Mineralogical Association of Canada

# Laser Ablation ICP-MS in the Earth Sciences: Current Practices and Outstanding Issues

**Editor**
Paul Sylvester

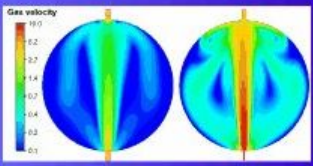


**Short Course Series**
**Volume**
**40**
VANCOUVER, BC, 2008
**Series Editor**
Robert Raeside

# Laser Ablation–ICP–MS in the Earth Sciences
# CURRENT PRACTICES AND OUTSTANDING ISSUES

Mineralogical Association of Canada
Short Course Series Volume 40

*Edited by*

**Paul Sylvester**
Department of Earth Sciences,
Memorial University of Newfoundland,
St. John's, Newfoundland & Labrador,
A1B 3X5, Canada

Short Course delivered in association with Goldschmidt 2008,
Vancouver, B.C., 19–20 July, 2008.

Agilent Technologies

VARIAN

## TABLE OF CONTENTS


Preface ix

1. Laser ablation–inductively coupled plasma–mass spectrometry (LA–ICP–MS); an introduction 1
   Henry Longerich

2. Formation of aerosols generated by laser ablation and their impact on elemental fractionation in LA–ICP–MS 19
   Detlef Günther & Joachim Koch

3. Computer modeling of laser ablation elemental microanalysis 35
   Davide Bleiner & Zhaoyang Chen

4. Comparison of femtosecond and nanosecond laser interactions with geologic matrices and their influence on accuracy and precision of LA–ICP–MS data 53
   Ingo Horn

5. Matrix effects in laser ablation ICP–MS 67
   Paul Sylvester

6. Laser ablation sampling strategies for concentration and isotope ratio analyses by ICP–MS 79
   Jan Kosler

7. Mass fractionation correction in laser ablation multiple-collector ICP–MS: implications for overlap corrections and precise and accurate *in situ* isotope ratio measurement 93
   Norman J. Pearson, William L. Griffin & Suzanne Y. O'Reilly

8. Sm–Nd and Sr isotope systematics in LREE-rich accessory minerals using LA–MC–ICP–MS 117
   Chris McFarlane & Malcolm McCulloch

9. A guide to depth profiling and imaging applications of LA–ICP–MS 135
   Jon Woodhead, John Hellstrom, Chad Paton, Janet Hergt, Alan Greig & Roland Maas

10. Reference materials for elemental and isotopic analyses by LA–(MC)–ICP–MS: successes and outstanding needs 147
    Klaus Peter Jochum & Brigitte Stoll

11. Calibration strategies for elemental analysis by LA–ICP–MS 169
    Simon Jackson

12. Analytical protocols for element concentration and isotope ratio measurements in fluid inclusions by LA–(MC)–ICP–MS 189
    Thomas Pettke

13. Major and trace element analysis of melt inclusions by laser ablation ICP–MS 219
    Paul R.D. Mason, Igor K. Nikogosian & Manfred J. van Bergen

14. Use of discrete-dynode secondary electron multipliers with Faradays – A 'reduced volume' approach for *in situ* U–Pb dating of accessory minerals within petrographic thin section by LA–MC–ICP–MS 241
    Antonio Simonetti, Larry M. Heaman & Thomas Chacko

15. Use of multiple channeltron ion counters for LA–MC–ICP–MS analysis of common lead isotopes in silicate glasses 265
    A. Kate Souders & Paul J. Sylvester

16. Data reduction strategies, uncertainty assessment and resolution of LA–(MC–)ICP–MS isotope data 283
    Matthew S.A. Horstwood

**Appendix. Software for Reduction of LA–ICP–MS Data**

A1. LAMTRACE data reduction software for LA-ICP-MS 305
Simon Jackson

A2. GLITTER: Data reduction software for laser ablation ICP–MS 307
W.L. Griffin, W.J. Powell, N.J. Pearson & S.Y. O'Reilly

A3. ComPbCorr – Software for common lead correction of U–Th–Pb analyses that do not report $^{204}$Pb 312
Tom Andersen

A4. LamDate and LamTool: spreadsheet-based data reduction for laser ablation ICP–MS 315
Jan Košler, Libor Forst & Jiří Sláma

A5. Analysis Management System (AMS) for reduction of laser ablation ICP–MS data 318
S.R. Mutchler, L. Fedele & R.J. Bodnar

A6. SILLS: A MATLAB-based program for the reduction of laser ablation ICP–MS data of homogeneous materials and inclusions 328
Marcel Guillong, Dimitri L. Meier, Murray M. Allan, Christoph A. Heinrich & Bruce W.D. Yardley

A7. Brief introduction to the Windows program Pepita: Data visualization and reduction, outlier rejection, calculation of trace element ratios and concentrations from LA–ICP–MS DATA 334
I. Dunkl, T. Mikes, K. Simon & H. von Eynatten

A8. Laser ablation data reduction software for concentration measurement – LARS-C 341
Antje Gebel

A9. Iolite: Software for spatially resolved LA–(QUAD and MC)–ICP–MS Analysis 343
John Hellstrom, Chad Paton, Jon Woodhead & Janet Hergt

**DETAILED LIST OF CONTENTS**


1. LASER ABLATION–INDUCTIVELY COUPLED PLASMA–MASS SPECTROMETRY (LA–ICP–MS); AN INTRODUCTION
**Henry Longerich**

INTRODUCTION 1
LA–ICP–MS 2
ICP 2
Mass spectrometer (MS) 2
Mass analyzers 3
Single collector sector 3
Multiple collector (MC) sector 6
Quadrupole (quad) MS 6
Time of flight (TOF) analyzers 7
Other analyzers 7
Interferences 7
Vacuum 9
Detector 10
Secondary electron multipliers (SEM) and channel electron multipliers (CEM) 10
Dynamic range of the detector system 11
ICP–MS 11
Laser ablation sampling system 13
Laser 13
To make or buy 15
CONCLUSIONS 16
ACKNOWLEDGEMENTS 16
REFERENCES 16

2. FORMATION OF AEROSOLS GENERATED BY LASER ABLATION AND THEIR IMPACT ON ELEMENTAL FRACTIONATION IN LA–ICP–MS
**Detlef Günther & Joachim Koch**

INTRODUCTION 19
Chronology and milestones of aerosol research in LA–ICP–MS – a summary 19
Visualization of LA aerosols – Part I: Expansion patterns and wall reactions 22
Visualization of LA aerosols – Part II: Aerosol structures and transport efficiences 26
CONCLUSION 29
ACKNOWLEDGEMENTS 32
REFERENCES 32

3. COMPUTER MODELING OF LASER ABLATION ELEMENTAL MICROANALYSIS
**Davide Bleiner & Zhaoyang Chen**

INTRODUCTION 35
METHODS 36
Structure of a simulation 36
Algorithms 37
Hardware 37
MODELING OF LASER MICROSAMPLING 37
Optical and thermal lengths 37
Sample ablation 38
Vapor plume characteristics 40

Laser intensity, wavelength, and pulse duration 41
MODELING OF LASER-INDUCED AEROSOL TRANSPORT 43
Fluid dynamics 43
Sample cell 44
Transport Line 47
MODELING OF LA–ICP–MS SIGNAL PROFILE 48
Single shot 49
Multiple shots 49
Operating conditions 49
REFERENCES 51

4. COMPARISON OF FEMTOSECOND AND NANOSECOND LASER INTERACTIONS WITH GEOLOGIC MATRICES AND THEIR INFLUENCE ON ACCURACY AND PRECISION OF LA–ICP–MS DATA
**Ingo Horn**
INTRODUCTION 53
THE ABLATION MECHANISM 53
FUNDAMENTAL ASPECTS IN FEMTOSECOND LASER ABLATION 54
Wavelength and energy density-dependent ablation rates 54
Pulse energy, energy density and pulse width 55
Aerosol structure and compositional analyses 55
Precision and accuracy 56
Isotope ratio determinations (Mg, Si, Fe, and Cu) 57
Laser-induced isotope fractionation 58
Accuracy and matrix dependency 59
CONCLUSION 61
ACKNOWLEDGEMENTS 62
REFERENCES 62

5. MATRIX EFFECTS IN LA–ICP–MS
**Paul Sylvester**
INTRODUCTION 67
MATRIX-DEPENDENT ELEMENTAL FRACTIONATION 68
TWO EXAMPLES OF NON-MATRIX-MATCHED CALIBRATION 70
Carbonate 70
Sulfide 73
MATRIX EFFECTS IN HIGH PRECISION *IN SITU* ISOTOPIC ANALYSES 75
SUMMARY 76
ACKNOWLDEGEMENTS 76
REFERENCES 76

6. LASER ABLATION SAMPLING STRATEGIES FOR CONCENTRATION AND ISOTOPE RATIO ANALYSES BY ICP–MS
**Jan Košler**
MASS DISCRIMINATION, ELEMENTAL/ISOTOPIC FRACTIONATION AND AEROSOL PROPERTIES 79
Instrument mass discrimination 79
Laser-induced fractionation 80
Aerosol particle size distribution 80
LASER ABLATION SAMPLING STRATEGIES 80
Stationary (static, single spot) ablation 80
Scanning (dynamic, raster) ablation 83

COMPARISON OF THE STATIONARY AND SCANNING ABLATION MODES 83
Precision and accuracy 83
Spatial resolution 84
Effects of sampling strategies on the ICP 85
APPLICATIONS OF LASER SCANNING AND STATIONARY ABLATION 86
CONCLUDING REMARKS 87
ACKNOWLEDGEMENTS 87
REFERENCES 88

7. MASS FRACTIONATION CORRECTION IN LASER ABLATION MULTIPLE-COLLECTOR ICP–MS: IMPLICATIONS FOR OVERLAP CORRECTIONS AND PRECISE AND ACCURATE *IN SITU* ISOTOPE RATIO MEASUREMENT
**Norman J. Pearson, William L. Griffin & Suzanne Y. O'Reilly**
INTRODUCTION 93
Instrumental Mass Bias – The Basics 95
Internal normalization 95
External correction 96
Standard sample bracketing 99
Mass bias corrections for laser ablation isotopic analysis 99
Method 1 99
Method 2 100
Method 3 100
Factors contributing to instrumental mass bias 101
Nebulizer gas experiments 102
Extraction lens voltage 103
Torch depth position 104
RF power 104
Cone design 105
Nebulizer gas composition 105
Laser-induced fractionation 106
Matrix effects 109
SUMMARY 110
ACKNOWLEDGEMENTS 110
REFERENCES 110

8. SM–ND AND SR ISOTOPE SYSTEMATICS IN LREE-RICH ACCESSORY MINERALS USING LA–MC–ICP–MS
**Chris McFarlane & Malcolm McCulloch**
INTRODUCTION 117
SM INTERFERENCE CORRECTIONS 118
LA–MC–ICP–MS compared to TIMS 118
SPECTRAL INTERFERENCES 120
BACKGROUNDS 120
PRECISION AND ACCURACY 120
Reference standards 121
DETERMINING $^{147}SM/^{144}ND$ 122
Factors influencing precision and accuracy of $^{147}Sm/^{144}Nd$ 123
APPLICATIONS 125
*In situ* Sm–Nd characterization of hydrothermal monazite 125
Sm–Nd isochron dating of hydrothermal and magmatic rocks 125
Coupled Nd and Sr isotope systematics of apatite 127
CONCLUSIONS 130
REFERENCES 131

9. A GUIDE TO DEPTH PROFILING AND IMAGING APPLICATIONS OF LA–ICP–MS
**Jon Woodhead, John Hellstrom, Chad Paton, Janet Hergt, Alan Greig & Roland Maas**
INTRODUCTION AND BACKGROUND 135
ANALYTICAL ISSUES AND THEIR RESOLUTION 135
Choice of Laser System 136
General Cell Design and Residence Times 136
Depth Profiling 136
Imaging 138
Mass Spectrometer Matters 138
Software 140
SOME EXAMPLES AND POSSIBILITES FOR THE FUTURE 140
Depth profiles 142
Elemental imaging 142
Isotopic imaging 142
Possibilities for the future 143
CONCLUSIONS 143
ACKNOWLEDGEMENTS 143
REFERENCES 143

10. REFERENCE MATERIALS FOR ELEMENTAL AND ISOTOPIC ANALYSES BY LA–(MC)–ICP–MS: SUCCESSES AND OUTSTANDING NEEDS
**Klaus Peter Jochum & Brigitte Stoll**
INTRODUCTION 147
DEFINITION OF A REFERENCE MATERIAL 147
REFERENCE MATERIALS FOR LA–(MC)–ICP–MS ANALYSIS 148
Synthetic reference glasses 148
a) NIST 600 series 148
b) USGS GS reference glasses 152
Geological reference glasses 153
a) USGS reference glasses 153
b) MPI-DING reference glasses 155
RMs for mineral analyses 158
a) 91500 zircon 159
b) Sulfides 159
c) Other RMs 160
CONCLUSIONS 163
REFERENCES 165

11. CALIBRATION STRATEGIES FOR ELEMENTAL ANALYSIS BY LA–ICP–MS
**Simon Jackson**
INTRODUCTION 169
CALIBRATION STRATEGIES 169
1. External calibration using solid samples only 171
2. External calibration using ablation of solid samples plus internal standardization 171
3. Calibration using aspirated solutions plus internal standardization 171
4. External calibration using ablation of liquid samples plus internal standardization 172
5. External calibration using normalization of totals to 100% 172
6. Isotope dilution calibration 172
Choice of internal standard 173
CALIBRATION STANDARDS 173
NIST SRM glasses 173

Other primary standards 175
Analysis of sulfides 175
Analysis of diamond and other carbon-based samples 176
Secondary standards 177
ACCURACY AND THE NEED FOR MATRIX MATCHING 177
Elemental fractionation 178
A case study on analysis of gold 179
DATA REDUCTION 180
Calculation of concentrations 180
Correction procedures for elemental fractionation 181
Signal selection and the mean count rate method 182
Intercept method 182
Slope method 182
Multi-internal standard correction procedure 182
CONCLUSIONS 184
ACKNOWLEDGEMENTS 185
REFERENCES 185

12. ANALYTICAL PROTOCOLS FOR ELEMENT CONCENTRATION AND ISOTOPE RATIO MEASUREMENTS IN FLUID INCLUSIONS BY LA–(MC)–ICP–MS
**Thomas Pettke**
INTRODUCTION 189
FLUID INCLUSIONS: CHARACTERISTICS RELEVANT FOR THEIR LA–ICP–MS ANALYSIS 191
SPECIFIC LA–ICP–MS INSTRUMENTAL REQUIREMENTS FOR FLUID INCLUSIONS 192
Step 1: Laser ablation of fluid inclusions 194
Aerosol transport system 194
Step 2: Ion production and recording 194
Optimization of the ICP–MS parameters 197
Analyte sensitivities 198
Spectral interferences 200
HOW TO SELECT, ANALYZE AND QUANTIFY A SERIES OF INDIVIDUAL FLUID INCLUSIONS 201
Selection criteria for fluid inclusions suitable for LA–ICP–MS analysis 201
The technique of fluid inclusion ablation 201
Representative recording of fast transient signals 203
Signal quantification strategies 204
Ways of improving on LODs 206
PRECISE AND ACCURATE ISOTOPE RATIO MEASUREMENTS USING LA–MC–ICP–MS: ACHIEVEMENTS AND PROSPECTS 208
FIGURES OF MERIT 209
Analytical precision 210
Internal precision 210
External precision 210
Analytical accuracy 211
ACKNOWLEDGEMENTS 212
REFERENCES 212

13. MAJOR AND TRACE ELEMENT ANALYSIS OF MELT INCLUSIONS BY LASER ABLATION ICP–MS
**Paul R.D. Mason, Igor K. Nikogosian & Manfred J. van Bergen**
INTRODUCTION 219
Information recorded by melt inclusions 220
REVIEW OF TECHNIQUES FOR STUDYING MELT INCLUSIONS 222

Electron and ion beam techniques: EMPA and SIMS 222
Nuclear microprobe 225
Spectroscopic methods 225
Laser ablation ICP–MS 226
LASER ABLATION ICP–MS: INSTRUMENTAL CONSTRAINTS AND CONSIDERATIONS 227
Laser ablation system 227
ICP–MS instrumentation 228
Ability to measure both accurately and precisely all elements of interest 228
Efficient as possible duty cycle 228
High sensitivity and low background count rates 229
Standards 229
Comparison of methodologies for melt inclusion analysis 229
SUMMARY AND FUTURE DEVELOPMENTS 233
Strengths of laser ablation ICP–MS 234
Weaknesses of laser ablation ICP–MS 234
Future developments 235
ACKNOWLEDGEMENTS 235
REFERENCES 235

14. USE OF DISCRETE-DYNODE SECONDARY ELECTRON MULTIPLIERS WITH FARADAYS – A 'REDUCED VOLUME' APPROACH FOR IN SITU U–PB DATING OF ACCESSORY MINERALS WITHIN PETROGRAPHIC THIN SECTION BY LA–MC–ICP–MS
**Antonio Simonetti, Larry M. Heaman & Thomas Chacko**
INTRODUCTION 241
MC–ICP–MS and laser ablation instrumentation 243
Discrete-dynode electron multipliers 243
Discrete-dynode–Faraday calibration: measurement of $^{206}Pb/^{238}U$ values 245
Standard ablation cell versus the 'SuperCell™'–Ion signal decay + 'washout' and 'sensitivity' 247
Petrographic examination, measurement protocol and data reduction 248
RESULTS 251
Background 251
Zircon – Cardamom Hills Massif, southern India 252
Zircon: Voisey's Bay Granite 256
Monazite: Queen Maud Block 258
Perovskite: Ice River Complex 259
SUMMARY 262
ACKNOWLEDGEMENTS 262
REFERENCES 262

15. USE OF MULTIPLE CHANNELTRON ION COUNTERS FOR LA–MC–ICP–MS ANALYSIS OF COMMON LEAD ISOTOPES IN SILICATE GLASSES
**A. Kate Souders & Paul J. Sylvester**
INTRODUCTION 265
PRINCIPLES OF MULTI-ION COUNTING WITH ELECTRON MULTIPLIERS 266
PROCEDURES FOR LA–MC–ICP–MS ANALYSES OF PB ISOTOPES USING MULTIPLE CHANNELTRONS 267
Instrumentation 267
Long term settings of Channeltrons 268
Sample preparation 268
Tasks for set-up of an analytical session of isotope ratio measurements 269
Analytical routine 270
Interference corrections for Hg on $^{204}Pb$ 272

ION COUNTER LINEARITY 272
ACCURACY AND PRECISION OF SILICATE GLASS ANALYSES 274
THE FUTURE 279
ACKNOWLEDGEMENTS 279
REFERENCES 279

16. DATA REDUCTION STRATEGIES, UNCERTAINTY ASSESSMENT AND RESOLUTION OF LA–(MC)–ICP–MS ISOTOPE DATA
**Matthew S.A. Horstwood**
INTRODUCTION 283
DATA REDUCTION 283
Laser-induced elemental fractionation 283
Monitor solutions 284
Complications when interpreting common Pb-affected data for accessory mineral geochronology 286
Isobaric interference corrections 288
UNCERTAINTY ASSESSMENT 290
Uncertainty propagation 290
Secondary and tertiary reference materials 293
Use of stable isotope ratios 294
Representation of data 295
Example of uncertainty propagation strategy 298
Example 298
Effect of U–Pb age discordance and uncertainty on εHf 298
SUMMARY 300
ACKNOWLEDGEMENTS 300
REFERENCES 300

**APPENDICES**

APPENDIX 1. LAMTRACE DATA REDUCTION SOFTWARE FOR LA–ICP–MS
**Simon Jackson**
INTRODUCTION 305
OPERATION 305
Data formatting and pre-integration 306
Calculation of element concentrations 306
Chemical profiling 306
U–Pb dating 306
Quality control and reporting 306
THE FUTURE 306
REFERENCES 307

APPENDIX 2. GLITTER: DATA REDUCTION SOFTWARE FOR LASER ABLATION ICP–MS
**William L. Griffin, W.J. Powell, Norman J. Pearson & Suzanne Y. O'Reilly**
INTRODUCTION 308
Overview 309
REFERENCES 311

APPENDIX 3. COMPBCORR – SOFTWARE FOR COMMON LEAD CORRECTION OF U–TH–PB ANALYSES THAT DO NOT REPORT $^{204}$PB
**Tom Andersen**
INTRODUCTION 312
ACKNOWLEDGEMENTS 314
REFERENCES 314

APPENDIX 4. LAMDATE AND LAMTOOL: SPREADSHEET-BASED DATA REDUCTION FOR LASER ABLATION ICP–MS
**Jan Košler, Libor Forst & Jiří Sláma**
INTRODUCTION 315
LamDate 315
LamTool 316
REFERENCES 316

APPENDIX 5. ANALYSIS MANAGEMENT SYSTEM (AMS) FOR REDUCTION OF LASER ABLATION ICP–MS DATA
**S.R. Mutchler, L. Fedele & R.J. Bodnar**
INTRODUCTION 318
USE OF MULTIPLE STANDARDS AND DRIFT CORRECTION 318
ELEMENTAL FRACTIONATION DURING ANALYSIS 319
FLUID INCLUSION ANALYSIS AND DATA REDUCTION 320
MELT INCLUSION ANALYSIS AND DATA REDUCTION 323
SUMMARY 327
ACKNOWLEDGEMENTS 327
REFERENCES 327

APPENDIX 6. SILLS: A MATLAB-BASED PROGRAM FOR THE REDUCTION OF LASER ABLATION ICP–MS DATA OF HOMOGENEOUS MATERIALS AND INCLUSIONS
**Marcel Guillong, Dimitri L. Meier, Murray M. Allan, Christoph A. Heinrich & Bruce W.D. Yardley**
INTRODUCTION 328
DESCRIPTION OF THE SOFTWARE 328
MATLAB and some general considerations 328
Main windows 329
Graphical user interface for signal integration 329
Spike/outlier detection based on Grubbs test 329
Drift correction and quality control 331
Quantification possibilities / calculation manager 331
Report writing possibilities 332
SUMMARY AND AVAILABILITY 333
ACKNOWLEDGEMENTS 333
REFERENCES 333

APPENDIX 7. BRIEF INTRODUCTION TO THE WINDOWS PROGRAM PEPITA: DATA VISUALIZATION AND REDUCTION, OUTLIER REJECTION, CALCULATION OF TRACE ELEMENT RATIOS AND CONCENTRATIONS FROM LA–ICP–MS DATA
**I. Dunkl, T. Mikes, K. Simon & H. von Eynatten**
INTRODUCTION 334
CONCEPT AND STRUCTURE OF THE SOFTWARE 334
PROGRAM DESCRIPTION 335
GUIDED TOUR OF THE PROGRAM 336
Installation 336
Functions of Pepita shown with the example files 336
Creation of a standard measurement file and performing the concentration calculation for an unknown 340
Customizing the input of Pepita for the format of user-defined data files 340
REFERENCES 340

APPENDIX 8. LASER ABLATION DATA REDUCTION SOFTWARE FOR CONCENTRATION MEASUREMENTS – LARS-C
**Antje Gebel**
INTRODUCTION 341
USING THE PROGRAM 341
SUMMARY 342
REFERENCES 342

APPENDIX 9. IOLITE: SOFTWARE FOR SPATIALLY RESOLVED LA–(QUAD AND MC)–ICP–MS ANALYSIS
**John Hellstrom, Chad Paton, Jon Woodhead & Janet Hergt**
INTRODUCTION 343
FLEXIBLE DATA REDUCTION MODULES 344
DATA VISUALIZATION AND EXPORT 345
STANDARDS 347
COMPATABILITY AND AVAILABILITY 347
DEVELOPMENT 348
REFERENCES 348

**Laser Ablation–ICP–MS in the Earth Sciences:**
**Current Practices And Outstanding Issues**

## PREFACE

Seven years ago, in 2001, the Mineralogical Association of Canada agreed to sponsor a short course on Laser Ablation–Inductively Coupled Plasma–Mass Spectrometry, or LA–ICP–MS, in the Earth Sciences. The course was held in conjunction with the joint annual meeting of the Geological Association of Canada and the Mineralogical Association of Canada (GAC–MAC) in St John's, Newfoundland. The MAC published a companion volume (number 29 of their Short Course Series) containing papers summarizing the lectures. At that time, LA–ICP–MS was just becoming a rather common fixture around Earth Sciences departments in universities and government research laboratories, and many geologists were understandably curious about how these instruments worked and what could be done with them. We therefore provided basic information on ICP–MS and laser instrumentation, as well as summaries of applications of the method in various subdisciplines of the Earth Sciences. The course was subtitled "Principles and Applications".

Seven years on, much has changed in LA–ICP–MS. The technique has matured and expanded markedly, both in terms of the specific instrumentation used and the application base it serves. Whereas in 2001, the primary use of the method in the Earth Sciences was for *in situ* analyses of trace element concentrations, today a significant and growing volume of work done with these instruments is centered around *in situ* isotopic analyses. The evolution toward isotopic applications in LA–ICP–MS has been made possible by the introduction of sector field-ICP–MS instruments, particularly those with multi-collector (MC) systems, into Earth Science laboratories. There are now some two hundred MC-sector field-ICP–MS instruments worldwide, many of them dedicated to geological applications, though not (yet) all interfaced with laser ablation systems. LA–MC–ICP–MS was described in the 2001 volume, but it was still in its infancy, and only beginning to be understood. Today a new generation of Earth scientists is exploring the geochemistry of a range of "non-traditional" isotopic systems with these instruments in ever increasing detail. Multiple ion counter systems on MC–ICP–MS instruments were barely used with laser ablation in 2001, whereas today they seem poised to extend *in situ* isotopic analyses to a whole range of elements present at only trace abundance levels in minerals.

There have been other changes since 2001. One of the most significant discoveries of the 1990s in this field was that laser ablation is more uniform and controlled with ultraviolet (UV) energy, which almost all minerals absorb efficiently, rather than with infrared radiation, which only dark-colored minerals absorb efficiently. By 2001, Nd:YAG (neodymium-doped yttrium aluminum garnet) lasers emitting with a UV wavelength of 266 nm were the most widely used for LA–ICP–MS, but there was mounting evidence that wavelengths deeper in the UV (213 and 193 nm) might be even better. Today, commercial deep UV lasers are the norm for laser ablation systems, and discussions about further improvements are centered on the pulse width of the lasers: specifically whether ultra-short pulse, femtosecond lasers significantly reduce elemental and isotopic fractionation in laser-produced aerosols compared to the conventional longer pulse, nanosecond lasers used today and, if so, why? Back in 2001, little was known about laser-produced aerosols, particularly the importance of generating a uniform population of nanometre-sized particles that are completely vaporized in the Ar plasma of the ICP. Now, the behavior of aerosols in the ablation cell and during their transfer to the ICP is an active area of research. Ablation cell design has finally become a serious concern, informed by observational data and quantitative computational models. In contrast, some technologies that seemed quite promising for LA–ICP–MS in 2001, most notably collision and reaction cells, and time of flight mass spectrometers, have not yet established niches in laser ablation studies, and are barely used for LA–ICP–MS today.

With all that has happened in LA–ICP–MS over the past seven years, and with the continuing interest in the method from Earth scientists, a new MAC short course and volume seemed timely.

The subtitle of this new volume is "Current Practices and Outstanding Issues". Chapters are intended primarily to describe the technologies and analytical procedures currently being used to collect data sets by LA–ICP–MS for applications in the Earth sciences. A secondary goal is to describe outstanding challenges or needs that are or should be the focus of ongoing studies. Topics of chapters were chosen to highlight fundamental issues in LA–ICP–MS rather than to try to describe or review all of the specific applications in the Earth sciences that are being (or could be) carried out using the method. Instead, specific applications, where discussed, are intended to illustrate analytical strategies and procedures that are being (or could be) applied to geologic samples more generally. There is a tradition of innovative use of new technologies to solve scientific problems in the Earth sciences and it is hoped that the ideas in this volume will lead to new applications and discoveries for LA–ICP–MS. The volume concludes with an appendix summarizing third party computer software currently available for reduction of LA–ICP–MS data. LA–ICP–MS is one of the most data-intensive analytical methods used in the Earth sciences, and converting raw count rates from the instrument into elemental concentrations or isotopic ratios is a non-trivial task.

I thank the authors and reviewers who made this volume possible; Rob Raeside, Short Course Series Editor, who once again, has produced a well-designed and attractive volume; the Goldschmidt Conference organizers who provided logistical assistance and a beautiful venue for the course; corporate sponsors *Varian Canada Inc*. and *Agilent Technologies*; and the MAC, whose continuing commitment to supporting education in the Earth sciences is well recognized and much appreciated by the community it serves.

Finally, in reflecting on the completion of this second MAC volume on LA–ICP–MS, I find myself reminded of the English film director, Michael Apted, who, every seven years, produces a documentary that revisits the lives of fourteen men and women who were first filmed as seven-year-old children in 1964, in a quest to understand what makes children the adults they become. It is too early to predict whether the evolution of LA–ICP–MS will be of sufficient continuing interest to Earth scientists to warrant another look at its development in seven years time. But it is safe to say that the technique, even without further improvements, is now fully capable of allowing geologists to make many significant discoveries for years to come. The challenge is there for them.

**Paul J. Sylvester**
St. John's
Newfoundland & Labrador
Canada

27 June 2008

# CHAPTER 1: LASER ABLATION–INDUCTIVELY COUPLED PLASMA–MASS SPECTROMETRY (LA–ICP–MS); AN INTRODUCTION

Henry Longerich,
Department of Earth Sciences,
Memorial University of Newfoundland,
St. John's, NL A1B 3X5, Canada
E-mail: Henry@esd.mun.ca

## INTRODUCTION

Laser ablation–inductively coupled plasma–mass spectrometry is a long name for this analytical instrument and technique which is why the acronym LA–ICP–MS was created and is commonly used. LA–ICP–MS is now so frequently used that the hyphens are some times omitted (LAICPMS). In our early reports we proposed the acronym LAM–ICP–MS where the "M" stood for microprobe. However this did not catch on in the user community. The microprobe aspects are however very important, due to the fact that LA is very well suited to micro-analytical applications, and is often very poorly suited for bulk analysis applications especially where the bulk analysis of a heterogeneous sample is required. In this introductory discussion the various parts of the LA–ICP–MS instrumentation will be introduced with attention to the suitability for laser ablation (LA) sampling applications. In later essays in this compilation more details will be given by a number of authors giving more specific descriptions and focussing on recent theoretical understanding, developments, and applications.

While this essay is not a detailed history, it is noted that the first use of LA with ICP–MS was published by Alan Gray (Gray 1985), soon after the first installation of the first commercial ICP–MS in 1984. Now the number of publications is very large as the technique has been widely accepted in many fields, with geology being an area in which there are many excellent applications. Any solid or liquid sample which can be contained in a suitable cell can be analyzed. At Memorial University, Newfoundland and Labrador, Canada, we put together a LA system in 1989 for use with our first generation, 1984, ICP–MS instrument. In 1992 our paper "The Application of Laser Ablation Microprobe–Inductively Coupled Plasma–Mass Spectrometry (LAM–ICP–MS) to *In Situ* Trace Element Determinations in Minerals" (Jackson *et al.* 1992) published in the *Canadian Mineralogist* was an important demonstration of the potential of the technique for quantitative trace element determinations for geological samples, and in recognition of this we received the Hawley Medal from the Mineralogical Association of Canada. For other introductions to ICP–MS, see various texts (Becker 2007, Montaser 1998, Jarvis *et al.* 1992, Nelms 2005).

Table 1-1 shows the components of a LA–ICP–MS. This essay will introduce the various essential parts of the instrumentation. Some of the other essays in this volume give more specific descriptions of instrumentation used for specific applications.

TABLE 1-1. COMPONENTS OF A LASER ABLATION–ICP–MS SYSTEM

| | |
|---|---|
| Laser Ablation (LA) | Laser |
| | Focussing, homogenization, beam steering, power control, power monitoring, sample observation |
| | Sample cell, computer driven movable sample stage |
| | Transport tubing |
| Inductively Coupled Plasma (ICP) | Ion source |
| Mass Spectrometer (MS) | Vacuum system |
| | Interface and ion lenses |
| | Analyzer (Quadrupole, Sector, Time of Flight, *etc.*) |
| | Detector (Transducer) |
| | Data Acquisition System and software |

Mineralogical Association of Canada Short Course 40, Vancouver, B.C., p. 1–18

**LA–ICP–MS**

The first part of the LA–ICP–MS is the LA (laser ablation) sample introduction system consisting of a laser with associated optics, an air-tight cell suitable for containing the sample, and tubing to transport the sample to the ICP by means of a flow of gas. The sample is transformed in the cell by the laser into an aerosol of small particles which are carried in a flow of gas to the ICP (inductively coupled plasma). In the ICP, gas (Ar often combined with He) is electrically heated to a high temperature forming a plasma. Plasma is a fluid similar to a gas, but containing a large number of free electrons and ions. The sample aerosol is carried into this plasma where it is further vaporized, atomized (note that strictly atomized means to convert a substance into very fine particles or droplets; the word atomized was employed before there was any knowledge of atoms), and finally ionized. The next part, the MS (mass spectrometer) which operates in vacuum, separates these ions based upon their mass to charge ratio, colloquially referred to simply as mass. The intensity (ions per second or current) of this ion beam is converted to an electrical signal which is measured and recorded. The mass/charge identifies the elemental composition and the intensity is functionally related to the concentration. One of the especially attractive characteristics of LA–ICP–MS, a hyphenated technique, which similar to some other hyphenated techniques, is that the LA is optimized for sampling, the ICP for ion production, and MS for separating the ions. Note however that these processes are not totally independent, and that optimization is a multidimensional procedure. This is compared to other techniques, for example the LAMMA (laser microprobe mass analysis) which used a laser to create ions which were directed into a Time of Flight MS for measurement. The success of LAMMA was severely hampered by the large matrix effects, in other words a large change in sensitivity for analytes in different matrices. Finally the ICP–MS has a detector system, computer interface, and computer. Each of these parts of the ICP–MS will be discussed in more detail with emphasis on their use with LA sampling.

**ICP**

In LA–ICP–MS the ICP is where the ions are formed for subsequent analysis. There are many other kinds of mass spectrometers which use a large variety of means and mechanics to produce ions. Electron Ionization (EI), Thermal Ionization (TI), and Secondary Ionization (SI) are three of the more common ways of generating ions for geological applications. The ion source which is of interest here is the ICP. Since early ICP emission spectroscopy was theoretically understood, it has been well known that the ICP was a good source of ions, as optical spectroscopists distinguish between emission from excited atoms and from excited ions. Further, for most of the periodic table, more than 99% of the atoms are converted to ions. The great achievement of ICP–MS instrumentation was to extract these ions into a vacuum where the pressure was low enough to produce good resolution of ions with differing mass to charge ratios. Interestingly, or rather boringly, all the commercial ICPs are very similar. The physical dimensions of the ICP torch are almost identical from instrument to instrument. Many are one piece made from fused quartz using precision, but conventional, glass-blowing techniques. Some are demountable allowing replacement of damaged parts without complete replacement or repair. The 'load coil' through which high power (>1 kW) radio frequency (RF) power is applied varies in the number and arrangement of the coils and the electrical grounding configuration. The load coil is fabricated from one-eighth inch outside diameter copper tubing, often coated, and cooled with water or Ar. The RF power has a frequency in the vicinity of 27 MHz or a second frequency near 40 MHz, which are the frequencies allowed by regulatory bodies which allocate radio frequencies to various applications (Wang *et al.* 2006).

**Mass Spectrometer (MS)**

It should be noted that mass spectrometer (MS) is a bit of a misnomer in that a MS does not measure mass. An electronic or mechanical balance is used to measure mass. A MS requires ions which are subsequently separated based on their mass to charge ratio. Fortunately in the ICP the majority of ions which are formed are singly charged, with the exception of some doubly charged ions from the alkaline and rare earth elements. The analyzer part of the MS is where the ions are separated from each other based upon their different mass/charge ratio. Commercial ICP–MS instruments were first delivered in 1984, with initial research reports published at that time. What delayed the creation of an ICP–MS instrument was the fact that ions are not able to travel very far (mean free path $\cong 0.1$ μm) at atmospheric pressure before they lose their charge or get deflected. A fundamental part of a MS

instrument (Fig. 1-1) is the vacuum system which lowers the pressure to allow the ions to travel (mean free path) more than a metre before impacting with another ion or neutral. The great breakthrough in the development of an ICP–MS was the interface where the pressure is lowered in steps through several orifices (three orifices separating four pressure regions and more in larger instruments) maintained at successively lower pressures. This stepwise lowering of pressure allows the ICP at atmospheric pressure to be connected to the MS which operates at low pressure. The last part of a complete MS requires some means of detecting or converting the ion beam intensity to a number which can be recorded using a suitable computer system.

***Mass analyzers.*** Mass spectrometers have been available from the early part of the twentieth century. The first mass spectrometers had analyzers which were based upon a Magnetic Sector Analyzer (MSA) to separate ions spatially based upon their mass to charge ratio (Fig. 1-2). Further developments led to the time of flight (TOF), and quadrupole (quad) analyzers. Other mass analyzers, including the ion trap (IT) and the ion cyclotron resonance (ICR), are not presently produced commercially with an ICP source. Commercially available ICP–MS currently are of three types, quadrupole (quad), TOF, and magnetic sector field (colloquially called simply sector or sector field) (Table 1-2). Sector instruments are available with either a single detector (collector) or in multiple collector (MC) designs. Since the applications and configuration for the single collector and MC designs are significantly different, it is useful to consider them separately. Sector analyzers used with an ICP source usually include an Electro Static Analyzer (ESA) which insures that the ion kinetic energies are all in a suitably narrow range (Fig. 1-3). The ESA is sometimes mistakenly thought of as a mass analyzer, but it is not used to separate ions according to their mass, but according to their energies. The ESA rejects ions with outlying energies. The Reverse Nier-Johnson configuration of MSA–ESA (Fig.1-4) can be used in single collector instruments while it is necessary to use the Nier-Johnson (ESA–MSA) configuration in MC instruments.

***Single collector sector*** instruments are based upon the principle that when high velocity charged particles (ions) pass through a magnetic field, ions are forced to travel in a curved path. In operation either the magnetic field or the accelerating potential of the ions can be changed to select the

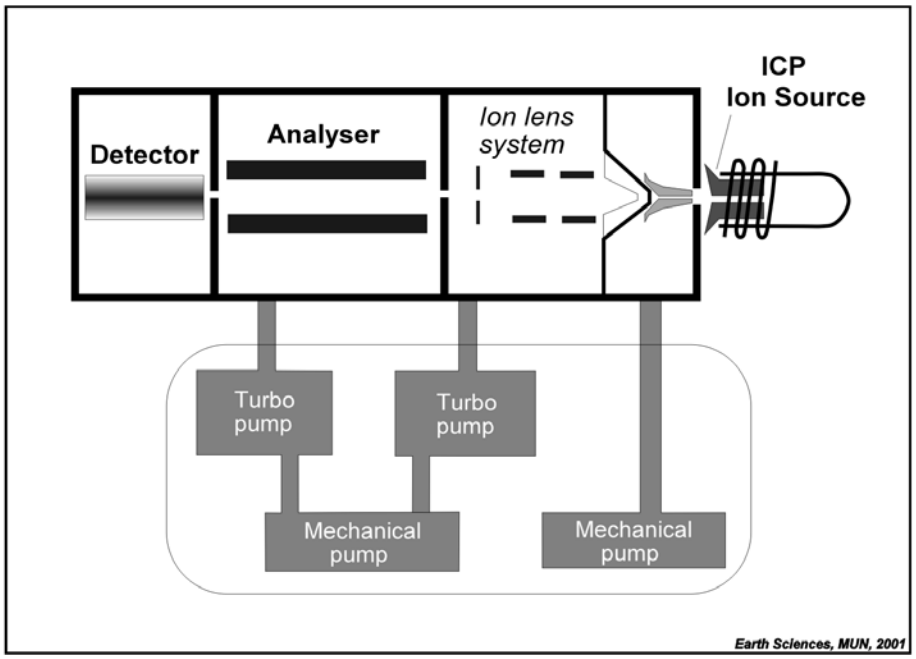


FIG 1-1. Schematic diagram of an inductively coupled plasma mass spectrometer showing the 4 main parts, as discussed in this chapter: the vacuum system; the ion source or ICP; the analyzer; and the detector.

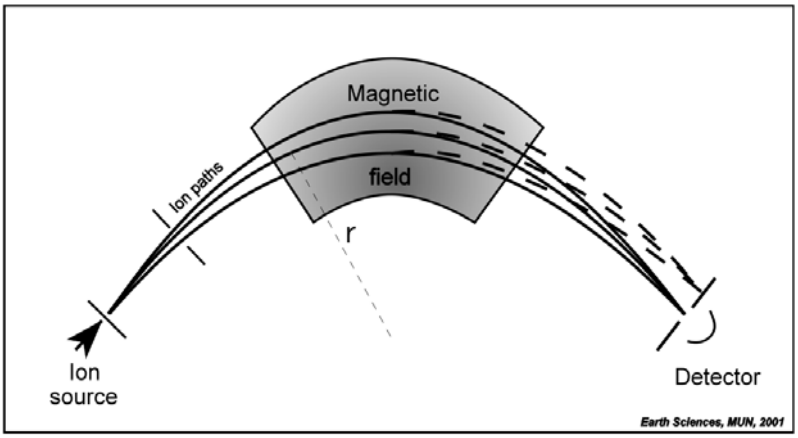


FIG 1-2. Schematic diagram of a Magnetic Sector Analyzer (MSA).

TABLE 1-2. SUMMARY OF THE VARIOUS CONFIGURATIONS AVAILABLE FOR ICP–MS INSTRUMENTS

| | **Time Of Flight (TOF)** | **Quadrupole (Quad)** | **Single Collector Sector** | **Multi Collector (MC)** |
|---|---|---|---|---|
| Cost | $ | $ | $$ | $$$ |
| Speed, time to change from one selected mass to another | Very fast | Fast | Depends upon the magnitude and number of jumps. Electrostatic fast, Magnetic slow | No mass jumps are usually implemented, but if needed are very slow |
| Sensitivity (signal per unit concentration) | Low | Medium to high depending upon design | High | High |
| Suppliers (some make different models) | 1 currently, formerly 2 | 4, a reduction from a few years ago | 1, with a second announced | Previously 4, currently 3 |
| Collision reaction cells | Not available | All, some optional | Not available | 1 only |
| Applications | Extremely fast scanning capability looking for a 'killer ap' | General use for elemental and isotopic analysis | General use for elemental and isotopic analysis | High precision isotope ratios |

ions which arrive at the fixed detector position. The magnetic field is changed by altering the current through an electromagnet which allows the user to select ions of a specific mass to charge ratio which reaches the detector. Ions with a smaller mass to charge ratio (*e.g.*, $Li^+$) are bent more and impact on an inside wall of the vacuum system or flight tube. In contrast, ions with high mass to charge ratio are not bent as much (*e.g.*, $U^+$) and impact on the outside of the flight tube. Ions of the selected mass will travel through the flight tube and exit through a slit. In single collector sector instruments, to obtain high resolution, the magnetic sector (MSA) is followed by an electrostatic sector (ESA), which eliminates ions with energies which are too high or too low. The configuration of MSA–ESA also

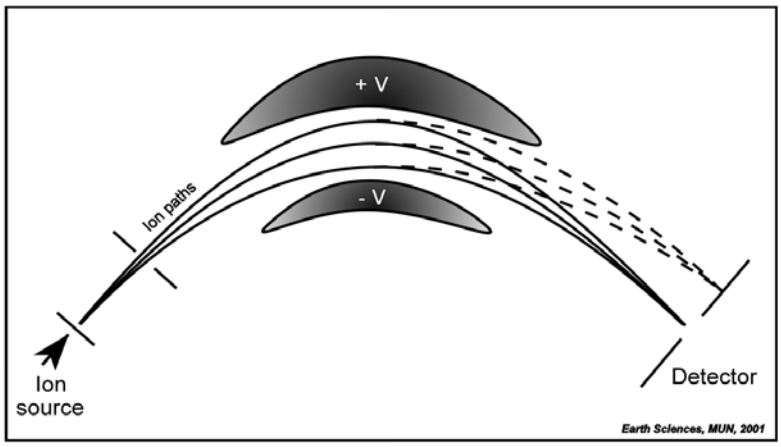


FIG 1-3. Schematic diagram of an Electrostatic Sector Analyzer (ESA).

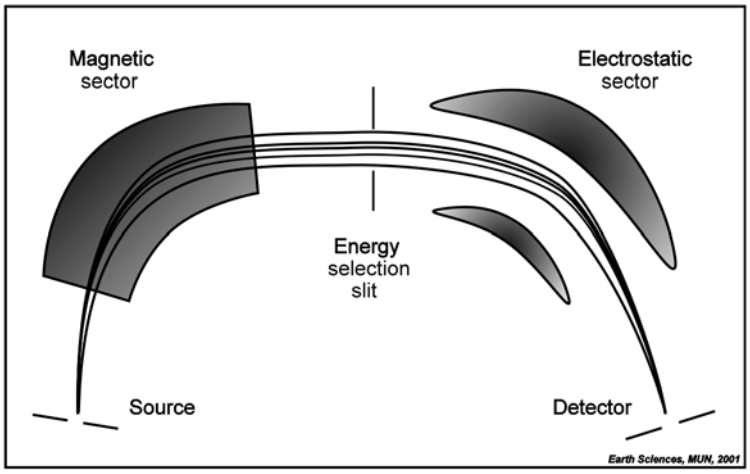


FIG 1-4. Schematic diagram of a double-focussing analyzer.

potentially gives better abundance sensitivity (a measure of the tailing of signal from large adjacent peaks) compared to an ESA–MSA configuration.

Single collector sector instrument advantages include low continuum backgrounds due to the curved path around which ions are forced to travel while high energy photons and neutrals travel straight impacting on the walls of the flight tube and are removed. Newer single collector analyzers have good sensitivity (signal per unit concentration), and have the potential to use high resolution to resolve some interferences (m/Δm resolution up to 12,000) although the use of high resolution is accompanied by an approximately proportional decrease in sensitivity. That is, a ten-fold increase in the resolution (*i.e.*, 300 to 3000) results in an approximate ten-fold reduction of sensitivity.

Single collector sector instrumentation disadvantages include a higher capital cost, and some peak jumping times where the magnetic field must be changed which are slower than for quads. A valid comparison between quad and sector instruments (Latkoczy & Günther 2002) with respect to sweep time (the total time required to make a measurement on all the masses in the parameter set) is difficult because the individual peak jumping times in sector instruments are a complicated function of the set of masses used in an application. This is because the selected mass can be changed, by changing either the accelerating potential applied to the ion beam and the ESA, or by changing the magnetic field. Changing accelerating potential is fast, but is possible only over a limited range typically from 100% to 130% of the mass selected by the magnet. Changing the magnetic field is, on the other hand, relatively slow as this requires a change in the high current (amperes) though the magnet, which is a large

inductor. This is a slow process, even with advanced laminated magnets. Several magnetic field changes are necessary to allow data acquisition over the entire useful mass range from $^{7}Li$ to $^{238}U^{16}O$.

***Multiple Collector (MC) Sector*** instruments use the same principle as a single collector MS, except that the ions are separated spatially, and this requires that the ions pass through the energy filter before being separated spatially by mass in the magnetic sector. Designs incorporate nine or more detectors at the focal plane of the magnet. There are several configurations of sector MS. The Nier-Johnson double focussing ESA–MSA configuration was formerly produced by three companies, one of which no longer produces this instrument. Another company offers a comparable instrument in which the MSA instead of being proceeded by an ESA uses a collision cell (*v.i.*) which is operated in a 'thermalizing' mode to produce an ion beam having a narrow range of energies. Typical specifications of MC instruments allow the simultaneous detection over a limited (17% to 20%) range of mass, allowing, for example, $^{6}Li$ to $^{7}Li$ or $^{204}Pb$ to $^{238}U$. Pseudo-high resolution is possible by using a small entrance slit accompanied by using one side of the detector as an exit slit. This pseudo-high resolution mode allows the separation of interferences and background from the analyte provided that all of the unwanted ions are on the same side of the analyte mass. Fortunately a large number of interferences are polyatomic ions containing low mass elements from the argon gas supply, air entrainment of the same elements, major element matrix, solvent water, and supporting acids when aqueous samples are introduced. These low mass polyatomic ions can often be separated from some of the common analyte ions which are measured, for example $^{40}Ar^{16}O$ on $^{56}Fe$ (Horn *et al.* 2006). Another ESA–MSA instrument configuration is the Mattauch-Hertzog which, using a different geometry of the magnet, allows a much larger mass range to be detected simultaneously. However the demonstrated sensitivities of this configuration have not matched that of the Nier-Johnson, and no commercial instruments of this type are currently available.

*Multiple Collector (MC) Sector instruments advantages* include the obvious advantage of simultaneous detection of several masses. This gives the 'multiplex advantage' in that all ions are detected all the time, resulting in a higher number of counts or integrated ion currents which in turn leads to lower uncertainties. Simultaneous detection also removes most, if not all, flicker noise resulting in a further reduction in the uncertainty. The applications of MC are usually limited to high precision isotope ratio determinations, for which an impressive list of applications has been reported. This has opened up new fields of research including especially elements with a high ionization potential *e.g.*, Hf (Halliday *et al.* 1996). The Mattauch-Hertzog configuration allows the detection of essentially the entire useful mass range (7 to 254 amu) simultaneously.

*Multiple Collector (MC) Sector instruments disadvantages* are that current designs are even slower (compared to single collector sector instruments) at switching between selected mass, making switching impractical in most LA applications. They have very high capital costs, much higher than the single collector sector. Without using magnetic switching they have a limited mass range. Applications are essentially limited to very precise isotope ratio determinations.

***Quadrupole (quad) MS*** were the first ICP–MS instruments commercially produced. Two companies initially produced quad instruments, and this was followed by other manufacturers. A quad mass analyzer works by applying a complex electrical field of alternating and direct current potentials to an array of four (quad) rods (poles). The ions are passed through the array of rods with the applied potentials allowing only the ions of the selected mass to pass. The quad is strictly a mass filter rather than a spectrometer in that ions can not be separated spatially.

*Quadrupole (quad) advantages* are most importantly their low cost. The low cost is enhanced by the small volume required for the analyzer. Current designs are the smallest of the commercial ICP–MS instruments, with most units being a 'desk top' design. Sensitivity varies between instruments, but can be excellent. Backgrounds are slightly higher than for sector instruments, but this is rarely a limitation as in operation few if any instruments meet continuum background specifications except at half integer masses. Peak jumping speeds are good and are essentially independent of the magnitude of the mass jump, but could be even better if manufacturers would be convinced that users would pay slightly more for higher speed mass switching.

*Quadrupole (quad) disadvantages* are that they do not have high resolution capability, or the multiplex and flicker reduction advantages of MC

sector instruments. High resolution quadrupoles are not commercially available, although research on high resolution modes of quad operation has been reported (Douglas & Houk 1985, Jarvis *et al.* 1992). In place of high resolution for interference and background reduction most quadrupole instruments offer optional collision/reaction cell capability (Tanner & Baranov 1999, Tanner *et al.* 2000, Tanner *et al.* 2002).

***Time Of Flight (TOF) analyzers*** were introduced a few years ago by two companies, only one of which is currently producing commercial instruments (Mahoney *et al.* 1997). The TOF produced a lot of user interest on its introduction due to the characteristics of very fast scanning (20,000 or more complete mass spectra per second) and simultaneous sampling (Mahoney *et al.* 1996). Fast scanning allows the detection of extremely fast transient signals while simultaneous sampling removes flicker noise, similar to that of MC but due to simultaneous sampling rather than simultaneous detection. The LECO instrument collects and holds sample ions for 5 μs prior to allowing the ions to 'drift' down the flight tube for 50 μs giving 20,000 spectra per second. Partially due to the 10% duty cycle, the resulting sensitivity was similar to first generation ICP–MS instruments, noting that quad instrumental sensitivities (signal before unit concentration) have increased more than 1000 fold in two decades of development. The most sensitive instruments with either sector or quad analyzers now have comparable sensitivities. The LECO instrument axial samples the ICP, meaning that the ICP is in line with the ion lenses and initial TOF ion path. This resulted in very high continuum background signals which, while specified at 200 cps, were closer to 400 cps when the ICP was tuned for maximum sensitivity. The orthogonal configuration of the GBC instrument results in a much lower continuum background. Due to the compression of the signal in time at the detector, the dynamic range of the instruments is severely limited. The ion counting range is limited compared to the other MS configurations by approximately two orders of magnitude, with the maximum analog signal also reached at similarly lower beam intensities. The TOF has not made a great market impact for LA, and has not demonstrated extensive use, however finding a critically important application, the so-called 'killer ap' could change this situation.

***Other analyzers*** including the Ion Trap (IT) which was briefly introduced commercially has been withdrawn from the market. The ion trap operates mathematically similarly to the quad with the important difference that ions are contained or 'trapped' and are then withdrawn sequentially as a function of mass from the trap. An apparent disadvantage of the IT is that the ICP supplies a large number of ions and neutrals from the Ar gas supply, which 'fill' the trap and limit the effectiveness of the IT.

**Interferences**

In the early days of ICP–MS we naively had the hope (with encouragement from the manufacturers) that ICP–MS was interference-free. Unfortunately, while the numbers of interferences are much less than in other techniques, important interferences and background polyatomic ions are present in ICP–MS. These interferences include isobaric elemental ions; polyatomic ions including especially carbides, nitrides, oxides, hydroxides, and argides; doubly charged elemental ions; *etc.* As precisions improve, an interference that was once insignificant becomes important. Thus for MC applications in which isotope ratios are measured with precisions now approaching a few parts per million, what was once an insignificant interference in elemental determinations obtained with a few percent relative standard deviation becomes very important. It is important here to define an 'interference' strictly as a source of signal intensity that adds to the intensity of the analyte of interest. This is different from multiplicative corrections including what we will define as matrix effects which are a function of the total sample transported. There are *four major paradigms to correct for or to remove interferences*.

For reasonable sized corrections, up to approximately 50% of the gross signal, *mathematical corrections* can be applied. For elemental determinations which typically have long term reproducibilities of a few percent, interferences are often small. However since elemental determinations are commonly done on end member minerals and other 'high purity' phases, the presence of interferences which in a whole rock sample would be insignificant can become problematic. Fortunately in LA, interferences are often significantly less than when dealing with solutions; for example the common polyatomic oxide ions are reduced by approximately one order of magnitude in LA

compared to conventional solution sample introduction. Thus interference corrections which need to be applied in solution nebulization sampling can sometimes be neglected in LA. This is most fortunate as measuring interference correction factors is difficult in LA due to the absence and difficulty of preparation of calibration materials with unusual elemental compositions, which are easily done using solutions.

When analyzing solutions (not the subject of this essay) *chemical separation* of the analyte from the matrix using various chromatographic methods can be used, and their use is highly recommended. In this case the source of the interfering elemental or polyatomic ion is removed from the sample before it is introduced to the ICP. This procedure is not applicable for LA. However the presence of a large number of reports involving the high precision determination of isotope ratios of solution samples which use chromatographic separations does indicate the magnitude of interference problems for high precision isotope ratio determinations.

Thirdly the application of *high resolution* mass spectrometry is available with sector analyzers including both single and multi-collector instruments. These instruments have several different resolutions available. High or medium resolution works to remove some interferences and backgrounds from the analyte due to the mass defect of elemental atoms in which some proton and neutron mass is converted to energy ($E = mc^2$) to hold the nucleus together. Figure 1-5 shows the relationship of the exact mass relative to the nominal mass (total integer number of protons plus neutrons), which gives a minimum near $^{56}$Fe. Thus polyatomic ions made up of elements with lower nominal mass than Fe (especially hydrides, oxides, hydroxides, and argides) are heavier in exact mass than elements in the vicinity of Fe. For example, the heavy polyatomic ion $^{40}Ar^{16}O$ can be separated from the lighter $^{56}$Fe. Thus if a suitable high resolution instrument setting is available then some, but not all, interferences can be separated. A summary of the required resolution needed for some separations has been published (Becker & Dietze 1997). Note that not all interferences can be separated, contrary to the wish of manufacturers and users. For example the separation of $^{14}$N from $^{14}$C is not possible using available high resolutions (up to 12,000), even though this application would not be useful anyway, due to the high background of N and C in the ICP. Similarly other mono-elemental ions with the same nominal mass cannot be

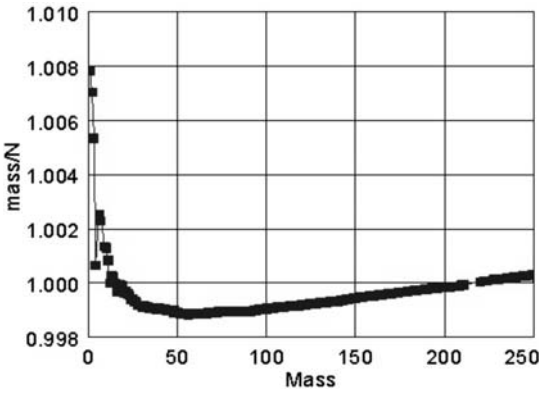


FIG 1-5. Mass defect shown as exact mass divided by the integer number of neutrons plus protons. Note the minimum mass defect and highest nuclear stability is at $^{56}$Fe.

separated with current resolving capabilities. Furthermore, polyatomic ions of elements lower in nominal mass than Fe, for example $^{53}Cr^{40}Ar$, can not be separated from $^{93}$Nb, which has a nominal mass higher than Fe (Hattendorf *et al.* 2001). A disadvantage of high resolution is the loss of sensitivity where sensitivity at low resolution (300) can be 200 times higher than at high resolution (10,000). Many applications use a medium resolution (3,000 to 4,000) where the loss of sensitivity is not as great.

Finally, *Collision/Reaction Cells* are currently available on quad instruments and on one of the MC instruments (Tanner *et al.* 2002). The cells are placed before the analyzer and are filled with a gas with which the sample ions and neutrals are allowed to react. With a suitable gas, reactions take place which can remove unwanted interfering and background ions from the system. More complicated schemes have been reported, for example converting the analyte to a fluoride where the fluoride polyatomic ion can then be measured without interference (Moens *et al.* 2001, Vanhaecke *et al.* 2003). The disadvantage of reaction cells are that new interferences can also be created (Hattendorf & Günther 2004), however a large number of successful applications have been reported for specific analytical problems. As with many procedures, this one, while solving one problem (remove an interference), can create new problems (new interferences). In both LA and solution nebulization the development of good procedures for multi-elemental determinations of a large number of analytes is difficult. The use of low molecular weight hydrogen (Hattendorf & Günther 2000, Mason & Kraan 2002) or helium gas in the

cell has been demonstrated to be most general. In some selected applications such as the analysis of fluid and melt inclusions (Günther *et al.* 2001, de Hoog *et al.* 2001, Mason *et al.* 2008, Pettke, 2008) good results have been reported. In the MC instrument the cell is used with a low mass reaction gas to 'thermalize' the ions, averaging out their energies to achieve the result of an electrostatic sector which removes ions with energies outside the desired range. The collision cell thus substitutes for the ESA, with the potential advantage of averaging the energies instead of removing the outliers.

**Vacuum**

Commercial instruments today use three or more regions of successively lower pressure (Fig. 1-6). The ICP is at atmospheric pressure. The plasma is 'sucked' though an orifice, the sampler (approximately 1 mm in diameter) into the expansion region where the pressure is reduced by approximately 1,000 fold. The pressure is further reduced by an additional 10,000 fold after passing through the second orifice, the skimmer, which is comparable in size to the sampler orifice. In most instruments an additional larger orifice separates this region from the analyzer and detector region where the pressure is reduced around 100 fold more. In sector instruments with their larger size and the presence of entrance and exit 'slits' additional pumps may be used to achieve even lower pressures in the analyzer and detector regions. For low uncertainty, very low pressures are needed to limit unwanted collisions and reactions. The number of different kinds of vacuum pumps and vacuum gauges has decreased in the more than two decades since ICP–MS instruments were first produced. The more limited number of pumping systems suggests that the newer systems are much more reliable, clean, and easy to operate. Rotary pumps are always found in these instruments. These pumps are mechanical, powered by a mid-size electrical motor. The pumps use oil to make good seals, and this oil needs to be replaced regularly for the same reasons automotive engine oil is regularly changed. The regions past the skimmer require lower pressures which are in most instruments pumped with turbo molecular pumps, colloquially known as 'turbo' pumps backed by a rotary pump. In large MC instruments, ion pumps may also be used in the flight tube or detector region to obtain very low pressures and better precisions. In summary the pumps used on available instruments are all very similar and are usually not a special consideration in purchasing decisions.

**Detector**

The last of the major parts of a MS is the detector. This is a 'transducer' which changes the ion current to a series of electrical pulses or to a potential (voltage) which can be converted into a number suitable for computer acquisition. There are two modes of operation, digital (pulse counting) and

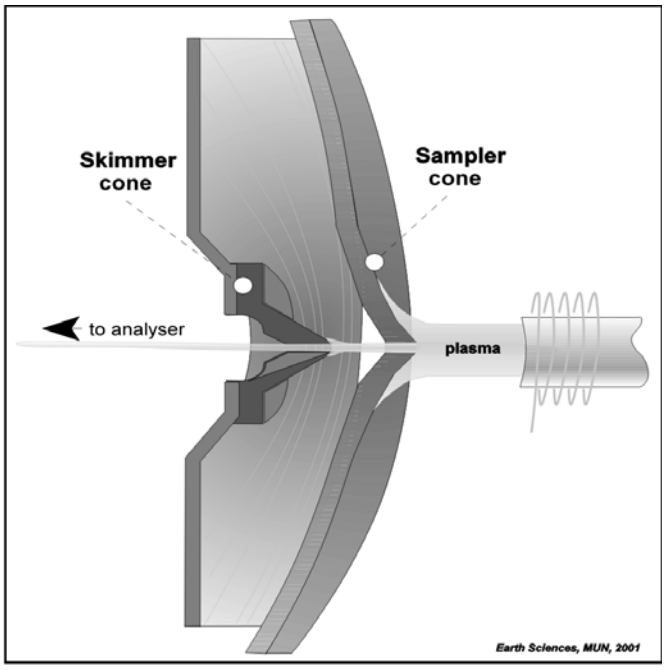


FIG 1-6. Schematic cross-section of the interface region of the ICP–MS, with the plasma being "sampled" by the sampler cone, then "skimmed" further by the next cone, before being directed toward the analyzer to the left.

analog. For low ion currents it is possible and better (more precise) to count the number of ions per unit time. At high ion currents, there are too many ions per unit time to count, and then an analog mode is used. The detectors require some careful evaluation as they are at the present time the weak link in the system. The invention of a new and better detector has the potential to have a great impact on the capabilities of the instruments and could open some new applications, while improving old ones.

***Secondary Electron Multipliers (SEM) and Channel Electron Multipliers (CEM)*** operate on the same principle, with the SEM having discrete dynode plates while the CEM has a single continuous area. In operation, an ion hits the first plate (some times called the conversion dynode) or the front area of the detector where the energy of an impacting ion produces a few (half dozen or so) electrons. These emitted electrons then in turn impact on the next plate or part of the detector again being amplified. After a dozen or so repeats of this amplification process around $10^8$ electrons are produced from each ion. The detector has the important characteristic of low noise amplification. For small ion beam intensities up to approximately $10^6$ ions per second each current pulse is converted to a potential pulse and is counted using digital electronics. For higher ion beam intensities an analog mode can be used where the current from the detector is converted to a potential which is then converted to a number by an integrating digital volt meter. An important desirable characteristic of SEM/CEM detectors is that their response is essentially instantaneous. Each ion which produces an electrical pulse does so nearly instantaneous with an output pulse width of nanoseconds. There is no delay in response of the detector system in the digital mode.

The *disadvantages of the electron multiplying detectors* are firstly that they do not have a quantum efficiency of 100%, which is apparent when optimizing the applied high voltage. In optimization the applied potential is increased until the derivative of the signal with respect to the applied potential approaches zero, ***i.e.***, a plot of signal ***vs.*** applied potential levels. Then the potential is decreased slightly to increase the life time of the device. In both digital and analog modes this characteristic (less than 100% conversion efficiency) of the detector makes high precision measurements difficult. In applications using several detectors (MC–ICP–MS) in the digital mode, the precision is limited due to the drift in cross (between detector) calibration, and since drift becomes more significant at higher ion currents this limits MC applications using ion counting to moderate ion count rates. One of the characteristics of these detectors is that they deteriorate a little bit with each ion impact, leading to drift of response, so in use they must be optimized periodically. Their dynamic range (lowest to highest ion current) at the low end (one ion) is excellent, but at the high end is limited by deterioration of the detector and a decreased gain response resulting in non linear response. At the high end of ion counting ($10^5$ to $10^6$ or more ions per second) dead time or pulse pile up corrections need to be applied. While dead time decreases the measured count rate, the correction can be made with reasonably good accuracy using well known equations, but only at moderate count rates.

An *ideal detector* would be 100% efficient. Every ion would be detected and the response to every ion would be identical, which unfortunately is not a characteristic of electron multiplying devices. However the *Faraday detector* system has these two important properties of 100% efficiency and a uniform response for each ion impact, and this is the reason for its wide use and application. The principle of the Faraday detector is very simple in that a conventional current to potential (voltage) operational amplifier is used to convert the ion current to a potential, which is in turn converted to a number by a suitable integrating digital voltmeter, which can be a voltage to frequency converter (VFC) followed by a digital counter. For each ion which impacts the detector 'cup' an electron is forced through the feed back resistor producing a potential output (E = I*R). These detectors have a long history in MC instruments, being used for decades in Thermal Ionization (TI) source instruments. Cross calibration is required to obtain high accuracy in MC instruments, but there are several good paradigms which are used to accomplish this, including peak hopping (dynamic), using a stable current source for amplifier calibration, and swapping amplifiers between detectors. Their main disadvantage is the limited dynamic range at low signals. In conventional resistor feedback amplifiers there is a component of noise which is a constant of nearly 2,000 cps for a 1-second integration time due to resistor noise from the very large $10^{11}$ ohm (100 GΩ) feed-back resistor. Another serious disadvantage of the Faraday detector is also related to the high valued resistor used in the feed-back circuitry which, with

the small parasitic capacitance of the system, gives a 'high value' of the decay time (capacitance multiplied by resistance). The amplifier is thus not able to follow changes in the signal 'instantaneously'. For 'stable' signals this is not a major concern, but for LA applications care must be taken in data interpretation and analysis, especially when Faradays are used with ion counters in high precision isotope ratio applications.

Some instruments use an electron multiplier in analog and digital operating modes. An instrument is also available which uses two modes of an electron multiplier which is switched with a Faraday. MC instruments all offer at least one ion counter and multiple Faradays. MC instruments are also available with multiple electron multipliers. As mentioned different instruments use different detectors, with some options available to the buyer of MC instruments. However there is no really ideal detector available and buyers need to evaluate the detector system on any system very carefully. Analog systems using integrating operational amplifier configurations in place of resistive feedback are now coming into use and promise improved performance with respect to speed.

***Dynamic Range of the Detector system*** Due to the necessity of measuring major elemental signals along with ultra-trace elemental signals a dynamic range which is as large as possible is important. This currently requires the use of two or more detectors and/or detector modes. An arrangement with an ion counting and an analog mode can allow dynamic ranges from 1 cps to more than 1 billion cps ($10^9$) or nine orders of magnitude. A higher range is available with Faraday detectors now capable of maximum outputs of 50 volts equivalent to 3 billion cps. With the special order of a smaller value feedback resistor an additional order of magnitude can be obtained. Note that while the useful range of each detector type or mode overlaps, in most ranges one of the detectors or modes is superior. Roughly digital ion counting is optimal over the entire ion counting range from 1 cps to $10^6$ cps, noting the need for dead time correction at high signals. The Faraday detector can be used from the resistor noise background signal of $10^3$ cps to the maximum potential of the amplifier which gives $10^9$ cps or more, for newer amplifier configurations. In the mid range of $10^3$ to $10^6$ ion counting is superior with respect to noise figures of merit.

There are other ways of increasing the dynamic range of the system other than those mentioned. These systems attenuate high ion currents rather than change detectors or detector modes. It is possible to decrease the ion current by changing the transmission of the mass analyzer in various ways. These include changing resolution (higher resolution gives lower sensitivity), especially useful on a quad where fast changes in resolution are possible, and by changes in ion lens settings. These techniques have some problems due to other characteristics which are affected including, importantly, mass bias and matrix effects, but with careful calibration can be very useful techniques (Heinrich *et al.* 2003). Currently sector instruments do not allow a quick resolution change, although there is the possibility of systems having a faster resolution change by using motorized slits rather than a system in which the slits are switched. CEM/SEM detectors with variable sensitivity have been designed allowing an extended range, eliminating some of the disadvantages of multi mode (digital and analog) systems. These detectors reduce sensitivity by changing the applied high voltage. However note that precision will be lost as Poisson counting statistics precision will be affected.

**ICP–MS**

In conclusion any ICP–MS can be and has been used with laser ablation (LA) sampling. There are important differences in cost and capability depending upon the instrument chosen. The two major types of applications are high precision isotope ratio measurements and quantitative trace element determinations. Single collector instruments all have isotope ratio determination capability, but with a precision that will not match that obtainable using MC instruments. The decision should be made on "suitably for purpose" considerations, as not all isotope ratio measurements require the best precision possible. Some precision figures of merit are given in (Günther-Leopold *et al.* 2004).

General *Figure of Merit* considerations in ICP–MS evaluation for LA are sensitivity, background, detection limit, settling time, and drift. Cost is, of course, the final consideration. Reliability of the instrument and the company, while harder to quantify, are very important.

*Sensitivity*, the signal detected per unit concentration is a very important consideration for LA. While the signal obtained in an acquisition is a function of the laser as well as the mass spectrometer, here it is the transmission efficiency

of ions from the ICP to the detector which needs to be specified. However this specification is not easily amendable to a robust evaluation because we do not have a convenient portable and stable sample source to make the measurements. The possibility of measuring sensitivity using a gas supply containing traces of analytes is possible, but difficult. Sensitivity measurement using a 'standard' concentric nebulizer with a 'standard' spray chamber may be the best available. However this is not completely adequate as the 'wet' aerosol produced has differences compared to a LA aerosol which is usually dry. Desolvation removes most, but not all, of the water, usually only approaching a dry plasma. The various nebulizers and spray chambers which are in use have some significant differences in efficiency from one to another. A further complication in sensitivity comparisons is that sensitivity can vary from unit to unit along with large adjustable variations as a function of mass as optimization is changed (Latkoczy *et al.* 2005). Since the beginning of ICP–MS gains in sensitivity have been more than 1,000 fold, with a theoretical maximum that is still 1,000 fold higher than the best of today's units. For laser sampling of the smallest pits (<10 μm), very high sensitivity is required if low detection limits are required. There is no limit to the useful sensitivity which new instruments may make available, because very small pits have a large number of interesting and useful applications. While the majority of LA is carried out with pits in the range of 30 μm to 50 μm, pits smaller than 3 μm can be obtained with care. However with these small pits (note that the pit depth should be no more than approximately the pit diameter to minimize elemental fractionation effects) the amount of sample aerosol produced is insufficient to provide the low detection limits and high precision needed for many applications, remembering the cubic relationship between diameter and volume.

*Background* is for the most part low in all ICP–MS instruments. It is the very low background in ICP–MS which relative to sensitivity (signal to background or signal to noise) is much better compared with ICP–OES (optical emission spectrometer ) instruments. It is this high signal to background ratio which gives ICP–MS very low detection limits. While lower backgrounds are better, most applications are not carried out near the limit of detection. As with sensitivity, the background obtained using LA with a dry plasma is not necessarily the same as for a wet plasma as very different optimization conditions are required. The background consists of a continuum, a signal which is constant over the entire mass range. Additional background signals come from elemental and polyatomic ions from the gas supply and atmospheric air entrainment (especially H, C, N, O, Ar, Kr, and Xe) and from 'memory' from previous samples. In many situations memory will be found to be the most important part of the background. Furthermore, the phenomenon of memory is one of the least studied due to the difficulty of carrying out the meaningful long term studies required. Note that continuum, polyatomic ion, and memory background are affected by all of the ICP optimization parameters, including especially power, gas flows, and torch position.

*Detection Limit* is a function of the sensitivity and the background noise, which is in turn a function of the background. Lower background and higher sensitivity produce lower detection limits. As the sensitivity is a function of a large number of variables, including most importantly the mass (volume) of sample ablated, the detection limit varies widely making comparison between facilities and different analytical paradigms very difficult.

*Settling Time* is the time for the system to make a 'peak hop' from one mass to another and for the signal to stabilize. There are two components of the settling time, the time for the analyzer (quadrupole, sector, TOF, *etc.*) to stabilize at a new selected mass, and the time for the detector to settle to a new ion beam intensity. The effective settling time is the longer of the two. Quadrupole analyzers are generally fast with settling times from 0.1 to a few ms. While one or two ms is typical, this time could be reduced by an additional expense using a larger power supply which would switch and settle faster into the inductively, resistive, and capacitive (LRC) load of the quads. Sector instruments are very slow when magnetic field changes are required, but are fast when only electrostatic changes are used. This makes a general statement comparing quad to sector instruments difficult as the time required to complete a sweep of all masses in a sector instrument depends upon the selected set of masses. No magnet changes would be required when a set of masses over a limited range (from the lowest mass to 130% of this mass) are determined, for example in isotope ratio determinations where the range of the electrostatic analyzer can be sufficient. TOF and MC, with simultaneous sampling have a zero settling time. Faster is better as faster settling gives more efficient data collection where less time is lost to settling with more

available for sample signal integration. As well the shorter dwell times (the time interval used to integrate the signal at a signal mass) could be used resulting in a larger number of complete mass scans per unit time (Longerich *et al.* 1996). Detector settling times vary from instantaneous settling for electron multiplying detectors up to a second or more for resistive feedback amplifiers. The time required when a change in detector mode is used or when the detector is changed also needs to be taken into consideration. In conclusion the limit on settling time depends upon the analyzer and detector(s) used.

*Drift*, the change in sensitivity (signal per unit concentration) is a very important parameter, and is one which is impossible to predict in the long term. The manufacturers have made great strides in reducing drift. However note that ICP–MS instruments exhibit a much higher drift than do almost all of the other elemental analysis instruments with which we are familiar. Paradigms which correct for drift are important, but not easily tested for robustness, the characteristic of the paradigm to produce high quality results when the instrument is drifting. The use of internal standardization is an important paradigm to correct for drift. Internal standardization is however not perfect as it is well known that drift is a function of mass and ionization potential, thus different elements drift differently.

**Laser Ablation sampling system**

A laser ablation sampling system consists firstly of a laser of sufficient power. The output laser beam, after being steered to the sample using mirrors and/or prisms, is focussed onto the sample using a lens. Apertures may be inserted into the beam path, along with other optics to improve beam homogeneity. Optics to observe the sample are also needed, which due to the high energy of the laser must consist of a video system to protect the eyes of the operator from potentially damaging laser energy. The sample is contained in some kind of air-tight cell through which a flow of gas carries the ablated sample aerosol to the ICP. The transport system usually uses quarter-inch OD tubing with lengths of one to two metres. Specialized systems which allow shorter transport distances have been used for fundamental studies, but are inconvenient for routine analyses. Interestingly and amazingly, any cell which can and has been fabricated works, although some designs are better than others, meaning higher transport efficiency and faster flush-out of a previous sample. The observation that "all cells work" has resulted in the lack of an imperative need for research and development in cell design including fundamental studies of the fluid dynamics (Koch *et al.* 2004a) of laser-created aerosol transport (Bleiner & Günther 2001). In this collection of essays there is a review of recent progress in cell design by Bleiner & Chen (2008). The other interesting observation on various cells is that the efficiency of sample mass transport is surprising high and that the geometry of the cells has not changed significantly when compared to earlier work (Arrowsmith & Hughes 1988). Higher efficiency is very desirable because if 100% transport efficiency is reached then laser-induced elemental fractionation processes taking place in the laser cell and transport system will be reduced, and better analytical signals would result.

***Laser***. Any laser and optical set up with sufficient power to ablate the sample is capable of being used for LA analysis (Table 1-3). A minimum power (the ablation threshold) is required in the vicinity of one mJ per pulse, although it is actually the energy density (irradiance in J per unit area) which is the critical parameter together with pulse width. The first report of LA–ICP–MS used a ruby laser operating in the red (694 nm) region of the visible spectrum. The most commonly used laser energies today are based upon the *Nd:YAG (Neodymium: Yttrium Aluminum Garnet)* laser. This is a solid state laser in which the garnet rod is excited using a flash lamp similar to flash lamps used in photography. This laser's fundamental energy output is at a wavelength of 1064 nm in the near infrared (NIR). Typical lasers produce hundreds of mJ per pulse of energy, which is much more than optimal for micro LA but can be used when a 'bulk' analysis is wanted. This wavelength was used in our, and other, early work, where it quickly became apparent that quality results producing good ablation pits formed only when the sample had high absorptivity at this wavelength. This especially included samples containing the transition element, Fe, for which there is a crystal field splitting energy causing high absorption near 1064 nm. On the other hand important minerals not containing a transition element (*e.g.*, calcite, apatite, quartz, feldspar, fluorite, feldspars, *etc.*) ablated poorly in what we described as "catastrophic" ablation (Jackson *et al.* 1992). These catastrophic pits are very deep, very large, very ragged or ruptured along crystal axes, and produce large particles. While these minerals

TABLE 1-3. SUMMARY OF LASERS COMMONLY USED FOR LASER ABLATION

| | | |
|---|---|---|
| Nd:YAG solid state | 1064 nm | Fundamental wavelength, used for bulk sampling. |
| | 266 nm | Good compromise between ease of use, durability, and cost. Applicable for a large number of sample types. |
| | 213 nm | Better compromise, but more expensive than a 266 nm and requires more maintenance. Applicable for a larger number of sample types than the 266 nm. |
| | 193 nm | Obtained using OPO (Optical Parametric Oscillator) optics. Allows the advantage of a solid state laser, with the disadvantage of more complicated optics. Most general applicability. |
| ArF Excimer gas | 193 nm | Higher cost, but uses fundamental wavelength, eliminating the need for frequency multiplying crystals and their maintenance and alignment. Most general purpose wavelength. |

are described as transparent, what microscopists mean by transparent usually refers to the absorptivity in the visible. For LA the absorptivity at the wavelength of the laser radiation is the important property of the sample.

Using suitable crystals the *frequency* of the laser output can be *multiplied*. The 1064 nm *wavelength* output from the Nd:YAG can be doubled (532 nm), tripled (355 nm), quadrupled (266 nm), or quintupled (213 nm) (Jeffries *et al.* 1998, Guillong *et al.* 2003, Horn *et al.* 2003). The 532 nm (green) is rarely used (Figg & Kahr 1997), although it has been reported to work well for green, chlorophyll containing samples. The tripled is rarely used other than to create 213 nm by combining the doubled with the tripled to create the quintupled (2+3=5). The 213 nm output can also be obtained by combining the fundamental with the quadrupled (1+4=5). The 266 nm energy is one of the commonly used LA energy, being a compromise between ease and economy of use with a general applicability to a large number of, but not all, materials. While many materials do absorb at 266 nm, the photon energy is not so high as to require more expensive and exotic optical materials and flushed optical paths. The higher energy 213 nm and 193 nm are now more commonly being purchased because of their more general applicability. The quintupled (213 nm) energy is more versatile than 266 nm since it is highly absorbed by a wider range of materials and has found a place in many laboratories. A higher energy photon energy at 193 nm produced using an Optical Parameter Oscillator (OPO) is also obtained from the Nd:YAG laser (Horn *et al*. 2003) and has been produced commercially.

The 193 nm wavelength, which is now found in many laboratories, can also be obtained from an *Excimer ArF* which emits energy at near the boundary between the UV and the Vacuum UV (VUV), where radiation is absorbed by air. The Excimer laser is more complicated to operate and more expensive to purchase than solid state lasers. However the higher photon energy has been found to have a number of very desirable characteristics and thus the choice of many laboratories, especially those which analyze a very wide range of materials. Being the fundamental wavelength of the laser eliminates the need for the frequency multiplying crystals and the need to align the optical set up for frequency multiplying and separation. Specialized optics including reflecting (mirror) optics rather than refracting (bending) optics are used at 193 nm. A supply of argon (Ar) and fluorine (F) gases are required which must be periodically changed. In use, Ar and F gas fill a closed cell, into which the excitation energy comes from an electrical discharge through the gas cell.

Recent development has seen the use of *femtosecond* (fs = $10^{-15}$ s) *lasers* (Margetic *et al.* 2001, Gonzalez *et al.* 2006, Gonzalez *et al.* 2004, Poitrasson *et al.* 2005, Russo *et al.* 2002, Bian *et al.* 2005, Bian *et al.* 2006, Koch *et al.* 2005, Koch *et al.* 2004 a or b?, Koch *et al.*2006). These lasers have a much shorter pulse width (around 10,000 times shorter) of several hundred femtoseconds compared to the previously mentioned nanosecond (ns = $10^{-9}$ s) Nd:YAG and ArF Excimer lasers which have pulse widths of a few ns. The much shorter pulse width limits the phenomenon of sample melting at the ablation site, resulting in some reported advantages. The cost is much higher than for any of

the ns lasers with set-up and maintenance also being more time-consuming. Wavelengths from the NIR to the UV have been used (Horn *et al.* 2006). Currently there are no complete 'turn key' fs laser systems available, although a microscope and optical system to be used with a user-supplied fs laser is available. Some essays in this collection report on some of the recent work with these fs lasers, principally Horn (2008).

The *quantum mechanics and energy levels* which go into making a laser are very interesting, but in simple terms, a Nd:YAG laser concentrates photon energy in time. In a Nd:YAG laser a flash lamp with a pulse width on the order of 1 ms ($10^{-3}$ sec) is concentrated in time forming a laser output pulse with a duration of around 10 ns ($10^{-8}$ sec) giving an increase in energy (Joules/sec) by a factor of 100,000 ($10^5$). This laser beam is around 5 mm in diameter at the exit of the Nd:YAG rod, and because it is a coherent radiation the diameter increases only slightly over a distance of one metre or so. For typical micro LA applications this 5 mm beam is focussed using a lens by a factor of around 100 to a smaller beam with a diameter of 50 μm, an optical demagnification of 100. Thus overall the energy density is increased in time and space by 10,000,000 ($10^5$ x $10^2$) times, giving a typical energy density on the sample surface of 100,000 W (Joule/second).

For all these laser systems *variable power control* is required in order to have a suitable sampling rate which depends upon the sample matrix and the beam size. In typical analyzes a laser pit of 60 μm diameter and depth would be formed in 60 seconds at a rate of 1 μm per second. At a laser repetition rate of 10 Hz this gives a boring rate of 0.1 μm per pulse (Horn *et al.* 2001). Due to the high output energy of lasers, optical attenuation is used in a beam splitting configuration. Absorbing filters are not used because of the likelihood of damage to such a filter. In most LA systems the property of polarization of the laser beam is used, which fortunately is a fundamental property of lasers. With frequency multiplied energies there may be a need to 'clean up' the polarization using an additional polarizer. Then rather than use the property of variable extinction using cross polarizers, a 'half wave plate' placed in the beam path is rotated giving different angles of polarization. This beam is passed through a prism which splits the two modes of polarization, one of which is directed to the sample while the other is harmlessly directed to a 'beam dump' where the energy is safely absorbed. The beam dump can be simply a hole drilled into a metal block. Optical systems which image an aperture onto the sample allow the same energy density (energy per unit area) to be maintained for different crater diameters.

To maintain reproducibility there is an obvious need for *energy meters* which must be suitable for the particular laser used. The meter can be placed in the beam path for monitoring the energy when not ablating. An alternative is to split the energy so that a known fraction is directed to the meter while the remainder is focussed onto the sample allowing continuous monitoring of the laser energy during ablation.

**To Make or Buy**

This is best described by a triangular plot of time, money, and knowledge. Lots of money; then buy a 'turn key' LA system. Lots of time; then money can be saved by shopping for the best buy, begging, learning, building, and borrowing. Lots of knowledge and experience; then money can be saved and the system put together in a short time at a reasonable cost. When we put together our first and subsequent LA systems (Australia, Japan, and Italy) there was no good choice other than to construct a system in-house. In addition to cost, a system made in-house has the advantages of flexibility for future research and development. There are now several 'turn key' commercial laser systems complete and ready to use based upon the lasers mentioned above, including all required optics, a sample cell, and motorized stage. For 'do it yourself' researchers, there are systems supplied without a laser, intended to be coupled with a 'customer supplied' laser.

## CONCLUSIONS

All ICP–MS instruments can be used with LA sampling. High sensitivity is important, especially for small pits and very low concentrations. Single detector sector or quadrupole instruments are used for quantitative elemental analysis and moderate precision isotope ratio work. Multicollector instruments are needed for the highest precision isotope ratio determinations.

The current state of the art of the detector components of the mass spectrometers are the weakest links in the system, and hopefully the future may see some innovative new devices. The limitations of present day detectors include settling time, linearity, stability, and dynamic range. At the present time, the capabilities of the detector are one

of the most important purchasing decision considerations for the buyer of a new instrument.

The optimal laser wavelength depends primarily on the absorptivity of the sample. Laser wavelengths with ns pulse width of 1064, 266, 213, and 193 nm are used for most recently reported work, and all are available in commercial units. The higher photon energy (shorter wavelength) works for a wider range of samples as in general photon absorptivity for all sample types increases with higher photon energy. Buying considerations are primarily determined by the range of sample types to be analyzed. As for the mass spectrometer, price, and maintenance are often important criteria.

## ACKNOWLEDGEMENTS

Recognition must be given to a large number of researchers who have contributed to the development and adoption of LA in more than two decades since the first LA–ICP–MS report of Gray in 1985. Thanks especially to my collaborators at Memorial University over many years including especially (in alphabetical order) Brian Fryer, Detlef Günther, Ingo Horn, Simon Jackson, Teresa Jeffries, Jan Košler, David Strong, and many others including especially support from technical services and research assistants who in the early years of LA–ICP–MS contributed in many ways to the development of this powerful and now widely accepted technique. Thanks to Paul Sylvester who organized this publication and two day short course as well as its predecessor in 2001. As well, note must be made to discussions in the hallway with Noel James who put the idea into our heads that a LA system would be a good idea. Thanks to Detlef Günther for a careful review and the addition of many helpful citations which can lead the reader to a portion of an immense literature on LA which is available today. Thanks to "Jiggs" Diegor who drafted the MS figures.

## REFERENCES

ARROWSMITH, P. & HUGHES, S.K. (1988): Entrainment and transport of laser ablated plumes for subsequent elemental analysis. *Appl. Spectrosc.* **42**, 1231-1239.

BECKER, J.S. & DIETZE, H.J. (1997): Investigations on cluster and molecular ion formation by plasma mass spectrometry. *Fresenius J Anal Chem.* **359**, 338-345.

BECKER, S. (2007): *Inorganic Mass Spectrometry; Principles and Applications*, Wiley-VCH Verlag GmbH & Co., 514 p.

BIAN, Q.Z., KOCH, J., LINDNER, H., BERNDT, H., HERGENRODER, R. & NIEMAX, K. (2005): Non-matrix matched calibration using near-IR femtosecond laser ablation inductively coupled plasma optical emission spectrometry. *J. Analyt. Atom. Spectrom.* **20**, 736-740.

BIAN, Q.Z., GARCIA, C.C., KOCH, J. & NIEMAX, K. (2006): Non-matrix matched calibration of major and minor concentrations of Zn and Cu in brass, aluminum and silicate glass using NIR femtosecond laser ablation inductively coupled plasma mass spectrometry. *J. Analyt. Atom. Spectrom.* **21**, 187-191.

BLEINER, D. & GÜNTHER, D. (2001): Theoretical description and experimental observation of aerosol transport processes in laser ablation inductively coupled plasma mass spectrometry. *J. Analyt. Atom. Spectrom.* **16**, 449-456.

BLEINER, D & CHEN, Z. (2008): Computer modeling of laser ablation elemental microanalysis. *In* Laser Ablation ICP–MS in the Earth Sciences: Current Practices and Outstanding Issues (P. Sylvester, *ed*.). *Mineral. Assoc. Can. Short Course Series* **40**, 35-52.

DE HOOG, J.C.M., MASON, P.R.D. & VAN BERGEN, M.J. (2001): Sulfur and chalcophile elements in subduction zones: constraints from a laser ablation ICP–MS study of melt inclusions from Galunggung Volcano, Indonesia. *Geochim. Cosmochim. Acta* **65**, 3147-3164.

DOUGLAS, D.J. & HOUK, R.S. (1985): Inductively coupled plasma mass-spectrometry (ICP–MS). *Prog. Analyt.l Atom. Spectroscopy* **8**, 1-18.

FIGG, D. & KAHR, M.S. (1997): Elemental fractionation of glass using Laser Ablation Inductively Coupled Plasma Mass Spectrometry. *Appl Spectrosc* **51**,1185-1192.

GONZALEZ, J., LIU, C.Y., MAO, X.L. & RUSSO, R.E. (2004): UV–femtosecond laser ablation–ICP–MS for analysis of alloy samples. *J. Analyt. Atom. Spectrom.* **19**, 1165-1168.

GONZALEZ, J., DUNDAS, S.H., LIU, C.Y., MAO, X.L. & RUSSO, R.E. (2006): UV–femtosecond and nanosecond laser ablation–ICP–MS: Internal and external repeatability. *J. Analyt. Atom. Spectrom.* **21**, 778-784.

GRAY, A.L. (1985): Solid sample introduction by laser ablation for inductively coupled plasma source mass spectrometry. *Analyst* **110**, 551-556.

GUILLONG, M., HORN, I. & GÜNTHER, D. (2003): A comparison of 266 nm, 213 nm and 193 nm produced from a single solid state Nd:YAG laser for laser ablation ICP MS. *J. Analyt. Atom. Spectrom.* **18**, 1224-1230.

GÜNTHER, D., HATTENDORF, B. & AUDÉTAT, A. (2001): Multi-element analysis of melt and fluid inclusions with improved detection capabilities for Ca and Fe using laser ablation with a dynamic reaction cell ICP–MS. *J. Analyt. Atom. Spectrom.* **16**, 1085-1090.

GÜNTHER-LEOPOLD, I., WERNLI, B., KOPAJTIC, Z. & GÜNTHER, D. (2004): Measurement of isotope ratios on transient signals by MC–ICP–MS. *Anal. Bioanal. Chemistry* 378, 241-249.

HALLIDAY, A., REHKAMPER, M., LEE, D.C. & YI, W. (1996): Early evolution of the Earth and Moon – New constraints from Hf–W isotope geochemistry. *Earth Planet. Sci. Lett.* **142**, 75-89.

HATTENDORF, B. & GÜNTHER, D. (2000): Characteristics and capabilities of an ICP–MS with a dynamic reaction cell for dry aerosols and laser ablation. *J. Analyt. Atom. Spectrom.* **15**, 1125-1131.

HATTENDORF, B. & GÜNTHER, D. (2004): Suppression of in-cell generated interferences in a reaction cell ICPMS by bandpass tuning and kinetic energy discrimination. *J J. Analyt. Atom. Spectrom.* **19**, 600-606.

HATTENDORF, B., GÜNTHER, D., SCHÖNBÄCHLER, M. & HALLIDAY, A. (2001): Simultaneous Ultra Trace Determination of Zr and Nb in Chromium Matrices with ICP–DRCMS. *Anal. Chem.* **73**, 5494-5498.

HEINRICH, C.A., PETTKE, T., HALTER, W.E., AIGNER-TORRES, M., AUDETAT, A., GÜNTHER, D., HATTENDORF, B., BLEINER, D., GUILLONG, M. & HORN, I. (2003): Quantitative multi-element analysis of minerals, fluid and melt inclusions by laser ablation–inductively coupled plasma–mass spectrometry. *Geochim Cosmochim Acta* **67**, 3473-3497.

HORN, I. (2008): Comparison of femtosecond and nanosecond laser interactions with geologic matrices and their influence on accuracy and precision of LA–ICP–MS data. *In* Laser Ablation ICP–MS in the Earth Sciences: Current Practices and Outstanding Issues (P. Sylvester, *ed.*). *Mineral. Assoc. Can. Short Course Series* **40**, 53-65.

HORN, I., GUILLONG, M. & GÜNTHER, D. (2001): Wavelength dependent ablation rates for metals and silicate glasses using homogenized laser beam profiles implications for LA ICP MS. *Appl. Surf. Sci.* **182**, 91-102.

HORN, I., GÜNTHER, D. & GUILLONG, M. (2003): Evaluation and design of a solid state 193 nm OPO Nd:YAG laser ablation system. *Spectrochim. Acta B* **58**, 1837-1846.

HORN, I., VON BLANCKENBURG, F., SCHOENBERG, R., STEINHOEFEL, G. & MARKL, G. (2006): *In situ* iron isotope ratio determination using UV femtosecond laser ablation with application to hydrothermal ore formation processes. *Geochim. Cosmochim. Acta* **70**, 3677-3688.

JACKSON, S.E., LONGERICH, H.P., DUNNING, G.R. & FRYER, B.J. (1992): The application of laser ablation microprobe; inductively coupled plasma mass spectrometry (LAM ICP MS) to *in situ* trace element determinations in minerals. *Can. Mineral* 30, Part 4, 1049-1064.

JARVIS, K.E., GRAY, A.L. & HOUK, R.S. (1992): *Handbook of inductively coupled plasma mass spectrometry.* Blackie, Chapman and Hall, New York, 380 pp.

JEFFRIES, T.E., JACKSON, S.E. & LONGERICH, H.P. (1998): Application of a frequency quintupled Nd:YAG source ($\lambda$=213 nm) for laser ablation inductively coupled plasma mass spectrometric analysis of minerals. *J. Analyt. Atom. Spectrom.* **13**, 935-940.

KOCH, J., SCHALDACH, G., BERNDT, H. & NIEMAX, K. (2004a): Numerical simulation of aerosol transport in atomic spectrometry. *Anal. Chem.* **76**, 130A-136A.

KOCH, J., VON BOHLEN, A., HERGENRÖDER, R. & NIEMAX, K. (2004b): Particle size distributions and compositions of aerosols produced by near IR femto and nanosecond laser ablation of brass. *J. Analyt. Atom. Spectrom.* **19**, 267-272.

KOCH, J., LINDNER, H., VON BOHLEN, A., HERGENRODER, R. & NIEMAX, K. (2005): Elemental fractionation of dielectric aerosols produced by near infrared femtosecond laser ablation of silicate glasses. *J. Analyt. Atom. Spectrom.* **20**, 901-906.

KOCH, J., WÄLLE, M., PISONERO & J., GÜNTHER, D. (2006): Performance characteristics of ultra violet femtosecond laser ablation inductively coupled plasma mass spectrometry at 265 and 200 nm. *J.*

*Analyt. Atom. Spectrom.* **21**, 932-940.

LATKOCZY, C. & GÜNTHER, D. (2002): Enhanced sensitivity in inductively coupled plasma sector field mass spectrometry for direct solid analysis using laser ablation (LA–ICP–SFMS). *J. Analyt. Atom. Spectrom.* **17**, 1264-1270.

LATKOCZY, C., BECKER, S., DUCKING, M., GÜNTHER, D., HOOGEWERFF, J.A., ALMIRALL, J.R., BUSCAGLIA, J., DOBNEY, A., KOONS, R.D., MONTERO, S., VAN DER PEIJL, G.J.Q., STOECKLEIN, W.R.S., TREJOS, T., WATLING, J.R. & ZDANOWICZ, V.S. (2005): Development and evaluation of a standard method for the quantitative determination of elements in float glass samples by LA–ICP–MS. *J Forensic Sci* **50**, 1327-1341.

LONGERICH, H.P., JACKSON, S.E. & GÜNTHER, D. (1996): Laser ablation inductively coupled plasma mass spectrometric transient signal data acquisition and analyte concentration calculation. *J. Analyt. Atom. Spectrom* **11**, 899-904.

MAHONEY, P.P., LI, G.Q. & HIEFTJE, G.M. (1996): Laser ablation–inductively coupled plasma mass spectrometry with a time-of-flight mass analyser. *J. Analyt. Atom. Spectrom* **11**, 401-405.

MAHONEY, P.P., RAY, S.J. & HIEFTJE, G.M. (1997): Time-of-flight Mass Spectrometry for Elemental Analysis. *Appl Spectrosc* **51**, A 16-A 28.

MARGETIC, V., BOLSHOV, M., STOCKHAUS, A., NIEMAX, K. & HERGENRODER, R. (2001): Depth profiling of multi-layer samples using femtosecond laser ablation. *J. Analyt. Atom. Spectrom.* **16**, 616-621.

MASON, P.R.D. & KRAAN, W.J. (2002): Attenuation of spectral interferences during laser ablation inductively coupled plasma mass spectrometry (LA–ICP–MS) using an rf only collision and reaction cell. *J. Analyt. Atom. Spectrom.* **17**, 858-867.

MASON, P.R.D., NIKOGOSIAN, I.K. & VAN BERGEN, M. (2008): Major and trace element analysis of melt inclusions by laser ablation ICP–MS. *In* Laser Ablation ICP–MS in the Earth Sciences: Current Practices and Outstanding Issues (P. Sylvester, *ed*.). *Mineral. Assoc. Can. Short Course Series* **40**, 219-239.

MOENS, L., VANHAECKE, F., BANDURA, D., BARANOV, V. & TANNER, S. (2001): Elimination of isobaric interferences in ICP-MS, using: ion-molecule reaction chemistry: Rb/Sr age determination of magmatic rocks, a case study. J. Analyt. Atom. Spectrom. **16**, 991-994.

MONTASER, A. (*Ed*) (1998): *Inductively Coupled Plasma Mass Spectrometry*. Wiley-VCH, New York, 964 pp.

NELMS, S.M. (*Ed*) (2005), *ICP Mass Spectrometry Handbook*, Blackwell Publishing, Oxford (UK), 485 pp.

PETTKE, T. (2008): Analytical protocols for element concentration and isotope ratio measurements in fluid inclusions by LA–(MC–)ICP–MS. *In* Laser Ablation ICP–MS in the Earth Sciences: Current Practices and Outstanding Issues (P. Sylvester, *ed*.). *Mineral. Assoc. Can. Short Course Series* **40**, 189-217.

POITRASSON, F., FREYDIER, R., MAO, X., MAO, S.S. & RUSSO, R.E. (2005): Femtosecond laser ablation ICP MS analysis of trace elements in solids. *Geochim Cosmochim Acta* **69**, A54.

RUSSO, R.E., MAO, X.L., GONZALEZ, J.J. & MAO, S.S. (2002): Femtosecond laser ablation ICP–MS. *J. Analyt. Atom. Spectrom.* **17**, 1072-1075.

TANNER, S.D. & BARANOV, V.I. (1999): A dynamic reaction cell for inductively coupled plasma mass spectrometry (ICP–DRC–MS). II. Reduction of interferences produced within the cell. *J. Am. Soc. Mass Spectrom.* **10**, 1083-1094.

TANNER, S.D., BARANOV, V.I. & VOLLKOPF, U. (2000): Dynamic reaction cell for inductively coupled plasma mass spectrometry (ICP–DRC–MS). Part III. Optimization and analytical performance. *J. Analyt. Atom. Spectrom.* **15**, 1261-1269.

TANNER, S.D., BARANOV, V.I. & BANDURA, D.R. (2002): Reaction cells and collision cells for ICP–MS: A tutorial review. *Spectrochim Acta Part **B*** **57**, 1361-1452.

VANHAECKE, F., DE WANNEMACKER, G., BALCAEN, L. & MOENS, L. (2003): The use of dynamic reaction cell – ICP mass spectrometry to facilitate Rb-Sr age determination. *In* Geochronology: linking the isotope record with petrology and textures, D. Vance, W. Müller & I.M. Villa, *eds*. Geol. Soc. London, Special Publication **220**, 173-181.

WANG, Z.K., HATTENDORF, B. & GÜNTHER, D. (2006): Analyte response in Laser Ablation Inductively Coupled Plasma Mass Spectrometry *J. Am. Soc. Mass Spectrom.* **17**, 641-651.

# CHAPTER 2: FORMATION OF AEROSOLS GENERATED BY LASER ABLATION AND THEIR IMPACT ON ELEMENTAL FRACTIONATION IN LA–ICP–MS

Detlef Günther & Joachim Koch,
ETH Zurich, Laboratory of Inorganic Chemistry,
Hönggerberg HCI, CH–8093 Zurich,
E-mail: guenther@inorg.chem.ethz.ch, koch@inorg.chem.ethz.ch

## INTRODUCTION

Ever since its birth in the mid 1980s, laser ablation–inductively coupled plasma mass spectrometry (LA–ICP–MS) using nanosecond laser sources (Gray 1985) has attracted growing attention and is, nowadays, considered a "routine" method for element and isotope-specific analyses of various solid samples (Durrant 1999, Günther *et al.* 1999, Becker *et al.* 2000a, b, 2002, Poitrasson 2003, Horn *et al.* 2006). The broad interest in LA–ICP–MS is mainly due to its capability of direct micro-analysis, conceptual simplicity, a high degree of flexibility, the development of advanced tuning and calibration strategies, as well as the technological progress in laser and ICP–MS instrumentation during the last decade. Nevertheless, achieving sufficient accuracy by LA–ICP–MS occasionally turns out to be less trivial than the simplicity of the analysis suggests, especially, for non-matrix-matched calibration. In fact, numerous authors (Cromwell *et al.* 1995, Outridge *et al.* 1996, 1997, Mank & Mason 1999, Borisov *et al*. 2000, Liu *et al.* 2000, Russo *et al.* 2000 Poitrasson *et al.* 2003, Kuhn & Günther 2003, 2006, Jackson *et al.* 2004, Liu *et al.* 2005, Košler *et al.* 2005, Poitrasson 2005, Saetveit *et al.* 2008) have reported on non-representative sampling or temporal changes in elemental responses during LA which were found to affect the accuracy of quantification severely even *if* matrix-matched standards were used. Both effects which are commonly referred to as "elemental fractionation" represent limiting factors that all analyses based on non-matrix-matched calibration are subject to.

A thorough examination of the mechanisms underlying elemental fractionation has been initiated in order to understand its complexity and relationship to laser-, transport-, and ICP-induced effects, noting that these are correlated in a multiplicative manner. For instance, the size distribution of particles released or compositional changes between sample and the generated aerosol phase determines selective material losses during the transport period as a result of, for example, gravitational settling or diffusion, which, in turn, defines the structure (*i.e.*, homogeneity, size distribution) and aggregation state of aerosols reaching the ICP. The composition and physical properties of this aerosol fraction will control evaporation, diffusion rate, and ionization efficiency inside the ICP (Olesik & Bates 1995, Alexander *et al.* 1998, Guillong & Günther 2002, Aeschliman *et al.* 2003, Kuhn & Günther 2004a, b, Kuhn *et al.* 2005, Olesik & Kinzer 2006). Thus, response ratios calculated on the basis of non-matrix-matched calibration may result in significant deviations of concentrations from "true" values. In Figure 2-1, a schematic of most influential and interactive parameters is shown.

This article reviews the literature published on the expansion and transport phenomena of aerosols produced by LA under atmospheric conditions and is intended to give a progress report on experimental findings of aerosol research relevant to LA–ICP–MS. However, it does not provide a review of theoretical considerations or modeling work addressing the fundamental mechanisms of material ejection during LA (Hergenröder 2006a, b, see also Bleiner & Chen 2008), which are still not completely understood given the large variety of parameters involved (wavelength, fluence, pulse width and others, see Figure 2-1). In the following subsection, the history of research efforts made to examine structure, compositions, and transport properties of laser-produced aerosols as potential sources of elemental fractionation is summarized and discussed. Subsequently, an update on the latest activities carried out in the research group for Trace Element and Microanalysis at ETH Zurich (Switzerland) is given.

### Chronology and milestones of aerosol research in LA–ICP–MS – A summary

The first evidence for material losses during the transport period of laser-produced aerosols was already reported in 1985 by Gray, who found a significant amount of debris deposited around the

Mineralogical Association of Canada Short Course 40, Vancouver, B.C., p. 19–34.

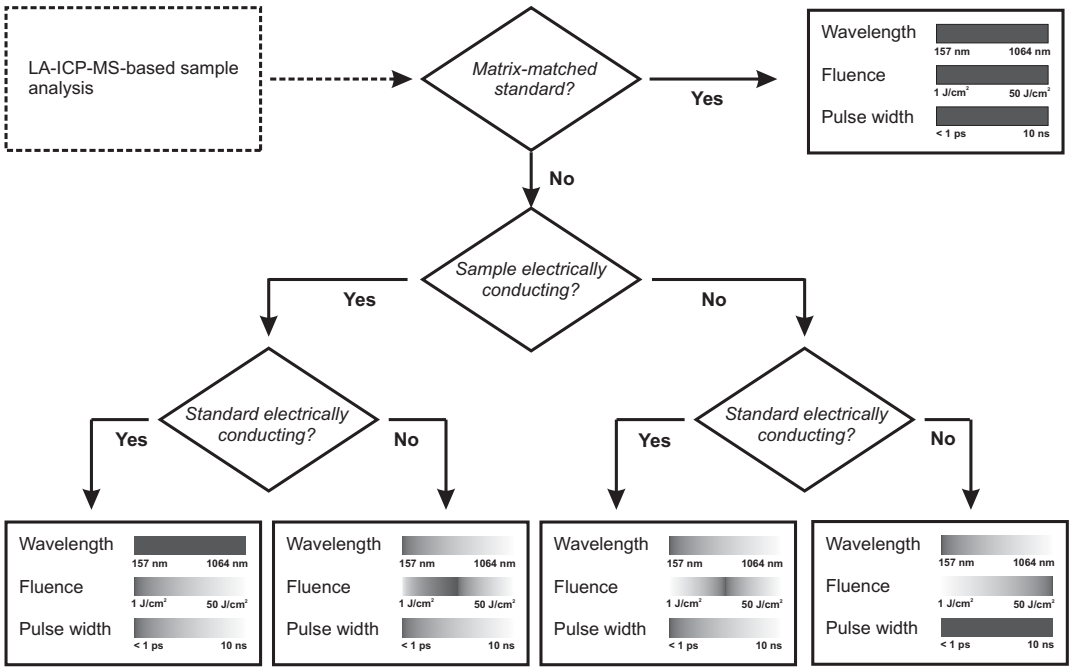


FIG. 2-1 Interaction and optimization scheme for the most influential parameters in LA–ICP–MS analyses for quantitative analysis. The intensity of the grey shading for wavelength, pulse width and fluence indicate increasing performance. Dark grey indicates no significant influence. However, UV-fs will always increase the performance with respect to precision and accuracy.

rim of ablation craters, indicating that the mass carried to the ICP is smaller than that initially ablated. At that time, LA–ICP–MS analyses were predominantly accomplished using near-infrared (NIR) nanosecond (ns) laser sources and Ar as the carrier gas. In 1988, the transport efficiency of laser-produced aerosols was measured by Arrowsmith & Hughes (1988) who determined a value of approximately 40% for Mo particles. The authors, furthermore, modeled the transport efficiency as a function of the primary particle size distribution, taking into account diffusional, gravitational, and inertial losses. It was shown that particles below 0.01 µm and above a few micrometres are subject to pronounced losses when transported over distances larger than one metre. The structure and shape of these particles were measured by Chenery *et al.* (1992) and Thompson *et al.* (1990) using scanning electron microscopy (SEM). These studies revealed (i) a strong dependence between the size distribution and the material analyzed, and, (ii) a selective transport of particles < 10 µm in diameter.

Shortly after, a series of experiments on the influence of different laser wavelengths with respect to the performance characteristics of LA–ICP–MS was carried out (Jeffries *et al.* 1995, 1996), followed by the first characterization of elemental behavior during fractionation published by Fryer *et al.* (1995). In this paper, elemental fractionation indices were defined on the basis of temporal changes in Ca-normalized responses over two equal parts of an acquired signal. Retrospectively, this is probably not the most robust indicator since the absence of any changes in relative responses does not necessarily imply that accurate analyses will be obtained (Guillong & Günther 2002, Günther 2002). Figg & Kahr (1997) and Alexander *et al.* (1998) pointed out the important role that particle size distributions play in the context of elemental fractionation. They furthermore assumed that a considerable portion of particles settles during the transport period and/or might not completely vaporize inside the ICP. However, most of the results presented were based on ICP–MS responses only, a monitor that already incorporates all contributing sources of fractionation namely aerosol generation, aerosol transport, vaporization, and ionization in the ICP. This made a distinction of the relative importance of laser-, transport-, and ICP-induced elemental fractionation impossible. By contrast, Outridge *et al.* (1996, 1997) analyzed aerosol particles produced by NIR–ns–LA which were filtered at different positions within the

transport system allowing the authors to separate laser- and transport-induced effects. This work showed that the laser-generated aerosols become enriched in volatile elements, especially when significant heat transfer into the sample takes place.

In 1998, Eggins *et al.* (1998) proposed the use of He as the in-cell carrier gas to reduce the amount of debris around the crater rim and thus to increase the sensitivity by a factor of approximately five. Based on these findings, paradigms have changed and researchers have been refocusing on the investigation of particle size distributions, aerosol compositions, and transport efficiencies since it became obvious that conclusions previously drawn using Ar as carrier gas could not be transferred directly to the observations made for He (Günther & Heinrich 1999a). In addition, the implementation of excimer lasers that emit in the deep UV spectral range with a 193 nm wavelength raised the question of the most suitable wavelength for LA–ICP–MS again. As a consequence, a number of comparative measurements have been made by, for example Liu *et al.* (2000), Russo *et al.* (2000), Jeffries *et al.* (1996) and Günther & Heinrich (1999b). Unfortunately, most of these comparisons must be considered inconclusive, since more than one laser or operating parameter was varied during the experimental work. Furthermore, the mass of material introduced into the ICP–MS changed significantly. However, some advantages of using shorter wavelengths have been demonstrated. For example, Jeffries *et al.* (1998) demonstrated that the risk of crack formation or catastrophic material removal during LA of highly transparent materials such as calcite can be minimized at wavelengths shorter than 266 nm. Similar improvements have also been observed when using a 193 nm (Günther *et al.* 1997) or a 157 nm (Telouk *et al.* 2003) laser for ablation.

In 2001, a first experimental indication for incomplete vaporization of refractory (oxide-forming species) particles inside the ICP was given by Horn *et al.* (2001) who analyzed various, differently absorbing silicate glasses. It was shown that LA of the most transparent glass gave lower sensitivities of the main constituents Si, Ca *etc.*, even though their ablation rate was higher than those found for the more opaque glasses. In addition, it was shown that the U/Th signal ratio during the analysis of silicate glass aerosols was dependent on the upper cut-off size of the particle size distributions which was attributed to an incomplete vaporization of larger particles. The cut-off size was varied by filtering aerosols prior to their entry into the ICP using mineral wool (Guillong & Günther 2002). One year later, Aeschliman *et al.* (2003) photographed trajectories of Y-rich particles passing through and even beyond the ICP. This provided visual evidence for the existence of a critical particle size for complete vaporization. At the same time, Guillong *et al.* (Guillong *et al.* 2003) published a study on the particle size distribution of aerosols generated using different wavelengths. For the first time, LA–ICP–MS was performed using an optical parametric oscillator (OPO, Horn *et al.* 2003), which allowed use of the three most widely employed wavelengths, 266 nm (Nd:YAG 4$^{th}$ harmonic), 213 nm (Nd:YAG 5$^{th}$ harmonic), and 193 nm (ArF) without otherwise changing the beam properties, *i.e.*, diameter and intensity profile and constant ICP–MS operating conditions. It was shown that the amount of larger, micrometre-sized particles generated, as well as the mean particle size of aerosols produced by LA of transparent silicate glasses decreases with shorter wavelength from 266 nm to 193 nm. This effect is barely observable for opaque materials. On the basis of optical particle counting (OPC), mean particle diameters of 5 nm to 25 nm were measured which is consistent with data reported by Kuhn *et al.* (2005) and Košler *et al.* (2005).

Despite the abovementioned drawbacks originating from elemental fractionation, LA–ICP–MS using nanosecond laser radiation has been successfully applied to the elemental and isotopic analysis of various non-conducting materials such as silicate glasses and minerals (Jackson *et al.* 1992, Gao *et al.* 2002, Yuan *et al.* 2004, Jackson *et al.* 2004, Jochum *et al.* 2005, Jochum *et al.* 2006 a, b, Jochum *et al.* 2007). For metals and semi-conductors, however, elemental and isotope ratio determinations turned out to be extremely demanding since the formation of a far-reaching heat-affected zone provokes material re-distribution during the ablation process (Bleiner & Grasser 2004, Bleiner 2005, Bleiner *et al.* 2007). Thus, the total composition of aerosols released by ns–LA may deviate considerably from the bulk value if fractionation-prone matrices such as metal alloys are analyzed (Outridge 1996, Outridge 1997, Kuhn & Günther 2003, Jackson & Günther 2003, Liu *et al.* 2004, Kuhn *et al.* 2006,). To suppress the occurrence of these effects and approach the "ideal" conditions of stoichiometric LA, Margetic *et al.* (2000) introduced and demonstrated some advantages of femtosecond (fs) pulse width laser

sources. Over the last ten years, fs–LA as a way to create stoichiometric aerosols has been proven in several studies dealing with the compositional analysis of impacted or size-classified material (Koch *et al.* 2004, 2005, 2006, Perdian *et al.* 2008a, b). It was demonstrated, that the application of NIR–fs pulses permits creation of aerosols consisting mainly of particles within the so-called mesoscopic size range (~10 nm up to ~100 nm) that can be transported efficiently over large distances (Arrowsmith & Hughes 1988) and the overall composition of which exactly matches that of the sample if LA settings such as wavelength, fluence, and type of carrier gas are chosen properly.

In 2007 and 2008, the transport efficiency of such aerosols was measured by Garcia *et al.* (2007, 2008) using low pressure impaction and pre- and post-ablation sample weighing. Values of up to 90% were reported which, furthermore, were independent of carrier gas, gas flow fields, and cell volume, which is in agreement to experimental cell studies (Bleiner & Günther 2001) but appears to be in contrast to data recently given by Bleiner & Chen (2008). However, efficiencies were measured without correcting for material deposited around the crater which, although often negligible for LA in a He atmosphere, cannot be disregarded if heavier carrier gases such as Ar are used. Consequently, the procedure described by Garcia (2007) does not allow determination of the transport efficiency according to its original meaning, that is the ratio of transported and ablated mass unless deposition can be excluded completely. Therefore, relative fraction of debris accumulating in an Ar atmosphere was also measured and found to be larger than 30% for ultraviolet (UV)–fs–LA applying moderate fluences of < 10 J/cm$^2$ (Garcia *et al.* 2008).

In order to learn more about the nature of particle dispersion during the transport period and the initial stages of LA (≤ 1 ms), from 2002 on, aerosols have been visualized by various techniques including light scattering and shadowgraphic imaging. For example, Russo *et al.* (1999) studied the expansion of non-condensed vapor immediately after the ablation event whereas Hirata *et al.* (2007) monitored the particulate phase, *i.e.*, condensed particles. Lately, a series of three articles dealing with the visualization of aerosols (i) expanding under Ar and He atmosphere (ii) striking the inner wall of ablation cells and (iii) moving through a transport tube towards the ICP was published by Koch *et al.* (2007, 2008a, b).

**Visualization of LA aerosols – Part I: Expansion patterns and wall reactions**

In the literature on the fundamentals of LA, several mechanisms underlying the formation of laser-produced aerosols such as condensational growth, phase explosion, and critical point phase separation have been discussed (Yoo *et al.* 2001, Hergenröder 2006a, b, c). Although no direct evidence has yet been reported, condensation of supersaturated vapor to particles is generally considered the most important mechanism for ns– as well as fs–LA. However, the mean diameter of particles grown from supersaturated vapor must be restricted to a few tens of nanometres.

In fact, the mean diameter of particle size distributions found is well below 100 nm, implying that nucleation and condensation are the dominant mechanisms since there is no other process known resulting in the formation of nano-sized particles only. However, for bimodal particle size distributions covering a range from 10 nm up to 1 µm as, for example shown in Figure 2-2, a different or at least coexistent mechanism has to be taken into account since particles significantly larger than 100 nm cannot be formed by condensation due to the high cooling rate of the expanding plasma which is in the range of $10^{10}$–$10^{11}$ K/s (Luk'yanchuk *et al.* 1998). Coexisting processes, that can result in the formation of micro-sized particles are, for instance, hydrodynamic instabilities or phase explosion (Yoo *et al.* 2001), *i.e.*, the explosive-like relaxation of a supercritical liquid which could act as a single source for both smaller and larger particles since it produces a mixture of droplets and vapor. It should be stressed that particles originating from condensational growth tend to form larger aggregates in the course of LA because of collisions, as can be seen in Figure 2-3 (Kuhn *et al.* 2005). From an analytical point of view, however, the formation of those aggregates proves favorable since it reduces potential diffusion losses during the transport period. Further information on the aggregation state of laser-produced aerosols can be found in Kuhn *et al.* (2004a, 2005) and Koch *et al.* (2004, 2005).

To visualize particles released by LA, shadowgraphic techniques have most commonly been utilized (Yoo *et al.* 2001, Hirata & Miyazaki 2007). In particular, the implementation of laser-based set-ups offers unique features including high temporal resolution or the possibility of monitoring any event that changes the refractive index such as shockwaves or density fluctuations of the expanding

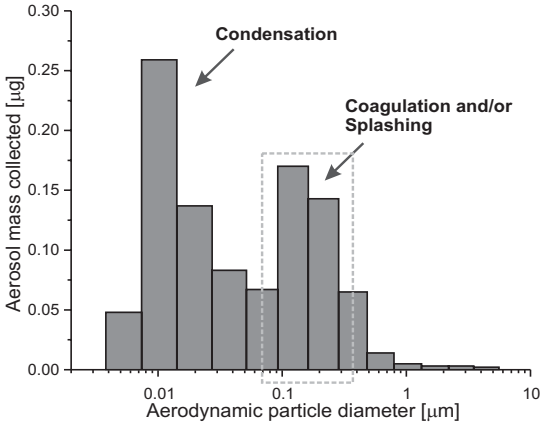


FIG. 2-2 Typical particle size distributions of an aerosol generated by UV–fs–LA of brass. The bimodal structure suggests the existence of, at least, two independent mechanisms such as condensational growth and hydrodynamic instabilities, *i.e.*, splashing which control the aerosol formation

material. However, the contrast achievable by shadowgraphy strongly decreases for less dense structures. It is, thus, inappropriate for observing dispersed nanoparticles and aggregates which represent the dominant part of aerosols formed. Moreover, depth resolution is missing since shadowgraphic imaging is a line-of-sight measurement. In comparison, laser scattering offers the best possible contrast and a depth resolution given by the thickness of the light sheet passing through the volume monitored.

The optical layout and trigger scheme is shown in Figure 2-4. Both, ns and fs pulses of 1.5–2.0 mJ output energy and 10 ns or 150 fs duration, respectively, were generated by a Ti:Sapphire chirped pulse amplification (CPA) laser system emitting at a wavelength of 795 nm (Legend, Coherent Inc., Santa Clara, Ca, USA). A pulsed, frequency-doubled, and vertically polarized Nd:YAG laser (Minilite PIV, Continuum, Santa Clara, CA, USA) was employed as a light source for the scattering set-up providing temporal resolution of 5 ns. The utilization of vertically polarized laser radiation enabled to simultaneously access to the Rayleigh ($d < 0.05 \cdot \lambda$), Debye ($0.05 \cdot \lambda < d < \lambda$), and Mie ($d > 0.05 \cdot \lambda$) particle size ranges. Light scattered towards the observation camera, therefore, originated from particles sizes covering the entire spectrum generated by LA.

In the left panel of Figure 2-5, the progressive expansion of aerosols generated by NIR ns-LA of brass using Ar is shown. As can be seen, aerosols were captured in a laterally moving vortex ring due to the formation of a dense plasma right above the target surface. In addition, particles remained confined within a volume of approximately 0.01 $cm^3$. Taking into account a mass removal of 1–10 ng/shot and a mean particle size of 100 nm, this value corresponds to a number density of $2 \times 10^{13}$–$2 \times 10^{14}$ $cm^{-3}$, which yields a particle collision frequency of $10^4$–$10^5$ Hz if a temperature of 300 K is assumed. Therefore, NIR–ns–LA applying Ar as aerosol carrier has to be regarded as a most unfavorable configuration for suppressing the formation of larger particles since aerosols produced this way are subject to pronounced coalescence and aggregation of liquid and already solidified droplets, respectively. These findings are in agreement with the increased production of micrometer particles, recently observed for NIR–

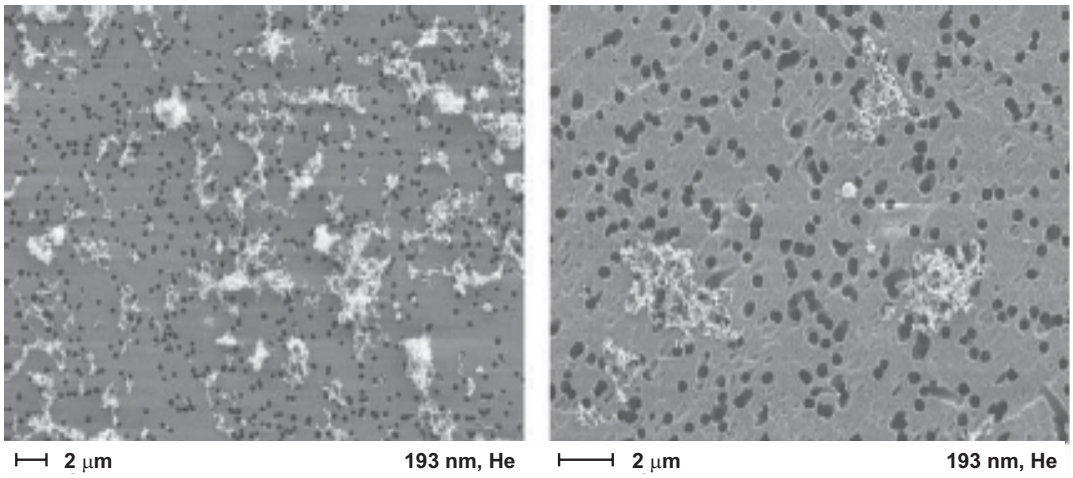


FIG. 2-3 Scanning electron micrograph of both primary particles and larger aggregates filtered during UV–ns–LA of $CaF_2$ (with kind permission of Springer Science+Business Media).

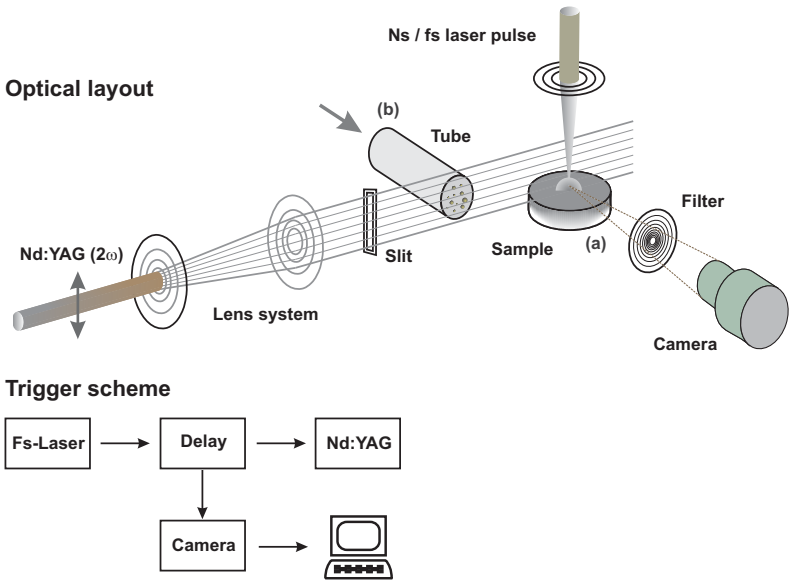


FIG. 2-4 Optical layout and trigger scheme used for the visualization of aerosols during their initial stage of expansion (**a**) and transport period (**b**).

ns–LA carried out using similar experimental conditions.

In fact, the expansion dynamics of aerosols released in an Ar atmosphere was found to be comparatively slow whereas the degree of aerosol dispersion for NIR–ns–LA, for example, using He drastically increased as a result of its lower viscosity and the absence of any plasma shielding which is an inherent feature of fs–LA. Therefore, the range of maximum expansion (*i.e.*, stopping distance) differed by a factor of approximately four, as can be seen in the right panel of Figure 2-5. Initial aerosol velocities calculated from expansion plots acquired at early delay times amounted to 30 m/s. Please note, that the expansion patterns shown in Figure 2-5 were captured for different carrier gases as well as pulse widths, thus, representing end member cases of LA.

Because of the high initial velocity of aerosols released in a He atmosphere, the inner walls of ablation cells are obviously exposed to a continuous flow of particles if their dimensions are smaller than the corresponding lateral or vertical stopping distances, which, at first glance suggests that severe deposition of material is likely. In Figure 2-6, the hydrodynamic motion of aerosol particles striking a solid boundary is shown. Apparently, the aerosol rapidly expands during the initial stage of the ablation process. Right after striking the boundary, particles form a small vortex which propagates along the boundary surface with a mean velocity of approximately 0.5 m/s. During further expansion, the vortex slows down and, eventually, reaches a stopping distance of about 20 mm. At this stage, the vortex has grown to a diameter of 3 mm due to centripetal forces.

To determine the relative amount of aerosol mass adsorbed under those conditions, a cleaned glass substrate was mounted 10 mm above the brass target, *i.e.*, far below the aerosol stopping distance expected for the LA conditions chosen. Fluence and repetition rate were set to 10 J/cm$^2$ and 10 Hz, respectively. The laser radiation (800 nm wavelength, 150 fs pulse duration) beam was delivered right through the glass substrate. During LA, the cell was flushed with He at a flow rate of 1.0 L/min. The transported aerosol fraction was filtered through a polycarbonate membrane attached to the outlet of the ablation cell. Particles deposited on both the membrane and glass substrate were dissolved in nitric acid and quantified by solution nebulization (SN)–ICP–MS. The results are summarized in Table 2-1 and indicate an adsorption efficiency of around 1 % which is in agreement with the minor degree of cell contamination usually found for LA at atmospheric pressures. Furthermore, the mean composition of deposited and transported particles differed by less than 3% and suggested a slightly higher adsorption of smaller, Zn-enriched aggregates. Nevertheless, compositional changes of transported *versus* total mass were smaller than 0.5%, as can be derived from Table 2-1.

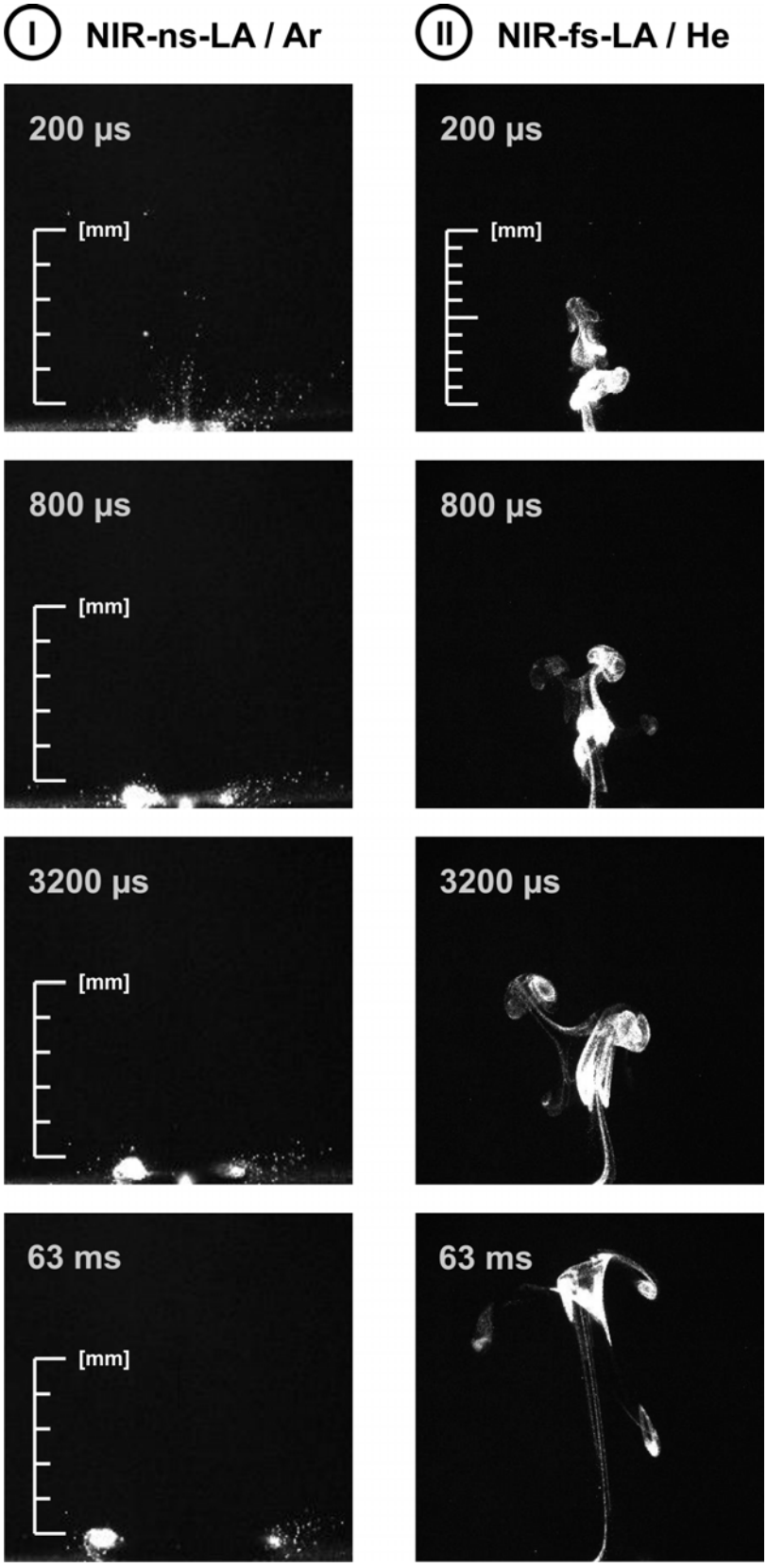


FIG. 2-5 Expansion patterns of aerosols generated by NIR ns– and NIR–fs–LA of brass in a quiescent Ar and He atmosphere, respectively (with kind permission of Elsevier Limited).

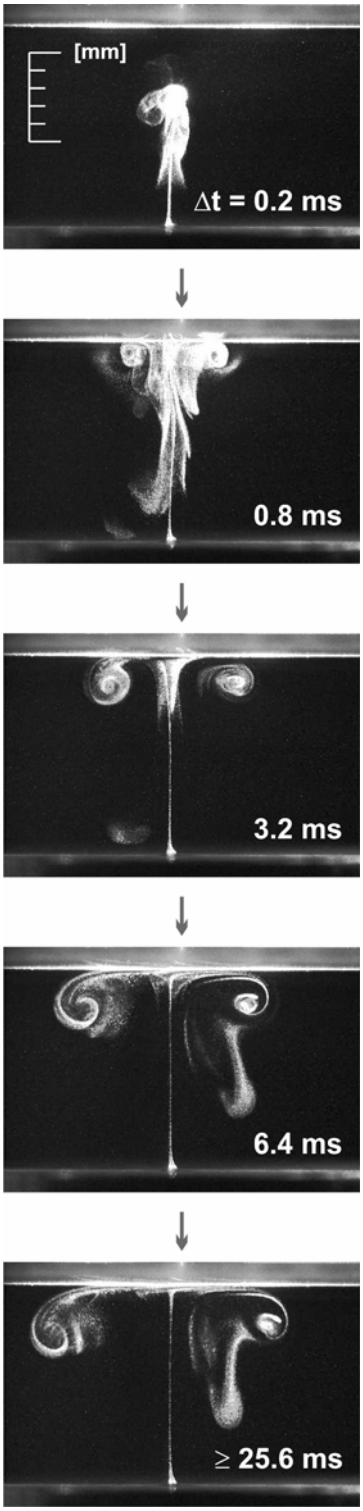


FIG. 2-6 Hydrodynamic motion of aerosol particles striking a solid boundary in a stationary He atmosphere (with kind permission of Elsevier Limited).

**Visualization of LA aerosols – Part II: Aerosol structures and transport efficiencies**

The expansion patterns shown in Figures 2-5 and 2-6 suggest that aerosols generated by LA at atmospheric pressures consist only of very few dispersed particles while most of the aerosol mass remains confined within cohesive, string-like aggregates. The overall dispersion can, thus, be understood as a mixture of kinetic expansion originating from the LA process itself and diffusional dispersion occurring shortly after. Assuming that He is used as the carrier gas and particle sizes of ≤ 50 nm the diffusion rate amounts to < 100 µm/s which means that aerosol aggregates cannot break up on their way to the ICP if no dispersive elements such as nozzles are inserted into the transport system (Pisonero *et al.* 2006).

In the upper part of Figure 2-7, aerosol dispersion is shown for the lateral cross-section of a transport tube attached to the outlet of a cylindrical ablation cell carrying a laminar flow of He at 1.0 L/min. Apparently an almost stationary but anisotropic dispersion pattern was formed. Furthermore, the aerosol appears to be separated into two phases consisting of dispersed particles which accumulate at the boundary layer of several vortex channels and larger aggregates moving inside. The formation of these phases is, most probably, due to the above mentioned heterogeneity (dispersed particles and string-like aggregates) of aerosols. Note, that both phases hardly reach certain regions of the cross section, which are highlighted by the white circles in Figure 2-7.

Inserting a 0.5 mm wide nozzle into the inlet of the ablation cell raised the kinetic energy of the flow field by a factor of approx. 200 and resulted in a stronger degree of aerosol homogenization. A sequence of three consecutive frames, shown in the lower part of Figure 2-7 reveals particles to be almost uniformly dispersed over the entire cross section. However, the occurrence of aerosol aggregates and blank regions could not be suppressed completely, as can be seen in the middle frame[1]. To illustrate the differences between laminar in-cell flow with and without an inlet nozzle, the respective velocity fields simulated by computational fluid dynamics (CFD, Software package: ANSYS CFX 11, Berlin, Germany) are shown in Figure 2-8.

[1] Compared to this, aerosol transportation under Ar atmosphere led to a complete dispersion provided that the flow rate was set to values larger than 0.5 L/min. For further details please refer to (Koch *et al.* 2007).

TABLE 2-1. ZN- AND CU-SPECIFIC ANALYSIS GENERATED BY FS-LA OF BRASS

| | **Deposited fraction** | | **Transported fraction** | |
|---|---|---|---|---|
| | Cu [%] | Zn [%] | Cu [%] | Zn [%] |
| **Mass** | 0.99 ± 0.14 | 1.16 ± 0.21 | 99.0 ± 0.14 | 98.8 ± 0.21 |
| **Composition** | 57.3 ± 3.50 | 42.7 ± 3.50 | 60.9 ± 0.90 | 39.1 ± 0.90 |

Results from the Zn- and Cu-specific analysis of a glass substrate exposed to an aerosol generated by repetitive fs-LA of brass under He atmosphere and a polycarbonate membrane used to filter out the transported aerosol fraction. The total composition of the aerosol was calculated from both deposited and transported mass fractions and amounted to Cu : Zn = 60.9 : 39.1 (Certified value: Cu : Zn = 61.2 : 37.7)

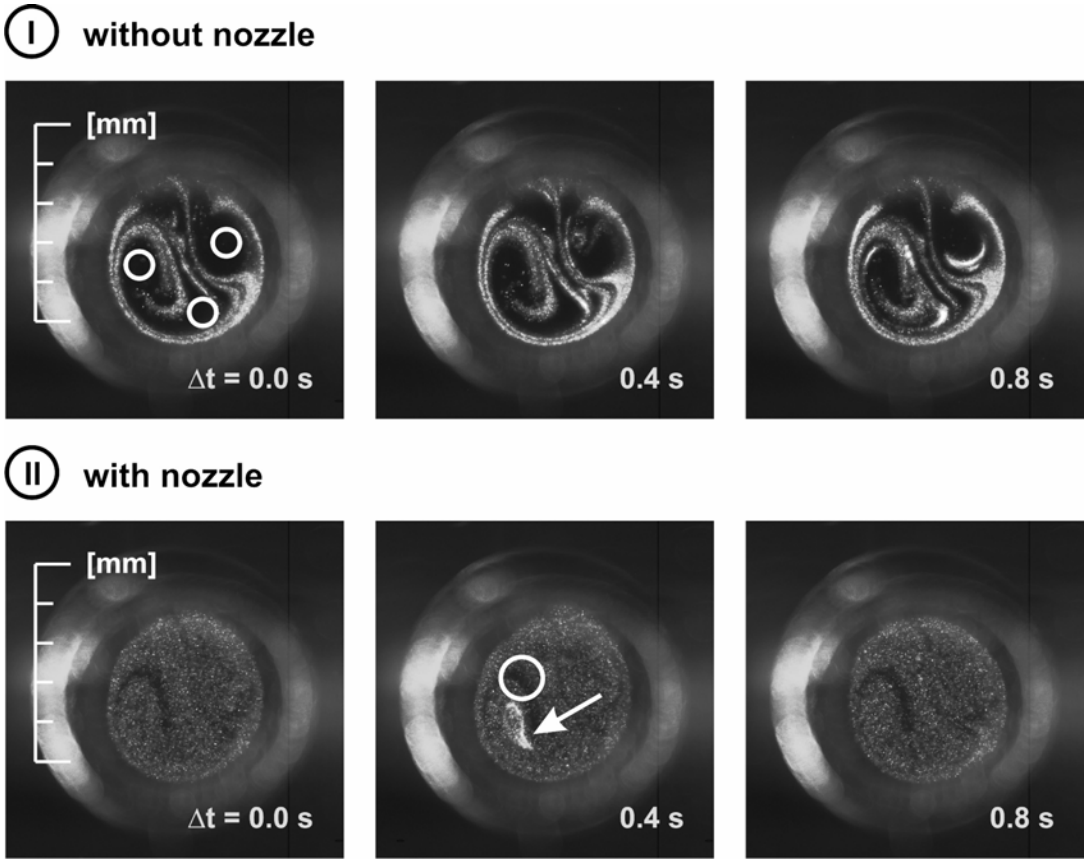


FIG. 2-7 Aerosol dispersion visualized over the cross section of a transport tube attached to the outlet of an ablation cell applying a flow rate of 1.0 L/min He and inlet diameters of 2.0 mm (without nozzle) and 0.5 mm (with nozzle).

According to Koch *et al.* (2007), the transport and entrainment of large aerosol aggregates as shown in Figure 2-8 may account for drastic density and temperature fluctuations inside the ICP during analysis, which probably changes signal intensities and their ratios. Therefore, their influence on signal stability, precision, and accuracy of ICP–MS analyses was examined. For this purpose, aerosols were generated by LA of silicate glass applying the same conditions used above. The Si signal is exemplarily shown in Figure 2-9. As expected, the application of laminar in-cell flow without an inlet nozzle yielded noisy signals due to aerosol aggregates randomly reaching the ICP (Koch *et al.* 2008a). Changing the in-cell flow mode by inserting the nozzle led to smoother signals as a result of disintegration of large aggregates into smaller ones. Nevertheless, the majority of element:Ca ratios were nearly unaffected, as can be seen in Figure 2-10. Most major and trace elements were subject to deviations of less than 2.5 %. In contrast Si, Zn, and Cd experienced pronounced shifts of approximately 3–5% due to a delayed evaporation of larger aggregates suppressing diffusion losses inside the

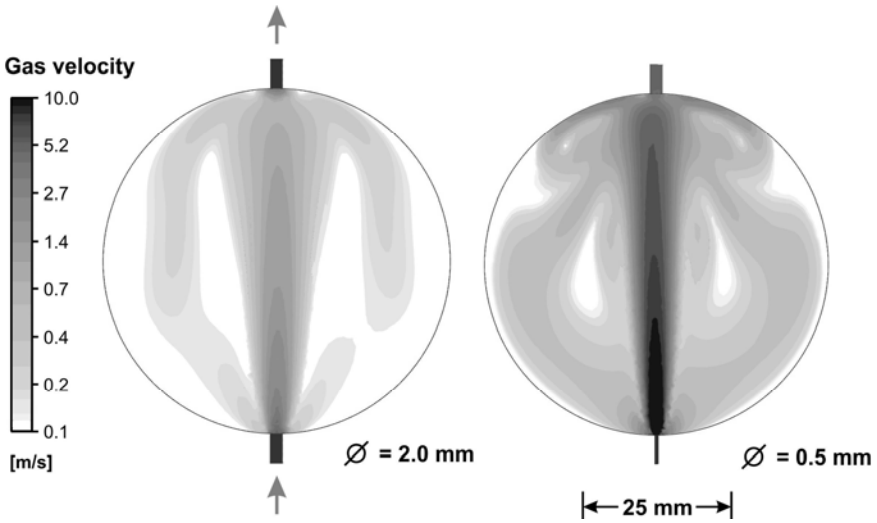


FIG. 2-8 Simulation of the velocity field built up inside the ablation cell used (radius: 22.5 mm, height: 20 mm) assuming inlet diameters of 2.0 mm (without nozzle) and 0.5 mm (with nozzle) and a flow rate of 1.0 L/min He.

ICP when applying laminar in-cell flow. After entering the ICP primary nano-particles, the aggregates are composed of, will melt, most likely coagulate, and form larger particles. Such particles would expose a smaller contact surface to the ICP compared to the initial aggregate. Therefore, the position for complete evaporation of volatile compounds, which is known to depend on the size and composition of aerosol aggregates, might be axially shifted using laminar flow.

The existence of stoichiometric aerosols as demonstrated by the data shown in Table 2-1 already suggests particulate losses during the transport period to be minor. Nevertheless, the transport efficiency of laser-produced aerosols was recently measured by low pressure impaction and pre- and post-LA target weighing to support this assumption. For this, UV–fs–LA of a brass target was performed in both He and argon atmospheres using the same ablation cell as shown in Figure 2-8. Throughout this study, transport efficiencies were calculated on the basis of two independent measurements. For analysis the collected particles were dissolved in nitric acid and subsequently quantified by SN-ICP-MS, as described above. Even though the number of experimental runs does not represent a statistically meaningful sample, the overall uncertainty was calculated from their relative standard variation plus a residual contribution originating from unknown losses inside the impactor, which altogether were assumed to be 10%.

Table 2-2 lists transport efficiencies determined with argon and He as the aerosol carrier and applying laminar flow with and without an inlet nozzle. As can be seen, values ranged from around 85% up to 95% which indicate only marginal losses for argon as well as He taking into consideration the experimental uncertainty specified. It should be emphasized that the transport efficiencies specified in Table 2-2 do not account for debris around the crater rim, as already discussed above. To correct the mass balance for debris, in addition, LA of a certified, 5 µm (+/– 5%) thick Cr layer (Kocour, Chicago (IL), USA) was performed in an argon atmosphere. This enabled release of a well defined aerosol mass, given by crater diameter, layer thickness, and Cr bulk density, thus making a discrimination of transport and cell extraction efficiency possible. In this way, a deficit of 35% between crater and transported mass was measured.

Assuming the degree of surface deposition for brass and Cr particles to be similar and losses arising from aerosol wall reactions to be negligible (see above), the actual transport efficiency, *i.e.*, the ratio of collected to ablated mass amounts to 55% up to 65%. It should, however, be stressed that the amount of debris is strongly dependent on the LA conditions (fluence, wavelength, gas pressure, *etc*.) as well as geometric issues involving the relative focus position and crater size. The value given should, therefore, not be treated as a reference valid for all LA configurations.

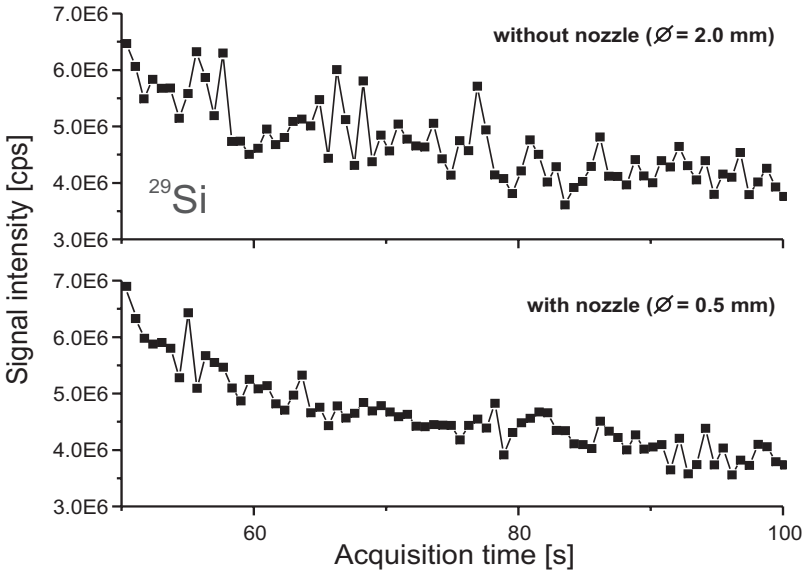


FIG. 2-9 The ICP–MS response for Si measured during NIR–fs–LA of silicate glass with and without the utilization of a 0.5 mm wide inlet nozzle.

**CONCLUSION**

The history and achievements of aerosol research with respect to LA–ICP–MS was reviewed and discussed. Moreover, a progress report on current research activities dealing with the visualization and compositional analysis of laser-produced aerosols was given. In this context, specific expansion and transport phenomena of aerosols generated by ns– and fs–LA of brass and silicate glass using He and Ar as carrier gases were investigated. It could, for example, be shown that aerosols form symmetric vortices when striking a solid boundary during their kinetic stage of expansion. The amount of material adsorbed under such conditions fell below 1%. Furthermore, the mean composition of adsorbed and transported brass particles differed by less than 3% and suggested a slightly higher adsorption of smaller,

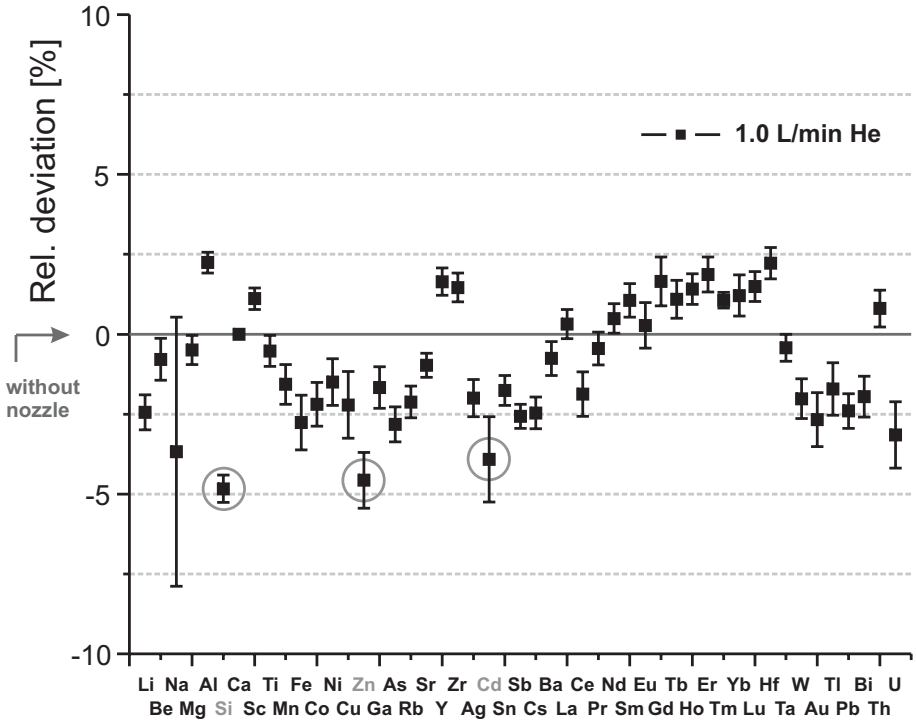


FIG. 2-10. Changes of Ca-normalized ICP–MS responses after inserting a 0.5 mm wide nozzle in the inlet of the ablation cell. The data points of most critical elements (Si, Zn, and Cd) are highlighted by circles. Please note, that the changes plotted do not necessarily suggest a minor or stronger degree of elemental fractionation when performing matrix or non-matrix matched analyses (see text).

TABLE 2-2 TRANSPORT EFFICIENCIES OF BRASS AEROSOLS GENERATED BY UV–FS–LA UNDER AR AND HE ATMOSPHERE APPLYING LAMINAR AND TURBULENT IN-CELL FLOW CONDITIONS.

| ***Helium*** | *Cu [%]** | *Zn [%]** | *Total [%]* |
|---|---|---|---|
| laminar | 62.8 ± 1.6 | 35.6 ± 1.0 | 92.0 ± 5.0 |
| turbulent | 62.8 ± 1.6 | 36.2 ± 1.0 | 89.0 ± 5.0 |
| **Argon** | | | |
| laminar | 66.7 ± 1.6 | 31.9 ± 1.0 | 92.0 ± 5.0 |
| **turbulent** | 65.4 ± 1.6 | 34.2 ± 1.0 | 88.0 ± 5.0 |

Reference value Cu : Zn = 61.2 : 37.3. Values given in the first two columns refer to the main constituents Cu and Zn whereas the total transport efficiency (third column) was calculated on the basis of Cu-, Zn-, Pb-, and Sn-specific aerosol masses. Note, that transport efficiencies given were not corrected for debris re-deposited on the sample surface (see text).

Zn-enriched aggregates. In contrast, the overall composition of transported particles matched the target material to within 99.5% and indicates minor material losses during the transport period. In fact, the transport efficiency measured by low pressure impaction and pre- and post-LA target weighing was found to be almost complete when disregarding the mass precipitated around the crater rim (which appears to be inherent to LA at atmospheric pressures). Depending on the in-cell flow conditions and carrier gas chosen, values varied in between 85% and 95% implying that elemental fractionation as a result of material deposition can only happen if, for instance, unrealistic small ablation cells are used which have dimensions that fall below the stopping distance of laser-induced plasmas. In such cases, reactive matter such as uncondensed vapor and small clusters reach the walls which gives rise to severe deposition.

In addition, aerosols were visualized over the cross-section of a transport tube attached to the outlet of an ablation cell. For instance, LA applying low speed in-cell flow and He as carrier resulted in stationary but anisotropic dispersion patterns. Aerosols were separated into two coexisting phases consisting of dispersed particles which accumulate at the boundary layer of several channel flows arranged along the tube axis and large aggregates moving inside. However, inserting a 0.5 mm wide nozzle in the inlet of the ablation cell flow made these channels disappear and lead to an almost homogeneous dispersion pattern due to the build-up of a high speed, quasi-turbulent in-cell flow. Furthermore, the absence of large aerosol aggregates enhanced the signal statistics, *i.e.*, precision and altered the Ca-normalized ICP–MS responses for Si, Zn, and Cd during LA of silicate glass by approximately 5%. This, most probably, arose from higher diffusion losses of these elements in the ICP. However, this finding does not allow us to predict whether a better accuracy will be achieved for LA–ICP–MS analyses using non-matrix matched calibration, an issue future investigations have to reveal. At the present stage, it only demonstrates the important role of the aerosol structure and that the degree of particle dispersion might be the key parameter for improving the precision of analysis.

## ACKNOWLEDGEMENTS

The research was financially supported by ETH Zurich and Swiss National Science Foundation. The authors would like furthermore to thank Rolf Dietiker and Markus Wälle for substantial contributions to numerical simulations and transport efficiency measurements, respectively. Comments made by Davide Bleiner helped to improve the manuscript.

## REFERENCES

AESCHLIMAN, D.B., BAJIC, S.J., BALDWIN, D.P. & HOUK, R.S. (2003): High speed digital photographic study of an inductively coupled plasma during laser ablation: comparison of dried solution aerosols from a microconcentric nebulizer and solid particles from laser ablation. *J. Analyt. Atom. Spectrom.* **18**, 1008-1014.

ALEXANDER, M.L., SMITH, M.R., HATMAN, J.S., MENDOZA, A. & KOPPENAAL, D.W. (1998): Laser ablation inductively coupled plasma mass spectrometry. *Appl. Surf. Sci.* **127-129**, 255-261.

ARROWSMITH, P. & HUGHES, S.K. (1988): Entrainment and transport of laser ablated plumes for subsequent elemental analysis. *Appl. Spectrosc.* **42**, 1231-1239.

BECKER, J.S., PICKHARDT, C. & DIETZE, H.J. (2000a): Laser ablation inductively coupled

plasma mass spectrometry for determination of trace elements in geological glasses. *Mikrochim. Acta* **135**, 7180.

BECKER, J.S. & DIETZE, H.J. (2000b): Inorganic mass spectrometric methods for trace, ultratrace, isotope, and surface analysis. *Int. J. Mass Spectrom.* **197**, 1-35.

BECKER, J.S. (2002): Applications of inductively coupled plasma mass spectrometry and laser ablation inductively coupled plasma mass spectrometry in materials science. *Spectrochim. Acta B* **57**, 1805-1820.

BLEINER, D. (2005): Mathematical modelling of laser induced particulate formation in direct solid microanalysis. *Spectrochim. Acta B* **60**, 49-64.

BLEINER, D & CHEN, Z. (2008): Computer modeling of laser ablation elemental microanalysis. *In* Laser Ablation ICP–MS in the Earth Sciences: Current Practices and Outstanding Issues (P. Sylvester, *ed*.). *Mineral. Assoc. Can. Short Course Series* **40**, 35-52.

BLEINER, D. & GASSER, P. (2004): Structural features of laser ablation particulate from Si target, as revealed by focused ion beam technology. *Appl. Phys. A Mater.* **79**, 1019-1022.

BLEINER, D. & GÜNTHER, D. (2001) Theoretical Description and Experimental Observation of Aerosol Transport Processes in Laser Ablation Inductively Coupled Plasma Mass Spectrometry. *J. Analyt. Atom. Spectrom.* **16**, 449-456

BLEINER, D., BOGAERTS, A., BELLONI, F. & NASSISI, V. (2007): Laser induced plasmas from the ablation of metallic targets: The problem of the onset temperature, and insights on the expansion dynamics. *J. Appl. Phys*. **101**, 83301-1-5.

BORISOV, O.V., MAO, X.L. & RUSSO, R.E. (2000): Effects of crater development on fractionation and signal intensity during laser ablation inductively coupled plasma mass spectrometry. *Spectrochim. Acta B* **55**, 1693-1704.

CHENERY, S., HUNT, A. & THOMPSON, M. (1992): Laser ablation of minerals and chemical differentiation of the ejecta. *J. Analyt. Atom. Spectrom.* **7**, 647-652.

CROMWELL, E.F. & ARROWSMITH, P. (1995): Fractionation effects in laser ablation inductively couples plasma mass spectrometry. *Appl. Spectrosc.* **49**, 1652-1660.

DURRANT, S.F. (1999): Laser ablation inductively coupled plasma mass spectrometry: achievements, problems, prospects. *J. Analyt. Atom. Spectrom*. **14**, 1385 1403.

EGGINS, S.M., KINSLEY, L.P.J. & SHELLEY, J.M.G. (1998): Deposition and element fractionation processes during atmospheric pressure laser sampling for analysis by ICP MS. *Appl. Surf. Sci.* **129**, 278-286.

FIGG, D. & KAHR, M.S. (1997): Elemental fractionation of glass using laser ablation inductively coupled plasma mass spectrometry. *Appl. Spectrosc.* **51**, 1185-1192.

FRYER, B.J., JACKSON, S.E. & LONGERICH, H.P. (1995): Design, operation and role of the laser ablation microprobe coupled with an inductively coupled plasma mass spectrometer (LAM ICP MS) in the earth sciences. *Can. Mineral.* **33**, 303-312.

GAO, S. GAO, S., LIU, X., YUAN, H., HATTENDORF, B., GÜNTHER, D., CHEN, L. & HU, S. (2002): Determination of forty two major and trace elements in USGS and NIST SRM glasses by laser ablation inductively coupled plasma mass spectrometry. *Geostand. Newsl.* **26**, 181-196.

GARCIA, C.C., LINDNER, H. & NIEMAX, K. (2007): Transport efficiency in femtosecond laser ablation inductively coupled plasma mass spectrometry applying ablation cells with short and long washout times. *Spectrochim. Acta Part B* **62**, 13-19

GARCIA, C.C., WAELLE, M., LINDNER, H., KOCH, J., NIEMAX, K. & GÜNTHER, D. (2008): Femtosecond laser ablation inductively coupled plasma mass spectrometry: Transport efficiencies of aerosols released under argon atmosphere and the importance of the focus position. *Spectrochim. Acta Part B* **63**, 271-276.

GRAY, A.L. (1985): Solid sample introduction by laser ablation for inductively coupled plasma source mass spectrometry. *Analyst* **110**, 551-556.

GUILLONG, M. & GÜNTHER, D. (2002): Effect of particle size distribution on ICP induced elemental fractionation in laser ablation inductively coupled plasma mass spectrometry. *J. Analyt. Atom. Spectrom.* **17**, 831-837.

GUILLONG, M., HORN, I. & GÜNTHER, D. (2003): A comparison of 266 nm, 213 nm and 193 nm produced from a single solid state Nd:YAG laser for laser ablation ICP MS. *J. Analyt. Atom. Spectrom.* **18**, 1224-1230.

GÜNTHER, D. (2002) Laser ablation inductively coupled plasma mass spectrometry. *Anal. Bioanal. Chem.* **372**, 31-32.

GÜNTHER, D. & HEINRICH, C.A. (1999a): Enhanced sensitivity in laser ablation ICP mass spectrometry using helium argon mixtures as aerosol carrier Plenary lecture. *J. Analyt. Atom. Spectrom.* **14**, 1363-1368.

GÜNTHER, D. & HEINRICH, C.A. (1999b): Comparison of the ablation behaviour of 266 nm Nd:YAG and 193 nm ArF excimer lasers for LA ICP MS analysis. *J. Analyt. Atom. Spectrom.* **14**, 1369-1374.

GÜNTHER, D., FRISCHKNECHT, R., HEINRICH, C.A. & KAHLERT, H.-J. (1997): Capabilities of a 193 nm Excimer Laser for Laser Ablation Inductively Coupled Plasma Mass Spectrometry Microanalysis of Geological Materials. *J. Analyt. Atom. Spectrom.* **12**, 939-944.

GÜNTHER, D., JACKSON, S.E. & LONGERICH, H.P. (1999): Laser ablation and arc/spark solid sample introduction into inductively coupled plasma mass spectrometers. *Spectrochim. Acta B* **54**, 381 409.

HERGENRÖDER, R. (2000): A comparison of nanosecond and femtosecond laser induced plasma spectroscopy of brass samples. *Spectrochim. Acta B* **55**, 1771-1785.

HERGENRÖDER, R. (2006a): A model of non congruent laser ablation as a source of fractionation effects in LA ICP MS. *J. Analyt. Atom. Spectrom.* **21**, 505-516.

HERGENRÖDER, R. (2006b): Hydrodynamic sputtering as a possible source for fractionation in LA ICP MS. *J. Analyt. Atom. Spectrom.* **21**, 517-524.

HERGENRÖDER, R. (2006c): A model for the generation of small particles in laser ablation ICP MS. *J. Analyt. Atom. Spectrom.* **21**, 1016 1026.

HIRATA, T. & MIYAZAKI, Z. (2007): High speed camera imaging for laser ablation process: For further reliable elemental analysis using inductively coupled plasma mass spectrometry. *Anal. Chem.* **79**, 147-152.

HORN, I., GUILLONG, M. & GÜNTHER, D. (2001): Wavelength dependent ablation rates for metals and silicate glasses using homogenized laser beam profiles implications for LA ICP MS. *Appl. Surf. Sci.* **182**, 91-102.

HORN, I., GÜNTHER, D. & GUILLONG, M. (2003): Evaluation and design of a solid state 193 nm OPO Nd:YAG laser ablation system. *Spectrochim. Acta B* **58**, 1837-1846.

HORN, I., VON BLANCKENBURG, F., SCHOENBERG, R., STEINHOEFEL, G. & MARKL, G. (2006): In situ iron isotope ratio determination using UV femtosecond laser ablation with application to hydrothermal ore formation processes. *Geochim. Cosmochim. Acta* **70**, 3677-3688.

JACKSON, S.E. & GÜNTHER, D. (2003): The nature and source of laser induced isotopic fractionation in laser ablation-multicollector-inductively coupled plasma-mass spectrometry. *J. Analyt. Atom. Spectrom.*, **18**, 205-212.

JACKSON, S.E., LONGERICH, H.P., DUNNING, G.R. & FRYER, B.J. (1992): The application of laser ablation microprobe; inductively coupled plasma mass spectrometry (LAM ICP MS) to in situ traceelement determinations in minerals. *Can. Mineral.* **30**, Part 4, 1049-1064.

JACKSON, S.E., PEARSON, N.J., GRIFFIN, W.L. & BELOUSOVA, E.A. (2004): The application of laser ablation-inductively coupled plasma-mass spectrometry to in situ U–Pb zircon geochronology. *Chem. Geol.* **211**, 47-69.

JEFFRIES, T.E., PERKINS, W.T. & PEARCE, N.J.G. (1995): Comparisons of infrared and ultraviolet laser probe microanalysis inductively coupled plasma mass spectrometry in mineral analysis. *Analyst* **120**, 1365-1371.

JEFFRIES, T.E., PEARCE, N.G., PERKINS, W.T. & RAITH, A. (1996): Chemical fractionation during infrared and ultraviolet laser ablation inductively coupled plasma mass spectrometry: Implications for mineral microanalysis. *Analyt. Comm.* **33**, 35-39.

JEFFRIES, T.E., JACKSON, S.E. & LONGERICH, H.P. (1998): Application of a frequency quintupled Nd:YAG source ($\lambda$ = 213 nm) for laser ablation inductively coupled plasma mass spectrometric analysis of minerals. *J. Analyt. Atom. Spectrom.* **13**, 935-940.

JOCHUM, K.P., PFANDER, J., WOODHEAD, J.D., WILLBOLD, M., STOLL, B., HERWIG, K., AMINI, M., ABOUCHAMI, W. & HOFMANN, A.W. (2005): MPI–DING glasses: New geological reference materials for in situ Pb isotope analysis. *Geochem. Geophys. Geosyst.* **6**, Q10008.

JOCHUM, K.P., STOLL, B. & HERWIG, K. (2006a): Improved in situ Pb isotope analysis of low Pb

samples by LAICP MS using a solid state 193 nm Nd: YAG laser. *Geochim. Cosmochim. Acta* **70**, A294.

JOCHUM, K.P. & WILLBOLD, M. (2006b): Reference materials in geoanalytical research. Review for 2004 and 2005. *Geostandards and Geoanalytical Research* **30**, 143-156.

JOCHUM, K.P., STOLL, B., HERWIG, K. & WILLBOLD, M. (2007): Validation of LA ICP MS trace element analysis of geological glasses using a new solid state 193 nm Nd:YAG laser and matrix matched calibration. *J. Analyt. Atom. Spectrom.* **22**, 112-121.

KOCH, J., VON BOHLEN, A., HERGENRÖDER, R. & NIEMAX, K. (2004): Particle size distributions and compositions of aerosols produced by near IR femto and nanosecond laser ablation of brass. *J. Analyt. Atom. Spectrom.* **19**, 267-272.

KOCH, J., LINDNER, H., VON BOHLEN, A., HERGENRÖDER, R. & NIEMAX, K. (2005): Elemental fractionation of dielectric aerosols produced by near infrared femtosecond laser ablation of silicate glasses. *J. Analyt. Atom. Spectrom.* **20**, 901-906.

KOCH, J., WÄLLE, M., PISONERO & J., GÜNTHER, D. (2006): Performance characteristics of ultra violet femtosecond laser ablation inductively coupled plasma mass spectrometry at 265 and 200 nm. *J. Analyt. Atom. Spectrom.* **21**, 932-940.

KOCH, J., SCHLAMP, S., ROSGEN, T., FLIEGEL, D. & GÜNTHER, D. (2007): Visualization of aerosol particles generated by near infrared nano and femtosecond laser ablation. *Spectrochimica Acta Part B* **62**, 20-29.

KOCH, J., WÄLLE, M., DIETIKER, R. & GÜNTHER, D. (2008a): Analysis of Laser-Produced Aerosols by Inductively Coupled Plasma Mass Spectrometry: Transport Phenomena and Elemental Fractionation. *Anal. Chem.*, **80,** 915-921.

KOCH, J., WÄLLE, M., SCHLAMP, S., RÖSGEN, T. & GÜNTHER, D. (2008b): Expansion phenomena of aerosols generated by laser ablation under helium and argon atmosphere. *Spectrochim. Acta B* **63**, 37-41.

KOŠLER, J., WIEDENBECK, M., WIRTH, R., HORVORKA, J., SYLVESTER, P. & MIKOVA, J. (2005): Chemical and phase composition of particles produced by laser ablation of silicate glass and zircon implications for elemental fractionation during ICP MS analysis. *J. Analyt. Atom. Spectrom.* **20**, 402-409.

KUHN, H.R. & GÜNTHER, D. (2003): Elemental fractionation studies in laser ablation inductively coupled plasma mass spectrometry on laser induced brass aerosols. *Anal. Chem.* **75**, 747-753.

KUHN, H.R. & GÜNTHER, D. (2004a): Laser ablation ICP MS: particle size dependent elemental composition studies on filter collected and online measured aerosols from glass. *J. Analyt. Atom. Spectrom.* **19**, 1158-1164.

KUHN, H.R. & GÜNTHER, D. (2004b): Size related vaporisation and ionisation of laser induced glass particles in the inductively coupled plasma. *Anal. Bioanal. Chem.* **378**, 1069-1074.

KUHN, H.R. & GÜNTHER, D. (2005): The agglomeration state of nanosecond laser generated aerosol particles entering the ICP. *Anal. Bioanal. Chem.* **383**, 434-441.

KUHN, H.R., GUILLONG, M. & GÜNTHER, D. (2004b): Size related vaporisation and ionisation of laser induced glass particles in the inductively coupled plasma. *Anal. Bioanal. Chem.* **378**, 1069-1074.

KUHN, H.-R., KOCH, J., HERGENRÖDER, R., NIEMAX, K., KALBERER, M., GÜNTHER, D. (2005): Evaluation of different techniques for particle size distribution measurements on laser-generated aerosols. *J. Analyt. Atom. Spectrom.*, **20**, 894-900

KUHN, H.R., PEARSON, N.J. & JACKSON, S.E. (2006): Laser ablation ICP MS: Particle size dependent isotopic fractionation of copper in laser generated aerosols. *Geochim. Cosmochim. Acta* **70**, A337.

LIU, H.C., BORISOV, O.V., MAO, X.L., SHUTTLEWORTH, S. & RUSSO, R.E. (2000): Pb/U fractionation during Nd:YAG 213 nm and 266 nm laser ablation sampling with inductively coupled plasma mass spectrometry. *Appl. Spectrosc.* **54**, 1435 1442.

LIU, C., MAO, X. L., MAO, S. S., ZENG, X., GREIF, R. & RUSSO, R. E. (2004): Nanosecond and femtosecond laser ablation of brass: Particulate and ICPMS measurements. *Anal. Chem.* **76**, 379-383.

LIU, C.Y., MAO, X.L., MAO, S.S., GREIF, R. & RUSSO, R.E. (2005): Particle size dependent chemistry from laser ablation of brass. *Anal. Chem.* **77**, 6687-6691.

LUK'YANCHUK, B.S., MARINE, W. & ANISIMOV,

S.I. (1998): Condensation of vapor and nanoclusters formation within the vapor plume, produced by ns-laser ablation of Si. *Laser Phys.*, **8**, 291-302.

MANK, A.J.G. & MASON, P.R.D. (1999): A critical assessment of laser ablation ICP MS as an analytical tool for depth analysis in silica based glass samples. *J. Analyt. Atom. Spectrom.* **14**, 1143-1153.

MARGETIC, V., PAKULEV, A., STOCKHAUS, A., BOLSHOV, M., NIEMAX, K., OLESIK, J.W. & BATES, L.C. (1995): Characterization of aerosols produced by pneumatic nebulizers for inductively couples plasma sample introduction effect of liquid and gas flow rates on volume based drop size distributions. *Spectrochim. Acta Part B* **50**, 285-303.

MARGETIC, V., PAKULEV, A., STOCKHAUS, A., BOLSHOV, M., NIEMAX, K. (2000): A comparison of nanosecond and femtosecond laser-induced plasma spectroscopy of brass samples. *Spectrochim. Acta Part B* **55**, 1771-1785.

OLESIK, J.W., BATES, L.C. (1995): Characterization of aerosols produced by pneumatic nebulizers for inductively couples plasma sample introduction effect of liquid and gas flow rates on volume based drop size distributions. *Spectrochim. Acta Part B* **50**, 285-303.

OLESIK, J.W. & KINZER, J.A. (2006): Measurement of monodisperse droplet desolvation in an inductively coupled plasma using droplet size dependent peaks in Mie scattering intensity. *Spectrochim. Acta B* **61**, 696-704.

OUTRIDGE, P.M., DOHERTY, W. & GREGOIRE, D.C. (1996): The formation of trace element enriched particulates during laser ablation of refractory materials. *Spectrochim. Acta B* **51**, 1451-1462.

OUTRIDGE, P.M., DOHERTY, W. & GREGOIRE, D.C. (1997): Ablative and transport fractionation of trace elements during laser sampling of glass and copper. *Spectrochim. Acta B* **52**, 2093-2102.

PERDIAN, D.C., BAJIC, S.J., BALDWIN, D.P. & HOUK, R.S. (2008a): Time-resolved studies of particle effects in laser ablation inductively coupled plasma mass spectrometry. *J. Analyt. Atom. Spectrom.* **23**, 325-335.

PERDIAN, D.C., BAJIC, S.J., BALDWIN, D.P. & HOUK, R.S. (2008b): Time-resolved studies of particle effects in laser ablation inductively coupled plasma mass spectrometry. *J. Analyt. Atom. Spectrom.* **23**, 336-341.

PISONERO, J., FLIEGEL, D. & GÜNTHER, D. (2006): High efficiency aerosol dispersion cell for laser ablation–ICP–MS. *J. Analyt. Atom. Spectrom.* **21**, 922-931.

POITRASSON, F., MAO, X.L., MAO, S.S., FREYDIER, R. & RUSSO, R.E. (2003): Comparison of ultraviolet femtosecond and nanosecond laser ablation inductively coupled plasma mass spectrometry analysis in glass, monazite, and zircon. *Anal. Chem.* **75**, 6184-6190.

POITRASSON, F., FREYDIER, R., MAO, X., MAO, S.S. & RUSSO, R.E. (2005): Femtosecond laser ablation ICP MS analysis of trace elements in solids. *Geochim. Cosmochim. Acta* **69**, A54.

RUSSO, R.E., MAO, X.L., LIU, H.C., YOO, J.H. & MAO, S.S. (1999): Time resolved plasma diagnostics and mass removal during single pulse laser ablation. *Appl. Phys. A Mater.* **69**, 887-894.

RUSSO, R.E., MAO, X.L., BORISOV, O.V. & LIU, H.C. (2000): Influence of wavelength on fractionation in laser ablation ICP MS. *J. Analyt. Atom. Spectrom.* **15**, 1115-1120.

SAETVEIT, N.J., BAJIC, S.J., BALDWIN, D.P., HOUK, R.S. (2008): Influence of particle size on fractionation with nanosecond and femtosecond laser ablation in brass by online differential mobility analysis and inductively coupled plasma mass spectrometry. *J. Analyt. Atom. Spectrom.* **23**, 54-61.

TELOUK, P., ROSE KOGA, E.F. & ALBAREDE, F. (2003): Preliminary results from a new 157 nm laser ablation ICP MS instrument: New opportunities in the analysis of solid samples. *J. Geostandards and Geoanalysis* **27**, 5-11.

THOMPSON, M., CHENERY, S. & BRETT, L. (1990): Nature of particulate matter produced by laser ablation – implications for tandem analytical systems. *J. Analyt. Atom. Spectrom.* **5**, 49-55.

YOO, J.H., BORISOV, O.V., MAO, X.L. & RUSSO, R.E. (2001): Existence of phase explosion during laser ablation and its effects on inductively coupled plasma–mass spectroscopy. *Anal. Chem.* **73**, 2288-2293.

YUAN, H.L, GAO, S., LIU, X.M., LI, H.M., GÜNTHER, D. & WU, F.Y. (2004): Accurate U Pb age and trace element determinations of zircon by laser ablation inductively coupled plasma mass spectrometry. *Geostandards and Geoanalytical Research* **28**, 353-370.

# CHAPTER 3: COMPUTER MODELING OF LASER ABLATION ELEMENTAL MICROANALYSIS

Davide Bleiner
Swiss Federal Institute of Technology, Sonneggstrasse 3,
8092 Zurich, Switzerland
E-mail: bleinerd@ethz.ch

*and*

Zhaoyang Chen
Lawrence Berkeley National Laboratory, 1 Cyclotron Road,
Berkeley CA 94720
E-mail: ZChen@lbl.gov

## INTRODUCTION

More and more research groups, though not specialized in computational methods, have become users of simulation packages to obtain fundamental and applied insights and optimize their analytical procedures. Hence, although this handbook's focus is on laboratory practice, it is informative to address benefits of integrating simulations with experimental studies. Besides, after an introduction on the pros, we give some elements to help beginners to start up. Finally, a selection of results are presented concerning important aspects in LA–ICP–MS, such as the laser-assisted microsampling, the transport of the laser-induced aerosol, and how one can relate the experimental parameters to the LA–ICP–MS signal structure. The reader will get familiar with the strengths, but also with some potential pitfalls in simulations: a computer processes any kind of input following the specific algorithm it was instructed to deploy. As the saying goes "Garbage in, garbage out!" Hence, apparently misleading results, sometimes encountered in the literature, are not due to an inherent lack of realism in the practice of simulations, but rather to the weakness of the specific computational approach. The situation is not so much different from the experiments: the use of a wrong calibration curve, the erratic fluctuation of the laser pulse energy, the selection of inappropriate isotopes or internal standards, *etc.* are all sources of bad results.

To discuss the benefits, one should first consider that a computational model is able to treat virtually all kinds of parametric values, even the most extreme ones. For instance, one might want to investigate the laser vaporization process. Considering the extreme temperatures involved, ns or shorter times and μm, or even nm, length scales, it is difficult to have detailed experimental information matching the process-tracking ability of equations. Second, a computational model allows tests and comparisons of a large number of parameter configurations. If one wants to develop a high efficiency ablation chamber, it might be time-consuming and expensive to design, manufacture, and operate each individual cell design, especially in a preliminary design review. Third, dedicated simulations may help to unravel contributions to the observed combined output, since some parameters are experimentally linked. For instance, one knows that a variation of carrier gas flow rate has concomitant effects, such as the flush across the sample chamber, the particles' speed, the ion residence time in the ICP, the ICP temperature, *etc.* Simulation has the ability to scan one process at a time, while fixing the coupled ones, and give information on their relative importance. Last, but not least, computer modeling is essentially low cost research, with a high output rate. All that is required is software, hardware (both helpful also in experimental studies!), and some understanding of the fundamental equations. If the time scale for experiment campaigns is typically from months to years, in the case of computations the temporal scale is typically much shorter (apart from the coding stage!).

On the other hand, a computational model is always an approximated version of the physical model, which in its turn is an approximation of nature. One has to be sure that all assumptions made are such that the scope of the model and the variance of the experiment match. The reduction of a physical model into a computational model passes through a meaningful mathematical approach for the sake of *realism*, but also considerations of the most efficient use of the hardware resources. For

Mineralogical Association of Canada Short Course 40, Vancouver, B.C., p. 35–52.

instance, the computation of particle vaporization in the ICP does not need to be performed in 3D, given the spherical symmetry of the problem, and since in all directions the physical laws are invariant. On the contrary, a 1D code may be more manageable and rapid. The "essentialization" of a computational model is beneficial for the calculation time, and also in terms of quality of results. In fact, the spared computational resources allow a higher degree of computational resolution and low error. There are three kinds of error in a numerical computation. First, the *round-off (machine) error* is related to the clipping of a real number to the machine precision in floating point values. Secondly, *truncation error* is related to the termination of the iterative method to an approximate solution different from the exact solution. Last, the *discretization error*, is related to the mismatch between the continuum physical problem and the numerical grid. Another important notion is that of *numerical stability*: an algorithm is numerically stable if an error, once it is generated, does not grow during the calculation.

## METHODS

There are two problem-solving approaches, namely "continuous" analytical solutions or "discrete" numerical solutions. Unfortunately, in some cases analytical solutions are hard to compute, or do not exist at all. For instance, the shockwave created in the ICP–MS interface (Mach disc) shows a sudden variation of pressure, temperature, gas speed and density in the upstream and downstream regions, associated with the governing laws in the subsonic and transonic regions. In some other cases, there is a transcendent dependence of a variable, and one cannot solve the equation analytically. For instance, many useful equations have the form $f(x) = x\, e^{-x}$ that cannot be solved analytically for x. The only way to overcome these situations is to compute point by point numerical solutions. The selection of the numerical scheme is of primary importance for both the realism and the computational resources involved in the simulation.

### Structure of a Simulation

In principle, three main steps can be identified in the progression of a simulation, namely:

- *Coding.* The writing of a computer code begins with the definition of the so-called pseudo-code (Chapman 2003). In its essence, the program should: (i) read input data, (ii) process them according to a set of governing equations, (iii) write output data files. To do so, a pseudo-code is then converted into a source code, following the syntax of the chosen programming language. When the source code is written (and debugged!), one needs to compile it to generate an executable program for the operating platform.
- *Pre-processing & the Solver*. A numerical calculation is performed across a certain computational domain with specific boundary conditions. This implies defining a numerical grid, and its border-line values, mapping the physical extension of the simulated object. The grid's nodes are the points where the governing equations are solved. The grid resolution, *i.e.*, how closely spaced the nodes are, determines the physical detail that can be reproduced. However, too many nodes limit the speed of computation, demanding more resources. The solution of the discretized equation is given by a specific numerical scheme. In the *explicit scheme*, the values for the $n^{th}$ step are directly computed from known values at the previous step. This approach is easy to code, virtually correct if infinite precision arithmetic would be available, but potentially less stable than the so-called *implicit schemes*. The latter are iterative methods that are typically more complex to code, but offer better stability, though convergence to the "exact solution" is only within a certain tolerance limit (residuals). The user should always check that the residuals are within an acceptable error for the characteristic magnitudes of the simulated problem. For more information on numerical methods see for instance the handbook by Hoffman (Hoffman 2001).
- *Post-Processing.* After running the code, the last step involves the visualization of the output data in the form of tables, plots (1, 2,or 3D), or even movies, *i.e.*, stacking a number of plots such that each frame has a temporal delay to the next. There is an internal temporal delay, *i.e.*, relative to the "instant" of computation, and an external temporal delay, *i.e.*, relative to the time of visualization. For instance, the simulation of the laser ablation plume expansion may be done with 10 frames of internal temporal delay of 500 ns. The whole movie might be ideally set to play for 10–15 s. Indeed, a movie that is completed in 500 ns x 10 frames = 5 μs would hardly highlight anything!

**Algorithms**

The number of computational techniques is large, based on different algorithmic principles, making some more suitable for one task than for another. Therefore, one should be well aware of the strengths and weaknesses of each. Here we provide a limited list of computational techniques, and suggest some useful readings for the interested reader.

- *Molecular Dynamics.* MD is a form of computer simulation wherein atoms are allowed to interact for a period of time under the action of inter-atomic potentials, giving a view of their motion. Since molecular systems of N particles imply $N^2$ interactions, a "virtual experiment" has to be restricted to short durations or length scales, due to limitations in computational resources. More information in the handbook by Rapaport (Rapaport 2004).
- *Monte Carlo.* There is no one MC method, but the term describes a large and widely used class of approaches based on stochastic algorithms. In fact, the MC method relies on random number generation and a cutoff criterion for structuring the output. More information in the handbook by Ross (Ross 2006).
- *Hydrodynamics.* HD codes are based on a set of differential equations that describe the conservative transport of some physical properties, such as mass, momentum, energy, *etc.* The general form for a space/time conservation equation is

$$\frac{\partial \phi}{\partial t} + \nabla \cdot f = s \qquad (1)$$

where $\phi$ is the physical property conserved, $f$ is a function describing the flux of $\phi$ and s is the so-called source term that describes the generation (or removal) of $\phi$ across the domain. More information in the handbook by Anderson (Anderson 1995).

- *Kinetic Codes.* A kinetic description is achieved by solving the interaction between particles, such as mechanical or electromagnetic collisions. The standard procedure for plasmas is to implement the Boltzmann equation or its reduced forms, *e.g.*, the Vlasov equation, the Fokker-Planck equation. More information is found in the handbook by Hockney and Eastwood (1998) or Sukop & Thorne (2005).

**Hardware**

Although nowadays commodity computers are able to process complex assignments, until a few years ago simulations were exclusively associated with large centralized facilities. Table 3-1 summarizes the most important milestones in the history of supercomputers. The peak speed is given as operations per second (OPS) or floating point operation per second (FLOPS), evaluated running a benchmark code (Linpack). Twice a year the *top500.org* organization compiles a list of the most powerful machines in the world. These machines are more efficient when operated with parallel codes. Parallel computing is a programming technique in which large programs are divided into smaller instruction blocks, solved in "parallel", as opposed to traditional sequential-instruction codes (see for instance the handbook, Fountain, 2006).

## MODELING OF LASER MICROSAMPLING

**Optical and Thermal Lengths**

The process of laser-assisted microsampling involves a number of physical processes. In this chapter the focus is on the results, but some background information on the fundamentals is

TABLE 3-1: MILESTONES OF SUPERCOMPUTER DEVELOPMENT.

| Year | Machine | Peak Speed (ops) | Location |
|---|---|---|---|
| 1942 | Atanosov-Berry | 30 | USA |
| 1944 | Flower Colossus | 5 k | UK |
| 1961 | IBM 7030 | 1.2 M | USA |
| 1976 | Cray 1 | 250 M | USA |
| 1984 | M–13 | 2.4 G | USSR |
| 1993 | Fujitsu NWT | 124.50 G | Japan |
| 1997 | Intel Asci Red 9152 | 1.338 T | USA |
| 2002 | NEC Earth Simulator | 35.86 T | Japan |
| 2005 | IBM Blue Gene L | 280 T | USA |
| 2007 | IBM Blue Gene | 478.2 T | USA |

The computation speed is given in operations per second (ops) determined running a benchmark code.

important to understand the simulations. For laser pulses in the ns time scale (or longer) one can assume thermal equilibrium and use the heat conduction equation to describe the space- and time-dependent temperature distribution within the irradiated sample (see for instance Incropera *et al.* 2006). The equation defines the time-dependent and space-dependent balance between laser energy deposition and heat or radiation losses:

$$\frac{\partial T}{\partial t} - u(t)\frac{\partial T}{\partial z} = (1-R)\alpha I(t)e^{-\alpha z} + D_h \frac{\partial^2 T}{\partial z^2} \quad (2)$$

here given in the simplest 1D version, considering the temperature (T) as a function of depth (z) and time (t). The source term, on the right hand side, is related to the net laser energy transmitted and absorbed into the sample (I(t) is the laser intensity time profile, α is the absorption coefficient, R is the reflectivity), and the one delocalized by thermal diffusion ($D_h$). The energy is used to heat the target, spatially and temporally, inducing phase changes, while surface recession takes place at speed *u(t)*. The so-called Stefan problem is a particular kind of boundary value problem for the heat conduction equation, adapted to the case in which a phase boundary can move with time (Gupta 2003). The heat conduction equation is controlled by two important groups of sample parameters, *optical properties* and *thermal properties*. Among the former, the reflectivity limits the energy transmission and depends on the laser wavelength, angle of incidence, and polarization. For instance, IR radiation has a high reflectivity for many materials in contrast to UV radiation. The non-reflected intensity (1–R) propagates through the material thickness and is partially absorbed. The depth-dependent absorption follows a characteristic exponential rate of absorption, *i.e.* the absorption coefficient α as in the Lambert-Beer law. The length scale $L_{opt} = 1/\alpha$ is called *optical penetration length*, which gives the length scale for optical effects. On the other hand, a characteristic distance for thermal processes is the heat penetration length, calculated from the thermal diffusivity ($D_h$) and the time scale for heating that is in our case the laser pulse duration (τ), namely $L_{th} = 2\sqrt{D_h \tau}$.

The spatial distribution of the laser ablation effects is dictated by the largest among the two characteristic length scales. For conductive and opaque metallic samples, the laser energy is conducted across a thermal volume larger than the optical volume, since $L_{ther} > L_{opt}$ This means that the effective pit size is typically larger than the laser spot size, and the spatial resolution does not depend merely on the focusing. For refractory and transparent samples, the laser pulse is trapped within the optical volume, since $L_{ther} < L_{opt}$. The extent of sample transparency must be evaluated with respect to the laser wavelength, *e.g.*, a "transparent" calcite sample is opaque for a deep UV excimer wavelength.

**Sample Ablation**

Mass ablation may be in the form of either a continuum vapor plume (hydrodynamic model) or discrete particles (kinetic model) depending on the degree of vapor coupling, pulse duration, and observation time after irradiation. In the laser ablation regime, collision effects become increasingly important for laser intensities $>10^8$ W/cm$^2$, as shown below. The collisions redistribute the kinetic energy across a distance of translational instability known as the Knudsen layer (KL). Within the KL one cannot define any temperature because the particles are not in thermal equilibrium. Upstream from the KL, the sample has the "surface temperature". Downstream from the KL, an unsteady adiabatic expansion (see Kelly *et al.* in Miller & Haglund 1998) of the laser plume takes place showing a temperature profile, as also shown below. To quantify the mass recession, as a simulation output, two parameters are commonly used, *i.e.* the *ablation yield* and the *ablation rate*. The former is defined as the number of ablated particles per laser pulse. The latter is defined as the number of ablated particles per unit irradiated area and unit time. It is clear that the ablation rate changes as function of repetition rate since it is time normalized.

Figure 3-1 shows the calculated temperature distributions inside a selection of metallic samples, as a function of depth and time. In all cases, the temperature is at a maximum in a shallow surface layer, when the laser pulse reaches its peak intensity (here a Gaussian profile of 10 ns width was modeled). Nevertheless, the temperature change shows persistence beyond the laser pulse duration. There are significant sample-dependent differences in the calculated peak temperature, ranging from approximately 3,000 K in the case of Zn and Al, to about 7,000 K for Fe, Cu, and Mn, and above 10,000 K in the case of Mo. This pronounced difference is mainly attributed to: (i) optical absorption coefficient, (ii) reflectivity, and (iii) thermal diffusivity. The optical absorption

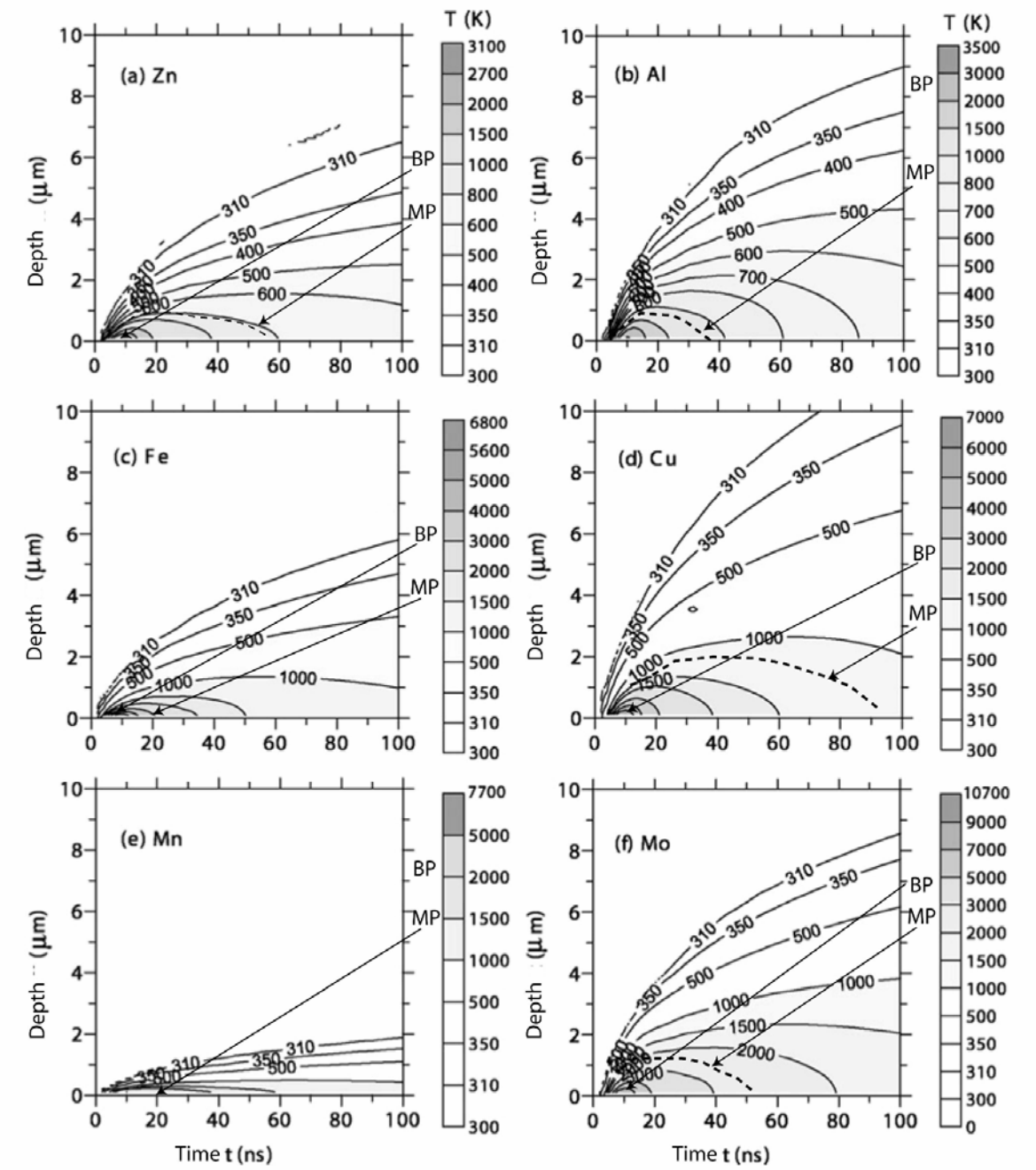


Fig. 3-1: Calculated temperature distribution inside a selection of sample metals (**a**, zinc; **b**, aluminum; **c**, iron; **d**, copper; **e**, manganese; **f**, molybdenum), as a function of depth (mm) and time (ns). Standard laser conditions, *i.e.* $I = 10^9$ W/cm$^2$, $\lambda =$ 266 nm, $\tau = 10$ ns. MP is melting point, BP is boiling point. One notes that different combinations of optical and thermal properties have radically different effects, as explained in the text, hence affecting the elemental microanalysis. Modified from Bleiner *et al.* (2006) with permission.

coefficients of Al and Mo are higher than those of all other metals, *i.e.* that laser energy is more efficiently trapped. Al has, however, a high reflectivity of 92%, which means that only 8% of the laser irradiance is transmitted to the bulk. Similar considerations for Zn can be made. Besides, samples with high thermal diffusivity rapidly adjust local temperature perturbation because heat quickly diffuses to the bulk. Thermal diffusivity is here highest for Cu and Al, *i.e.* the heat largely extends

in the depth. On the other hand, Mn has a low thermal diffusivity, *i.e.* the temperature rise was limited to a shallow depth.

Figure 3-2 shows the simulated maximum surface temperature in the various metals and gives the corresponding calculated melt or evaporation depth induced upon ablation. Although Mo reaches the highest surface temperature, the evaporation depth is calculated to be only 32 nm, which is lower than for most other metals, due to its low thermal diffusivity and high BP. Cu and Fe have similar surface and BP, hence their evaporation depths are also comparable in the order of 45–50 nm. For Zn, the calculated evaporation depth is relatively high, around 60 nm, in spite of its low temperature, due to its low BP. Mn appears to have the highest evaporation depth of about 80 nm attributed to its high temperature and relatively low BP, whereas for Al the model predicts a very low evaporation depth, of only 0.3 nm, due to its rather low attained temperature (3580 K), in comparison with its BP (2790 K). The computed melt depth ranges from 0.3 μm in the case of Mn, to almost 1.5 μm for Cu. This trend is strongly correlated with the thermal conductivity of the different metals. Indeed, Mn has a very low thermal conductivity, so that the confined temperature rise induces a shallow melt pool. Cu, on the other hand, has a large thermal conductivity and hence a larger melt depth. Obviously, the surface temperature and melting point of the different materials also determine the melt depth. The low melting point of Al and Zn, for instance, explains why these metals have a relatively large melt depth, in spite of the relatively low surface temperature. This suggests that, at least for certain metals, such as Al, laser-induced evaporation is not the dominating mechanism resulting in material ablation, but melt ejection plays an important role. This result was confirmed by calculations at higher laser intensity (2 GW/cm$^2$) and also crater profilometry (Bleiner *et al.* 2006).

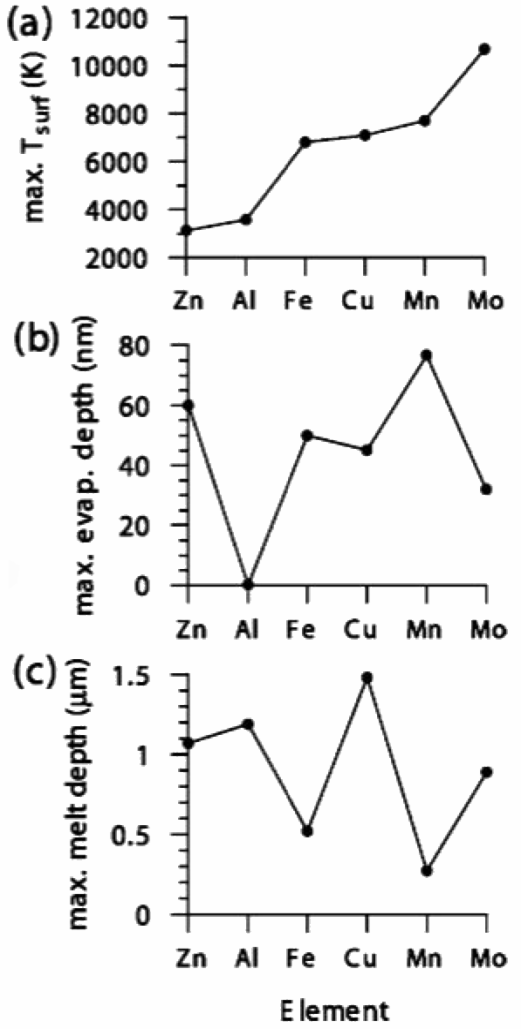


Fig. 3-2: Calculated maximum surface temperature **(a)**, evaporation **(b)** and melt **(c)** depths for a selection of sample metals. The plots in **(b)** and **(c)** allow assessing the relative role of vaporization and melt expulsion, partly responsible for elemental fractionation in multi-elemental samples. Reproduced from Bleiner *et al.* (2006) with permission.

**Vapor Plume Characteristics**

In Fig. 3-3, the calculated plume characteristics for a selection of metallic samples are compared (Bleiner *et al.* 2006). The metal vapor number density increases drastically from Al to Mn in close correlation with the evaporation depth. The same applies to most of the other plume characteristics shown. The plume length indicates the position where the vapor density has dropped to negligible values, whereas the shock front position denotes the end of the background gas compression front. Compared to the other metals, Al shows the most significant difference in ablation characteristics, which is attributed to the very low amount of evaporation as possibly explained for its high reflectivity, thermal conductivity, and low melting point. As mentioned above, calculations predict that still at $10^9$ W/cm$^2$ practically no vapor plume is formed for Al, and for a laser irradiance of twice as high the Al vapor density, plume velocity, plume length, plume temperature, ionization degree and electron density are still lower than the

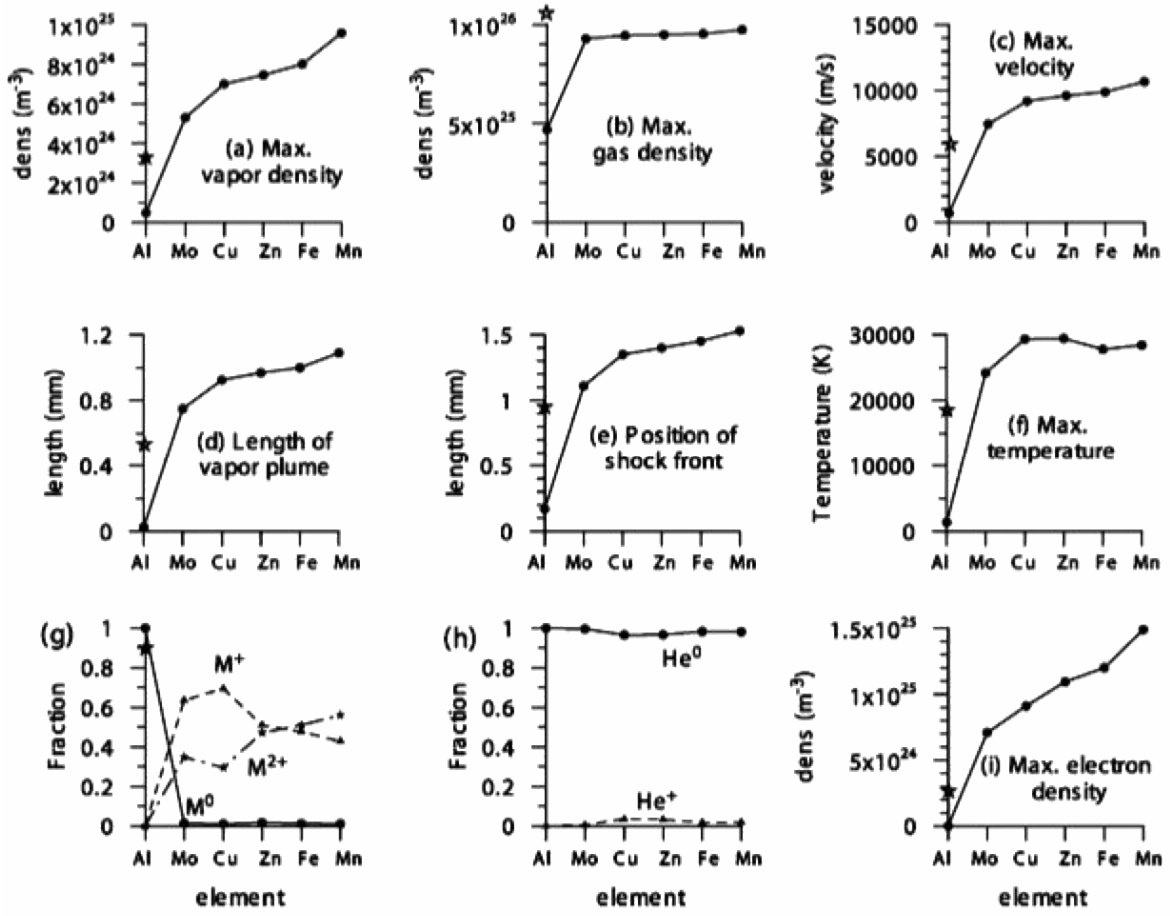


Fig. 3-3: Calculated laser-induced vapor plume characteristics for a selection of sample metals. The star indicates results for Al at 2 GW/cm$^2$ laser intensity as opposed to the 1 GW/cm$^2$ for all other calculations. Background gas is He. Reproduced from Bleiner *et al.* (2006) with permission.

corresponding values for the other metals at a laser irradiance of $10^9$ W/cm$^2$.

The formation of a laser plasma within a time scale shorter than the pulse duration interferes with the propagation of the incoming laser. The interaction involves either reflection, depending on the wavelength-dependent plasma critical density, or absorption of the laser pulse by means of multiphoton ionization or inverse Bremsstrahlung. It is clear that the ionization degree of the He background gas is considerably lower than the ionization degree of the metal vapor since He has a much higher ionization potential (24.58 eV) than the metal atoms (in the range 7 to 9.4 eV), and even the second ionization potential of the metals is lower than the first ionization potential of He. Whereas the He gas is almost completely in atomic form, the metal vapor is mainly ionized, except for the case of Al, which is still largely in atomic form. These observations on the atomic optical states are of particular importance in combination with LIBS (Laser-induced Breakdown Spectrometry, Radziemski & Cremers 1989), and are discussed in detail elsewhere (Bleiner *et al.* 2006). In this handbook, we keep the focus on the information relevant to LA–ICP–MS.

**Laser Intensity, Wavelength, and Pulse Duration**

The effects of laser intensity are shown in a series of 1D numerical simulations with Cu (Bogaerts & Chen 2005, Chen & Bogaerts 2005). Fig. 3-4 summarizes single-shot microsampling characteristics as a function of laser intensity for the widely used 266 nm beam. The surface temperature (**a**) shows that well above the threshold of $10^8$ W/cm$^2$, boiling is the dominating mass removal mechanism. Microsampling might become less stoichiometric when boiling and melting have comparable relevance, *e.g.*, at about the threshold regime. For that we indicate a minimum LA–ICP–

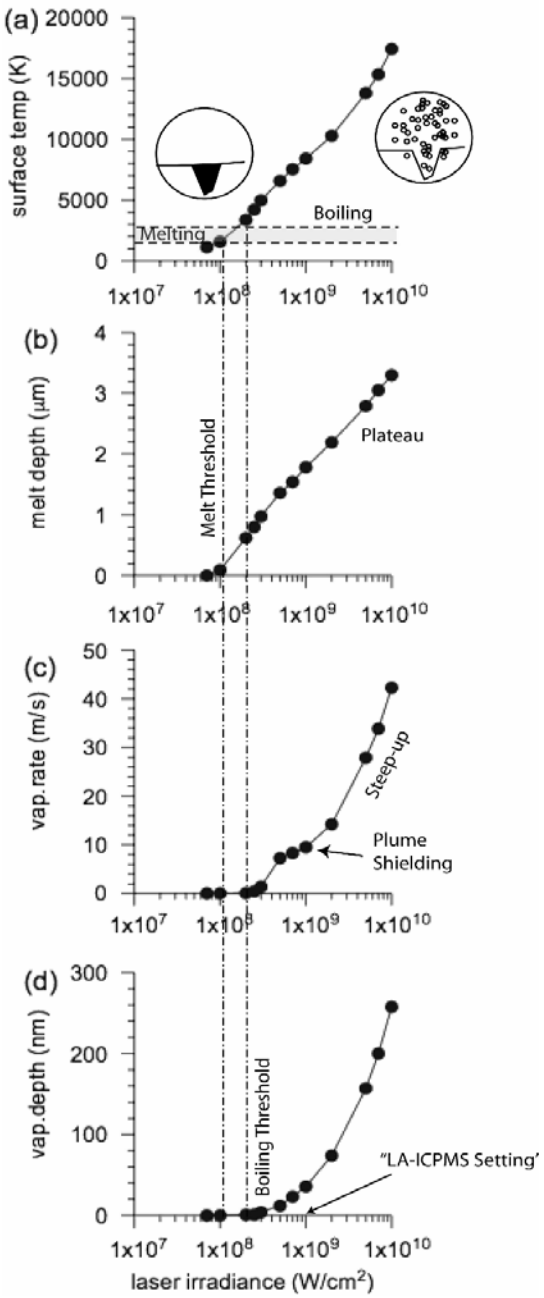


Fig. 3-4: Calculated surface temperature **(a)**, melt depth **(b)**, vaporization rate **(c)**, and vaporization depth **(d)** of Cu as a function of laser standard conditions given in Fig. 3-1. Modified from Bogaerts & Chen (2005) with permission.

MS intensity for good practice. The vaporization rate (**c**) gives the speed of surface recession, which is important for depth profiling calibration. Experimental geometry of the laser crater can be compared with the vaporization (**d**) and melt depth (**b**) computed.

The laser wavelength is important for the influence it has on the reflectivity and absorption both in the sample and in the expanding plume. Results are shown (Fig. 3-5) at the main harmonics of the Nd:YAG laser to demonstrate the general effects produced at IR, visible, and UV spectral ranges. For instance, the reflectivity of copper drops by a factor of three from the first Nd:YAG harmonic (1064 nm, IR) to the fourth harmonic (266 nm, UV), *i.e.*, from 97% to 34%. Moreover, a shorter wavelength corresponds to a higher photon energy, *i.e.*, higher sample ablation efficiency, shorter penetration length, and higher photo-ionization probability in the plasma. The performance of the IR beam is in general poorer than that for the other wavelengths, and the visible and UV beams are comparable for metal ablation. The IR beam is limited by the high reflectivity at the sample surface, and severe plasma absorption. The visible beam (532 nm) is less efficiently coupled to the sample due to higher reflectivity, but its "softer" plume is less opaque than the one induced with an UV beam. The fact that visible and UV beams are quite analogous in metal ablation characteristics depends thus on two opposing processes that compensate: ablation efficiency and plasma absorption.

The laser pulse duration is another important parameter, especially when its extension is considered over a wide time-scale, from the femtosecond (fs) up to the millisecond (ms). This has indeed a significant impact on the fundamental mechanisms of ablation. Clearly, for a constant fluence, the variation of the pulse duration has also an immediate influence on the pulse intensity. The most interesting aspects to discuss are the changes in ablation characteristics between the long pulse (μs-scale or longer), the short pulse (ns-scale), and the ultra-short pulse regime (ps-scale or shorter). The long pulse regime can be simulated using a macroscopic treatment of laser heating, whereas the shorter pulses give rise to more and more significant contribution from microscopic processes. With ultra-short pulses stationary conditions are never reached (see also the handbook by Rulliere 2004). For this reason the vast majority of codes for the ultra-short pulses are based on MD or two-temperature HD codes. The main results found in a number of computational studies of the ultra-short pulse ablation are (Bäuerle 2000): (i) very high pressure within the interaction volume, with hypersonic ejection and strong compression wave; (ii) high heating rate, which is much faster than the

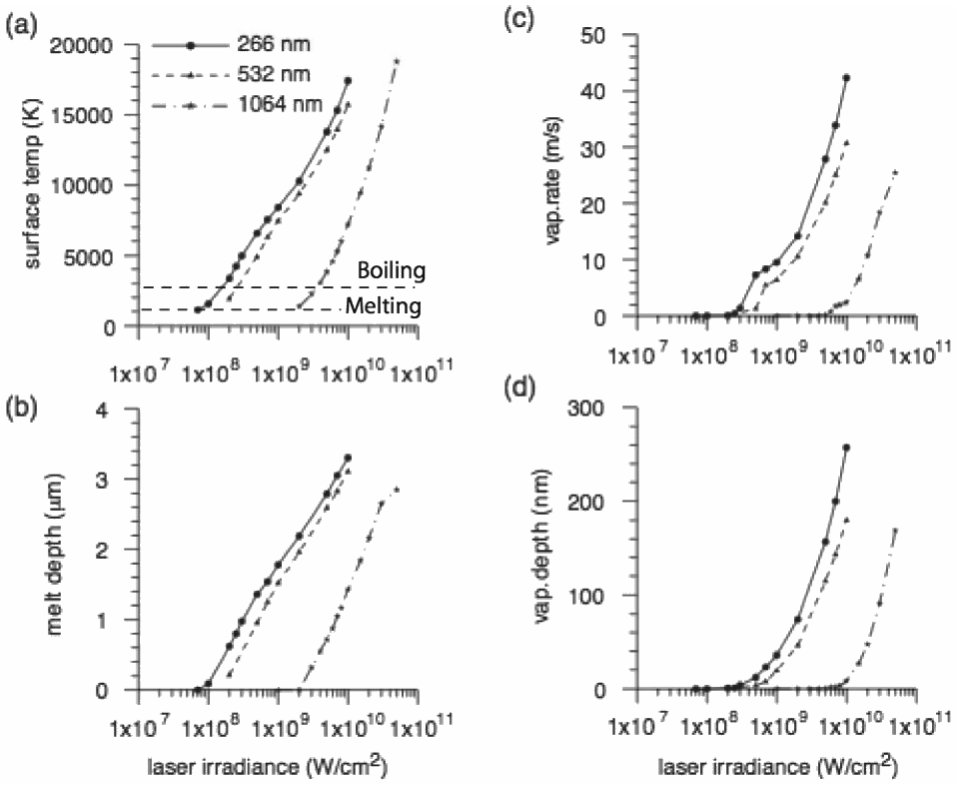


Fig. 3-5: Calculated surface temperature **(a)**, melt depth **(b)**, vaporization rate **(c)**, and vaporization depth **(b)** of Cu as a function of laser irradiance for three laser wavelengths. Modified from Bogaerts & Chen (2005) with permission.

thermal diffusion speed of any sample; (iii) lower ablation threshold fluence than for ns-pulses, and non-linear increase of the ablation rate with the fluence; (iv) significant role of spinodal breakdown (phase explosion), *i.e.*, sample boiling close the critical point; (v) no vapor/plasma plume develops during the pulse and mass ablation takes place only after the pulse; (vi) minimal thermal effects (cool ablation), apart from post-pulse effects. In metals, the conduction band electrons mainly absorb the radiation.

## MODELING OF LASER-INDUCED AEROSOL TRANSPORT

### Fluid Dynamics

In LA–ICP–MS a carrier gas flowing through the set-up volume transports the laser-induced aerosol to the mass spectrometer. The first issue to address concerning the aerosol transport is the flow pattern of the carrier gas. Subsequently, one can add an ensemble of particles in the treatment, moving along the gas streamlines. The governing equations are obtained from conservation of mass and momentum. The Navier-Stokes equations govern the motion of the fluid phase, in the sense of balance of momentum changes as a function of pressure and dissipative viscous forces across the fluid. The laminar gas velocity profile through a channel is parabolic, with the mean velocity that is the half of the maximum velocity. The parabolic profile develops dynamically from the initial flat profile at the tube entrance (free stream flow) over an entry distance. Across this entry distance, there is a shear stress region close to the tube walls, *i.e.* a region of rapid velocity change, which is called the boundary layer (see also Schichtling *et al.* 2004). The boundary layer thickness increases from the tube entrance downstream until the flow becomes fully developed. This dynamic evolution influences the gas velocity profile as well as the transport of the LA-induced particles. The treatment of solid particles that move along the fluid phase is complex. Due to the physical heterogeneity of the particle ensemble, the various types of forces acting on the particles might be less or more significant depending on particle size and morphology. Details are discussed by Bleiner & Bogaerts (2006). Two more governing equations had to be coded, in order to account for viscous turbulence (see also the handbook by Tennekes & Lumley (1972).

The discrete phase (the aerosol!) must be matched to the physical properties of the ablated sample. In our model we used experimental curves of particle size distributions, showing bimodal curves with modes at about 30 nm and 0.5–2 µm (not shown). Some other physical properties are adopted from tables, such as density, or assuming the particles are spherical. As a boundary condition, the gas inlet was set to 1.0 L/min.

**Sample Cell**

The injection of carrier gas into a standard "drum-shaped" ablation cell induces circulation. In fluid dynamics, circulation is the line integral around a closed curve of the fluid velocity. Circulation is related to vorticity by the Kelvin-Stokes theorem (see also Greitzer *et al.* 2007), namely vorticity is the fluid circulation per unit area taken around an infinitesimal loop. In simple words, vorticity is the local angular rate of rotation of the chamber gas. Both simulations and our own experiments (see also Bleiner 2002), have highlighted the occurrence of circulation in the chamber flow pattern. This has direct consequences on the calculated particle trajectories. The fact that that carrier gas rotates across the cell is inherently negative because it favors fractional transport, retards the particle extraction, and leads to signal broadening.

Figure 3-6 shows calculated velocity distributions in a 100 $cm^3$ ablation cell (aspect ratio is 1.0, *i.e.* the width is equal to the height), across the horizontal and vertical planes. The most evident effect is that the gas inlet jet expands longitudinally for almost the entire diameter of the ablation cell (high efficiency transport region), whereas the gas moves significantly slower at the margins (low efficiency transport regions), and mostly backwards. Local fluctuations of the gas flow pattern can induce a temporal side displacement of the gas plume axis from the inlet-outlet axis. All samples that are ablated in off-axis positions across the cell consequently provide more modest sensitivity, also considering the fact that the gas flow lines point backward. In large ablation cells, aerosol circulation is a severe problem that causes transport delay, signal tailing and also sample cross-contamination. For the interested reader, simulations of the particles trajectories are shown by Bleiner & Bogaerts (2007).

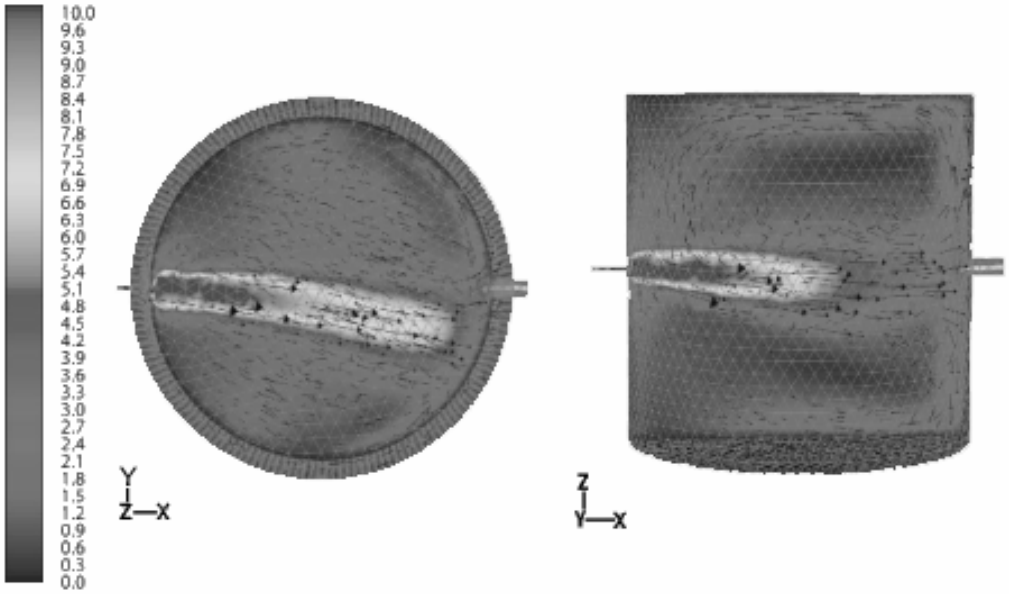


Fig. 3-6: Calculated gas flow pattern across a 100 $cm^3$ ablation cell flushed with 1.0 L/min Ar. The color scale indicates the gas speed in m/s. The cell geometry is the "drum" design (top view on the right, and side view on the left). The inlet is on the right hand side of each view, facing the outlet on the opposite side. The latter is matched to the ordinary transport tubing size. A central region of fast forward gas movement induces shear circulation with the marginal zones. In the latter the gas is slow and moves backwards. The flow accelerates at the outlet to vent the slight pressure buildup inside the chamber. The flow pattern extracts articles that are transported in the central region, while tend to disperse all others. The cropping of the low efficiency margins would improve gas flow confinement, but limit the available space for samples. Reproduced from Bleiner & Bogaerts (2007) with permission – see color version of illustration on Plate 1.

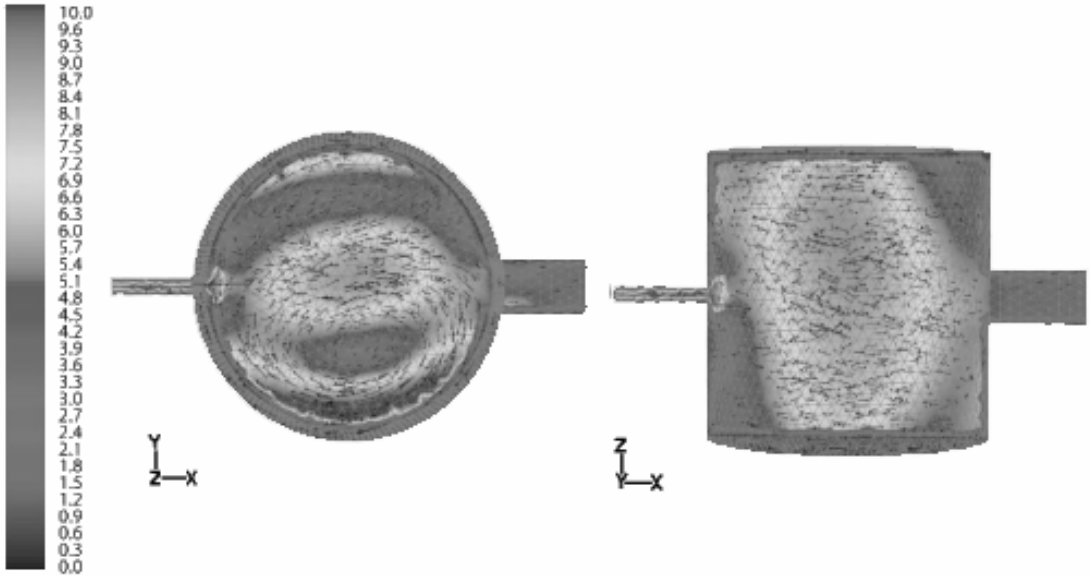


Fig. 3-7: Calculated gas flow pattern across a 2.5 $cm^3$ ablation cell flushed with 1.0 L/min Ar. The color scale indicates the gas speed in m/s. The cell geometry is the "Drum" design (top view on the right, and side view on the left). The inlet is on the right hand side of each view, facing the outlet on the opposite side. The latter is matched to the ordinary transport tubing size. Significant circulation takes place with rapid rotation of the gas in two neighboring counter-rotating sub-cells. The right hand side sub-cell (see top view) rotates clockwise. The flow is unsteady and fluctuating as a function of time. The flow pattern forces the particles into rapid motion and statistically the latter may encounter the outlet. Reproduced from Bleiner & Bogaerts (2007) with permission - see color version of illustration on Plate 1.

Figure 3-7 shows calculated velocity distributions in a 2.5 $cm^3$ ablation cell, across the horizontal and vertical planes. The general structure of the flow is characterized by the presence of two side vortices that spin around two eccentric vertical axes. The vorticity direction in the two sub-cells is opposite, *i.e.*, clockwise for the right hand one and counter-clockwise for the left hand one. The motion of the gas in both margins of the cell is backwards, *i.e.*, the gas flows to compensate the forward motion along the inlet-outlet axis. Rapid time-dependent fluctuations are observed since the flow is highly unsteady. This cell designs works as a particle stirrer and the extraction is stochastic, based on the probability that a rapidly moving particle may encounter the outlet. Again, for the interested reader, simulations of the particles trajectories are shown in Bleiner & Bogaerts (2007).

So far, we have shown how substantially larger and smaller cells have both drawbacks and advantages. Computer-aided design modifications may favor an enhancement of the performance. The analytical figures that might drive a design improvement are essentially two: (i) maximization of extraction efficiency, and (ii) enhancement of transport speed. The latter condition is important to ensure a fast rising signal of modest tailing, which is a requirement for depth-profiling analysis.

Figure 3-8 summarizes the computed values of the extraction efficiency for the various cell designs simulated. The efficiency is obtained counting the particles at the outlet divided by the total number of particles in the ablation cell. The essential characteristics of the design analysis progress are summarized in Table 3-2, highlighting the specific advantage and drawback to address.

Finally, we show computational results obtained using helium (He) instead of argon (Ar) as a carrier gas. The main physical differences between the two gases are the mass density (Ar is 1.7837 $kg/m^3$, and He is 0.1785 $kg/m^3$), which influences their diffusivity, the atom cross-section (the empirical covalent radius of Ar is 97 pm, and for He is 32 pm), and the mean free path (at atmospheric pressure it is 70 nm for Ar, and for He is 193 nm). The viscosity is rather similar. The thermal conductivity, which is very different, is not of relevance for gas flow pattern computations at constant temperature.

Figure 3-9 summarizes velocity calculated with He as carrier gas, at for 0.5 L/min and 1.0 L/min. In both velocity distribution plots one notes that the central gas plume is much wider than for the case of Ar, as shown above. Interestingly, even

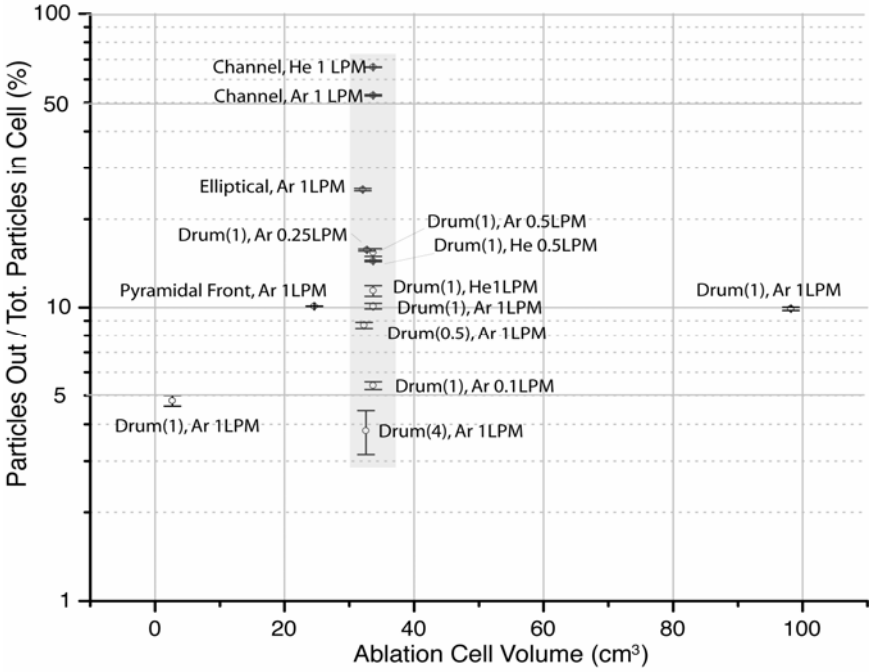


Fig. 3-8. Computed relative number of particles extracted from different cell designs using either Ar or He as carrier, shown as a function of cell volume. The data are indicated with precision figure due to the statistical outcome of the extraction process. The 'drum' is a standard cylindrical cell with its axis of symmetry orthogonal to inlet-outlet axis. The aspect ratio, *i.e.* width to height ratio, of each drum cell is given in parentheses. 'Elliptical' is a 'drum' cell stretched along the inlet-outlet axis. 'Pyramidal Front' is a half 'Drum' cell completed with a pyramidal outlet region, to eliminate gas back-circulation regions. 'Channel' is a cylindrical cell whose symmetry axis is coincident with the inlet-outlet axis. Gas flow rate in L/min (LPM). Reproduced from Bleiner *et al.* (2006) with permission.

TABLE 3-2: ESSENTIAL CHARACTERISTICS OF VARIOUS POSSIBLE DESIGNS

| **Design** | **Advantage** | **Disadvantage** |
|---|---|---|
| Drum | Large space for mounting several samples. | Narrow high efficiency zone, and wide low efficiency margins. Strong gas circulation |
| Elliptical | Reduction of the low efficiency zone. | Circulation still present across the entire volume. |
| Droplet-Shaped | Reduction of circulation to the rounded side, with flow collimation in the apical side. | Input mass flow rate must be matched to the outlet flow rate. |
| Channel-Shaped | Plug flow pattern, offering optimal confinement of the gas flow. | Enlarging the channel diameter to mount more samples may increase the Reynolds and induce loss of laminarity. |
| Eye-Shaped (as in Gurevich & Hergenroeder 2007) | Compromise solution to inject gas and extract it without flow separation | Depending on the wall profile, flow separation might occur. |

Essential characteristics of various possible designs, highlighting advantages and disadvantages. An important aspect of the cell design is that the axis of geometrical symmetry must lie parallel with the axis of gas primary flow. In the standard "Drum" design, the geometry axis is orthogonal to the gas inlet axis. This condition determines circulation because of a shear layer induced at the sides of the inlet jet. Circulation favors fractional transport, retards the particle extraction, and leads to signal broadening.

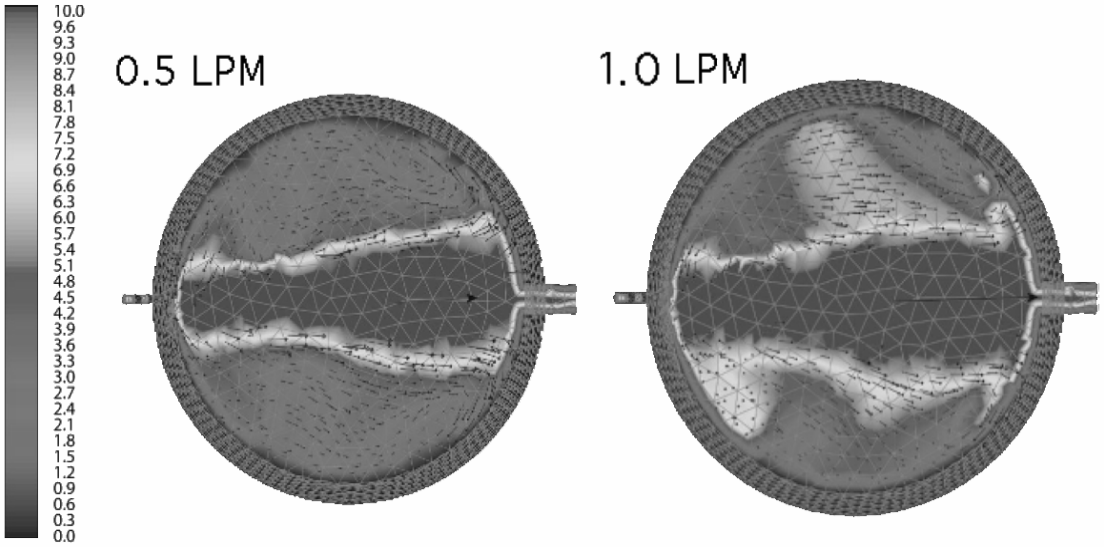


Fig. 3-9: Calculated gas speed inside a 33 $cm^3$ drum cell, with He as carrier gas at 0.5 L/min (left) and 1.0 L/min (right). The color scale gives the gas velocity in m/s. A larger high efficiency area in the center is visualized as compared to the case with Ar carrier gas. Reproduced from Bleiner & Bogaerts (2007) with permission - color version of illustration on Plate 2.

in the marginal regions there is no significant back-flow. In fact, even though the speed difference between the center and the boundary can be as high as a factor of 10 in the module, almost all velocity vectors point forwards, especially at 1 L/min. Again, for the interested reader, simulations of the particles trajectories are shown in Bleiner & Bogaerts (2007).

**Transport Line**

A few research groups have experimentally investigated the gas flow through the transport tube (Moenke-Blankenburg *et al.* 1990, Moenke-Blankenburg 1993, Bleiner 2002), also from the perspective of potential fractional transport, and suggested changes to improve the performance. Simulations have therefore the possibility to complement the observations made, supporting the data with the fundamental predictions made from first principles.

The velocity profiles, as well as the boundary layer thickness calculated, are very different for the various carrier gases (Bleiner & Bogaerts 2006) and in general the heavier gases guarantee more uniform transport conditions as a function of radial distance than the lighter gases. On the other hand, the maximum velocity of He is a factor of 1.7 greater than that of Ar, hence He provides faster sample introduction and signal rise. The range of all Reynolds numbers is well within the domain of laminar flow. Among the two main carrier gases, He provides better laminar conditions, in spite of the higher velocity, due to a lower mass density by a factor of 10.

Figure 3-10 shows a side view of the simulated particles trajectories in the tubing, with particle sizes highlighted by different colors. As a first general observation one notes that the trajectories of the finer particles are less straight-forward than those of the heavier particles. This however did not influence the transport efficiency that was in general close to 99%, for the open tube condition. It should be said that in the model the walls of the numerical grid were reflecting barriers, so that losses due to particles sticking to the tubing were not accounted for. As a second statement, one notes that the heavier particles move by saltation along the tube bottom, whereas the finer ones are suspended in the gas. However, in the case of Ar as carrier gas, the size-dependent gradation is less strong than in the case of He as carrier gas. Moreover, in the case of He the fine particles follow jagged traces, and the larger particles experience long step leaps with collision with the walls. This effect should be attributed to the higher flow velocity of He compared to Ar, and the more complex flow structure in parallel lanes. In conclusion one observes that Ar provides essentially size-independent transport efficiency. In the case of He, the transport of fine particles is less efficient, in a short period of time, than that of the large particles, due to the erratic trajectories. This

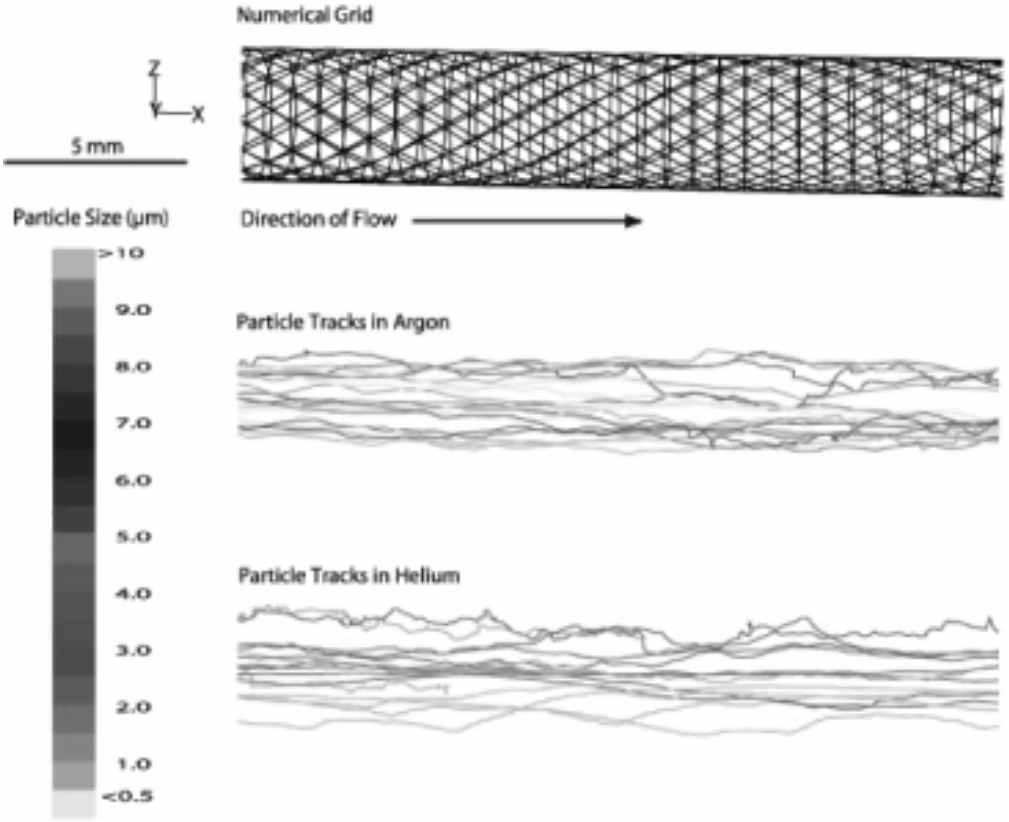


Fig. 3-10: Simulated particle trajectories in the tubing for Ar or He as carrier gas. The color scale gives the particle size in μm. In the case of He fine particles follow jagged traces floating in the gas mass, and the coarse particles experience long step leaps with collision with the walls. Ar provides essentially size-independent transport efficiency. Reproduced from Bleiner & Bogaerts (2006) with permission - color version of illustration on Plate 2.

result can be physically motivated with the longer mean free path of He versus Ar, and more pronounced slipping effects for the finer particles.

## MODELING OF LA–ICP–MS SIGNAL PROFILE

The use of pulsed lasers has introduced large flexibility in the sampling procedure. In fact, one can select the number or the rate of pulses, in order to control the sample introduction or the depth profiling. Under ideal conditions, the ablation, transport, and ICP atomization of the sample are instantaneous processes (delta function), so that no signal dispersion is to be considered. In the experiments, however, one deals with a combination of signal-broadening factors that contribute to the final measured profile. Considering the whole laser-assisted sample introduction process, such factors can be generally attributed to the duration of the laser pulse, the duration of the set-up elution period, and the duration of the ICP atomization.

The time scale of the laser pulse is 7–9 orders of magnitude shorter than the whole sample introduction process, *i.e.*, 1–100 ns pulse width *versus* a few seconds for the sample introduction or single shot signal dispersion. Thus, the laser pulse can be assumed "instantaneous", and irrelevant in the final signal broadening. On the contrary, the time scale of particle transport is of great importance. It is clearly influenced by several experimental factors, *e.g.* cell/tube geometry, carrier gas, *etc.*, and hence this process is far from being a delta function. The time scale of the ICP-atomization is a function of the particle residence time in the plasma, depending on the analyte volatility. The particle residence time is of the order of a few tens of ms (Niu & Houk 1996), and thus is 2–3 orders of magnitude shorter than the characteristic time-scale for LA–ICP–MS signal. Thus, the latter can also be neglected without any sacrifice in computational realism.

From this brief analysis on contributions to the observed signal dispersion, the coding can be

computationally lighter and physically more focused, considering the detailed aspects of the particle transport only. Generally speaking, the ICP-vaporization has its contribution to the LA–ICP–MS signal intensities, but to simplify the treatment is of practical use to model the ICP–MS response with normalized sensitivity (element-independent). Depending on whether one single laser shot or multiple pulses are delivered, the signal structure will vary significantly. Therefore, the two situations of single or multiple shot(s) will be discussed in separate sections.

**Single Shot**

The rate of particle extraction through the outlet is a function of time-dependent particle number density. Hence, when many particles are in a small setup, these elute fast, but when just a few particles remain, the elution speed drops, especially in a large setup. This behavior is described using a first order rate equation. From this exponential elution law, one can solve for the rate constant and obtain the flush rate (k) as a function of gas flow rate (F) and setup volume (V), as follows:

$$k = -\frac{1}{\Delta t} Ln\left[N(t)/N_0\right] = -\frac{F}{V_{eff}} Ln\left[1-\varepsilon\right] \qquad (3)$$

where ε is the extraction efficiency or the ratio between the particles out of the cell ($N_o$–$N(t)$) over the total particle in the cell ($N_o$). The effective volume $V_{eff}$ is the geometrical volume of the ablation set-up minus the dead volume. The dead volume is the sum of the space occupied by the target sample(s), plus the regions that are not swept by the carrier gas, due to the specific gas flow pattern. The analytical expression for the single-shot LA–ICP–MS signal is as follows (Fig. 3-11):

$$I_{pulse}(t) = \Re \cdot 2ke^{-k(t-to)}\left[1-e^{-k(t-to)}\right]h(t-t_o) \quad (4)$$

The LA–ICP–MS signal profile is ultimately the product of the ICP–MS analyte-specific response factor ($\Re$), the flush factor, the exponential evacuation of the cell combined with the co-exponential filling of the transport line. The amplitude of the signal is given by the factor 2k. To add more realism to the mathematical treatment, the Heaviside step function is applied centered on the signal onset time $t_o$. The step function is needed for the fact that an experimental measurement abruptly passes from background level to a user-generated analytical signal (Bleiner *et al.* 2005).

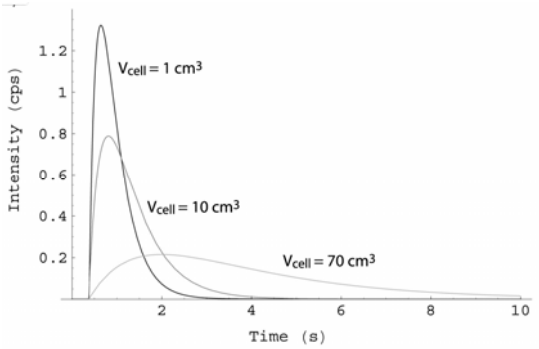


Fig. 3-11: Calculated LA–ICP–MS single shot signal profiles for a selection of ablation cell volumes: the smaller the cell volume, the sharper the signal. The signal profile is smooth because in-cell circulation issues are not modeled in this treatment. Reproduced from Bleiner & Bogaerts (2006) with permission.

**Multiple Shots**

In LA–ICP–MS measurement, several laser pulses are typically delivered at a constant repetition rate. Under this scheme, each signal data point receives the "filling contribution" of the last pulse and the "eluting contribution" of all previous pulses not yet evacuated from the set-up, as explained in detail by Bleiner *et al.* (2005). The combined signal profile (Fig. 3-12), resulting from a series of pulses at a given time interval, or repetition rate, is calculated from the convolution integral among the single shot profile $I_{pulse}(t)$ and the pulse delivery distribution function S(t). The sample delivery function can be visualized as the function that states when a certain sample pulse occurs, for how long, how high, and at what rate the whole sequence is delivered. For standard LA–ICP–MS systems, the pulse delivery distribution is a steady sequence of identical sample introduction pulses (*i.e.*, reproducible and identical amplitude, phase, width), with a pulsation period determined by the laser pulse repetition rate. One should note that the individual pulses are not strictly the laser pulses, rather "pulses of sample introduction".

**Operating Conditions**

Fig. 3-13 shows the effect of gas flow rate (a) and tube length or diameter (b) on signal intensity. One notes a steady increase of signal up to 1.2 L/min, where the signal increase rate begins to slow down. At and above 1.5 L/min the signal increase almost plateaus and is more and more comparable with the measurement precision. This model focuses on sample introduction and does not consider that the overall tendency at high flow rates is toward

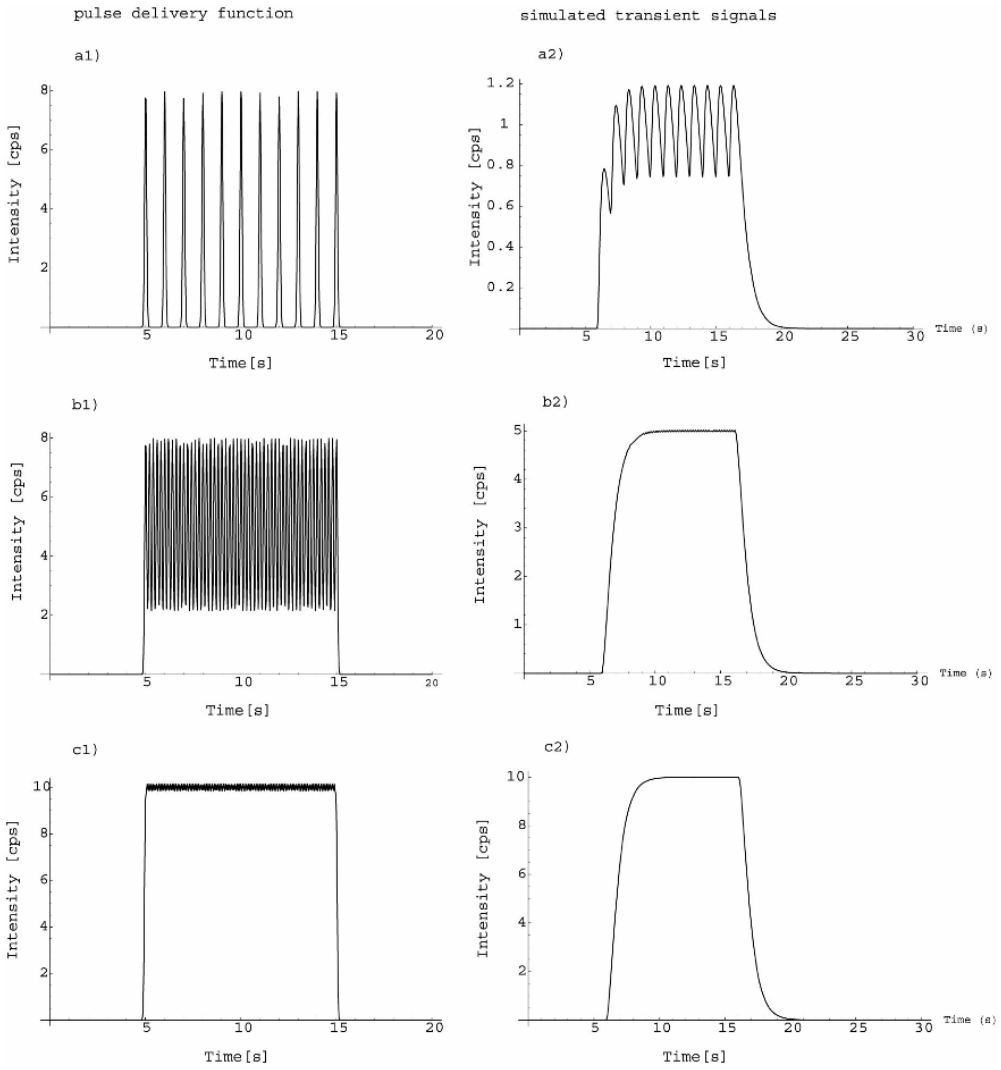


Fig. 3-12: Simulated signal profiles from a sequence of sample introduction pulses at 1 Hz (a1), 5 Hz (b1), and 10 Hz (c1), convoluted with the individual single shot profiles (shown above). For low repetition rate the transient signal is jagged (a2), whereas at higher repetition rate it becomes smoother (b2 and c2). Reproduced from Bleiner & Bogaerts (2006) with permission.

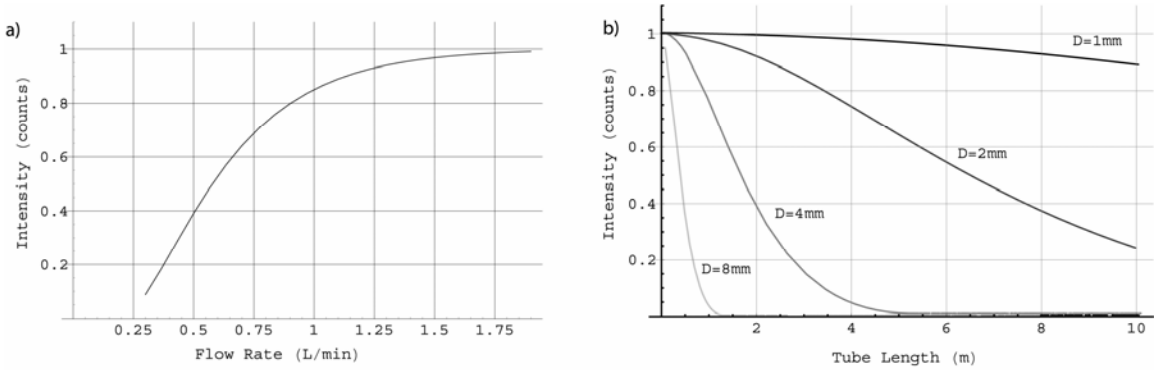


Fig. 3-13: Calculated effect of gas flow rate **(a)** and tube diameter/length **(b)** on signal intensity, due to sample introduction. Reproduced from Bleiner & Bogaerts (2006) with permission.

poorer sensitivities, due to pronounced ICP cooling effects (approximations and scope of the model!). The variation of time-integrated signals as a function of tube length for several tube diameters shows that narrow tube widths (*e.g.*, D = 1 mm) produce sharp signals, less affected by the length of the transport tubing because for narrow tubes the total volume increase as a function of tube length is modest. Thus, uniform dispersion conditions are kept over large tube lengths. Due to the power of four dependency of the pressure drop on the tube radius (Hagen-Poiseuille law), a small reduction of tube width dramatically improves transport characteristics for a given gas and flow rate. Wide tube cross-sections (*e.g.*, D = 8 mm) produce more prominent deterioration of sensitivity, poorer reproducibility, and worse limits of detection.

## REFERENCES


ANDERSON, J.D. (1995): *Computational Fluid Dynamics*. McGraw-Hill, 574p.

BÄURLE, D. (2000): *Laser Processing and Chemistry*. Springer, 649p.

BLEINER, D. (2002): *The Optimization of a laser ablation inductively coupled plasma mass spectrometry system for the detection of short transient signals*. PhD thesis, ETH Zurich.

BLEINER, D. & BOGAERTS, A. (2006): Computer simulations of laser ablation sample introduction for plasma-source elemental microanalysis. *J.Anal. Atom. Spectrom.* **21**, 1161-1174

BLEINER, D. & BOGAERTS, A. (2007): Computer simulations of sample chambers for laser ablation – inductively coupled plasma spectrometry. *Spectroch. Acta* Part B, **62**, 155-168.

BOGAERTS, A. & CHEN, Z. (2005): Effect of laser parameters on laser ablation and laser-induced plasma formation: A numerical modelling investigation. *Spectroch. Acta*: Part B, **60**, 1280-1307.

BLEINER, D., BELLONI, F., DORIA, D., LORUSSO A. & NASSISI, V. (2005): Overcoming pulse mixing and signal tailing in laser ablation inductively coupled plasma mass spectrometry depth profiling. *J. Anal. Atom. Spectrom.* **20**, 1337-1343.

BLEINER, D., CHEN, Z., AUTRIQUE, D. & BOGAERTS, A. (2006): Role of laser-induced melting and vaporization of metals during ICP-MS and libs analysis, investigated with computer simulations and experiments. *J. Anal. Atom. Spectrom.* **21**, 910-921.

CHAPMAN, S.J. (2003): *Fortran 90/95 for Scientists and Engineers*. Mc Graw-Hill, 814p.

CHEN, Z. & BOGAERTS A. (2005): Laser ablation of Cu and plume expansion into 1 atm ambient gas. *J. Appl. Phys.* **97**, 1-12.

FOUNTAIN, T.J. (2006): *Parallel Computing: Principles and Practice*. Cambridge University Press, 346p.

GREIZER, E.M., TAN, C.S., & GRAF, M.B. (2007): *Internal Flow: Concepts and Applications*. Cambridge University Press, 2007, 707p.

GUPTA, S.C. (2003): *The Classical Stefan Problem: basic concepts, modelling and analysis*. JAI Press, 385p.

GUREVICH E.L. & HERGENROEDER, R. (2007): A simple laser ICP-MS ablation cell with wash-out time less than 100 ms. *J. Anal. Atom. Spectrom.* **22**, 1043-1050.

HOCKNEY, R.W. & EASTWOOD, J.W. (1998): *Computer Simulation Using Particles*. Taylor and Francis, 564p.

HOFFMAN, J.D. (2001): *Numerical Methods for Engineers and Scientists*. CRC.

INCROPERA, F.P., DEWITT, D.P., BERGMAN, T.L. & LAVINE, A.S. (2006): *Introduction to Heat Transfer*. Wiley, 1024p.

LINPACK. Technical report, www.netlib.org/linpack.

MILLER, J.C. & HAGLUND, R.F. (1998): *Laser Ablation and Desorption*. Academic Press.

MOENKE-BLANKENBURG, L. (1993): Laser ICP spectrometry. *Spectroch. Acta. Rev*. **15**, 1-37.

MOENKE-BLANKENBURG, L., GAECKLE, M. GUENTHER, D. & KAMMEL, J. (1990): Processes of laser ablation and vapour transport to the ICP. *In* Plasma source mass spectrometry (K.E. Jarvis & A.L. Gray, *eds.*). Royal Society of Chemistry, Cambridge, UK, 1-17.

NIU, H. & HOUK, R.S. (1996): Fundamental aspects of ion extraction in inductively coupled plasma mass spectrometry. *Spectroch. Acta* Part B **51**, 779-815.

RADZIEMSKI, L. & CREMERS D. (1989): *Laser-induced Plasmas and Applications*. CRC, 437p.

RAPAPORT, D.C. (2004): *The Art of Molecular Dynamics Simulation*. Cambridge University Press, 568p.

ROSS, S.M. (2006): *Simulation*. Academic Press, 298p.

RULLIERE, C. (2004): *Femtosecond Laser Pulses: Principles and Experiments*. Springer, 426p

SCHLICHTLING, H., GERSTEN, K., KRAUSE, E., OERTEL, H. JR. & MAYES, C. (2004): *Boundary Layer Theory*. Springer, 799p

SUKOP, M.C. & THORNE, D.T. JR. (2005): *Lattice Boltzmann Modeling: An Introduction for Geoscientists and Engineers*. Springer, 172p.

TENNEKES, H. & LUMLEY, J.L. (1972): *A first course in turbulence*. MIT Press, 1972, 300p.

# CHAPTER 4: COMPARISON OF FEMTOSECOND AND NANOSECOND LASER INTERACTIONS WITH GEOLOGIC MATRICES AND THEIR INFLUENCE ON ACCURACY AND PRECISION OF LA–ICP–MS DATA

Ingo Horn
Institute for Mineralogy
Leibniz University Hannover
Callinstr. 3
D–30167 Hannover
Germany
Email: i.horn@mineralogie.uni-hannover.de

## INTRODUCTION

Today's commercially available laser ablation systems are generally based on either Nd:YAG or Excimer lasers which produce a variety of different wavelengths at pulse durations between 3 and 25 nanoseconds (ns; $10^{-9}$ sec). Consensus has been reached in the earth science community on the use of ultraviolet (UV) pulses for ablation of materials of geological interest, because most of these materials absorb strongly in the UV region and that absorption is a material-constant. The most commonly used wavelengths are 213 nm, the quintupled frequency of the Nd:YAG laser, and 193 nm, the fundamental wavelength of the ArF excimer laser. The main drawback of ns laser ablation is laser-induced elemental and isotopic fractionation, which has been described in a variety of publications (Cromwell & Arrowsmith 1995, Eggins *et al.* 1998, Hirata 1997, Jackson & Günther 2003, Košler *et al.* 2005, Kuhn & Günther 2003, Liu *et al.* 2000, Longerich *et al.* 1996, Mank & Mason 1999). However, general technological improvements have now made femtosecond (fs; $10^{-15}$ sec) laser systems available for ICP–MS, and there is some evidence that laser-induced fractionation is significantly reduced or eliminated using them. Femtosecond lasers are more expensive than nanosecond lasers because several solid state lasers are employed in these systems. No "turn key" commercial fs–LA system is currently available but this situation may change in the near future.

Similarly to ns laser ablation, frequency conversion of the fundamental wavelengths of fs lasers to the UV region can be performed (Russo *et al.* 2002), although no consensus has yet been reached on whether UV is desirable for fs ablation. Wavelengths similar to those known from ns laser ablation are accessible in the second, third and fourth harmonics of the fundamental wavelengths of fs lasers. Fundamental differences however arise from the fact that fs pulses deposit the energy onto the target material faster than thermal diffusion transports the energy away from the ablation area. This allows ablated materials to be heated to much higher temperatures compared to ns laser pulses. The timescale of this process is in the sub-picosecond ($<10^{-12}$ sec) range.

The analytical advantage of femtosecond laser ablation lies within the possibility of reduction of elemental and the elimination of isotopic fractionation to below levels that can be detected by LA–ICP–MS (Horn & von Blanckenburg 2007). Pecheyran *et al.* (2007) and Koch *et al.* (2006) illustrated that with respect to elemental fractionation fs laser ablation generally improved the results obtainable. Fernandez *et al.* (2007) summarized various fs laser systems that have been coupled to ICP-based instrumentation. Wavelengths between 1030 and 196 nm can be employed in such systems. The improvements of fs over ns laser ablation are discussed in this chapter with respect to the obtainable precision and accuracy of measurements on geological materials.

## THE ABLATION MECHANISM

Fundamental studies carried out on metals illustrate that the ablation mechanism of ns laser pulses is dominated by thermal effects, which is also true for femtosecond laser ablation. This generally results in melting of the material ablated (Horn *et al.* 2001, Kuhn & Günther 2003, Mao *et al.* 1998, Margetic *et al.* 2001b). The thermal ablation mechanism of ns laser pulses leads to elemental fractionation, which is regarded as a severe analytical limitation for the application of mineral dating using U/Pb geochronology and other geological applications. A small number of laboratories employ fs laser pulses for the

Mineralogical Association of Canada Short Course 40, Vancouver, B.C., p. 53–65.

determination of concentrations of minor and trace elements mainly in conjunction with quadrupole ICP–MS, or for the determination of isotope ratios of heavy stable isotope systems such as Si and Fe using multi-collector ICP–MS systems (Bian *et al.* 2006, González *et al.* 2004, Horn *et al.* 2006b, Margetic *et al.* 2001a, Poitrasson *et al.* 2003, Samek *et al.* 2004). Shorter laser-induced plasma life times are observed in fs ablation when compared to the ns ablation process, allowing for more efficient energy transfer to the sample without interaction of ejected material with the incoming laser pulse. It is clear that fundamental differences exist between the ablation mechanism of fs and ns pulses and that research is still far from a complete understanding (Miotello & Kelly 1995, Yoo *et al.* 2000, Zeng *et al.* 2005).

Several ablation mechanisms have been discussed in the literature which include vaporization, fragmentation, spallation, explosive boiling (or phase explosion), spinodal decomposition (or critical point phase separation). Most of these processes occur at least in part outside of thermodynamic equilibrium (Perez & Lewis 2003). The ablation process always appears to involve more than one of the above processes. Since the ablation process occurs partly outside the thermodynamic equilibrium, theoretical consideration by molecular dynamics simulations of femtosecond pulse interactions may help to increase our understanding. Cheng & Xu (2005) and Lorazo *et al.* (2006) investigated nickel and silicon target materials using molecular dynamics simulations across an energy density range of ~0.2 to 1.5 J/cm$^2$. Their simulations illustrated that two different ablation mechanisms occur depending on the laser fluence (laser energy per unit area, *e.g.*, J/cm$^2$). At low fluence, the process is dominated by *explosive boiling* while at high fluence, *spinodal decomposition* or *critical point phase separation* is the dominant ablation mechanism.

Figure 4-1 is a time sequence that illustrates the development of phases formed during ablation of solid crystalline Si. The phase diagram of Si and the thermodynamic pathways after femtosecond and nanosecond pulse interaction are shown (modified after Lorazo *et al.* 2006). Material is elevated to supercritical temperatures of ~10000 K during fs ablation. Cooling leads to nucleation of liquid and vapor at the intersection with the liquid–vapor phase boundary followed by the formation of nm sized melt droplets and gas. For ns pulse interaction with solid matter, pulse widths of 3 – 25 *10$^{-9}$ s are

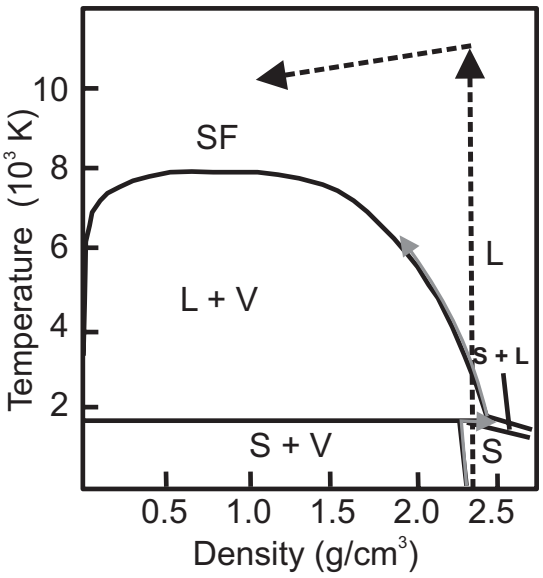


FIG. 4-1: Schematic illustration of the thermodynamic pathway in Si for fs (dashed line) and ns (solid grey line) ablation. For details see text in Lorazo *et al.* (2006) (figure after Lorazo *et al.* 2006). S=solid; L=liquid; V= vapor, SF=critical point.

applied, which is too slow to compensate for thermal diffusion taking place on time scales of $10^{-11}$ s (Russo *et al.* 1999). The result is that heating to supercritical temperatures is not achieved and there is the formation of a melt layer (Fig. 4-1). For details on the thermodynamic pathways under fs, ps and ns ablation, see Lorazo *et al.* (2006).

## FUNDAMENTAL ASPECTS IN FEMTOSECOND LASER ABLATION

### Wavelength and energy density-dependent ablation rates

The recent study by Hirata & Kon (2008) illustrated that the ablation rate of fs pulses at a wavelength of 780 nm in the infrared (IR) is 7 to 10 times higher than with Excimer laser ablation at 193 nm at an identical fluence at the sample. For borosilicate glass a fs ablation rate of ~0.8 µm/pulse was determined using an energy density of 5 J/cm$^2$. Measurements with a fluence of 30 J/cm$^2$ on borosilicate glass by Ben-Yakar & Byer (2002) reported an ablation rate of 0.6 µm/pulse using a wavelength of 800 nm while Kim *et al.* 2000 reported ablation rates for metals and silicon of 0.2 to 2 nm/pulse at the ablation threshold. Freydier *et al.* (2008) investigated Pb/U ratio stability as a function of pulse width using 800 nm and 266 nm fs pulses for ablation. The resulting crater depth at 800 nm indicated an ablation rate of ~ 0.4 µm/pulse for

NIST 612 which is similar to the observations of Hirata & Kon (2008) and Ben-Yakar & Byer (2002), and almost twice as fast as reported for a 193 nm Excimer laser system (Horn *et al.* 2001). At a repetition rate of 5 Hz and an acquisition time of 120 seconds, a crater depth of ~ 250 µm would be excavated. For a standard thin section thickness of 30 µm, a measurement time of only 15 seconds could be realized under these conditions before drill-through, which would limit the achievable precision.

Measurements performed by Chmeleff *et al.* (2008) using 196 nm fs pulses at an energy density of 1.5 J/cm$^2$ show ablation rates of ~10 nm/pulse for synthetic diopside glass. For comparison, using commercially available laser ablation systems, rates for ns laser ablation have been reported for a variety of different matrices. They range from 0.1 to 1.5 µm/pulse, depending on the nature of the material and energy density on the sample (Horn *et al.* 2001).

**Pulse energy, energy density and pulse width**

Most commercially available single stage amplified femtosecond laser systems reach output energies between 1 and 3.5 mJ in the IR. If higher pulse energies are required a second amplification stage can be used, generating several tenths of mJ additional energy. Amplification can be performed using regenerative, chirped pulses, or multi-pass systems. Femtosecond pulses can only be generated if the optical medium used (laser rod) generates a wavelength spectrum with several oscillation modes or wavelengths. Energy densities used for analytical purposes vary significantly, ranging from 1.5 J/cm$^2$ (Horn & von Blanckenburg 2007) to 20 J/cm$^2$ (Hirata & Kon (2008)). However, Chmeleff *et al.* (2008) reported that Si isotope measurements decrease in precision at higher energy densities and that this seems to be material dependent.

Up until now, pulse widths between 60 and 400 fs have been used for analytical purposes, even so Freydier *et al.* (2008) carried out experiments between 60 and 3000 fs in order to evaluate the performance differences. A 'low energy' high repetition rate ablation procedure using 1030 nm was applied by Pecheyran *et al.* (2007) and Fernandez *et al.* (2007). Pulse energies of up to 200 µJ/pulse were applied at a repetition rate of up to 10000 Hz, excavating craters of several hundred micrometres in only a few seconds; this could be called micro-machining coupled to ICP–MS. In the deep UV region up to 50 µJ/pulse (Koch *et al.* 2006) have been generated of which only a few µJ/pulse reach the sample surface with repetition rates of up to 150Hz (Chmeleff *et al.* 2008).

**Aerosol structure and compositional analyses**

According to the literature, ns–LA–ICP–MS using non-matrix-matched calibration has successfully been applied to the analyses of various silicate glasses and geological materials (Gao *et al.* 2002, Guillong *et al.* 2003, Günther & Hattendorf 2005, Hattendorf & Günther 2003, Resano *et al.* 2003). For metals and semi-conductors, however, quantification by non-matrix-matched calibration turned out to be extremely difficult since diffusion of heat out of the irradiated volume generally results in melting and material re-distribution during the LA process. As a consequence, the overall composition of aerosols formed by ns LA can severely depart from the expected bulk value, especially if intensively fractionating matrices such as metal alloys are analyzed (Kuhn & Günther 2003, Liu *et al.* 2005). To suppress these effects, the laser pulse duration needs to fall below the material-specific thermal relaxation time, which is in the range of a few hundred fs, as discussed above. Reducing the pulse duration down to this region has, therefore, been suggested to improve the LA characteristics and to approach to the concept of matrix-independent, "stoichiometric" LA (Bian *et al.* 2006, Garcia *et al.* 2008).

Over the last five years, the performance features of fs LA as a way to create such 'stoichiometric' aerosols has been thoroughly examined in several studies ranging from the compositional analysis of aerosol particles collected directly from the laser through to ICP–MS- and optical emission spectrometry (OES)-based studies. For instance, aerosol particles produced by near infrared (NIR)–fs–LA of brass (Koch *et al.* 2004) and silicate glass (Koch *et al.* 2005) were classified by low pressure impaction and analyzed using total reflection X-ray fluorescence (TXRF). These studies demonstrated that the application of fs pulses creates aerosols mainly consisting of primary particles and aggregates covering a size range of approximately 10 nm up to 100 nm. Aerosols of this size range can be efficiently transported over larger distances (~1 m) (Arrowsmith & Hughes 1988). Their compositions will be representative of the bulk sample (Fig. 4-2) as long as the LA settings such as wavelength and fluence are chosen appropriately (Garcia *et al.* 2008, Koch *et al.* 2004, Koch *et al.* 2005). The recent study of Wälle *et al.*

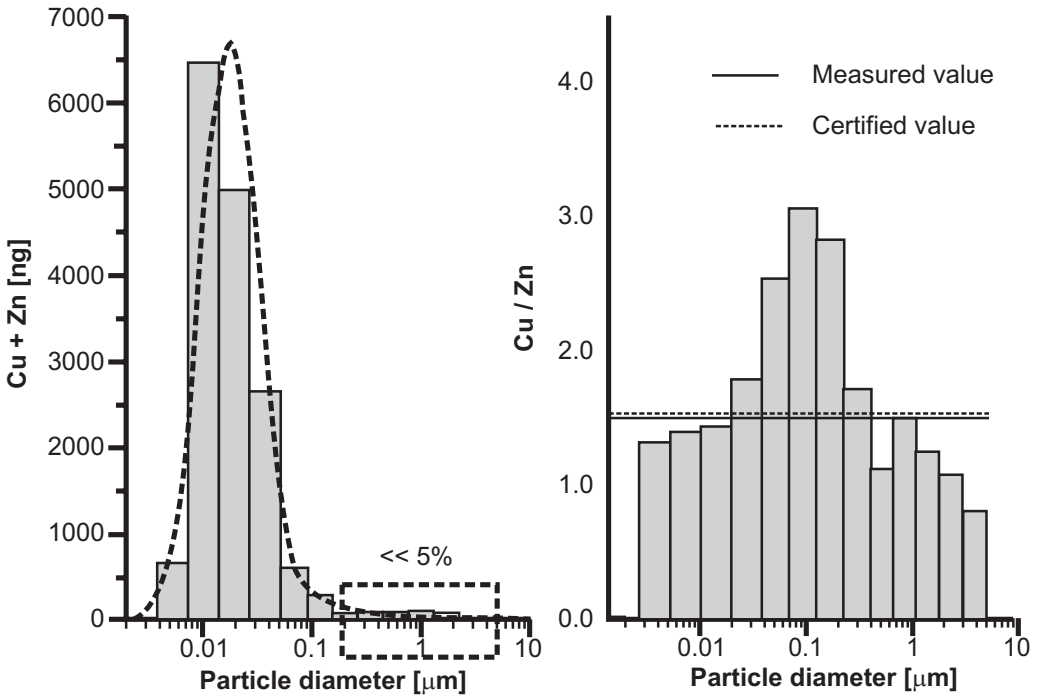


FIG. 4-2: Size-dependent particle mass distribution and composition of aerosols generated by near-IR (775 nm) fs–LA of brass under He atmosphere and a fluence of 2.5 $Jcm^{-2}$ (total number of shots:1.5 x $10^4$). The dashed grey curve is a log-normal fitting curve (after Koch *et al.* 2004).

(2008) reconfirmed the absence of elemental fractionation in aerosols produced during fs LA of brass through quadrupole ICP–MS analysis using on-line addition of liquid standards. Depending on the element considered, accuracies better than 99% were achieved.

**Precision and accuracy**

In order to provide evidence for the increase in precision and accuracy obtainable with fs laser ablation, investigations have focused on the determination of Pb/U ratios (Freydier *et al.* 2008, Hirata & Kon (2008), Horn & von Blanckenburg 2007, Poitrasson *et al.* 2003). Comparison of ns and fs laser ablation for U/Th elemental ratios were investigated by González *et al.* (2008) and for elemental concentration determinations by González *et al.* (2006). Their results revealed a significant bias during ns laser ablation, which is not observed during fs laser ablation. The expected U/Th elemental ratio for the NIST 610 reference material is 1.007 if calculated from certified values (Horn & von Blanckenburg 2007). González *et al.* (2008) determined a ratio of 0.98 using fs laser ablation while ns ablation gave a ratio of 1.75. These results are in agreement with those obtained by Horn & von Blanckenburg (2007) (Fig. 4-3). Poitrasson *et al.* (2003) reported an external level of precision of 0.4 and 2.8 % (2SD) for the $^{206}Pb/^{238}U$ ratio in NIST 610 and 612 respectively using a quadrupole-based mass spectrometer in conjunction with a UV (266 nm) fs laser ablation system. This is 2 to 3 times better than that obtained by ns laser ablation, under similar conditions, if no correction through standardization is applied. Freydier *et al.* (2008) determined the day to day precision for $^{206}Pb/^{238}U$ ratio determinations of NIST612 to be 2% (1σ) when calibrated against NIST610, which has been reported to be inhomogeneous at similar levels in its elemental concentrations (Eggins & Shelley 2002) and Pb/U ratios (Horn & von Blanckenburg 2007). Horn & von Blanckenburg (2007) further illustrated that a precision of better than 0.4% (2σ) for the $^{206}Pb/^{238}U$ ratio in NIST 610 can be obtained even though counting statistical limitations apply when using Faraday cups in multi-collection mode for the detection. Horn & von Blanckenburg (2007) used a wavelength of 196 nm and similar pulse width to that of Poitrasson *et al.* (2003).

Besides the Pb/U and U/Th ratio determinations, Cu/Zn ratios by ns and fs laser ablation also have been compared. Cu/Zn ratios have been investigated using ns laser ablation by Liu *et al.*

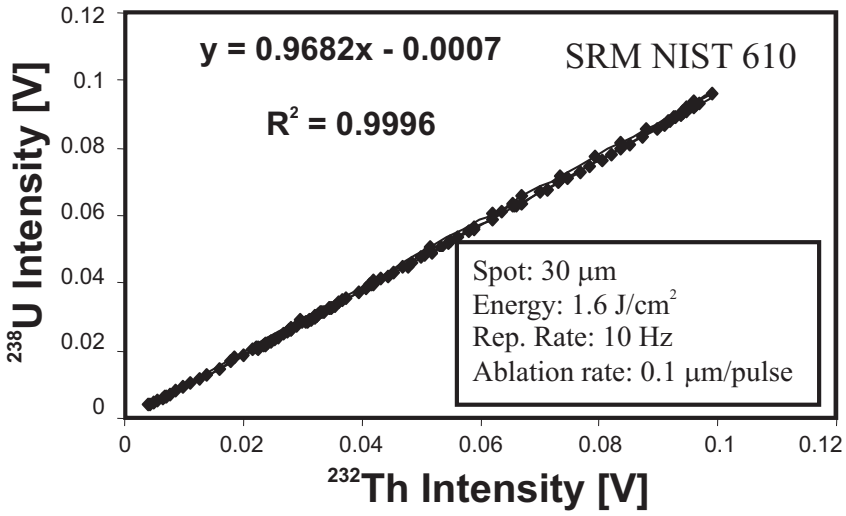


FIG. 4-3: Intensity variations of U and Th for ablation of a single spot of NIST 610 using a UV (196 nm) fs laser ablation system and Faraday cups on a Thermo-Finnigan Neptune MC–ICP–MS (modified after Horn & von Blanckenburg 2007).

(2004) and Kuhn & Günther (2003) while fs laser ablation was assessed by Margetic *et al.* (2000) and Margetic *et al.* (2001b). Further investigations have focused on the determination of isotope ratios of Mg, Fe, Cu and Si by fs and ns laser ablation. So far, comparisons between fs and ns laser ablation have been made only for Fe and Si isotopes with respect to the obtainable precision and accuracy.

**Isotope ratio determinations (Mg, Si, Fe, and Cu)**
Košler *et al.* (2005), Hirata & Kon (2008), Horn *et al.* (2006a) and Horn & von Blanckenburg (2007) have investigated Fe isotope ratio determinations by laser ablation. Košler *et al.* (2005) used a ns laser ablation system operating at 213 nm (~5 ns pulse width) while Hirata & Kon (2008) performed experiments at 780 nm (227fs pulse width) and 193 nm (20 ns pulse width). Horn & von Blanckenburg (2007) and Horn *et al.* (2006a) used 196 nm at a pulse width of ~200 fs. Košler *et al.* (2005) illustrated that spot analyses could not be carried out successfully for ns laser ablation under the conditions used. They reported a transient shift in Fe isotope ratios which is correlated with the depth of the ablation crater and relates to changes in the particle size distribution of the ablated aerosol. The observed variations are ~4 ‰ which is close to the isotopic variations for Fe observed so far in natural samples (Fig. 4-4). Hirata & Kon (2008) compared the performance of fs versus ns laser ablation with respect to precision of Fe isotope measurements. Their results indicate no significant improvements when using IR fs laser ablation. The precision, here recalculated as $\delta^{56}$Fe values, are 0.32 ‰ for IR fs and 0.36 ‰ for UV ns laser ablation. However, these results are largely related to instrumental

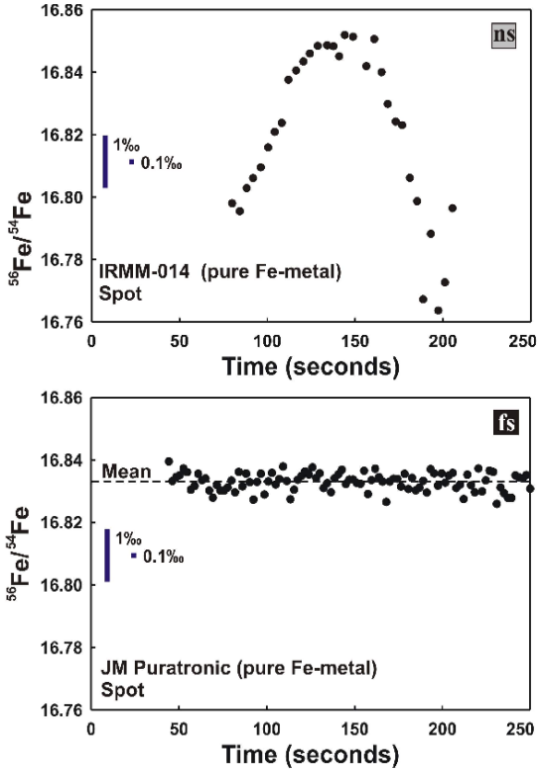


FIG. 4-4: A comparison of ns and fs spot analysis of Fe isotope ratios in pure Fe-metal under similar analytical conditions using a Thermo-Finnigan Neptune MC–ICP–MS for detection. TOP: ns ablation of IRMM-014 reference material using 213 nm for ns ablation (after Košler *et al.* 2005). BOTTOM: fs ablation of JM Puratronic reference material using 196 nm for fs ablation (after Horn & von Blanckenburg 2007).

fluctuation rather than to the ablation process differences.

Jackson & Günther (2003) investigated Cu isotope ratios using ns laser ablation. The results obtained illustrate a significant bias, depending on the particle size distribution introduced to the ICP of the mass spectrometer, similar to that observed for Fe when using ns laser ablation (Fig. 4-5). Jackson & Günther (2003) reported a precision of better than 1 ‰ for $^{65}Cu/^{63}Cu$ could be achieved when larger particles (>0.5 µm) were removed by filtering. They suggested that the dominant source of isotopic fractionation in ns ablation of Cu (under the high laser fluence conditions employed in their study) was the preferential volatilization of $^{63}Cu$ during incomplete vaporization and ionization in the ICP of particles greater than approximately 0.5 µm in diameter.

Norman *et al.* (2006) revealed that, in addition to Fe and Cu, isotope measurements of Mg are subject to an isotope fractionation effect when using ns LA–MC–ICP–MS. Young *et al.* (2002) did not report a similar Mg isotope fractionation effect but it may only be observed when more than one well characterized isotope standard reference material is used.

The precision obtained for isotope ratios by fs laser ablation is somewhat dependent on the abundance of the isotopes of interest and their mass range. Chmeleff *et al.* (2008) reported Si isotope analyses using UV fs laser ablation on various matrices that had been thoroughly analyzed by round robin testing (Reynolds *et al.* 2006). They found an external precision of ~0.2 ‰ (2σ) for the $^{28}Si/^{30}Si$ in two international reference materials (IRMM-018 and NBS 28). These are two of three solid international reference materials available for Si isotopes and are composed of Si and $SiO_2$, respectively (Chmeleff *et al.* 2008). For Fe isotopes a slightly better external precision of ~0.1 ‰ (2σ) was obtained for the $^{56}Fe/^{54}Fe$ ratio for a variety of matrices (Horn *et al.* 2006a) with the variation depending on their internal homogeneity. These matrices include Fe oxides/hydroxides, Fe carbonates, sulfides, metals, metal alloys, and silicates. The results indicate that laser ablation is capable of producing a precision for the isotope systems of Si and Fe which is similar to that obtained by conventional solution nebulization MC–ICP–MS after chromatographic separation.

**Laser-induced isotope fractionation**

The problems encountered by Jackson & Günther (2003), Košler *et al.* (2005) and Norman *et al.* (2006) for ns laser ablation described above are similar and seem to apply to the isotopic systems of Mg, Fe and Cu. In heavy stable isotope analysis a ratio of a heavy isotope over a light isotope is compared to that of a standard, with the difference usually reported in ‰. This is required because the absolute ratios cannot be extracted directly due to the mass discrimination produced by space charge effects and ion optics in ICP–MS. The mass discrimination however stays relatively constant, after initial effects during instrumental warm-up, for ICP-based instrumentation. In the case of isotope fractionation the ratio (*e.g.*, $^{56}Fe/^{54}Fe$, $^{65}Cu/^{63}Cu$) increases with increasing crater depth during a spot analysis. This correlates with a change from larger particles to smaller particles in ablated aerosols with increasing crater depth (Kuhn *et al.* 2004).

This transient component of fractionation is superimposed on the mass discrimination of the ICP–MS system (see examples of Jackson & Günther 2003, Košler *et al.* 2005, Norman *et al.* 2006). This is shown schematically in Figure 4-6

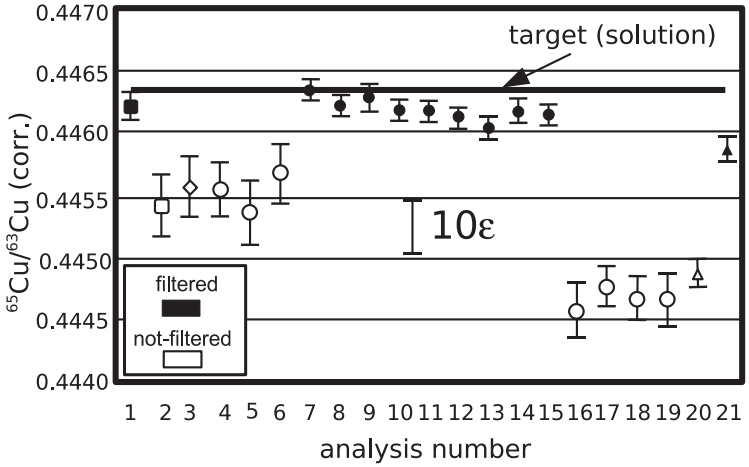


FIG. 4-5: Mass discrimination corrected $^{65}Cu/^{63}Cu$ ratios for glass wool-filtered and non-filtered line scan UV ns ablations of a pure copper disc in Ar atmosphere. Different symbols and shapes represent analyses performed on different days using operating conditions optimized daily (after Jackson & Günther 2003).

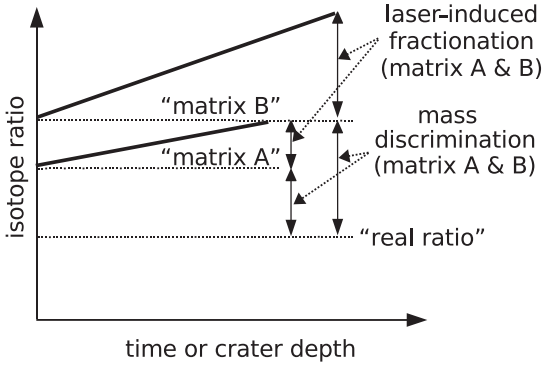


FIG. 4-6: Schematic illustration of instrumental mass discrimination during solution nebulization (dashed lines) and laser-induced isotope fractionation (solid lines) of isotope ratios for two different matrices (A & B) in solution (dashed lines) and for laser ablation (solid lines). For different matrices the transient laser induced component is superimposed onto the constant mass discrimination of the mass spectrometer. Mass discrimination may be different for solution nebulization ("wet plasma") and laser ablation ("dry plasma") conditions (Figure modified after Horn & von Blanckenburg 2007).

and for Mg isotopes ratios measured in olivine of variable composition in Figure 4-7. Laser induced fractionation is a mass-dependent effect and therefore even in a three-isotope plot (*e.g.*, $\delta^{56}$Fe *vs.* $\delta^{57}$Fe) it is indistinguishable from drift in mass discrimination.

A model for isotope fractionation has been proposed by Horn & von Blanckenburg (2007) based on thermal diffusion (Fig. 4-8), which can also explain the U/Th fractionation observed during ns laser ablation. Their model involves slightly different diffusivities for the heavy and a light isotope, resulting in the preferential release of the light isotope due to kinetic fractionation. Isotope specific diffusion studies have not been carried out for many elements. Li diffusion in liquid Li has been studied and resulted in a diffusivity difference of 30% between the two isotopes of Li (Lodding *et al.* 1970).

**Accuracy and matrix dependency**

Accuracy is generally investigated through the determination of reference materials. This is more difficult to achieve for micro-analysis as only a limited number of reference materials have been certified on the micro-scale. For stable isotope analysis of Fe IRMM-14 is used as a primary standard, while NBS 28 is used for Si isotope analysis. Neither of these international reference materials is certified for micro-analysis. The Institute of Reference Materials and Measurements (IRMM) offers certified isotopic solid materials for stable isotope analyses for the elements Li, B, Si, Fe and Pt. Silicon is the only system where more than 2 solid standard reference materials exist (IRMM-017, IRMM-018a and NBS 28). Due to this limitation, tests for accuracy commonly have to be carried out using materials previously analyzed by solution nebulization after chromatographic separation.

Chmeleff *et al.* (2008) illustrated the accuracy obtainable for fs laser ablation of IRMM-017 for silicon isotope analysis using NBS 28 as the bracketing standard. The results obtained are in good agreement with those compiled by Reynolds *et al.* (2006). Chmeleff *et al.* (2008) determined values of $\delta^{29}$Si of –0.65‰ and a $\delta^{30}$Si of –1.25‰ for IRMM-017 whereas Reynolds *et al.* (2006) reported a $\delta^{29}$Si of – 0.63‰ and a $\delta^{30}$Si of –1.28‰. Other materials, previously investigated through a

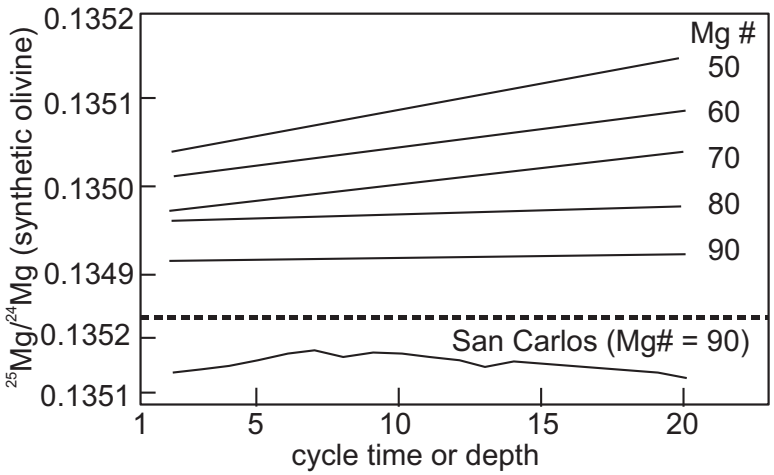


FIG. 4-7: Mg isotope analyses of synthetic olivine with different Mg-numbers (Mg #) determined by 193 nm ns ablation coupled to a Thermo-Finnigan Neptune MC–ICP–MS. Measured ratios of $^{25}$Mg/$^{24}$Mg increase towards higher values during spot analyses to different degrees depending on the Mg # of the analyzed olivine. The transient component added onto the mass discrimination of the mass spectrometer changes the $^{25}$Mg/$^{24}$Mg by ~1‰ over 20 measurement cycles (~80 s). (Figure modified after Norman *et al.* 2006)

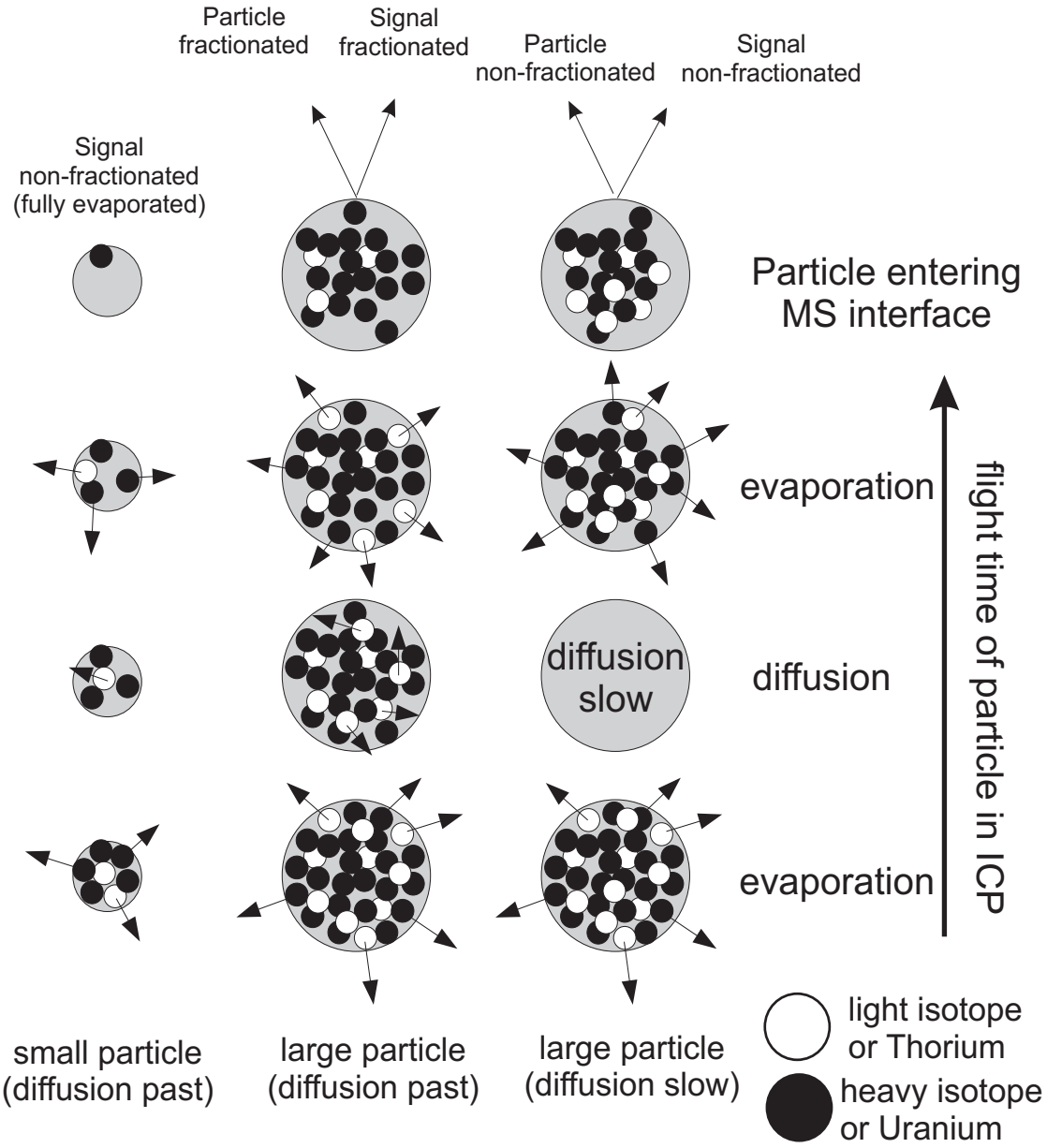


FIG. 4-8: Model for the generation of isotope and U/Th fractionation during laser ablation. The paths of particles of different size through the inductively coupled plasma of the mass spectrometer are illustrated. Three scenarios are envisioned: **Right** column – illustration of a large particle (not to scale) entering the ICP, being successively vaporized. The particle stays relatively cold so that diffusivity differences between light and heavy isotopes (or U and Th) are negligible. After the initial evaporation of atoms from the particle, even if the light isotope is preferentially evaporated, the remaining heavy isotopes have to be removed first before lighter isotopes can be evaporated. The remaining particle and the evaporated atoms would have isotope ratios that would not be fractionated. **Middle** column – if diffusion, slightly different between the light and heavy isotope, does play a role, it is likely that after the initial vaporization lighter isotopes would diffuse to the particle surface and be evaporated preferentially. The resulting measurement (evaporated atoms) and remaining particle would then be fractionated with respect to isotope ratios being enriched in the light isotope relative to the heavy isotope. **Left** column **–** this illustrates the path of a small particle that is completely evaporated and therefore produces a signal in the ICP–MS that is not fractionated in isotope ratios (or Th/U). The proposed model can explain the observations made for U/Th ratios because U and Th are expected to have different thermal diffusivities (Th diffusion being faster than U diffusion). Figure is modified after Horn & von Blanckenburg 2007.

round robin testing show similar results illustrating that UV fs laser ablation can achieve results comparable to that of solution nebulization ICP–MS (Fig. 4-9). Similar results for Fe isotope ratio analysis were obtained by Horn *et al.* (2006b) for a wide spectrum of matrices (Fig. 4-10).

Additional evidence that elemental fractionation is less dominant for fs laser ablation than ns ablation comes from determinations of Pb/U and U/Th ratios. Horn & von Blanckenburg (2007) demonstrated that elemental fractionation with respect to Pb/U ratios is below the detectability of a multi-collector ICP–MS system equipped with Faraday cups such that calibration for zircon and baddeleyite analysis can be performed successfully using NIST 610 or zircon as a bracketing standard when using UV–fs–laser ablation. A calibration performed on zircon grains and applied to the Phalabowra baddeleyite has been shown to produce 'reversely discordant' U–Pb data when using 193 nm ns laser ablation (Horn *et al.* 2000) while UV–fs ablation produces 'normally discordant' U–Pb results. The ages derived from UV–fs ablation are only slightly older than those measured by TIMS for the baddeleyite which is to be expected for micro-analyses compared to bulk analyses. Freydier *et al.* (2008) pointed out that the accuracy of $^{206}Pb/^{238}U$ measured by LA–ICP–MS may be biased (on the order of 10%) when lasers with pulse widths of >200 fs are used for cross-calibration of NIST610 and NIST612.

## CONCLUSION

Femtosecond laser ablation has not yet been proven undoubtedly to eliminate elemental or isotopic fractionation. Data provided by the recent studies of Freydier *et al.* (2008) and Hirata & Kon (2008) still show behavior similar to that observed for ns laser ablation with respect to Pb/U fractionation which is in contrast to observations made by Horn & von Blanckenburg (2007). Whether these different results are related to different wavelengths used (IR vs UV) or the result of the large differences in the ablation rates and energy densities still has to be investigated. Results obtained on U/Th ratios on the other hand demonstrate clear improvements in precision and accuracy for fs ablation (González *et al.* 2008, Horn & von Blanckenburg 2007). For heavy stable isotope ratio determinations, significant improvements have been reported by Horn *et al.* (2006b) for fs laser ablation. Horn & von Blanckenburg (2007) and Chmeleff *et al.* (2008), illustrated that a precision and accuracy close to that obtained by conventional solution nebulisation coupled to MC–ICP–MS can be obtained for the Fe and Si isotope systems. Femtosecond laser ablation has been applied to only a limited number of isotopic systems which makes a full comparison between fs and ns laser ablation difficult at the present time.

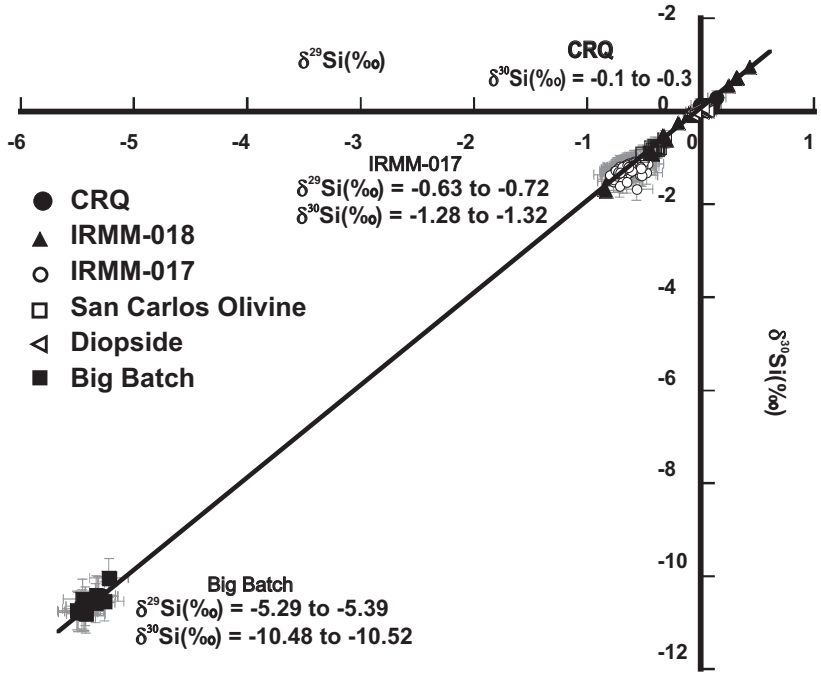


FIG. 4-9: Accuracy illustrated for UV fs laser ablation in a 3 isotope plot for Si stable isotope analysis. Values given are reference values for IRMM-017, Big Batch and Caltech Rose Quartz (CRQ) (modified after Chmeleff *et al.* 2008). Error bars are 2 standard deviations of the mean of all cycles of individual measurements. A linear regression line of y = 1.96x + 0.01 fits the data.

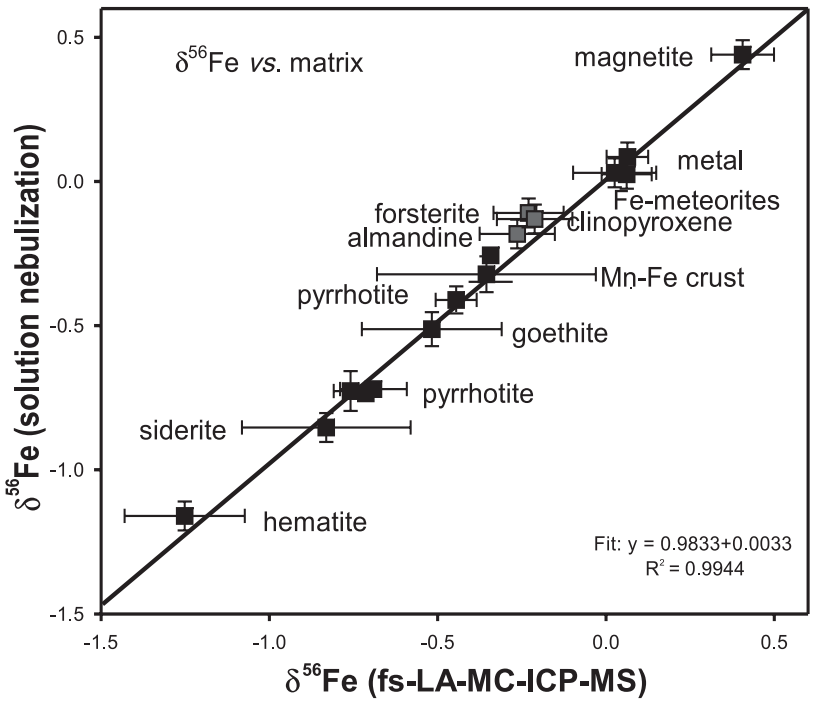


FIG. 4-10: Matrix independency of UV fs laser ablation is illustrated here in comparison to bulk solution nebulization ICP–MS after chromatographic separation of Fe in a variety of minerals (modified after Horn *et al.* 2006b). 2σ error bars are shown; larger error bars reflect sample inhomogeneity (*e.g.*, Mn–Fe crust, goethite, siderite and hematite).

**ACKNOWLEDGEMENTS**

I would like to thank Detlef Günther, Joachim Koch and Paul Sylvester for help in the preparation of this short course chapter.

**REFERENCES**

ARROWSMITH, P. & HUGHES, S.K. (1988): Entrainment and transport of laser ablated plumes for subsequent elemental analysis. *Appl. Spectrosc.* **42**, 1231-1239.

BEN-YAKAR, A. & BYER, R. (2002): Femtosecond laser machining of fluidic microchannels for miniaturized bioanalytical systems. *Proc. SPIE - The International Society for Optical Engineering* **4637**, 212-217.

BIAN, Q., GARCIA, C., KOCH, J. & NIEMAX, K. (2006): Non-matrix matched calibration of major and minor concentrations of Zn and Cu in brass, aluminum and silicate glass using NIR femtosecond laser ablation inductively coupled plasma mass spectrometry. *J. Analyt. Atom. Spectrom.* 21, 187-191.

CHENG, C. & XU, X. (2005): Mechanisms of decomposition of metal during femtosecond laser ablation. *Phys. Rev. B: Condens. Matter* **72**, 1-15.

CHMELEFF, J., HORN, I, STEINHOEFEL, G & VON BLANCKENBURG, F. (2008): *In situ* determination of precise stable Si isotope ratios by UV–femtosecond laser ablation high-resolution multi-collector ICP–MS. *Chem. Geol.* **249**, 155-166.

CROMWELL, E. & ARROWSMITH, P. (1995): Fractionation effects in laser ablation inductively coupled plasma mass spectrometry. *Appl. Spectrosc.* **49**, 1652-1660.

EGGINS, S. & SHELLEY, J. (2002): Compositional heterogeneity in NIST SRM 610-617 glasses. *Geostandard Newslett.* **26**, 269-286.

EGGINS, S., KINSLEY, L. & SHELLEY, J. (1998): Deposition and element fractionation processes during atmospheric pressure laser sampling for analysis by ICP–MS. *Appl. Surf. Sci.* **129**, 278-286.

FERNANDEZ, B., CLAVERIE, F., PECHEYRAN, C., DONARD, O. & CLAVERIE, F. (2007): Direct analysis of solid samples by fs–LA–ICP–MS. *Trends in Analyt. Chem.* **26**, 951-966.

FREYDIER, R., CANDAUDAP, F., POITRASSON, F., ARBOUET, A., CHATEL, B. & DUPRE, B. (2008): Evaluation of infrared femtosecond laser ablation for the analysis of geomaterials by ICP–MS. *J. Analyt. Atom. Spectros.* **23**, 702-710.

GAO, S., LIU, X., YUAN, H., HATTENDORF, B., GÜNTHER, D., CHEN, L. & HU, S. (2002): Determination of forty two major and trace elements in USGS and NIST SRM glasses by laser ablation–inductively coupled plasma– mass

spectrometry. *Geostandard Newslett.* **26**, 181-196.

GARCIA, C., LINDNER, H., VON BOHLEN, A., VADLA, C. & NIEMAX, K. (2008): Elemental fractionation and stoichiometric sampling in femtosecond laser ablation. *J. Analyt. Atom. Spectrom.* **23**, 470-478.

GONZÁLEZ, J., LIU, C., MAO, X. & RUSSO, R. (2004): UV-femtosecond laser ablation–ICP–MS for analysis of alloy samples. *J. Analyt. Atom. Spectrom.* **19**, 1165-1168.

GONZÁLEZ, J., DUNDAS, S., LIU, C., MAO, X. & RUSSO, R. (2006): UV-femtosecond and nanosecond laser ablation–ICP–MS: Internal and external repeatability. *J. Analyt. Atom. Spectrom.* **21**, 778-784.

GONZÁLEZ, J., OROPEZA, D., MAO, X. & RUSSO, R. (2008): Assessment of the precision and accuracy of thorium (232Th) and uranium (238U) measured by quadrupole based inductively coupled plasma-mass spectrometry using liquid nebulization, nanosecond and femtosecond laser ablation. *J. Analyt. Atom. Spectrom.* **23**, 229-234.

GUILLONG, M., HORN, I. & GÜNTHER, D. (2003): A comparison of 266 nm, 213 nm and 193 nm produced from a single solid state Nd : YAG laser for laser ablation ICP–MS. *J. Analyt. Atom. Spectrom.* **18**, 1224-1230.

GÜNTHER, D. & HATTENDORF, B. (2005): Solid sample analysis using laser ablation inductively coupled plasma mass spectrometry. *Trends in Analyt. Chem.* **24**, 255-265.

HATTENDORF, B. & GÜNTHER, D. (2003): Strategies for method development for an inductively coupled plasma mass spectrometer with bandpass reaction cell. Approaches with different reaction gases for the determination of selenium. *Spectrochim. Acta*, Part B **58**, 1-13.

HIRATA, T. (1997): Soft ablation technique for laser ablation inductively coupled plasma mass spectrometry. *J. Analyt. Atom. Spectrom.* **12**, 1337-1342.

HIRATA, T. & KON, Y. (2008): Evaluation of the Analytical Capability of NIR Femtosecond Laser Ablation–Inductively Coupled Plasma Mass Spectrometry. *Analyt. Sci.* **24**, 345-353.

HORN, I. & VON BLANCKENBURG, F. (2007): Investigation on elemental and isotopic fractionation during 196 nm femtosecond laser ablation multiple collector inductively coupled plasma mass spectrometry. *Spectrochim. Acta B* **62**, 410-422.

HORN, I., RUDNICK, R. & MCDONOUGH, W. (2000): Precise elemental and isotope ratio determination by simultaneous solution nebulization and laser ablation–ICP–MS: application to U–Pb geochronology (vol 164, pg 283 2000): *Chem. Geol.* **167**, 405-425.

HORN, I., GUILLONG, M. & GÜNTHER, D. (2001): Wavelength dependant ablation rates for metals and silicate glasses using homogenized laser beam profiles – implications for LA–ICP–MS. *Appl. Surf. Sci.* **182**, 91-102.

HORN, I., SCHOENBERG, R. & VON BLANCKENBURG, F. (2006a): Comment on "Analysis of Fe isotopes in sulfides and iron meteorites by laser ablation high-mass resolution multi-collector ICP mass spectrometry" by J. Košler, R. B. Pedersen, C. Kruber, and P. J. Sylvester. *J. Analyt. Atom. Spectrom.* **21**, 211-213.

HORN, I., VON BLANCKENBURG, F., SCHOENBERG, R., STEINHOEFEL, G. & MARKL, G. (2006b): In situ iron isotope ratio determination using UV–femtosecond laser ablation with application to hydrothermal ore formation processes. *Geochim. Cosmochim. Acta* **70**, 3677-3688.

JACKSON, S. & GÜNTHER, D. (2003): The nature and sources of laser induced isotopic fractionation in laser ablation–multicollector–inductively coupled plasma–mass spectrometry. *J. Analyt. Atom. Spectrom.* **18**, 205-212.

KIM, M., TAKAO, T., OKI, Y. & MAEDA, M. (2000): Thin-layer ablation of metals and silicon by femtosecond laser pulses for application to surface analysis. *Japan. J. Appl. Phys.* **39**, 6277-6280.

KOCH, J., VON BOHLEN, A., HERGENRÖDER, R. & NIEMAX, K. (2004): Particle size distributions and compositions of aerosols produced by near-IR femto- and nanosecond laser ablation of brass. *J. Analyt. Atom. Spectrom.* **19**, 267-272.

KOCH, J., LINDNER, H., VON BOHLEN, A., HERGENRÖDER, R. & NIEMAX, K. (2005): Elemental fractionation of dielectric aerosols produced by near-infrared femtosecond laser ablation of silicate glasses. *J. Analyt. Atom. Spectrom.* **20**, 901-906.

KOCH, J., WALLE, M., PISONERO, J. & GÜNTHER, D. (2006): Performance characteristics of ultra-violet femtosecond laser ablation inductively coupled

plasma mass spectrometry at similar to 265 and similar to 200 nm. *J. Analyt. Atom. Spectrom.* **21**, 932-940.

KOŠLER, J., PEDERSEN, R., KRUBER, C. & SYLVESTER, P. (2005): Analysis of Fe isotopes in sulfides and iron meteorites by laser ablation high-mass resolution multi-collector ICP mass spectrometry. *J. Analyt. Atom. Spectrom.* **20** 192-199.

KUHN, H. & GÜNTHER, D. (2003): Elemental fractionation studies in laser ablation inductively coupled plasma mass spectrometry on laser-induced brass aerosols. *Analyt. Chem*. **75**, 747-753.

KUHN, H., GUILLONG, M. & GÜNTHER, D. (2004): Size-related vaporisation and ionisation of laser-induced glass particles in the inductively coupled plasma. *Analyt. & Bioanalyt. Chem.* **378**, 1069-1074.

LIU, H., BORISOV, O., MAO, X., SHUTTLEWORTH, S. & RUSSO, R. (2000): Pb/U fractionation during Nd : YAG 213 nm and 266 nm laser ablation sampling with inductively coupled plasma mass spectrometry. *Appl. Spectrosc.* **54**, 1435-1442.

LIU, C., MAO, X., MAO, S., ZENG, X., GREIF, R. & RUSSO, R. (2004): Nanosecond and Femtosecond Laser Ablation of Brass: Particulate and ICPMS Measurements. *Analyt. Chem.* **76**, 379-383.

LIU, C., MAO, X., MAO, S., GREIF, R. & RUSSO, R. (2005): Particle size dependent chemistry from laser ablation of brass. *Analyt. Chem*. **77**, 6687-6691.

LODDING, A., MUNDY, J. & OTT, A. (1970): Isotope inter-diffusion and self-diffusion in solid lithium metal. *Phys Status Solidi* **38**, 559-569.

LONGERICH, H., GUENTHER, D. & JACKSON, S. (1996): Elemental fractionation in laser ablation inductively coupled plasma mass spectrometry. Fresenius J. *Analyt. Chem*. 355, 538-542.

LORAZO, P., LEWIS, L. & MEUNIER, M. (2006): Thermodynamic pathways to melting, ablation, and solidification in absorbing solids under pulsed laser irradiation. *Phys. Rev. B: Condens. Matter* **73**, 1-22.

MANK, A. & MASON, P. (1999): A critical assessment of laser ablation ICP–MS as an analytical tool for depth analysis in silica-based glass samples. *J. Analyt. Atom. Spectrom.* **14**, 1143-1153.

MAO, X., CIOCAN, A. & RUSSO, R. (1998): Preferential vaporization during laser ablation inductively coupled plasma atomic emission spectroscopy. Appl. Spectrosc. 52, 913-918.

MARGETIC, V., PAKULEV, A., STOCKHAUS, A., BOLSHOV, M., NIEMAX, K. & HERGENRÖDER, R. (2000): A comparison of nanosecond and femtosecond laser-induced plasma spectroscopy of brass samples. *Spectrochim. Acta, Part B* **55**, 1771-1785.

MARGETIC, V., BOLSHOV, M., STOCKHAUS, A., NIEMAX, K. & HERGENRÖDER, R. (2001a): Depth profiling of multi-layer samples using femtosecond laser ablation. *J. Analyt. Atom. Spectrom.* **16**, 616-621.

MARGETIC, V., NIEMAX, K. & HERGENRÖDER, R. (2001b): A study of non-linear calibration graphs for brass with femtosecond laser-induced breakdown spectroscopy. *Spectrochim. Acta, Part B* **56**, 1003-1010.

MIOTELLO, A. & KELLY, R. (1995): Critical assessment of thermal models for laser sputtering at high fluences. *Appl. Phys. Lett.* **67**, 3535-3537.

NORMAN, M., MCCULLOCH, M., O'NEILL, H. & YAXLEY, G. (2006): Magnesium isotopic analysis of olivine by laser-ablation multi-collector ICP–MS: Composition dependent matrix effects and a comparison of the Earth and Moon. *J. Analyt. Atom. Spectrom.* **21**, 50-54.

PECHEYRAN, C., CANY, S., CHABASSIER, P., MOTTAY, E. & DONARD, O. (2007): High repetition rate and low energy femtosecond laser ablation coupled to ICPMS detection: A new analytical approach for trace element determination in solid samples. *J. Phys.: Conf. Series* **59**, 112-117.

PEREZ, D. & LEWIS, L. (2003): Molecular-dynamics study of ablation of solids under femtosecond laser pulses. *Phys. Rev. B: Condens. Matter* **67**, 1841021–18410215.

POITRASSON, F., MAO, X., MAO, S., FREYDIER, R. & RUSSO, R. (2003): Comparison of ultraviolet femtosecond and nanosecond laser ablation inductively coupled plasma mass spectrometry analysis in glass, monazite, and zircon. *Analyt. Chem*. **75**, 6184-6190.

RESANO, M., VANHAECKE, F., HUTSEBAUT, D., DE CORTE, K. & MOENS, L. (2003): Possibilities of laser ablation–inductively coupled plasma–mass spectrometry for diamond fingerprinting. *J. Analyt. Atom. Spectrom.* **18**, 1238-1242.

REYNOLDS, B.C., GEORG, R.B., OBERLI, F., WIECHERT, U. & HALLIDAY, A.N. (2006): Re-assessment of silicon isotope reference materials using high-resolution multi-collector ICP–MS. *J. Analyt. Atom. Spectrom.* **21**, 266-269.

RUSSO, R., MAO, X., LIU, H., YOO, J. & MAO, S. (1999): Time-resolved plasma diagnostics and mass removal during single-pulse laser ablation. *Appl. Phys. A* **69**, S887-S894.

RUSSO, R., MAO, X., GONZÁLEZ, J. & MAO, S. (2002): Femtosecond laser ablation ICP–MS. *J. Analyt. Atom. Spectrom.* **17**, 1072-1075.

SAMEK, O., MARGETIC, V., MICHELS, A., NIEMAX, K., HERGENRÖDER, R. & VON WIRÉN, N. (2004): Femtosecond laser analytical mass spectrometry applied to plant samples. *Appl. Phys.* A **79**, 957-960.

WÄLLE, M., KOCH, J. & GÜNTHER, D. (2008): Analysis of brass and silicate glass by femtosecond laser ablation inductively coupled plasma mass spectrometry using liquid standard calibration. *J. Analyt. Atom. Spectrom.* B803563F.

YOO, J., JEONG, S., MAO, X., GREIF, R. & RUSSO, R. (2000): Evidence for phase-explosion and generation of large particles during high power nanosecond laser ablation of silicon. *Appl. Phys. Lett.* **76**, 783-785.

YOUNG, E., ASH, R., GALY, A. & BELSHAW, N. (2002): Mg isotope heterogeneity in the Allende meteorite measured by UV laser ablation–MC–ICPMS and comparisons with O isotopes. *Geochim. Cosmochim. Acta* **66**, 683-698.

ZENG, X., MAO, X., GREIF, R. & RUSSO, R. (2005): Experimental investigation of ablation efficiency and plasma expansion during femtosecond and nanosecond laser ablation of silicon. *Appl. Phys.* A **80**, 237-241.

## CHAPTER 5: MATRIX EFFECTS IN LASER ABLATION–ICP–MS

Paul J. Sylvester
Micro-Analysis Facility, INCO Innovation Center (MAF-IIC) and Department of Earth Sciences,
Memorial University, St. John's, Newfoundland A1B 3X5 Canada
E-mail: pauls@esd.mun.ca

### INTRODUCTION

When an analytical technique gives a result that is dependent on the chemical composition or physical nature of the sample introduced to the instrument, the technique is said to exhibit 'matrix effects'. If the result cannot be corrected other than by normalization against a calibration standard that has a composition or physical form similar to that of the sample, a procedure called 'matrix-matching', the technique is said to 'suffer' from matrix effects. Laser ablation–inductively coupled plasma–mass spectrometry (LA–ICP–MS) exhibits severe matrix effects in the sense that laser sampling can result in hugely variable amounts of material being delivered to the ICP–MS, depending on how well the laser beam couples to the sample. Happily however, calibration strategies have been developed to correct for the variable 'ablation yields', most notably, internal standardization to an element of known concentration in the sample (see summary by Jackson 2008), so that LA–ICP–MS does not suffer greatly from this type of matrix effect. Matrix-dependent spectral interferences are also not generally a problem for LA–ICP–MS, as oxide production rates, one of the main sources of interferences in solution–ICP–MS, are very low under the 'dry plasma' conditions of LA–ICP–MS (Kent & Ungerer 2005).

More insidious are laser- or ICP-induced, volatility-controlled fractionations between elements that differ from matrix to matrix. The fractionations result in matrix-dependent differences in the relative sensitivities (signal intensity, usually expressed in counts per second, divided by element concentration, usually given in micrograms per gram or parts per million) of elements recorded by the mass spectrometer (Fig. 5-1). Unlike matrix-dependent variations in ablation yield, internal standardization using a single element will not accurately correct for matrix-dependent differences in relative sensitivities between elements because different elements will require different correction factors. That said, the reality is that for a great many applications in the Earth sciences, groups of particular elements in silicate minerals or glasses such as Ca, Sc, Sr, Y, Zr, Ba, the rare earth elements, Hf, Th and U, do not exhibit large differences in relative sensitivities in different matrices. Thus concentration data can be produced with accuracies of about 5 to 10% using internal standardization without matrix matching (*e.g.*, Kurosawa *et al*. 2006, Jochum *et al*. 2007). Poorer accuracy of course will result for elements that exhibit larger differences in relative sensitivities in different matrices such as Rb and Sr in different silicate glasses (*e.g.*, Jochum *et al*. 2007, and Fig. 5-1). For these cases, matrix matching or non-traditional instrumentation (*e.g.*, Horn 2008) or calibration strategies (*e.g.*, Jackson 2008) would be needed to determine concentrations accurately to 5% by LA–ICP–MS.

This chapter is largely a brief introduction to the extent to which matrix-matching is necessary for external calibration of elemental analyses of non-silicates in LA–ICP–MS using instrumentation

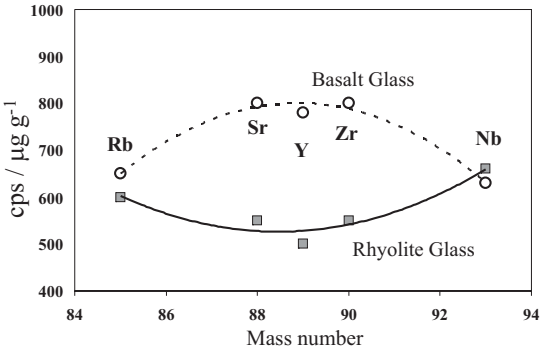


FIG. 5-1. Schematic illustration of matrix-dependent mass response curves in laser ablation–ICP–MS. Curves are shown from Rb to Nb for basalt and rhyolite glasses, based on the Li borate fused glass data of Yu *et al*. (2003). Absorption of laser energy tends to be greater in iron-rich, basalt glass compared to iron-poor, rhyolite glass. This leads to greater ablation yields and thus higher element sensitivities in the basalt. Because the relative sensitivities of the elements are different in basalt and rhyolite, external calibration using a single standard material, even with internal standardization, will produce somewhat inaccurate results.

Mineralogical Association of Canada Short Course 40, Vancouver, B.C., p. 67–78.

commonly available, and with single element internal standardization. Compared to the silicate minerals, there have been few studies of the nature and extent of matrix effects in non-silicate mineral classes of interest to earth scientists, particularly the carbonate minerals for environmental applications and the sulfides for mineral deposit research. Because matrix matching is likely to be most necessary where there are large elemental fractionations in LA–ICP–MS, or where fractionating element pairs need to be measured to much better than 5% accuracy (*e.g.*, Pb/U ratios for U–Pb geochronology), I begin with an overview of the causes of elemental fractionation in LA–ICP–MS and the instrumental procedures that are used to minimize it. (Data reduction strategies used to correct for elemental fractionation are given in this volume by Jackson 2008.) I then discuss two examples of elemental analyses of carbonate and sulfide matrices recently performed in the laboratory in terms of their implications for the accuracy of non-matrix matched calibration. I conclude with some comments on matrix effects in isotopic analyses made by LA–ICP–MS.

## MATRIX-DEPENDENT ELEMENTAL FRACTIONATION

Elemental fractionation in LA–ICP–MS refers to changes in the relative proportions of chemical elements in a sample relative to its original composition that are produced during analysis. (Changes in the relative proportions of isotopes are referred to as isotopic fractionation, and also occur in LA–ICP–MS; see Pearson *et al*. 2008.) The changes may be produced during laser sampling, during transport of the sample-derived aerosols to the ICP, or in the Ar plasma of the ICP itself. The extensive history of studies on elemental fractionation in LA–ICP–MS and the current understanding of the important variables involved are reviewed elsewhere in this volume (Günther & Koch 2008, Horn 2008, Jackson 2008). Here we focus only on the instrumentation and data collection practices that are commonly used to reduce the matrix-dependency on elemental fractionation (Table 5-1).

The six main processes thought to play a role in elemental (and isotopic) fractionation are illustrated in Figure 5-2 and are:

1) redistribution of elements among subsolidus phases formed in the area directly around the ablation pit during sample heating by laser energy (*e.g.*, Košler *et al*. 2005 suggested that Pb was preferentially volatilized relative to U when ablated zircon thermally decomposed into baddeleyite and quartz).
2) non-congruent evaporation of more volatile elements from melt formed in the ablation pit (*e.g.*, Hergenröder 2006).
3) fractional condensation of the cooling plume of sample vapor rising from the ablation site, precipitating refractory condensates onto the walls of the ablation pit, the sample surface and ablation cell surfaces at the expense of more volatile species (*e.g.*, Eggins *et al*. 1998).
4) differential transport of particles (quenched melt droplets, vapor phase condensates, agglomerates and sample fragments) of differing sizes and compositions out of the ablation cell and through the transfer tubing to the ICP torch (*e.g.*, Koch *et al*. 2002).
5) incomplete vaporization of particles larger than ~150 nm in size in the Ar plasma of the ICP, biasing signal responses in favor of more volatile elements (*e.g.*, Guillong *et al*. 2003).
6) suppression of signal intensities for volatile elements relative to refractory elements in the Ar plasma due to loading it with large masses of laser-derived aerosols (Kroslakova & Günther 2007).

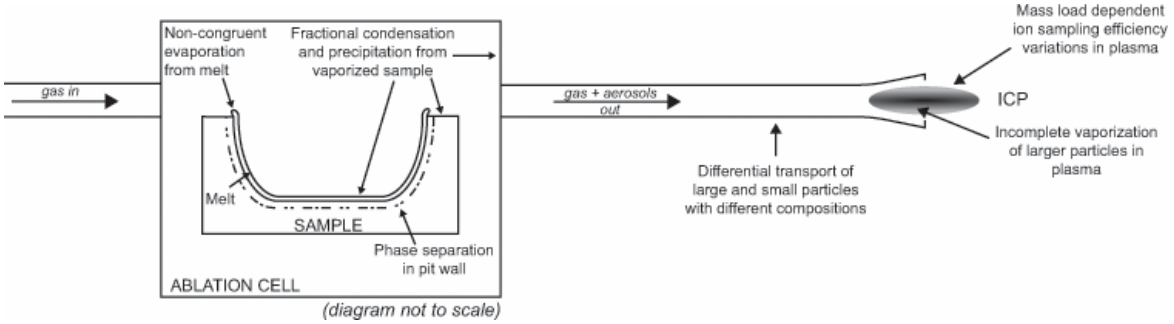


FIG. 5-2. Possible causes of elemental (and isotopic) fractionation in LA–ICP–MS, showing where in the system each could occur. See text for discussion.

TABLE 5-1: INSTRUMENTATION AND OPERATING CONDITIONS FOR MINIMIZATION OF ELEMENTAL FRACTIONATION IN LA-ICP-MS

| Parameter | Description | Explanation | Reference |
|---|---|---|---|
| Laser wavelength | Particles produced with 193 nm ablation are smaller and more uniform than for 213 nm or 266 nm ablation, leading to more complete evaporation in the Ar plasma of the ICP | Deep ultraviolet light is absorbed more efficiently by most minerals, particularly transparent ones. Laser energy is concentrated in a smaller sample volume which is more completely vaporized | Guillong *et al.* (2003) |
| Laser pulse duration | All commercial laser systems currently available for LA-ICP-MS have nanosecond pulse widths but femtosecond lasers have shown promising results in reducing melting at the ablation site and reducing particle sizes in the aerosols | The ultra-short femtosecond pulse length does not allow significant time for thermal diffusion into the surrounding material, as occurs during the nanosecond pulse | Fernández *et al.* (2007) |
| Laser energy | Fluence (energy per area) must be sufficiently high and uniform across the laser beam profile that ablation occurs without producing large particles by cracking or splintering | Insufficient absorption of laser energy by the target will lead to fragmentation rather than vaporization of the sample | Günther & Hattendorf (2005) |
| Sampling strategy | Shallow ablation pits (depth to width ratios of 1:1 or less) or line scans or box rasters exhibit the least elemental fractionation. Short ablation times or low laser repetition rates (2-5 Hz) may be used to limit pit depths provided that sensitivity is sufficient | In deeper pits, there is a change in particle size distribution with ablation time as laser beam loses focus and the energy density decreases on the pit floor | Košler (2008) |
| Ablation conditions | Same crater diameters and ablation times should be used for standards and samples | Ion generation takes place in different zones of the Ar plasma depending on the size of the mass loads of the ablated sample | Kroslakova & Günther (2007) |
| Sample cell design | Existing cell designs induce circulation of sample aerosols with velocities much slower at the boundaries than across the center but other designs to limit circulation are possible | Circulation in the cell can lead to fractional transport of aerosols and retard particle extraction, particularly from the cell edges | Bleiner & Chen (2008) |
| Ablation chamber gas | Development of surface condensates is reduced by ablating in an ambient atmosphere of He instead of Ar and is accompanied by an increase in ICP-MS sensitivity for 193 nm ablation | Aerosol plume expands more rapidly into the lighter He gas and is thus more efficiently removed from the cell | Eggins *et al.* (1998) |
| ICP carrier gas | Combining a small amount of $N_2$ (2–4 ml/min) into the carrier gas flow reduces elemental fractionation between Th and U | $N_2$ can compact Th and U sensitivity maxima to a similar position within the Ar plasma | Eggins *et al.* (2005) |
| ICP tuning | Plasma operating conditions should be adjusted so that the $^{238}U/^{232}Th$ intensity ratio in NIST 610 is approximately 1. A key parameter is the sampling depth in the Ar plasma (distance between the torch and sample cone) | $^{238}U$ and $^{232}Th$ have similar ionization energies, masses and isotopic abundances and thus should have similar concentration-normalized intensities if complete atomization is occurring in the plasma | Günther & Hattendorf (2005) |

The relative importance of each of these processes is a matter of some debate and ongoing study but in recent years it has become clear that fractionations occurring in the Ar plasma are at least as important as those produced during laser sampling itself, and perhaps much more so.

From the standpoint of matrix effects, the processes causing elemental fractionation would be of little concern to the analyst if samples and non-matrix-matched external calibration standards exhibited the same fractionation behavior under the same ablation conditions. If this were the case then the elemental fractionations would simply cancel out when the count rates of the analytes in samples were translated to concentrations by reference to the count rates of the standard. Sadly however this is not true for some elemental fractionations and thus a great deal of effort has gone into optimizing the instrumentation and experimental conditions used for LA–ICP–MS that minimize the fractionations. These are listed and briefly explained in Table 5-1.

One of the key principles underlying these practices is to reduce melting of the sample at the ablation site, so that the aerosol stream to the ICP contains few large melt particles that will be incompletely vaporized in the Ar plasma. Another is to reduce time-dependent elemental fractionation at the ablation site and provide more constant mass loads on the Ar plasma. Some of these practices have both negative and positive consequences, requiring decision trade-offs: for example, sampling by scanning or rastering reduces fractionation at the ablation site and produces more constant mass loads on the ICP, but can result in the formation of a greater proportion of larger particles than conventional spot analyses (*e.g.*, see summary by Košler 2008). Thus, matrix matching should be considered where particular applications require highly accurate and precise measurements that cannot be achieved by other means.

## TWO EXAMPLES OF NON-MATRIX-MATCHED CALIBRATION

To illustrate the quality of data that can be expected for non-matrix-matched laser ablation analysis of non-silicates, silicate glass standards were used to measure Ca carbonate (USGS MACS-1) and Fe–Cu–Zn sulfide (USGS MASS-1) reference materials for a set of elements of particular interest to earth scientists. The analyses were made using a Finnigan Element-XR high resolution ICP–MS coupled to a GeoLas laser ablation system equipped with a Lambda Physik ComPex Pro 110 ArF excimer laser operating at a wavelength of 193 nm with a pulse width of 20 ns. Identical ablation conditions were used for the carbonate and silicate pairs (59 μm spot, 5 Hz, 3 J/cm$^2$), and sulfide and silicate pairs (40 μm spot, 10 Hz, 3 J/cm$^2$). To compare the sulfide and carbonate data more directly, we only consider the results over about the same number of pulses (~300) for both experiments, which translates to an ablation interval of ~60 s for carbonate and ~30 s for sulfide. All ablations were performed in a He atmosphere.

The carbonate and sulfide samples were both pressed powder pellets and thus differ dramatically not only in composition from the silicate glass standard but also in their physical character, thereby maximizing the lack of matrix matching in the analyses. The silicate glass standards used for external calibration were NIST 612 (for the carbonate) and NIST 610 (for the sulfide). Jochum & Stoll (2008) have noted that the overwhelming majority of LA–ICP–MS analyses published in the literature are calibrated against these glasses. They are synthetic soda-lime silicate, trace element-spiked glass reference materials with similar compositions – the main difference being that NIST 610 has approximately ten times higher abundances of trace elements than NIST 612. Ca was used for internal standardization of the carbonate analyses, whereas Fe was used for the sulfide analyses. Six to eight analyses were made of each of MACS-1 and MASS-1 over two or three analytical sessions and the individual analyses reported here were chosen to be representative of all of the analyses made.

### Carbonate

Results of the carbonate analysis are given in Table 5-2 and Figures 5-3 and 5-4. The concentrations for all elements measured in MACS-1 (B, Mn, Cu, Zn, Sr, La, Ce, Nd, Pb) using NIST 612 as the external calibration standard and Ca as the internal standard fall well within the 1 σ uncertainties of the preferred values and the measurements. For B, Mn, Sr, La, Ce and Nd, the absolute correspondence between measured and preferred concentrations is better than 5%, and thus much better than would be expected from the stated uncertainties (5–13% on the preferred concentrations for MACS-1 and on the measurements made here). This is a remarkable result in that the accuracy of the measured concentrations for the carbonate is just as good as the best analyses for silicates using NIST 612 as the calibration standard.

TABLE 5-2: COMPARISON OF ELEMENTAL FRACTIONATION INDICES AND SENSITIVITIES IN CARBONATE AND SILICATE MATRICES UNDER IDENTICAL ABLATION CONDITIONS

| **Element** | **B** | **Ca** | **Mn** | **Cu** | **Zn** | **Sr** | **La** | **Ce** | **Nd** | **Pb** |
|---|---|---|---|---|---|---|---|---|---|---|
| **Isotope** | **11** | **43** | **55** | **63** | **66** | **86** | **139** | **140** | **146** | **208** |
| **USGS MACS-1 Synthetic calcium carbonate pressed powder pellet** | | | | | | | | | | |
| Preferred concs (ppm)[1] | 25.3 | 392800 | 118 | 124 | 123 | 219 | 126 | 114 | 125 | 121 |
| SD | ± 2.4 | ± 26200 | ± 12 | ± 5 | ± 16 | ± 20 | ± 12 | ± 7 | ± 9 | ± 11 |
| Background corrected mean count rates (cps) | | | | | | | | | | |
| Gas background | 110 | 693 | 1720 | 195 | 20 | 1283 | 26 | 14 | 2 | 18 |
| 1st 30 secs of ablation | 1911 | 412332 | 87289 | 59442 | 14749 | 30401 | 275552 | 258686 | 56615 | 272633 |
| SE of mean | ± 69 | ± 4404 | ± 748 | ± 912 | ± 204 | ± 411 | ± 2847 | ± 3426 | ± 717 | ± 3641 |
| 2nd 30 secs of ablation | 1707 | 346672 | 74944 | 50647 | 12990 | 25322 | 226023 | 210174 | 46315 | 244986 |
| SE of mean | ± 52 | ± 3454 | ± 738 | ± 450 | ± 191 | ± 315 | ± 2636 | ± 2228 | ± 610 | ± 1601 |
| Total 1 min ablation | 1810 | 379502 | 81216 | 55044 | 13862 | 27821 | 250787 | 234430 | 51424 | 258587 |
| SE of mean | ± 44 | ± 4062 | ± 755 | ± 642 | ± 160 | ± 338 | ± 2953 | ± 2987 | ± 660 | ± 2331 |
| Fractionation Index[2] | 0.90 | 0.84 | 0.86 | 0.85 | 0.88 | 0.84 | 0.82 | 0.81 | 0.82 | 0.90 |
| SD | ± 0.04 | ± 0.01 | ± 0.01 | ± 0.02 | ± 0.02 | ± 0.02 | ± 0.01 | ± 0.01 | ± 0.01 | ± 0.01 |
| Sensitivity (cps/ppm)[3] | 89 | 716 | 691 | 644 | 406 | 1289 | 1990 | 2317 | 2383 | 4080 |
| SD | ± 9 | ± 48 | ± 72 | ± 29 | ± 52 | ± 120 | ± 196 | ± 136 | ± 177 | ± 357 |
| **NIST 612 Synthetic soda-lime silicate glass** | | | | | | | | | | |
| Preferred concs (ppm)[1] | 35 | 85049 | 38 | 37 | 38 | 78.4 | 35.8 | 38.7 | 35.9 | 38.57 |
| SD | ± 3 | ± 1429 | ± 1 | ± 3 | ± 4 | ± 0.2 | ± 0.4 | ± 0.4 | ± 0.4 | ± 0.20 |
| Background corrected mean count rates (cps) | | | | | | | | | | |
| Gas background | 64 | 597 | 1665 | 156 | 20 | 1051 | 41 | 38 | 2 | 50 |
| 1st 30 secs of ablation | 3108 | 106729 | 32353 | 19367 | 6221 | 13004 | 93881 | 100427 | 18573 | 89750 |
| SE of mean | ± 82 | ± 1156 | ± 460 | ± 271 | ± 159 | ± 209 | ± 1153 | ± 1237 | ± 288 | ± 822 |
| 2nd 30 secs of ablation | 2513 | 78694 | 23845 | 14655 | 4733 | 9436 | 69319 | 74121 | 14094 | 68329 |
| SE of mean | ± 83 | ± 1218 | ± 417 | ± 280 | ± 137 | ± 191 | ± 1160 | ± 1139 | ± 267 | ± 1016 |
| Total 1 min ablation | 2810 | 92364 | 28064 | 16972 | 5477 | 11191 | 81399 | 87274 | 16333 | 78864 |
| SE of mean | ± 64 | ± 1517 | ± 478 | ± 287 | ± 124 | ± 205 | ± 1381 | ± 1459 | ± 282 | ± 1171 |
| Fractionation Index[2] | 0.81 | 0.74 | 0.75 | 0.76 | 0.76 | 0.75 | 0.74 | 0.74 | 0.76 | 0.76 |
| SD | ± 0.03 | ± 0.01 | ± 0.02 | ± 0.02 | ± 0.03 | ± 0.02 | ± 0.02 | ± 0.01 | ± 0.02 | ± 0.01 |
| Sensitivity (cps/ppm)[3] | 100 | 804 | 739 | 663 | 517 | 1448 | 2276 | 2550 | 2645 | 3902 |
| SD | ± 9 | ± 19 | ± 23 | ± 55 | ± 56 | ± 27 | ± 46 | ± 50 | ± 54 | ± 61 |
| **Calculated concentration for MACS-1 using NIST 612 as external standard and Ca as internal standard** | | | | | | | | | | |
| Calculated concs (ppm)[4] | 25 | IS | 124 | 135 | 108 | 219 | 124 | 117 | 127 | 142 |
| SD | ± 3 | | ± 10 | ± 15 | ± 14 | ± 16 | ± 9 | ± 9 | ± 10 | ± 11 |

Notes: (1) Preferred concentrations for MACS-1 are from Stephen Wilson (pers. comm.) and for NIST 612 are from GeoReM (http://georem.mpch-mainz.gwdg.de/). (2) Fractionation Index is the ratio of the mean count rate of the second half of the ablaion interval relative to that of the first half. (3) Element sensitivity normalized for isotopic abundances: 11B (80.1%), 43Ca (0.135%), 55Mn (100%), 63Cu (69.17%), 66Zn (27.9%), 86Sr (9.86%), 139La (99.91%), 140Ce (88.45%), 146Nd (17.2%), 208Pb (52.4%). (4) Calculation using equation given by Longerich *et al.* (1996).

It is not possible to determine whether Cu, Zn and Pb can be calibrated as accurately against NIST 612 as the other elements measured in MACS-1: we would need better precision on the preferred values for the carbonate. Two lines of evidence however suggest that accurate analyses for Cu, Zn and Pb are possible. Firstly, the pattern of elemental fractionation in MACS-1 is very similar to that in NIST 612. A 'fractionation index' calculated as the mean intensity of the second half of the ablation signal relative to that of the first half and plotted in Fig. 5-4 shows that while the laser signal falls more rapidly with ablation of NIST 612 than of MACS-1, the relative losses in signal from element to element are very similar in both matrices. When the fractionation indices for the two samples are ratioed against each other and normalized to Ca = 1, it is clear that the total variation in elemental

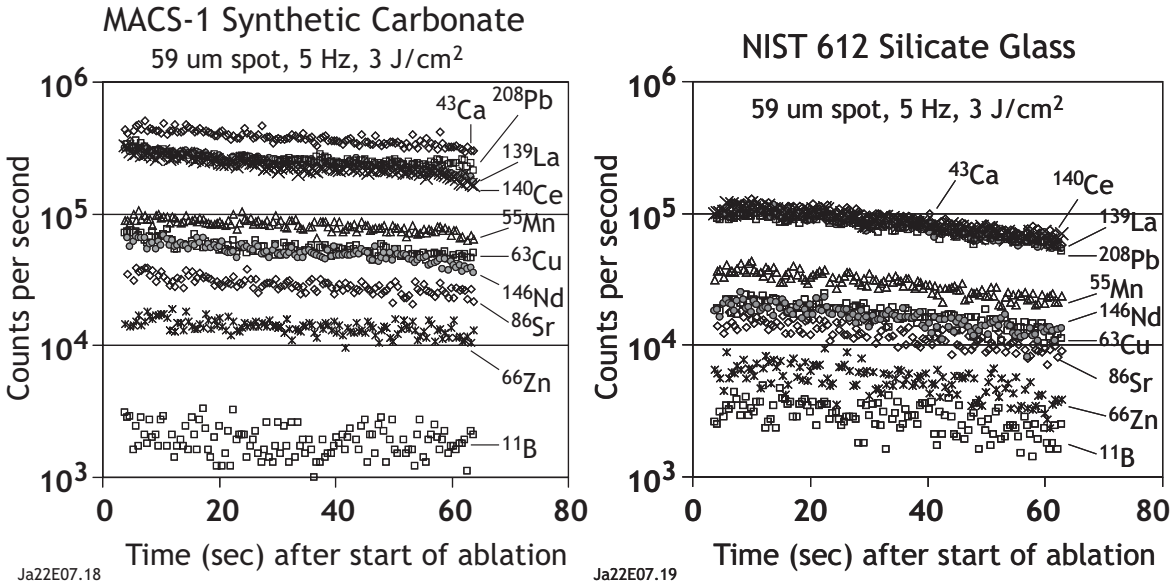


FIG. 5-3. Time-resolved element spectra for MACS-1 (left) and NIST 612 (right) under identical ablation conditions. For both samples, the data for the first 4 seconds of ablation are more scattered and thus omitted for clarity.

fractionation between the carbonate and silicate is less than 10%. Secondly the calculated sensitivities for the elements are very similar in MACS-1 and NIST 612. Thus corrections for differences in sensitivity, using the internal standard element Ca, would be small. The implication of the observations is that, like B, Mn, Sr, La, Ce and Nd, concentrations of Cu, Zn and Pb can be determined in carbonates with accuracies of better than 10%, even when using NIST 612 as the calibration standard.

These results are largely consistent with the limited number of previous studies on carbonate analyses by LA–ICP–MS using non-matrix matched calibration. For instance, Tanaka *et al.* (2007) reported that all of the rare earth elements (except La) could be measured accurately in carbonates to better than 10% using NIST glass calibration. Hathorne *et al.* (2008) noted that fractionation factors for Sr, Ba and the rare earths are the same in calcite as in NIST 612, but that fractionation factors for Li, Mg and Cu were matrix-dependent. They presented scanning electron microscope images indicating that many of the larger particles (>200 nm) formed during ablation of calcite by photomechanical fracturing, rather than by hydrodynamic sputtering (melting and splashing) as in NIST 612, and suggested that this may play a role in the different fractionation behavior observed for Li, Mg and Cu.

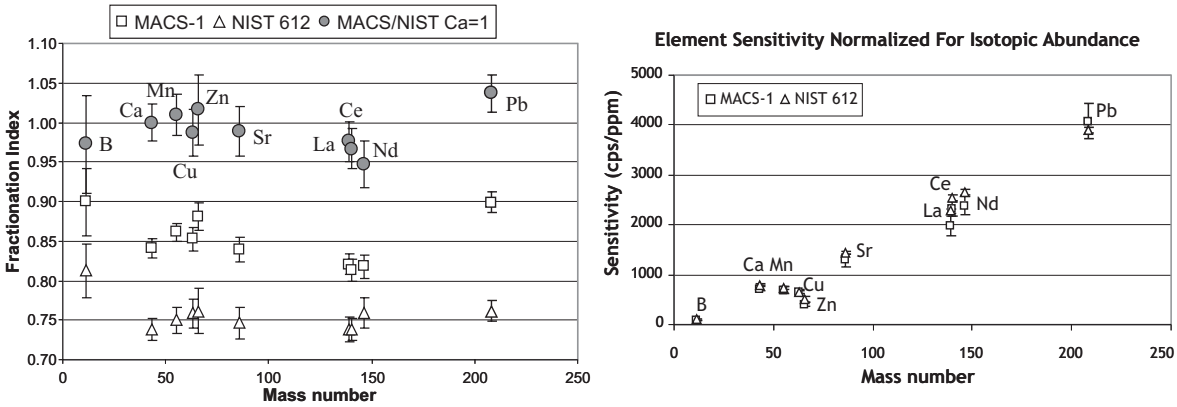


FIG. 5-4. Comparison of fractionation indices (left) and sensitivity factors (right) for MACS-1 and NIST 612 under identical ablation conditions.

## Sulfide

Results of the sulfide analysis are given in Table 5-3 and Figures 5-5 and 5-6. In contrast to the similar element sensitivities found for carbonate and silicate, element sensitivities are generally ~50% greater in sulfide than in silicate. This is probably due to greater absorption of laser energy by the transition metals enriched in the sulfide. Also, whereas element signals in carbonate decreased more slowly during ablation than in silicate, they decreased much more rapidly in sulfide compared to in silicate.

Despite these differences, the agreement between the concentrations calculated for MASS-1 using NIST 610 as the calibration standard (with Fe as the internal standard) and the preferred values for

TABLE 5-3: COMPARISON OF ELEMENTAL FRACTIONATION INDICES AND SENSITIVITIES IN SULFIDE AND SILICATE MATRICES UNDER IDENTICAL ABLATION CONDITIONS

| **Element** | **S** | **Fe** | **Co** | **Ni** | **Cu** | **Zn** | **Ag** | **Pt** | **Au** |
|---|---|---|---|---|---|---|---|---|---|
| **Isotope** | **34** | **57** | **59** | **60** | **65** | **68** | **109** | **195** | **197** |
| **USGS MASS-1 Synthetic sulfide pressed powder pellet** | | | | | | | | | |
| Preferred concs (ppm)[1] | 276000 | 156000 | 67 | 170 | 134000 | 210000 | 67 | 73 | 47 |
| SD | | | | ± 24 | | | | | |
| Background corrected mean count rates (cps) | | | | | | | | | |
| Gas background | 15093 | 9306 | 3397 | 23540 | 4540 | 878 | 167 | 0 | 4 |
| 1st 15 secs of ablation | 4661179 | 7401586 | 148806 | 60073 | 64757838 | 50539583 | 69058 | 45973 | 75318 |
| SE of mean | ± 90967 | ± 326739 | ± 4743 | ± 1656 | ± 2775615 | ± 1801645 | ± 3051 | ± 1768 | ± 3421 |
| 2nd 15 secs of ablation | 2634318 | 2792528 | 60254 | 27178 | 27284112 | 21884051 | 30559 | 18701 | 34400 |
| SE of mean | ± 81726 | ± 138700 | ± 2530 | ± 633 | ± 1157319 | ± 908497 | ± 1290 | ± 859 | ± 1382 |
| Total 30 sec ablation | 3647749 | 5097057 | 104530 | 43626 | 46020975 | 36211817 | 49809 | 32337 | 54859 |
| SE of mean | ± 125209 | ± 305545 | ± 5361 | ± 1429 | ± 2522523 | ± 1849452 | ± 2653 | ± 1772 | ± 2879 |
| Fractionation Index[2] | 0.57 | 0.38 | 0.40 | 0.45 | 0.42 | 0.43 | 0.44 | 0.41 | 0.46 |
| SD | ± 0.02 | ± 0.03 | ± 0.02 | ± 0.02 | ± 0.03 | ± 0.02 | ± 0.03 | ± 0.02 | ± 0.03 |
| Sensitivity (cps/ppm)[3] | 308 | 1542 | 1560 | 979 | 1114 | 920 | 1544 | 1309 | 1167 |
| SD | ± 11 | ± 92 | ± 80 | ± 142 | ± 61 | ± 47 | ± 82 | ± 72 | ± 61 |
| **NIST 610 Synthetic soda-lime silicate glass** | | | | | | | | | |
| Preferred concs (ppm)[1] | 693 | 458 | 405 | 459 | 430 | 456 | 239 | 3.2 | 23 |
| SD | ± 69 | ± 9 | ± 23 | ± 4 | ± 24 | ± 19 | ± 19 | ± 0.1 | ± 4 |
| Background corrected mean count rates (cps) | | | | | | | | | |
| Gas background | 15389 | 8437 | 3840 | 21360 | 4148 | 920 | 172 | 1 | 6 |
| 1st 15 secs of ablation | 11887 | 12176 | 431462 | 121945 | 119786 | 59650 | 138207 | 1092 | 18545 |
| SE of mean | ± 166 | ± 237 | ± 5811 | ± 1626 | ± 1871 | ± 998 | ± 2490 | ± 52 | ± 371 |
| 2nd 15 secs of ablation | 7816 | 7060 | 270820 | 78549 | 80096 | 36690 | 92936 | 849 | 12951 |
| SE of mean | ± 148 | ± 147 | ± 7488 | ± 1912 | ± 2431 | ± 1142 | ± 2346 | ± 65 | ± 424 |
| Total 30 sec ablation | 9851 | 9618 | 351141 | 100247 | 99941 | 48170 | 115571 | 970 | 15748 |
| SE of mean | ± 142 | ± 201 | ± 9824 | ± 2317 | ± 2572 | ± 1436 | ± 2984 | ± 43 | ± 413 |
| Fractionation Index[2] | 0.66 | 0.58 | 0.63 | 0.64 | 0.67 | 0.62 | 0.67 | 0.78 | 0.70 |
| SD | ± 0.02 | ± 0.02 | ± 0.02 | ± 0.02 | ± 0.02 | ± 0.02 | ± 0.02 | ± 0.07 | ± 0.03 |
| Sensitivity (cps/ppm)[3] | 331 | 991 | 867 | 833 | 754 | 563 | 1004 | 896 | 685 |
| SD | ± 33 | ± 28 | ± 55 | ± 21 | ± 46 | ± 29 | ± 84 | ± 49 | ± 120 |
| **Calculated concentration for MASS-1 using NIST 610 as external standard and Fe as internal standard** | | | | | | | | | |
| Calculated concs (ppm)[4] | 164924 | IS | 77 | 128 | 127264 | 220325 | 66 | 69 | 51 |
| SD | ± 20825 | | ± 8 | ± 10 | ± 13331 | ± 21129 | ± 8 | ± 6 | ± 10 |

Notes: (1) Preferred concentrations for MASS-1 are from Wilson *et al.* (2002) except Ni (Stephen Wilson, pers. comm.) and Pt (unpublished solution ICP-MS data, Memorial University) for NIST 610 are from GeoReM (http://georem.mpch-mainz.gwdg.de/). (2) Fractionation Index is the ratio of the mean count rate of the second half of the ablaion interval relative to that of the first half. (3) Element sensitivity normalized for isotopic abundances: 34S (4.29%), 57Fe (2.119%), 59Co (100%), 60Ni (26.2231%), 65Cu (30.83%), 68Zn (18.75%), 109Ag (48.161%), 195Pt (33.832%), 197Au (100%). (4) Calculation using equation given by Longerich *et al.* (1996). No overlap corrections were made for 179Hf16O on 195Pt and 181Ta16O on 197Au in NIST 610 because they are 5% or less for typical laser tuning conditions (Sylvester & Eggins 1997).

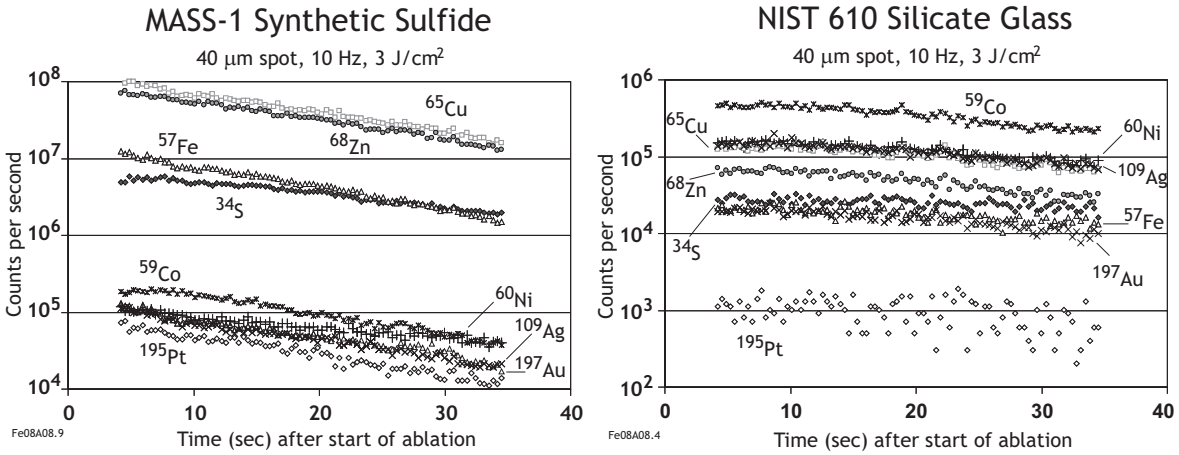


FIG. 5-5. Time-resolved element spectra for MASS-1 (left) and NIST 610 (right) under identical ablation conditions. For both samples, the data for the first 4 seconds of ablation are more scattered and thus omitted for clarity.

MASS-1 is within ~5% for Cu, Zn, Ag and Pt; ~10% for Au; ~16% for Co; ~25% for Ni; and ~40% for S. Uncertainties on the concentration estimates for MASS-1 are not well known but Wilson *et al*. (2002) estimated the homogeneity of the major elements, S, Fe, Cu and Zn, to be better than 5% at the 20 μm scale, based on replicate electron microprobe analyses. Using LA–ICP–MS analyses, they estimated the homogeneity of Co, Ag and Pt to be better than ~20% on the 25 μm scale and ~10% on the 50 μm scale. Gold was found to be more heterogeneous (better than 20% only at the 50 μm scale), and Ni was not determined. Thus, the results presented here suggest that the NIST 610 glass may be used to measure concentrations of Cu, Zn, Ag, Pt and Au in sulfide minerals with an accuracy of better than 10% using Fe as an internal standard.

The large discrepancy between the measured and expected result for S is probably the result of a large interference (~40%) of $^{16}O^{18}O^{+}$ on $^{34}S$, the isotope measured in our experiment, produced by ionization of oxygen present in the silicate glass that is not also present in the sulfide. As can be seen in Fig. 5-6, the apparent sensitivity calculated for S in NIST 610 is very similar to that in MASS-1, whereas all of the other elements measured in the samples have lower sensitivities in NIST 610. Other isotopes of S available for measurement would also be affected by this interference ($^{16}O^{16}O^{+}$ on $^{32}S$, $^{16}O^{17}O^{+}$ on $^{33}S$), making it very difficult to measure S, or to use the element as an internal standard, for sulfide analyses calibrated against a silicate. One may have suspected that $^{40}Ar^{16}O^{1}H^{+}$ may have produced a significant interference on $^{57}Fe$ in NIST 610, again using the oxygen derived from the sample matrix, but this does not appear to be the case.

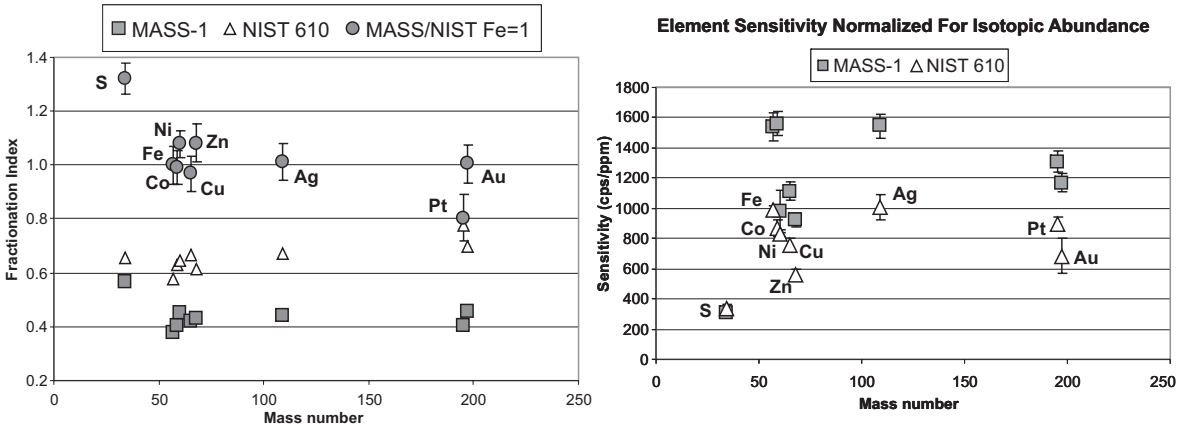


FIG. 5-6. Comparison of fractionation indices (left) and sensitivity factors (right) for MASS-1 and NIST 610 under identical ablation conditions.

The origin of the discrepancies for Co and Ni are not clear but may reflect inaccuracies in the preferred values for MASS-1. In NIST 610, calculated sensitivities decrease progressively with increasing mass from $^{57}$Fe (~1000 cps/ppm) to $^{68}$Zn (~600 cps/ppm) (Fig. 5-6). A similar trend is apparent from $^{57}$Fe (~1600 cps/ppm) to $^{68}$Zn (~900 cps/ppm) in MASS-1 except that Co falls above the trend (~1600 cps/ppm) and Ni below (~1000 cps/ppm). Thus the preferred values for in MASS-1 may be too low for Co and too high for Ni.

Platinum shows significantly more time-dependent fractionation relative to Fe in MASS-1 compared to in NIST 610 than do the other elements measured (Fig. 5-6). The ablations carried out here were rather short (~30 sec at 10 Hz or 300 pulses) in order to minimize fractionation but larger errors for Pt would result if longer ablations were carried out under these conditions. In fact, comparison of Figs. 5-4 and 5-6 indicates that, over 300 pulses, time-dependent inter-element fractionation is generally larger in the sulfide compared to silicate (~30% including Pt), than it is in the carbonate compared to silicate (~10%). This suggests caution in using silicate as a calibration standard for sulfide under ablation conditions that would lead to more inter-element fractionation than found here (*e.g.*, longer ablations, greater laser repetition rates, use of 213 or 266 nm wavelength lasers, *etc*.).

There have been almost no detailed comparisons of matrix effects between sulfide and silicate in LA–ICP–MS reported previously. Halter *et al*. (2004) presented data, however, showing that mean measurements of Fe, Co, Ni and Cu in synthetic pyrrhotite, chalcopyrite and millerite grains made by LA–ICP–MS with NIST 610 calibration agreed with those made by electron microprobe analyses of the same grains. The agreement was reported as being within 1 standard deviation of the mean of five to nine analyses, mostly between 1 and 5 % RSD.

## MATRIX EFFECTS IN HIGH PRECISION *IN SITU* ISOTOPIC ANALYSES

A growth area for applications of LA–ICP–MS in the earth sciences is high precision, *in situ* isotope ratio measurements of geological materials using sector field ICP instruments, particularly those with multicollector arrays. These instruments are capable of making much more precise measurements of isotopic ratios than conventional ICP instruments equipped with quadrupole mass spectrometers. This opportunity brings increased challenges to define the extent of matrix effects at a much more precise level than are needed for measurements of elemental concentrations. In this volume, Pearson *et al*. (2008) review the methods used to correct for instrumental mass biases in isotopic measurements and the role that matrix effects play in those biases, mainly through plasma loading and polybaric spectral interferences.

Research into the extent of matrix effects in isotopic measurements has begun in earnest only recently, but several studies have identified significant biases already. These are particularly relevant where instrumental mass bias corrections must be made by external calibration against a standard rather than using an invariant ratio pair of the element of interest. For instance, Mason *et al.* (2006) found that *in situ* measurements of $\delta^{34}$S made on a pressed powder pellet of elemental sulfur were consistently lighter (by 3 to 5‰) than the expected value, when calibrated against a silver sulfide pressed powder pellet. Norman *et al.* (2006) reported a composition-dependent matrix effect in which systematically heavier isotopic compositions of Mg were measured in synthetic olivine with Mg numbers (= % atomic Mg/[Mg+Fe]) decreasing from 90 to 50. With regard to high precision measurements of isotope pairs of different elements, Bernal *et al.* (2005) determined a 3% matrix bias for [$^{230}$Th/$^{238}$U] activity ratios in a hematite reference material when calibrated against an aluminosilicate glass. Košler *et al.* (2002) noted biases in Pb/U ratios between silicate glass and zircon in the context of developing calibration strategies for high precision $^{206}$Pb/$^{238}$U and $^{207}$Pb/$^{235}$U measurements for *in situ* U–Pb zircon geochronology by LA–ICP–MS. Almost all laboratories performing such analyses now use some form of matrix matching to achieve sufficiently accurate age dates for zircon.

Recent studies of femtosecond laser ablation report little or no isotopic fractionation during analysis and thus the potential to collect much more accurate isotope ratio data without matrix matching than by conventional nanosecond laser ablation (see Horn 2008). Although femtosecond lasers are comparatively expensive and can be difficult to operate properly, they may well prove to find an important niche in high precision isotopic ratio analysis, where their advantages would be most useful.

## SUMMARY

LA–ICP–MS is an unusually forgiving analytical method for matrix differences between samples and standards when proper correction procedures such as internal standardization are used. A large number of elements including the rare earth elements, and many of the alkaline earth and high field strength elements can be measured in silicates to better than 10% accuracy using a silicate standard that is significantly different in bulk composition than the unknowns (*e.g.*, NIST 610/612 glasses) provided that inter-element fractionation during analysis is limited. Matrix matching may improve data accuracy to better than 5% for silicates although this has not yet been demonstrated rigorously for a wide variety of silicate minerals.

With a 193 nm wavelength, nanosecond laser, a silicate standard may be used to analyze B, Mn, Cu, Zn, Sr, La, Ce, Nd and Pb in carbonates using Ca as the internal standard, and to analyze Cu, Zn, Ag, Pt and Au in sulfides using Fe as the internal standard with accuracies of ~10% or better. Matrix effects between sulfide and silicate are large, however, so matrix matching is recommended for sulfide analyses provided suitable reference materials become available.

Matrix matching is required for element pairs that fractionate strongly during laser ablation (*e.g.*, Pb and U) and need to be determined to a high level of precision and accuracy (such as in U–Pb geochronology). The extent to which matrix matching is needed for high precision measurements of isotopic ratios is not yet clear. This may become a niche area for the use of femtosecond lasers in LA–ICP–MS.

## ACKNOWLEDGEMENTS

Steve Wilson is thanked for providing the USGS MACS-1 and MASS-1 reference materials. Mike Tubrett collected the carbonate data with Bursin Isler and the sulfide data with Louis Cabri. Kate Souders assisted with the preparation of the manuscript.

## REFERENCES

BERNAL, J.-P., EGGINS, S.M. & MCCULLOCH, M.T. (2005): Accurate *in situ* $^{238}U$–$^{234}U$–$^{232}Th$–$^{230}Th$ analysis of silicate glasses and iron oxides by laser–ablation MC–ICP–MS. *J. Anaytl. Atom. Spectrom.*, **20**, 1240–1249.

BLEINER, D & CHEN, Z. (2008): Computer modeling of laser ablation elemental microanalysis. *In* Laser Ablation ICP–MS in the Earth Sciences: Current Practices and Outstanding Issues (P. Sylvester, *ed*.). *Mineral. Assoc. Can. Short Course Series* **40**, 35-52.

EGGINS, S.M., KINSLEY, L.P.J. & SHELLEY, J.M.G. (1998): Deposition and element fractionation processes during atmospheric pressure laser sampling for analysis by ICPMS. *Appl. Surf. Sci.* **129**, 278-286.

EGGINS, S.M., GRUN, R., MCCULLOCH, M.T., PIKE, A.W.G., CHAPPELL, J., KINSLEY, L., MORTIMER, G., SHELLEY, M., MURRAY-WALLACE, CHRISTOPH SPOTLE, C.V. & TAYLOR, L. (2005): *In situ* U-series dating by laser-ablation multi-collector ICPMS: new prospects for Quaternary geochronology. *Quat. Sci. Rev.* **24,** 2523–2538.

FERNÁNDEZ, B., CLAVERIE, F., PECHEYRAN, C., DONARD, O. & CLAVERIE, F. (2007): Direct analysis of solid samples by fs–LA–ICP–MS. *Trends in Analyt. Chem.* **26**, 951-966.

GUILLONG, M., HORN, I. & GÜNTHER, D. (2003): A comparison of 266 nm, 213 nm and 193 nm produced from a single solid state Nd:YAG laser for laser ablation ICP–MS. *J. Analyt. Atom. Spectrom.* **18**, 1224-1230.

GÜNTHER, D. & HATTENDORF, B. (2005): Solid sample analysis using laser ablation inductively coupled plasma mass spectrometry. *Trends in Analyt. Chem.* **24**, 255-265.

GÜNTHER, D. & KOCH, J. (2008): Formation of aerosols generated by laser ablation and their impact on elemental fractionation in LA–ICP–MS. *In* Laser Ablation ICP–MS in the Earth Sciences: Current Practices and Outstanding Issues (P. Sylvester, *ed*.). *Mineral. Assoc. Can. Short Course Series* **40**, 19-34.

HALTER, W.E., PETTKE, T. & HEINRICH, C.A. (2004): Laser–ablation ICP–MS analysis of silicate and sulfide melt inclusions in an andesitic complex I: analytical approach and data evaluation. *Contrib. Mineral. Petrol.* **147**, 385-396.

HATHORNE, E.C., JAMES, R.H., SAVAGEY, P. & ALARD, O. (2008): Physical and chemical characteristics of particles produced by laser ablation of biogenic calcium carbonate. *J. Analyt. Atom. Spectrom.*, **23**, 240–243.

HERGENRÖDER, R. (2006): A model of noncongruent laser ablation as a source of fractionation effects in LA–ICP–MS. *J. Analyt. Atom. Spectrom.* **21**, 505-516.

HORN, I. (2008): Comparison of femtosecond and nanosecond laser interactions with geologic matrices and their influence on accuracy and precision of LA–ICP–MS data. *In* Laser Ablation ICP–MS in the Earth Sciences: Current Practices and Outstanding Issues (P. Sylvester, *ed*.). *Mineral. Assoc. Can. Short Course Series* **40**, 53-65.

JACKSON, S.E. (2008): Calibration strategies for elemental analysis by LA–ICP–MS *In* Laser Ablation ICP–MS in the Earth Sciences: Current Practices and Outstanding Issues (P. Sylvester, *ed*.). *Mineral. Assoc. Can. Short Course Series* **40**, 169-188.

JOCHUM, K.P. & STOLL, B. (2008): Reference materials for elemental and isotopic analyses by LA–(MC)–ICP–MS: successes and outstanding needs. *In* Laser Ablation ICP–MS in the Earth Sciences: Current Practices and Outstanding Issues (P. Sylvester, *ed*.). *Mineral. Assoc. Can. Short Course Series* **40**, 147-168.

JOCHUM, K.P., STOLL, B., HERWIG, K. & WILLBOLD, M. (2007): Validation of LA–ICP–MS trace element analysis of geological glasses using a new solid-state 193 nm Nd:YAG laser and matrix-matched calibration. *J. Analyt. Atom. Spectrom*. **22**, 112-121.

KENT, A.J.R. & UNGERER, C.A. (2005): Production of barium and light rare earth element oxides during LA–ICP–MS microanalysis. *J. Analyt. Atom. Spectrom.* **20**, 1256 – 1262.

KOCH, J., FELDMANN, I., JAKUBOWSKI, N. & NIEMAX, K. (2002): Elemental composition of laser ablation aerosol particles deposited in the transport tube to an ICP. *Spectrochim. Acta Part B: Atom. Spectrosc.* **57**, 975-985.

KOŠLER, J. (2008): Laser ablation sampling strategies for concentration and isotope ratio analyses by ICP–MS. *In* Laser Ablation ICP–MS in the Earth Sciences: Current Practices and Outstanding Issues (P. Sylvester, *ed*.). *Mineral. Assoc. Can. Short Course Series* **40**, 79-92.

KOŠLER, J., FONNELAND, H., SYLVESTER, P., TUBRETT, M. & PEDERSEN, R. (2002): U–Pb dating of detrital zircons for sediment provenance studies – a comparison of laser ablation ICP–MS and SIMS techniques. *Chem. Geol.* **182**, 605-618.

KOŠLER, J., WIEDENBECK, M., WIRTH, R., HOVORKA, J., SYLVESTER, P. & MÍKOVÁ, J. (2005): Chemical and phase composition of particles produced by laser ablation of silicate glass and zircon – implications for elemental fractionation during ICPMS analysis. *J. Analyt. Atom. Spectrom.* **20**, 402-409.

KROSLAKOVA, I. & GÜNTHER, D. (2007): Elemental fractionation in laser ablation–inductively coupled plasma–mass spectrometry: evidence for mass load induced matrix effects in the ICP during ablation of a silicate glass. *J. Analyt. Atom. Spectrom.* **22**, 51-62.

KUROSAWA, M., SHIMA, K., ISHII, S. & SASA, K. (2006): Trace element analysis of fused whole-rock glasses by laser ablation–ICP–MS and PIXE. *Geostand. & Geoanalyt. Res.* **30**, 17 – 30.

LONGERICH, H.P., JACKSON, S.E. & GÜNTHER, D. (1996): Laser Ablation-Inductively Coupled Plasma-Mass Spectrometric transient signal data acquisition and analyte concentration calculation. *J. Analyt. Atom. Spectrom.*, **11**, 899-904.

MASON, P.R.D., KOŠLER, J., DE HOOG, J.C.M., SYLVESTER, P.J. & MEFFAN-MAIN, S. (2006): *In situ* determination of sulfur isotopes in sulfur-rich materials by laser ablation multiple-collector inductively coupled plasma mass spectrometry (LA–MC–ICP–MS). *J. Analyt. Atom. Spectrom.* **21**, 177 – 186

NORMAN, M., MCCULLOCH, M., O'NEILL, H. & YAXLEY, G. (2006): Magnesium isotopic analysis of olivine by laser-ablation multi-collector ICP–MS: Composition dependent matrix effects and a comparison of the Earth and Moon. *J. Analyt. Atom. Spectrom.* **21**, 50-54.

PEARSON, N.J., GRIFFIN, W.L. & O'REILLY, S.Y. (2008): Mass fractionation correction in laser ablation multiple-collector ICP–MS: implications for overlap corrections and precise and accurate *in situ* isotope ratio measurement. *In* Laser Ablation ICP–MS in the Earth Sciences: Current Practices and Outstanding Issues (P. Sylvester, *ed*.). *Mineral. Assoc. Can. Short Course Series* **40**, 93-116.

SYLVESTER, P.J. & EGGINS, S.M. (1997): Analysis of Re, Au, Pd, Pt and Rh in NIST glass certified reference materials and natural basalt glasses by laser ablation ICP–MS. *Geostand. Newslett.: J. Geostand. & Geoanalys.* **21**, 215-229.

TANAKA, K, TAKAHASHI, Y. & SHIMIZU, H. (2007): Determination of rare earth element in carbonate

using laser-ablation inductively-coupled plasma mass spectrometry: An examination of the influence of the matrix on laser-ablation inductively-coupled plasma mass spectrometry analysis. *Analytica Chimica Acta* **583**, 303–309.

WILSON, S.A., RIDLEY, W.I. & KOENIG, A.E. (2002): Development of sulfide calibration standards for the laser ablation inductively coupled plasma mass spectrometry technique. *J. Analyt. Atom. Spectrom.* **17**, 406-409.

YU, Z., NORMAN, M.D. & ROBINSON, P. (2003): Major and trace element analysis of silicate rocks by XRF and laser ablation ICP–MS using lithium borate fused glasses: matrix effects, instrument response and results for international reference materials. *Geostand. & Geoanalyt. Res.* **27**, 67–89.

# CHAPTER 6: LASER ABLATION SAMPLING STRATEGIES FOR CONCENTRATION AND ISOTOPE RATIO ANALYSES BY ICP–MS

Jan Košler
Centre for Geobiology and Department of Earth Science,
University of Bergen,
Allegaten 41,
N–5007 Bergen, Norway.
E-mail: jan.kosler@geo.uib.no

## MASS DISCRIMINATION, ELEMENTAL/ ISOTOPIC FRACTIONATION AND AEROSOL PROPERTIES

Laser ablation plasma source mass spectrometry (LA–ICP–MS) is now a widely accepted method for analysis of trace element and isotope composition in earth, biological and material sciences. The first application of the LA–ICP–MS technique for analysis of trace elements in minerals (Jackson *et al.* 1992) demonstrated its great potential with respect to detection capabilities and spatial resolution, but also its limitations, namely in analytical precision and accuracy. The precision and accuracy of trace element concentration analysis by LA–ICP–MS is limited by availability of suitable standard reference materials, their characterization uncertainty and commonly poor homogeneity on the scale of sampling by the laser beam. In addition, both trace element concentration and isotope ratio measurements suffer from the effects of isobaric interferences, instrument (spectrometer) mass discrimination/bias and laser-induced fractionation of elements and isotopes.

### Instrument mass discrimination

The non-uniform molar sensitivity across the mass range (*i.e.*, instrument mass discrimination/ bias) that is typical of all mass spectrometric measurements results from differential transmission of ions from the ion source to the detector (*cf.* Pearson *et al.* 2008). The molar sensitivity is commonly reversely (but not linearly) proportional to the mass of ions and in a typical ICP mass spectrometer varies from <1% to 20% per amu for heavy and light isotopes, respectively. There is no single cause of variation of molar sensitivity with mass but it is often assumed that the main source of this effect is in the ICP region (Maréchal *et al.* 1999) or in the ICP–MS interface, and that it is dominated by space charge effects (Douglas & Tanner 1988, Allen *et al.* 1997, Gillson *et al.* 1988, Heumann *et al.* 1998, Jakubowski *et al.* 1998). The extent of mass discrimination can be, to some extent, controlled by choice of instrument operation parameters, such as RF power, electrostatic lens settings, parameters of collision and reaction cell and settings of instrument components that modify the beam path, shape and energy distribution (*e.g.*, zoom lens or ion energy filters). It is suggested that the observed change of molar sensitivity with mass results from cumulative effect of manipulation of ions along their path from the source to the detector.

Correction schemes for ICP–MS mass discrimination have been largely adopted from thermal ionization mass spectrometry (TIMS) where empirical linear, power and exponential law equations are used. However, mass discrimination in TIMS and ICP–MS is dominated by processes in their very different ion sources and hence the physical reasons for mass discrimination and the mathematical formulas that should be used to correct for it are fundamentally different for the two techniques. Mass discrimination in ICP–MS results in offset of measured isotopic/elemental ratios that is, to a first order, independent of time. In contrast, mass discrimination in TIMS is smaller but changes with time due to isotopic distillation during evaporation of the sample from the filament. In addition, ICP–MS offers the possibility of "external" mass discrimination correction that utilizes known and measured isotopic ratios of one element to correct for mass discrimination of isotopes of another element. However, it has been shown in at least the case of Tl and Pb, that the difference in chemistry of these two elements produces a difference in their mass fractionation that limits the accuracy of the correction (Rehkämper & Mezger 2000, Kamenov *et al.* 2004). Several studies (Maréchal *et al.* 1999, Vance & Thirlwall 2002, Ingle *et al.* 2003, Wombacher & Rehkämper 2003) have proposed the use of alternate empirical equations (to TIMS) to correct

Mineralogical Association of Canada Short Course 40, Vancouver, B.C., p. 79–92.

for mass discrimination in ICP–MS, namely the generalized power law (GPL) proposed by Maréchal *et al.* (1999) and Albarède *et al.* (2004). This law uses an exponent the value of which is normally determined from repeat analyses of standards so that the GPL equation can quantify different mass dependencies.

**Laser-induced fractionation**

Laser-induced fractionation of elements and isotopes is a progressive change in the ratios of measured signals of certain element/isotope pairs with increasing number of laser pulses applied to the sample. Fractionation may occur at the ablation site, during transport of ablated material to the plasma source of ICP–MS, and in the plasma itself (by incomplete volatilization of delivered particles). Fractionation at the ablation site is commonly linked to phase changes, such as evaporation–condensation (Eggins *et al.* 1998, Hergenröder 2006a), melting (Kuhn & Günther 2003, Hergenröder 2006b) or solid state phase transformation (Košler *et al*. 2005a). Provided that different particles generated by incongruent laser ablation vary in size, chemical and isotopic fractionation is likely to take place within the ablation cell and during the transport of ablated aerosol from the cell to the ICP. Several studies have demonstrated that complete atomization and ionization of particles produced by laser ablation in the ICP is subject to their size and composition and also temperature and particle trajectory in the plasma (Olesik 1997, Guillong & Günther 2002, Aeschliman *et al.* 2003, Wang *et al.* 2006, Perdian *et al.* 2008a, b). Although the transit time of a particle through the ICP at a speed of ~28 $m.s^{-1}$ (Aeschliman *et al.* 2003) is less than 1 ms, there is evidence for chemical and isotopic fractionation in the plasma that results in different parts of the ICP having different chemical and isotopic composition at a given time (*e.g.*, Wang *et al.* 2006). Sampling just part of the ICP, as is the case in all commercially available ICP–MS instruments, inevitably results in elemental and isotopic bias which has been referred to as plasma-induced fractionation (Guillong & Günther 2002, Jackson & Günther 2003). Given that the extent of particle evaporation varies also with the size of particles, the spatial composition of the ICP depends on the particle size distribution in the ablated aerosol. Collectively, the laser-induced fractionation consists of two components: (1) constant bias that results from non-stoichiometric ablation and (2) time-dependent fractionation that results from changes in particle composition, number and size distribution during the analysis (Guillong & Günther 2002, Košler *et al.* 2005a).

**Aerosol particle size distribution**

The size distribution of particles produced during laser ablation has been shown to exert a significant control on the nature and size of elemental and isotopic fractionation (Guillong & Günther 2002, Jackson & Günther 2003, Kozlov *et al.* 2003, Košler at al. 2005a, b, Günther & Koch 2008). Major factors affecting the size distribution of particles reaching the ICP are the fluence, wavelength and pulse duration of the laser, the aspect ratio of the laser pit, the composition of the sample carrier gas, and the size-dependent transport efficiency of the ablated particles. It has been shown that particle size distribution changes during a single analysis subject to the parameters listed above but it also depends on absorption of laser radiation by the sample (Horn *et al.* 2001) and the sampling strategy, *i.e.*, scanning (raster) or stationary (single spot) ablation (Fig. 6-1). The effect of sampling mode on analytical figures of merit has been widely discussed in the community over the past ~10 years, especially in the context of Pb/U fractionation and the accuracy and precision of Pb/U ratio measurement during ablation of accessory minerals (Parrish *et al.* 1999, Guillong & Günther 2002, Horstwood *et al.* 2003, Gonzáles *et al.* 2004). The major difference between the two sampling modes is a rapid decrease in particle size and signal intensity for ablation with a stationary beam compared to the more steady signal and less change in particle size distribution while the laser beam scans across the sample surface. Difference in temporal change of particle size distribution between the two sampling modes has, for most sample matrices, laser ablation and ICP parameters, a significant effect on instrument mass bias and laser-induced fractionation, and also on analytical figures of merit.

## LASER ABLATION SAMPLING STRATEGIES

**Stationary (static, single spot) ablation**

Stationary, static or single spot ablation is laser ablation sampling at a fixed lateral position of the target sample for a period of time, normally the duration of a single analysis. Pulsed lasers are used in most cases and the amount of material ablated per analysis is proportional to the laser spot size (~area

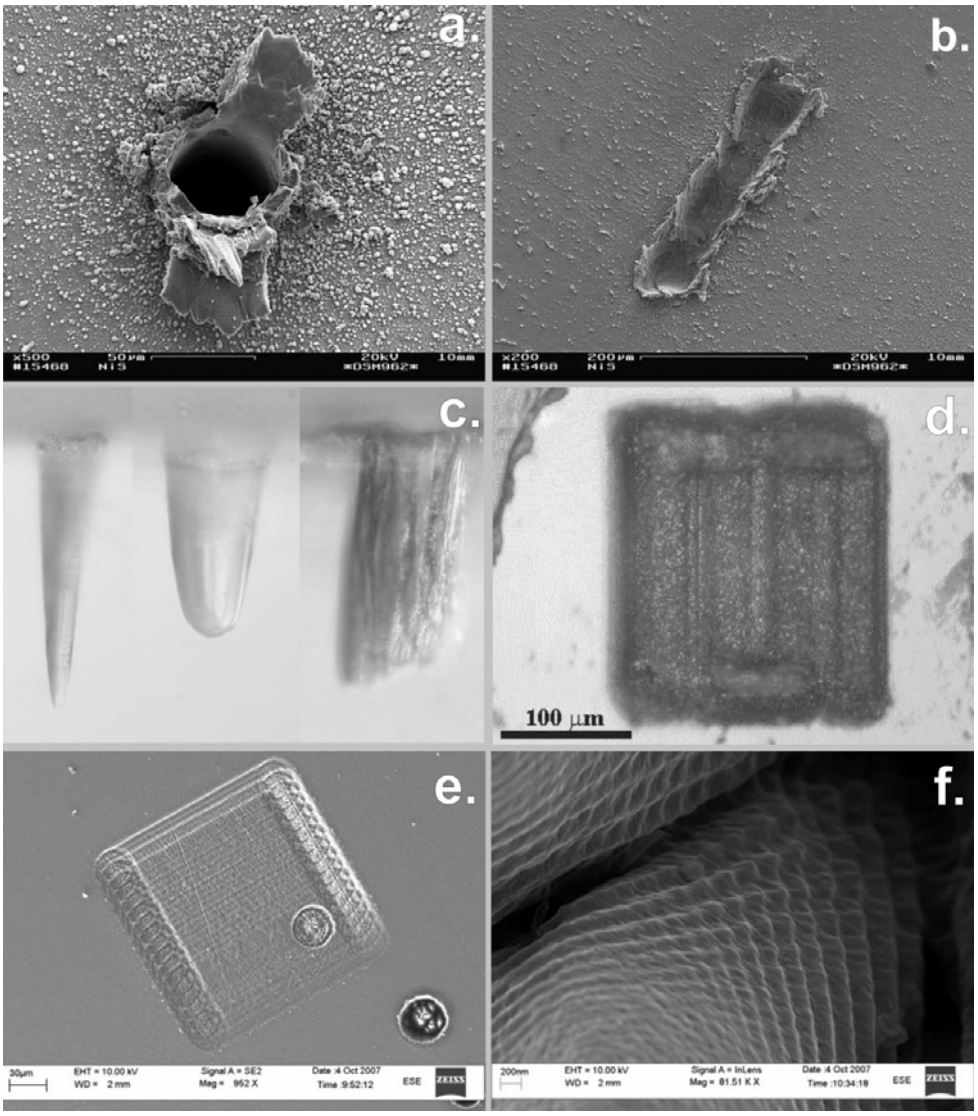


FIG. 6-1. Sampling strategies using different types of lasers. SEM images of static (**a**) and scanning (**b**) ablation craters in NiS produced with a non-homogenized 266 nm Nd:YAG laser; optical microscope images of laser craters produced by static ablation (**c**) (side view, crater diameters are 30 and 60 µm); and box raster laser scanning (**d**) in zircon ablated by a non-homogenized 266 nm Nd:YAG laser (modified from Košler & Sylvester 2003), SEM images of box raster and single laser pits produced by a non-homogenized 196 nm femtosecond laser in zircon (**e**) and a corresponding detail of the bottom of the laser crater (**f**).

irradiated by incident laser beam), laser pulse repetition rate and time length of ablation, and the material properties in combination with the laser wavelength and fluence. Horn *et al.* (2001) studied the rate of ablation in metals and in silicate glasses using a solid state 266 nm laser and a 193 nm excimer laser in order to determine the vertical (z) spatial resolution of laser ablation analysis. They found that the rate of ablation for a given sample composition was almost independent of the laser wavelength but it varied with fluence and material properties of the ablated sample (namely its melting point and absorption at the relevant laser wavelength). At the same time, the observed differences in the depth of penetration in samples with different absorption of the laser light (such as the NIST-600 series glasses) were smaller, and the measured signal intensities were higher for the shorter laser wavelength, suggesting differences in particle formation for the two wavelengths. Typically, laser ablation analysis is performed on a flat sample surface which has been polished to aid

visual control of the ablation process. Subject to the laser wavelength and its absorption by the sample, this may lead to unwanted reflection of laser light during the initial phase of the ablation, poor coupling of the laser to the polished sample surface and uneven ablation, resulting in the formation of large (μm size) as well as small (nm size) particles at the start of an analysis (Fig. 6-2a). The initial burst of large and small particles is accompanied by a short-lived increase of signal following which only smaller particles form and the signal intensity decays at a slower rate. This initial part of the signal is very often omitted from analysis because it is believed to yield non-reproducible analytical data.

The ablation conditions during stationary sampling change rapidly and can result in fast decay of transient signal during laser ablation ICP–MS analysis. As the laser penetrates into the sample and forms a deepening ablation crater, the beam becomes out of focus and the laser energy density at the bottom of the crater decreases. Ultimately, the ablation stops for lack of available energy to ablate. However, temporal increase in the ablation rate due to internal reflections within the crater has also been reported (Eggins *et al*. 1998). For many elements and isotopes, the stationary laser ablation sampling results in elemental or isotopic fractionation. This is primarily due to change in the particle size distribution, particle composition and mass load of the ICP. Several strategies have been proposed to suppress the fractionation and to improve the quality of the signal and analytical precision obtained from the initial part of the ablation. These include soft ablation (a slow increase of laser energy at the start of the ablation to improve coupling of laser with the sample; Hirata 1997) and active focusing (continuous re-focusing of the laser at the bottom of the ablation crater by slow rising of

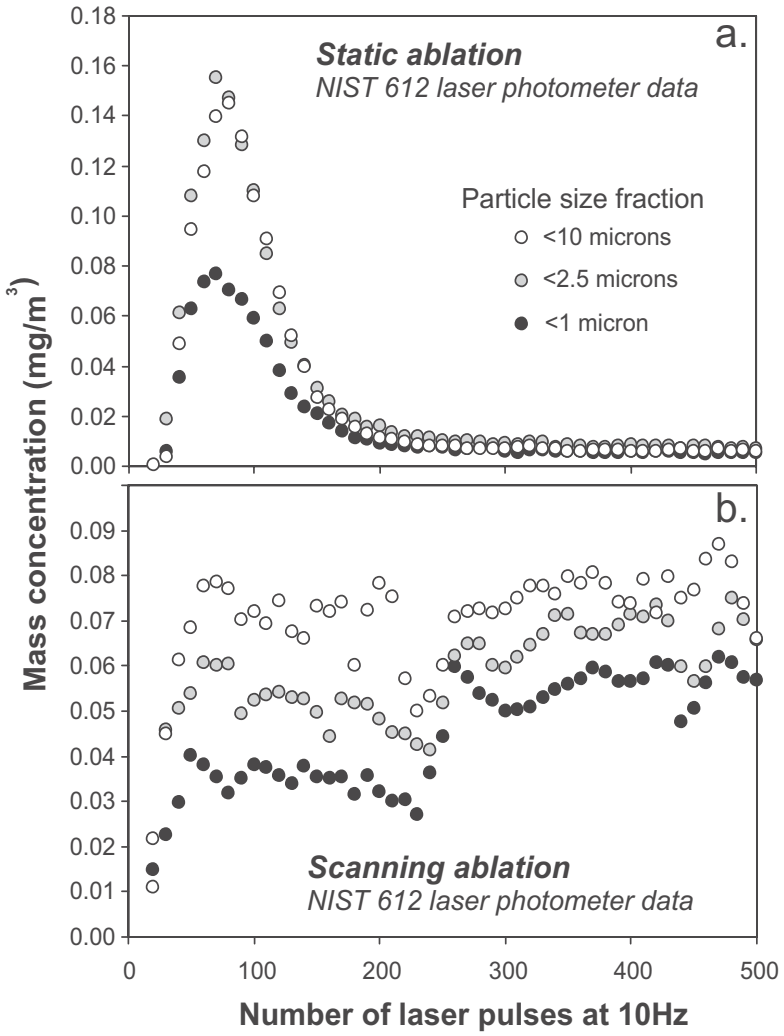


FIG. 6-2. Temporal variations of mass concentrations of particles determined by a TSI DustTrak 8520 laser photometer which has a capability to detect particles >0.3 μm (data from Košler *et al.* 2005a). The aerosol was generated by ablating NIST-612 soda-lime glass in a He atmosphere with a 266 nm Nd:YAG laser fired at 10 Hz repetition rate. Mass concentrations of particles smaller than 10, 2.5 and 1 μm suggest that no particles in the 10–2.5 μm size range were present during the first 250 pulses of the static ablation experiment while proportions of particles in the 2.5–1 and 1–0.3 μm fractions were almost equal. The scanning experiment produced aerosol with almost equal distributions in the three size fractions throughout the first 500 laser pulses.

the sample stage; Hirata & Nesbitt 1995). However, due to difficulties in automating and in reproducibility of these sampling strategies, neither of them has been widely used.

**Scanning (dynamic, raster) ablation**

Scanning (dynamic, raster) laser ablation sampling involves moving the sample (stage) under the stationary laser beam, creating a groove (raster) in the sample surface. As a result, the laser beam does not penetrate deep into the sample and the ablation is similar (though not identical) to the initial phase of stationary ablation (*i.e.*, formation of both large μm size and small nm size particles). The raster is normally achieved by programming the stage motion and, subject to the available sample surface, its pattern can vary in size, shape and number of passes of the laser over the same parts of the sample. Compared to stationary ablation, the supply of particles to the ICP and their size distribution are relatively constant (Fig. 6-2b), reducing the time-dependent variation in signal intensity, producing more constant plasma mass load and suppressing the elemental and isotopic fractionation. Similar to stationary ablation (single spot analysis), the amount of ablated material and depth of penetration during scanning ablation are proportional to the size of laser spot (~area irradiated by incident laser beam), laser fluence, repetition rate, material ablated in combination with laser wavelength, scanning speed and length of the raster. Scanning laser ablation was first demonstrated to be a useful sampling technique for ICP–MS trace element measurement in corals (Sinclair *et al.* 1998) and meteorites (Campbell & Humayun 1999) because it produced sufficiently stable and long signal for obtaining precise concentration values and provided good spatial resolution required for the analysis. It has subsequently been adopted by the geological community and used particularly for U–Pb dating of accessory minerals (Parrish *et al.* 1999) because it leads to suppression of the time-dependent variation of the measured Pb/U ratios. Optimization of the laser ablation parameters in the scanning mode (at a given beam diameter and laser energy) includes adjustments to the scanning speed and the laser repetition rate. Different combinations of scanning speed (0.75 to 100 μm/s) and laser pulse frequency (5 to 20 Hz) have been proposed as "ideal" for suppressing the time-dependent variation of the measured elemental or isotopic ratios and thereby improving the precision and accuracy of the measurement (Gonzáles *et al.* 2004, Bennett *et al.* 2005, Perdian *et al.* 2008a, b). However, no consensus on these optimum values has so far been arrived at by the laboratories that utilize this technique.

## COMPARISON OF THE STATIONARY AND SCANNING ABLATION MODES

**Precision and accuracy**

Suppression of the time-dependent variations of elemental and isotopic ratios during laser beam scanning allows estimation of a mean value of the measured ratios because the measured signals have a Poisson distribution that is approximating normal symmetrical distribution. The uncertainty can then be estimated as the standard deviation of the population or standard deviation ("error") of the mean. This is not possible when the signal intensity ratios show a time-dependent drift (fractionation), as is often the case with stationary laser ablation. In such a case the value of the mean is subject to the ablation time interval used in the analysis and it is not representative of the analysis as a whole. Accordingly, the calculation of the mean and uncertainty must be based on assumptions other than symmetrical distribution of the observed elemental and isotopic ratios. Mathematical solutions such as linear regression of the measured elemental and isotopic ratios and calculation of the mean ratio value and its uncertainty at the start of ablation (Sylvester & Ghaderi 1997) have to be applied to obtain a reliable estimate of statistical parameters of the measurement. As a result of better stability of the measured signal intensity ratios and generally higher signal intensities during laser beam scanning, this sampling strategy yields precision that is typically 2–5 times better than static laser ablation.

The accuracy of element concentration measurements by laser ablation ICP–MS depends primarily on the reproducibility of sample and calibration standard measurements, similarities in the ablation behavior of samples and reference materials, and on the homogeneity and characterization of the reference materials used for calibration. Accuracy of isotope ratio measurements may further depend on measurements of reference element and isotope ratios that are needed for mass discrimination and fractionation corrections, unless the corrections can be made from measurements of a simultaneously aspirated standard solution (*e.g.*, Mason *et al.* 2006). Stationary laser ablation has

been reported to produce element concentration data with better accuracy than scanning laser ablation analysis. The experiments of Guillong & Günther (2002) suggest that, especially with particle filtering, stationary ablation in He (266 nm, 80 μm beam diameter, 10 Hz) can produce more accurate U/Th data for silicate glasses compared to the scanning sampling mode. However, the accuracy of the measured U/Th ratios is expected to vary with number of instrument tuning parameters, including the sampling position of the ICP. In another study Gonzáles *et al.* (2004) used a UV laser (213 nm) coupled to a quadrupole ICP–MS to measure U, Th and Pb concentrations in a volcanic rock, utilizing the NIST600 series glasses for calibration and Ca or Si as internal standards. Although their results suggest that accuracy of the scanning laser ablation analysis (100 μm spot diameter, 21 J/cm$^2$, 10 Hz, 50 μm/s, ablation in Ar) was ~2 times worse compared to the stationary mode of sampling, they did not rule out the potential contribution of sample heterogeneity to this poorer performance.

**Spatial resolution**

In comparing spatial resolution (the ability to resolve chemical and isotopic heterogeneities in 3D) of different laser ablation sampling modes, the volume of ablated sample material should be compared either to the obtained precision of elemental/isotopic determination or to the total number of analyte counts registered by the detector. Different techniques have been used to measure the volume of laser ablation craters, including SEM imaging (Eggins *et al.* 2003), using optical or mechanical profilometers (Horn *et al.* 2001), imaging the craters filled with fluorescing liquid by scanning confocal microscopy (Carlson *et al.* 2007, T. Hrstka pers. com.) or imaging the craters in transmitted light (Horn *et al.* 1999, Košler & Sylvester 2003). The latter technique was used to image laser craters produced by stationary and scanning laser ablation modes in mineral garnet (Fig. 6-3). Two chemically and optically different natural garnet grains (cubic Fe–Mg–Ca–Mn silicates) were used in this study: Fe-rich light pink almandine and Mg-rich dark red pyrope. The garnet was sectioned and polished to form an edge so that the ablation craters could be observed and their dimensions measured in 3D using a petrographic microscope. The laser ablation conditions were similar to those used for trace element analysis in silicate minerals. The laser was a 213 nm Nd:YAG that was fired at 10 Hz repetition rate and 3 J/cm$^2$ for 90 seconds (total of 900 pulses) to produce round laser pits that were 25 and 40 μm in diameter in the garnet. In addition, 150x25 and 150x40 μm trenches were produced by using identical ablation conditions while moving the stage under stationary laser beam at a speed of 10 μm/s. This set-up allowed for volume of ablated material to be calculated from dimensions of craters in the two garnet grains. The results suggest that for the laser parameters used in this experiment, the volume of material ablated using the laser scanning mode is *ca*. 15% larger than the volume of material

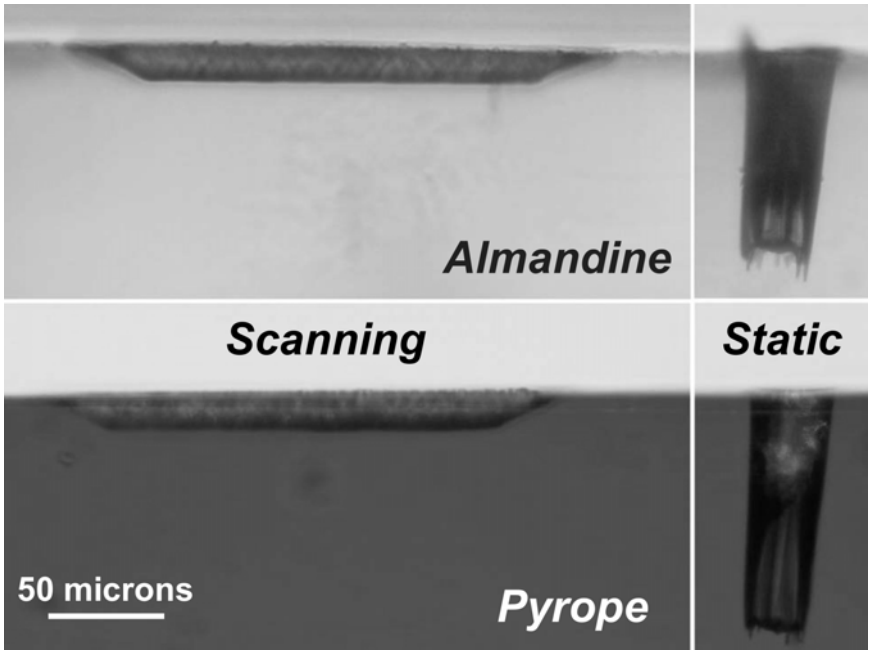


FIG. 6-3. Side view of craters produced by scanning (left) and static (right) laser ablation in almandine (top) and pyrope (bottom) garnets. The volume of craters produced by laser scanning is *ca.* 15% larger compared to the volume of craters formed during static ablation. See text for more details.

ablated by stationary ablation, irrespective of laser beam diameter and color of the garnet. The total number of counts obtained from laser scanning during ablation of different sample matrices and for different lasers and ablation conditions is 20–100% larger compared to signal intensities obtained from stationary ablation sampling (Campbell & Humayun 1999, Guillong & Günther 2002, Košler *et al.* 2003, Mason *et al.* 2006, Chmeleff *et al.* 2008). The ablation time required for achieving comparable precision with the two sampling strategies is at least 20% shorter for laser scanning and accordingly, the spatial resolution of laser scanning ablation is similar, or better, compared to the stationary ablation.

Most geological and biological samples are heterogeneous on the micro-scale and imaging the analyzed surface by optical or by electron beam techniques prior to laser ablation analysis has proven practical to resolve the sample heterogeneities spatially. Laser ablation close to the previously imaged sample surface is therefore essential for matching the image and analytical data as closely as possible (*cf.* Fig. 6-4). The 2D resolution of the laser scanning ablation on the exposed sample surface is worse compared to the stationary ablation sampling. However, its better 3D spatial resolution and the ability to correlate the laser ablation signal with images of sample surface make the laser scanning a preferred sampling mode for many geological and biological applications of LA–ICP–MS.

**Effects of sampling strategies on the ICP**

The number and size distribution of particles produced by laser ablation can have a significant effect on the ICP and as a consequence on both the degree of space charge and the extent of plasma-induced fractionation. Laser beam scanning generally produces aerosols with more constant

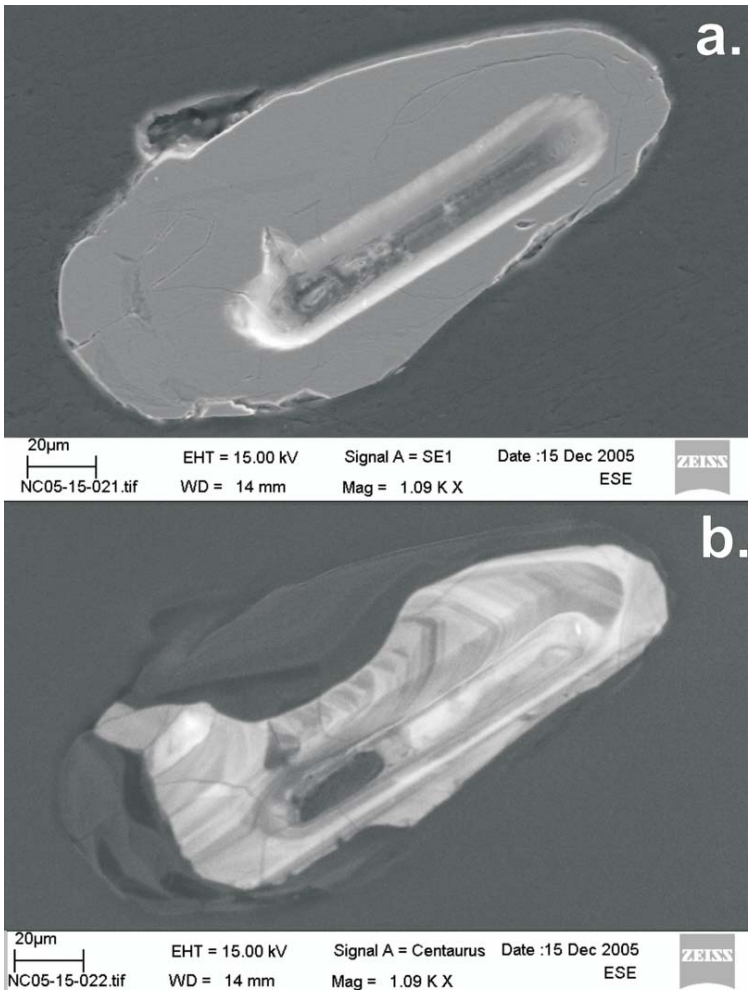


FIG. 6-4. Secondary electron (**a**) and cathodoluminescence (**b**) images of a zircon grain with ablation grove produced by scanning the laser across the grain surface. The CL image shows that on one side of the grove the ablation penetrated into the dark (U-rich) rim part of the zircon grain (courtesy of A. Ksienzyk), pointing to the importance of sample imaging prior to, and possibly also after, the analysis by LA–ICP–MS.

particle number and size distribution over the time of analysis compared to the stationary beam sampling and accordingly, the plasma mass load is less variable for the laser scanning mode. Studies of plasma mass load effects during ablation of silicate samples (Kroslakova & Günther 2007) suggested a significant matrix effect that leads to a decrease of volatile element/Ca intensity ratios with increasing plasma mass load and which is more pronounced for elements with low melting points. Such matrix effects will vary with changes in the plasma mass load (such as observed during stationary beam ablation) and they may even exceed the contribution of laser-induced fractionation to the observed temporal changes in the signal intensity ratios. It has been suggested that thermal effects from laser radiation may alter sample domains adjacent to laser ablation craters (Košler *et al.* 2005a). The ablation and re-sampling of previously heated areas of the sample increases with decreasing speed of laser scanning (Perdian *et al.* 2008a); greater overlap of successive laser spots, more extensive re-heating and re-ablation leads to a greater contribution of large particles and larger changes in the plasma mass load.

Other techniques that improve the stability of plasma mass load during the analysis include the use of shorter laser wavelength (Guillong *et al.* 2003, Télouk *et al.* 2003), use of shorter laser pulses (Russo *et al.* 2002, Poitrasson *et al.* 2003, Koch *et al.* 2004, 2006, Horn *et al.* 2006, Horn & von Blanckenburg 2007) and improved aerosol transport efficiency, *e.g.*, by ablation in He (Eggins *et al.* 1998). It is expected that in combination with the laser scanning ablation, these techniques will result in improved precision and reproducibility of laser ablation ICP–MS measurements.

## APPLICATIONS OF LASER SCANNING AND STATIONARY ABLATION

The choice of the laser ablation sampling mode is subject to the sample matrix, the analyzed element/isotope and its concentration and the precision and reproducibility required by the application. Analyses that require high precision and accuracy and that are prone to inter-element or isotope fractionation, such as measurements of isotopic ratios of light and mid-mass isotopes and U–Th–Pb dating of accessory minerals, generally benefit from using the laser scanning ablation mode. Laser scanning is also preferred for analyses where high spatial resolution is needed to detect and avoid small particles or inclusions (O'Neill & Eggins 2002). On the other hand, stationary ablation analysis is simple to implement and can be easily automated for non-attended runs. It is commonly used for trace element analysis where there is no significant elemental fractionation between analytes and internal standard and for isotopic ratio measurements of heavy isotopes, such as Sr, Hf, Os and Pb. Stationary ablation is also well suited for laser ablation depth profiling (*e.g.*, Mank & Mason 1999, Woodhead *et al.* 2008) although recent development in excimer laser and ablation cell technology indicate that laser scanning with a line-shaped beam and fast flushing ablation cell is also well suited for analysis of chemical and diffusion profiles in natural samples, such as silicate minerals (Spandler *et al.* 2007).

Laser scanning ablation (raster mode) has been successfully used for U–Th–Pb dating of accessory minerals (Parrish *et al.* 1999, Košler *et al.* 2001, 2002, Li *et al.* 2001, Cox *et al.* 2003, Horstwood *et al*. 2003, Woodhead *et al.* 2004, Sláma *et al.* 2008). The main benefit has been in significant reduction of the Pb/U elemental fractionation (Fig. 6-5) that is thought to originate mainly from thermally induced phase changes in the ablated minerals (Košler *et al.* 2005a). Stationary laser beam ablation has also been successfully used to date accessory minerals by several laboratories (Horn *et al.* 2000, Jeffries *et al.* 2003, Tiepolo 2003, Jackson *et al.* 2004, Simonetti *et al.* 2005, Sláma *et al.* 2008). The latter approach relies mainly on external calibration of the Pb/U

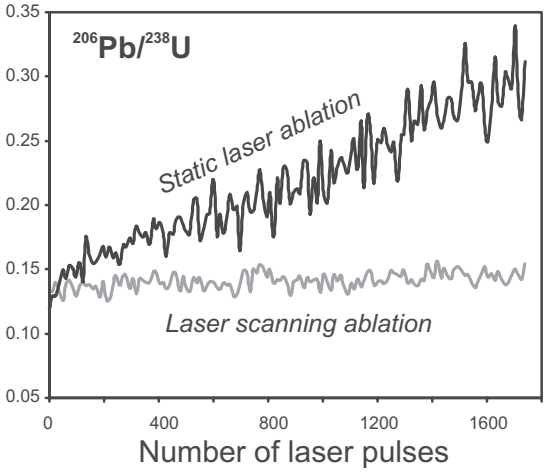


FIG. 6-5. Time-resolved Pb/U ratios obtained from static and laser scanning ablation of zircon 91500 with a Nd:YAG 266 nm laser (10 Hz repetition rate) in He atmosphere. Data are not corrected for mass discrimination; the reported TIMS value of the $^{206}Pb/^{238}U$ ratio is 0.1796 (Wiedenbeck *et al.* 1995).

fractionation, its correction by mathematical functions (Horn *et al.* 2000), short ablation time (Simonetti *et al.* 2005) or use of short pulse (femtosecond) lasers that reduce heat transfer to the sample (Horn & von Blanckenburg 2007). Comparison of analytical precision and accuracy achieved by the two sampling techniques has proven difficult because of differences in analytical protocols and data reduction procedures used by individual laboratories.

*In situ* isotope ratio measurements by laser ablation ICP–MS represent a relatively novel technique that became available in the mid 1990s due to implementation of instruments with the capability for simultaneous detection of multiple isotopes (*i.e.*, multicollector ICP–MS). Laser ablation sampling strategy exerts an important control on the precision and accuracy of isotope ratio measurements, especially for light and mid-mass isotopes and ablation with nanosecond pulse lasers. Precision of isotope ratio measurements required for most geological and biological applications varies between 1 and 0.05 permil and accordingly tight control over the instrument mass discrimination, laser-induced isotopic fractionation, and the effects of plasma mass load are essential. Due to higher isotope signal intensities and better signal stability, scanning laser ablation sampling has been preferred over stationary beam ablation for isotope ratio measurement of copper (Jackson & Günther 2003), iron (Košler *et al.* 2005b), sulfur (Bendall *et al.* 2006, Mason *et al.* 2006) and silicon (Chmeleff *et al.* 2008). Other studies used stationary ablation and relied on external calibration of Cu and Fe isotopic ratios (*e.g.*, Graham *et al.* 2004). Isotopic compositions of Fe in metals and sulfides and Si in silicates have been successfully analyzed by UV femtosecond laser ablation (Horn *et al.* 2006, Chmeleff *et al.* 2008). The scanning femtosecond laser ablation provides higher signal intensities but because of a uniform and small aerosol particle size distribution produced by the femtosecond pulses, no significant differences were found in the precision and accuracy of isotopic ratios measured by the two laser sampling modes (Horn *et al.* 2006). In contrast, ablation of metals and sulfides with stationary nanosecond laser beam can result in significant (up to several permil) fractionation of Fe and Cu isotopes (Jackson & Günther 2003, Košler *et al.* 2005b) that has been attributed to variations in isotopic composition of different aerosol size fractions (Fig. 6-6). The combination of scanning laser ablation and external calibration by matrix-matched standards can significantly improve precision and accuracy of analyses made with nanosecond laser ablation ICP–MS (Košler *et al.* 2005b).

## CONCLUDING REMARKS

This paper provides a review and comparison of two laser ablation sampling modes – stationary (static, single spot) and scanning (dynamic, raster) that can be employed by laser ablation ICP–MS users. The choice of laser ablation sampling mode is an important analysis parameter as it can affect both the quality analytical data and their interpretation. Stationary ablation provides excellent 2D resolution of the analyzed sample surface, is easy to set up for automated runs, and yields precise and accurate elemental and isotopic data for samples, elements and isotopes that do not suffer from severe elemental or isotopic fractionation. Because stationary ablation can penetrate several tens to hundreds microns into the sample, the analytical data obtained can be difficult to correlate with compositional maps/images of the sample surface. Stationary ablation can be also used for composition mapping (by combination and interpolation of data from multiple discrete measurements) and for depth profiling.

Scanning ablation provides more flexibility in sampling different parts of the sample and, because it normally penetrates less than 10 micrometres below the analyzed surface, the analytical data can be correlated with compositional images obtained by other (*e.g.*, electron microbeam) techniques. In combination with a low volume (fast flushing) ablation cell, scanning ablation can be used for compositional mapping (Woodhead *et al*. 2008) and profiling in the plane of the analyzed sample surface. Compared to stationary ablation, scanning ablation commonly yields higher signal intensities and can be used to suppress temporal variations in the measured element/isotope signal intensity ratios (laser-induced elemental and isotopic fractionation) and as a result improve measurement precision. The 3D spatial resolutions achievable with the two sampling modes are comparable.

## ACKNOWLEDGEMENTS

Assistance with the aerosol particle collection was provided by Jan Hovorka and Jitka Míková, Nicola McLoughlin, Anna Ksienzyk and Michael Wiedenbeck helped with obtaining optical and SEM sample images, Ingo Horn operated the femtosecond laser at the University of Hannover.

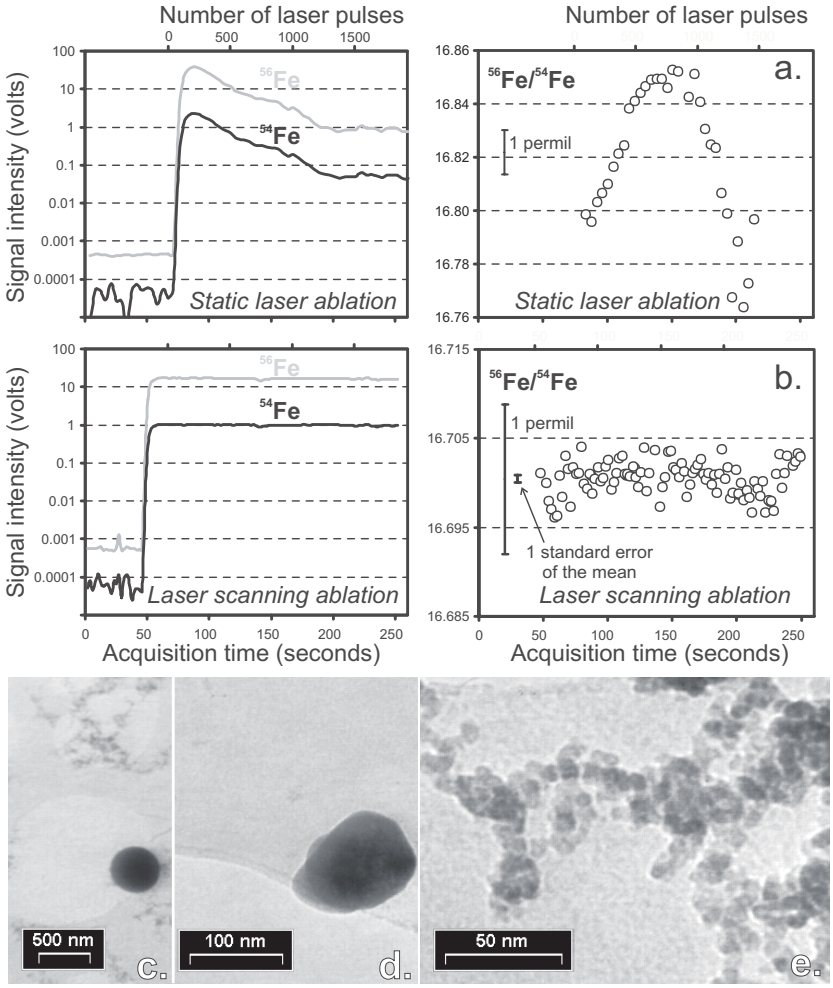


FIG. 6-6. Iron isotopic fractionation during the ablation of IRMM-014 Fe metal isotopic standard with a 213 nm Nd:YAG laser in He atmosphere (modified from Košler *et al.* 2005b). The laser ablation parameters were as follows: 40 μm laser crater diameter, 10 Hz and 5.5 J cm$^2$ for the static laser ablation (**a**), and 80 μm laser crater diameter, 10 Hz, 5.5 J cm$^2$ and 10 μm s$^{-1}$ stage speed for the laser raster analysis (**b**). The TEM images show different types of particles produced during the ablation, including spherical melt droplets (**c**), non-spherical particles (**d**) and fine particles that formed by condensation from vapour phase (**e**).

Steve Eggins and an anonymous reviewer are thanked for providing helpful comments on the manuscript.

## REFERENCES

AESCHLIMAN, D.B., BAJIC, S.J., BALDWIN D.P. & HOUK, R.S. (2003): High-speed digital photographic study of an inductively coupled plasma during laser ablation: comparison of dried solution aerosols from a microconcentric nebulizer and solid particles from laser ablation. *J. Anal. At. Spectrom.* **18**, 1008-1014.

ALBARÈDE, F., TÉLOUK, P., BLICHERT-TOFT, J., BOYET, M., AGRANIER, A. & NELSON B. (2004): Precise and accurate isotopic measurements using multiple-collector ICPMS. *Geochim. Cosmochim. Acta*, **68**, 2725-2744.

ALLEN, L.A., LEACH, J. J. & HOUK, R.S. (1997): Spatial location of the space charge effect in individual ion clouds using monodisperse dried microparticulate injection with a twin quadrupole inductively coupled plasma mass spectrometer. *Anal. Chem.* **69**, 2384-2391.

BENDALL, C., LAHAYE, Y., FIEBIG, J., WEYER, S. & BREY, G.P. (2006): In situ sulfur isotope analysis by laser ablation MC–ICPMS. *Appl. Geochem.* **21**, 782-787.

BENNETT, V., JACKSON, V.A., RIVERS, T., RELF, C.,

HORAN, P. & TUBRETT, M. (2005): Geology and U–Pb geochronology of the Neoarchean Snare River terrane: tracking evolving tectonic regimes and crustal growth mechanisms. *Canad. J. Earth Sci.* **42**, 895-934.

CAMPBELL, A.J. & HUMAYUN, M. (1999): Trace element microanalysis in iron meteorites by laser ablation ICPMS. *Anal. Chem.* **71**, 939-946.

CARLSON, A.L., COGHLAN, L.G., GILLENWATER, A.M. & RICHARDS-KORTUM, R.R. (2007): Dual-mode reflectance and fluorescence near-video-rate confocal microscope for architectural, morphological and molecular imaging of tissue. *J. Microscopy* **228**, 11–24.

CHMELEFF, J., HORN, I., STEINHOEFEL, G. & VON BLANCKENBURG, F. (2008): In situ determination of precise stable Si isotope ratios by UV–femtosecond laser ablation high-resolution multi-collector ICP–MS. *Chem. Geol.* **249**, 155-166.

COX, R.A., WILTON, D.H.C. & KOŠLER, J. (2003): Laser-ablation U–Th–Pb in situ dating of zircon and allanite: An example from the October Harbour granite, central coastal Labrador, Canada. *Can. Mineral.* **41**, 273-291.

DOUGLAS, D.J. & TANNER, S.D. (1988): Fundamental considerations in ICP–MS. *In* Inductively Coupled Plasma Mass Spectrometry (A. Montaser ed.). *Wiley-VCH*, 615-679.

EGGINS, S.M., KINSLEY, L.P.J. & SHELLEY, J.M.M. (1998): Deposition and element fractionation processes during atmospheric pressure laser sampling for analysis by ICPMS. *Appl. Surf. Sci.* **129**, 278-286.

EGGINS, S., DE DECKKER, P. & MARSHALL, J. (2003): Mg/Ca variation in planktonic foraminifera tests: implications for reconstructing palaeo-seawater temperature and habitat migration. *Earth Planet. Sci. Lett.* **212**, 291-306.

GILLSON, G.R., DOUGLAS, D.J., FULFORD, J.E., HALLIGAN, K.W. & TANNER, S.D. (1988): Nonspectroscopic interelement interferences in inductively coupled plasma mass-spectrometry. *Anal. Chem.*, **60**, 1472-1474.

GONZÁLES, J., FERNÁNDES, A., MAO, X. & RUSSO, R.E. (2004): Scanning vs. single spot laser ablation (λ=213 nm) inductively coupled plasma mass spectrometry. *Spectrochim. Acta B* **59**, 369-374.

GRAHAM, S., PEARSON, N., JACKSON, S., GRIFFIN, W. & O'REILLY, S.Y. (2004): Tracing Cu and Fe from source to porphyry: in situ determination of Cu and Fe isotope ratios in sulfides from the Grasberg Cu–Au deposit. *Chem. Geol.* **207**, 147-169.

GUILLONG, M. & GÜNTHER, D. (2002): Effect of particle size distribution on ICP-induced elemental fractionation in laser ablation–inductively coupled plasma–mass spectrometry. *J. Anal. At. Spectrom.* **17**, 831-837.

GUILLONG, M., HORN, I. & GÜNTHER, D. (2003): A comparison of 266 nm, 213 nm and 193 nm produced from a single solid state Nd:YAG laser for laser ablation ICP–MS. *J. Anal. At. Spectrom.* **18**, 1224-1230.

GÜNTHER, D. & KOCH, J. (2008): Formation of aerosols generated by laser ablation and their impact on elemental fractionation in LA–ICP–MS. *In* Laser Ablation ICP–MS in the Earth Sciences: Current Practices and Outstanding Issues (P. Sylvester, *ed*.). *Mineral. Assoc. Can. Short Course Series* **40**, 19-34.

HERGENRÖDER, R. (2006a): A model for the generation of small particles in laser ablation ICP–MS. *J. Anal. At. Spectrom.* **21**, 1016-1026.

HERGENRÖDER, R. (2006b): A model of non-congruent laser ablation as a source of fractionation effects in LA–ICP–MS. *J. Anal. At. Spectrom.* **21**, 505-516.

HEUMANN, K.G., GALLUS, S.M., RÄDLINGER, G. & VOGL, J. (1998): Precision and accuracy in isotope ratio measurements by plasma source mass spectrometry. *J. Anal. At. Spectrom.* **13**, 1001-1008.

HIRATA, T. & NESBITT, R.W. (1995): U–Pb isotope geochronology of zircon: Evaluation of the laser probe–inductively coupled plasma mass spectrometry technique. *Geochim. Cosmochim. Acta*, **59**, 2491-2500.

HIRATA, T. (1997): Soft ablation technique for laser ablation–inductively coupled plasma–mass spectrometry. *J. Anal. At. Spectrom.* **12**, 1337-1342.

HORN, I. & VON BLANCKENBURG, F. (2007): Investigation on elemental and isotopic fractionation during 196 nm femtosecond laser ablation multiple collector inductively coupled plasma mass spectrometry. *Spectrochim. Acta B* **62**, 410-422.

HORN, I., RUDNICK, R.L. & MCDONOUGH, W.F. (1999): In-situ non matrix matched U/Pb and

Pb/Pb dating of zircon by excimer LA–ICP–MS. *J. Conf. Abstr.* **4**, 799.

HORN, I., RUDNICK, R.L. & MCDONOUGH, W.F. (2000): Precise elemental and isotope ratio measurement by simultaneous solution nebulisation and laser ablation–ICP–MS: application to U–Pb geochronology. *Chem. Geol.* **167**, 405-425.

HORN, I., GUILLONG, M. & GÜNTHER, D. (2001): Wavelength dependant ablation rates for metals and silicate glasses using homogenized laser beam profiles – implications for LA–ICP–MS. *Appl. Surf. Sci.* **182**, 91-102.

HORN, I., VON BLANCKENBURG, F., SCHOENBERG, R., STEINHOEFEL, G. & MARKL, G. (2006): In situ iron isotope ratio determination using UV femtosecond laser ablation with application to hydrothermal ore formation processes. *Geochim. Cosmochim. Acta* **70**, 3677-3688.

HORSTWOOD, M.S.A., FOSTER, G.L., PARRISH, R.R., NOBLE, S.R. & NOWELL G.M. (2003): Common-Pb corrected in situ U–Pb accessory mineral geochronology by LA–MC–ICP–MS. *J. Anal. Atom. Spectr.* **18**, 837-846.

INGLE, C.P., SHARP, B.L., HORSTWOOD, M.S.A., PARRISH, R.R. & LEWIS, D.J. (2003): Instrument response functions, mass bias and matrix effects in isotope ratio measurements and semi-quantitative analysis by single and multi-collector ICP–MS. *J. Anal. At. Spectrom.* **18**, 219-229.

JACKSON, S.E. & GÜNTHER, D. (2003): The nature and sources of laser induced isotopic fractionation in laser ablation multicollector inductively coupled plasma mass spectrometry. *J. Anal. At. Spectrom.* **18**, 205-212.

JACKSON, S.E., LONGERICH, H.P., DUNNING, G.R. & FRYER, B.J. (1992): The application of laser-ablation microprobe–inductively coupled plasma mass spectrometry LAM–ICP–MS to in-situ trace element determinations in minerals. *Can. Mineral.* **30**, 1049-1064.

JACKSON, S.E., PEARSON, N.J., GRIFFIN, W.L. & BELOUSOVA, E.A. (2004): The application of laser ablation–inductively coupled plasma–mass spectrometry to in situ U–Pb zircon geochronology. *Chem. Geol.* **211**, 47-69.

JAKUBOWSKI, N., MOENS, L., & VANHAECKE, F. (1998): Sector field mass spectrometers in ICP–MS. *Spectrochim. Acta B* **53**, 1739-1763.

JEFFRIES, T.E., FERNANDEZ-SUAREZ, J., CORFU, F. & ALFONSO, G.G. (2003): Advances in U–Pb geochronology using a frequency quintupled Nd:YAG based laser ablation system (λ= 213 nm) and quadrupole based ICP–MS. *J. Anal. At. Spectrom.* **18**, 847-855.

KAMENOV, G.D., MUELLER, P.A. & PERFIT, M.R. (2004): Optimization of mixed Pb–Tl solutions for high precision isotopic analyses by MC–ICP–MS. *J. Anal. At. Spectrom.* **19**, 1262-1267.

KOCH, J., VON BOHLEN, A., HERGENRÖDER, R. & NIEMAX, K. (2004): Particle size distributions and compositions of aerosols produced by near-IR femto- and nanosecond laser ablation of brass. *J. Anal. At. Spectrom.* **19**, 267-272.

KOCH, J., WALLE, M., PISONERO, J. & GÜNTHER, D. (2006): Performance characteristics of ultra-violet femtosecond laser ablation inductively coupled plasma mass spectrometry at ~265 and ~200 nm. *J. Anal. At. Spectrom.* **21**, 932–940.

KOŠLER, J. & SYLVESTER, P.J. (2003): Present trends and the future of zircon in geochronology: laser ablation ICPMS. *Rev. Mineral. Geochem.* **53**, 243-275.

KOŠLER, J., TUBRETT, M. & SYLVESTER, P. (2001): Application of laser ablation ICPMS to U–Th–Pb dating of monazite. *Geostand. Newslett.*, **25**, 375-386.

KOŠLER, J., FONNELAND, H., SYLVESTER, P., TUBRETT, M. & PEDERSEN, R. (2002): U–Pb dating of detrital zircons for sediment provenance studies – a comparison of laser ablation ICP–MS and SIMS techniques. *Chem. Geol.* **182**, 605-618.

KOŠLER, J., SIMONETTI, A., SYLVESTER, P., COX, R., TUBRETT, M. & WILTON, D. (2003): Laser ablation ICPMS measurements of Re/Os ratios in molybdenite and implications for Re–Os geochronology. *Can. Mineral.* **41**, 307-320.

KOŠLER, J., WIEDENBECK, M., WIRTH, R., HOVORKA, J., SYLVESTER, P. & MÍKOVÁ, J. (2005a): Chemical and phase composition of particles produced by laser ablation of silicate glass and zircon – implications for elemental fractionation during ICPMS analysis. *J. Anal. At. Spectrom.* **20**, 402-409.

KOŠLER, J., PEDERSEN, R., KRUBER, C. & SYLVESTER, P. (2005b): Analysis of Fe isotopes in sulfides and iron meteorites by laser ablation high-mass resolution multicollector ICP mass spectrometry. *J. Anal. At. Spectrom.* **20**, 192-199.

KOZLOV, B., SAINT, A. & SKROCE, A. (2003):

Elemental fractionation in the formation of particulates, as observed by simultaneous isotopes measurement using laser ablation ICP–oa–TOFMS. *J. Anal. At. Spectrom.* **18**, 1069–1075.

KROSLAKOVA, I. & GÜNTHER, D. (2007): Elemental fractionation in laser ablation–inductively coupled plasma–mass spectrometry: evidence for mass load induced matrix effects in the ICP during ablation of a silicate glass. *J. Anal. At. Spectrom.* **22**, 51-62.

KUHN, H.R. & GÜNTHER, D. (2003): Elemental fractionation studies in laser ablation inductively coupled plasma mass spectrometry on laser-induced brass aerosols. *Anal. Chem.* **75**, 747-753.

LI, X., LIANG, X., SUN, M., GUAN, H., MALPAS, J.G. (2001): Precise $^{206}Pb/^{238}U$ age determination on zircons by laser ablation microprobe–inductively coupled plasma–mass spectrometry using continuous linear ablation. *Chem. Geol.* **175**, 209-219.

MANK, A.J.G. & MASON, P.R.D. (1999): A critical assessment of laser ablation ICP–MS as an analytical tool for depth analysis in silica-based glass samples. *J. Anal. At. Spectrom.* **14**, 1143-1153.

MARÉCHAL, C., TÉLOUK, P. & ALBARÈDE, F. (1999): Precise analysis of copper and zinc isotopic compositions by plasmasource mass spectrometry. *Chem. Geol.* **156**, 251-273.

MASON, P.R.D., KOŠLER, J., HOOG, J.C.M., SYLVESTER, P.J. & MEFFAN-MAINE, S. (2006): In situ determination of sulfur isotopes in sulfur-rich materials by laser ablation multiple-collector inductively coupled plasma mass spectrometry (LA–MC–ICP–MS). *J. Anal. At. Spectrom.* **21**, 177-186.

OLESIK, J.W. (1997): Investigating the fate of individual sample droplets in inductively coupled plasmas. *Applied Spectroscopy* **51**, 158A-175A.

O'NEILL, H.ST.C. & EGGINS, S.M. (2002): The effect of melt composition on trace element partitioning: an experimental investigation of the activity coefficients of FeO, NiO, CoO, $MoO_2$ and $MoO_3$ in silicate melts. *Chem. Geol.* **186**, 151-181.

PARRISH, R.R., NOWELL, G., NOBLE, S.R., HORSTWOOD, M., TIMMERMAN, H., SHAW, P. & BOWEN, I.J. (1999): LA–PIMMS: A new method of U–Th–Pb geochronology using micro-sampling techniques. *J. Conf. Abstr.* **4**, 799.

PEARSON, N.J., GRIFFIN, W.L. & O'REILLY, S.Y. (2008): Mass fractionation correction in laser ablation multiple-collector ICP–MS: implications for overlap corrections and precise and accurate *in situ* isotope ratio measurement. *In* Laser Ablation ICP–MS in the Earth Sciences: Current Practices and Outstanding Issues (P. Sylvester, *ed.*). *Mineral. Assoc. Can. Short Course Series* **40**, 93-116.

PERDIAN, D.C., BAJIC, S.J., BALDWIN, D.P. & HOUK, R.S. (2008a): Time-resolved studies of particle effects in laser ablation inductively coupled plasma–mass spectrometry. Part 1. Investigation of nanosecond and femtosecond pulse width lasers and devices for particle size selection. *J. Anal. At. Spectrom.* **23**, 325-335.

PERDIAN, D.C., BAJIC, S.J., BALDWIN, D.P. & HOUK, R.S. (2008b): Time-resolved studies of particle effects in laser ablation inductively coupled plasma–mass spectrometry. Part 2. Investigation of $MO^+$ ions, effect of sample morphology, transport gas, and binding agents. *J. Anal. At. Spectrom.* **23**, 336-341.

POITRASSON, F., MAO, X., MAO, S., FREYDIER, R. & RUSSO, R. (2003): Comparison of ultraviolet femtosecond and nanosecond laser ablation inductively coupled plasma mass spectrometry analysis in glass, monazite, and zircon, *Anal. Chem.* **75**, 6184-6190.

REHKÄMPER, M. & MEZGER, K. (2000): Investigation of matrix effects for Pb isotope ratio measurements by multiple collector ICP–MS: verification and application of optimized analytical protocols. *J. Anal. At. Spectrom.* **15**, 1451-1460.

RUSSO, R., MAO, X., GONZALES, J. & MAO, S. (2002): Femtosecond laser ablation ICP–MS. *J. Anal. At. Spectrom.* **17**, 1072-1075.

SIMONETTI, A., HEAMAN, L.M., HARTLAUB, R.P. CREASER, R.A., MACHATTIE, T.G. & BÖHM, C. (2005): U–Pb zircon dating by laser ablation–MC–ICP–MS using a new multiple ion counting Faraday collector array. *J. Anal. At. Spectrom.* **20**, 677-686.

SINCLAIR, D.J., KINSLEY, L.P.J. & MCCULLOCH, M.T. (1998): High resolution analysis of trace elements in corals by laser ablation ICP–MS. *Geochim. Cosmochim. Acta* **62**, 1889-1901.

SLÁMA, J., KOŠLER, J., CONDON, D.J., CROWLEY,

J.L., GERDES, A., HANCHAR, J.M., HORSTWOOD, M., MORRIS, G.A., NASDALA, L., NORBERG, N., SCHALTEGGER, U., SCHOENE, B., TUBRETT, M.N. & WHITEHOUSE, M.J. (2008): Plešovice zircon – a new natural reference material for U–Pb and Hf isotopic microanalysis. *Chem. Geol.* **249**, 1-35.

SPANDLER, C., O'NEILL, H.ST.C. & KAMENETSKY, V.S. (2007): Survival times of anomalous melt inclusions from element diffusion in olivine and chromite. *Nature* **447**, 303-306.

SYLVESTER, P.J. & GHADERI, M. (1997): Trace element analysis of scheelite by excimer laser ablation–inductively coupled plasma–mass spectrometry (ELA–ICP–MS) using a synthetic silicate glass standard. *Chem. Geol.* **141**, 49-65.

TÉLOUK, P., ROSE-KOGA E.F., ALBARÈDE, F. (2003): Preliminary results from a new 157 nm laser ablation ICP–MS instrument: New opportunities in the analysis of solid samples. *Geostand. Newslett.*, **27**, 5-11.

TIEPOLO, M. (2003): In situ Pb geochronology of zircon with laser ablation–inductively coupled plasma–sector field mass spectrometry. *Chem. Geol.* **199**, 159-177.

VANCE, D. & THIRLWALL, M. (2002): An assessment of mass discrimination in MC–ICPMS using Nd isotopes. *Chem. Geol.* **185**, 227-240.

WANG, Z., HATTENDORF, B. & GÜNTHER, D. (2006): Vaporization and ionization of laser ablation generated aerosols in an inductively coupled plasma mass spectrometer – implications from ion distribution maps. *J. Anal. At. Spectrom.* **21**, 1143-1151.

WIEDENBECK, M., ALLÉ, P., CORFU, F., GRIFFIN, W.L., MEIER, M., OBERLI, F., VON QUADT, A., RODDICK, J.C. & SPIEGEL, W. (1995): Three natural zircon standards for U–Th–Pb, Lu–Hf, trace element and REE analyses. *Geostand. Newsl.* **19**, 1-23.

WOMBACHER, F. & REHKÄMPER, M. (2003): Investigation of the mass discrimination of multiple collector ICPMS using neodymium isotopes and the generalised power law. *J. Anal. At. Spectrom.* **18**, 1371-1375.

WOODHEAD, J., HERGT, J., SHELLEY, M., EGGINS, S. & KEMP, R. (2004): Zircon Hf–isotope analysis with an excimer laser, depth profiling, ablation of complex geometries, and concomitant age estimation *Chem. Geol.* **209**, 121-135.

WOODHEAD, J., HELLSTROM, J., PATON, C., HERGT, J., GREIG, A. & MAAS, R. (2008): A guide to depth profiling and imaging applications of LA–ICP–MS. *In* Laser Ablation ICP–MS in the Earth Sciences: Current Practices and Outstanding Issues (P. Sylvester, *ed.*). *Mineral. Assoc. Can. Short Course Series* **40**, 135-145.

# CHAPTER 7: MASS FRACTIONATION CORRECTION IN LASER ABLATION MULTIPLE-COLLECTOR ICP–MS: IMPLICATIONS FOR OVERLAP CORRECTIONS AND PRECISE AND ACCURATE *IN SITU* ISOTOPE RATIO MEASUREMENT

Norman J. Pearson, William L. Griffin and Suzanne Y. O'Reilly
GEMOC ARC National Key Centre, Department of Earth and Planetary Sciences,
Macquarie University, NSW 2109, Australia
E-mail: npearson@els.mq.edu.au

## INTRODUCTION

Over the past decade techniques for isotopic measurement using the multiple collector (MC–) inductively coupled plasma–mass spectrometer (ICP–MS) have been developed to a level where the typical within-run (internal) precision and between-run (external) precision are comparable to TIMS (*e.g.*, Nd – Luais *et al.* 1997; Hf – Blichert-Toft 2001; Pb – Woodhead 2002). The ICP source is highly efficient at ionizing elements with high ionization potentials, and the MC–ICP–MS has become the instrument of choice to investigate the mass-dependent isotopic fractionation of light and heavy metals (*e.g.*, Li – Tomascak 2004; Mg – Young & Galy 2004; Fe – Beard & Johnson 2004, Dauphas & Rouxel 2006; Cu, Zn – Maréchal *et al.* 1999, Albarède 2004; Mo – Anbar 2004; Tl – Nielsen *et al.* 2004). The development of these 'non-traditional' stable isotope systems has benefited from the possibility of correcting instrumental mass bias by introducing an 'external' element along with the sample (*e.g.*, Tl for Pb – Longerich *et al.* 1987, Belshaw *et al.* 1998; Zn or Ni for Cu – Maréchal *et al.* 1999, Archer & Vance 2004; Yb for Lu – Griffin *et al.* 2000). Another significant advantage of the MC–ICP–MS is the capability to attach a laser ablation microprobe and perform *in situ* isotopic measurements. This has led most notably to the combined U–Pb and Lu–Hf isotopic analysis of zircon (*e.g.*, Griffin *et al.* 2000 2004b, Woodhead *et al.* 2004, Kemp *et al.* 2006) as well as studies of a range of other isotopic systems, including both radiogenic ones (*e.g.*, Sr – Schmidberger *et al.* 2003, Woodhead *et al.* 2005, Nd – Foster & Vance 2006, McFarlane & McCulloch 2007, 2008; Os – Pearson *et al.* 2002, Alard *et al.* 2005) and non-traditional stable isotopes (*e.g.*, Cu, Fe – Graham *et al.* 2004; Fe – Horn *et al.* 2006; Mg – Young *et al.* 2002, Pearson *et al.* 2006).

There are many advantages to be gained by LAM–MC–ICP–MS analysis, the most important being the potential information that can be obtained at the high spatial resolution. Like other microanalytical techniques laser ablation MC–ICP–MS produces data that can be interpreted in a spatial context and integrated with microstructural and other geochemical datasets. Other advantages include the removal of the sample digestion and chemical purification procedures, high sample throughput, little or no memory and no solvent interferences. Despite the advances in recent years there remains a perception that the accuracy and precision of the *in situ* measurements suffer in comparison to solution measurements because of matrix effects and isobaric interferences. Other issues that also need to be addressed are the availability of suitable reference materials, especially for matrix matching in studies of mass-dependent isotopic fractionation, and laser-induced isotopic fractionation.

There are many factors that contribute to the accuracy and precision of *in situ* measurements. As illustrated in Figure 7-1, these can be considered as the interplay between parameters related to the sample, the laser operating conditions and processes in the mass spectrometer. To date most of the *in situ* studies fall into two general categories related to sample composition. The first includes those that have concentrated on radiogenic isotope systems in which the elements of interest are trace or minor elements in common rock-forming minerals (*e.g.*, Sr in clinopyroxene, carbonate, feldspar) or accessory phases (*e.g.*, Hf in zircon, rutile; Nd in apatite, titanite; Os in mantle sulfide). The second group includes the study of mass-dependent isotopic fractionation of elements that are major constituents in the minerals of interest (*e.g.*, Cu in chalcopyrite; Fe in pyrite, metallic Fe; Mg in forsteritic olivine). The precision of an individual measurement is primarily a function of the number of ions counted and therefore depends on the concentration of the element in the mineral, the size of the laser pit, the sensitivity of the mass spectrometer and the

Mineralogical Association of Canada Short Course 40, Vancouver, B.C., p. 93–116.

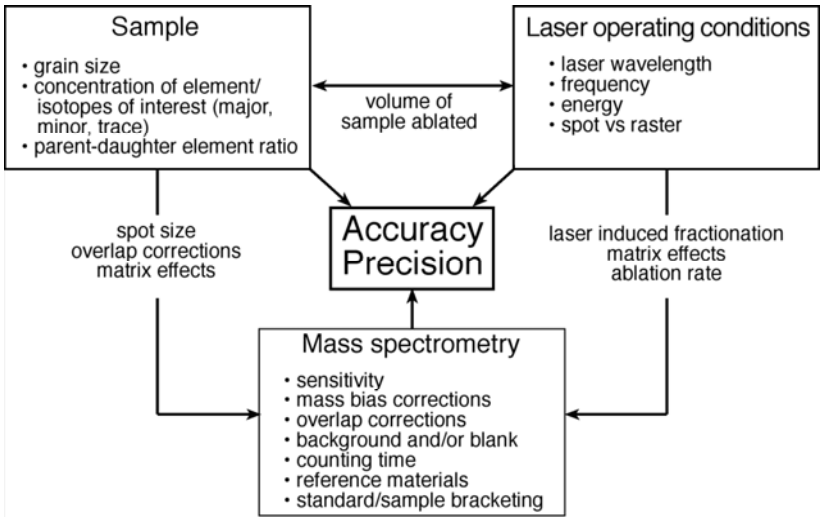


FIG. 7-1. A schematic diagram showing the parameters that affect the accuracy and precision of *in situ* isotope ratio measurements by laser ablation MC–ICP–MS.

counting time. The combination of the size of the mineral grain and the sensitivity of the mass spectrometer dictates the sampling strategy. The choice between static ablation and scanning ablation should take into consideration the required precision and the impact of laser-induced fractionation (Košler 2008). This raises the issue of whether the laser is used simply as a solid-sampling device in order to maximize the volume of material introduced in the mass spectrometer, thereby homogenizing the sample but improving precision. The alternative approach is to use the laser as a microprobe to add isotopic data to internal variations identified using optical images or other geochemical data. This technique invariably involves using a smaller spot size with the consequent effect on precision. In deciding which approach to use it is worth considering that the first may give a very precise but geologically meaningless result if the sample is heterogeneous. This is also true for the comparison of data obtained by solution analysis of mineral separates and by LAM–MC–ICP–MS. For example, Griffin *et al.* (2006a) demonstrated that reference zircon 91500 shows considerable heterogeneity in $^{176}Hf/^{177}Hf$, with a bimodal distribution about a mean value that is within the uncertainty of solution measurements. Although Corfu (2007) attributed the spread in $^{176}Hf/^{177}Hf$ to analytical artifacts, no relationships are observed between the corrected $^{176}Hf/^{177}Hf$ and other isotopic ratios (*e.g.*, $^{176}Lu/^{177}Hf$, $^{176}Yb/^{177}Hf$) to support this explanation (Griffin *et al.* 2007). Furthermore no correlations are observed between the stable isotope ratios ($^{180}Hf/^{177}Hf$ and $^{178}Hf/^{177}Hf$) and $^{176}Hf/^{177}Hf$ to indicate residual mass-dependent errors.

The parameters listed under the mass spectrometer heading in Fig. 7-1 are common to both solution and *in situ* analysis. Included in this group is the correction for mass-dependent instrumental bias, which is the most important factor affecting accuracy and external precision. Mass bias is an isotopic fractionation produced by the variable transmission of the ion beam in the mass spectrometer. In the MC–ICP–MS the mass fractionation processes take place mainly in the plasma and interface regions (see discussion below in section Factors Contributing to Mass Bias). The effect of instrumental mass bias on the accuracy and precision of isotopic measurements using MC–ICP–MS solution analysis was thoroughly investigated by Albarède *et al.* (2004). In comparison with conventional solution analysis, the added complexity associated with the *in situ* method primarily concerns the 'dirty' nature of the sample. This may cause matrix effects that can change instrumental mass fractionation and produce isotopic interferences (isobaric and other molecular overlaps) that also require procedures to correct mass bias. Isobaric interferences present a major problem in nearly all of the radiogenic isotopic systems of most interest to geochemists: $^{87}Rb$ on $^{87}Sr$, $^{144}Sm$ on $^{144}Nd$, $^{176}Lu$ and $^{176}Yb$ on $^{176}Hf$, $^{187}Re$ on $^{187}Os$. Matrix-related molecular interferences must also be considered, for example in Ca-rich minerals such as calcite, apatite and clinopyroxene there is the potential interference from Ca dimers, as well as the production of doubly charged REE

ions that must be corrected for accurate Sr isotope measurement. Sample matrix is also a significant factor in restricting the *in situ* study of the non-traditional isotope systems to relatively simple mineral compositions.

The main purpose of this paper is to extend the study by Albarède and co-workers and to examine the role of mass bias on the accuracy and precision of isotopic analysis by laser ablation MC–ICP–MS. The first part presents a brief review of the theoretical basis for isotopic normalization using a ratio of the same element (internal normalization) and investigates the factors that affect the magnitude of the mass fractionation. These results are then used as the framework to explore further the techniques of isotopic normalization using a different element (external normalization) and standard sample bracketing. The final part of the paper examines the potential issues related to laser-induced isotopic fractionation and plasma loading, which have been shown to be directly related to the laser operating conditions and the transient nature of the signal (*e.g.*, Jackson & Günther 2003, Kühn *et al.* 2007).

**Instrumental Mass Bias – The Basics**

Although it is generally considered that mass bias in the MC–ICP–MS is greater than in TIMS (*e.g.*, Rehkämper *et al.* 2001), the same mass-fractionation laws are applied to correct for instrumental mass bias. A general phenomenological theory for the mass fractionation produced by the MC–ICP–MS was first presented by Maréchal *et al.* (1999) and has been reviewed in several studies (*e.g.*, Wombacher & Rehkämper 2003, Ingle *et al.* 2003, Albarède *et al.* (2004). The concepts presented by the Lyon group were based on the previous studies by Hofmann (1971), Russell *et al.* (1978), Hart & Zindler 1989), Habfast, (1999) & Platzner (1997). Maréchal *et al.* (1999) showed that the exponential and power 'laws' for correction of mass fractionation (Russell *et al.* 1978) are special cases of a more general mass fractionation law they termed the 'generalized power law'. The expression for the generalized power law is:

$$R_{true} = R_{meas} \bullet f^{(M_2^n - M_1^n)} \qquad (1)$$

where $R_{true}$ is the true isotopic ratio ($M_2/M_1$) of two isotopes of mass $M_1$ and $M_2$, $R_{meas}$ is the value measured by the mass spectrometer, $f$ is the mass fractionation coefficient and $n$ is the exponential variable.

The generalized power law is equivalent to the power 'law' for n = 1:

$$R_{true} = R_{meas} \bullet f^{(M_2 - M_1)} \qquad (2)$$

and approaches the exponential 'law' for $n \rightarrow 0$:

$$R_{true} = R_{meas} \bullet (M_2 / M_1)^f \qquad (3)$$

Both the exponential and power laws have been applied widely in MC–ICP–MS studies. Many studies have favored the 'exponential law', originally presented by Russell *et al.* (1978) and this has an advantage over other non-linear forms of correction because the mass difference is expressed as absolute isotope masses. Support for the exponential law is given by Blicher-Toft *et al.* (1997), Luais *et al.* (1997), Belshaw *et al.* (1998), Hirata *et al.* (1998), Maréchal *et al.* (1999), Griffin *et al.* (2000), White *et al.* (2000) and Pearson *et al.* (2002) for a range of isotope systems (Cu, Nd, Hf, Os, Pb). These studies demonstrated that internal normalization using the exponential law produced results that agree with TIMS reference values to within about 50–100 ppm. The power law was preferred by Hirata (1996, 1997) and Rehkämper & Halliday (1998), as it provided a better fit than the exponential law to their Pb isotope data. Of these studies, Rehkämper & Halliday (1998), Maréchal *et al.* (1999) and Pearson *et al.* (2002) provided the most thorough comparison of the application of the different fractionation laws to MC–ICP–MS. Subsequent studies by Vance & Thirlwall (2002) and Wombacher & Rehkämper (2003) have shown that the common mass fractionation laws do not accurately correct the instrumental mass bias produced in plasma source mass spectrometers. The implications of these studies are considered further in the following discussion of the three main procedures used to correct mass bias in MC–ICP–MS.

***Internal Normalization.*** The best procedure to correct for mass bias is 'internal' normalization. This approach requires that the mass fractionation coefficient can be determined using a pair of stable isotopes with a known or 'true' isotopic ratio. A widely utilized property of the generalized power law is that a linear array is produced when one measured isotope ratio is plotted against another on a log-log plot. The expression for the exponential 'law' defines a linear relationship between ln ($R_{true}$ / $R_{meas}$) and ln ($M_2/M_1$) and the slope of the line gives the mass fractionation coefficient, $f$(Fig. 7-2). In the

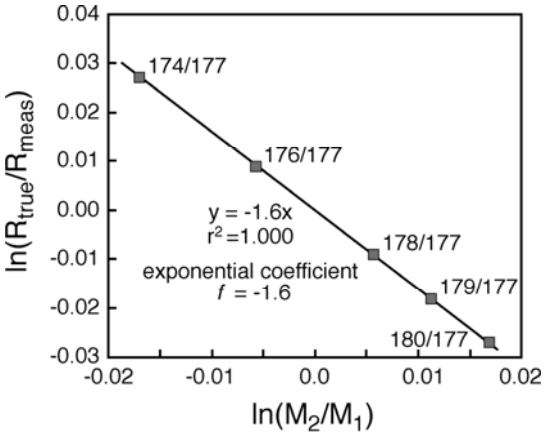


FIG. 7-2. $Ln(R_{true}/R_{meas})$ *vs*. $ln(M_2/M_1)$ plot for an analysis of JMC475 Hf. The linear array indicates the validity of the exponential mass fractionation law and the slope (–1.6) gives the value for the exponential coefficient *f*.

case of the power law, there is a linear relationship between ln ($R_{true}$ / $R_{meas}$) and ΔM, with the slope equal to ln *g*. The linear array in the log-log plot of two isotope pairs has a slope approximately equal to the ratio of the mass differences of the two pairs of isotopes (Fig. 7-3). While a precise line can be generated by running the same sample over a short time, the linear array produced over a longer time provides a more robust indication of instrumental mass fractionation behavior. The spread of values along the line indicates the relative variation in mass bias and the limiting values define the range of absolute *f* values (*ca*. –1.4 to –2.25). The slope of the line in Fig. 7-3 is 1.994 ± 0.004; this is within error of the theoretical slope for the exponential law (1.995) but is lower than the slope predicted by the

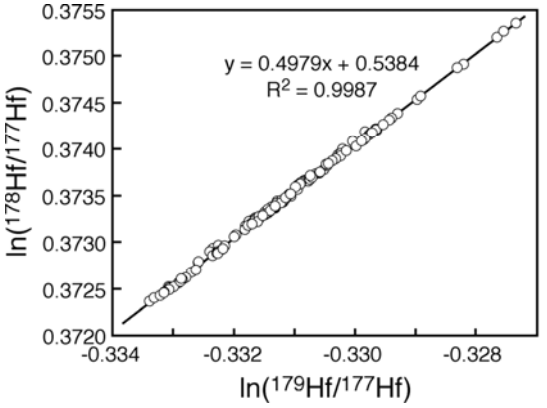


FIG. 7-3. Plot of $ln(^{178}Hf/^{177}Hf)$ *vs*. $ln(^{179}Hf/^{177}Hf)$ for the JMC475 Hf solution. The data points are from 132 analyses over a period of 5 years and show the long-term robustness of the instrumental mass fractionation on the Nu Plasma.

power law (2.001).

Although the exponential (kinetic) law has been adopted widely there are indications that it does not accurately correct mass fractionation with mass-dependent residual errors, especially where there is a relatively large mass difference between isotopes (*e.g.*, Albarède *et al.* 2004, White *et al.* 2000, Maréchal *et al.* 1999, Woodhead 2002, Pearson *et al.* 2002, Archer & Vance 2004). Vance & Thirlwall (2002) and Wombacher & Rehkämper (2003) obtained significant deviations in $^{150}Nd/^{144}Nd$ (>500 ppm and >200 ppm respectively) from TIMS reference values, using $^{146}Nd/^{144}Nd$ and an exponential law to correct mass fractionation. Applying the generalized power law to the same Nd analyses, Wombacher & Rehkämper (2003) showed that the instrumental mass fractionation on two Nu Plasma instruments was accurately described with the value of the exponent variable $n = –0.23$. This approach may improve the absolute accuracy of isotope measurements by MC–ICP–MS but it requires the careful calibration of *n*. Variations in *n* from –0.2 to –0.4 were observed during routine operation and these were attributed to variations in operating conditions (*e.g.*, torch position, gas flows, acceleration voltages). The range of values is also lower than the value of *n* of approximately –0.5 obtained for Nd isotopes on the Micromass Isoprobe by Vance & Thirlwall (2002) and suggests differences between different instrument types. Application of the generalized power law to the Hf isotope data presented in Fig. 7-2 produces a best fit with $n = –0.24 \pm 0.02$. Correction of the data using the exponential law gives values for $^{176}Hf/^{177}Hf$ within 15 ppm of the reference value of 0.282160 (Nowell *et al.* 1998), and better than 50 ppm for $^{178}Hf/^{177}Hf$ and 25 ppm for $^{180}Hf/^{177}Hf$ (reference values from Stevenson & Patchett 1990). Applying a generalized power law correction with $n = –0.24$ reduces these errors to less than 10 ppm, 40 ppm and 5 ppm respectively. It is important to note that the value of *n* is within error of that obtained for Nd by Wombacher & Rehkämper (2003) and supports a consistent instrumental mass bias behavior in the mass range from Nd to Hf for different Nu Plasma instruments.

***External Correction.*** The linear relationship on log-log plots also holds when isotope ratios of different elements are plotted, and this has formed the basis for the 'external' or 'doped' correction procedure. External mass bias correction has proved successful for a number of applications on the MC–ICP–MS

and several studies have investigated the mass bias behavior of different element pairs (*e.g.*, Cu–Zn, Maréchal *et al.* 1999; Re–Ir, Os–Ir, Pearson *et al.* 2002; Pb–Tl, Belshaw *et al.* 1998, Rehkämper & Halliday 1998, White *et al.* 2000, Woodhead 2002). The fundamental assumption in this method is that the fractionation coefficients of the two elements are proportional. The slope of the line on the log-log plot then defines the relationship between the *f* factors and the intercept value is a function of the 'true' isotopic values of the two isotope pairs. This method was applied by Belshaw *et al*. (1998) to establish the 'true' isotopic composition of Tl using the known 'true' composition of SRM981 Pb. This Tl isotopic composition was then used with success in a number of studies to monitor mass discrimination of Pb of unknown isotopic composition. A log-log plot of Pb *versus* Tl obtained from a mixed Tl–Pb (SRM981) solution on the Nu Plasma at GEMOC shows that over an extended period of time there is a consistent relationship between the two elements (Fig. 7-4). Although the slope of the line is not exactly the same as the value predicted from the exponential mass relationship, the values obtained for the various Pb isotopic ratios are within error of the values of Todt *et al.* (1996). Nevertheless the corrected data retain a residual mass-dependent uncertainty and various methods have been employed to eliminate this error (*e.g.*, Maréchal *et al.* 1999, White *et al.* 2000, Woodhead 2002). White *et al.* (2000) showed that the mass discrimination behavior of Pb and Tl on a VG

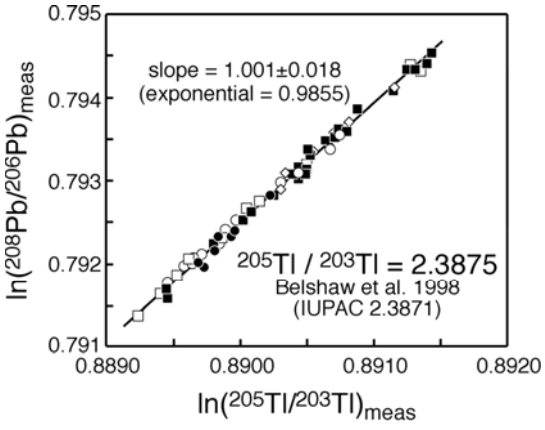


FIG. 7-4. Plot of $\ln(^{208}Pb/^{206}Pb)$ *vs*. $\ln(^{205}Tl/^{203}Tl)$ of a mixed Pb (SRM981) and Tl (SRM997) solution. The data points are from 55 analyses over a 3-year period. The slope of the line (1.001±0.018) is slightly higher than the theoretical value derived from the mass relationship of the exponential (0.9855).

Plasma54 was not adequately modeled using the exponential law and that the relationship varied from session to session. Accordingly they advocated the determination of empirical relationships between isotopic ratios for each analytical session. Rehkämper & Mezger (2000) used an empirically optimized Tl normalization and found it necessary to adjust the Tl isotopic ratio each day on a Micromass Isoprobe. Although the variations in $^{205}Tl/^{203}Tl$ are within the uncertainty of the certified reference value for NIST SRM 997 Tl, the procedure of daily calibration has been criticized. Thirlwell (2001) considered that inadequate tail corrections could explain the analytical artifacts observed by Rehkämper & Mezger (2000). In a follow-up study Thirlwell (2002) described the effect of matrix composition (pure standard matrix *versus* silicate sample matrix) on the measured Tl isotopic composition and the propagation of these variations on the accuracy of the corrected Pb isotope ratios. These studies prompted Woodhead (2002) to take the approach of running standards with different amounts of matrix to generate a wide spread in mass bias, thereby improving the precision on the empirical mass bias behavior of Pb and Tl. This approach was subsequently used by Archer & Vance (2004) in their study of Cu isotopes, in which Zn was used as an external dopant. All of these studies emphasized the importance of instrument stability in precisely defining either the exponential or the empirical slopes. The results from the various Pb–Tl studies also raise the question as to whether a 'true' value obtained on one instrument using the relationship between two elements can be applied to another instrument. As stated above the practice of adjusting the 'true' value of the normalizing standard has been challenged. While a tail correction might be appropriate for the Micromass Isoprobe, peak tailing is less likely to be an issue on the Nu Plasma and the ThermoFinnigan Neptune as the abundance sensitivities is an order of magnitude lower. This led Baxter *et al.* (2006) to revise the exponential model for mass bias correction using a 'doped' internal standard and the revised expression eliminated any dependency on the 'true' isotopic ratio of the internal standard.

Ingle *et al.* (2003) took a different approach to modeling and correcting instrumentally derived mass fractionation by treating the bias in measured isotope ratios as a function of instrument response across the mass range Li to U. This response function has been reported to be a monotonically

increasing function of isotope mass, with both quadratic expressions and the exponential function of Russell *et al.* (1978) producing equally good fits to the experimental data. Rather than determine a value for *f* using two masses in the mass range of interest, Ingle *et al.* (2003) derived a polynomial expression from the instrument response function for a Thermo Elemental VG Axiom MC–ICP–MS to correct isotope ratio data. They showed that a polynomial expression gave a better fit to the experimental data compared to the power and exponential models, and in doing so demonstrated that it produced more accurate isotope ratios. Recently Doherty *et al.* (2008) investigated the application of the general polynomial technique and determined a linear isotope mass bias function on a Nu Plasma MC–ICP–MS for 'internal standardization' using a dopant element to correct isotope ratio measurements (*e.g.*, Tl–Pb, Sm–Eu and Ni–Cu). They concluded that if either the exponential law of Russell *et al.* (1978) or the polynomial function derived by Ingle *et al.* (2003) are applied to the correction of isotope ratio measurements on an instrument where the mass bias is linear, then the corrected data will retain a significant residual mass-dependent error.

To investigate the consistency of mass bias behavior as a consequence of instrument design further, data were compiled from three Nu Plasma instruments: Nu005 and Nu034 at GEMOC, Macquarie University, and an unnumbered instrument at Nu Instruments, Wrexham. The measurements were carried out on Nu005 using a wide angle skimmer cone and an Edwards EM28 roughing pump and a wide angle skimmer cone and an Edwards EM2 80 roughing pump ("Big 80"). This configuration was also used on Nu034 and the factory instrument. The data were produced from a mixed Yb–Hf solution and involved the independent measurement of Yb and Hf mass bias coefficients. In accordance with the exponential mass bias correction, linear arrays were produced on log-log plots of isotope ratios for Hf and Yb (Fig. 7-5), but significantly the data from the three instruments define a single line. The slopes of the lines in the Hf–Yb plots are lower than those predicted from the mass relationship of the exponential law. The experimentally derived slope for $\ln(^{179}Hf/^{177}Hf)$ *vs*. $\ln(^{173}Yb/^{172}Yb)$ is 0.4833 (theoretical exponential value = 0.5159) and for $\ln(^{179}Hf/^{177}Hf)$ *vs*. $\ln(^{172}Yb/^{171}Yb)$ the slope is 0.4821 (theoretical exponential value = 0.5189).

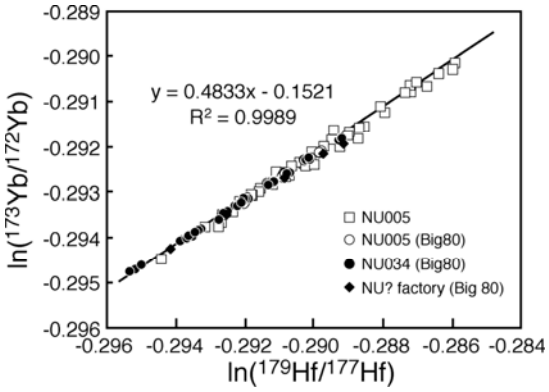


FIG. 7-5. Plot of $\ln(^{173}Yb/^{172}Yb)$ *vs*. $\ln(^{179}Hf/^{177}Hf)$ of a mixed Hf (JMC475) and Yb solution showing the similarity of mass bias behavior between three Nu Plasma MC–ICP–MS (Nu005 with and without the Big80 pump, Nu034 and Nu factory.

Figure 7-6 presents a plot of $f\,Hf(^{179}Hf/^{177}Hf)$ *vs*. $f\,Yb(^{173}Yb/^{172}Yb)$ for all instruments and instrument configurations. *f* Hf was calculated using the invariant value ($R_{True}$) of 0.7325 for $^{179}Hf/^{177}Hf$ and *f* Yb was calculated using the IUPAC recommended value of 0.7392 for $^{173}Yb/^{172}Yb$. The data define a strong linear relationship (slope = 0.920 ± 0.005 (σ)) that indicates that the mass bias relationship between Hf and Yb is consistent from one instrument to another over time and for a range of operating conditions. The data from Nu005 also show that there is no apparent change in the relative mass bias behavior of these two elements related to interface configuration, including skimmer design. However, the absolute values for the mass bias

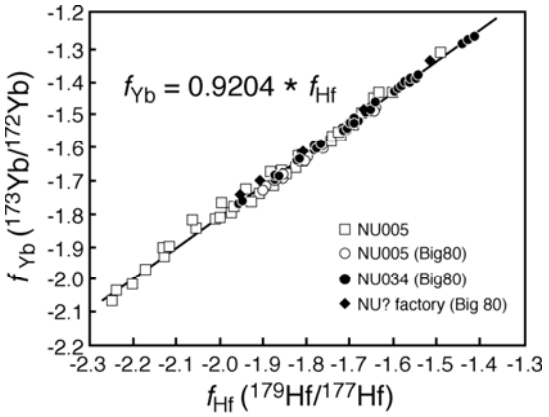


FIG. 7-6. Plot of exponential mass bias coefficient *f* for Yb ($^{173}Yb/^{172}Yb$) vs Hf ($^{179}Hf/^{177}Hf$). Data as in Fig 7-5. The linear array gives a constant relationship between *f* Hf and *f* Yb, but because the slope is not equal to one it indicates that the mass fractionations of Yb and Hf are not the same.

coefficient are higher (more negative) for the original narrow angle skimmer design. Values for *f* Hf using the wide angle skimmer range from –1.4 to –1.9, while values up to –2.2 were produced using the narrow angle skimmer. While this clearly demonstrates that the mass bias coefficients for Hf and Yb are not equal, it does establish a long term correlation for variations in mass bias and one that is consistent from instrument to instrument from the same manufacturer. The results obtained on the Nu Plasma are also similar to those reported by Wu *et al.* (2006), who determined a line of best fit with a slope of 0.912 relating *f*Yb and *f*Hf on a Neptune. Furthermore the studies suggest that the processes responsible for instrumental mass discrimination on the two types of instrument, and perhaps in plasma source mass spectrometry in general, produce mass discrimination of similar magnitude and mass dependence.

***Standard Sample Bracketing.*** The final method for mass bias correction is to measure samples of known isotopic composition interspersed with unknown samples to monitor any change in instrumental mass bias over time. This standard sample bracketing technique to correct for mass bias has been adopted from gas source mass spectrometry and is widely used where there are no internal isotope pairs or the addition of an external dopant is not a viable option (*e.g.*, Li, Mg). The method involves the interpolation of mass bias of an unknown sample from the inferred mass bias values obtained from a pair of standard runs, one preceding and one following the sample. The assumption in this technique is that the mass bias changes uniformly with time, but it is also critical that the matrices of the sample and the standards are identical. Several studies have demonstrated the effects of sample matrix on mass fractionation (*e.g.*, Galy *et al.* 2001, Zhu *et al.* 2002, Woodhead 2002) and this may necessitate matrix matching of samples and standards for laser ablation analysis, especially for studies of mass-dependent isotopic fractionation.

**Mass Bias Corrections for Laser Ablation Isotopic Analysis**

The two main issues encountered in the accurate measurement of *in situ* radiogenic isotope ratios such as $^{87}Sr/^{86}Sr$, $^{143}Nd/^{144}Nd$, $^{176}Hf/^{177}Hf$ and $^{187}Os/^{188}Os$ are the corrections for mass bias and the isobaric interferences of the parent/daughter isotopes. The mass bias corrections of Sr, Nd, Hf and Os are relatively straightforward as each element has a pair of interference-free stable isotopes that can be used for normalization. The same is not true for the parent isotopes, with Rb, Lu and Re each having only two isotopes, one of which is the interferent on the daughter isotope. Using the Lu–Hf isotope system as an example, the following discussion looks at the various approaches that can be adopted to overcome the problem of mass bias correction for the isobaric interferences.

An exponential mass bias correction is widely used for Hf isotope analysis (*e.g.*, Griffin *et al.* 2000, Blichert-Toft *et al.* 1997, Woodhead *et al.* 2004) using $^{179}Hf/^{177}Hf = 0.7325$. There are several approaches to deal with the REE overlaps but three methods are outlined below. However, while Yb has multiple isotopes free from isobaric overlap ($^{171}Yb$, $^{172}Yb$, $^{173}Yb$), Lu only has two isotopes and one of these overlaps with $^{176}Hf$. Hence for *in situ* analysis assumptions will always need to be made for the mass bias of Lu.

***Method 1***. In this method it is assumed that $f\,Hf = f\,Yb = f\,Lu$ and the mass bias obtained for Hf is also applied to the REE mass bias correction. With this approach, usually only one Yb isotope is measured (either $^{173}Yb$ or $^{172}Yb$). Griffin *et al.* (2000) tested this correction method by analyzing solutions of JMC475 spiked with Yb and JMC475 spiked with Lu.

A CETAC MCN6000 desolvation nebulizer was used to introduce the solutions into the MC–ICP–MS and 'dry plasma' conditions were created by removal of the solvent. The 'true' values for $^{172}Yb/^{176}Yb$ and $^{175}Lu/^{176}Lu$ were adjusted to give the 'true' $^{176}Hf/^{177}Hf$ of JMC475. The Yb and Lu isotopic compositions derived from the solution analyses were then used to correct the laser analyses. The other main assumptions in this approach are that the instrumental mass bias for 'dry plasma' solution analysis and laser analysis are the same and that the day to day variation in mass bias does not shift appreciably from the conditions under which the spiked solution experiments were performed. The accuracy and precision of the method are shown by the analysis of reference zircon (91500, 61308) but are also qualified by noting that the accuracy of the correction procedure was demonstrated for $^{176}Yb/^{177}Hf \leq 0.25$ and $^{176}Lu/^{177}Hf \leq 0.10$. This still encompasses the vast majority of typical zircon ($^{176}Yb/^{177}Hf \leq 0.1$ and $^{176}Lu/^{177}Hf \leq 0.002$; Belousova *et al.* 2002, Griffin *et al.* 2004b, Griffin *et al.* 2006b).

***Method 2.*** A number of studies have adopted an approach in which the mass bias of Hf and Yb are measured independently (*e.g.*, Woodhead *et al.* 2004, Iizuka & Hirata 2005, Wu *et al.* 2006, Kemp *et al.* 2006). The Woodhead *et al.* (2004) and the Iizuka & Hirata (2005) studies were performed on Nu Plasma MC–ICP–MS and because of the configuration of the collector block the $^{173}Yb/^{171}Yb$ ratio was measured. Woodhead *et al.* (2004) tested different values of the true isotopic composition of Yb and recommended the values reported by Chu *et al.* (2002). Kemp *et al.* (2006) preferred the value of $^{176}Yb/^{172}Yb = 0.5862$ determined by Segal *et al.* (2003), and it is worth noting that this is the closest value to the 'true' ratio reported by Griffin *et al.* (2000; $^{176}Yb/^{172}Yb = 0.5865$). The natural isotopic abundances of $^{171}Yb$ and $^{173}Yb$ are 14.28% and 16.13% respectively, and for the majority of natural zircon analyses the beam intensities produced by laser ablation for these two Yb isotopes would typically be ≤20 mV. With such low beam sizes, the uncertainty on the measured *f* Yb makes a significant contribution to the uncertainty on the corrected $^{176}Hf/^{177}Hf$. Whereas Woodhead *et al.* (2004) and Kemp *et al.* (2006) determined *f* Yb for each time interval, Iizuka & Hirata (2005) used the mean $^{173}Yb/^{171}Yb$ ratio of the entire analysis to obtain a more precise value for *f* Yb. This procedure was adopted by Wu *et al.* (2006) and they showed a two-fold improvement in the $^{176}Hf/^{177}Hf$ precision of individual analyses using a mean *f* Yb value. Although this approach might be valid for homogeneous zircon, Wu *et al.* (2006) conceded that it could lead to inaccuracies in complexly zoned zircon. This would certainly be an issue if *f* Yb was related to the Yb concentration but there have been no reports of such a correlation. As mentioned above, the mass bias of Lu cannot be determined directly in laser ablation analysis and Woodhead *et al.* (2004) made the assumption that *f* Yb = *f* Lu. Although the magnitude of the Lu interference is much smaller than that of Yb they preferred to use *f*Yb rather than *f* Hf because of the close geochemical affinities of Yb and Lu.

***Method 3.*** The third method is to determine the mass bias relationship between Hf and Yb, and as in Method 2 assume that *f* Yb = *f* Lu. External mass bias correction has proved successful for a number of applications on the MC–ICP–MS and several studies have investigated the mass bias behavior of different element pairs (*e.g.*, Cu–Zn, Maréchal *et al.* 1999; Re–Ir, Os–Ir, Pearson *et al.* 2002, Woodhead 2002). Whereas Chu *et al.* (2002) proposed this method for Hf and REE, Woodhead *et al.* (2004) considered that their long term correlation between Hf and Yb mass bias could not be expressed in a robust mathematical formulation. In contrast the results presented in the preceding section indicate a robust mass bias relationship between Yb and Hf both between different instruments and over time. This finding is further supported by the results of laser ablation analysis of zircon standard 61308 which also show there is no fundamental difference in mass bias behavior of Hf and HREE (Fig. 7-7). This zircon was selected because its high REE contents, compared with other reference zircon samples, allow more precise measurement of *f*Yb. The 61308 data lie on an extension of the solution trend and the higher (less negative) *f* values are attributed to the effects of the zircon matrix and the addition of He to the sample gas (see discussion below). The main conclusion to be drawn from this plot is that there is in fact a consistent relationship between the mass bias values for Hf and REE using 'dry' plasma sample introduction techniques.

The three methods described above provide an overview of the different ways the problem of the REE overlap correction on Hf has been addressed. While advocates of Method 2 claim that this method is more accurate, the published results for zircon reference materials show no systematic differences that can be attributed to the correction procedures. For example, at GEMOC the long term average for $^{176}Hf/^{177}Hf$ for the Mud Tank zircon by laser ablation and corrected using Method 1 is 0.282523 ± 43 (n = 2190; uncertainty is 2σ; Griffin *et al.*

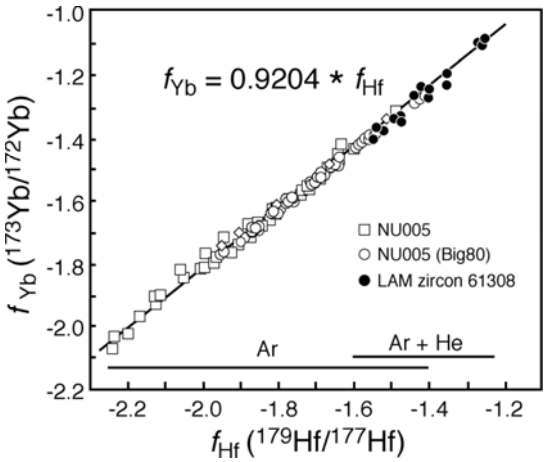


FIG. 7-7. Plot of exponential mass bias coefficient *f* for Yb ($^{173}Yb/^{172}Yb$) *vs.* Hf ($^{179}Hf/^{177}Hf$) showing results for solution analysis (data as in Fig. 7-6) and laser ablation analysis of reference zircon standard 61308.

2006a), and the solution value is 0.282521 ±4 (n = 3). This compares favorably with the values obtained using Method 2 and published in Woodhead & Hergt (2005) of 0.282504 ±44 (n = 158) by laser ablation and 0.282507 ±6 (n = 5) by solution. The Mud Tank zircon is characterized by low REE/Hf ratios with values for $^{176}Yb/^{177}Hf$ = 0.0045 ±0.0023 and $^{176}Lu/^{177}Hf$ = 0.00011 ±5. Zircon standard 61.308 has higher REE/Hf ratios ($^{176}Lu/^{177}Hf$ = 0.00186 in 61.308A and $^{176}Lu/^{177}Hf$ = 0.00228 in 61.308B; Wiedenbeck *et al.* 1995) and provides a more rigorous test of the overlap correction procedures. The long term average for $^{176}Hf/^{177}Hf$ for 61.308 using correction Method 1 is 0.283004 ±57 (n = 97; uncertainty is 2σ), which is within error of published solution analyses. Wiedenbeck *et al.* (1995) reported a mean $^{176}Hf/^{177}Hf$ value of 0.282977 ±14 for 61.308A and 0.282977 ±6 for 61.308B and when these values are corrected to a JMC475 value of 0.282160, they produce a mean $^{176}Hf/^{177}Hf$ of 0.283995. A number of measurements have also been performed over several analytical sessions using a collector configuration that allowed correction of the REE overlap using Method 1 and Method 2. The results show no systematic bias between the two correction methods: $^{176}Hf/^{177}Hf$ = 0.282990 ±32 (n = 10, 2σ) for Method 1 and $^{176}Hf/^{177}Hf$ = 0.282301 ±50 for Method 2. The larger uncertainty for Method 2 reflects the greater uncertainty introduced by the direct measurement of the Yb mass bias.

To summarize, the choice of method for the deconvolution of an overlap requires careful assessment of the mass bias both in terms of within-run variations and analytical precision, and the longer term instrument stability to establish the working range of *f* values for the correction. In order to do this it is important to consider the factors that control instrumental mass bias.

**Factors Contributing to Instrumental Mass Bias**

While most studies on mass bias in MC–ICP–MS have concerned the development of models to explain the observed mass-dependent fractionation, the sources of the fractionation and the magnitude and stability of the phenomenon remain poorly understood. However, it is also important that the observed mass discrimination can be explained by the processes that produce the fractionation (Wombacher & Rehkämper 2003, Andrén *et al.* 2004). Fundamental studies that have investigated the influence of ICP–MS operating parameters on optimized signal intensities have provided the basis for our understanding of the transport of the sample into the ICP, ion production in the ICP, ion extraction from the ICP and ion transport through the mass spectrometer (*e.g.*, Vanhaecke *et al.* 1993, Heumann *et al.* 1998, Houk & Praphairaksit 2001, Lehn *et al.* 2002, Holliday & Beauchemin 2004, and references therein). From these it is generally considered that mass bias in plasma source mass spectrometry is generated within the plasma, as well as in the interface region between the sampler and skimmer cones, and immediately behind the skimmer cone. Based on ion physics Freedman (2002) showed that instrumental mass bias in MC–ICP–MS is the sum of sub-equal contributions produced in the plasma and in the extraction process (behind the cones).

The physical properties of the plasma control the vaporization, atomization and ionization of the sample (Houk & Prashairaksit 2001), with parameters such as gas kinetic temperature and electron density parameters having a significant effect on diffusion rates in the ICP and kinetic energy of the ion transmitted through the interface. It is commonly accepted that only ions from the central channel of the plasma can be effectively sampled into the mass spectrometer (Douglas & French 1988, Vanhaecke *et al.* 1993). Processes resulting in the preferential vaporization of light isotopes from dry aerosol particles or mass-dependent diffusion contribute to mass bias and element fractionation (Vanheacke *et al.* 1993, Hobbs & Olesik 1997, Houk *et al.* 1997, Aeschliman *et al.* 2003). Albarède *et al.* (2004) also suggested that the very high temperature of the plasma is the prime source of the mass fractionation, producing a spread in ion energies and as a consequence more complex trajectories in the mass spectrometer. All of these studies emphasize the role of temperature in the central channel of the ICP and directly in front of the sample cone orifice as being critical to the degree of ionization. Instrument operating parameters that control the plasma temperature include RF power, gas flow rates and sampling depth (Lehn *et al.* 2002).

Another process that is considered to be one of the main causes of mass fractionation comes under the general heading of space–charge effects (*e.g.*, Tanner 1991, Heumann *et al.* 1998). These effects occur within the vacuum interface region (between the sampler and skimmer cones), behind the skimmer cone and into the ion optics. After ionization the mutual repulsion of the charged

particles results in the preferential transmission of the heavy ions: the lighter ions are more easily deflected leaving the heavy ions in the central ion beam. Niu & Houk (1996) identified hydrodynamic entrainment by the expanding plasma behind the cones as a cause of mass fractionation. The transmission of ions through the interface region and ion optics depends on the ion kinetic energies, the spread in ion energies of a given m/z and the range of m/z. In addition to the factors listed above that control plasma temperature and hence ion energies, other parameters that will influence space–charge effects include the interface vacuum and the acceleration potential of the ion extraction. The space–charge phenomenon can also be considered as a consequence of the total ion beam intensity (plasma loading) and is very much dependent on the composition and concentration of the sample matrix. Because of the complex matrices of natural minerals, the composition and the amount of material ablated are significant factors that could affect isotopic fractionation in the ICP–MS, and are likely to be especially significant in studies of mass-dependent isotopic fractionation. Therefore it is important to understand the effects of different ICP–MS operating conditions on mass bias and to be able to separate these from the effects that can be attributed directly to the introduction of solid particles by laser ablation.

Several recent studies have emphasized the influence of ICP–MS operating conditions on elemental analyte response and mass spectra produced by laser ablation ICP–MS (Rodushkin, *et al.* 2002, Wang *et al.* 2006). However, to date there has only been the one detailed study specifically undertaken by Andrén *et al.* (2004) on a Finnigan Neptune MC–ICP–MS to understand the effects of instrument operating parameters on the physical processes responsible for instrumental mass bias. In order to understand better the factors that influence the mass bias behavior and response of the mass spectrometer, the remainder of this section will explore the effects of different instrument operating and tuning parameters on mass bias on the Nu Plasma. The results presented here are from experiments performed using 'dry plasma' solution analysis with a desolvation nebulizer and they will provide a framework to investigate then in the following section the effects of factors directly related to the *in situ* measurement.

Tuning or operating conditions that are most likely to contribute to the mass bias behavior include: nebulizer gas flow, extraction lens voltage, RF power, torch depth position, cone design and condition, and nebulizer gas composition. A series of experiments was undertaken on the Nu Plasma MC–ICP–MS in an attempt to isolate the effects of each of these parameters on instrumental mass bias. It is acknowledged at the outset that changing an individual parameter while keeping all other parameters constant essentially detunes the instrument and may not truly reflect the variations that might be observed during routine operation. Nevertheless the results of the experiments provide a valuable set of empirical relationships to help understand the processes that control mass fractionation in the mass spectrometer.

***Nebulizer gas experiments.*** Nebulizer gas flow for 'wet' plasma solution analysis, or membrane gas flow in the case of the desolvation nebulizer (DSN) and 'dry' plasma, is one of the basic parameters used to tune the mass spectrometer. Generally the tuning procedure for isotopic analysis is simply to adjust the nebulizer gas flow to maximize sensitivity and not be concerned about oxide or doubly charged ion production. This approach is unlike the conventional procedure for tuning a quadrupole or single sector instrument for trace element analysis and can be adopted because of the purity of the sample solutions and the restricted mass range in most isotopic measurements. Fig. 7-8a shows the signal response for a 50 ppb solution of JMC475 Hf as a function of changing the membrane gas flow on the Nu Instruments DSN100, while keeping all other instrument parameters constant. In this example the Hf signal increases with increasing gas flow until a maximum voltage is reached, after which any further increase in gas flow causes the voltage to decrease. A deviation of ± 0.1 litres per minute (l/min) from the optimum membrane gas flow of 2.7 l/min, results in a relative loss in sensitivity of approximately 10%. In contrast, the mass bias represented by the exponential mass bias coefficient *f*, shows a near linear trend with the change in gas flow, with the mass fractionation being greater at higher gas flow (Fig. 7-8b). The range in *f* values obtained is from –1.40 to –1.78. The experiment was repeated using a Yb-doped Hf solution, and Yb shows the same relationship with gas flow as Hf for both sensitivity and mass bias. However, the Hf/Yb ratio in Fig. 7-8a shows a monotonic decrease with increasing gas flow, indicating that any changes in gas flow during a session could affect the measured isotopic ratio between the two elements.

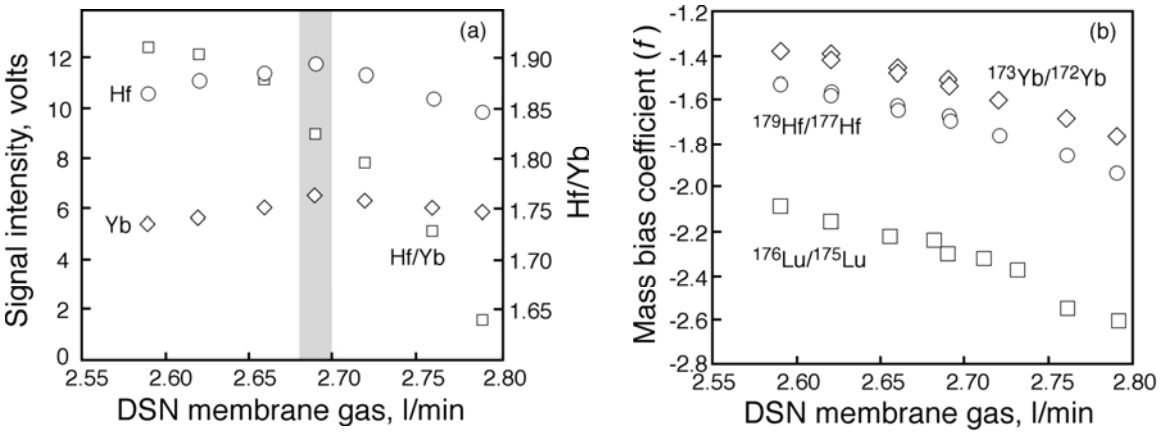


FIG. 7-8 (**a**) Plot of Hf and Yb signal intensity (volts) and Hf/Yb ratio *versus* desolvation nebulizer (DSN) membrane gas flow (l/min) for a mixed Yb–Hf solution; (**b**) Plot of exponential mass bias coefficient *f* for Yb ($^{173}$Yb/$^{172}$Yb) and Hf ($^{179}$Hf/$^{177}$Hf) *versus* DSN membrane gas flow (l/min).

The study of the effect of gas flow on mass bias was expanded to cover a wider mass range from Mg to Pb. The results are presented in Fig. 7-9 and show that the strong inverse relationship between *f* and gas flow is a feature of high mass. With decreasing atomic number the curves become flatter and between Sr and Cu the slope changes from negative to positive. Further studies are currently being undertaken to understand these relationships but the results confirm that if an external dopant is going to be used to correct for mass bias it should be an element of similar mass.

***Extraction lens voltage.*** Ion extraction from the plasma on the Nu Plasma MC–ICP–MS is controlled by a series of ion lens systems operated at high voltage, interspersed with sets of steering lenses. The interface, which constitutes the first extraction lens HV1 (sampler and skimmer cones), is held at the highest potential (4 kV) and the collector array is at ground potential, so the ions are accelerated at the start of their paths through the mass spectrometer. The voltage on HV1 is matched to the ESA and ion transmission has a very narrow plateau region of approximately 20 volts. As a consequence when HV1 is adjusted off this plateau, the signal transmission decreases dramatically to background levels. Because of this HV1 is essentially a constant parameter in day to day operation. The second extraction lens, HV2, is located directly behind the skimmer cone and is much more sensitive to the mode of sample introduction, particularly if it is 'wet' or 'dry' plasma, and the nebulizer gas flow. Fig. 7-10a shows the signal response for a solution of JMC475 Hf, introduced using the DSN100, as a function of changing the voltage on HV2 and keeping all other instrument parameters constant. Over an operating range of 400 volts (200 volts either side of the optimum tune value of approximately 2.53 kV) the signal response is an upwardly convex curve, with a loss of approximately 10% transmission at ±100 volts and approximately 25% at ±200 volts. The exponential mass bias coefficient *f* shows an upwardly concave trend with less negative values at higher values of HV2 voltage (Fig. 7-10b). The range of *f* values is from –1.82 at 2.33 kV to –1.45 at 2.73 kV. The relative changes in signal intensity and in *f* values of approximately 0.4 in response to a change in HV2 voltage of 400 V are essentially the same as those produced by a change in membrane gas flow of 0.2 l/min. As in the gas flow

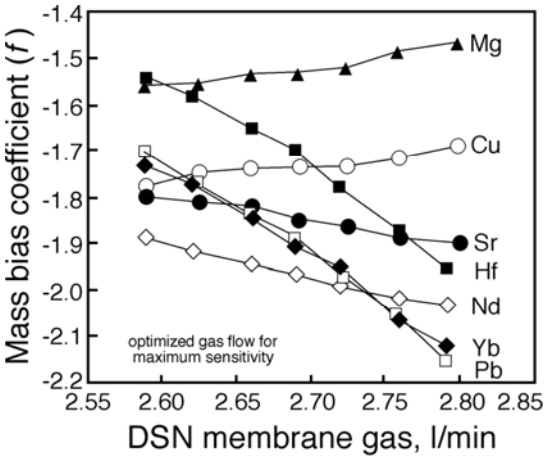


FIG. 7-9. Plot of exponential mass bias coefficient (*f*. values for selected elements (Mg, Cu, Sr, Nd, Yb, Hf, Pb) *versus* DSN membrane gas flow (l/min).

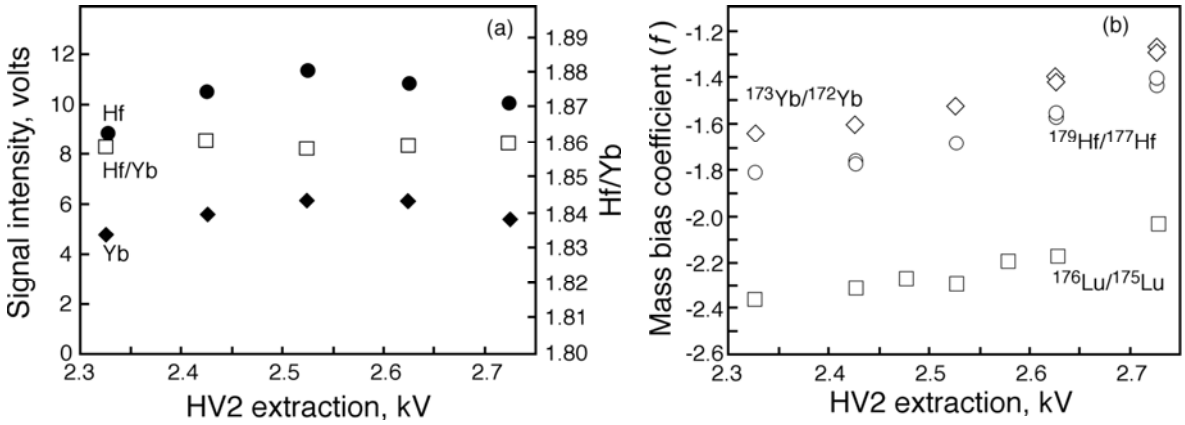


FIG. 7-10. (**a**) Plot of Hf and Yb sensitivity (volts), and Yb/Hf ratio *versus* HV2 extraction lens voltage (kV) for a mixed Yb–Hf solution; (**b**) Plot of exponential mass bias coefficient *f* for Yb ($^{173}$Yb/$^{172}$Yb) and Hf ($^{179}$Hf/$^{177}$Hf) *versus* HV2 extraction lens voltage (kV).

experiments (Fig. 7-9), the mass fractionation behavior of Yb isotopes is very similar to that of Hf isotopes. In contrast to the gas flow experiments, there is no systematic change observed in Hf/Yb over the 400 volt range of HV2 operation.

***Torch depth position.*** Adjustment of the torch position along the vertical and horizontal axes of the plane parallel to the interface, away from a point directly in line with the sampler cone orifice, has the obvious effect of reducing sensitivity and also leads to less negative *f* values. Adjustment of the torch in and out along the horizontal axis perpendicular to the interface has the effect of changing the length of travel of the sample within the plasma and the position at which the plasma is sampled. At shallow torch depths, where the torch is closer to the cones, a hotter part of the plasma is sampled, whereas at greater torch depths the temperature of the plasma is lower. The effect of sample depth on the *f* coefficient for Hf is shown in Fig. 7-11. Over a depth range of 0.5 mm the values for *f* change from –1.6 at the position closest to the cones to –1.35 when the torch is farthest from the cones. This is accompanied by a 15–20% loss in sensitivity.

The tuning of the MC–ICP–MS is a complex interplay between these and many other parameters, and isolating the effects of individual parameters during routine operation is difficult. As stated above the common practice is to tune the instrument for maximum sensitivity, so given the effect that most of the parameters exert on sensitivity it is unlikely that the instrument would be operated with any one of the parameters shifted significantly from an optimum setting. Any small offset in one tuning parameter from optimum is likely to be compensated by the adjustment of one of the other parameters. For instance, the subtle loss in sensitivity due to a slightly lower than optimum nebulizer gas flow could be recovered by reducing the HV2 voltage or decreasing the torch depth, with little or no effect on mass bias.

***RF Power.*** The adjustment of the forward power to the plasma is not normally considered to be a routine tuning parameter. Typically the RF power is set at a fixed value and the other tune parameters are adjusted to achieve maximum sensitivity. In general most applications use a 'hot' plasma with RF power in the range 1200–1400 watts. There are many well documented studies that have used cold plasma (RF <1000 watts) with the prime aim of eliminating Ar-based interferences (*e.g.*, on Fe isotopes, Kehm *et al.* 2003) or reducing matrix-

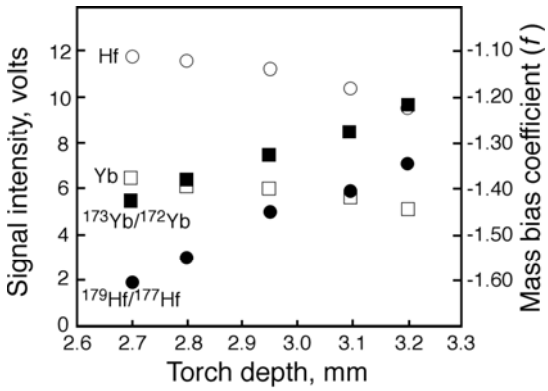


FIG. 7-11. Plot of signal intensity (volts) and exponential mass bias coefficient *f* for Yb ($^{173}$Yb/$^{172}$Yb) and Hf ($^{179}$Hf/$^{177}$Hf) *versus* torch depth for a mixed Yb–Hf solution.

induced fractionation (*e.g.*, of Li isotopes, Bryant *et al.* 2003). Although RF power can be considered as a constant factor in instrument operating conditions this does not mean that the absolute wattage does not affect instrumental mass bias. Figure 7-12. shows a plot of RF power *versus* signal intensity and *f* mass bias coefficient for Hf. For this set of experiments the instrument was initially tuned at 1300 watts as indicated by the maximum signal intensity. The important feature of the diagram is the linear increase in mass bias coefficient from approximately –1.7 at 1200 watts to approximately –1.5 at 1350 watts.

***Cone design.*** Two basic skimmer cone designs are currently available for the Nu Plasma: a standard "narrow" skimmer recommended for 'wet' plasma and a wide angle skimmer for 'dry' plasma. Until the wide angle skimmer became available in 2001 all types of analysis were carried out using the standard "narrow" skimmer cone. Table 7-1 shows average Hf mass bias coefficients for 'dry plasma' analysis on the Nu Plasma for JMC475 Hf solution introduced using a desolvation nebulizer and during the laser ablation analysis of zircon. There are fundamental differences in the *f* values for the standard "narrow" skimmer cone and the wide angle skimmer. While the solution and laser values are very similar for the standard "narrow" skimmer, the *f* values obtained from the laser analyses are less negative than those from the solution measurements using the wide angle skimmer. There are several possible explanations for this shift. One possibility is that the difference in *f* values for solution and laser ablation might be due to the fact that desolvation systems do not produce completely dry

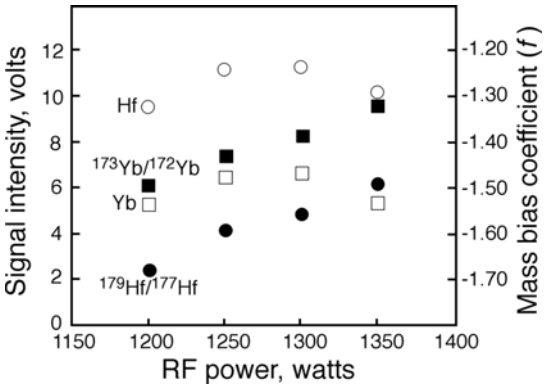


FIG. 7-12. Plot of signal intensity (volts) and exponential mass bias coefficient *f* for Yb ($^{173}Yb/^{172}Yb$) and Hf ($^{179}Hf/^{177}Hf$) *versus* forward RF power (watts) for a mixed Yb–Hf solution.

aerosols and this difference in fluid content might affect fractionation processes in the plasma.

Another two possibilities relate more directly to the laser ablation procedures: the first might be that it is due to the use of He in the laser analyses and the second could be that it is related to laser-induced isotopic fractionation.

***Nebulizer gas composition.*** The benefits of using He as the carrier gas in the ablation sample cell are well documented (*e.g.*, Eggins *et al.* 1998, Horn & Günther 2003) and the practice is widely used in trace element and isotope ratio analysis. A sequence of experiments was undertaken to test the effect of the addition of He on Hf mass bias. In the first set of analyses only Ar was used to transport the sample to the ICP with the laser cell being placed in the sample line between the desolvation nebulizer (DSN) and the ICP. A series of bracketed JMC475 solution/laser analyses was performed and the results show a consistent shift of approximately 0.05 to less negative values of *f* for the laser measurements (Fig. 7-13). A second set of experiments was then performed with only He in

TABLE 7–1: COMPARISON OF AVERAGE MASS BIAS COEFFICIENTS FOR HF OBTAINED BY SOLUTION ANALYSIS USING A DESOLVATION NEBULIZER AND LASER ABLATION.

| | n | *f*(Hf) | 2σ |
|---|---|---|---|
| **JMC475** | | | |
| NU005 standard skimmer | 79 | –1.987 | 0.285 |
| NU005 Wide angle skimmer | 190 | –1.683 | 0.222 |
| NU005 Big80 | 110 | –1.686 | 0.160 |
| **LAM zircon** | | | |
| NU005 standard skimmer | 1295 | –2.052 | 0.319 |
| NU005 Wide angle skimmer | 14061 | –1.464 | 0.310 |
| NU005 Big80 | 12211 | –1.522 | 0.267 |

Comparison of average mass bias coefficients for Hf obtained by solution analysis of JMC475 using a desolvation nebulizer (MCN6000 or DSN-100) and laser ablation of zircon. Results for three different combinations of cone design and interface pump are presented. Standard "narrow" skimmer = Nu Type A standard skimmer cone (319–284) and Edwards EM28 rotary pump; Wide angle skimmer = Nu Type B 'wide angle' skimmer cone (319–497) and Edwards EM28 rotary pump; Big80 = Nu Type B 'wide angle' skimmer cone (319–497) and Edwards EM2 80 rotary pump.

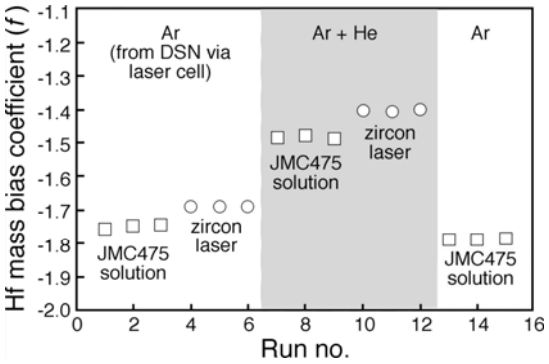


FIG. 7-13. Time series of experiments to show the effect of nebulizer gas composition on *f* for Hf ($^{179}Hf/^{177}Hf$). Analysis numbers 1–3 and 13–15 are of a standard Hf solution using a desolvation nebulizer, but with the laser sample cell in the gas line between the DSN and ICP. Analysis numbers 4–6 are laser ablation measurements of Mud Tank zircon, using Ar from the DSN as the sole nebulizer gas. For analysis numbers 7 to 12, He has been introduced to the nebulizer gas between the DSN and laser cell. The results for the bracketing analyses of JMC475 at the start and end of the run sequence indicate little change in instrument mass bias with time (*ca.* 3 hours).

the laser cell and with the Ar from the DSN introduced via a three-way connector downstream from the laser cell. The mass spectrometer was not turned off between the two sets of measurements and only the gas flows were retuned to give the same $^{180}Hf$ signal intensity for the JMC475 solution. The addition of the He resulted in a shift in *f* of approximately 0.3 for both the solution and laser analyses. Again the *f* values for the laser analyses were offset by approximately 0.05 from the solution values. The tubing was then changed back to the original setup and the JMC475 re-analyzed to establish if there had been any long term drift in mass bias over the period of the experiments (approximately 3 hours).

One observation to explain why the addition of He to the carrier gas stream causes this shift in mass bias is an associated slight increase in the interface pressure. Although the combined volume of Ar plus He introduced must remain similar to the flow rate of Ar by itself, the He must be more difficult for the pump to remove. Further evidence for this explanation comes from the measurement of the interface pressure using two different capacity roughing pumps. An Edwards EM28 pump was supplied initially with the Nu Plasma, but since 2003 a large capacity Edwards EM2 80 pump has been used (the "Big 80" configuration). Under an Ar gas load the typical interface pressure for the EM28 is 2.5–2.7 mbar and for the EM2 80 it is 0.75 mbar. With the addition of He, the pressure in the interface using the EM28 increases to approximately 2.9–3.0 mbar, whereas for the EM2 80 the increase is not as large with typical values of 0.9–1.0 mbar. The ability of the two different pumps to remove the He might explain the subtle difference in average *f* values in Table 7-1 depending on which type of pump is used. Although it should be noted that the values are within error of each other, the values obtained with the Big 80 configuration are closer to the solution values. Nevertheless it would seem that the change in interface pressure must affect the ion extraction processes and produce the shift in mass bias.

**Laser-induced Fractionation**

Particle size distribution is also considered to be a significant factor responsible for isotopic fractionation in laser ablation; the incomplete ionization of larger particles in the plasma results in preferential transmission of lighter isotopes (Jackson & Günther 2003, Kühn *et al.* 2007, Günther & Koch 2008). This probably should be considered as a laser-induced phenomenon, but the isotopic fractionation is being produced in the plasma rather than at the site of ablation.

The intrinsic physics of the laser design and operating conditions are considered to be the main factors that contribute to laser-induced elemental and isotopic fractionation (*e.g.*, Guillong *et al.* 2003, Kühn *et al.* 2007, Horn & von Blanckenburg 2007, Košler 2008, Horn 2008). These factors include laser pulse width, wavelength, repetition rate (which in turn controls ablation rate and pit aspect ratio), and energy density. A series of experiments was carried out to examine the effects of varying the most common operating conditions on mass fractionation: repetition rate, spot size and energy. The measurements were made of Hf isotopes in the Mud Tank zircon standard using a New Wave UP213 laser ablation system.

Figure 7-14a shows the effect of repetition rate on sensitivity, both in terms of signal intensity and as a function of time. At high repetition rates the signal intensity is significantly greater but decreases markedly with time, whereas at low repetition rates the signal is essentially steady state. A plot of *f* values *versus* time for an individual analysis at a given frequency (Fig. 7-14b) shows that mass fractionation behaves quite differently. At 2 Hz the *f* value increases rapidly in the first 15–20 seconds after the laser is turned on but then

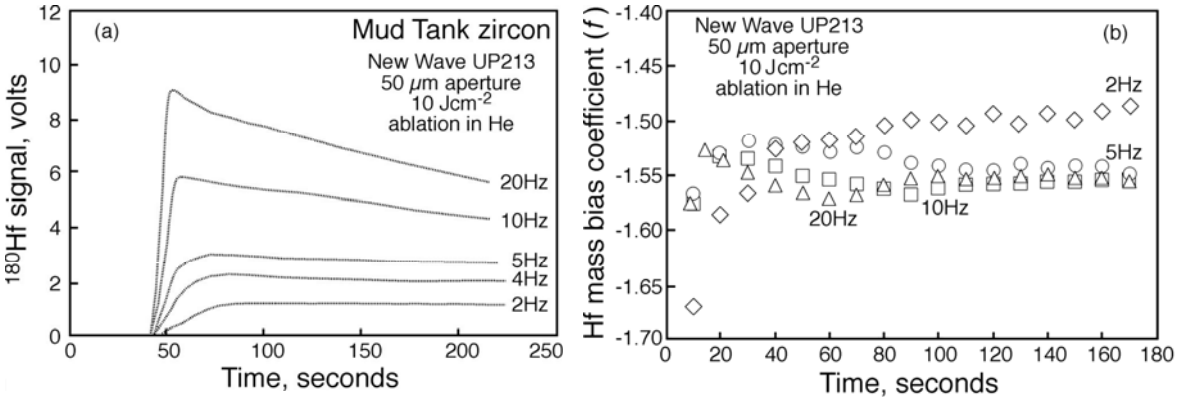


FIG. 7-14. Plots showing the effect of laser repetition rate on the measurement of Hf isotopes in zircon. (**a**) signal sensitivity (180Hf volts) *versus* time as a function of repetition rate (Hz); (**b**) exponential mass bias coefficient *f* for Hf ($^{179}Hf/^{177}Hf$) *versus* time as a function of repetition rate (Hz)

continues to increase at a steady rate, albeit slowly, until the laser is turned off. The initial increase in *f* is much more rapid at 5 Hz, and reaches a maximum after approximately 20 seconds. The value stays nearly constant for the next 60 seconds and then shows a very subtle decline until the end of the analysis. A maximum *f* value is also reached after 20 seconds at 10 Hz, but then almost immediately it starts to drop until at around 90 seconds it levels out (or increases slightly) for the remainder of the analysis. The pattern displayed by the 20 Hz analysis is similar to the 10 Hz one but the initial peak in *f* values is sharper due to the higher laser repetition rate. Both the 10 and 20 Hz patterns are very similar to those obtained by Kühn *et al.* (2007) for copper isotopes, with the dip in mass fractionation in the middle of the analysis attributed to a change in particle size distribution and ablation process with depth. There is also a clear relationship between repetition rate and the absolute value of the *f* mass fractionation factor (Fig. 7-15). With increasing repetition rate the *f* value becomes progressively more negative but significantly, the normalized $^{176}Hf/^{177}Hf$ values are within the long term range of values for the Mud Tank zircon. Although the mass fractionation behavior appears to vary with repetition rate, the fractionation process is mass-dependent as shown in the log-log plot of pairs of Hf isotopes from a single ablation analysis (Fig. 7-16), allowing for correction using another isotope pair (Fig. 7-17). The results of the experiments indicate that although an isotopic fractionation appears to be produced by the laser ablation process under certain operating conditions, application of the exponential law to correct for instrumental mass bias using an internal pair of isotopes appears to account for this fractionation.

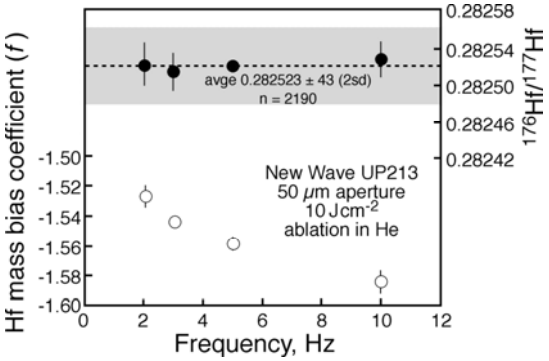


FIG. 7-15. Plot of laser repetition rate (Hz) *versus* exponential mass bias coefficient *f* value for Hf ($^{179}Hf/^{177}Hf$). The values for $^{176}Hf/^{177}Hf$ have been corrected using the exponential law and normalized to ($^{179}Hf/^{177}Hf$).

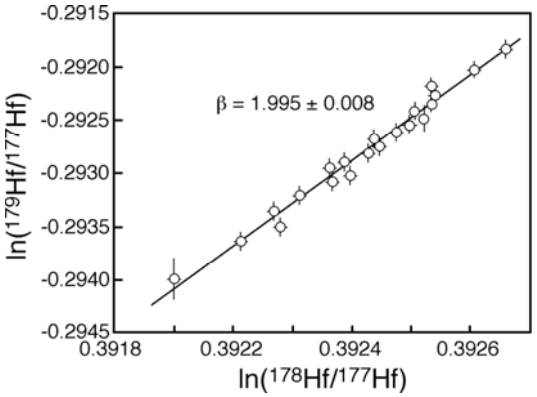


FIG. 7-16. Plot of $\ln(^{178}Hf/^{177}Hf)$ vs $\ln(^{179}Hf/^{177}Hf)$ from a single laser ablation analysis of Mud Tank zircon. Each data point is the average for a 10 second interval (50 x 0.2 second measurements) and the error bars are 1 standard deviation.

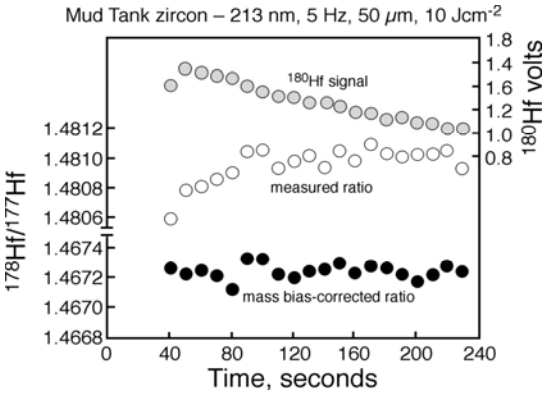


FIG. 7-17. Time-resolved analysis plot of laser ablation of Mud Tank zircon showing signal intensity ($^{180}$Hf, volts), as well as the measured and mass bias-corrected $^{178}$Hf/$^{177}$Hf.

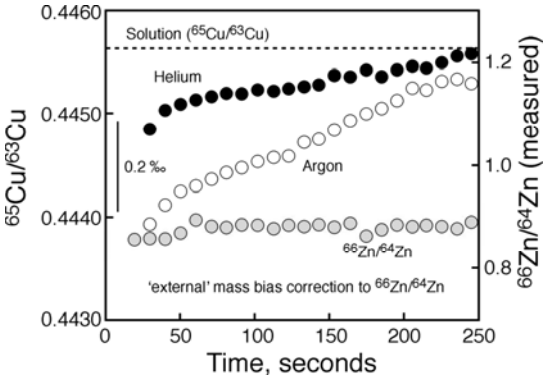


FIG. 7-18. Time-resolved analysis plot of laser ablation of Cu metal in argon and in helium, showing the steady change in $^{65}$Cu/$^{63}$Cu with time (after Jackson & Günther 2003). The $^{65}$Cu/$^{63}$Cu ratios were corrected for instrumental mass bias using a desolvated Zn solution introduced into the nebulizer gas line.

The likelihood of laser-induced isotopic fractionation has important implications for the *in situ* measurement of mass-dependent isotopic systems. First and foremost it underlines the importance of having matrix-matched reference materials to enable the standard sample bracketing technique to be employed. It also causes some concerns where an external dopant is introduced using a desolvation nebulizer and used to correct mass bias. The solution allows monitoring of the mass bias stability of the instrument over time but might not adequately correct the mass fractionation of the solid material as was demonstrated in a series of experiments by Jackson & Günther (1993). In these experiments they ablated Cu metal using laser of different wavelengths and under a range of different laser conditions, and used a Zn solution to correct for instrumental mass bias, but they were unable to obtain an accurate isotopic composition of the Cu metal (Fig. 7-18). If the external dopant method is to be employed then it is necessary to keep the laser operating conditions constant and a stable energy output becomes a critical factor. This is to ensure that the ratio of ablated material to desolvated solution does not change, so that any long term drift in the mass bias of the solution only reflects the change in instrumental mass bias. The results of the Jackson & Günther study also indicate that a combination of standard sample bracketing and the external doping technique provides the best approach.

One laser ablation application where the external dopant method has been used with success is the *in situ* analysis of Re–Os isotopes in sulfides in mantle-derived peridotite (*e.g.*, Pearson *et al.* 2002, Griffin *et al.* 2004a, Alard *et al.* 2005). Pearson *et al.* (2002) demonstrated consistent mass bias behavior for Os–Ir and Ir–Re solutions on the Nu Plasma and this led to the use of Ir as an external dopant to correct for mass bias. Although Os has more than one pair of stable isotopes that can be used for mass bias correction, there are potential isobaric interferences from Pt isotopes that have to be considered. Rhenium only has two isotopes, one of which overlaps with $^{187}$Os, so assumptions have to be made regarding its mass bias behavior. Mass bias normalization using the introduced Ir solution provides independent corrections for both Os and Re, and enables a more precise measurement of instrument mass bias because the solution signal intensity is typically ≥1 order of magnitude higher than the Os and Re signals derived from the sulfide. The problems observed in the Cu study by Jackson & Günther (2003) do not appear to affect the *in situ* measurement of Os–Re isotopes in a sulfide matrix. Figure 7-19a presents time-resolved signal intensities for selected isotopes for the Ir dopant solution and Os in the Ni sulfide mineral, as well as uncorrected ratios for selected isotope ratios. An isotope ratio plot (Fig. 7-19b) shows that the Ir ratio remains unaffected when the laser is turned on and the Os ratio also stays constant during the ablation. These features are emphasized by the tight cluster of points in the log-log plot (Fig. 7-20) rather than a linear trend that would be produced by time-dependent fractionation.

The combined effect of changing spot size and/or energy is to vary the amount of material introduced into the ICP. Mass loading in the ICP has been recently shown to have a large effect on

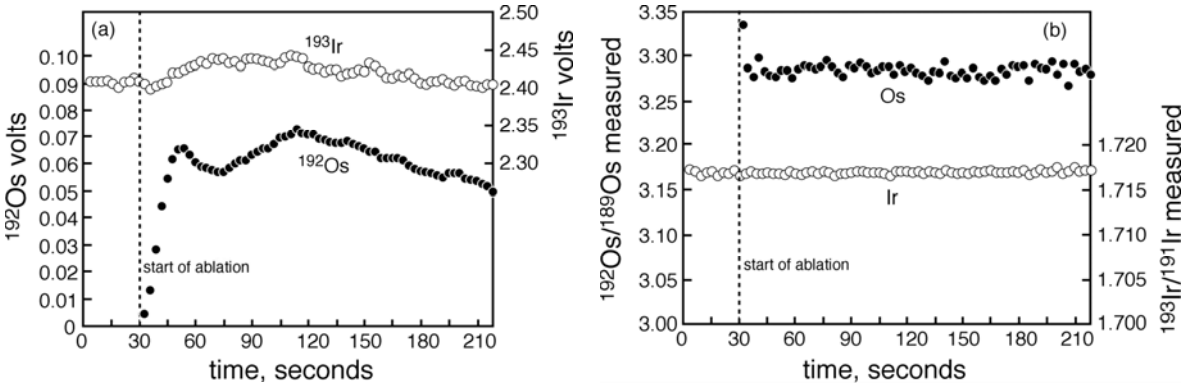


FIG. 7-19. Time-resolved analysis plots of laser ablation of an Os-doped (200 ppm) synthetic Ni–S (PGE–A) and desolvated Ir solution. (a) $^{193}$Ir and $^{192}$Os signal intensity (volts) *versus* time; (b) uncorrected $^{193}$Ir/$^{191}$Ir and $^{192}$Os/$^{189}$Os ratios *versus* time.

elemental fractionation in the laser ablation of silicates (Kroslakova & Günther 2007). The influence of plasma loading on mass bias can be evaluated in a plot of the mass bias coefficient *f* *versus* total signal intensity obtained from laser ablation of Mud Tank zircon using different spot sizes and beam energies (Fig. 7-21). Although the measurements are not from a single analytical session, there does not appear to be any significant relationship. A controlled study of the effect of spot size was undertaken at fixed repetition rate (5 Hz) and energy (10 Jcm$^{-2}$) and the results show a more systematic control on mass fractionation. With increasing spot size rate the *f* value becomes progressively less negative but again the normalized $^{176}$Hf/$^{177}$Hf values are within the long term range of values for the Mud Tank zircon. Furthermore a plot of *f* values *versus* time for an individual analysis at a given spot size shows that mass fractionation behaves quite differently. At large spot sizes the time-dependent variation in *f* is near constant. At small spot sizes the pattern is very similar to those described for the 10 and 20 Hz experiments above.

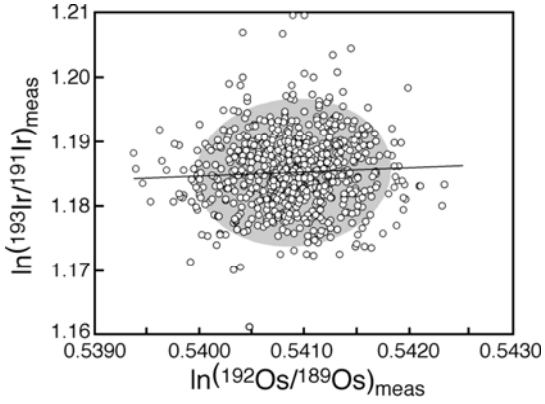


FIG. 7-20. Plot of ln($^{192}$Os/$^{189}$Os) vs ln($^{193}$Ir/$^{191}$Ir) from laser ablation analysis of an Os-doped (200 ppm) synthetic Ni–S (PGE–A) and desolvated Ir solution. Each point is a 0.2 second measurement and the shaded area represents the ±2σ error ellipse.

***Matrix effects.*** There is an increasing volume of data showing the effects of sample matrix on the mass bias behavior of a range of elements in the ICP (Carlson *et al.* 2001, Albarède *et al.* 2004, Pietruszka *et al.* 2006). As stated in the Introduction sample purification is commonly deemed to be necessary for accurate and precise measurement of mass-dependent isotope fractionation. This is also perceived to be a problem for laser ablation analysis because of the amount of 'dirty' matrix introduced into the mass spectrometer. However the agreement between the Hf isotope measurements of reference

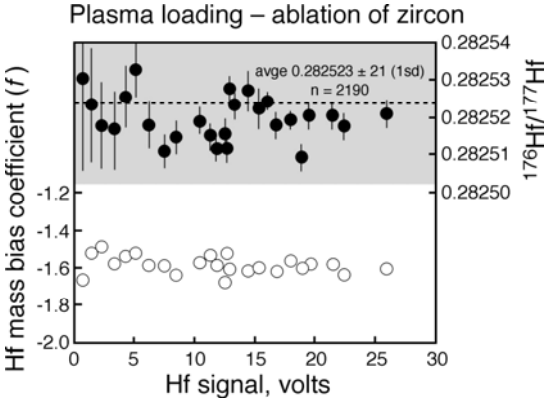


FIG. 7-21. Plot of Hf signal intensity (volts) vs exponential mass bias coefficient *f* for Hf ($^{179}$Hf/$^{177}$Hf) to investigate the potential effects of plasma loading. The results are from the laser ablation of Mud Tank zircon and the range in Hf signal was obtained by using different combinations of spot size and repetition rate. The values for $^{176}$Hf/$^{177}$Hf have been corrected using the exponential law and normalized to ($^{179}$Hf/$^{177}$Hf).

zircon (*e.g.*, Griffin *et al.* 2000, Woodhead & Hergt 2005, Iizuka & Hirata 2005) by digestion/solution analysis and by laser ablation indicates that in this case matrix effects are negligible. The question remains as to whether the systematic shift in mass bias with increasing volumes of ablated material is simply a plasma-loading effect or if there is also a matrix effect. The potential effect of a Zr-rich matrix on Hf mass bias was assessed by analyzing a series of 100 ppb Hf solutions doped with varying amounts of Zr (2, 5, 7 and 10 ppm). The spread of Zr/Hf ratios of the solutions (20 to 100) covers the range reported for typical zircon (Belousova *et al.* 2002). The results are presented in Figure 7-22a and show a systematic change to less negative *f* values for Hf with increasing Zr content. In a second set of experiments a suite of 10 ppm Zr solutions doped with different amounts of Hf (10 to 100 ppb) was analyzed to assess the effect of changing the Zr/Hf ratio while attempting to keep the total plasma loading near constant. The range of Zr/Hf ratios extends to much higher values (100 to 1000) than those typical for natural zircon compositions but significantly even at these high ratios there appears to be no relationship with the mass fractionation of Hf (Fig. 7-22b). Most importantly, in both sets of experiments the corrected $^{176}Hf/^{177}Hf$ values are well within the 2σ range of the long term average of the JMC475 in our laboratory.

Based on the results from the Zr-doped experiments a second series of analyses was undertaken to assess the affect of the addition of Zr on the relative mass bias behavior of Hf and Yb. The plot of *f* Hf *vs f* Yb (Fig. 7-23) shows that a linear array is produced for the Zr-doped solutions of JMC475. This array is parallel to the trend defined by the solutions without any Zr added but displaced to higher (less negative) *f* Hf values. The analyses were performed using a bracketing technique with the Hf–Yb solution and it would appear that while there is a shift in *f* Hf the addition of Zr has little affect on *f* Yb. Despite this behavior the slope of the line defined by the Zr-doped solutions is within uncertainty of that determined for the bracketing Zr-free solutions and also of the long term *f* Hf–*f* Yb slope. Thus although the addition of Zr shifts the absolute Hf bias, the exponential law is able to accommodate this offset.

It should also be remembered that many of the isotopic systems, such as Hf, have other pairs of stable isotopes that should be measured to monitor the relative impact of plasma loading and matrix on mass bias. The reporting of as many ratios as possible is advocated especially as the limits of the *in situ* MC–ICP–MS method are stretched to lower element concentrations, higher parent–daughter ratios and more complex mineral compositions.

## SUMMARY

There are many factors that influence the accuracy and precision of *in situ* isotope ratio measurement and these can be divided into 3 categories related to the sample, the mass spectrometer and the laser system.

Accuracy is mainly a function of correction procedures for mass bias, isobaric interferences and sample matrix effects, whereas precision is a function of signal intensity which is in turn dependent on sample composition, laser energy, spot size and mass spectrometer sensitivity, and ablation time.

The correction for mass-dependent instrumental bias is the most critical factor controlling accuracy and it is important to understand which parameters influence isotopic fractionation in LAM–MC–ICP–MS. Instrument

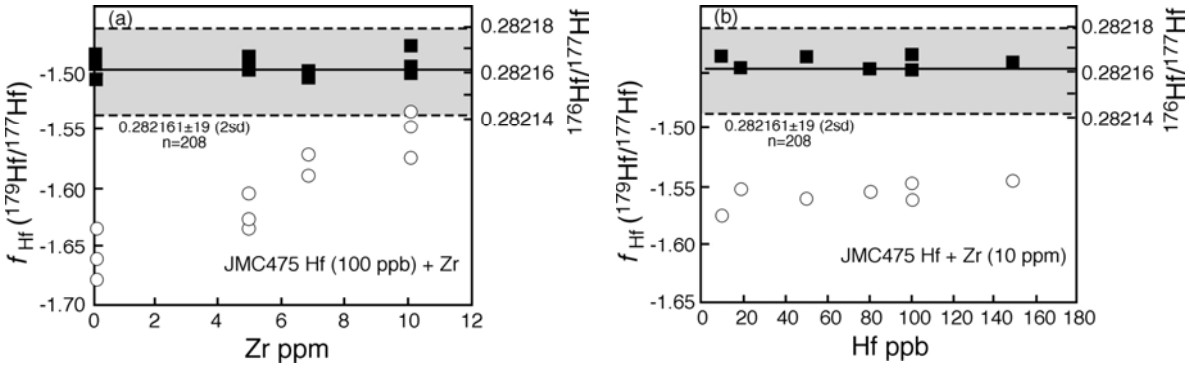


FIG. 7-22. The effect of matrix composition on the mass bias coefficient (*f* value for Hf ($^{179}Hf/^{177}Hf$). (**a**) when 100 ppb of Hf (JMC475) is doped with varying amounts of Zr; (**b**) when 10 ppm of Zr is doped with varying amounts of Hf.

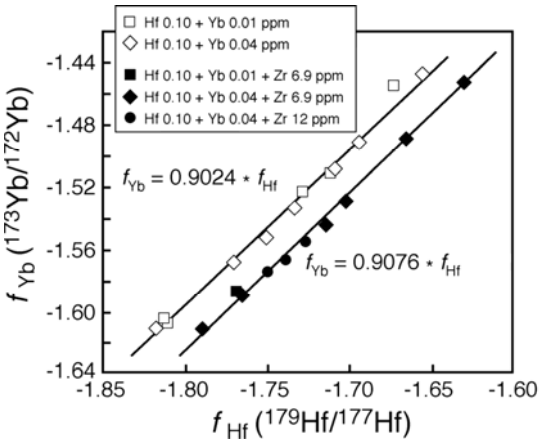


FIG. 7-23. Plot of exponential mass bias coefficient *f* for Yb ($^{173}$Yb/$^{172}$Yb) *vs* Hf ($^{179}$Hf/$^{177}$Hf) of mixed Hf (JMC475) + Yb + Zr solutions.

operating parameters that affect mass bias for solution analysis include nebulizer gas flow, RF power, extraction voltages, torch position and cone design. Additional factors affecting mass bias for laser ablation analysis are matrix (sample)-related and the laser operating conditions.

Matrix-related effects include plasma loading and polybaric interferences. Laser-induced isotopic fractionation is directly related to particle size distribution, which depends on the intrinsic design of the laser and on the operating conditions.

Mass bias correction using 'internal' stable isotope pairs appears to incorporate the possible effects of laser-induced fractionation. The consistent mass bias behavior of pairs of elements on the Nu Plasma also enables robust corrections for isobaric interferences of elements for which there is no independent measurement of mass bias (*e.g.*, Rb–Sr, Hf–Yb–Lu, Os–Ir–Re). The mass bias behavior of other types of instrument needs to be documented independently.

The interplay of all of the factors that influence accuracy and precision emphasizes the need for reference materials that are well characterized, not only with regard to their isotopic composition but also their major and trace element constituents.

## ACKNOWLEDGEMENTS

Many of the ideas and concepts presented in this paper have been germinating since the first experiments were carried out on Nu Plasma 005 in late 1998. In the intervening years many colleagues and visitors to GEMOC have contributed to our understanding of instrumental mass bias and laser-related processes. Aspects of this work have also been presented at various international meetings and the ensuing discussions with numerous people have provided further stimulation. Thanks go to Simon Jackson, Olivier Alard, Phil Freedman, Detlef Günther, Hansrudi Kühn, Helen Williams, Sune Nielsen, Tom Andersen and Stuart Graham. We are also indebted to the team at Nu Instruments for their on-going support.

This is contribution No. 534 from the ARC National Key Centre for the Geochemical Evolution and Metallogeny of Continents (http:/www.els.mq.edu.au/GEMOC). This study used instrumentation funded by ARC LIEF and DEST Systemic Infrastructure Grants, Macquarie University and Industry.

## REFERENCES

AESCHLIMAN, D.B., BAJIC, S.J., BALDWIN, D.P. & HOUK, R.S. (2003): High-speed digital photographic study of an inductively coupled plasma during laser ablation: comparison of dried solution aerosols from a microconcentric nebulizer and solid particles from laser ablation. *J. Analyt. Atom. Spectrom.***18**, 1008-1014.

ALARD, O., LUGUET, A., PEARSON, N.J., GRIFFIN, W.L., LORAND, J.-P., GANNOUN, A., BURTON, K.W. & O'REILLY, S.Y. (2005): *In situ* Os isotopes in abyssal peridotites: bridging the "isotopic gap" between MORB and their source mantle. *Nature* **436**, 1005-1008.

ALBARÈDE, F. (2004): The stable isotope geochemistry of copper and zinc. *In* Geochemistry of Non-traditional Stable Isotopes (Johnson, C.M., Beard, B.L. and Albarède, F., editors). *Rev. Mineral. & Geochem.* **55**, 409-427. Mineral. Soc. Amer., Washington DC.

ALBARÈDE, F., TELOUK, P., BLICHERT-TOFT, J., BOYET, M., AGRANIER, A. & NELSON, B. (2004): Precise and accurate measurements using multiple-collector ICP–MS. *Geochim. Cosmochim. Acta* **68**, 2725-2744.

ANBAR, A.D. (2004): Molybdenum stable isotopes: observations, interpretations and directions. *In* Geochemistry of Non-traditional Stable Isotopes (Johnson, C.M., Beard, B.L. and Albarède, F., editors). *Rev. Mineral. Geochem.* **55**, 429-454. Mineral. Soc. Amer., Washington DC.

ANDRÉN, H., RODUSHKIN, I., STENBERG, A., MALINOVSKY, D. & BAXTER, D.C. (2004): Sources of mass bias and isotope ratio variation

in multi-collector ICP–MS: optimization of instrumental parameters based on experimental observations. *J. Analyt. Atom. Spectrom.* **19**, 1217-1224.

ARCHER, C. & VANCE, D. (2004): Mass discrimination correction in multiple-collector plasma source mass spectrometry: and example using Cu and Zn isotopes. *J. Analyt. Atom. Spectrom.* **19**, 656-665.

BAXTER, D.C., RODUSHKIN, I., ENGSTRÖM, E. & MALINOVSKY, D., (2006): Revised exponential model for mass bias correction using an internal standard for isotope abundance ratio measurements by multi-collector inductively coupled plasma mass spectrometry. *J. Analyt. Atom. Spectrom.* **21**, 427-430.

BEARD, B.L. & JOHNSON, C.M. (2004): Fe isotopic variations in the modern and ancient earth and other planetary bodies. *In* Geochemistry of Non-traditional Stable Isotopes (Johnson, C.M., Beard, B.L. & Albarède, F., *eds*). *Rev. Mineral. Geochem.* **55**, 319-357. Mineral. Soc. Amer., Washington DC.

BELOUSOVA, E.A., GRIFFIN, W.L., O'REILLY, S.Y. & FISHER, N.I. (2002): Igneous zircon: trace-element composition as an indicator of source rock type. *Contrib. Mineral. Petrol.* **143**, 602-622.

BELSHAW, N.S, FREEDMAN, P.A., O'NIONS, R.K., FRANK, M. & GUO, Y. (1998): A new variable dispersion double-focusing plasma mass spectrometer with performance illustrated for Pb isotopes. *Int. J. Mass Spec. Ion. Proc.* **181**, 51-58.

BLICHERT-TOFT, J. (2001): On the Lu–Hf isotope geochemistry of silicate rocks. *Geostand. News.* **25**, 41-56.

BLICHERT-TOFT, J., CHAUVEL, C. & ALBARÈDE, F. (1997): Separation of Lu and Hf for high precision isotope analysis of rock samples by magnetic sector-multiple collector ICP–MS. *Contrib. Mineral. Petrol.* **127**, 248-260.

BRYANT, C.J., MCCULLOCH, M.T. & BENNETT, V.C. (2003): Impact of matrix effects on the accurate measurement of Li isotope ratios by inductively coupled plasma mass spectrometry (MC–ICP–MS) under 'cold' plasma conditions. *J. Analyt. Atom. Spectrom.* **18**, 734-737.

CARLSON, R.W., HAURI, E.H. & ALEXANDER, C.M.O'D. (2001): Matrix induced isotopic mass fractionation in the ICP–MS. *In:* Plasma Source Mass Spectrometry: The New Millennium. Holland, J.G. Tanner, S.D. (*eds.*). The Royal Society of Chemistry, Cambridge, pp. 288-297.

CHU, N-C., TAYLOR, R.N., CHAVAGNAC, V., NESBITT, R.W., BOELLA, R.M., MILTON, J.A., GERMAN, C.R., BAYON, G. & BURTON, K. (2002): Hf isotope ratio analysis using multi-collector inductively coupled plasma mass spectrometry: an evaluation of isobaric interference corrections. *J. Analyt. Atom. Spectrom.* **17**, 1567-1574.

CORFU, F. (2007): Comment to short communication 'Comment: Hf-isotope heterogeneity in zircon 91500' by W.L. Griffin, N.J. Pearson, E.A. Belousova & A. Saeed (Chemical Geology 233 (2006) 358–363). *Chem. Geol.* **233**, 350-353.

DAUPHAS, N. & ROUXEL, O. (2006): Mass spectrometry and natural variations in iron isotopes. *Mass Spectrom. Rev.* **25**, 515-550.

DOHERTY, W., GREGOIRE, C. & BERTRAND, N. (2008): Polynomial mass bias functions for the internal standardization of isotope ratio measurements by multi-collector inductively coupled plasma mass spectrometry. *Spectrochim. Acta Part B* **63**, 407-414.

DOUGLAS, D.J. & FRENCH, J.B. (1988): Gas dynamics of the inductively coupled plasma mass-spectrometry interface. *J. Analyt. Atom. Spectrom.* **3**, 743-747.

EGGINS, S.M., KINGSLEY, L.P.J. & SHELLEY, J.M.G. (1998): Deposition and elemental fractionation processes during atmospheric pressure laser sampling for ICP–MS. *App. Surf. Sci. 129*, 278-286.

FOSTER, G.L. & VANCE, D. (2006): *In situ* Nd isotopic analysis of geological materials by MC–ICP–MS. *J. Analyt. Atom. Spectrom.* **21**, 288-296.

FREEDMAN, P.A. (2002): Mass bias in ICP mass spectrometers. *Geochim. Cosmochim Acta* **66**, Abstracts of the 12th Annual Goldschmidt Conference A245.

GALY, A., BELSHAW, N.S., HALICZ, L. & O'NIONS, R.K. (2001): High-precision measurement of magnesium isotopes by multiple-collector inductively coupled plasma mass spectrometry. *Int. J. Mass. Spectrom.* **208**, 89-98.

GRAHAM, S., PEARSON, N.J., JACKSON, S.E., GRIFFIN, W.L. & O'REILLY, S.Y. (2004): Tracing Cu and Fe from source to porphyry: in situ determination of Cu and Fe isotope ratios in sulfides from the Grasberg Cu–Au deposit. *Chem.*

*Geol.* **207**, 147-169

GRIFFIN, W.L., PEARSON, N.J., BELOUSOVA, E., JACKSON, S.E., VAN ACHTERBERGH, E., O'REILLY, S.Y. & SHEE, S.R. (2000): The Hf isotopic composition of cratonic mantle: LAM–MC–ICP–MS analysis of zircon megacrysts in kimberlites. *Geochim. Cosmochim. Acta.* **64**, 133-147.

GRIFFIN, W.L., GRAHAM, S., O'REILLY, S.Y. & PEARSON, N.J. (2004a): Lithospheric evolution beneath the Kaapvaal Craton: Re–Os systematics of sulfides in mantle-derived peridotites. *Chem. Geol.* **208**, 89-118.

GRIFFIN, W.L., BELOUSOVA, E.A., SHEE, S.R., PEARSON, N.J. & O'REILLY, S.Y. (2004b): Archean crustal evolution in the northern Yilgarn Craton: U–Pb and Hf-isotope evidence from detrital zircons. *Precamb. Res.* **127**, 231-282.

GRIFFIN, W.L., PEARSON, N.J., BELOUSOVA, E.A. & SAEED, A. (2006a): Comment: Hf-isotope heterogeneity in zircon 91500. *Chem. Geol.* **233**, 358-363.

GRIFFIN, W.L., BELOUSOVA, E.A., WALTERS, S.G. & O'REILLY, S.Y. (2006b): Archean and Proterozoic crustal evolution in the Eastern Succession of the Mt Isa District, Australia: U–Pb and Hf-isotope studies of detrital zircons. *Aust. J. Earth Sci*. **53**, 125-150.

GRIFFIN, W.L., PEARSON, N.J., BELOUSOVA, E.A. & SAEED, A. (2007): Reply to "Comment to short-communication 'Comment: Hf-isotope heterogeneity in zircon 91500' by W.L. Griffin, N.J. Pearson, E.A. Belousova & A. Saeed (Chemical Geology 233 (2006) 358-363)" by F. Corfu. *Chem. Geol*. **244**, 354-356.

GUILLONG, M., HORN, I. & GÜNTHER, D. (2003): A comparison of 266 nm, 213 nm and 193 nm produced from a single solid state Nd:YAG laser for laser ablation ICP–MS. *J. Analyt. Atom. Spectrom*. **18**, 1224-1230.

GÜNTHER, D. & KOCH, J. (2008): Formation of aerosols generated by laser ablation and their impact on elemental fractionation in LA–ICP–MS. *In* Laser Ablation ICP–MS in the Earth Sciences: Current Practices and Outstanding Issues (P. Sylvester, *ed*.). *Mineral. Assoc. Can. Short Course Series* **40**, 19-34.

HABFAST, K. (1998): Fractionation correction and multiple collectors in thermal ionization isotope ratio mass spectrometry. *Int. J. Mass Spec.* **176**, 133–148.

HART, S.R. & ZINDLER, A. (1989): Isotopic fractionation laws: A test using calcium. *Int. J. Mass Spec. Ion. Proc.* **89**, 287-301.

HEUMANN, K.G., GALLUS, S.M., RÄDINGER, G. & VOGL, J. (1998): Precision and accuracy in isotope ratio measurements by plasma source mass spectrometry. *J. Analyt. Atom. Spectrom.* **13**, 1001-1008.

HIRATA, T. (1996): Lead isotopic analysis using multiple collector – inductively coupled plasma mass spectrometry coupled with modified external correction procedure for mass discrimination effect. *Analyst* **121**, 1407-1411.

HIRATA, T. (1997): Isotopic variations in germanium in iron and stony meteorites. *Geochim. Cosmochim. Acta.* **61**, 4439-4448.

HIRATA, T., HATTORI, M. & TANAKA, T. (1998): *In situ* osmium isotope ratio analyses of iridosmines by laser ablation–multiple collector–inductively coupled plasma mass spectrometry. *Chem. Geol*. **144**, 269-280.

HOBBS, S.E. & OLESIK, J.W. (1997) The influence of incompletely desolvated droplets and vaporizing particles on chemical matrix effects in inductively coupled plasma spectrometry: time-gated optical emission and laser induced fluorescence measurements. *Spectrochim. Acta Part B* **52**, 353-367.

HOFMANN, A. (1971): Fractionation corrections for mixed-isotope spikes of Sr, K and Pb. *Earth Planet. Sci. Lett.* **10**, 397-402.

HOLLIDAY, A.E. & BEAUCHEMIN, D. (2004): Spatial profiling of analyte signal intensities in inductively coupled mass spectrometry. *Spectrochim. Acta Part B* **59**, 291-311.

HORN, I. (2008): Comparison of femtosecond and nanosecond laser interactions with geologic matrices and their influence on accuracy and precision of LA–ICP–MS data. *In* Laser Ablation ICP–MS in the Earth Sciences: Current Practices and Outstanding Issues (P. Sylvester, *ed*.). *Mineral. Assoc. Can. Short Course Series* **40**, 53-65.

HORN, I. & GÜNTHER, D. (2003): The influence of ablation carrier gasses Ar, He and neon on the particle size distribution and transport efficiencies of laser-ablation induced aerosols: implications for LA–ICP–MS. *App. Surf. Sci.* **207**, 144-157.

HORN, I. & VON BLANCKENBURG, F. (2007):

Investigation on elemental and isotopic fractionation 196nm femtosecond laser ablation multi-collector inductively coupled mass spectrometry. *Spectrochim. Acta Part B 62*, 410-422.

HORN, I., VON BLANCKENBURG, F., SCHOENBERG, R., STEINHOEFEL, G. & MARK, G. (2006): *In situ* iron isotope ratio determination using UV–femtosecond laser ablation with application to hydrothermal ore formation processes. *Geochim. Cosmochim. Acta* **70**, 3677-3688.

HOUK, R.S. & PRAPHAIRAKSIT, N. (2001): Dissociation of polyatomic ions in the inductively coupled plasma. *Spectrochimica Acta Part B* **56**, 1069-1096.

HOUK, R.S., WINGE, R.K. & CHEN, X. (1997): High speed photographic study of wet droplets and solid particles in the inductively coupled plasma. *J. Analyt. Atom. Spectrom.* **12**, 1139-1148.

IIZUKA, T. & HIRATA, T. (2005): Improvements of precision and accuracy in in situ Hf isotope microanalysis of zircon using the laser ablation-MC–ICP–MS technique. *Chem. Geol*. **220**, 121-137.

INGLE, C.P., SHARP, B.L., HORSTWOOD, M.S.A., PARRISH, R.R. & LEWIS, J.D. (2003): Instrument response functions, mass bias and matrix effects in isotope ratio measurements and semi-quantitative analysis by single and multicollector ICP–MS. *J. Analyt. Atom. Spectrom.* **18**, 219-229.

JACKSON, S.E. & GÜNTHER D. (2003): The nature and sources of laser-induced isotopic fractionation in laser ablation-multi collector–inductively coupled plasma–mass spectrometry. *J. Anal. At. Spectrom.* **18**, 205-212.

KEHM K., HAURI E.H., ALEXANDER C.M.O. & CARLSON R.W. (2003). High precision iron isotope measurements of meteoritic material by cold plasma ICP–MS. *Geochim. Cosmochim. Acta* **67**, 2879-2891.

KEMP, A.I.S., HAWKESWORTH, C.J., PATERSON, B.A. & KINNY, P.D. (2006): Episodic growth of the Gondwana supercontinent from hafnium and oxygen isotopes in zircon. *Nature* **439**, 580-583.

KOŠLER, J. (2008): Laser ablation sampling strategies for concentration and isotope ratio analyses by ICP–MS. *In* Laser Ablation ICP–MS in the Earth Sciences: Current Practices and Outstanding Issues (P. Sylvester, *ed*.). *Mineral. Assoc. Can. Short Course Series* **40**, 79-92.

KROSLAKOVA, I. & GÜNTHER, D. (2007): Elemental fractionation in laser-ablation induced coupled mass spectrometry: evidence for mass load induced matrix effects in the ICP during ablation of silicate glass. *J. Analyt. Atom. Spectrom*. **22**, 51-62.

KÜHN, H.-R., PEARSON, N.J. & JACKSON, S.E. (2007): The influence of the laser ablation process on isotopic fractionation of copper in LA–MC–ICP–MS. *J. Analyt. Atom. Spectrom.* **22**, 547-552.

LEHN, S.A., WARNER, K.A., HUANG, M. & HIEFTJE, G.M. (2002): Effect of an inductively coupled plasma mass spectrometry sampler interface on electron temperature, electron number density, gas-kinetic temperature, and analyte emission intensity upstream in the plasma. *Spectrochim. Acta Part B* **57**, 1739-1751.

LONGERICH, H.P., FRYER, B.J. & STRONG, D.F. (1987): Determination of lead isotope ratios by inductively coupled plasma–mass spectrometry ICP–MS. *Spectrochim. Acta Part B* **42**, 39-48.

LUAIS, B., TÉLOUK, P. & ALBARÈDE, F. (1997): Precise and accurate neodymium isotope measurements by plasma–source mass spectrometry. *Geochim. Cosmochim. Acta* **61**, 4847-4854.

MARÉCHAL, C., TELOUK, P. & ALBARÈDE, F. (1999): Precise analysis of copper and zinc isotopic compositions by plasma–source mass spectrometer. *Chem. Geol.* **156**, 251-273.

MCFARLANE, C.R.M. & MCCULLOCH, M.T. (2007): Coupling of *in situ* Nd–Sm systematics and U–Pb dating of monazite and allanite with application to crustal evolution studies. *Chem. Geol*. **245**, 45-60.

MCFARLANE, C. & MCCULLOCH, M. (2008): Sm–Nd and Sr isotope systematics in LREE-rich accessory minerals using LA–MC–ICP–MS. *In* Laser Ablation ICP–MS in the Earth Sciences: Current Practices and Outstanding Issues (P. Sylvester, *ed*.). *Mineral. Assoc. Can. Short Course Series* **40**, 117-133.

NIELSEN, S., REHKÄMPER, M., BAKER, J. & HALLIDAY, A.N. (2004): The precise and accurate determination of thallium isotope compositions and concentrations in water samples by MC–ICP–MS. *Chem. Geol*. **204**, 109-124.

NIU, H. & HOUK, R.S. (1996): Fundamental aspects of ion extraction in inductively coupled plasma

mass spectrometry. *Spectrochim. Acta Part B* **51**, 779-815.

NOWELL, G.M., KEMPTON, P.D., NOBLE, S.R., FITTON, J.G., SAUNDERS, A.D., MAHONEY, J.J. & TAYLOR, R.N. (1998): High precision Hf isotope measurements of MORB and OIB by thermal ionisation mass spectrometry: insights into the depleted mantle. *Chem. Geol*. **149**, 211-233.

PEARSON, N.J., ALARD, O., GRIFFIN, W.L., JACKSON, S.E. & O'REILLY, S.Y. (2002): In situ measurement of Re–Os isotopes in mantle sulfides by laser ablation multicollector-inductively coupled plasma mass spectrometry: Analytical methods and preliminary results. *Geochim. Cosmochim. Acta* **66**, 1037-1050.

PEARSON, N.J., GRIFFIN, W.L., ALARD, O. & O'REILLY, S.Y. (2006): The isotopic composition of magnesium in mantle olivine: Records of depletion and metasomatism. *Chem. Geol*. **266**, 115-133.

PIETRUSZKA, A.J., WALKER, R.J. & CANDELA, P.A. (2006): Determination of mass-dependent molybdenum isotopic variations by MC–ICP–MS: an evaluation of matrix effects. *Chem. Geol*. **225**, 121-136.

PLATZNER, I.T. (1997): *Modern isotope ratio mass spectrometry*. John Wiley & Sons, Chichester. pp 1-514.

REHKÄMPER, M. & HALLIDAY, A.N. (1998): Accuracy and long-term reproducibility of lead isotope measurements by MC–ICP–MS using an external correction of mass discrimination. *Int. J. Mass Spec. Ion Proc*. **181**, 123-133.

REHKÄMPER, M. & MEZGER, K. (2000): Investigation of matrix effects for Pb isotope ratio measurements by multiple collector ICP–MS: verification and optimized analytical protocols. *J. Analyt. Atom. Spectrom.* **15**, 1451-1460.

REHKÄMPER, M., SCHÖNBÄCHLER, M. & STIRLING, C. (2001): Multiple collector ICP–MS: Introduction to instrumentation, measurement techniques and analytical capabilities. *Geostand. News*. **25**, 23-40.

RODUSHKIN, I., AXELSSON, M.D., MALINOVKSY, D. & BAXTER, D.C. (2002): Analyte- and matrix-dependent elemental response variations in laser ablation inductively coupled plasma mass spectrometry. *J. Analyt. Atom. Spectrom.* **17**, 1223-1230.

RUSSELL W.A., PAPANASTASSIOU, D.A. & TOMBRELLO, T.A. (1978): Ca isotope fractionation on the earth and other solar system materials. *Geochim. Cosmochim. Acta* **42**, 1075-1090.

SCHMIDBERGER, S.S., SIMONETTI, A. & FRANCIS, D. (2003): Small-scale Sr isotope investigation of clinopyroxenes from peridotite xenoliths by laser ablation–MC–ICP–MS – implications for mantle metasomatism. *Chem. Geol*. **199**, 317-329.

SEGAL, I., HALICZ, L. & PLATZNER, I.T. (2003): Accurate isotope measurements of ytterbium by multiple collection inductively coupled plasma mass spectrometry applying erbium and hafnium in an improved double external normalization procedure. *J. Analyt. Atom. Spectrom.* **18**, 1217-1223.

STEVENSON, R.K. & PATCHETT, P.J. (1990): Implications for the evolution of continental crust from Hf isotope systematics of Archean detrital zircons. *Geochim. Cosmochim. Acta.* **54**, 1683-1697.

TANNER, S.D. (1991): Space charge in ICP–MS: calculation and implication. *Spectrochim. Acta Part B* **47**, 809-823.

THIRLWELL, M. (2001): Inappropriate tail corrections can cause large inaccuracy in isotope ratio determination by MC–ICP–MS. *J. Analyt. Atom. Spectrom.* **16**, 1121-1125.

THIRLWELL, M.F. (2002): Multicollector ICP–MS analysis of Pb isotopes using a $^{207}$Pb–$^{204}$Pb double spike demonstrates up to 400 ppm/amu systematic errors in Tl-normalization. *Chem. Geol*. **184**, 255-279.

TODT, W., CLIFF, R.A., HANSER, A. & HOFMANN, A.W. (1996): Evaluation of a $^{202}$Pb–$^{205}$Pb double spike for high-precision lead isotope analysis. *In:* Earth Processes: Reading the Isotope Code (Hart, S.R. & Basu, A., *eds*) **95**, Am. Geophys. Union, Washington DC, pp 429-437.

TOMASCAK, P.B. (2004): Developments in the understanding and application of lithium isotopes in the earth and planetary sciences. *In* Geochemistry of Non-traditional Stable Isotopes (Johnson, C.M., Beard, B.L. & Albarède, F., editors). *Rev. Mineral. Geochem.* **55**, 153-195. Mineral. Soc. Amer., Washington DC.

VANCE, D. & THIRLWALL, M. (2002): An assessment of mass discrimination in MC–ICP–MS using Nd isotopes. *Chem. Geol.* **185**, 227-240.

VANHAECKE, F., DAMS, R. & VANDECASTLE, C. (1993): 'Zone model' as an explanation for signal behaviour and non-spectral interferences in inductively coupled mass spectrometry. *J. Analyt. Atom. Spectrom.* **8**, 433-438.

WANG, Z., HATTENDORF, B. & GÜNTHER, D. (2006): Analyte response in laser ablation inductively coupled plasma mass spectrometry. *J. Am. Soc. Mass Spectrom.* **17**, 641-651.

WHITE, W.M., ALBARÈDE, F. & TÉLOUK, P. (2000): High-precision analysis of Pb isotope ratios by multi-collector ICP–MS. *Chem. Geol*. **167**, 257-270.

WIEDENBECK M., ALLE P., CORFU F., GRIFFIN W.L., MEIER M., OBERLI F., VON QUADT A., RODDICK J.C. & SPIEGEL W. (1995): Three natural zircon standards for U-Th-Pb, Lu-Hf, trace-element and REE analyses. Geostand. News. 19, 1-23.

WOMBACHER, F. & REHKÄMPER, M. (2003): Investigation of the mass discrimination of multiple collector ICP–MS using neodymium isotopes and the generalized power law. *J. Analyt. Atom. Spectrom.***18**, 1371-1375.

WOODHEAD, J. (2002): A simple method for obtaining highly accurate Pb isotope data by MC–ICP–MS. *J. Analyt. Atom. Spectrom*. **17**, 1381-1385.

WOODHEAD, J. & HERGT, J. (2005): A preliminary appraisal of seven natural zircon reference materials for in situ Hf isotope determination. *Geostand. Geoanal. Res*. **29**, 183-195.

WOODHEAD, J., HERGT, J., SHELLEY, M., EGGINS, S. & KEMP, R. (2004): Zircon Hf-isotope analysis with an excimer laser, depth profiling, ablation of complex geometries and concomitant age estimation. *Chem. Geol*. **209**, 121-135.

WOODHEAD, J.D., SWEARER, S., HERGT, J, & MAAS, R. (2005): *In situ* Sr-isotope analysis of carbonates by LA–MC–ICP–MS: interference corrections, high spatial resolution and an example from otolith studies. *J. Analyt. Atom. Spectrom*. **20**, 22-27.

WU, F-Y., YANG, Y-H., XIE, L-W., YANG, J-H. & XU, P. (2006): Hf compositions of the standard zircons and baddelyites used in U–Pb geochronology. *Chem. Geol*. **234**, 105-126.

YOUNG, E.D. & GALY, A. (2004): The isotope geochemistry and cosmochemistry of magnesium. *In* Geochemistry of Non-traditional Stable Isotopes (Johnson, C.M., Beard, B.L. & Albarède, F., *eds*). *Rev. Mineral. Geochem.* **55**, 197-230. Mineral. Soc. Amer., Washington DC.

YOUNG, E.D., ASH, R.D., GALY, A. & BELSHAW, N.S. (2002): Mg isotope heterogeneity in the Allende meteorite measured by UV laser ablation–MC–ICP–MS and comparisons with O isotopes. *Geochim. Cosmochim. Acta*. **66**, 683-698.

ZHU, X.K., GUO, Y., WILLIAMS, R.J.P., O'NIONS, R.K., MATTHEWS, A., BELSHAW, N.S., CANTERS, R.W., DE WAAL, E.C., WESTER, U., BURGESS, B.K., & SALVATO, B. (2002): Mass fractionation processes of transition metal isotopes. *Earth Planet. Sci. Lett.* **200**, 47-62.

# CHAPTER 8: SM–ND AND SR ISOTOPE SYSTEMATICS IN LREE-RICH ACCESSORY MINERALS USING LA–MC–ICP–MS

Chris McFarlane[1,2] & Malcolm McCulloch[1]
[1]Australian National University, Research School of Earth Sciences, Mills Road, Canberra ACT Australia
[2]Current address: University of New Brunswick, Dept. of Geology, 2 Bailey Drive,
Fredericton NB E3B5A3, Canada
E-mail: crmm@unb.ca

## INTRODUCTION

The Sm–Nd isotopic system has been widely used in the geological and planetary sciences as a geochronometer and isotopic tracer. Isotope dilution and thermal ionization mass spectrometry (TIMS) on whole rock or single mineral aliquots has conventionally been used in order to achieve the high levels of precision (<0.005% on $^{143}Nd/^{144}Nd$) necessary to document the small variations in time-integrated Nd isotope ratios arising from ancient differentiation events. In doing so, however, isotopic heterogeneities (*e.g.*, inheritance, disequilibrium) preserved at the grain scale are lost. The importance of preserving and directly targeting these grain-scale isotope heterogeneities using ion microprobe and laser ablation (MC)–ICP–MS techniques has been highlighted by studies that combine *in situ* U–Pb dating and Lu–Hf isotope characterization of zircon (Gerdes & Zeh 2006, Griffin *et al.* 2004, Harrison *et al.* 2005, Machado & Simonetti 2001, Woodhead *et al.* 2004). This approach, now widely applied to detrital and magmatic zircon populations, has been used to address first order questions about ancient lithospheric differentiation.

By analogy, combining *in situ* U–Th–Pb dating and Sm–Nd isotope characterization with LA–MC–ICP–MS can also be used to trace ancient crustal differentiation events. The ~$10^3$-fold decrease in analytical volumes afforded by LA–MC–ICP–MS compared to conventional analytical methods necessitates a commensurate increase in the absolute concentration of Nd (and Sr) in the analyte material. This technique is, therefore, applicable to LREE- (and Sr-)enriched accessory minerals, most notably monazite, allanite, titanite, and apatite although a variety of other accessory phases might also be utilized such as LREE-epidote, xenotime (*e.g.*, Schaltegger *et al.* 2005), scheelite (*e.g.*, Brugger *et al.* 2000), britholite, bastnaesite, florencite, and REE-niobates. One of the main advantages of using *in situ* Sm–Nd characterization of these phases instead of Lu–Hf in co-precipitated zircon is that many REE-bearing accessory minerals can contain upwards of 10 wt% Nd (compared to ~1 wt% Hf in zircon). As a result, laser spot diameters can in some cases be reduced to <20 μm while still maintaining sufficiently high precision. This allows fine grained material and intragranular zoning features to be characterized isotopically at the same spatial resolution as *in situ* U–Th–Pb dating techniques. Integration of Sm–Nd systematics gathered in this way with textural, compositional, and geochronological datasets provides a powerful tool to understand the evolution of geological systems (Gregory *et al.* in review).

Precise U–Th–Pb dating of monazite, allanite, titanite, and apatite is now well established and can be carried out *in situ* using a variety of electron, ion, and laser microprobe techniques (*e.g.*, Gregory *et al.* 2007, Hermann & Rubatto 2003, Simonetti *et al.* 2006, Storey *et al.* 2006, Williams *et al.* 2007, Willigers *et al.* 2002). Until recently, however, *in situ* Nd isotope characterization of these accessory minerals at the sub-grain scale was largely untested. Several studies (Foster & Vance 2006, Foster & Carter 2007, McFarlane & McCulloch 2007) have now demonstrated the viability and utility of combined *in situ* U–Pb and Sm–Nd characterization of LREE-enriched accessory minerals.

The main analytical challenges facing accurate and precise *in situ* measurement of Sm–Nd systematics in LREE-enriched accessories include: 1) peak-stripping the $^{144}Sm$ interference on $^{144}Nd$; 2) critically assessing the accuracy of corrected ratios; and 3) obtaining as accurate as possible $^{147}Sm/^{144}Nd$. Overcoming these challenges allows *in situ* Sm–Nd systematics measured by LA–MC–ICP–MS to be applied to a variety of geological applications where high spatial resolution or high sampling throughout are needed to identify initial Nd heterogeneities. We demonstrate practical

Mineralogical Association of Canada Short Course 40, Vancouver, B.C., p. 117–133.

applications of this technique to monazite-bearing hydrothermal alteration assemblages and to rapid retrieval Sm–Nd isochron ages for calc-alkaline granitoid rocks. We also explore potential coupling of *in situ* Nd and Sr isotope characterization of apatite.

## SM INTERFERENCE CORRECTIONS

In the LREE-enriched accessory minerals amenable to LA–MC–ICP–MS Sm–Nd analyses, Sm/Nd ratios vary depending on the relative compatibilities of the REE in the crystal lattice and on mineral–melt or mineral–fluid REE fractionation. The resulting Sm/Nd in these accessories can therefore be quite variable but typically fall in the range 0.05 (*e.g.*, monazite, allanite) to 1.0 (*e.g.*, xenotime). This means that there is always an isobaric interference of $^{144}$Sm on $^{144}$Nd and there is no alternative but to peak-strip this interference in order to obtain accurate Nd isotope ratios.

This Sm interference correction is complicated by the fact that $^{146}$Nd/$^{144}$Nd, which by convention is used to normalize the other Nd isotope ratios, is also affected by Sm interference. As a result mass-bias correction of $^{144}$Sm interference on $^{144}$Nd cannot be applied directly from the measured $^{146}$Nd/$^{144}$Nd. This problem can be overcome in a variety of ways:

1) by using an iterative approach as outlined by Foster & Vance (2006);
2) using $^{146}$Nd/$^{145}$Nd (itself normalized to $^{146}$Nd/$^{144}$Nd measured using pure Nd solutions) to normalize interference-corrected Nd isotope ratios (Jackson *et al.* 2001), or
3) monitoring an additional interference free invariant ratio such as $^{147}$Sm/$^{149}$Sm to correct $^{144}$Sm/$^{149}$Sm independently for peak-stripping followed by normalizing of Nd isotope ratios to interference-free $^{146}$Nd/$^{144}$Nd (McFarlane & McCulloch 2007).

The latter two-stage interference and mass-bias approach is used in the present study.

All of these approaches rely on independently establishing a working instrumental value for $^{144}$Sm/$^{147,149}$Sm. For the iterative approach as outlined by Foster & Vance (2006) this can be accomplished by measuring a well characterized REE-doped secondary standard such as NIST610 and adjusting the $^{144}$Sm/$^{147}$Sm in order to obtain the independently measured (*e.g.*, using purified solutions) values for the natural Nd isotope ratios. Isotopic and inter-element homogeneity of the reference standard at the scale of a laser pit is, therefore, essential. This step is critical for samples with Sm/Nd > 0.1, above which the corrected Nd isotope ratios become sensitive to small changes in instrumental mass bias between sessions. The measured *versus* true values for $^{144}$Sm/$^{147}$Sm and $^{146}$Nd/$^{144}$Nd (0.7219) are then used to remove $^{144}$Sm interference on $^{144}$Nd iteratively. This approach has the advantage that interference corrections are applied using isotope ratios, rather than multiplication by a raw intensity that is subject to time-dependent variability.

In the present study and as described by McFarlane & McCulloch (2007), working instrumental values for invariant Sm ratios were measured once for a pure Sm solution using the same amplifier and cup configurations used for laser ablation (see Table 8-1a). Interference of $^{144}$Sm on $^{144}$Nd is then corrected by monitoring $^{149}$Sm and using a value for $^{144}$Sm/$^{149}$Sm obtained by doping Nd standard solutions (*e.g.*, nNd-1, La Jolla) with variable Sm and iteratively refining the $^{144}$Sm/$^{149}$Sm to give the true Nd isotope ratios. The measured $^{147}$Sm/$^{149}$Sm (1.06119) and adjusted $^{144}$Sm/$^{149}$Sm (0.2103) are then used for Sm interference corrections of subsequent laser ablation data. The resulting $^{146}$Nd/$^{144}$Nd$^{true}$ is corrected for Sm interference and instrumental mass bias in a single step for each measurement cycle. The interference-free $^{146}$Nd/$^{144}$Nd is then used to make the mass-bias correction for the other Nd isotope ratios using a value of 0.7219 and applying an exponential mass-bias law. Using a two-step interference and mass-bias correction in this way (*i.e.*, one for Sm and one for Nd) ensures that day to day and within-run variations in instrumental mass-bias are fully accounted for in the acquisition. The veracity of applying interference and mass-bias corrections determined by solution to laser ablation analysis can be demonstrated by comparing Nd isotope ratios measured on the same reference standards using both approaches (see Table 8-3 below). In all cases corrections established via analyses of pure and Sm-doped Nd standard solutions yield the same reference values obtained by both solution aspiration or laser ablation.

### LA–MC–ICP–MS compared to TIMS

Whereas solution MC–ICP–MS and LA–MC–ICP–MS values overlap within error, both methods yield interference and mass-bias corrected $^{143}$Nd/$^{144}$Nd that are typically low (*i.e.*, isotopically heavy) relative to available TIMS reference values. For example, solution analysis of nNd1 and La Jolla standards by McFarlane & McCulloch (2007)

TABLE 8-1. NEPTUNE MC–ICP–MS COLLECTOR CONFIGURATION FOR ND AND SR ISOTOPE MEASUREMENTS

(a) Nd configuration and *potential* interferences

| Cup | L4 | L3 | L2 | L1 | Ax | H1 | H2 | H3 | H4 |
|---|---|---|---|---|---|---|---|---|---|
| Amplifier | 5 | 9 | 1 | 3 | 8 | 7 | 2 | 6 | 4 |
| Analyte | $^{142}$Nd | $^{143}$Nd | $^{144}$Nd | $^{145}$Nd | $^{146}$Nd | $^{147}$Sm | $^{149}$Sm | $^{153}$Eu | $^{155}$Gd |
| | $^{142}$Ce | | $^{144}$Sm | | | | | | *$^{139}La^{16}O$* |
| Interferences | | | *$^{130}Ba^{14}N$* | | *$^{130}Ba^{16}O$* *$^{132}Ba^{14}N$* | *$^{133}Cs^{14}N$* | | | |
| | | *$^{103}Rh^{40}Ar$* | *$^{104}Pd^{40}Ar$* | *$^{105}Pd^{40}Ar$* | *$^{106}Pd^{40}Ar$* | | | | |

(b) Sr configuration and monitored interferences

| Cup | L4 | L3 | L2 | L1 | Ax | H1 | H2 | H3 | H4 |
|---|---|---|---|---|---|---|---|---|---|
| Amplifier | 7 | 6 | 1 | 3 | 2 | 5 | 8 | 9 | 4 |
| Analyte | $^{83}$Kr | $^{167}$Er$^{++}$ | $^{84}$Sr | $^{85}$Rb | $^{86}$Sr | $^{173}$Yb$^{++}$ | $^{87}$Sr | $^{88}$Sr | $^{177}$Hf$^{++}$ |
| | $^{166}$Er$^{++}$ | | $^{168}$Er$^{++}$ | $^{170}$Er$^{++}$ | | | | | |
| | | | $^{84}$Kr | | $^{86}$Kr | | | | |
| Interferences | | | $^{168}$Yb$^{++}$ | $^{170}$Yb$^{++}$ | $^{172}$Yb$^{++}$ | | $^{174}$Yb$^{++}$ | $^{176}$Yb$^{++}$ | |
| | | | | | | | $^{174}$Hf$^{++}$ | $^{176}$Hf$^{++}$ | |
| | | | | | | | $^{87}$Rb | | |

Potential interferences are shown in italics.

yielded $^{143}$Nd/$^{144}$Nd values (normalized to $^{146}$Nd/$^{144}$Nd = 0.7219) systematically 40 ppm lower than the reference TIMS values whereas Foster & Vance (2006) encountered offsets between 20 and 40 ppm. This result is superficially consistent with the observations of Vance & Thirwall (2002) who encountered an offset of a similar magnitude in $^{143}$Nd/$^{144}$Nd between TIMS and solution MC–ICP–MS (Isoprobe & Nu). In contrast our $^{145}$Nd/$^{144}$Nd for pure Nd solutions, Sm-doped solutions, and LA–MC–ICP–MS typically overlap within error with the canonical value of 0.348417 (Wasserburg *et al.* 1981). This discrepancy must, at some level, be related to inherent deviations of instrumental mass bias from the empirically derived exponential mass-bias law used to normalize Nd isotope ratios. However, other studies of mass-bias systematics on the Neptune MC–ICP–MS (Pearson & Nowell 2005) indicate that mass bias for Nd on these systems most closely fits the exponential law suggesting that other factors must also influence corrected isotope ratios.

For example, Hirata *et al.* (2003) have noted that calibrating and matching Faraday cup preamplifier response (*i.e.*, identifying those with slow *vs.* fast responses to transient intensity fluctuations) increases both the accuracy and precision of MC–ICP–MS isotope ratios. We have noted the same effect on the ANU Neptune. As shown in Table 8-1, our Nd (and Sr) instrument set-up has a unique cup–amplifier configuration that was optimized to assign amplifiers with as similar as possible responses to the most important Nd (and Sr) masses (*i.e.*, $^{143–146}$Nd, $^{84–88}$Sr). Amplifiers with significantly slower or faster responses to transient signals were relegated to analytes that do not contribute to the interference or mass-bias corrections. We feel, therefore, that our Neptune configuration is sufficiently optimized to generate precise Nd and Sr isotope ratios.

More importantly, Andrén *et al.* (2004) have quantified deviations of measured/true isotope ratios ($R_{norm}$) as a function of processes occurring in the plasma and in the interface regions between the skimmer and sampling cones and the extraction lens. These authors demonstrated that tuning the ICP–MS to achieve maximum intensity typically leads to isotopically heavy ratios compared to reference values. For example, subtle sub-mm changes in torch depth (Z) can lead to large deviations in $R_{norm}$ by up to 0.6% for $^{187}$Re/$^{185}$Re. For $^{143}$Nd/$^{144}$Nd sampled by LA–MC–ICP–MS, the magnitude of $R_{norm}$ encountered in two independent studies (McFarlane & McCulloch 2007, Foster & Vance 2006) is on the order of only 0.008%. It is possible, therefore, that very subtle changes in

tuning of either the torch depth or sample gas flow rate away from maximum sensitivity could bring the corrected $^{143}Nd/^{144}Nd$ into alignment with TIMS reference values. Further experimentation to verify the effect of ICP–MS tuning on corrected $^{143}Nd/^{144}Nd$ is therefore needed.

Independent of the exact cause of the offset in our corrected $^{143}Nd/^{144}Nd$, we have encountered a systematic 40 ppm offset relative to TIMS values over two years of data collection on reference standards using the ANU Helex + Neptune LA–MC–ICP–MS system. This consistency may reflect that fact that a single operator tunes the ICP–MS to achieve the same sensitivity for each new analytical session. For comparison purposes with conventional TIMS datasets, this 40 ppm empirical correction has been applied to the data in Tables 8-4, 8-5, and 8-7 and shown in Figure 8-3, 8-5, 8-6, 8-7 and 8-9 (see below).

## SPECTRAL INTERFERENCES

Table 8-1a shows a partial list of potential isobaric isotopic and polyatomic interferences that can affect Sm–Nd ratios acquired by LA–MC–ICP–MS. Whereas isobaric interference of $^{144}Sm$ on $^{144}Nd$ is always present in natural minerals, the magnitude of additional polyatomic interferences generated in the plasma will vary according to the absolute concentration of the interfering species in the target mineral, ionization potentials, instrument tuning, and auxiliary gas composition and flow rates.

First order control on the production and relative impact of these potential interferences can be obtained by characterizing the trace element composition of target minerals prior to LA–MC–ICP–MS. Table 8-2 shows a suite of major and trace element LA–ICP–MS data for the natural accessory minerals we have analyzed so far for Sm–Nd (monazite, allanite, titanite, and apatite) using LA–MC–ICP–MS.

Inspection of these data reveals that the potential isobaric interferences involving oxides, nitrides, and argides of Ba, Cs, and the PGEs listed in Table 8-1 are unlikely to be important owing to the low absolute concentration of these elements in the accessory minerals of interest. Although high Ba concentrations have been reported in hydrothermal overgrowths on titanite (Jung & Hellebrand 2007) and allanite can contain several hundred ppm Ba (Hermann 2002), the low natural isotopic abundances of $^{130}Ba$ (0.106%) and $^{132}Ba$ (0.102%) preclude significant generation of Ba-oxide and Ba-nitride interferences. For example, work by Foster & Vance (2006) has shown that $^{130}Ba^{16}O$ is negligible for Ba/Nd as high as 10 and at oxide production rates (measured using $^{254}UO/^{238}U$) of 3%. A similar conclusion was reached by Luais *et al.* (1997) and McFarlane & McCulloch (2007). Interferences on Sm and Nd isotopes arising from production of molecules involving elements in the carrier gas with high ionization potentials such as Xe and N ($^{129}Xe^{14}N$; $^{131}Xe^{16}O$) and H ($^{142}CeH$) are also assumed to be negligible and are removed by on-peak gas background subtraction.

## BACKGROUNDS

On-peak gas backgrounds must be measured and subtracted to obtain the most accurate Nd and Sr isotope ratios. In theory, the most robust approach to background measurement is to collect 20 to 40 seconds of gas background (laser off) prior to ablation and then subtract the mean background for each analyte over this interval from the measured unknown intensities. In practice, however, when analyzing minerals with high Nd concentration (*e.g.*, monazite and allanite) that yield peak/background $>10^5$ for the Nd isotopes, subtle changes in background intensities translate into ppm-level variations in corrected isotope ratios. In these situations obtaining an on-peak gas background measurement at the start and end of a session is sufficient, allowing very high sample throughput (*e.g.*, 25 analyses/hour). In contrast, for *in situ* Sm–Nd analysis of accessory minerals with low LREE content like apatite (*e.g.*, <2000 ppm Nd), variations in background intensities must be fully accounted for to ensure the most accurate and precise Nd isotope ratios. Furthermore, in cases where a number of minerals with variable REE content are analyzed, the analytical session should be planned such that targets are analyzed sequentially as a function of increasing REE concentration. This approach is likely to minimize memory effects that contribute to higher background levels, thereby guaranteeing the highest possible precision and accuracy for low REE accessory minerals.

## PRECISION & ACCURACY

Assuming the correct instrumental values for $^{144}Sm/^{147,149}Sm$, $^{147}Sm/^{149}Sm$ or $^{146}Nd/^{145}Nd$ can be determined alternative Sm-interference correction schemes yield identical results with $2\sigma$ (standard error) analytical uncertainties typically 10–40 ppm on $^{143}Nd/^{144}Nd$, depending on the Nd content of

TABLE 8-2. REE AND TRACE-ELEMENT CHEMISTRY OF NATURAL ACCESSORY MINERALS

| | Trebilcock monazite | | Daibosatsu allanite | | Fish Canyon Tuff titanite | | *Durango apatite | | †Phalabowra apatite | |
|---|---|---|---|---|---|---|---|---|---|---|
| | ($n$ = 20) | | ($n$ = 20) | | ($n$ = 10) | | ($n$ = 30) | | ($n$ = 5) | |
| (ppm) | Mean | 1σ | Mean | 1σ | Mean | 1σ | Mean | 1σ | Mean | 1σ |
| Be | 0.06 | 0.06 | 0.53 | 0.07 | 0.01 | 0.01 | - | - | <0.01 | |
| As | 311 | 27 | 93.4 | 20.6 | 36.2 | 13.1 | 802 | 23 | 18.1 | 2.3 |
| Rb | 2.02 | 0.1 | 0.7 | 0.1 | 1.15 | 0.5 | 0.06 | 0.01 | 0.04 | 0.0 |
| Sr | 2.30 | 0.7 | 2.0 | 0.5 | 27.0 | 9.3 | 475 | 11 | 4685 | 59 |
| Y | 21130 | 148 | 4273 | 551 | 5098 | 2005 | 456 | 13 | 191 | 18 |
| Pd | <0.01 | - | <0.01 | 0.0 | 0.02 | 0.00 | - | - | <0.01 | - |
| Cd | - | - | - | - | - | - | <0.12 | - | - | - |
| Cs | <0.01 | - | <0.01 | - | 0.03 | 0.01 | <0.07 | - | <0.01 | - |
| Ba | 0.16 | 0.05 | <0.03 | - | 0.05 | 0.04 | 1.44 | 0.06 | 74.5 | 2.9 |
| La | 63146 | 5833 | 56122 | 3024 | 3179 | 337 | 3370 | 87 | 1139 | 132 |
| Ce | 154722 | 1420 | 104506 | 5909 | 11063 | 1007 | 4282 | 116 | 2803 | 295 |
| Pr | 20893 | 1874 | 8494 | 401 | 1660 | 299 | 336 | 9 | 372 | 38 |
| Nd | 87868 | 7925 | 24397 | 716 | 7390 | 2000 | 1040 | 29 | 1581 | 154 |
| Sm | 32559 | 2341 | 3191 | 99 | 1576 | 652 | 127 | 3.3 | 266 | 25 |
| Eu | 157 | 8.3 | 4.1 | 1.5 | 168 | 45 | 15.3 | 0.4 | 54.0 | 5.3 |
| Gd | 21011 | 1054 | 1902 | 81 | 1174 | 535 | 109 | 3.2 | 166 | 16 |
| Tb | 2649 | 88 | 237 | 17 | 183 | 88 | 12.9 | 0.4 | 16.1 | 1.6 |
| Dy | 8726 | 172 | 1085 | 108 | 1047 | 492 | 73.9 | 3.0 | 60.2 | 5.7 |
| Ho | 800 | 5.9 | 165 | 19 | 199 | 87 | 14.3 | 0.5 | 7.73 | 0.7 |
| Er | 1090 | 18 | 349 | 48 | 505 | 201 | 38.6 | 1.3 | 13.3 | 1.4 |
| Tm | 93 | 2.6 | 42 | 6.3 | 69 | 24 | 4.9 | 0.2 | 1.17 | 0.1 |
| Yb | 395 | 14 | 267 | 41 | 436 | 123 | 27.8 | 0.9 | 5.41 | 0.6 |
| Lu | 28 | 1.3 | 33 | 4.8 | 49 | 11 | 3.65 | 0.1 | 0.60 | 0.1 |
| Pb | 802 | 87 | 5.3 | 0.3 | 1.74 | 0.14 | 0.53 | 0.0 | 79.5 | 15 |
| Th | 144085 | 2026 | 7893 | 1625 | 259 | 60 | 181 | 8.6 | 295 | 53 |
| U | 15827 | 1763 | 615 | 58 | 147 | 28 | 8.88 | 0.4 | 60.3 | 15 |
| Sm/Nd | 0.371 | | 0.131 | | 0.213 | | 0.122 | | 0.169 | |
| $^{147}Sm/^{144}Nd$ | 0.234 | | 0.082 | | 0.134 | | 0.077 | | 0.106 | |

*Data from Trotter & Eggins, 2006; †Preliminary values

target grains and the diameter of the laser crater. For example, Figure 8-1 shows how increasing the laser crater diameter for monazite analysis affects the calculated 2σ error (based 50 cycles with 2 second integration). The lower limit on analytical precision in most natural samples is, however, limited by grain scale homogeneity and the age of the target mineral.

Independent of the interference and correction scheme adopted, the ability to reproduce within error the accepted value for an invariant Nd or Sr ratio such as $^{145}Nd/^{144}Nd$ (0.348417) and $^{86}Sr/^{88}Sr$ (0.00678) provides an important check on the internal accuracy of an analysis. Our Neptune cup configuration limits our choice of invariant Nd isotope ratio to $^{145}Nd/^{144}Nd$ which we quote in addition to the corrected $^{143}Nd/^{144}Nd$. As a demonstration, Figure 8-2 shows the long term reproducibility on the calculated initial $^{143}Nd/^{144}Nd$ for the 270 Ma Trebilcock monazite standard over a one year period. Also shown is the deviation of $^{145}Nd/^{144}Nd$ from the canonical TIMS value (expressed in term of ε units relative to 0.348417). The long term $\varepsilon^{145}Nd$ for this dataset is 0.01 ± 0.06, demonstrating the long term internal accuracy of the measurements.

**Reference standards**

In addition to being able to reproduce the natural value for $^{145}Nd/^{144}Nd$, a critical test of the accuracy of corrected $^{143}Nd/^{144}Nd$ is the ability to reproduce reference values for independently

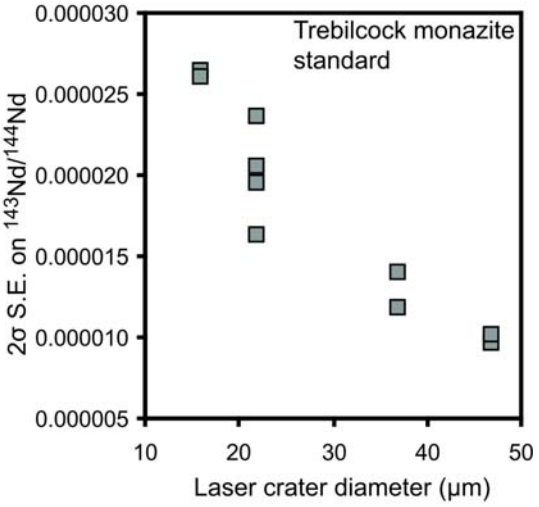


FIG. 8-1. Effect of increasing laser crater diameter on 2σ standard error for $^{143}Nd/^{144}Nd$ as measured on the Trebilcock monazite standard. The high Nd concentration of monazite (typically >9 wt.% Nd) allows high precision measurements to be obtained even for laser crater diameters of < 20 μm. TIMS-level (*e.g.*, <10 ppm) precision can be obtained on monazite for laser crater diameters of ~50μm.

characterized secondary standards. Routine analysis of NIST610 at the start of an analytical session can be used as a guide to the overall accuracy of the analytical protocol. The exclusive use of NIST610 to gauge the accuracy of unknown samples is, however, not recommended. This is in part because we have observed that the ablation behavior of NIST610 can be erratic and contrasts with that observed for the natural silicate and phosphate minerals listed in Table 8-3. This ablation behavior combined with the relatively low abundance of Sm and Nd in NIST610 adversely affects analytical precision. The presence of other trace elements doped at roughly the same concentration as Sm and Nd may also contribute to unwanted polyatomic interferences. Natural silicate and phosphate minerals also display a range of time-dependent ablation characteristics that in some cases favor the use of higher laser pulse repetition rates to increase signal intensities (*e.g.*, Durango apatite) or lower repetition rates (or rastering) to minimize time-dependent elemental fractionation (*e.g.*, Trebilcock monazite). This matrix-dependent behavior highlights the benefit of using independently characterized, matrix-matched natural or synthetic standards. Potential natural mineral standards are listed in Table 8-3.

## DETERMINING $^{147}Sm/^{144}Nd$

In order to use LA–MC–ICP–MS Sm–Nd characterization as a tool to investigate grain-scale variations in initial $^{143}Nd/^{144}Nd$, an accurate measure of $^{147}Sm/^{144}Nd$ must also be obtained. Using the two-stage interference and mass-bias correction approach adopted here, $^{147}Sm/^{144}Nd$ is calculated using the background-corrected $^{147}Sm$ and the interference-corrected $^{144}Nd$, the latter having already been corrected for mass bias relative to $^{147}Sm$ during peak-stripping. The veracity of this approach can be demonstrated by comparing $^{147}Sm/^{144}Nd$ calculated in this manner for a range of natural mineral standards that have been independently characterized using electron microprobe and quadrupole LA–ICP–MS (see McFarlane & McCulloch 2007). Whereas our $^{147}Sm/^{144}Nd$ results overlap independent estimates without further correction, Foster & Vance (2006) calculated $^{147}Sm/^{144}Nd$ using an alternative method that involved measuring $^{147}Sm/^{145}Nd$, mass-bias correcting this value to $^{146}Nd/^{144}Nd$, and multiplying the result by the canonical $^{145}Nd/^{144}Nd$. Using this approach, these authors described the need to apply a further normalization of the result for an unknown to the average $^{147}Sm/^{144}Nd$ obtained on NIST610 (*i.e.*, ~0.6277) during an analytical session.

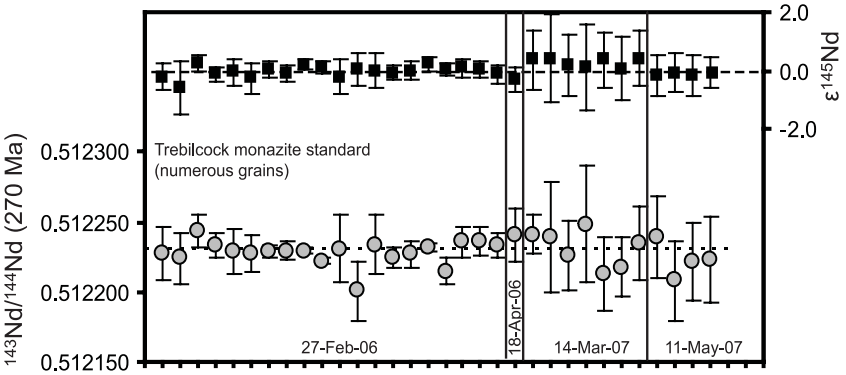


FIG. 8-2. Long term (2 year) internal ($\varepsilon^{145}Nd$) and external (initial $^{143}Nd/^{144}Nd$) reproducibility measured on numerous different grains of Trebilcock monazite liberated from a single large translucent fragment. The size of 2σ error bars in inversely proportional to laser crater diameter (see Fig. 8-1).

TABLE 8-3. POTENTIAL ND AND SR ISOTOPE MINERAL STANDARDS

(a) Sm-Nd isotope reference material

| Standard | Age (Ma) | Rock type | Nd (ppm) | $^{147}Sm/^{144}Nd$ (2σ) | $^{143}Nd/^{144}Nd$ (2σ) | Notes |
|---|---|---|---|---|---|---|
| Trebilcock monazite, Maine | 270 | Granitic pegmatite | ~98000 | 0.2322 (16)<br>0.2313 (10)<br>0.234 | 0.512593 (3)*<br>0.512586 (8)*<br>0.512623 (1)† | 2006-2008 ANU average, *n* = 33<br>June 2008 MUN, *n* = 11<br>Tomascak et al., (1998) |
| Daibosatsu allanite, Japan | 13 | Granitic pegmatite | ~25000 | 0.0840 (8)<br>0.0810 (20) | 0.512569 (3)*<br>0.512577 (10)*<br>0.512558 (8)** | 2006-2008 ANU average, *n* = 23<br>June 2008 MUN, *n* = 10<br>McFarlane & McCulloch (2007) |
| Siss3 allanite, Bergell intrusion | 34 | Tonalite | ~18600 | 0.1300 | 0.512352 (5)† | von Blanckenburg et al. (1992) |
| Fish Canyon Tuff titanite, Colorado | 28 | Felsic tuff | ~7400 | 0.1246 (80)<br>0.1143 (66) | 0.512170 (5)*<br>0.512171 (10)*<br>0.512171 (16)** | 2007 ANU average, *n* = 17<br>June 2008 MUN, *n* = 4<br>This study, multi-grain fraction |
| Fish Canyon Tuff apatite, Colorado | 28 | Felsic tuff | ~1400 | 0.0876 | 0.512213 (8)** | Foster & Vance (2006) |
| Durango apatite, Mexico | 31 | Fumarolic cavities | ~1000<br><br>~1600 | 0.0763 (14)<br>0.0765 (5)<br>0.0867 | 0.512449 (10)*<br>0.512469 (16)*<br>0.512483 (4)** | 2007 ANU average, *n* = 10<br>June 8 MUN, *n* = 7<br>Foster & Vance (2006) |

(b) Sr-isotope reference material for apatite

| | | | Sr (ppm) | $^{87}Rb/^{86}Sr$ | $^{87}Sr/^{86}Sr$ | |
|---|---|---|---|---|---|---|
| Durango apatite | 31 | | ~475 | <0.0001 | 0.70629 (2)† | 2007 ANU Triton |
| Phalabowra apatite | 2060 | Pegmatite | ~4500 | <0.0001 | 0.70738 (3)† | 2007 ANU Triton |

*analyzed by LA-MC-ICPMS; **analyzed by solution-MC-ICPMS; †analyzed by TIMS; MUN, Memorial Univ. of Nfld.

**Factors influencing precision and accuracy of $^{147}Sm/^{144}Nd$**

Laser-induced time-dependent fractionation of Sm/Nd is a potential source of error on measured $^{147}Sm/^{144}Nd$ (Günther & Koch 2008) but natural intragranular zoning makes it difficult to assess the impact of this process. The ~13 Ma Daibosatsu allanite is locally isotopically and chemically homogenous as demonstrated in Figure 8-3 by the monotonic decrease the $^{145}Nd$ ion beam signal and constant Eu* as a function of crater depth. This allows us to assess the potential for laser-induced Sm/Nd fractionation critically using a typical laser spot diameter (47 μm) and repetition rate (5 Hz). As expected, $^{155}Gd/^{142}Ce$ exhibits more severe time-dependent fractionation on the order 2.5%. By comparison, although $^{147}Sm/^{144}Nd$ fractionation is evident, the degree of laser-induced fractionation (<0.2%) is just barely resolvable outside the 2σ standard deviation on the mean. Although ablation in drilling mode using progressively smaller crater diameters will theoretically increase the degree of inter-element fractionation, this problem can be avoided by rastering the laser over the target area. The latter technique is particularly useful during analysis of Nd-rich accessory minerals like monazite and allanite. Assuming Sm/Nd fractionation levels can be minimized to <0.5% using appropriate ablation conditions, these time-dependent instrumental phenomena are likely to be completely obscured by natural percent level intragranular variations in Sm/Nd typically encountered in accessory minerals. A similar result has been obtained by several other studies investigating Yb/Hf and Lu/Hf fractionation during LA–MC–ICP–MS measurement of zircon (Hawkesworth & Kemp 2006, Lizuka & Hirata 2005, Woodhead *et al.* 2004).

In practice then, one of the most important variables affecting the precision and accuracy of $^{147}Sm/^{144}Nd$ is the degree of natural compositional zoning. This observation is analogous to LA–MC–ICP–MS analysis of Lu–Hf systematics in zircon, where magmatic differentiation can lead to large intragranular variations in Yb/Hf that must be taken into account to obtain the highest possible precision (Hawkesworth & Kemp 2006). Sm/Nd fractionation is also a common feature in magmatic accessory minerals where fractional crystallization, magma replenishment, mineral resorption, and sector zoning (*e.g.*, Rakovan *et al.* 1997) can lead to complex internal zoning patterns. Compositional zoning in metamorphic accessory minerals can be developed at similar scales and is controlled by

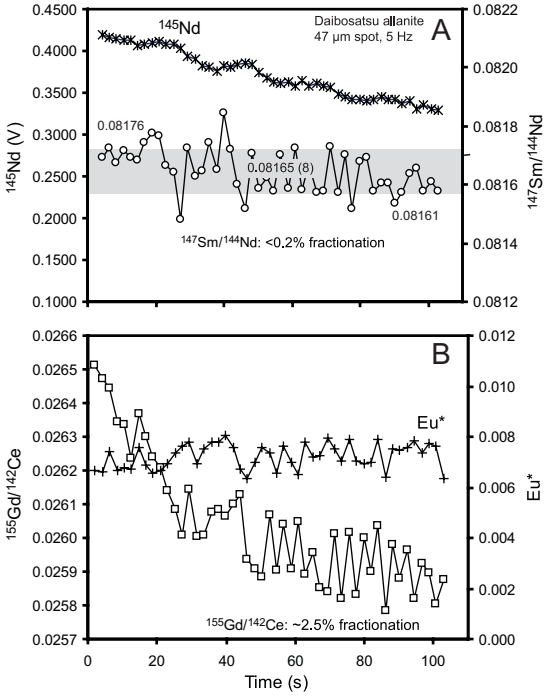


FIG. 8-3. Laser-induced time-dependent behavior measured on a chemically and isotopically homogeneous grain of Daibosatsu allanite. A) Deepening of the laser crater leads to a monotonic decrease in ion beam intensity as monitored by $^{145}$Nd and a <0.2% fractionation of $^{147}$Sm/$^{144}$Nd. This level of fractionation is typically much smaller than natural intragranular zoning in Sm/Nd. B) As expected $^{155}$Gd/$^{142}$Ce displays a significantly larger time-dependent fractionation of ~2.5%. The constant Eu* also attests to the chemical homogeneity of the target.

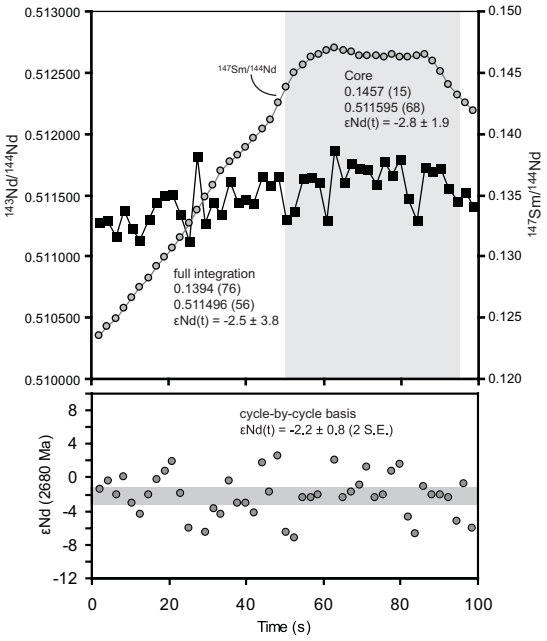


FIG. 8-4. Time series for a 2.68 Ga allanite grain from the Teton Ranges showing intracrystalline chemical and isotopic heterogeneity. The grain displays a discrete core as recorded by $^{147}$Sm/$^{144}$Nd. The corrected $^{143}$Nd/$^{144}$Nd also displays a monotonic increase approaching the core the mimics the increasing $^{147}$Sm/$^{144}$Nd ratio. Full integration of the time series yields a weighted mean 147Sm/144Nd with a ~5.5$ error that compromises the precision on the calculated εNd(*t*) value. A better estimate of εNd(*t*) can be obtained by either limiting the integration to the core region or by calculating εNd(*t*) on a cycle by cycle basis (as shown in lower panel) and taking the mean for this population. Both methods yield more precise and accurate εNd(t) values that overlap within error.

changes in mineral assemblage during prograde metamorphism, the generation and subsequent crystallization of partial melts, and by fluid-mediated recrystallization during periods of metasomatism.

Inspecting LA–MC–ICP–MS data off-line to identify discrete compositional zones characterized by different $^{147}$Sm/$^{144}$Nd is, therefore, an important step when analyzing old (*e.g.*, Precambrian) samples. Our experience is that almost all natural samples display intragranular variations in $^{147}$Sm/$^{144}$Nd locally on the order of 10%. The top half of Figure 8-4 shows the corrected $^{143}$Nd/$^{144}$Nd and $^{147}$Sm/$^{144}$Nd for an analysis (drilling mode) of allanite from an Archean (~2.68 Ga) orthogneiss from the Teton Ranges, Wyoming. This grain displays zoning in $^{147}$Sm/$^{144}$Nd from ~0.125 at the rim to ~0.145 in the core, a difference of ~14%. Integration of the entire 100 second time series yields a fairly precise $^{143}$Nd/$^{144}$Nd of 0.511496 (55), but the associated $^{147}$Sm/$^{144}$Nd of 0.1394 (76) has an anomalously large 1σ error of ~5.5%. This translates into an imprecise εNd(2.68 Ga) of –2.5 ± 3.8 and a potentially spurious depleted mantle model age ($t_{DM}$) of 3.33 Ga. In this case, a more accurate and precise measure of the Sm–Nd systematics of this grain can be obtained by either: 1) limiting the integration to the core region, or; 2) examining the εNd value on a cycle by cycle basis and calculating a mean for the population. The first approach applied to the core region of the grain in Figure 8-4 yields $^{143}$Nd/$^{144}$Nd of 0.511595 (68), $^{147}$Sm/$^{144}$Nd of 0.1457 (15) and corresponding εNd(2.68 Ga) and $t_{DM}$ of –2.8 ± 1.9 and 3.44 Ga respectively. Alternatively, calculating an independent εNd for each cycle demonstrates that the ablation volume records a uniform initial Nd value that is scattered about a mean of –2.2. The

main problem with calculating εNd in this manner, however, is assigning a realistic analytical error to each cycle of the analysis in order to demonstrate that the calculated values define a normal distribution.

## APPLICATIONS

Analysis of Sm–Nd systematics in LREE-enriched accessory minerals by LA–MC–ICP–MS is best applied to geological problems requiring combinations of high spatial resolution, high sample throughput (*e.g.*, provenance studies), or rapid turnaround time (*e.g.*, mineral exploration). The technique is also best applied in conjunction with conventional (*i.e.*, using mineral separates) or *in situ* U–Th–Pb geochronology studies on the same grains (*e.g.*, Simonetti 2008) enabling the calculation of precise εNd(t).

### *In situ* Sm-Nd characterization of hydrothermal monazite

Monazite, with upwards of 10 wt% Nd, can be analyzed using the smallest possible laser crater diameters (typically <20 μm; Figure 8-2) thereby enabling subgrain domains to be characterized for Nd isotope systematics at the same spatial resolution as ion microprobe or LA–(MC)–ICP–MS U–Pb geochronology (Simonetti *et al.* 2008). Co-precipitation of monazite and other REE-enriched accessory minerals (*e.g.*, apatite, titanite, allanite-epidote, bastnaesite) during hydrothermal alteration associated with orogenic lode gold (Rasmussen *et al.* 2006, Vielreicher *et al.* 2003) and iron oxide–copper–gold (IOCG) deposits (Corriveau 2007) can be exploited to date and fingerprint isotopically episodes of fluid infiltration. The high spatial resolution afforded by LA–MC–ICP–MS can also be used in these settings to trace the timing and sources of superimposed cross-cutting vein arrays.

Figure 8-5a shows a cluster of monazite and xenotime inferred to have co-precipitated with a potassic (biotite + K-feldspar) alteration assemblage associated with a small Cu–Au prospect in the Southern Curnamona Province (SCP), Australia. This mineralization is associated with an episode of regional IOCG-type alteration that has been previously constrained to ~1575 Ma based on Sm–Nd isochron dating of epidote–garnet alteration (Kent *et al.* 2000).

A combination of electron microprobe imaging, compositional mapping, and spot analysis was initially used to reveal internal zoning patterns and establish the major element chemistry of monazite. Because there is clear textural evidence for co-precipitation of monazite and xenotime, the $X_{Y+HREE}$ content of monazite can be used to calculate monazite–xenotime miscibility gap temperatures for this grain (*e.g.*, Gratz & Heinrich 1997, Heinrich *et al.* 1997). These thermometry estimates, superimposed on the Y X-ray map in Figure 8-5b, record the high temperature precipitation of this potassic alteration assemblage between 550 and 600°C (assuming 3 kbar).

The grain was then analyzed for Sm–Nd systematics by LA–MC–ICP–MS using a laser spot diameter of 16 μm, producing ~0.5V $^{145}$Nd (110000 ppm total Nd). Both analyses yielded εNd(1575 Ma) of ~ –5.6, consistent with other conventional Sm–Nd studies of hydrothermal alteration in the SCP (Kent *et al.* 2000). The LA–MC–ICP–MS analytical setup we employed also provides a measure of Eu* and LREE fractionation. For example, the small Eu* (~0.5) and steep LREE-fractionation ($[Ce/Gd]_{CN}$ ~7) together with the calculated εNd are consistent with monazite precipitation from fluids of crustal affinity, potentially derived through dehydration of the oxidized lower Willyama Supergroup meta-sedimentary pile.

Finally, monazite was analyzed by quadrupole LA–ICP–MS using a larger laser spot diameter of 40 μm (Figure 8-5c) to identify whether the grains preserve evidence for enrichment of trace metals likely to have accompanied Au mineralization. Comparison of quadrupole *versus* multiple collector laser ICP–MS data for Eu* and $(Ce/Gd)_{CN}$ also confirms the accuracy of the latter technique. This exercise reveals that hydrothermal monazite does contain trace levels of Mo, Sn, and Sb suggesting that it precipitated from the same hot hypersaline brines implicated in Cu–Au–(Mo) mineralization ((Skirrow *et al.* 1999).

### Sm–Nd isochron dating of hydrothermal and magmatic rocks

The demonstrated precision and accuracy of LA–MC–ICP–MS Nd isotope characterization can also be exploited as a reconnaissance Sm–Nd isochron geochronology tool. The different LREE-partitioning behavior of accessory minerals in magmatic, metamorphic, and hydrothermal systems can lead to a range of Sm/Nd in co-precipitated phases which can be exploited to generate statistically robust multi-point isochrons. Although the generation of Sm–Nd isochrons using LA–MC–ICP–MS has been demonstrated previously using

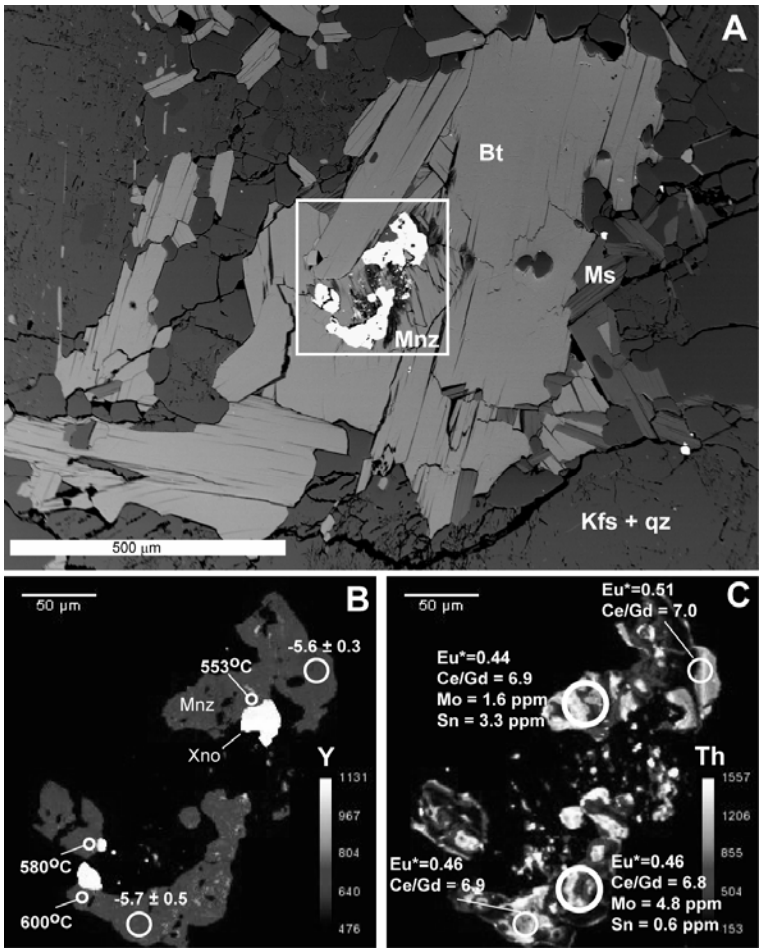


FIG. 8-5. **A**) Backscattered electron image of monazite (Mnz) cluster intergrowth with biotite (Bt) in a potassic alteration zone associated with Cu–Au mineralization in the Southern Curnamona Province, south Australia (Ms=muscovite; Kfs=K-feldspar; Qz=quartz). **B** & **C**) EPMA X-ray maps showing the distribution of Y and Th. Positions of EPMA analyses for monazite–xenotime thermometry, LA–MC–ICP–MS spots for Nd isotope characterization, and LA–ICP–MS spots for trace element quantification are shown. Integration of these textural, chemical, and isotopic datasets allows us to reconstruct the likely fluid composition and fluid sources responsible for hydrothermal mineralization.

titanite mineral separates with a range of Sm/Nd (GEMOC Annual Report 1999, Jackson *et al.* 2001), combining Sm–Nd data for two or more accessory minerals from the same sample or from adjacent samples of different bulk composition, can significantly increase the precision of *in situ* isochron ages. It may also be advantageous to employ Sm–Nd isochron ages in cases where the U–Pb system in minerals like zircon has been disturbed by recent or ancient Pb loss.

As an example, Figure 8-6a and Table 8-4 show the results of combining hydrothermal monazite, allanite, and LREE-enriched epidote from potassic and calcic-sodic alteration zones from two nearby Cu–Au prospects in the SCP described above. All analyses were obtained in standard polished thin sections with target locations guided by optical and BSE images. Large LREE epidote surrounded by quartz was analyzed with the largest possible laser spot diameter on the ANU Helex system (233 µm). This six point isochron yields a precise Sm–Nd age of 1561 ± 39 Ma (2σ) that overlaps with a conventional garnet–epidote Sm–Nd errorchron age of 1575 ± 85 Ma (Kent *et al.* 2000). Whereas these independent *in situ* and conventional datasets yield the same initial $^{143}Nd/^{144}Nd$, the textural control inherent to the *in situ* approach minimizes the potential for isotopic mixing (*e.g.*, by excluding older inherited inclusions) and allows anomalous data points to be rejected on the basis of legitimate petrographic or intragranular zoning criteria. These features facilitate the construction of statistically meaningful (*i.e.*, MSWD ~1) isochrons.

Another example, Figure 8-6b, shows the results of a LA–MC–ICP–MS Sm–Nd study of magmatic allanite and apatite separated from a ~2.1 Ga granodiorite from the Birimian of southeastern Mali, West Africa. Ion microprobe (SHRIMP) dating of magmatic zircon in conventional grain mount was used to define a near-concordant $^{207}Pb/^{206}Pb$ age of 2093 ± 5 Ma (1σ). Allanite and apatite separated from the same rock were hand picked to identify clear inclusion-free grains,

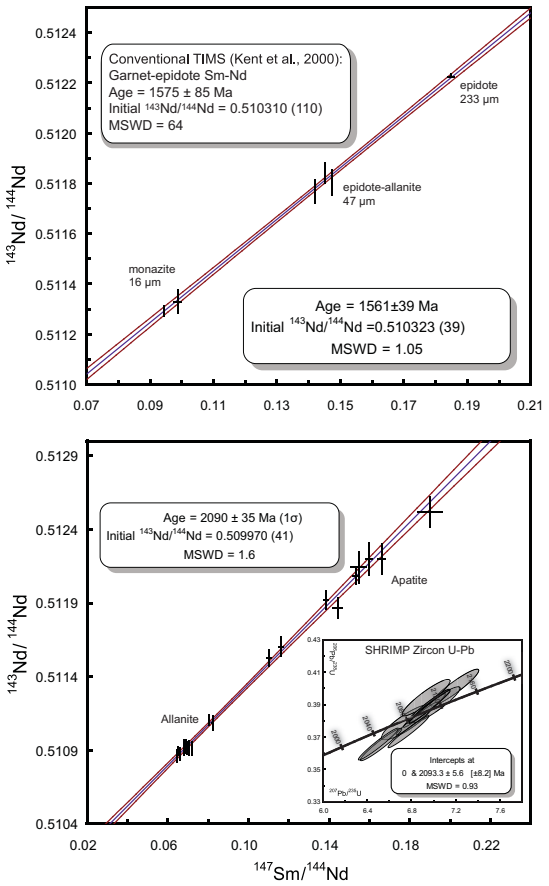


FIG. 8-6. Multiple-phase LA–MC–ICP–MS Sm–Nd isochron age for (**A**) regional hydrothermal alteration in the Southern Curnamona Province, South Australia and (**B**) a granodiorite sample from southeastern Mali, West Africa. Inset in (**A**) shows the results of a conventional TIMS-based Sm–Nd study for similar rocks. Inset in (**B**) shows the results of ion microprobe (SHRIMP) U–Pb dating of zircon extracted from the same mineral separate (author's unpublished data). The LA–MC–ICP–MS Sm–Nd isochron ages overlap within error the independently determined ages. Sm–Nd isotope data in (**A**) were collected in standard 30 µm thick thin sections whereas the allanite–apatite isochron in (**B**) was collected using a standard epoxy grain mount.

mounted in epoxy and then polished to the reveal the mid-section of the grains. Sm–Nd isotope data were collected using laser spot diameters of 47–62 µm for allanite and 105–137 µm for apatite, with larger spots used on larger grains. The resulting 20 point isochron for allanite ($n$ = 11) and apatite ($n$ = 9) yields a Sm–Nd age of 2090 ± 35 Ma (1σ) which is statistically indistinguishable from the independent zircon U–Pb ion microprobe age. An important feature of this LA–MC–ICP–MS Sm–Nd dating

TABLE 8-4. SUMMARY OF SM-ND ISOCHRON DATA

| | $^{147}Sm/^{144}Nd$ (2σ) | $^{143}Nd/^{144}Nd$ (2σ) | $^{145}Nd/^{144}Nd$ (2σ) |
|---|---|---|---|
| 2.1 Ga granodiorite, Birimian Belt of Mali, West Africa | | | |
| Ap-1 | 0.1386 (11) | 0.511921 (60) | 0.348425 (37) |
| Ap-2 | 0.1546 (35) | 0.512142 (105) | 0.348404 (57) |
| Ap-3 | 0.1660 (17) | 0.512202 (103) | 0.348405 (78) |
| Ap-4 | 0.1597(16) | 0.512200 (109) | 0.348420 (71) |
| Ap-5 | 0.1441 (20) | 0.511868 (70) | 0.348411 (44) |
| Ap-6 | 0.1161 (11) | 0.511604 (64) | 0.348403 (63) |
| Ap-7 | 0.1899 (61) | 0.512520 (101) | 0.348416 (68) |
| Ap-8 | 0.1532 (17) | 0.512084 (60) | 0.348406 (77) |
| Ap-9 | 0.1102 (11) | 0.511528 (53) | 0.348406 (46) |
| Alln-1 | 0.08041 (1) | 0.511104 (34) | 0.348431 (21) |
| Alln-2 | 0.08220 (7) | 0.511085 (48) | 0.348393 (32) |
| Alln-3 | 0.06483 (3) | 0.510897 (30) | 0.348400 (21) |
| Alln-4 | 0.07202 (7) | 0.510911 (43) | 0.348427 (20) |
| Alln-5 | 0.06960 (3) | 0.510914 (41) | 0.348428 (28) |
| Alln-6 | 0.07028 (2) | 0.510917 (47) | 0.348414 (21) |
| Alln-7 | 0.06611 (3) | 0.510884 (35) | 0.348416 (17) |
| Alln-8 | 0.06808 (6) | 0.510894 (26) | 0.348418 (16) |
| Alln-9 | 0.06469 (5) | 0.510860 (40) | 0.348410 (19) |
| Alln-10 | 0.06595 (9) | 0.510866 (29) | 0.348408 (24) |
| Alln-11 | 0.06898 (5) | 0.510926 (43) | 0.348418 (25) |
| Alln-12 | 0.06798 (4) | 0.510919 (48) | 0.348430 (22) |
| Hydrothermal alteration, southern Curnamona Province | | | |
| LREE-Epid | 0.1850 (10) | 0.512222 (12) | 0.348407 (10) |
| Alln-1 | 0.1475 (1) | 0.511804 (49) | 0.348418 (28) |
| Alln-2 | 0.1419 (1) | 0.511768 (45) | 0.348431 (35) |
| Alln-3 | 0.1450 (1) | 0.511841 (40) | 0.348410 (35) |
| Mnz-1 | 0.0944 (1) | 0.511293 (19) | 0.348414 (14) |
| Mnz-2 | 0.0987 (11) | 0.511330 (47) | 0.348402 (29) |

method is that in contrast to other microbeam techniques (*e.g.*, U–Pb dating by LA–ICP–MS or ion microprobe), the measured ratios are independent of external calibration to a reference standard.

**Coupled Nd and Sr isotope systematics of apatite**

We recently tested whether precise and accurate Nd and Sr isotope data can be collected sequentially from the same apatite mineral separates from a suite of calc-alkaline intrusive rocks. This capability is theoretically possible because apatite can contain several hundreds to thousands of ppm of both Nd and Sr and should contain negligible Rb (see Table 8-2). Collecting Nd and Sr isotope data from the same apatite grain mount would allow us to construct Nd–Sr diagrams rapidly for suites of intrusive rocks to identify potential mixing trends

between depleted and enriched reservoirs. These isotope tracer studies provide first order constraints on the petrogenesis of igneous rocks and may help to reveal magmatic processes (*e.g.*, assimilation and contamination) relevant to layered mafic and ultramafic intrusions (Boudreau & McCallum 1989) and intrusion-related Cu–Au deposits (Lang & Baker 2001). Preliminary results are surprisingly good with accurate measurement of Sr backgrounds (which can suffer from memory effects) being the main analytical challenge.

Whereas Sm–Nd characterization of apatite by LA–MC–ICP–MS is now well documented (Foster & Vance 2006, Foster & Carter 2007), methodologies to obtain precise and accurate *in situ* Sr isotope data for apatite and other geological materials are still being refined. Vroon *et al.* (2008) provided a concise overview of the current challenges still facing LA–MC–ICP–MS Sr isotope analyses of geological materials. Fietzke *et al.* (2008) have also demonstrated an alternative approach to Sr isotope measurement of marine carbonates by LA–MC–ICP–MS that improves analytical precision and which may be extendable to other geological materials. Although $^{87}$Rb interference on $^{87}$Sr in apatite is typically negligible, interferences on $^{84–88}$Sr occur as $^{84,86}$Kr in the carrier gas and from $^{40–48}$Ca-dimers and Ca-phosphates, and doubly charged HREE (*e.g.*, $^{168,170}$Er, $^{172,174,176}$Yb) and $^{176}$Hf generated during the ablation process. As a result, a cascade of interference and mass-bias corrections are required (see Vroon *et al.* 2008) to remove the gas background and isobaric molecular interferences in order to obtain accurate $^{87}$Sr/$^{86}$Sr, $^{84}$Sr/$^{86}$Sr, and $^{84}$Sr/$^{88}$Sr, the latter two invariant ratios being used to verify internal accuracy. We have also observed cryptic memory effects for $^{88}$Sr and $^{84}$Sr occurring either in the sample gas delivery tubing or on the ICP–MS cones. Lower transmission for Sr relative to Nd also necessitates targeting either large apatite grains (>~150 μm) or those unusually rich in Sr (*e.g.*, Phalabowra apatite).

In our experiment, raster analysis of NIST610 using a 233 μm spot and 6 Hz laser pulse repetition rate was used to tune the instrument, verify cup positions, and center the peaks. We first analyzed Nd isotopes in several suitably sized grains of apatite from each of eight samples ranging in composition from diorite to granite, using laser spot diameters of ~100 μm. Durango apatite was analyzed periodically throughout the session. We then switched to the Sr isotope configuration (see Table 8-1b) which monitors $^{83}$Kr, $^{84–88}$Sr, $^{85}$Rb, and doubly charged $^{167}$Er, $^{173}$Yb, and $^{177}$Hf with interference and mass-bias corrections applied offline using a sequential approach similar to the methodology described by Ramos *et al.* (2004). After retuning the instrument for Sr, an additional set of apatite grains from each sample was analyzed for Sr isotopes using a larger laser spot diameter of ~140 μm and a higher repetition rate of 6–7 Hz. Durango apatite was analyzed using the same ablation conditions between each set of unknowns. The combined Nd and Sr isotope results for Durango apatite are given in Table 8-5 and Figure 8-7. The reference $^{87}$Sr/$^{86}$Sr values for Durango and Phalabowra apatite were measured on the ANU ThermoFinnigan Triton TIMS using conventional purified solutions (M. Norman, pers. comm.)

The accumulation and slow decay of $^{88}$Sr and $^{84}$Sr memory between unknowns (Fig. 8-7) made it difficult to determine how and when to measure backgrounds. Although acquisition of an initial gas background prior to turning the laser on is the recommended approach to this problem, we were interested in resolving the behavior of the background over the course of an analytical session. As a result, we opted to measure a full 100 second background between each set of unknowns and used the mean for the last 20 second tail of this analysis for background subtraction on the next set of unknowns. This exercise demonstrated that in contrast to $^{84,88}$Sr, backgrounds for $^{83}$Kr, $^{86}$Sr, $^{87}$Sr, and the doubly charged REE were steady and low throughout the session. Whereas the growth of $^{88}$Sr memory is probably related to high intensity of $^{88}$Sr relative to the other isotopes of interest, the slow decay of $^{84}$Sr (the least abundant Sr isotope) is more difficult to explain. One possibility is that the ICP–MS cones were contaminated with a variety of interfering molecular species (*e.g.*, $^{84}$Kr, $^{40}$Ca$^{44}$Ca, $^{68}$Zn$^{16}$O, $^{168}$Er$^{++}$) during tuning on NIST610.

The combined Nd and Sr isotope data for Durango (and Phalabowra) apatite compiled in Table 8-5 demonstrate excellent reproducibility compared to the reference TIMS values. Although the mean $^{84}$Sr/$^{88}$Sr for Durango apatite is low compared to the canonical value of 0.0565, we note that in this experiment the positioning of Faraday cup L2 which monitors $^{84}$Sr was not optimal owing to the low intensity of $^{84}$Sr during tuning on NIST610. This problem together with the time-dependent decay of $^{84}$Sr background after ablation of NIST610 described above suggests that alternatives to NIST610 (*e.g.*, a Sr-rich natural

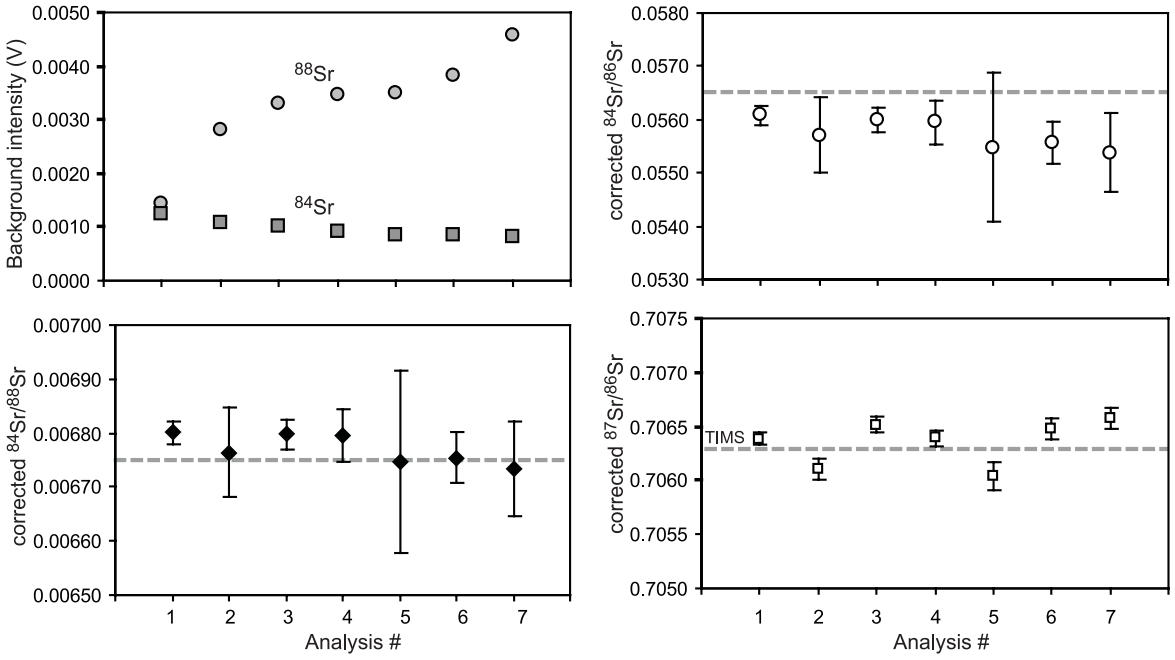


FIG. 8-7. Variations in mean $^{84,88}$Sr backgrounds and interference and mass-bias corrected Sr-isotope ratios for Durango apatite measured by LA–MC–ICP–MS.

TABLE 8-5. COMBINED *IN SITU* ND AND SR ISOTOPE CHARACTERIZATION OF DURANGO APATITE

| Durango apatite, 100-137 μm spot size, 6 Hz, ~9 Jcm$^{-2}$ | | | | | | | |
|---|---|---|---|---|---|---|---|
| | **$^{147}$Sm/$^{144}$Nd** | **$^{143}$Nd/$^{144}$Nd** | **$^{145}$Nd/$^{144}$Nd** | **Eu*** | **Ce/Gd** | | |
| Dur-1 | 0.0787 (1) | 0.512493 (45) | 0.348405 (25) | 0.418 | 9.68 | | |
| Dur-2 | 0.0778 (1) | 0.512491 (36) | 0.348411 (22) | 0.421 | 9.92 | | |
| Reference | | 0.512483 (20) | | | | | |
| | | | | Raw intensities | | | |
| | **$^{87}$Sr/$^{86}$Sr** | **$^{84}$Sr/$^{86}$Sr** | **$^{84}$Sr/$^{88}$Sr** | **V$^{84}$Sr** | **V$^{86}$Sr** | **V$^{87}$Sr** | **V$^{88}$Sr** |
| Dur-1 | 0.70639 (6) | 0.0561 (2) | 0.00680 (2) | 0.028 | 0.469 | 0.338 | 4.07 |
| Dur-3 | 0.70611 (10) | 0.0557 (7) | 0.00676 (8) | 0.010 | 0.157 | 0.114 | 1.36 |
| Dur-4 | 0.70652 (8) | 0.0560 (2) | 0.00680 (3) | 0.023 | 0.383 | 0.277 | 3.33 |
| Dur-5 | 0.70639 (8) | 0.0559 (4) | 0.00680 (5) | 0.021 | 0.351 | 0.254 | 3.05 |
| Dur-6 | 0.70604 (13) | 0.0555 (14) | 0.00675 (17) | 0.010 | 0.164 | 0.119 | 1.42 |
| Dur-7 | 0.70647 (10) | 0.0556 (4) | 0.00675 (5) | 0.013 | 0.207 | 0.149 | 1.80 |
| Dur-8 | 0.70657 (10) | 0.0554 (7) | 0.00673 (9) | 0.011 | 0.182 | 0.132 | 1.58 |
| Dur-10 | 0.70632 (8) | 0.0552 (5) | 0.00672 (6) | 0.015 | 0.253 | 0.183 | 2.20 |
| mean | 0.70638 (13) | 0.0560 (2) | 0.00679 (2) | | | | |
| ANU TIMS | 0.70629 (2) | | | | | | |
| Phalabowra apatite, 47 μm, 6 Hz, ~9 Jcm$^{-2}$ | | | | | | | |
| Phal-1 | 0.70729 (6) | 0.0561 (6) | 0.00678 (7) | 0.020 | 0.353 | 0.255 | 3.064 |
| Phal-2 | 0.70730 (5) | 0.0561 (6) | 0.00678 (8) | 0.019 | 0.351 | 0.254 | 3.050 |
| ANU TIMS | 0.70738 (3) | | | | | | |

standard like Phalabowra apatite) should be used for cup alignment and tuning. Both of the above factors are likely to have contributed to the slight deviations from the canonical values for $^{84}Sr/^{86}Sr$ and $^{84}Sr/^{88}Sr$. In contrast, $^{87}Sr/^{86}Sr$ for both Durango and Phalabowra standards overlap the TIMS results suggesting that in this case interferences other than Kr and doubly charged HREE (such as Ca-dimers and phosphates) have little affect on the corrected ratios outside 2σ analytical uncertainty.

The combined Nd and Sr isotope data for apatite from the 2100 Ma magmatic suite we analyzed as unknowns are summarized in Table 8-6 and shown in Figure 8-8. In this figure each data point represents the average initial Nd and Sr isotope value for the sample with 2σ errors on $^{143}Nd/^{144}Nd(t)$ propagated from uncertainties on the measured $^{147}Sm/^{144}Nd$ and $^{143}Nd/^{144}Nd$. This dataset, constructed over the course of one analytical session, clearly discriminates granitic rocks potentially contaminated by (older?) radiogenic Sr enriched sources.

## CONCLUSIONS

Analysis of Sm–Nd systematics in LREE-enriched accessory minerals by LA–MC–ICP–MS

TABLE 8-6. PRELIMINARY RESULTS OF COMBINED ND AND SR ISOTOPE ANALYSIS OF MAGMATIC APATITE IN GRAIN MOUNT

| | $^{87}Sr/^{86}Sr(i)$ (2σ) | $^{84}Sr/^{88}Sr$ (2σ) | $^{147}Sm/^{144}Nd$ (2σ) | $^{143}Nd/^{144}Nd$ (2σ) | $^{143}Nd/^{144}Nd$ (*i*) (2σ) *t* = 2100 Ma | $^{145}Nd/^{144}Nd$ (2σ) | Eu* |
|---|---|---|---|---|---|---|---|
| MANU-78 (Diorite) | | | | | | | |
| 78-1 | 0.70231 (16) | 0.00676 (8) | 0.140 (2) | 0.511941 (83) | 0.509969 (108) | 0.348404 (36) | 0.296 |
| 78-2 | 0.70232 (21) | 0.00674 (36) | 0.148 (1) | 0.512021 (57) | 0.509933 (64) | 0.348421 (31) | 0.305 |
| 78-3 | 0.70248 (21) | 0.00676 (18) | 0.186 (2) | 0.512568 (105) | 0.509957 (126) | 0.348400 (72) | 0.379 |
| 78-4 | 0.70223 (21) | 0.00675 (08) | | | | | |
| MANU-79 (Tonalite) | | | | | | | |
| 79-1 | 0.70244 (16) | 0.00679 (8) | 0.168 (1) | 0.512282 (32) | 0.509972 (27) | 0.348429 (21) | 0.070 |
| 79-2 | 0.70219 (15) | 0.00677 (9) | 0.181 (1) | 0.512457 (28) | 0.509969 (37) | 0.348403 (26) | 0.066 |
| 79-3 | 0.70226 (19) | 0.00675 (4) | 0.171 (1) | 0.512330 (49) | 0.509971 (56) | 0.348410 (49) | 0.067 |
| 79-4 | 0.70228 (17) | 0.00676 (6) | | | | | |
| MANU-102 (Tonalite) | | | | | | | |
| 102-1 | 0.70253 (25) | 0.00676 (8) | 0.245 (9) | 0.513406 (81) | 0.510026 (192) | 0.348420 (58) | 0.184 |
| 102-2 | 0.70229 (21) | 0.00677 (8) | 0.244 (1) | 0.513384 (74) | 0.510026 (85) | 0.348420 (36) | 0.106 |
| MANU-84 | | | | | | | |
| 84-1 | 0.70198 (7) | 0.00676 (6) | 0.138 (1) | 0.511883 (56) | 0.509936 (52) | 0.348404 (37) | 0.471 |
| 84-2 | 0.70196 (8) | 0.00678 (12) | 0.149 (1) | 0.512040 (58) | 0.509944 (55) | 0.348422 (36) | 0.557 |
| 84-3 | 0.70195 (9) | 0.00679 (7) | | | | | |
| 84-4 | 0.70211 (12) | 0.00677 (9) | | | | | |
| MANU-101 | | | | | | | |
| 101-1 | 0.70242 (10) | 0.00678 (7) | 0.243 (2) | 0.513323 (56) | 0.510014 (77) | 0.348410 (38) | 0.071 |
| 101-2 | 0.70254 (15) | 0.00678 (5) | 0.226 (6) | 0.513109 (62) | 0.510024 (140) | 0.348437 (36) | 0.063 |
| 101-3 | 0.70245 (9) | 0.00680 (5) | | | | | |
| MANU-86 | | | | | | | |
| 86-1 | 0.70241 (9) | 0.00673 (5) | 0.182 (5) | 0.512522 (94) | 0.509957 (154) | 0.348435 (32) | 0.071 |
| 86-2 | 0.70239 (11) | 0.00677 (5) | 0.209 (3) | 0.512872 (60) | 0.509933 (100) | 0.348398 (45) | 0.076 |
| 86-3 | 0.70232 (6) | 0.00678 (4) | 0.223 (3) | 0.513007 (60) | 0.509877 (96) | 0.348382 (32) | 0.088 |
| MANU-106 (Granite) | | | | | | | |
| 106-1 | 0.70264 (29) | 0.00673 (16) | 0.154 (1) | 0.512124 (48) | 0.509997 (61) | 0.348408 (27) | 0.105 |
| 106-2 | 0.70338 (34) | 0.00675 (21) | 0.148 (1) | 0.512046 (47) | 0.510000 (62) | 0.348414 (30) | 0.100 |
| MANU-103 (Granite) | | | | | | | |
| 103-1 | 0.70452 (44) | 0.00682 (18) | 0.208 (2) | 0.512898 (47) | 0.510027 (70) | 0.348406 (29) | 0.047 |
| 103-2 | 0.70337 (32) | 0.00682 (18) | 0.222 (2) | 0.513031 (51) | 0.509973 (76) | 0.348392 (26) | 0.067 |

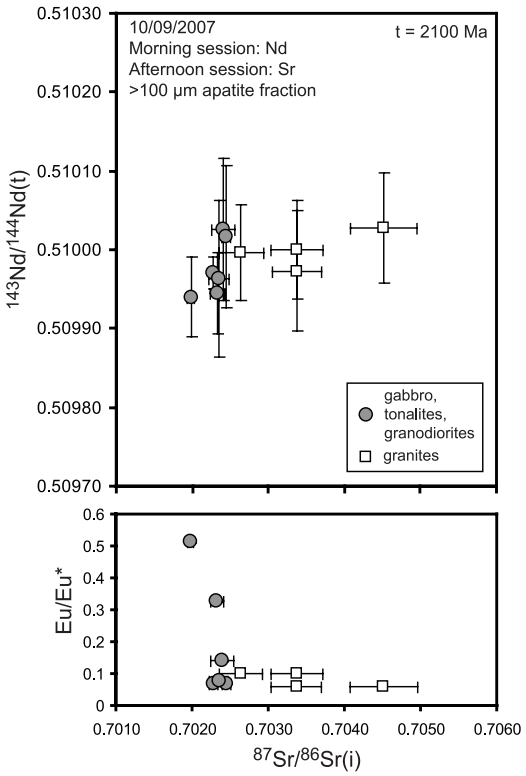


FIG. 8-8. Results of coupled Nd and Sr isotope analysis of magmatic apatite measured in conventional epoxy grain mounts using the LA–MC–ICP–MS techniques described in this study. This preliminary study reveals potential crustal contamination of granitic samples as manifest by the enriched Sr-isotope signature of magmatic apatite extracted from these samples.

represents a tool to investigate grain-scale Nd isotope heterogeneities at spatial resolutions well beyond the limits of conventional mineral separation and isotope dilution measurements. In accessory minerals significantly enriched in Nd (*e.g.*, monazite) laser spot diameters <20 µm can be utilized while still maintaining analytical precision on the order of tens of ppm. This capability allows us to probe grain-scale features such as alteration rims, zones of recrystallization, and fine intergrowths to identify Nd isotope disequilibrium. Combined with *in situ* U–(Th)–Pb dating by electron, ion, or laser microprobe techniques, accurate and precise εNd(t) can be calculated for discrete textural or compositional domains. This approach minimizes potential mixing between inherited sub-grain domains (*e.g.*, detrital cores) and provides a means (*e.g.*, using textural or compositional criteria) to identify and reject spurious data points that fall off Sm–Nd isochrons.

At the same time, the high sample throughput and capacity to obtain precise Sm–Nd data directly from thin sections can be exploited for regional reconnaissance studies of sedimentary provenance or to map Nd isotope reservoirs underlying major volcano-plutonic complexes rapidly. Coupled LA–MC–ICP–MS analysis of Nd and Sr isotopes in magmatic apatite and other Sr- and LREE-enriched minerals also holds promise as a tool to help identify magmas that have been affected by mixing or assimilation of enriched (*i.e.*, crustal) material. The same capabilities applied to magmatic and hydrothermal vein or replacement deposits might also be used to resolve the source(s) of fluids or magma batches associated with pulses of mineralization more clearly. Characterization and dissemination of widely available natural Nd and Sr isotope reference standards is a prerequisite for more widespread implementation of this LA–MC–ICP–MS technique.

## REFERENCES

ANDRÉN, H., RODUSHKIN, I., STENBERG, A., MALINOVSKY, D. & BAXTER, D.C. (2004): Sources of mass bias and isotope ratio variation in multi-collector ICP–MS: optimization of instrumental parameters based on experimental observations. *J. Analyt. Atom. Spectrom.* **19**, 1217-1224.

BOUDREAU, A.E. & MCCALLUM, I.S. (1989): Investigations of the Stillwater Complex: Part V. Apatites as indicators of evolving fluid composition. *Contrib. Mineral. Petrol.* **102**, 138-153.

BRUGGER, J., LAHAYE, Y., COSTA, S., LAMBERT, D. & BATEMAN, R. (2000): Inhomogeneous distribution of REE in scheelite and dynamics of Archaean hydrothermal systems (Mt. Charlotte and Drysdale gold deposits, Western Australia). *Contrib. Mineral. Petrol.* **139**, 251-264.

CORRIVEAU, L. (2007): Fe oxide copper–gold deposits: a Canadian perspective. *In:* Mineral deposits of Canada: A synthesis of major deposit-types, district metallogeny, the evolution of geological provinces, and exploration methods (W. Goodfellow, *ed.*), Mineral Deposits Division, Geological Association of Canada Special publication **5**.

FIETZKE, J., LIEBETRAU, V., GÜNTHER, D., GÜRS, K., HAMETNER, K., ZUMHOLZ, K., HANSTEEN, T. H. & EISENHAUER, A. (2008): An alternative data acquisition and evaluation strategy for improved isotope ratio precision using LA–MC–ICP–MS

applied to stable and radiogenic strontium isotopes in carbonates. *J. Analyt. Atom. Spectrom.* DOI: 10.1039/b717706b.

FOSTER, G. L. & CARTER, A. (2007): Insights into the patterns and locations of erosion in the Himalaya – A combined fission-track and in situ Sm–Nd isotopic study of detrital apatite. *Earth Planet. Sci. Lett.* **257**, 407-418.

FOSTER, G. & VANCE, D. (2006): *In situ* Nd isotopic analysis of geological materials by laser ablation MC–ICP–MS. *J. Analyt. Atom. Spectrom.* **288**, 288-296.

GERDES, A. & ZEH, A. (2006): Combined U–Pb and Hf isotope LA–(MC–)ICP–MS analyses of detrital zircons: Comparison with SHRIMP and new constraints for the provenance and age of an Armorican metasediment in Central Germany. *Earth Planet. Sci. Lett.*, **249** 47-61.

GRATZ, R. & HEINRICH, W. (1997): Monazite–xenotime thermobarometry: Experimental calibration of the miscibility gap in the binary system $CePO_4$–$YPO_4$. *Am. Mineral.* **82**, 772-780.

GREGORY, C.J., RUBATTO, D., ALLEN, C.M., WILLIAMS, I.S., HERMANN, J. & IRELAND, T. (2007): Allanite micro-geochronology: A LA–ICP–MS and SHRIMP U–Th–Pb study. *Chem. Geol.* **245**, 162-182.

GREGORY, C.J., MCFARLANE, C.R.M., HERMANN, J. & RUBATTO, D. (in review): Tracing the evolution of calc-alkaline magmas using micro-analysis of accessory minerals. *Submitted to Chem. Geol*.

GRIFFIN, W.L., BELOUSOVA, E.A., SHEE, S.R., PEARSON, N.J. & O'REILLY, S.R. (2004): Archean crustal evolution in the northern Yilgarn Craton: U–Pb and Hf-isotope evidence from detrital zircons. *Precambrian Res.* **131**, 231-282.

GÜNTHER, D. & KOCH, J. (2008): Formation of aerosols generated by laser ablation and their impact on elemental fractionation in LA–ICP–MS. *In* Laser Ablation ICP–MS in the Earth Sciences: Current Practices and Outstanding Issues (P. Sylvester, *ed*.). *Mineral. Assoc. Can. Short Course Series* **40**, 19-34.

HARRISON, T.M., BLICHERT-TOFT, J., MÜLLER, W., ALBAREDE, F., HOLDEN, P. & MOJZSIS, S.J. (2005): Heterogeneous Hadean Hafnium: Evidence of Continental Crust at 4.4 to 4.5 Ga. *Science* **310**, 1947-1950.

HAWKESWORTH, C.J. & KEMP, A.I.S. (2006): Using hafnium and oxygen isotopes in zircons to unravel the record of crustal evolution. *Chem. Geol.* **226**, 144-162.

HEINRICH, W., ANDREHS, G. & FRANZ, G. (1997): Monazite–xenotime miscibility gap thermometry. I. An empirical calibration. *J. Metamorph. Geol.* **15**, 3-16.

HERMANN, J. (2002): Allanite: thorium and light rare earth element carrier in subducted crust. *Chem. Geol.* **192**, 289-306.

HERMANN, J. & RUBATTO, D. (2003): Relating zircon and monazite domains to garnet growth zones; age and duration of granulite facies metamorphism in the Val Malenco lower crust. *J. Metamorph. Geol.* **21**, 833-852.

HIRATA, T., HAYANO, Y. & OHNO, T. (2003): Improvements in precision of isotopic ratio measurements using laser ablation–multiple collector–ICP–mass spectrometry: reduction of changes in measured isotopic ratios. *J. Analyt. Atom. Spectrom.* **18**, 1283-1288.

JACKSON, S.E., PEARSON, N.J. & GRIFFIN, W.L. (2001): In situ isotope ratio determination using laser ablation (LA)–magnetic sector–ICP–MS. *In:* Laser ablation–ICP–MS in the Earth Sciences: principles and applications (P. Sylvester, *ed.*), Mineral. Assoc. Can. Short Course Series **29**, 105-120.

JUNG, S. & HELLEBRAND, E. (2007): Textural, geochronological and chemical constraints from polygenetic titanite and monogenetic apatite from a mid-crustal shear zone: An integrated EPMA, SIMS, and TIMS study. *Chem. Geol.* **241**, 88-107.

KENT, A.J.R., ASHLEY, P. & FANNING, C.M. (2000): Metasomatic alteration associated with regional metamorphism: an example from the Willyama Supergroup, South Australia. *Lithos* **54**, 33-62.

LANG, J.R. & BAKER, T. (2001): Intrusion-related gold systems: the present level of understanding. *Min. Dep.* **36**, 477-489.

LIZUKA, T. & HIRATA, T. (2005): Improvements of precision and accuracy in *in situ* Hf isotope microanalysis of zircon using the laser ablation–MC–ICP–MS technique. *Chem. Geol.* **220**, 121-137.

LUAIS, B., TELOUK, P. & ALBAREDE, F. (1997): Precise and accurate neodymium isotopic measurements by plasma-source mass spectrometry. *Geochim. Cosmochim. Acta* **61**,

4847-4854.

MACHADO, N. & SIMONETTI, A. (2001): U–Pb dating and Hf isotopic composition of zircon by laser ablation–MC–ICP–MS. *In:* Laser ablation–ICP–MS in the Earth Sciences: principles and applications (P. Sylvester, *ed.*), Mineral. Assoc. Can. Short Course **29**, 121-146.

MCFARLANE, C.R.M. & MCCULLOCH, M.T. (2007): Coupling of *in situ* Sm–Nd systematics and U–Pb dating of monazite and allanite with applications to crustal evolution studies. *Chem. Geol.* **245**, 45-60.

PEARSON, D.G. & NOWELL, G.M. (2005): Accuracy and precision in plasma ionisation multi-collector mass spectrometry: constraints from Neodymium and Hafnium isotope measurements. In: *Plasma Source Mass Spectrometry: Current Trends and Future Developments* (G. Holland & D.R. Bandura, *eds.*), RSC Publishing, 284-314.

RAKOVAN, J., MCDANIEL, D.K. & REEDER, R. (1997): Use of surface-controlled REE sectoral zoning in apatite from Llallagua, Bolivia, to determine a single-crystal Sm–Nd age. *Earth Planet. Sci. Lett.* **146**, 329-336.

RAMOS, F.C., WOLFF, J.A. & TOLLSTRUP, D.L. (2004): Measuring $^{87}Sr/^{86}Sr$ variations in minerals and groundmass from basalts using LA–MC–ICP–MS. *Chem. Geol.* **211**, 135-158.

RASMUSSEN, B., SHEPPARD, S. & FLETCHER, I.R. (2006): Testing ore deposit models using in situ U–Pb geochronology of hydrothermal monazite: Paleoproterozoic gold mineralization in northern Australia. *Geology* **34**, 77-80.

SCHALTEGGER, U., PETTKE, T., AUDÉTAT, A., REUSSER, R. & HEINRICH, C.A. (2005): Magmatic-to-hydrothermal crystallization in the W–Sn mineralized Mole Granite (NSW, Australia) Part I: Crystallization of zircon and REE-phosphates over three million years – a geochemical and U–Pb geochronological study. *Chem. Geol.* **220**, 215-235.

SIMONETTI, A., HEAMAN, L., CHACKO, T. & BANERJEE, N.R. (2006): In situ petrographic thin section U–Pb dating of zircon, monazite, and titanite using laser ablation–MC–ICP–MS. *Int. J. Mass Spectrom.* **253**, 87-97.

SIMONETTI, A., HEAMAN, L.M. & CHACKO, T.. (2008): Use of discrete-dynode secondary electron multipliers with Faradays – a '*reduced volume*' approach for *in situ* U–Pb dating of accessory minerals within petrographic thin section by LA–MC–ICP–MS. *In* Laser Ablation ICP–MS in the Earth Sciences: Current Practices and Outstanding Issues (P. Sylvester, *ed.*). *Mineral. Assoc. Can. Short Course Series* **40**, 241-264.

SKIRROW, R.G., MAAS, R. & ASHLEY, P. (1999): New age constraints for Cu–Au(–Mo) mineralisation and regional alteration in the Olary–Broken Hill region. *AGSO Research Newsletter* **31**, 22-25.

STOREY, C.D., JEFFRIES, T.E. & SMITH, M. (2006): Common lead-corrected laser ablation ICP–MS U–Pb systematics and geochronology of titanite. *Chem. Geol.* **227**, 37-52.

VANCE, D. & THIRWALL, M. (2002): An assessment of mass discrimination in MC–ICP–MS using Nd isotopes. *Chem. Geol.* **185**, 227-240.

VIELREICHER, N.M., GROVES, D.I., FLETCHER, I.R., MCNAUGHTON, N.J. & RASMUSSEN, B. (2003): Hydrothermal monazite and xenotime geochronology: a new direction for precise dating of orogenic gold mineralization. *SEG Newsletter* **53**, 1-16.

VROON, P.Z., VAN DER WAGT, B., KOORNNEEF, J. M. & DAVIES, G.R. (2008): Problems in obtaining precise and accurate Sr isotope analysis from geological materials using laser ablation MC–ICP–MS. *Anal. Bioanal. Chem.* **390**, 465-476.

WASSERBURG, G.J., JACOBSEN, S.B., DEPAOLO, D. J. & MCCULLOCH, M.T. (1981): Precise determination of Sm:Nd ratios, Sm and Nd isotopic abundances in standard solutions. *Geochim. Cosmochim. Acta* **45**, 2311-2323.

WILLIGERS, B.J.A., BAKER, J.H., KROGSTAD, E.J. & PEATE, D.W. (2002): Precise and accurate in situ Pb–Pb dating of apatite, monazite, and sphene by laser ablation multiple-collector ICP–MS. *Geochim. Cosmochim. Acta* **66**, 1051-1066.

WILLIAMS, M.L., JERCINOVIC, M.J. & HETHERINGTON, C.J. (2007): Microprobe monazite geochronology: understanding geological processes by integrating composition and chronology. *Annual Reviews of Earth and Planetary Sciences* **35**, 137-175.

WOODHEAD, J., HERGT, J., SHELLEY, M., EGGINS, S. & KEMP, R. (2004): Zircon Hf-isotope analysis with an excimer laser, depth profiling, ablation of complex geometries, and concomitant age estimation. *Chem. Geol.* **209**, 121-135.

## CHAPTER 9: A GUIDE TO DEPTH PROFILING AND IMAGING APPLICATIONS OF LA–ICP–MS

Jon Woodhead, John Hellstrom, Chad Paton, Janet Hergt, Alan Greig, Roland Maas
School of Earth Sciences, The University of Melbourne,
Melbourne, Victoria, 3010, Australia
E-mail: jdwood@unimelb.edu.au

### INTRODUCTION AND BACKGROUND

Laser ablation ICP–MS is increasingly seen as a routine analytical tool for use in the Earth and environmental sciences and yet the vast majority of applications still employ static spot analyses or simple traverses. LA–ICP–MS systems, however, are also ideally suited to both depth profiling analysis and imaging[1] applications (the two considered together in this contribution since their successful implementation requires understanding of a number of common issues). Compared to existing methods, LA–ICP–MS offers the potential for rapid analysis, an extremely wide dynamic range, relatively clean mass spectrum, depth profiling on the tens of μm scale (*cf.* SIMS), utility at a variety of scales (from μm to cm), and multi-element/isotopic capability. Despite these obvious benefits, laser ablation remains largely under-utilized, particularly in the area of imaging, when compared with other analytical methodologies *e.g.* micro-XRF, SIMS. Although the exact reasons for this lag are unclear, one possibility is that LA–ICP–MS systems represent a melding of two different technologies from different manufacturers with neither routinely providing software appropriate to the task of image analysis. Furthermore, the considerable coding resources required to implement 'in house' off-line solutions are often beyond the capabilities of most institutions. This remains an outstanding issue for manufacturers and users alike.

In reality many ICP–MS laboratories deal with depth profiling issues on a regular basis, particularly in the field of U/Pb geochronology. In this case, however, the emphasis is usually on correcting for the effects of down-hole elemental fractionation, rather than exploring real isotopic and elemental variations with depth. In the recent literature, Mason & Mank (2001) and Margetic *et al.* (2001) discussed depth profiling in general and examples for elemental and isotopic analysis are presented by Eggins *et al.* (2003) and Woodhead *et al.* (2004) respectively. We are only now starting to see uptake of ICP–MS instrumentation for imaging purposes and much of this work to date has been undertaken in the biological sciences, typically examining elemental variation in tissue samples (*e.g.* Becker *et al.* 2005, Jackson *et al.* 2006). Image analysis of geological materials has been demonstrated by Treble *et al.* (2005) and we recently provided a preliminary exploration of imaging applications in the Earth sciences (Woodhead *et al.* 2007). In this publication we discuss in greater detail some of the analytical issues inherent to both depth profiling and imaging applications, with the benefit of additional practical experience acquired since our last contribution. This discussion is aimed largely at ICP–MS operators who may not previously have considered these techniques although seasoned users may also find some aspects of interest.

### ANALYTICAL ISSUES AND THEIR RESOLUTION

Laser ablation systems are unique among *in situ* analytical technologies in that material sampling is conducted at (near) atmospheric pressures with the ablated material carried into the ion source by a gas stream, typically a mixture of helium and argon. Transport efficiencies are never 100% and indeed it is typical for some high-temperature condensation to occur out of the ablation 'plume' with redeposition back on to the sample surface (phenomena employed to great effect in the electronics industry for production of thin films (*e.g.*, Ashfold *et al.* 2003). These characteristics present some particular challenges for laser ablation studies which can become more pronounced during depth profiling or imaging applications. In the following sections we consider

[1] The terms 'imaging' and 'mapping' are often used interchangeably although a 'map' is, strictly speaking, a two-dimensional 'image' of a surface. Since laser ablation has the potential for establishing elemental distributions in three-dimensions, the generic term 'imaging' is preferred here.

Mineralogical Association of Canada Short Course 40, Vancouver, B.C., p. 135–145.

the possibilities for both mixing and resampling of ablation products, and how these effects can be avoided or at least minimized.

**Choice of laser system**

Many studies have been undertaken comparing the performance characteristics of different laser systems (*e.g.*, Russo *et al.* 2000, Gonzalez *et al.* 2002, Guillong *et al.* 2003) and their conclusions will not be reiterated here. We do note however the obvious limitations of laser systems which are unable to maintain a 'top hat' beam profile during drilling for depth-profiling applications. In addition lasers which couple better with the sample of interest produce more efficient ablation and tend to reduce the effects of resampling (see later sections). In both regards shorter wavelength lasers such as 193nm ArF excimers are preferred for imaging purposes.

**General cell design and residence times**

For the purpose of bulk (spot or raster) analysis it is usual practice to incorporate some form of smoothing device into ablation cell design. Many variants of this have been proposed (*e.g.*, Tunheng & Hirata 2004) but their purpose is usually to remove any high frequency oscillations from the sample stream (in particular those related to pulsing of the laser); consequently they act to mix ablated sample components thoroughly and in so doing remove noise from the signal. Although such an approach is highly desirable in many 'bulk analysis' applications, serving (for example) to lower RSD's, this is not the case during depth profiling or imaging where resolution is a key issue, and sample mixing of this type would only serve to blur the signal. It is important, therefore, as a first step towards optimizing a system for such applications that any smoothing devices be either removed or at least their operating characteristics be quantified. A variety of ways can be used to achieve this, but perhaps the easiest is to operate the laser at a low pulse rate while observing the signal at the mass spectrometer both with and without any smoothing devices fitted (see, *e.g.,* Woodhead *et al.* 2007). In this way a time constant for flushing of the cell can be established and from this appropriate pulse rates and, in the case of imaging, tracking speeds determined. Similarly cells designed with low working volumes will reduce mixing phenomena and greatly assist in profiling and imaging applications (*e.g.*, Eggins *et al.* 2005). In cases where this is not a primary design feature it may be possible to fabricate inserts which reduce the working volume (*e.g.*, Simonetti *et al.* 2008), and these can be used specifically for applications requiring high resolution.

**Depth profiling**

The application of depth profiling involves using the laser to drill down into the sample for the purposes of establishing depth–composition relationships. While this is commonly a useful goal in itself it should also be realized that depth profiling is, in addition, the best method for investigation of elemental/isotopic variation at extremely high resolution because, in this mode, theoretical resolution is limited by the depth of a single ablation pulse (typically ~0.1 μm) and this is usually far less than what can be obtained during raster analysis (limited by the diameter of a single laser spot, typically ~10 μm or so). Thus, wherever ultra-high resolution is required it may be advisable to orient samples to allow depth rather than raster analysis. In practice, however, depth profiling can be complicated by a number of phenomena not observed in typical bulk or raster analyses and it is these aspects that may have resulted in the limited uptake of the method.

The first of these issues is the potential for resampling of material in passing down-hole. This can have a variety of causes; for example, as ablation pits deepen it not only becomes more difficult for ablation products to escape but there can also be significant redeposition on the pit walls (*e.g.*, Eggins *et al.* 1998); as a result subsequent pulses may re-entrain earlier ablation products. In addition, in laser systems which are focused onto the sample surface ablation pits can diverge from the ideal 'top hat' profile with depth, with resultant removal of sidewall materials in addition to those from the base of the pit. Both processes serve to blur the depth–composition relationship. Any behavior of this type must be quantified prior to embarking on depth-profiling studies and this is most easily accomplished using composite test samples. Typically thin slivers of two or more materials of interest (ideally of known composition *e.g.* NIST glasses) are bonded together to form a layer composite with one or more compositional boundaries then present in the sample at known depths (the latter can be accurately constrained by SEM imaging of a vertical section through the composite). It is then a relatively simple matter to perform a variety of drilling experiments under differing conditions of spot size and ablation rate in

order to characterize the performance of a given analytical system. An example is shown in Figure 9-1a, using a natural zircon composite.

Downhole elemental fractionation is a well know phenomenon in laser ablation studies (*e.g.*, Fryer *et al.* 1995) and typically in bulk analysis such effects are 'averaged out' by integrating for a given time period and then normalizing to an internal standard element such as calcium (determined by other means or estimated from stoichiometric considerations). In the case of U/Pb geochronology, where the U/Pb ratio must be determined with a greater degree of accuracy a variety of other methods have been adopted to correct for the effects of downhole elemental fractionation such as extrapolation of the time–composition relationship to time t=o (*e.g.*, Košler *et al.* 2002, Horstwood 2008). However, these methods are unsuitable for

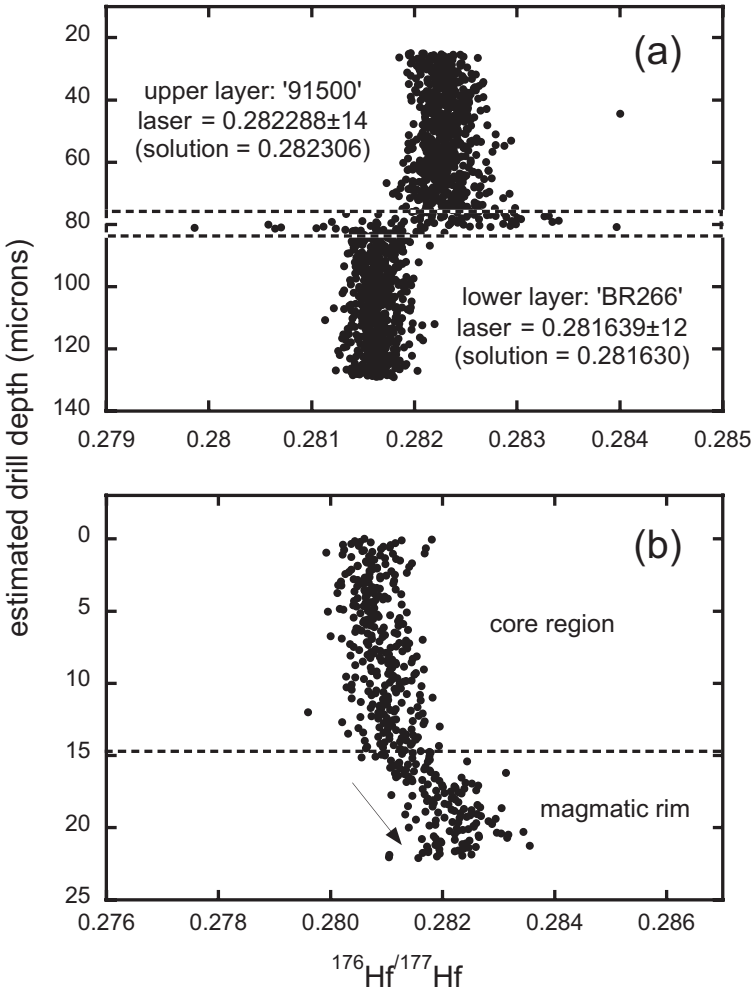


FIG. 9-1. **a)** The results of a drilling experiment employing a composite material formed from two zircon reference materials. In drilling down through the sample, in this case with a ~60 µm spot, the isotopic composition of the two layers are readily distinguished (with some minor disruption during ablation of the epoxy layer between the two). In addition isotopic compositions acquired for both the upper and lower layers agree well with those determined from solution analyses, suggesting no significant mixing during ablation. In this figure each spot represents a 0.2 second data acquisition, with 2 S.E. uncertainties quoted based upon integration of all values within a given layer. A series of parallel experiments using different spot sizes is described in Woodhead *et al.* (2004) and demonstrates the feasibility of laser depth profiling for all but very high aspect ratio pits: for optimum performance using this system we prefer to keep aspect ratios lower than 2:1 (depth:width). **b)** a more typical; 'real world' example of a zircon derived from granite of the Lachlan Fold Belt of SE Australia. In this case ablation begins in the core of the zircon (since the sample is a grain mount, polished to reveal the zircon structure) but, towards the end, passes through a magmatic rim of different isotopic composition. Separate integration of the two domains can provide additional petrogenetic insights when compared to a simple spot analysis.

actually documenting (rather than correcting for) downhole elemental variations. The only realistic approach in this case is to calibrate the downhole fractionation process by reference to a standard or material of known composition and, ideally, one that is matrix-matched to the samples under study. The calibrated elemental fractionation parameters can then be applied to unknown depth–composition profiles. Alternatively, a number of experimental approaches may be employed in an attempt to minimize fractionation effects, *e.g.*, active focusing (Hirata & Nesbitt 1995), ablation under low pressure (*e.g.*, Fliegel & Günther 2006), or femtosecond laser ablation (*e.g.*, Hergenröder *et al.* 2006, Hirata & Kon 2008). Finally we note that it is clear from all previous studies that elemental fractionation effects are strongly related to ablation pit aspect ratio (*e.g.*, Mason & Mank 2001, Woodhead *et al.* 2004) and will be exacerbated (and hence harder to model or correct for) for high aspect ratios. As a consequence ablation of a wider sample area by repeated rastering might also offer some benefits (*e.g.*, Košler 2008).

Fortunately, for the majority of isotopic applications downhole elemental fractionation is of little concern, and isotope ratios will be corrected internally for mass bias effects using an internal isotope pair (*e.g.*, $^{86}Sr/^{88}Sr$). Only in cases where significant age corrections must be made, and hence parent/daughter ratios must be accurately measured, will the above considerations come in to play.

**Imaging**

Images are typically produced by ablation of a number of parallel transects, the data from which are then combined digitally using appropriate software. In the production of elemental and isotopic images by LA–ICP–MS one of the most important considerations for obtaining appropriate resolution is the combination of spot size and translation rate. This will depend upon the results of experiments conducted to determine the residence time of materials within the cell (see above) which will vary from system to system. With our own ablation cell, for example, we typically translate the stage so as to obtain several laser pulses in the time taken to move the distance of one laser spot diameter (*e.g.*, Woodhead *et al.* 2007). Needless to say, some form of pre-ablation surface cleaning is almost always required before image acquisition (for any form of laser ablation analysis): we typically conduct the pre-ablation process at a slightly larger spot size than will be used for the actual analysis and employ more rapid translation and repetition rates. The latter can result in introduction of considerable material into the sample stream and it is advisable to disconnect the cell from the ICP–MS during this process.

The ability to produce 2-dimensional images using laser ablation raises further potential for resampling of ablation products or high temperature condensates either ahead of a translating laser spot or in traversing alongside (and hence through the ablation products of) recent transects, a phenomenon Woodhead *et al.* (2007) termed 'surface resampling'. Once more the key to understanding this process and thus limiting its deleterious effects is to perform a variety of experiments prior to imaging in order to understand system behavior better. It is important that every operator perform such tests since the degree to which these phenomena will affect a given experiment will undoubtedly be highly system-specific.

The easiest way to document likely effects is to employ composite materials of widely differing composition. In our previous studies we have used a sandwich of a NIST 610 glass juxtaposed with a NIST 616 glass (Fig. 9-2). Since the latter has extremely low trace element abundances it can effectively be used to monitor the condensate blanket formed from ablation of the adjacent NIST 610 glass. By running a variety of traverses both parallel and perpendicular to the boundary between the two glasses it is possible to document the effect of surface resampling. Once the effect has been quantified for typical analytical conditions it is then a simple matter to adjust ablation parameters, particularly raster spacing, to minimize such effects.

Finally it is important to realize that some ablation cell designs have unidirectional (as opposed to cyclonic, for example) internal gas flows. In these cases the direction of stage translation relative to gas flow can exert a significant influence of ablation behavior. To avoid artifacts generated by any processes of this type it is advisable to perform all raster analyses in the same direction (*i.e.*, returning to the same end of the ablation area before each traverse), rather than rastering backwards and forwards as is often the norm.

**Mass spectrometer matters**

The potential pitfalls when attempting depth profiling or imaging by LA–ICP–MS are not restricted to the ablation system itself; a variety of other factors related to the mass spectrometer being employed must also be considered. Some of the

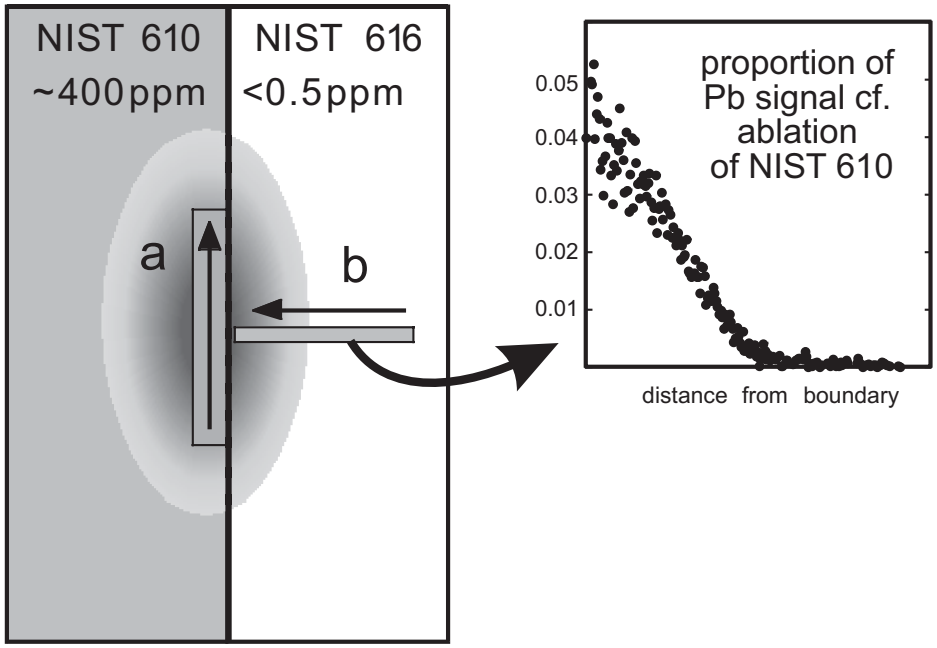


FIG. 9-2. One method for estimating optimum track spacing during parallel rasters. A composite material is produced by mounting NIST 610 and 616 glass standards adjacent to each other. Using the spot size, repetition rate and stage translation rate appropriate to the experiment under consideration, an ablation track is then produced along the boundary between the two glasses on the NIST 610 side (path 'a'). An ablation/condensate blanket spreads out onto the surrounding area and dominates elemental abundances on the low concentration NIST 616 glass side. A perpendicular track can then be made (using a smaller spot size to obtain higher resolution) which will then chart its encounter with the condensate blanket as the ablation site is approached (path 'b'). By performing a similar ablation in the NIST 610 it is possible to calibrate this 'resampling' phenomenon in terms of a proportion of the signal obtained from the original sample (see inset). Tracks can then be spaced appropriately to minimize resampling artifacts or at least contain them within acceptable limits.

more common instrumental idiosyncrasies of concern are outlined below and it is worth noting that these may be more conspicuous in imaging applications than during normal bulk analysis protocols where data are averaged over longer time intervals.

One common source of problems in elemental analysis by quadrupole ICP–MS is the calibration of detectors between different modes of operation, *e.g.*, pulse counting and analog detection. While minor errors in the accuracy of such cross calibrations may commonly go unnoticed in conventional laser ablation work, in the production of images, especially of materials where concentrations of some elements may hover around the detector 'trip point', any inaccuracies will often produce unexpected artifacts in the final images.

Similarly, in MC–ICP–MS instruments that employ mixed collector arrays (*e.g.*, both Faraday cups and ion counters), problems can be encountered with so-called 'tau effects'. These result from the relatively slow response of the faraday cup preamplifiers to changes in signal intensity (which can be a few seconds) compared to ion counters. Although algorithms are generally incorporated into the instrument software to calibrate this response, problems do occur in some cases, with the most typical symptom being an apparent change in isotope ratio correlated with rapid change in signal intensity (*e.g.* Hirata *et al.* 2003). Any such inadequacies will rapidly become evident in images derived from samples with large concentration gradients and hence rapidly fluctuating signal intensities. The veracity of the tau correction is easily monitored by measuring an isotope pair simultaneously in a faraday cup ion counter configuration and opening/closing the laser shutter, thereby simulating rapidly changing signal intensity. Measured isotope ratios should remain constant throughout this process.

Mass fractionation, isobaric interferences, and matrix effects are no less important in profiling or imaging than in solution of bulk laser analyses and must be treated accordingly. The majority of applications will involve a single matrix and so, for trace element analysis, it is usually sufficient to employ an internal standardization although this

must now be performed on a scan by scan basis. Similarly in isotopic studies an internal mass bias correction (if available) should be performed on each individual scan. For samples in which this is not possible (*e.g.*, Pb isotope analysis) the only recourse is to assess the likely magnitude of any bias effect via ablation of different matrices of known isotopic composition.

Instrumental drift is a phenomenon common to most mass spectrometers and, since large image maps can take many hours to complete, should be corrected for. Ideally reference materials should be measured at the start and end of any long analytical experiment and an extrapolated drift correction applied to each scan of the analysis period. In the production of large image maps we also allow a ~30–60 second pause at the start or end of each individual transect so that baselines can also be monitored and any variation modeled throughout the analysis period.

Finally it should be remembered that many mass spectrometers will have a finite file length structure and thus analytical periods may have to be constructed appropriately; in the worst case scenario some instruments will crash if the file length is exceeded. On some systems we have also observed unpredictable behavior if graphic displays of signal intensity are invoked during very long (hours) analyses since the amount of data stored can cause the PC to crash. Both situations can easily invoke a state of apoplexy in the operator and should be avoided!

**Software**

We noted at the start of this paper that one factor which may be responsible for the slow uptake of LA–ICP–MS for imaging and depth-profiling applications is a lack of appropriate software. This situation is understandable from a manufacturer's point of view since almost every operator will require a different approach, but nevertheless this remains a major hindrance for future development. Our laboratory struggled for a number of years in trying to use the common data-handling software packages (*e.g.*, Microsoft Excel) in this regard but eventually abandoned this in favor of writing our own code using the Igor Pro programming environment. This change was necessitated by the very large quantities of data involved and the obvious advantages of using a package designed for signal processing applications.

In designing a software utility for time-resolved analysis of any type, obvious requirements are abilities to manipulate data at the individual time-slice level, correct data for variable baselines and instrumental drift through often long analytical sessions and, finally, to perform a variety of calculations on the resulting very large data sets (*e.g.*, correction of interferences, calculation of isotope ratios). The software needs to be sufficiently flexible to be able to handle individual time-slices of slightly different duration – a phenomenon of quadrupole instruments where detectors can take a finite, and variable, amount of time to 'decide' which mode they wish to operate in for a given count rate. It can be surprisingly difficult to detect the exact start and end of some traverses if they extend beyond the bounds of irregular samples into the mounting medium where signals approximate those of the baseline. In order to construct images from such data it is very helpful if the laser ablation stage is able to record and time-stamp its location accurately at any point in its travel. Image scan lines may be delimited on the basis of automated detection of 'laser on' and 'laser off' events in the time-resolved data-set where an image lies entirely with the bounds of a sample, or in most cases by even time-based division of the data. For visualization purposes data should be interpolated to constant distance spacing to ensure that each scan row contains the same number of points. Images can then be displayed using any of a number of commercially available graphing software packages, although we have written our own code to automatically generate composite images of the type shown in Figure 9-3c.

**SOME EXAMPLES AND POSSIBILITIES FOR THE FUTURE**

Here we show some examples of depth profiling and imaging obtained in the University of Melbourne laboratory. Two different mass spectrometers were employed: elemental analyses were performed on a prototype of the Varian 810 quadrupole ICP–MS whereas isotopic analyses were conducted using a Nu Plasma multi-collector ICP–MS. The Varian instrument uses an electron multiplier for ion detection whereas in this work the Nu Plasma was used solely with Faraday cup detection. Both instruments were mated to deep UV laser ablation probes. The design attributes and capabilities of the HelEx ('HeliumExcimer') laser ablation system used in this study have been described in some detail in previous publications (*e.g.*, Eggins *et al.* 1998, Woodhead *et al.* 2004, 2005, and most thoroughly in Eggins *et al.* 2005). In

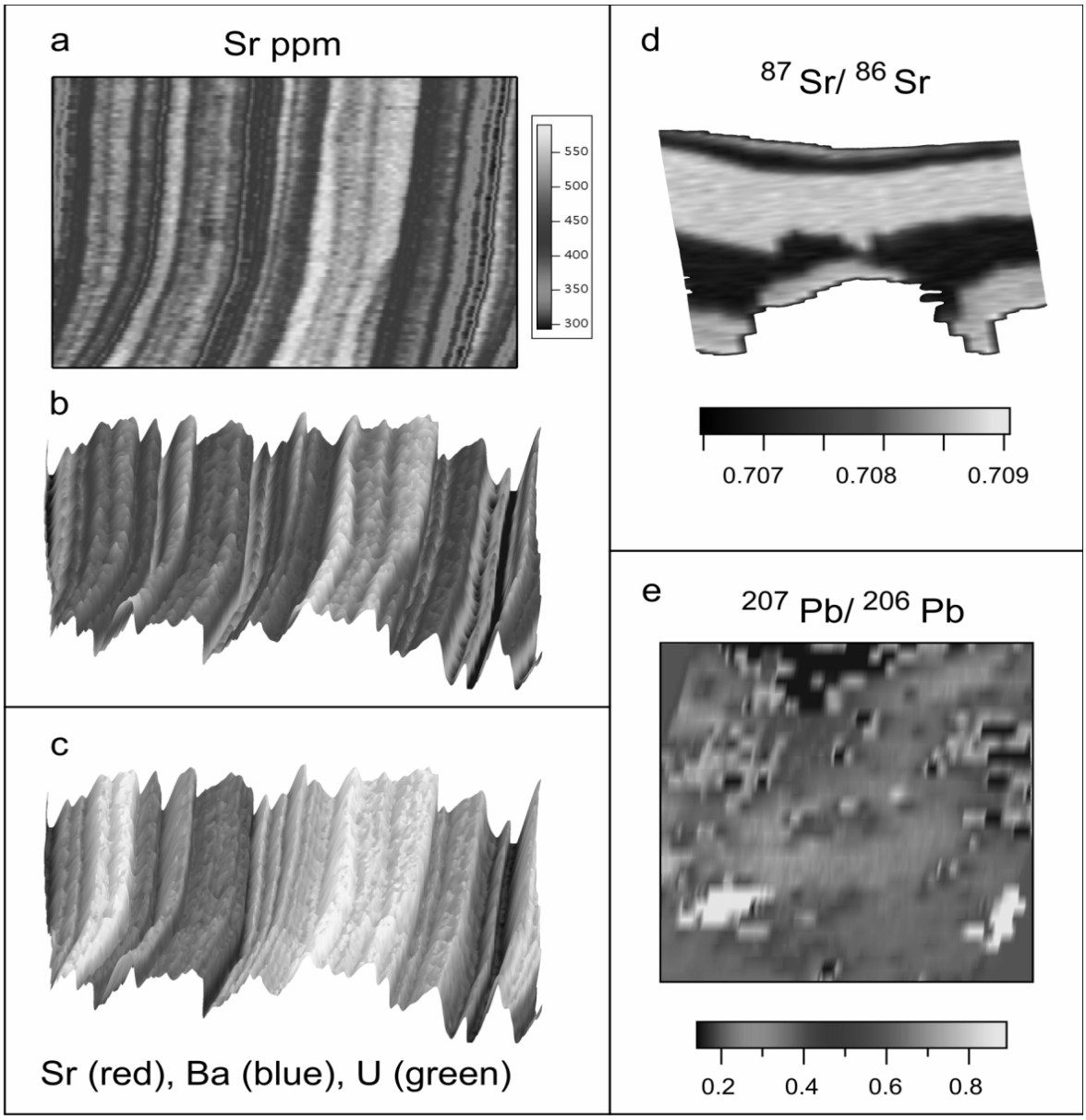


FIG. 9-3. Examples of imaging applications. **a–c)** trace element images of an ~11 x 16 mm section of speleothem. **a)** and **b)** both show Sr content in ppm: **a)** is a simple 2-dimensional representation but in **b)** the z-axis is also contoured in terms of Sr content to highlight subtle variations. **c)** is an example of a multi-element representation where additional colours have been added to plot **b)** to highlight high concentrations of two other elements, Ba and U. If required the z-axis could be used to represent variation in a fourth element. **d)** shows variation in $^{87}Sr/^{86}Sr$ ratio in a section of fish otolith ~2 x 2.4 mm in size. High ratios represent growth in a marine environment (present day seawater has an $^{87}Sr/^{86}Sr$ ratio of ~0.709) whereas lower ratios represent migration into brackish or freshwater environments. **e)** shows Pb-isotope variation in a perthitic feldspar within an area ~2.4 x 2.6 mm in size. Yellow tones indicate so-called 'common' Pb with $^{207}Pb/^{206}Pb$ ratios ~1 whereas the darker blue tones indicate highly radiogenic Pb with $^{207}Pb/^{206}Pb$ ratios approaching 0.2. Such variations are not entirely unexpected in a feldspar which has a significant U content of heterogeneous distribution (the granite is 450 Ma old) but do serve to illustrate that bulk feldspar analysis is not appropriate in such circumstances, unless an accurate correction can be made for radiogenic ingrowth. See Plate 3 for color version.

brief, the system incorporates a Lambda Physik Compex 110 ArF laser which produces a 24 x 8 mm beam of UV light at 193 nm with a pulse length of 24 ns. The image of an aperture (of variable size and shape) illuminated by the laser beam is then demagnified and projected onto the sample surface using a simple optical system, to produce very well defined ablation pits with near-vertical sides. Power density on the sample was estimated to be <5 J $cm^{-2}$. Ablation was performed in a helium atmosphere to minimize sample redeposition from the ablation plume (Kuper & Brannon, 1992, Eggins et al, 1998, Horn & Gunther, 2003). Under these conditions a 55 μm diameter spot and repetition rate of 5Hz will provide a sensitivity of ~1–2 mV/ppm for most elements on a NIST 610 glass reference material (Nu Plasma with Faraday cup detection) and ~10,000 cps/ppm on a NIST 612 glass standard (Varian ICPMS with electron multiplier detection, operated in normal sensitivity mode), for ThO/Th levels <0.5%.

As noted previously, prior to trace element analysis, samples are usually pre-ablated to clean the surface, using a spot of slightly larger size than the one eventually employed for analysis, traversed across the sample at relatively high speed compared to the actual analysis; during this process the ablation system is usually disconnected temporarily from the mass spectrometer. For the construction of elemental and isotopic images the translation of the ablation cell beneath the laser beam was computer controlled following pre-digitized paths, with translation rates, spot sizes and pulse repetition rates chosen to provide appropriate signal intensities. The following examples illustrate the use of imaging and depth profiling at a variety of scales.

**Depth profiles**

Previous discussion considered the ablation of a zircon composite shown in Figure 9-1a, modified from Woodhead *et al.* (2004). In Figure 9-1b we show a more typical 'real world' example, ablation of a zircon sample from the granites of SE Australia. Ablation actually began in the core of the crystal since this grain mount was polished to reveal the internal structure of the zircon. Toward the end of the analysis period the laser beam entered a zone in the region of the bottom rim of the crystal which has a significantly different Hf-isotope ratio. Most time-resolved software can easily integrate these two domains separately but it is advisable to characterize the laser behavior first using experiments such as that documented in Figure 9-1a before trying to interpret such results in terms of geological significance.

**Elemental imaging**

Figure 9-3 a–c shows trace element variations in a speleothem sample from the caves beneath the Nullarbor Plain of Western Australia. The cave deposits from this area have recently become accessible to study due to the development of new methods for their chronology (Woodhead *et al.* 2006). Because they are of considerable age (~2–10 Ma), however, we prefer to produce elemental images of the samples rather than assuming that simple line traverses record paleoclimate information faithfully. In this way it is possible to screen samples for apparent aberrations in the data such as alteration along micro-cracks or variations resulting from crystal growth effects.

In this particular case the area analyzed is approximately 11 x 16 mm in size and the image was produced from 80 parallel line traverses using a 121 μm spot. The total track length is 1300 mm and, using a stage translation rate of 4.8 mm/min, this represents around 5.5 hours of acquisition time. Three different images are shown demonstrating a variety of different visualization options (see figure caption). Individual elements can be singled out for study (Sr concentration is shown in **a**) but it may also be useful to employ the third dimension – the 'z' axis – to highlight subtle variations in element distribution; in the case of panel **b** we have also contoured the z-axis in terms of Sr concentration. More elaborate constructions can easily be imagined. Panel **c** takes the information from **b** and adds variation in another two elements, Ba and U. In this way it is possible to produce easily readable 'maps' that highlight hotspots in a variety of elements.

**Isotopic imaging**

The rapid proliferation of MC–ICP–MS instruments raises the intriguing possibility of obtaining images of the isotopic composition of a potentially very large range of elements; two examples are shown here, the first an $^{87}Sr/^{86}Sr$ isotope map of a fish otolith (see also Woodhead *et al.* 2007) and the second a Pb-isotope map of a K-feldspar.

The otolith is taken from a diadromous fish and shows areas of both high (~0.709) and low (~0.706) $^{87}Sr/^{86}Sr$ ratio, representing growth in marine and freshwater environments, respectively.

In this case the area ablated is approximately 2 x 2.4 mm in size and the image was produced from 28 parallel scans using a 71 μm spot. The total track length is 56 mm and, using a stage translation rate of 9.5 μm/s, this represents a total acquisition time of 98 minutes. At the time we performed this analysis, this time was longer than the allowable file length for the Nu Plasma MC–ICP–MS and so the image was constructed from 2 separate files stitched together. The Nu file structure has since been modified to allow for longer files. The $^{87}Sr/^{86}Sr$ ratio was internally corrected for mass bias effects using an $^{86}Sr/^{88}Sr$ ratio of 0.1194, with on line Ca argide and Rb corrections as documented in Woodhead *et al.* (2005).

The feldspar is taken from a high heat-producing granite from the Mount Painter region of South Australia (see McLaren *et al*., 2006). These granite plutons typically have very high concentrations of U and Th and bulk rock analyses are somewhat unusual in that they commonly display very radiogenic compositions. In this image it appears that there are distinct domains of more radiogenic composition (low $^{207}Pb/^{206}Pb$), reflecting the time-integrated heterogeneous distribution of U and Th. For the Pb-isotope map the analysis area is ~2.6 x 2.4 mm and the image was produced from 28 parallel scans using a 93 μm spot. Stage translation was 1.8mm/minute, with acquisition taking 37 minutes. In this case internal correction for mass bias is not possible and an external correction was applied based upon analysis of the NIST 610 glass run at the start and end of the ablation period (NIST Pb-isotope data from Woodhead & Hergt, 2001), although mass bias was relatively stable throughout the analysis period.

### Possibilities for the future

Applications of LA–ICP–MS are very much in their infancy and it is possible to envisage considerable further development both in terms of image processing and hardware. Recently Yuan *et al.* (2008) demonstrated the feasibility of splitting a single laser ablation stream during spot analysis and directing these into two different mass spectrometers for simultaneous acquisition of trace element and isotopic information. Clearly such an approach would be of enormous interest for imaging purposes, although the use of time of flight instrumentation could also be investigated in this regard.

Another area in which laser ablation could play a unique role would be in a combination of depth profiling and imaging methodologies to provide a 3-dimensional image capability. This would require the careful control of spot size in successive sets of parallel rasters (gradually decreasing as in a 'drill cascade', *e.g.*, Günther *et al.* 1997) and also drill rate but preliminary experiments suggest that this is an entirely achievable goal.

## CONCLUSIONS

Laser ablation sampling is ideally suited to depth profiling applications and the production of high resolution images. Compared to existing methods, LA–ICP–MS offers relatively rapid analysis (in terms of area covered per unit time), an extremely wide dynamic range, a relatively clean mass spectrum, depth profiling on the tens of μm scale, imaging at a variety of scales (from μm to cm), and multi-element/isotopic capability. A thorough understanding of system behavior is however essential prior to undertaking any such analyses but this can easily be accomplished by reference to relatively simple ablation experiments.

## ACKNOWLEDGEMENTS

Paul Devine, Roger Kemp, David Milton, and Sandra McLaren are thanked for providing the sample materials used for imaging. This work was in part made possible by a grant (to Hergt & Woodhead) from the Hermon Slade Foundation. Klaus-Peter Jochum and Takafumi Hirata are thanked for valuable comments on the manuscript.

## REFERENCES

ASHFOLD, M.N.R., CLAEYSSENS, F., FUGE, G.M. & HENLEY, S.J. (2003): Pulsed laser ablation and deposition of thin films. *Chem. Soc. Reviews* 33, 23-31.

BECKER, J.S., ZORIY, M.V., PICKHARDT, C., PALOMERO-GALLAGHER, N. & ZILLES, K. (2005): Imaging of Copper, Zinc, and Other Elements in Thin Section of Human Brain Samples (Hippocampus) by Laser Ablation Inductively Coupled Plasma Mass Spectrometry *Anal. Chem.* **77**, 3208-3216.

EGGINS, S.M., KINSLEY, L.P.J. & SHELLEY, J.M.G. (1998): Deposition and elemental fractionation processes during atmospheric pressure laser sampling for analysis by ICP–MS. *Applied Surface Science* **127-129**, 278-286.

EGGINS, S., DE DECKKER, P. & MARSHALL, J. (2003): Mg/Ca variation in planktonic

foraminifera tests: implications for reconstructing palaeo-seawater temperatures and habitat migration. *Earth Planet. Sci. Lett.* **212**, 291-306.

EGGINS, S.M., GRUN, R., MCCULLOCH, M.T., PIKE, A.W.G., CHAPPELL, J., KINSLEY, L., MORTIMER, G., SHELLEY, M., MURRAY-WALLACE, C.V. & TAYLOR, L (2005): In situ U-series dating by laser ablation multi-collector ICPMS: new prospects for Quaternary geochronology. *Quat. Sci, Rev,* **24**, 2523-2538.

FLIEGEL, D, & GÜNTHER, D. (2006): Low pressure laser ablation coupled to inductively coupled plasma mass spectrometry. *Spectrochim. Acta Part **B*** **61**, 841-849.

FRYER, B.J., JACKSON, S.E. & LONGERICH, H.P. (1995): The design, operation and role of the laser ablation microprobe coupled with an inductively coupled plasma mass spectrometer. *Can. Mineral.* **33**, 303-312.

GONZALEZ, J., MAO, X.L., ROY, J., MAO, S.S. & RUSSO, R.E. (2002): Comparison of 193, 213 and 266 nm laser ablation ICPMS. *J. Analytical Atomic Spectrometry* **17**, 1108-1113.

GUILLONG, M., HORN, I & GÜNTHER, D. (2003): A comparison of 266 nm, 213 nm and 193 nm produced from a single solid state Nd:YAG laser for laser ablation ICP–MS. *J. Analytical Atomic Spectrometry* **18**, 1224-1230.

GÜNTHER, D., FRISCHKNECHT, R., HEINRICH, C & KAHLERT, H-J. (1997): Capabilities of an argon fluoride 193 nm excimer laser for laser ablation inductively coupled plasma mass spectrometry microanalysis of geological materials. *J. Analytical Atomic Spectrometry* **12**, 939-944.

HERGENRÖDER, R., SAMEK, O. & HOMMES, V. (2006): Femtosecond laser ablation elemental mass spectrometry. *Mass Spectrometry Reviews* **25**, 551-572.

HIRATA, T. & KON, Y. (2008): Evaluation of the analytical capability of NIR femtosecond laser ablation inductively coupled plasma mass spectrometry. *Analytical Sciences* **24**, 345-353.

HIRATA, T. & NESBITT, R.W. (1995): U–Pb isotope geochronology of zircon: evaluation of the laser-probe inductively coupled plasma mass spectrometry technique. *Geochim. Cosmochim. Acta* **59**, 2491-2500.

HIRATA, T., HAYANO, Y. & OHNO, T. (2003): Improvements in precision of isotopic ratio measurements using laser ablation–multiple collector–ICP–mass spectrometry: reduction of changes in measured isotopic ratios. *J. Analytical Atomic Spectrometry* **18**, 1283-1288.

HORN, I. & GÜNTHER, D. (2003): The influence of ablation carrier gasses Ar, He, and Ne on the particle size distribution and transport efficiencies of laser ablation-induced aerosols: implications for LA–ICP–MS. *Applied Surface Science* **207**, 144-157.

JACKSON, B., HARPER, S., SMITH, L & FLINN, J. (2006): Elemental mapping and quantitative analysis of Cu, Zn, and Fe in rat brain sections by laser ablation ICP–MS. *Analytical & Bioanalytical Chemistry* **384**, 951-957.

KOŠLER, J., FONNELAND, H., SYLVESTER, P., TUBRETT, M. & PEDERSEN, R.B. (2002): U–Pb dating of detrital zircons for sediment provenance studies – a comparison of laser ablation ICPMS and SIMS techniques. *Chem. Geol.* **182**, 605-618.

KUPER, S. & BRANNON, J. (1992): Ambient gas effects on debris formed during KrF laser ablation of polyamide. *App. Physics Lett.* **60**, 1633-1635.

MARGETIC, V., BOLSHOV, M., STOCKHAUS, A., NIEMAX, K. & HERGENRÖDER, R. (2001): Depth profiling of multi-layer samples using femtosecond laser ablation. *J. Analytical Atomic Spectrometry* **16**, 616-621.

MASON, P.R.D. & MANK, A.J.R. (2001): Depth analysis by laser ablation ICP–MS. *In* Laser ablation IC–PMS in the Earth Sciences, (Sylvester, P., *ed.*) *Mineral. Assoc. Can. Short Course Series* **29**, 93-103.

MCLAREN, S., SANDIFORD, M., POWELL, R., NEUMANN, N. & WOODHEAD, J. (2006): Paleozoic intraplate crustal anatexis in the Mount Painter province, South Australia: timing, thermal budgets and the role of crustal heat production. *J. Petrol.* **47**, 2281-2302.

RUSSO, R.E., MAO, X.L., BORISOV, O.V. & LIU, H. (2000): Influence of wavelength on fractionation in laser ablation ICP–MS. *J. Analytical Atomic Spectrometry* **15**, 1115-1120.,

SIMONETTI, A., HEAMAN, L.M. & CHACKO, T.. (2008): Use of discrete-dynode secondary electron multipliers with Faradays – a '*reduced volume*' approach for *in situ* U–Pb dating of accessory minerals within petrographic thin section by LA–MC–ICP–MS. *In* Laser Ablation ICP–MS in the Earth Sciences: Current Practices and Outstanding Issues (P. Sylvester, *ed.*).

*Mineral. Assoc. Can. Short Course Series* **40**, 241-264.

TREBLE, P.C., CHAPPELL, J. & SHELLEY, J.M.G. (2005): Complex speleothem growth processes revealed by trace element mapping and scanning electron microscopy of annual layers. *Geochim. Cosmochim. Acta* **69**, 4855-4863.

TUNHENG, A. & HIRATA, T. (2004): Development of signal-smoothing device for precise elemental analysis using laser ablation ICP–mass spectrometry. *J. Analytical Atomic Spectrometry* **19**, 932-934.

WOODHEAD, J.D. & HERGT, J.M. (2001): Strontium, neodymium, and lead isotope analyses of NIST glass certified reference materials: SRM 610, 612, 614. *Geostandards Newsletter* **25**, 261-266.

WOODHEAD, J., HERGT, J., SHELLEY, M., EGGINS, S. & KEMP, R. (2004): Zircon Hf-isotope analysis with an excimer laser, depth profiling, ablation of complex geometries, and concomitant age estimation. *Chem. Geol.* **209**, 121-135

WOODHEAD, J.D., SWEARER, S., HERGT, J. & MAAS, R. (2005): *In situ* Sr-isotope analysis of carbonates by LA–MC–ICP–MS: interference corrections, high spatial resolution and an example from otolith studies. *J. Analytical Atomic Spectrometry* **20**, 22-27.

WOODHEAD, J.D., HELLSTROM, J., MAAS, R., DRYSDALE, R., ZANCHETTA, G., DEVINE, P. & TAYLOR, E. (2006): U–Pb geochronology of speleothems by MC–ICPMS. *Quat. Geochron.* **1**, 208-221.

WOODHEAD, J., HELLSTROM, J., HERGT, J., GREIG, A. & MAAS, R. (2007): Isotopic and elemental imaging of geological materials by laser ablation Inductively Coupled Plasma mass spectrometry. *Geostandards & Geoanalytical Research* **31**, 331-343.

YUAN, H.-L., GAO, S., DAI, M.-N, ZONG, C.-L, GUNTHER, D., FONTAINE, G.H., LIU, X.-M. & DIWU, C (2008): Simultaneous determinations of U–Pb age, Hf isotopes and trace element compositions of zircon by excimer laser ablation quadrupole and multiple collector ICP–MS. *Chem. Geol.* **247**, 100-118.

# CHAPTER 10: REFERENCE MATERIALS FOR ELEMENTAL AND ISOTOPIC ANALYSES BY LA–(MC)–ICP–MS: SUCCESSES AND OUTSTANDING NEEDS

Klaus Peter Jochum and Brigitte Stoll
Max-Planck-Institut für Chemie, Postfach 3060,
55020 Mainz, Germany
E-mail: kpj@mpch-mainz.mpg.de

## INTRODUCTION

Reference materials (RMs) play an important role in laser ablation ICP mass spectrometry (LA–ICP–MS) and LA–multicollector (MC)–ICP–MS. They are used as samples for calibration, development of methods, quality control, quality assurance and for inter-laboratory comparisons of concentration and isotope data. They are commonly used in many fields, such as geochemistry, cosmochemistry, biogeochemistry, environmental research and forensic elemental analysis. The accuracy of LA–(MC)–ICP–MS measurements depends on bration against RMs to ensure comparability over time and among laboratories. The quality of the LA–(MC)–ICP–MS data is therefore dependent on the accurate characterization of suitable RMs, for without such RMs it is difficult to produce reliable data sets. Calibration procedures for LA–ICP–MS of geological samples using reference materials are described and discussed in detail by Jackson (2008).

A quantitative trace element analysis requires the knowledge of an empirical relative sensitivity factor (RSF). This factor corrects for differences in ablation behavior, ion formation, transmission, and detection of the various elements as well as mass fractionation effects. It is calculated by dividing the measured (uncorrected) concentration in a RM by the "true" concentration (*e.g.,* the certified value). A RSF can be influenced by the matrix of the sample (Kroslakova & Günther 2007). Whereas RSFs obtained from LA–ICP–MS analyses of the same matrix (*e.g.,* basaltic glass) are very similar using 193 nm and 213 nm Nd:YAG lasers, they differ significantly up to 15% from the RSFs obtained from the analysis of the synthetic NIST SRM 612 glass (Jochum *et al.* 2007). This matrix dependence, which is lower for UV-fs lasers (Mozna *et al.* 2006) and higher for ≥ 266 nm Nd:YAG lasers, has been explained by a different size distribution of particles produced by the ablation for synthetic NIST glass and geological glasses (Guillong *et al.* 2005). When the calibration material and the unknown geological sample have a similar absorptivity, then the particle size distribution is similar, resulting in more accurate data. A detailed review and discussion on the formation of the aerosols generated by laser ablation is given by Günther & Koch (2008).

For *in situ* isotope analysis, LA–ICP–MS and especially LA–MC–ICP–MS have become important tools (*e.g.,* Paul *et al.* 2005, Jochum *et al.* 2006a, Tiepolo *et al.* 2006). Mass discrimination is a main source of error in isotope ratio measurements, because the measured isotope ratios differ from the "true" values due to fractionation processes that are mass-dependent, such as instrumental mass discrimination and laser ablation-induced fractionation (see Pearson *et al.* 2008, Košler 2008). Therefore RMs with well known isotope compositions are needed for external calibration (Paul *et al.* 2005, Jochum *et al.* 2006a).

## DEFINITION OF A REFERENCE MATERIAL

According to the International Organization for Standardization (ISO) Guide 30 (ISO 1992) definition, a RM is a "material or substance one or more of whose property values are sufficiently homogeneous and well established to be used for the calibration of an apparatus, the assessment of a measurement method, or for assigning values to materials". Recently, ISO/REMCO (2005) established an approved definition of a RM: "material, sufficiently homogeneous and stable with respect to one or more specified properties, which has been established to be fit for its intended use in a measurement process". Many RMs produced to date fit these ISO definitions, but only a small number fit the definition of certified RMs (CRMs), being "reference materials, accompanied by a certificate, one or more of whose property values are certified by a procedure which establishes traceability to an accurate realization of the unit in which the property values are expressed, and for which each certified value is accompanied by an uncertainty at a stated level of confidence" (ISO 1992, Kane & Potts 1999) and "characterized by a metrologically valid procedure for one or more

Mineralogical Association of Canada Short Course 40, Vancouver, B.C., p. 147–168.

specified properties, accompanied by a certificate that states the value of the specified property, its associated uncertainty, and a statement of metrological traceability" (ISO/REMCO 2005).

## REFERENCE MATERIALS FOR LA–(MC)–ICP–MS ANALYSIS

Homogeneity is a fundamental requirement for any RM. It is not an inherent property of the material, but is specific to both element and analytical test portion mass (Kane 2002). A RM for LA–(MC)–ICP–MS should not only be homogeneous at bulk analytical tests (100 mg range) but also homogeneous at the µg range.

Table 10-1 lists the RMs, which are most useful for calibration and quality control in LA–(MC)–ICP–MS. The major and trace element homogeneity of these samples was studied using the micro-analytical methods electron probe microanalysis (EPMA), secondary ion mass spectrometry (SIMS), synchrotron radiation–XRF (SR–XRF) and LA–ICP–MS (see below for details). An extensive study is that of Kempenaers *et al.* (2003), who investigated possible micro-heterogeneity of many USGS, MPI-DING and NIST reference glasses using SR–XRF. A procedure based on repeated analysis of the reference glass in many locations allowed the minimum sampling mass needed for a representative analysis to be calculated. When selected chalcophile elements (*e.g.,* Cu, Zn) are not considered, the minimal representative mass drops to about 20 ng for all reference glasses. This corresponds to a sample volume of about 20 x 20 x 20 $\mu m^3$, *i.e.*, somewhat smaller than what is typically vaporized during a LA–(MC)–ICP–MS series.

The RMs of Table 10-1 can be divided into four groups: synthetic reference glasses, geological reference glasses, natural and synthetic minerals. Advantages and disadvantages of the use of these materials for element and isotope analysis are discussed in detail.

### Synthetic reference glasses

#### *a) NIST 600 series*

For calibration purposes, most LA–ICP–MS analysts presently use the synthetic glass standard reference materials (SRM) of the 600 series (SRM 610–617) of the National Institute of Standards and Technology (NIST). The chemical compositions of the pairs SRM 610–611, 612–613, 614–615, 616–617 are identical; they only differ in their shape. Typical applications of the NIST glasses in LA–

TABLE 10-1: REFERENCE MATERIALS FOR USE IN LA–(MC)–ICP–MS

| Reference material | Material type | Rock type / mineral |
|---|---|---|
| **NIST** | | |
| SRM 610 | synthetic glass | |
| SRM 612 | synthetic glass | |
| SRM 614 | synthetic glass | |
| **USGS** | | |
| BCR-2G | geological glass | basalt |
| BHVO-2G | geological glass | basalt |
| BIR-1G | geological glass | basalt |
| GSC-1G | synthetic glass | basalt |
| GSD-1G | synthetic glass | basalt |
| GSE-1G | synthetic glass | basalt |
| MASS-1 (PS-1) | synthetic mineral | sulfide |
| MACS-1 | synthetic mineral | Ca carbonate |
| **MPI-DING** | | |
| KL2-G | geological glass | basalt |
| ML3B-G | geological glass | basalt |
| ATHO-G | geological glass | rhyolite |
| StHs6/80-G | geological glass | andesite |
| GOR128-G | geological glass | komatiite |
| GOR132-G | geological glass | komatiite |
| T1-G | geological glass | quartz-diorite |
| BM90/21-G | geological glass | peridotite |
| **University of Münster** | | |
| TNT666 | synthetic glass | titanite |
| TNT777 | synthetic glass | titanite |
| TNT150 | synthetic glass | titanite |
| TNT1500 | synthetic glass | titanite |
| CPX666 | synthetic glass | clinopyroxene |
| CPX777 | synthetic glass | clinopyroxene |
| DAC666 | synthetic glass | dacite |
| DAC777 | synthetic glass | dacite |
| STDP5 | synthetic glass | phosphate |
| STDP3-150 | synthetic glass | phosphate |
| STDP3-1500 | synthetic glass | phosphate |
| **University of Heidelberg** | | |
| Sy | synthetic mineral | rutile |
| Diss | natural mineral | rutile |
| R19 | natural mineral | rutile |
| R10 | natural mineral | Rutile |
| **Others** | | |
| 91500 zircon | natural mineral | zircon |
| $Fe_{1-x}S$ | synthetic mineral | sulfide |
| $(Fe,Ni)_{1-x}S$ | synthetic mineral | sulfide |
| $(Fe,Cu)_{1-x}S$ | synthetic mineral | sulfide |
| TIT-200 | synthetic mineral | titanite |

ICP–MS are the analyses of geological glasses (*e.g.*, Jochum *et al*. 2007), broken glass in forensic elemental analysis (e.g., Trejos & Almirall 2004), minerals (e.g., Ionov *et al.* 2004), biological and environmental samples (e.g., Wyndham *et al.* 2004).

SRM 610 and SRM 612 are the most widely used NIST glasses. These samples have the advantage that the concentrations of all trace elements are similar and high enough (*ca*. 400 µg/g for NIST SRM 610, *ca*. 40 µg/g for NIST SRM 612) for a precise primary calibration (Fig. 10-1). The importance of these glasses as calibration materials in LA–(MC)–ICP–MS is demonstrated by the evaluation of publications in the geochemical GeoReM database for reference materials of geological and environmental interest (http://georem.mpch-mainz.gwdg.de, Jochum *et al.* 2005a). For example, 89% of 27 LA–(MC)–ICP–MS laboratories involved in the certification process of the geological MPI-DING glasses (Jochum *et al.* 2006b) used the NIST glasses and 11% the BCR-2G glass from the United States Geological Survey (USGS) for calibration. In addition, NIST SRM 610 and NIST SRM 612 are the two most clicked reference materials of the GeoReM database (status May 2008) also demonstrating the common use of these reference glasses for microanalysis.

However, there are some major drawbacks concerning the NIST SRM glasses. It has been pointed out by Kane (1998) that, with the exception of eight elements certified by NIST (Ag, Fe, Ni, Pb, Rb, Sr, Th, U), the trace element composition of these glasses is not yet sufficiently well established to match the International Organization for Standardization (ISO) guidelines for certifying RMs. In addition, these reference materials are not certified for use at the microbeam scale. A further drawback of the NIST glasses for use in geochemistry is that the major element compositions of the samples are very different from those of any geological matrix (Figs. 10-1, 10-2a, b, d, 10-3). This may lead to severe analytical problems due to matrix effects (*e.g.*, Yu *et al.* 2003; Jochum *et al.* 2007). This is especially true for LA–ICP–MS measurements done with lasers having wavelengths of 266 nm or higher, where element fractionation is relatively high.

Most analysts so far use the compilation data for NIST SRM 610 and 612 from Pearce *et al.* (1997). These authors provided data for 61 major and trace elements. Other useful compilations are from Rocholl *et al.* (1997) and Eggins (2003). The new software of the GeoReM database contains "GeoReM preferred values" and their uncertainties for the NIST glasses and other RMs as evaluated by the GeoReM team. These data yield best possible estimates of the "true" values obtained by modern analytical techniques (Jochum & Nohl 2008). The main criterion for selecting the GeoReM preferred values is whether or not the data are certified. Such data are accompanied by an uncertainty and have a

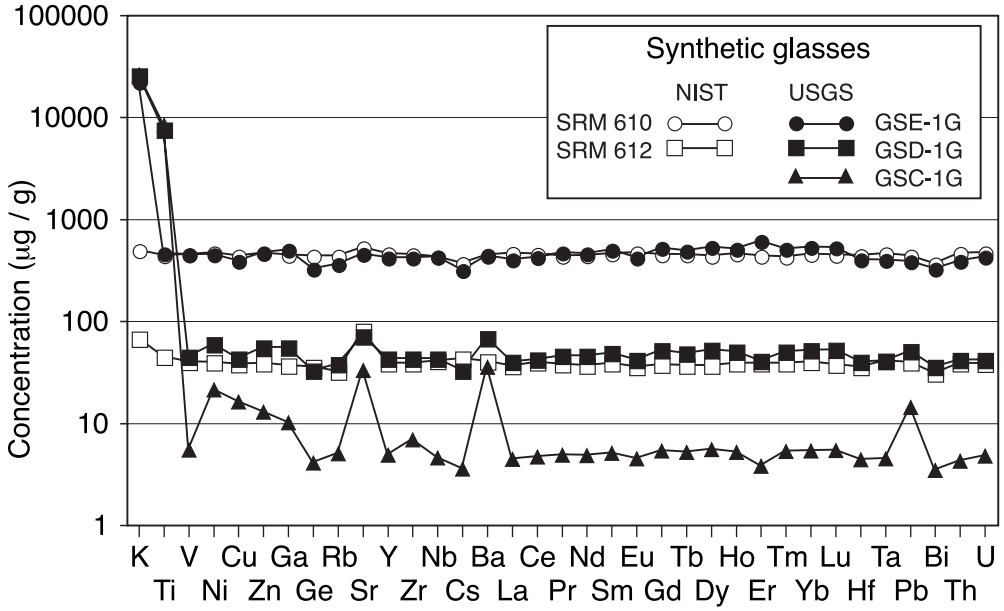


FIG. 10-1: GeoReM preferred values for synthetic NIST and USGS reference glasses. In contrast to the NIST samples, the USGS glasses have a geological (basaltic) major element composition.

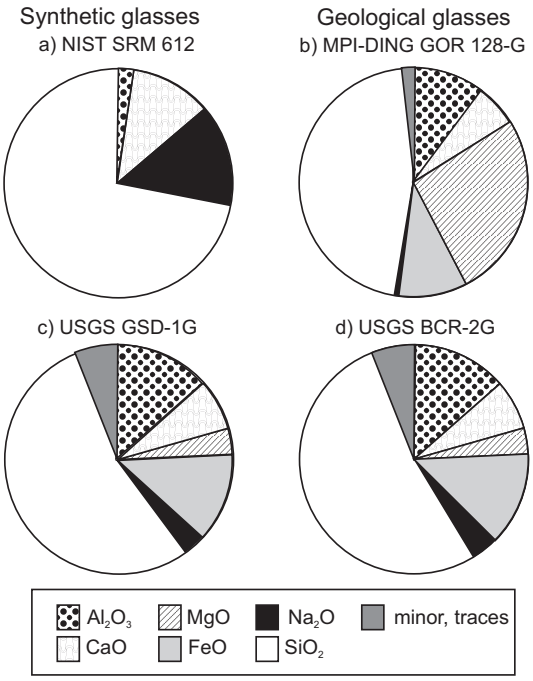


FIG. 10-2: Major element composition (concentrations in %m/m) of two synthetic and two geological reference glasses. The major element composition (particularly with respect to MgO and FeO) of the synthetic NIST SRM 612 **a)** is completely different from those of the geological (komatiitic) MPI-DING GOR 128-G **b)** and (basaltic) USGS BCR-2G **d)** glasses. The matrix composition of the synthetic USGS GSD-1G glass **c)** is similar to that of the geological USGS BCR-2G glass **d)**.

high level of confidence. Unfortunately, since there are only few certified data available, the GeoReM preferred values were chosen on the basis of data determined using high precision and definitive methods, such as isotope dilution–thermal ionization mass spectrometry (ID–TIMS). When the above criteria cannot be met, the GeoReM preferred values were selected from other bulk analytical methods, such as ICP–MS, microanalytical techniques (*e.g.,* LA–ICP–MS, SIMS) and, lastly, compilations from older publications. Table 10-2 lists the GeoReM preferred values for NIST SRM 610, 612 and 614.

The NIST glasses were also used to determine the mass bias for isotope ratio measurements. Until now, high precision B, Li, Sr, Nd and Pb isotope data are available for these reference glasses (Table 10-2). The investigations of Baker *et al.* (2004) showed some evidence for isotopic heterogeneity of Pb. It is likely that the glass and the added Pb dopant were not completely mixed during the preparation of the glasses. NIST SRM 612 has been used to determine the mass discrimination of Pb isotopes for the isotope LA–(MC)–ICP–MS analyses of reference materials (Paul *et al*. 2005, Jochum *et al.* 2006a) and melt inclusions (Jochum *et al.* 2006c).

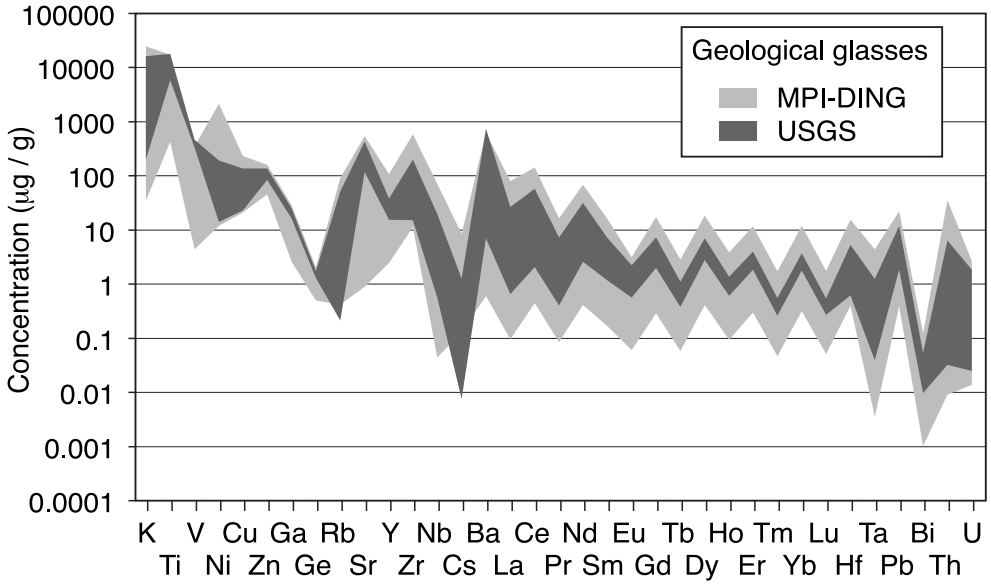


FIG. 10-3: Ranges of trace element concentrations of the geological MPI-DING and USGS reference glasses (see Tables 10-4 and 10-5).

TABLE 10-2: GEOREM PREFERRED VALUES OF THE SYNTHETIC REFERENCE GLASSES NIST SRM 610, SRM 612 AND SRM 614.

| | | NIST SRM 610 | NIST SRM 612 | NIST SRM 614 | | | NIST SRM 610 | NIST SRM 612 | NIST SRM 614 |
|---|---|---|---|---|---|---|---|---|---|
| Ag | µg/g | 239 | 22 | 0.42 | Ni | µg/g | 458.7 | 38.8 | 1 |
| $Al_2O_3$ | %m/m | 2.04 | 2.11 | 1.99 | P | µg/g | 343 | 51 | 13 |
| As | µg/g | 317 | 37 | 0.66 | Pb | µg/g | 426 | 38.57 | 2.32 |
| Au | µg/g | 23 | 5.1 | 0.45 | Pr | µg/g | 430 | 37.2 | 0.76 |
| B | µg/g | 356 | 35 | 1.4 | Rb | µg/g | 425.7 | 31.4 | 0.855 |
| Ba | µg/g | 435 | 39.7 | 3.2 | Sb | µg/g | 369 | 38 | 0.78 |
| Be | µg/g | 466 | 38 | 0.67 | Sc | µg/g | 441 | 41 | 1.6 |
| Bi | µg/g | 358 | 30 | 0.58 | Se | µg/g | 109 | | |
| CaO | %m/m | 11.5 | 11.9 | 11.9 | $SiO_2$ | %m/m | 70.0 | 71.9 | 72.3 |
| Cd | µg/g | 259 | 28.3 | 0.58 | Sm | µg/g | 451 | 38.1 | 0.75 |
| Ce | µg/g | 448 | 38.7 | 0.81 | Sn | µg/g | 396 | 38 | 1.6 |
| Co | µg/g | 405 | 35 | 0.85 | Sr | µg/g | 515.5 | 78.4 | 45.8 |
| Cr | µg/g | 405 | 36 | 1.8 | Ta | µg/g | 452 | 40 | 0.79 |
| Cs | µg/g | 361 | 42 | 0.66 | Tb | µg/g | 443 | 36 | 0.73 |
| Cu | µg/g | 430 | 37 | 1.37 | Th | µg/g | 457.2 | 37.79 | 0.748 |
| Dy | µg/g | 427 | 36 | 0.74 | Ti | µg/g | 434 | 44 | 3.4 |
| Er | µg/g | 426 | 38 | 0.74 | Tl | µg/g | 61 | 15.1 | 0.28 |
| Eu | µg/g | 461 | 35 | 0.76 | Tm | µg/g | 420 | 38 | 0.73 |
| Fe | µg/g | 458 | 51 | 19 | U | µg/g | 461.5 | 37.38 | 0.823 |
| Ga | µg/g | 438 | 36 | 1.5 | V | µg/g | 442 | 39 | 1.0 |
| Gd | µg/g | 444 | 36.7 | 0.75 | W | µg/g | 445 | 40 | 0.88 |
| Ge | µg/g | 426 | 35 | 0.89 | Y | µg/g | 450 | 38 | 0.80 |
| Hf | µg/g | 432 | 35 | 0.70 | Yb | µg/g | 445 | 39.2 | 0.77 |
| Ho | µg/g | 449 | 38 | 0.74 | Zn | µg/g | 456 | 38 | 2.5 |
| In | µg/g | 441 | 43 | 0.88 | Zr | µg/g | 440 | 38 | 0.84 |
| K | µg/g | 486 | 66.3 | 30 | $^{11}B/^{10}B$ | | 4.049 | 4.048 | 4.052 |
| La | µg/g | 457 | 35.8 | 0.72 | $^{143}Nd/^{144}Nd$ | | 0.511927 | 0.51193 | 0.51192 |
| Li | µg/g | 485 | 42 | 1.6 | $^{206}Pb/^{204}Pb$ | | 17.045 | 17.095 | 17.838 |
| Lu | µg/g | 435 | 36.9 | 0.73 | $^{207}Pb/^{204}Pb$ | | 15.504 | 15.511 | 15.537 |
| Mg | µg/g | 465 | 77 | 35 | $^{207}Pb/^{206}Pb$ | | 0.9096 | 0.9073 | 0.8704 |
| Mn | µg/g | 485 | 38 | 1.4 | $^{208}Pb/^{204}Pb$ | | 36.964 | 37.005 | 37.486 |
| Mo | µg/g | 410 | 38 | 0.8 | $^{208}Pb/^{206}Pb$ | | 2.168 | 2.1647 | 2.0995 |
| $Na_2O$ | %m/m | 13.4 | 14.0 | 13.6 | $^{87}Sr/^{86}Sr$ | | 0.709699 | 0.709063 | 0.708363 |
| Nb | µg/g | 419 | 40 | 0.81 | $\delta^7Li$ | ‰LSVEC | 32.5 | 31.2 | 20.5 |
| Nd | µg/g | 431 | 35.9 | 0.74 | | | | | |

***b) USGS GS reference glasses***

As mentioned above one of the major drawbacks of the NIST 600 glasses is that their major element compositions are very different from any geological matrix. Therefore, the USGS prepared the four synthetic reference glasses GSA-1G, GSC-1G, GSD-1G, GSE-1G with a geological (basaltic) major element composition having many trace elements in similar abundances at different concentration levels (GSE-1G: *ca*. 500 µg/g, GSD-1G: *ca*. 50 µg/g, GSC-1G: *ca*. 5 µg/g; GSA-1G: blank, < 0.01 µg/g) (Figs. 10-1, 10-2c). Meanwhile first analytical results of the elemental composition have been published (Jochum *et al.* 2005b, Guillong *et al.* 2005, Jochum *et al.* 2007) using different analytical techniques. The GeoReM preferred values for GSC-1G, GSD-1G and GSE-1G are listed in Table 10-3. The determination of the isotopic composition of Li, B, Ca, Sr, Nd, Pb is in progress and will be published elsewhere (Jochum, pers. comm..).

Jochum *et al.* (2005b) investigated the homogeneity of the GS glasses. The relative standard deviation (RSD) obtained from EPMA analyses within areas of about 100 µm in diameter is better than 1%, *i.e*., well within the repeatability range of EPMA. Chemical heterogeneities of major elements at larger (mm) size are also not detectable. RSD values for refractory lithophile trace elements obtained from LA–ICP–MS using spot sizes of 40–120 µm varied between about 1–10%. They are within the range of LA–ICP–MS repeatability indicating that possible chemical trace element heterogeneities for lithophile elements in the GS samples are not detectable. Only the chalcophile element Cu seems to be heterogeneously distributed.

As demonstrated by many authors (*e.g.*, Jochum *et al.* 2007), matrix-matched calibration is necessary for accurate LA–ICP–MS. Figure 10-4 shows the RSFs for several elements determined in the basaltic glasses GSD-1G, KL2-G and the synthetic reference glass NIST SRM 612 (Jochum

TABLE 10-3: GEOREM PREFERRED VALUES OF THE USGS SYNTHETIC REFERENCE GLASSES GSC-1G, GSD-1G AND GSE-1G.

| | | GSC-1G | GSD-1G | GSE-1G |
|---|---|---|---|---|
| Ag | µg/g | 4.1 | 23 | 200 |
| $Al_2O_3$ | %m/m | 13.5 | 13.4 | 13 |
| As | µg/g | 3.2 | 27 | 260 |
| B | µg/g | 26 | 50 | 330 |
| Ba | µg/g | 34.8 | 67 | 427 |
| Be | µg/g | 4.5 | 46 | 490 |
| Bi | µg/g | 3.4 | 35 | 320 |
| CaO | %m/m | 7.1 | 7.2 | 7.4 |
| Cd | µg/g | 1.9 | 18 | 160 |
| Ce | µg/g | 4.62 | 41.4 | 414 |
| Co | µg/g | 5.9 | 40 | 380 |
| Cr | µg/g | 10.3 | 42 | 400 |
| Cs | µg/g | 3.5 | 32 | 310 |
| Cu | µg/g | 16 | 42 | 380 |
| Dy | µg/g | 5.41 | 51.2 | 524 |
| Er | µg/g | 3.72 | 40.1 | 595 |
| Eu | µg/g | 4.4 | 41 | 410 |
| FeO(t) | %m/m | 13.7 | 13.3 | 12.7 |
| Ga | µg/g | 10 | 54 | 490 |
| Gd | µg/g | 5.29 | 50.7 | 514 |
| Ge | µg/g | 4 | 32 | 320 |
| Hf | µg/g | 4.3 | 39 | 395 |
| Ho | µg/g | 5.1 | 49 | 501 |
| In | µg/g | 4.5 | 38 | 370 |
| K | µg/g | 25700 | 25300 | 21800 |
| La | µg/g | 4.36 | 39.1 | 392 |
| Li | µg/g | 5.9 | 43 | 430 |
| Lu | µg/g | 5.33 | 51.5 | 518 |
| MgO | %m/m | 3.6 | 3.6 | 3.5 |
| Mn | µg/g | 176 | 220 | 590 |

| | | GSC-1G | GSD-1G | GSE-1G |
|---|---|---|---|---|
| Mo | µg/g | 4.6 | 39 | 390 |
| $Na_2O$ | %m/m | 3.6 | 3.6 | 3.9 |
| Nb | µg/g | 4.5 | 42 | 420 |
| Nd | µg/g | 4.72 | 44.7 | 453 |
| Ni | µg/g | 21 | 58 | 440 |
| P | µg/g | 1000 | 860 | 70 |
| Pb | µg/g | 14 | 50 | 378 |
| Pr | µg/g | 4.8 | 45 | 460 |
| Rb | µg/g | 4.92 | 37.3 | 356 |
| Sb | µg/g | 5.3 | 43 | 450 |
| Sc | µg/g | 5.4 | 52 | 530 |
| Se | µg/g | 0.2 | 2 | 20 |
| $SiO_2$ | %m/m | 52.6 | 53.2 | 53.7 |
| Sm | µg/g | 5.00 | 47.8 | 488 |
| Sn | µg/g | 5.3 | 29 | 280 |
| Sr | µg/g | 32.3 | 69.4 | 447 |
| Ta | µg/g | 4.4 | 40 | 390 |
| Tb | µg/g | 5.1 | 47 | 480 |
| Th | µg/g | 4.2 | 41 | 380 |
| $TiO_2$ | %m/m | 1.37 | 1.24 | 0.075 |
| Tl | µg/g | 0.27 | 0.9 | 2.0 |
| Tm | µg/g | 5.2 | 49 | 500 |
| U | µg/g | 4.7 | 41 | 420 |
| V | µg/g | 5.4 | 44 | 440 |
| W | µg/g | 4.5 | 43 | 430 |
| Y | µg/g | 4.8 | 42 | 410 |
| Yb | µg/g | 5.29 | 50.9 | 520 |
| Zn | µg/g | 12.7 | 54 | 460 |
| Zr | µg/g | 6.8 | 42 | 410 |

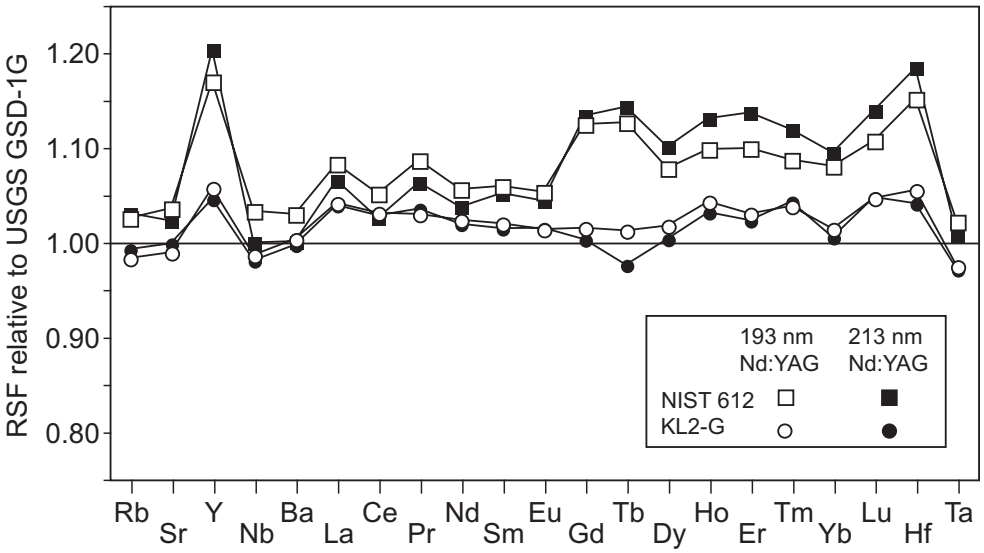


FIG. 10-4: Relative sensitivity factors (RSFs) of the NIST SRM 612 glass and the KL2-G glass obtained with LA–ICP–MS using 193 nm and 213 nm Nd:YAG laser ablation systems, respectively (Jochum *et al.* 2007). The data for the natural basaltic KL2-G glass agree well with the RSFs of the synthetic, but basaltic, GSD-1G glass and disagree with those of the synthetic NIST 612 glass.

*et al.* 2007). It clearly shows a significant difference of the RSFs between the basaltic and the synthetic samples. The RSFs obtained from the NIST 612 glass are higher for both laser types indicating systematic lower concentrations in basalts when using NIST 612 as calibration material. Discrepancies are lower for the 193 nm than for the 213 nm laser.

**Geological reference glasses**

To provide RMs of natural composition for microanalytical work, the USGS as well as the Max-Planck-Institut für Chemie in cooperation with D. Dingwell (MPI-DING) have prepared large amounts of homogeneous reference glasses. These samples have the advantage that they have a natural rock composition showing the typical zigzag patterns of even/uneven atomic numbered elements (Fig. 10-3). These RMs are especially useful as secondary standards and as calibration materials for elements having concentrations greater than several µg/g. The natural abundances of some trace elements are too low to permit a precise calibration.

***a) USGS reference glasses***

The USGS glasses comprise the basaltic glasses BCR-2G, BHVO-2G and BIR-1G (USGS 1996, 2004). They were prepared by melting kilogram aliquots of (powdered) BCR-2 (Columbia River basalt), BHVO-2 (basalt Hawaiian Volcanic Observatory), and BIR-1 (Icelandic basalt) at 1540°C under a nitrogen atmosphere (Wilson & Taggart, unpublished). The USGS reference glasses TB-1G (made from basalt from near Denver, Colorado) and NKT-1G (prepared from nephelinite from near the town of Knippa, Texas) have not seen wide use yet (Elburg *et al.* 2005).

The homogeneity of BCR-2G, BHVO-2G and BIR-1G was studied in detail by Rocholl (1998), Kempenaers *et al.* (2003) and Jochum *et al.* (2005b). The investigations of Rocholl (1998) show an overall homogeneity for major and most lithophile trace elements of BCR-2G for scales of a few tens of micrometres to a few tens of centimetres. Norman *et al.* (2004) determined the distribution of chalcophile and siderophile elements in glass fragments of the USGS glasses. Their results show clear evidence for small scale heterogeneities of Pt and Re, since the glasses were prepared in Pt crucibles.

The USGS reference glasses have been extensively analyzed by many laboratories using different techniques (see GeoReM database). This is especially true for BCR-2G, where up to 50 analytical data for some elements were published. Therefore, the GeoReM preferred values (Table 10-4) have a high degree of confidence. This is also demonstrated by a comparison of the GeoReM preferred values of the BCR-2G glass with the original rock powder BCR-2. The GeoReM preferred values of 40 elements in BCR-2G, BCR-2 and also BCR-1 agree within uncertainty limits of

TABLE 10-4: GEOREM PREFERRED VALUES OF THE USGS REFERENCE GLASSES BCR-2G, BHVO-2G AND BIR-1G.

| | | BCR-2G | BHVO-2G | BIR-1G | | | BCR-2G | BHVO-2G | BIR-1G |
|---|---|---|---|---|---|---|---|---|---|
| $Al_2O_3$ | %m/m | 13.4 | 13.6 | 15.5 | Nd | µg/g | 28.9 | 24.5 | 2.37 |
| Ba | µg/g | 683 | 131 | 6.5 | $P_2O_5$ | %m/m | 0.37 | 0.29 | 0.027 |
| Be | µg/g | 2.3 | 1.3 | 0.1 | Pb | µg/g | 11 | 1.7 | 3.7 |
| CaO | %m/m | 7.06 | 11.4 | 13.3 | Pr | µg/g | 6.7 | 5.35 | 0.37 |
| Ce | µg/g | 53.3 | 37.6 | 1.89 | Pt | µg/g | 0.78 | 0.46 | 0.92 |
| Co | µg/g | 38 | 44 | 52 | Rb | µg/g | 47 | 9.2 | 0.197 |
| Cr | µg/g | 17 | 293 | 392 | Sb | µg/g | 0.35 | 0.3 | 0.56 |
| Cs | µg/g | 1.16 | 0.10 | 0.007 | Sc | µg/g | 33 | 33 | 43 |
| Cu | µg/g | 21 | 127 | 119 | $SiO_2$ | %m/m | 54.4 | 49.3 | 47.5 |
| Dy | µg/g | 6.44 | 5.28 | 2.55 | Sm | µg/g | 6.59 | 6.1 | 1.09 |
| Er | µg/g | 3.70 | 2.56 | 1.7 | Sn | µg/g | 2.6 | 2.6 | 2.3 |
| Eu | µg/g | 1.97 | 2.07 | 0.517 | Sr | µg/g | 342 | 396 | 109 |
| FeO(t) | %m/m | 12.4 | 11.3 | 10.4 | Ta | µg/g | 0.78 | 1.15 | 0.036 |
| Ga | µg/g | 23 | 22 | 15 | Tb | µg/g | 1.02 | 0.92 | 0.35 |
| Gd | µg/g | 6.71 | 6.16 | 1.85 | Th | µg/g | 5.9 | 1.22 | 0.03 |
| Ge | µg/g | 1.5 | 1.6 | 1.2 | $TiO_2$ | %m/m | 2.27 | 2.79 | 1.04 |
| Hf | µg/g | 4.84 | 4.32 | 0.57 | Tm | µg/g | 0.51 | 0.34 | 0.24 |
| Ho | µg/g | 1.27 | 0.98 | 0.56 | U | µg/g | 1.69 | 0.403 | 0.023 |
| In | µg/g | 0.11 | 0.10 | 0.086 | V | µg/g | 425 | 308 | 326 |
| K | µg/g | 14900 | 4270 | 183 | Y | µg/g | 35 | 26 | 14.3 |
| La | µg/g | 24.7 | 15.2 | 0.609 | Yb | µg/g | 3.39 | 2.01 | 1.64 |
| Li | µg/g | 9 | 4.4 | 3 | Zn | µg/g | 125 | 102 | 78 |
| Lu | µg/g | 0.503 | 0.279 | 0.248 | Zr | µg/g | 184 | 170 | 14 |
| MgO | %m/m | 3.56 | 7.13 | 9.4 | $^{206}Pb/^{204}Pb$ | | 18.765 | 18.733 | 18.867 |
| MnO | %m/m | 0.19 | 0.17 | 0.19 | $^{207}Pb/^{204}Pb$ | | 15.626 | 15.571 | 15.665 |
| Mo | µg/g | 270 | 3.8 | 0.075 | $^{208}Pb/^{204}Pb$ | | 38.73 | 38.27 | 38.487 |
| $Na_2O$ | %m/m | 3.23 | 2.4 | 1.85 | $^{87}Sr/^{86}Sr$ | | 0.705003 | 0.703469 | 0.703105 |
| Nb | µg/g | 12.5 | 18.3 | 0.52 | $\delta^7Li$ | ‰LSVEC | 4.5 | | 5.4 |

approximately 1–5% (Fig. 10-5). Exceptions are noted for some elements (Cr, Pb, W, and especially Mo, Pt (not shown in the figure)) that were introduced during sample preparation processes of the powders and the glass.

In addition to trace element analyses, isotope data are also available. Sr and Nd isotopes are identical within uncertainty limits to their unfused counterparts (Raczek *et al.* 2003; Elburg *et al.* 2005). However, the Pb isotopic ratios of the USGS glasses and the unfused powders are not identical in all cases. It was speculated by Elburg *et al.* (2005) that the Pb isotope data obtained from small amounts of glass material do not necessarily reproduce other splits of the glass.

To provide matrix-matched calibration some authors used the basaltic USGS reference glasses as calibration materials for the determination of trace elements of basalts. An example is the recent work of Stoll *et al.* (2008), who analyzed basaltic RMs including the new Brazilian RM BRP-1, basalts from Hawaii and basaltic Martian meteorites. They reported that 80% of the LA–ICP–MS RM data are within 10% of the GeoReM preferred values (Fig. 10-6).

***b) MPI-DING reference glasses***

Eight silicate MPI-DING glasses were prepared by directly fusing and stirring 50–100 g rock powder and chips (Jochum *et al.* 2000). Direct fusion without alteration of the composition was performed at temperatures in the range of 1400–1600°C. The glasses comprise two tholeiitic basaltic examples from the Hawaiian volcanoes Kilauea (KL2-G) and Mauna Loa (ML3B-G), andesite from the St. Helens (USA) eruption (StHs6/80-G), two komatiite examples from Gorgona Island (GOR128-G, GOR132-G), peridotite from the Ivrea Zone of Italy (BM90/21-G), rhyolite from Iceland (ATHO-G), and quartz diorite from the Italian Alps (T1-G).

The major element homogeneity was evaluated by means of EPMA profiles (Jochum *et al.* 2000). Except for the two komatiite examples, RSD variations (0.3–2%) in the MPI-DING glasses are similar to the ranges of analytical repeatability of EPMA analyses. This indicates that possible chemical heterogeneities are smaller than the analytical uncertainty and hence not detectable. Unequivocal mineralogical and chemical heterogeneities in the µm range were observed in a few fragments of GOR128-G and GOR132-G, in which quenched olivine crystals formed. However these crystals are concentrated in small and limited areas and are negligible for most LA–ICP–MS applications. Trace element investigations (Jochum *et al.* 2000, 2006b) showed that RSD variations (0.1–4%) of refractory lithophile elements (*e.g.*, Sr, Ba, REE, Zr, Nb) were well within analytical errors. Heterogeneous distribution had been observed for some chalcophile (Cu, Sn, Bi) and siderophile (Ir, Pt, Au) elements. Such heterogeneities have been explained by loss of volatile components from the molten glass surface (Eggins & Shelley 2002) and of siderophile elements to the platinum crucible.

Data for nine isotope systems (H, O, B, Li, Ca, Sr, Nd, Hf, Pb) are available (Jochum *et al.* 2006b), mainly obtained by high precision analytical techniques. Possible large scale and small scale isotopic heterogeneities were tested by micro-analytical techniques. LA–MC–ICP–MS analyses using 60–80 µm spot sizes show no evidence for heterogeneities of B isotopes. Slight micro-heterogeneities of Li isotopes could be observed for

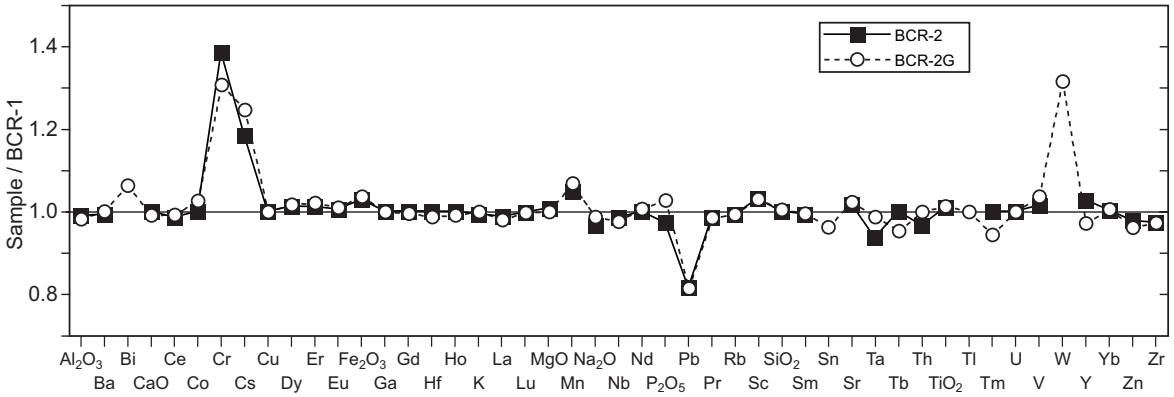


FIG. 10-5: Comparison of the GeoReM preferred values for the USGS rock powders BCR-1, BCR-2 and the BCR-2G glass. Nearly all element concentrations agree within uncertainty limits.

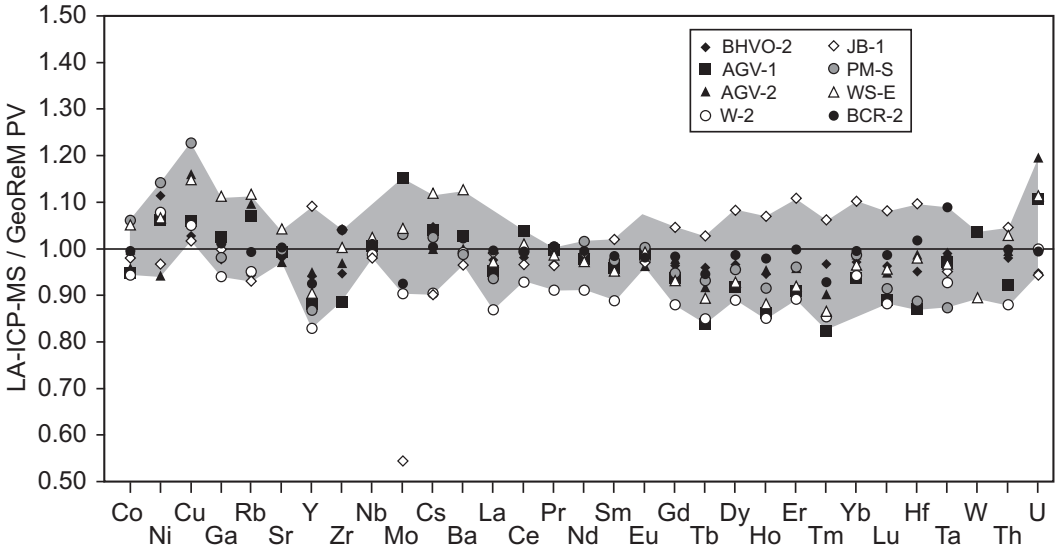


FIG. 10-6: LA–ICP–MS data for international reference materials (Stoll *et al.* 2008). They are compared with the GeoReM preferred values. Matrix-matched calibration was performed using the basaltic reference glasses KL2-G, ML3B-G, BCR-2G and BHVO-2G.

GOR128-G and ML3B-G using SIMS. Heterogeneities of Pb isotopes are found for ML3B-G by high precision TIMS and MC–ICP–MS measurements using different glass chips. The differences in Li and Pb isotopes are small and lower than the reproducibility obtained from LA–(MC)–ICP–MS.

The MPI-DING glasses were certified (Jochum *et al.* 2006b) by adapting the recommendations for the certification of geological reference materials of the International Association of Geoanalysts (IAG) (Kane 2002, Kane *et al.* 2003). Altogether, more than 60 qualified geochemical laboratories worldwide contributed to the analyses. The reference values for up to 74 elements and 9 isotope systems were derived from the results of 16 independent techniques (Table 10-5). The MPI-DING glasses therefore belong to the best characterized reference materials for *in situ* microanalytical trace element and isotopic work. They found broad acceptance in many laboratories worldwide. Some examples are the quantification of LA–ICP–MS measurements of glass fibers using KL2-G and ML3B-G (Becker *et al.* 2002). The basalt glass KL2-G and the komatiite glass GOR132-G were used as matrix-matched calibration materials for LA–ICP–MS analyses of basaltic and komatiitic glasses (Jochum *et al.* 2007). The certified MPI-DING reference glasses can also be used to improve analytical data. For example, Fig. 10-7 shows the results of the KL2-G reference glass obtained from four different LA–ICP–MS laboratories (data published in Jochum *et al.* 2006b). Whereas the REE data of laboratories 1 to 3 are within the uncertainty ranges of the "true" values, those of laboratory 4 are significantly higher than the "true" values. Non-matrix matched calibration or analytical problems may be the reason for these discrepancies.

At the present time, LA–(MC)–ICP–MS data for the MPI-DING glasses exist for B, Sr and Pb isotopes. The LA–MC–ICP–MS data of B isotopes agree with the high precision data of two TIMS laboratories (Fig. 10-8). *In situ* Pb isotope measurements were performed by single collector (Jochum *et al.* 2006a) and multi-collector (Paul *et al.* 2005, Souders & Sylvester 2008) ICP–MS. Figure 10-9 shows the published $^{208}Pb/^{206}Pb$ and $^{207}Pb/^{206}Pb$ ratios of the different MPI-DING glasses. The LA–ICP–MS and the LA–MC–ICP–MS data differ agree within uncertainty limits (ca. 0.1–0.2 %) with the high-precision TIMS and solution MC–ICP–MS values (Jochum *et al.* 2006b).

The MPI-DING glasses are also useful for *in situ* LA–ICP–MS analyses of Sr isotopes. Jochum *et al.* (2006c) determined $^{87}Sr/^{86}Sr$ ratios in Hawaiian melt inclusions using a spot size of 50 µm. Various corrections were made for the determination of $^{87}Sr/^{86}Sr$: dead time of the ion counting system; blank; isobaric interference of Kr (about 2 % if $^{86}Sr$ = 30 µg/g); possible interferences from doubly charged REE and Hf; isobaric interference of $^{87}Rb$ on $^{87}Sr$ (should not exceed 30% or Rb/Sr = 0.1 for precise analysis); mass bias correction for $^{87}Sr$ using $^{88}Sr$ and the corrected $^{86}Sr$; final correction for

TABLE 10-5: GEOREM PREFERRED VALUES OF THE GEOLOGICAL MPI-DING REFERENCE GLASSES.

| | | KL2-G | ML3B-G | GOR128-G | GOR132-G | ATHO-G | T1-G | StHs6/80-G | BM90/21-G |
|---|---|---|---|---|---|---|---|---|---|
| Ag | µg/g | 0.15 | 0.03 | <0.5 | 0.04 | 0.3 | 0.1 | 0.02 | <0.3 |
| $Al_2O_3$ | %m/m | 13.3 | 13.6 | 9.91 | 11 | 12.2 | 17.1 | 17.8 | 2.33 |
| As | µg/g | 0.17 | 0.28 | <0.1 | 0.16 | 1.4 | 0.96 | 2.73 | <0.03 |
| B | µg/g | 2.73 | 2.5 | 23.5 | 17.2 | 5.7 | 4.1 | 11.8 | 4.2 |
| Ba | µg/g | 123 | 80.1 | 1.06 | 0.815 | 547 | 388 | 298 | 0.533 |
| Be | µg/g | 0.88 | 0.62 | 0.034 | 0.08 | 3.2 | 2 | 1.2 | 0.01 |
| Bi | µg/g | 0.036 | 0.006 | 0.0009 | 0.007 | 0.05 | 0.1 | 0.11 | 0.0015 |
| Br | µg/g | | <0.2 | <0.3 | <0.2 | 1.2 | 0.3 | 0.8 | <0.1 |
| CaO | %m/m | 10.9 | 10.5 | 6.24 | 8.45 | 1.7 | 7.1 | 5.28 | 2.1 |
| Cd | µg/g | 0.09 | 0.1 | 0.072 | 0.08 | 0.5 | 0.2 | 0.1 | 0.1 |
| Ce | µg/g | 32.4 | 23.1 | 0.45 | 0.393 | 121 | 127 | 26.1 | 0.471 |
| Cl | µg/g | 26 | 7.5 | 12 | 6.2 | 430 | 113 | 231 | 0.7 |
| Co | µg/g | 41.2 | 41.2 | 92.4 | 92.7 | 2.13 | 18.9 | 13.2 | 97.6 |
| $CO_2$ | %m/m | 0.00052 | 0.00047 | 0.00044 | 0.00058 | 0.00037 | 0.00063 | 0.00044 | 0.0006 |
| Cr | µg/g | 294 | 177 | 2272 | 2528 | 6.1 | 20.9 | 16.9 | 2190 |
| Cs | µg/g | 0.115 | 0.14 | 0.24 | 7.45 | 1.08 | 2.69 | 1.75 | 1.07 |
| Cu | µg/g | 87.9 | 112 | 63.8 | 205 | 18.6 | 18.8 | 41.5 | 37.9 |
| Dy | µg/g | 5.22 | 4.84 | 1.98 | 2.15 | 16.2 | 4.5 | 2.22 | 0.361 |
| Er | µg/g | 2.54 | 2.44 | 1.4 | 1.56 | 10.3 | 2.49 | 1.18 | 0.264 |
| Eu | µg/g | 1.92 | 1.67 | 0.264 | 0.255 | 2.76 | 1.21 | 0.953 | 0.053 |
| F | µg/g | 177 | 70 | 25 | 22 | 0.7 | 321 | 320 | 2.6 |
| FeO(t) | %m/m | 10.7 | 10.9 | 9.81 | 10.1 | 3.27 | 6.44 | 4.37 | 6.8 |
| Ga | µg/g | 20 | 19.6 | 8.67 | 10.4 | 25.3 | 19.4 | 20.9 | 2.3 |
| Gd | µg/g | 5.92 | 5.26 | 1.17 | 1.19 | 15.3 | 5.31 | 2.59 | 0.253 |
| Ge | µg/g | 1.3 | 1.1 | 0.96 | 0.68 | 1.8 | 1.8 | 1.1 | 0.44 |
| $H_2O$ | %m/m | 0.015 | 0.015 | 0.026 | 0.026 | 0.014 | 0.026 | 0.025 | 0.014 |
| Hf | µg/g | 3.93 | 3.22 | 0.349 | 0.357 | 13.7 | 3.88 | 3.07 | 0.52 |
| Ho | µg/g | 0.961 | 0.906 | 0.443 | 0.507 | 3.43 | 0.86 | 0.42 | 0.083 |
| In | µg/g | 0.24 | 0.2 | 0.067 | 0.09 | 0.17 | 0.3 | 0.5 | 0.19 |
| Ir | µg/g | 0.1 | 0.03 | 0.063 | 1.28 | 0.09 | 0.2 | 0.02 | 0.065 |
| $K_2O$ | %m/m | 0.48 | 0.385 | 0.036 | 0.0308 | 2.64 | 1.96 | 1.29 | 0.00372 |
| La | µg/g | 13.1 | 8.99 | 0.121 | 0.0842 | 55.6 | 70.4 | 12 | 0.223 |
| Li | µg/g | 5.1 | 4.5 | 10.4 | 8.9 | 28.6 | 19.9 | 20.7 | 2.2 |
| Lu | µg/g | 0.285 | 0.286 | 0.206 | 0.237 | 1.54 | 0.354 | 0.168 | 0.045 |
| MgO | %m/m | 7.34 | 6.59 | 26 | 22.4 | 0.103 | 3.75 | 1.97 | 34.3 |
| MnO | %m/m | 0.165 | 0.17 | 0.176 | 0.154 | 0.106 | 0.127 | 0.076 | 0.109 |
| Mo | µg/g | 3.6 | 16.7 | | 30.5 | 4.8 | 4.2 | 2 | 19 |
| $Na_2O$ | %m/m | 2.35 | 2.4 | 0.574 | 0.83 | 3.75 | 3.13 | 4.44 | 0.115 |
| Nb | µg/g | 15 | 8.61 | 0.099 | 0.073 | 62.4 | 8.87 | 6.94 | 0.039 |
| Nd | µg/g | 21.6 | 16.7 | 0.784 | 0.689 | 60.9 | 41.4 | 13 | 0.367 |
| Ni | µg/g | 112 | 107 | 1074 | 1187 | 13 | 10.6 | 23.7 | 1900 |
| O | %m/m | 44.4 | 44.7 | 44.4 | 44.0 | 48.7 | 46.4 | 47.9 | 45.8 |
| $P_2O_5$ | %m/m | 0.232 | 0.23 | 0.025 | 0.036 | 0.025 | 0.168 | 0.164 | <0.0004 |
| Pb | µg/g | 2.07 | 1.38 | 0.345 | 19.5 | 5.67 | 11.6 | 10.3 | 0.57 |
| Pr | µg/g | 4.6 | 3.43 | 0.1 | 0.089 | 14.6 | 12.4 | 3.2 | 0.075 |
| Pt | µg/g | 16 | 8.8 | 11.1 | 13 | 8 | 6 | 1 | 20 |

TABLE 10-5 (CONTD.): GEOREM PREFERRED VALUES OF THE GEOLOGICAL MPI-DING REFERENCE GLASSES.

| | | KL2-G | ML3B-G | GOR128-G | GOR132-G | ATHO-G | T1-G | StHs6/80-G | BM90/21-G |
|---|---|---|---|---|---|---|---|---|---|
| Rb | µg/g | 8.7 | 5.8 | 0.406 | 2.1 | 65.3 | 79.7 | 30.7 | 0.374 |
| Re | µg/g | 0.0007 | 0.0007 | 0.0006 | 0.0009 | 0.0005 | 0.0018 | 0.0009 | 0.0008 |
| S | µg/g | 7.7 | 1.2 | 4.3 | 1.8 | 0.6 | 2.6 | 2.7 | 1.2 |
| Sb | µg/g | 0.14 | 0.11 | 0.01 | 0.06 | 0.32 | 0.25 | 0.2 | 0.037 |
| Sc | µg/g | 31.8 | 31.6 | 32.1 | 36.5 | 7 | 26.9 | 11.5 | 13.3 |
| Se | µg/g | 0.07 | 0.06 | <0.03 | <0.03 | 0.1 | 0.05 | 0.04 | <0.009 |
| $SiO_2$ | %m/m | 50.3 | 51.4 | 46.1 | 45.5 | 75.6 | 58.6 | 63.7 | 53.1 |
| Sm | µg/g | 5.54 | 4.75 | 0.525 | 0.508 | 14.2 | 6.57 | 2.78 | 0.147 |
| Sn | µg/g | 1.54 | 1.14 | 0.224 | 0.34 | 5.41 | 2 | 1.1 | 0.4 |
| Sr | µg/g | 356 | 312 | 30 | 15.3 | 94.1 | 284 | 482 | 0.78 |
| Ta | µg/g | 0.961 | 0.555 | 0.019 | 0.031 | 3.9 | 0.464 | 0.42 | 0.0031 |
| Tb | µg/g | 0.89 | 0.797 | 0.248 | 0.269 | 2.51 | 0.773 | 0.371 | 0.051 |
| Th | µg/g | 1.02 | 0.548 | 0.008 | 0.009 | 7.4 | 31.3 | 2.28 | 0.054 |
| $TiO_2$ | %m/m | 2.56 | 2.13 | 0.288 | 0.306 | 0.255 | 0.755 | 0.703 | 0.062 |
| Tl | µg/g | | 0.008 | <0.003 | 0.001 | 0.07 | 0.13 | 0.11 | 0.006 |
| Tm | µg/g | 0.331 | 0.324 | 0.204 | 0.234 | 1.52 | 0.354 | 0.172 | 0.041 |
| U | µg/g | 0.548 | 0.442 | 0.0121 | 0.048 | 2.37 | 1.71 | 1.01 | 0.084 |
| V | µg/g | 309 | 268 | 189 | 214 | 3.91 | 190 | 90.3 | 61 |
| W | µg/g | 0.37 | 0.35 | 15.5 | 25.4 | 9.3 | 0.69 | 0.47 | 0.49 |
| Y | µg/g | 25.4 | 23.9 | 11.8 | 12.9 | 94.5 | 23.9 | 11.4 | 2.18 |
| Yb | µg/g | 2.10 | 2.06 | 1.41 | 1.61 | 10.5 | 2.38 | 1.13 | 0.28 |
| Zn | µg/g | 110 | 108 | 74.7 | 76.8 | 141 | 74 | 67 | 39.9 |
| Zr | µg/g | 152 | 122 | 10 | 9.9 | 512 | 144 | 118 | 20 |
| $^{143}Nd/^{144}Nd$ | | 0.51295 | 0.512875 | 0.513234 | 0.513282 | 0.513009 | 0.512326 | 0.512894 | 0.512598 |
| $^{176}Hf/^{177}Hf$ | | 0.283109 | 0.283067 | | | | | | |
| $^{206}Pb/^{204}Pb$ | | 19.03 | 18.72 | 18.52 | 19.25 | 18.383 | 18.728 | 18.9 | |
| $^{207}Pb/^{204}Pb$ | | 15.632 | 15.60 | 15.62 | 15.72 | 15.48 | 15.679 | 15.614 | |
| $^{207}Pb/^{206}Pb$ | | 0.82146 | 0.8334 | 0.8439 | 0.8166 | 0.84204 | 0.83724 | 0.82616 | |
| $^{208}Pb/^{204}Pb$ | | 38.524 | 38.454 | 38.28 | 38.71 | 38.111 | 38.973 | 38.515 | |
| $^{208}Pb/^{206}Pb$ | | 2.0243 | 2.0542 | 2.068 | 2.011 | 2.073 | 2.081 | 2.0379 | |
| $^{87}Sr/^{86}Sr$ | | 0.703517 | 0.703805 | 0.706888 | 0.707156 | 0.703224 | 0.710093 | 0.703497 | 0.706276 |
| $\delta^{11}B$ | ‰NIST951 | | | 13.55 | 7.11 | | | -4.48 | |
| $\delta^{17}O$ | ‰VSMOW | 4.31 | 4.28 | 4.83 | 4.34 | 1.59 | 3.89 | 3.21 | 4.27 |
| $\delta^{18}O$ | ‰VSMOW | 8.63 | 8.35 | 9.43 | 8.52 | 3.2 | 7.53 | 6.12 | 8.4 |
| $\delta^{44}/^{40}Ca$ | ‰NIST915a | 0.67 | 0.67 | 0.66 | 0.49 | 0.84 | 0.73 | 0.74 | 1.29 |
| $\delta^{7}Li$ | ‰LSVEC | 4.1 | 4.4 | 14.4 | 8.9 | 17.1 | 2.1 | 3.6 | |
| δD | ‰VSMOW | | | | | | -117 | -95 | |

$^{87}Sr/^{86}Sr$ (caused by unknown mass discrimination for Rb) using well documented MPI-DING reference glasses KL2-G, ML3B-G and the USGS BHVO-2G with known $^{87}Sr/^{86}Sr$ and similar matrix. An external precision (RSD) of the Sr isotope measurements of 0.02 % was achieved. Agreement with TIMS data was within 0.01–0.04%.

**RMs for mineral analyses**

Well characterized RMs are needed for accurate chemical and isotopic analyses of minerals by LA–(MC)–ICP–MS (see Horstwood 2008). However, only a few of such RMs are available. Notable exceptions are natural and synthetic zircon, titanite and sulfide RMs as well as some others (*e.g.*, carbonate, phosphate, rutile), which are under development or recently produced.

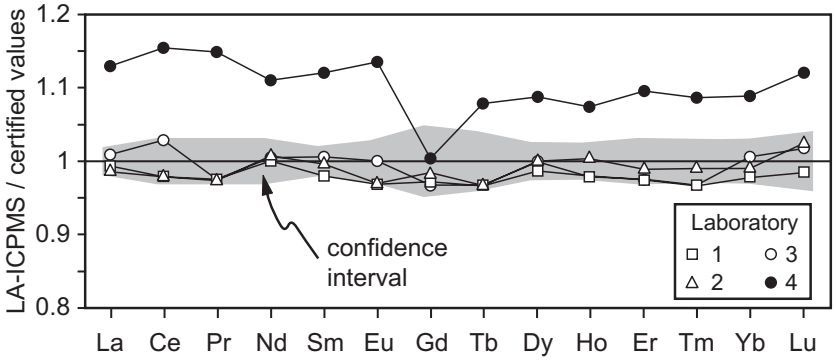


FIG. 10-7: REE data for KL2-G obtained from 4 different LA–ICP–MS laboratories (data in Jochum *et al.* 2006b). They are compared with the certified values (Table 10-5). The data of laboratories 1–3 agree with the certified values. The results of laboratory 4 are significantly higher presumably because of calibration difficulties.

***a) 91500 zircon***

Some natural zircon samples (such as BR266 (see Simonetti *et al.* 2008), Temora-1, Temora-2, Monastery; see GeoReM database for further samples) were used as RMs. However, for most of them only small amounts of sample and few analytical data are available. The 91500 crystal has become by far the best characterized zircon RM currently available. This sample consists of one crystal with an original mass of 238 g, which was provided by the Harvard Mineralogical Museum in Cambridge, USA (Wiedenbeck *et al.* 1995). It was collected near Kuehl Lake, Renfrew County, Ontario, Canada. In 2004, Wiedenbeck *et al.* (2004) published a second detailed report including data from various techniques. In particular, the authors investigated the suitability of 91500 for calibrating *in situ* analyses. In Fig. 10-10 the REE data of 5 LA–ICP–MS laboratories are compared with the GeoReM preferred values of 91500 zircon, which are listed in Table 10-6. Unfortunately, Wiedenbeck *et al.* observed banding in the zircon. Other authors (Woodhead & Hergt 2005, Iizuka & Hirata 2005) found potential micrometre-scale heterogeneity. However, it appears that 91500 is relatively homogeneous in $^{176}Hf/^{177}Hf$ at the *ca.* 50 μm scale and seems to be very well suited for calibrating *in situ* Hf isotopic analyses. Consistent results are also found for oxygen isotopes.

It may be expected that the 91500 zircon will continue to play an important role in geoanalysis over the coming years. Despite of this, Wiedenbeck *et al.* (2004) recommended its use not as a primary calibrator but as a secondary RM for quality control purposes.

***b) Sulfides***

The determination of trace elements, such as the highly siderophile elements (HSE) Re, Os, Ir, Ru, Rh and Pd, in natural sulfide minerals is important in basic, economic and environmental geochemistry. LA–ICP–MS is a powerful technique for *in situ* analysis of trace elements in sulfides. Ideally, matrices and trace element concentrations of RMs should be as close as possible to the unknowns. However, there is a lack of suitable RMs for primary calibration. For this reason, most laboratories synthesize their own calibration materials for sulfide analysis. There are several methods to prepare such samples. Ballhaus

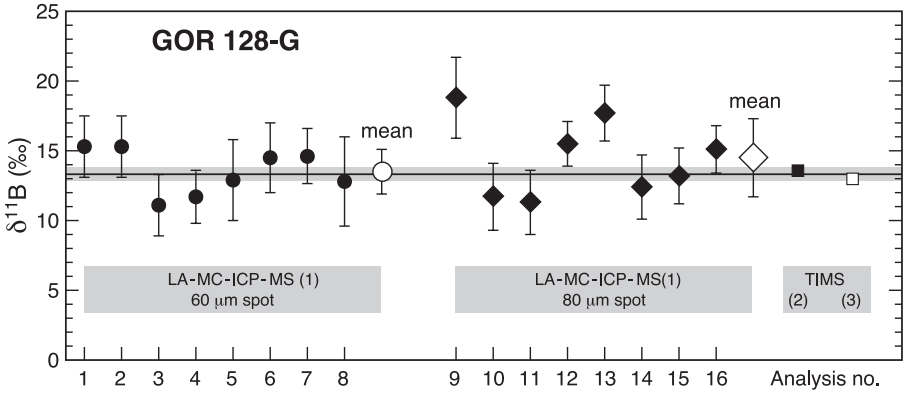


FIG. 10-8: $\delta^{11}B$ values (relative to NIST SRM 951) for the komatiitic GOR 128-G glass obtained from LA–MC–ICP–MS analyses using two different spot sizes (1: Tiepolo *et al.* 2006). Nearly all single spot analyses overlap the high precision TIMS values (2: Rosner & Meixner 2004; 3: S. Tonarini, unpublished) at the 1σ level.

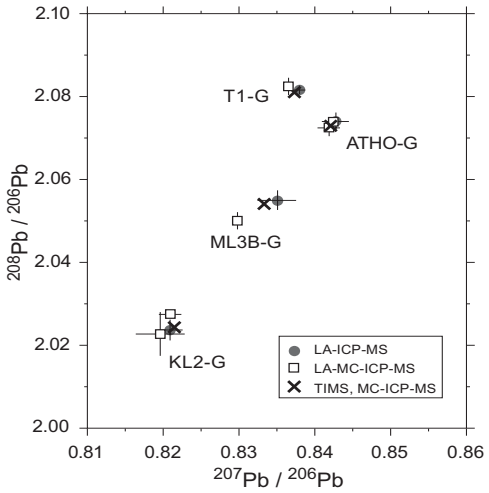


FIG. 10-9: $^{208}Pb/^{206}Pb$ *vs.* $^{207}Pb/^{206}Pb$ for MPI-DING reference glasses. LA–ICP–MS (Jochum *et al.* 2006a) and LA–MC–ICP–MS (Paul *et al.* 2005, Souders & Sylvester 2008) data are compared with high precision TIMS and MC–ICP–MS values (Jochum *et al.* 2006a). Error bars indicate ±1 SD.

& Sylvester (2000) synthesized $Fe_{1-x}S$ monosulfide aggregates with theoretical density, which contain noble metals of about 5–10 µg/g. Another method is to synthesize sulfide RMs at one atm. in $SiO_2$ glass capsules (Cabri *et al.* 2003). Noble metal concentrations were analyzed by ICP–MS and ranged between 20 and 50 µg/g (Mungall *et al.* 2005).

The USGS prepared *ca*. 200 g of a sulfide RM, PS-1 (later renamed by them, MASS-1) by precipitating amorphous metal sulfides from solution (Wilson *et al.* 2002). Homogeneity was tested by EPMA and LA–ICP–MS. Preliminary composition data of 23 elements in MASS-1 are listed in Table 10-6. However, this RM does not contain platinum-group elements (PGE). New homogeneous PGE sulfide RMs for LA–ICP–MS work were recently prepared by Wohlgemuth-Ueberwasser *et al.* (2007). The compositions are $(Fe,Ni,Cu)_{1-x}S$ monosulfides synthesized from metal powders and elemental S. Re and PGE were added as solutions. Following synthesis at 1 atm. the sulfides were sintered at 1.5 to 2 GPa to obtain pellets with theoretical density. Homogeneity of the RMs is different: the most homogeneous sulfides are the $Fe_{1-x}S$ and $(Fe,Ni)_{1-x}S$ compositions followed by the $(Fe,Cu)_{1-x}S$ composition. The NiS sample is the most heterogeneous RM. The abundances of Re and the PGE of the homogeneous sulfide RMs were analyzed by isotope dilution using ICP–MS (Wohlgemuth *et al.* 2007; see Table 10-6). Concentrations range from 35 to 60 µg/g.

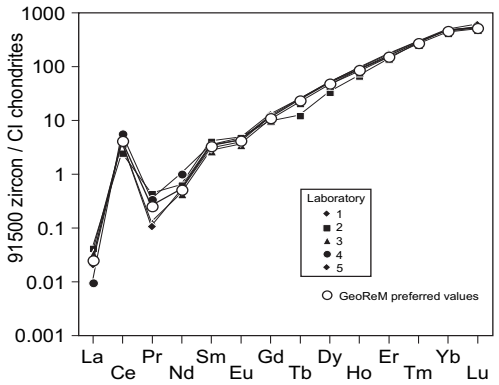


FIG. 10-10: CI chondrite-normalized REE data of 91500 zircon obtained from 5 different LA–ICP–MS laboratories (Wiedenbeck *et al.* 2004). The figure also shows the GeoReM preferred values.

***c) Other RMs***

Odegard *et al.* (2005) prepared the titanite ($CaTiSiO_5$) glass calibration material TIT-200. A titanite matrix doped with minor and trace elements at about 200 µg/g was fused in graphite electrodes at 1600–1700°C. Backscattered electron images indicated good homogeneity. The homogeneity in the titanite glass was assessed by LA–ICP–MS analyses. Table 10-6 shows preliminary analytical data.

MACS-1 is a synthetic calcium carbonate pellet RM, which was developed for LA–ICP–MS. This sample was used as quality control material for coral LA–ICP–MS analysis (Munksgaard *et al.* 2004, Mertz-Kraus *et al.* 2008). Table 10-7 shows the recommended values and the results of two LA–ICP–MS laboratories. The LA–ICP–MS data agree well with the recommended values, except for Al and Mg, where large discrepancies were found. The new synthetic carbonate MACS-2 is under development. Another microanalytical RM, the synthetic phosphate MAPS-2, was produced by the USGS.

Klemme *et al.* (2008) prepared 11 synthetic silicate and phosphate glasses (TNT666, TNT777, TNT150, TNT1500, CPX666, CPX777, DAC666, DAC777, STDP5, STDP3-150, STDP3-1500) to serve as reference materials for *in situ* micro-analysis of clinopyroxene, apatite and titanite, and other phosphate and titanite phases. The glasses are homogeneous in major and trace elements down to the micrometre scale. The authors also provided provisional recommended and information values (Table 10-8). Because two TNT glasses have been characterized in Hf isotopes, they may also be of interest to those who intend to measure the Hf isotopic composition of titanite.

TABLE 10-6: PRELIMINARY WORKING VALUES FOR MINERAL RMS (SEE TEXT FOR DETAILS).

| | | 91500 zircon | MASS-1 (PS-1) sulfide | $Fe_{1-x}S$ sulfide | $(Fe,Ni)_{1-x}S$ sulfide | $(Fe,Cu)_{1-x}S$ sulfide | TIT-200 titanite | Sy rutile | Diss rutile | R19 rutile | R10 rutile |
|---|---|---|---|---|---|---|---|---|---|---|---|
| Ag | µg/g | | 67 | | | | | | | | |
| As | µg/g | | 65 | | | | | | | | |
| Au | µg/g | | 47 | | | | | | | | |
| Ba | µg/g | 0.06 | | | | | | | | | |
| Bi | µg/g | | 7 | | | | | | | | |
| Cd | µg/g | | 70 | | | | | | | | |
| Ce | µg/g | 2.6 | | | | | 180 | | | | |
| Co | µg/g | | 67 | | | | 230 | | | | |
| Cr | µg/g | 1.5 | 37 | | | | 180 | | | | |
| Cu | µg/g | | 134000 | 100 | 100 | 21500 | | | | | |
| Dy | µg/g | 12 | | | | | 200 | | | | |
| Er | µg/g | 25 | | | | | 190 | | | | |
| Eu | µg/g | 0.24 | | | | | 190 | | | | |
| Fe | %m/m | | 15.6 | 60.5 | 55.4 | 58.2 | 0.025 | | | | |
| Ga | µg/g | | 50 | | | | | | | | |
| Gd | µg/g | 2.2 | | | | | 180 | | | | |
| Ge | µg/g | | 50 | | | | | | | | |
| $H_2O$ | %m/m | | 13.6 | | | | | | | | |
| Hf | µg/g | 5900 | | | | | 180 | 0.0954 | 5.081 | | 38.8 |
| Hg | µg/g | | 57 | | | | | | | | |
| Ho | µg/g | 4.8 | | | | | 210 | | | | |
| In | µg/g | | 50 | | | | | | | | |
| Ir | µg/g | | | 63.4 | 32.3 | 31.9 | | | | | |
| La | µg/g | 0.006 | | | | | 200 | | | | |
| Lu | µg/g | 13 | | | | | 200 | | | | |
| Mn | µg/g | | 260 | | | | 210 | | | | |
| Mo | µg/g | | 61 | | | | | | | | |
| $Na_2O$ | %m/m | | 3.3 | | | | | | | | |
| Nb | µg/g | 0.79 | | | | | 180 | | 146.3 | | 2633 |
| Nd | µg/g | 0.24 | | | | | 190 | | | | |
| Ni | µg/g | 0.07 | | 100 | 47200 | 100 | 200 | | | | |

TABLE 10-6 (CONTD.): PRELIMINARY WORKING VALUES FOR MINERAL RMS (SEE TEXT FOR DETAILS).

| | | 91500 zircon | MASS-1 (PS-1) sulfide | $Fe_{1-x}S$ sulfide | $(Fe,Ni)_{1-x}S$ sulfide | $(Fe,Cu)_{1-x}S$ sulfide | TIT-200 titanite | Sy rutile | Diss rutile | R19 rutile | R10 rutile |
|---|---|---|---|---|---|---|---|---|---|---|---|
| Os | µg/g | | | 71.9 | 36.9 | 46.6 | | | | | |
| P | µg/g | 24 | | | | | | | | | |
| Pb | µg/g | 15 | | | | | | | | | |
| Pd | µg/g | | | 60.4 | 34 | 41.2 | | | | | |
| Pr | µg/g | 0.024 | | | | | 190 | | | | |
| Pt | µg/g | | | 60.2 | 32.3 | 33.8 | | | | | |
| Re | µg/g | | | 61 | 34.2 | 38.1 | | | | | |
| Rh | µg/g | | | 57.2 | 34 | 35.7 | | | | | |
| Ru | µg/g | | | 59.9 | 35.1 | 36.7 | | | | | |
| S | %m/m | | 27.6 | 39.1 | 39.1 | 38.3 | | | | | |
| Sb | µg/g | | 55 | | | | | | 0.410 | 1.26 | 2.02 |
| Sc | µg/g | | | | | | 190 | | | | |
| Se | µg/g | | 53 | | | | | | | | |
| Si | µg/g | | | | | | 146000 | | | | |
| $SiO_2$ | %m/m | 32.7 | | | | | | | | | |
| Sm | µg/g | 0.5 | | | | | 200 | | | | |
| Sn | µg/g | | 55 | | | | | | | 123 | |
| Sr | µg/g | 0.052 | | | | | | | | | |
| Ta | µg/g | 0.5 | | | | | | 0.00371 | 7.66 | | 504 |
| Tb | µg/g | 0.86 | | | | | 190 | | | | |
| Th | µg/g | 30 | | | | | 180 | | | | |
| Ti | µg/g | 6 | | | | | 228000 | | | | |
| Tm | µg/g | 6.9 | | | | | 190 | | | | |
| U | µg/g | 80 | | | | | 170 | | | | 34.4 |
| V | µg/g | | 63 | | | | 180 | | | | |
| W | µg/g | | | | | | 160 | | | 59 | |
| Y | µg/g | 140 | | | | | 200 | | | | |
| Yb | µg/g | 74 | | | | | 200 | | | | |
| Zn | %m/m | | 21 | | | | | | | | |
| Zr | µg/g | | | | | | 190 | | 98.03 | 264 | 789 |
| $ZrO_2$ | %m/m | 66.2 | | | | | | | | | |
| $^{176}Hf/^{177}Hf$ | | 0.282306 | | | | | | | | | |
| $\delta^{18}O$ | ‰SMOW | 9.9 | | | | | | | | | |

TABLE 10-7: LA-ICP–MS DATA AND RECOMMENDED VALUES FOR MACS-1.

| Element | recommended (1) | LA-ICP-MS (2) | LA-ICP-MS (3) | LA-ICP-MS (4) |
|---|---|---|---|---|
| Al | 110±16 | 312±49 | | 31±4 |
| Ba | 114±8 | 130±1 | 117±11 | 115±6 |
| Cd | | | | 82±6 |
| Ce | | | 116±12 | 123±10 |
| Cu | 124±5 | 122±5 | | |
| Dy | | | 124±14 | 135±12 |
| Er | | | 120±14 | 128±11 |
| Eu | | | 0.005±0.001 | 0.0049±0.0009 |
| Gd | | | 115±12 | 128±11 |
| Hf | | | 0.010±0.001 | 0.008±0.001 |
| Ho | | | 0.010±0.001 | 0.0052±0.0005 |
| La | 126±12 | 126±1 | 125±12 | 139±11 |
| Lu | | | 0.0030±0.0002 | 0.0026±0.0003 |
| Mg | 10 | 28.0±1.1 | | 11.8±0.6 |
| Mn | 118±12 | 126±2 | | 122±9 |
| Nb | | | 0.002±0.001 | 0.0018±0.0009 |
| Nd | | | 125±12 | 135±12 |
| Pb | 121±11 | 115±1 | 125±12 | 115±5 |
| Pr | | | 0.006±0.001 | 0.0063±0.0008 |
| Rb | | 0.098±0.039 | 0.075±0.01 | 0.065±0.030 |
| Sm | | | 120±12 | 134±12 |
| Sr | 219±20 | 249±1 | 211±10 | 215±7 |
| Ta | | | | 0.0011±0.0002 |
| Tb | | | 0.020±0.002 | 0.021±0.002 |
| Th | | | | 0.011±0.001 |
| Tm | | | | 0.0039±0.0006 |
| U | | 0.006±0.001 | 0.004±0.001 | 0.004±0.001 |
| Y | | | 0.052±0.010 | 0.054±0.004 |
| Yb | | | 123±15 | 132±10 |
| Zn | 123±16 | 118±2 | | 98±5 |
| Zr | | | 0.020±0.001 | 0.016±0.003 |

Concentrations in µg/g. Uncertainties are 1 SD. **(1)** S. Wilson (USGS) in Munksgaard *et al.* 2004; **(2)** Munksgaard *et al.* New Wave UP213 laser ablation system (Jochum *et al*. 2007)2004; **(3)** this work, MPI Mainz laboratory, using Element 2 ICPMS; **(4)** MPI-Mainz laboratory (Mertz-Kraus *et al*. 2008).

Recently, Luvizotto *et al.* (2008) prepared and analyzed a synthetic (Sy) and three natural (Diss, R19, R10) rutile RMs. Provisional concentration values for Zr, Nb, Sn, Sb, Hf, Ta, W and U are given in Table 10-6. The authors also presented concentrations of other elements (V, Cr, Fe, Mo, Lu, Pb, Th) as well as Pb and Hf isotope data.

## CONCLUSIONS

The demand for suitable reference glasses has increased considerably in the past few years because of the wide use of microanalytical techniques. At present there are 17 synthetic and geological glasses and 22 mineral samples (see Table 10-1) which are used worldwide in LA–(MC)–ICP–MS laboratories. The MPI-DING glasses have recently been certified (Jochum *et al.* 2006b), so that they belong to the best characterized RMs for microanalytical work. For the USGS basaltic glasses BCR-2G, BHVO-2G, BIR-1G and the synthetic NIST 600 glasses reliable reference values exist. An important step was the

TABLE 10-8: RECOMMENDED AND INFORMATION (IN PARANTHESES) VALUES OF THE UNIV. OF MÜNSTER (UM) REFERENCE GLASSES (KLEMME ET AL. 2008).

| | | **TNT666** | **TNT777** | **TNT150** | **TNT1500** | **CPX666** | **CPX777** | **DAC666** | **DAC777** | **STDP5** | **STDP3-150** | **STDP3-1500** |
|---|---|---|---|---|---|---|---|---|---|---|---|---|
| $Al_2O_3$ | %m/m | | | 0.11 | 0.12 | 8.72 | 8.72 | 15.33 | 15.32 | | 13.5 | 13.1 |
| B | µg/g | (47) | | (66) | (144) | (97.8) | (6.3) | (86.6) | (3.1) | (59.1) | (65.6) | (158.6) |
| Ba | µg/g | 16.2 | 977 | 155 | 1347 | 10 | 1228 | (5.3) | 1268 | 1438 | 155 | (1520) |
| Be | µg/g | (69) | | (144) | (203) | (82.7) | | (83.2) | (0.5) | (88.3) | (10.7) | (99.5) |
| CaO | %m/m | 28.04 | 27.91 | 28.16 | 27.30 | 25.21 | 25.02 | 8.08 | 7.97 | 31.81 | 21.1 | 20.4 |
| Ce | µg/g | 1058 | (0.38) | 125 | 1319 | (1382) | (2.9) | 1299 | (3) | 1501 | 147 | (1522) |
| Cs | µg/g | 528 | (3) | 97 | 705 | 946 | (2.4) | 1139 | (10) | 1355 | 142 | (1495) |
| Er | µg/g | | | | | (0.07) | | | | | | (0.23) |
| Eu | µg/g | | (0.15) | | | | | | | | | (0.16) |
| Ga | µg/g | (12) | 506 | (2) | | (581) | (5) | 568 | (10) | | 15 | (42.9) |
| Gd | µg/g | 996 | | 126 | 1279 | 1170 | (1) | 1222 | | 1375 | 124 | (1281) |
| Hf | µg/g | 1262 | (2.5) | 150 | 1611 | 1329 | (3) | 1419 | (3) | 1344 | 145 | (1306) |
| $K_2O$ | %m/m | 0.08 | 0.06 | 0.084 | 0.10 | 0.024 | 0.018 | 3.19 | 3.2 | | | |
| La | µg/g | 1032 | (0.73) | 116 | 1173 | (1169) | (12) | 1217 | (4) | 1216 | 118.7 | (1241) |
| Li | µg/g | 52 | | 93 | (183) | 65 | 63 | 71 | 71 | 89 | 12 | (99) |
| Lu | µg/g | (0.21) | 1343 | 143.2 | 1469 | (1) | 1357 | | 1517 | 1429 | 137 | (1407) |
| MgO | %m/m | | | | | 14.09 | 14.06 | | | | 10.7 | 10.4 |
| $Na_2O$ | %m/m | 0.016 | | 0.013 | 0.024 | 0.04 | 0.029 | 4.37 | 4.2 | | | |
| Nb | µg/g | 44.96 | 790 | 169 | 1357 | (4.9) | 841 | (4) | 921 | 1285 | 146 | (1521) |
| Nd | µg/g | (0.07) | (0.27) | (0.403) | (0.58) | (0.08) | (0.27) | | (0.29) | | (0.2) | (0.4) |
| $P_2O_5$ | %m/m | | | | | | | | | 65.91 | 7.8 | 7.6 |
| Pb | µg/g | 974 | (3.4) | 89 | 851 | (1470) | (5) | 1394 | (5) | 1414 | 151 | (1584) |
| Pr | µg/g | | 967 | 123 | 1342 | (0.21) | (0.2) | (2) | 1258 | 1443 | 132 | (1425) |
| Rb | µg/g | 6.4 | 309 | 114 | 1059 | 7 | 638 | (11.2) | 838 | 1447 | 145 | (1545) |
| $SiO_2$ | %m/m | 30.14 | 29.96 | 29.97 | 28.86 | 42.9 | 42.9 | 64.32 | 64.04 | | 46.51 | 45.1 |
| Sm | µg/g | | 1019 | 126 | 1278 | | 1181 | (3) | 1294 | 1346 | 127.4 | (1282) |
| Sr | µg/g | 626 | (8.7) | 140 | 1321 | (1167) | (8) | 767 | (4) | 1434 | 196 | (1474) |
| Ta | µg/g | 3.29 | 1470 | 150.4 | 1489 | (2.1) | (1613) | (5) | 1744 | 1463 | 170 | (1518) |
| Th | µg/g | (0.32) | (1309) | 121 | 1314 | (2) | 1874 | (4) | 1898 | 1235 | 149 | (1434) |
| $TiO_2$ | %m/m | 39.65 | 39.55 | 39.86 | 38.86 | 6.91 | 6.92 | 2.76 | 2.73 | | | |
| U | µg/g | (5.8) | 1630 | 145 | 1366 | (5) | 1966 | (5) | 2025 | 1378 | 144 | (1446) |
| Y | µg/g | (1.5) | (564) | 119 | (1269) | 2 | 714 | 2 | 780 | 1473 | 138 | (1426) |
| Yb | µg/g | (0.19) | (1) | | 1.62 | | (1.5) | | (1.6) | | | (1.5) |
| Zr | µg/g | 667 | 16.99 | 225.4 | 1622 | 685 | (11) | 749 | (9) | 1335 | 142 | (1301) |
| $^{176}Hf/^{177}Hf$ | | | | 0.282305 | 0.282326 | | | | | | | |

development of the USGS GS glasses, which are ideal calibration materials for geological samples because of their basaltic matrix and their high trace element content. It is expected that this set of samples will substitute for the NIST 600 glasses for many geological applications in the future. However, so far only a few analyses are available.

Because of the wide field of LA–(MC)–ICP–MS applications, an increasing need exists for glasses with natural compositions. So far, only the MPI-DING glasses cover the entire spectrum from ultramafic to highly siliceous compositions. In all reference glasses most elements are homogeneously distributed. However, this is not valid for some chalcophile and siderophile elements, such as the PGE. This means that there is a particular need for well calibrated chalcophile and siderophile reference glasses for LA–ICP–MS analysis.

For *in situ* isotope analysis an increasing need also exists for well characterized RMs and CRMs to satisfy the requirements for new LA–(MC)–ICP–MS applications (*e.g.*, Pb, Sr isotopes and new stable isotope systems, such as B, Li, Ca). Isotope data for B, Li, Sr, Nd and Pb are available for the NIST SRM 610 and 612 glasses. Even more isotope systems (H, O, Li, B, Ca, Sr, Nd, Hf, Pb) have been investigated for the MPI-DING glasses. An extensive isotope study of the USGS GSD-1G glass is now in progress. However, more isotope analyses are required for satisfactory characterization of these reference glasses.

For mineral LA–(MC)–ICP–MS investigations there is a great lack of suitable RMs. Only few samples are distributed worldwide and well analyzed, *e.g.*, 91500 zircon and some sulfide RMs. No international reference materials for garnet, olivine and other minerals exist. An important step has been the recent preparation and characterization of 11 homogeneous titanite, clinopyroxene, dacite and phosphate glasses by the University of Münster (Klemme *et al.* 2008). However, the sample amount of 15 g for each glass limits the wide use of these RMs. Reasons for the low number of RMs are severe heterogeneities in natural minerals and difficulties in the preparation of homogeneous synthetic samples. The production of large amounts of homogeneous certified mineral samples is therefore an urgent task for RM producers.

Unfortunately, most reference materials for *in situ* microanalytical work are not yet certified. To overcome this, the International Association of Geoanalysts (IAG) has undertaken to serve as a certifying body and to develop a protocol for the certification of geological and environmental RMs. The certification procedure of the MPI-DING glasses (Jochum *et al.* 2006) followed these rules.

## REFERENCES

"GeoReM numbers", which identify the references in the GeoReM database are provided below.


BAKER, J., PEATE, D., WAIGHT, T. & MEYZEN, C. (2004): Pb isotopic analysis of standards and samples using a $^{207}Pb$–$^{204}Pb$ double spike and thallium to correct for mass bias with a double-focusing MC–ICP–MS. *Chem. Geol.* **211**, 275-303. (GeoReM 150)

BALLHAUS, C. & SYLVESTER, P. (2000): Noble metal enrichment process in the Merensky Reef, Bushveld Complex. *J. Petrol.* **41**, 545-561.

BECKER, J.SU., PICKHARDT, C., HOFFMANN, N., HÖCKER, H. & BECKER, J.SA. (2002): Multi-element analysis of alkaline-resistant glass and basalt glass fibers using laser ablation ICP–MS: A useful tool in technical textile quality control. *At. Spectrosc.* **23**, 1-6.

CABRI, L.J., SYLVESTER, P.J., TUBRETT, M.N., PEREGOEDOVA, A. & LAFLAMME, L.H.G. (2003): Comparison of LAM–ICP–MS and Micro-PIXE results for palladium and rhodium in selected samples of Noril'sk and Talnakh sulfides. CAN. MINERAL. **41**, 321-329.

EGGINS, S.M. (2003): Laser ablation ICP–MS analysis of geological materials prepared as lithium borate glasses. *Geostand. Newslett.* **27**, 147-162. (GeoReM 64)

EGGINS, S.M. & SHELLEY, J.M.S. (2002): Compositional heterogeneity in NIST SRM 610-617 glasses. *Geostand. Newslett.* **26**, 269-286. (GeoReM 168)

ELBURG, M., VROON, P., VAN DER WAGT, B. & TCHALIKIAN, A. (2005): Sr and Pb isotopic composition of five USGS glasses (BHVO-2G, BIR-1G, BCR-2G, TB-1G, NKT-1G). *Chem. Geol.* **223**, 196-207. (GeoReM 480)

GEOREM DATABASE: http://georem.mpch-mainz.gwdg.de

GUILLONG, M., HAMETNER, K., REUSSER, E., WILSON, S.A. & GÜNTHER, D. (2005): Preliminary characterization of new glass reference materials (GSA-1G, GSC-1G, GSD-1G and GSE-1G) by laser ablation-inductively coupled plasma-mass spectrometry using 193 nm, 213 nm and 266 nm wavelengths. *Geostand.*

*Geoanalyt. Res*. **29**, 315-331. (GeoReM 881)

GÜNTHER, D. & KOCH, J. (2008): Formation of aerosols generated by laser ablation and their impact on elemental fractionation in LA–ICP–MS. *In* Laser Ablation ICP–MS in the Earth Sciences: Current Practices and Outstanding Issues (P. Sylvester, *ed*.). *Mineral. Assoc. Can. Short Course Series* **40**, 19-34.

HORSTWOOD, M.S.A. (2008): Data reduction strategies, uncertainty assessment and resolution of LA–(MC–)ICP–MS isotope data. *In* Laser Ablation ICP–MS in the Earth Sciences: Current Practices and Outstanding Issues (P. Sylvester, *ed*.). *Mineral. Assoc. Can. Short Course Series* **40**, 283-303.

IIZUKA,T. & HIRATA, T. (2005): Improvements of precision and accuracy in *in situ* Hf isotope microanalysis of zircon using the laser ablation–MC–ICP–MS technique. *Chem. Geol*. **220**, 121-137. (GeoReM 1057)

INTERNATIONAL ORGANIZATION FOR STANDARDIZATION (ISO) (1992): *Terms and definitions used in connection with reference materials*, 2nd ed., ISO Guide **30**, 8 pp. Geneva.

IONOV, D., BLICHERT-TOFT, J. & WEIS, D. (2004): Hf isotope compositions and HREE variations in off-craton garnet and spinel peridotite xenoliths from central Asia. *Geochim. Cosmochim. Acta* **69**, 2399-2418. (GeoReM 398)

ISO/REMCO (2005): Reference number ISO/REMCO N 766. www.iso.ch/REMCO

JACKSON, S.E. (2008): Calibration strategies for elemental analysis by LA–ICP–MS *In* Laser Ablation ICP–MS in the Earth Sciences: Current Practices and Outstanding Issues (P. Sylvester, *ed*.). *Mineral. Assoc. Can. Short Course Series* **40**, 169-188.

JOCHUM, K.P. & NOHL, U (2008): Reference materials in geochemistry and environmental research and the GeoReM database. *Chem. Geol.*, doi:10.1016/j.chemgeo.2008.04.002

JOCHUM, K.P., DINGWELL, D.B., ROCHOLL, A., STOLL, B., HOFMANN, A.W. & 31 coauthors (2000): The preparation and preliminary characterization of eight geological MPI-DING reference glasses for *in situ* microanalysis. *Geostand. Newslett.* **24**, 87-133. (GeoReM 3)

JOCHUM, K.P., NOHL, U., HERWIG, K., LAMMEL, E., STOLL, B. & HOFMANN, A.W. (2005a): GeoReM: A new geochemical database for reference materials and isotopic standards. *Geostand. Geoanal. Res*. **29**, 333-338.

JOCHUM, K.P., WILLBOLD, M., RACZEK, I., STOLL, B. & HERWIG, K. (2005b): Chemical characterization of the USGS reference glasses GSA-1G, GSC-1G, GSD-1G, GSE-1G, BCR-2G, BHVO-2G and BIR-1G using EPMA, ID–TIMS, ID–ICP–MS and LA–ICP–MS. *Geostand. Geoanalyt. Res.* **29**, 285-302. (GeoReM 492)

JOCHUM, K.P., STOLL, B., HERWIG, K. & WILLBOLD, M. (2006a): Improvement of *in situ* Pb isotope analysis by LA–ICP–MS using a 193 nm Nd:YAG laser. *J. Anal. At. Spectrom*. **21**, 666-675. (GeoReM 1047)

JOCHUM, K.P., STOLL, B., HERWIG, K.P., WILLBOLD, M., HOFMANN, A.W., AMINI, M. & 47 coauthors (2006b): MPI-DING reference glasses for *in situ* microanalysis: New reference values for element concentrations and isotope ratios. *Geochem. Geophys. Geosyst*. **7**, No. 2, Q02008, doi:10.1029/2005GC001060. (GeoReM 658)

JOCHUM, K.P., SOBOLEV, A.V., KUZMIN, D. & HOFMANN, A.W. (2006c): A sensitive LA–ICP–MS technique for Sr and Pb isotope analysis using a new solid-state 193 nm laser and application to Mauna Loa melt inclusions. *EOS Trans. AGU* **87(52**), Fall Meet. Suppl., Abstract

JOCHUM, K.P., STOLL, B., HERWIG, K. & WILLBOLD, M. (2007), Validation of LA–ICP–MS trace element analysis of geological glasses using a new solid-state 193 nm Nd:YAG laser and matrix-matched calibration. *J. Anal. Atom. Spectrom*., 22, 112-121. (GeoReM 1248)

KANE, J.S. (1998): An assessment of the suitability of NIST glass SRM literature data for the derivation of reference values. *Geostand. Newsl*. **22**, 15-31.

KANE, J.S. (2002): Fitness-for-purpose of reference material reference values in relation to traceability of measurement, as illustrated by USGS BCR-1, NIST SRM 610 and IAEA NBS28. *Geostand. Newslett.* **26**, 7-29.

KANE, J.S. & POTTS, P.J. (1999): An interpretation of ISO Guidelines for the certification of geological reference materials. *Geostand. Newslett.* **23**, 209-221.

KANE, J.S., POTTS, P.J., WIEDENBECK, M., CARIGNAN, J. & WILSON, S. (2003): International Association of Geoanalysts' protocol for the certification of geological and environmental refer-

ence materials. *Geostand. Newslett*. **27**, 227-244.

KEMPENAERS, L., JANSSENS, K., JOCHUM, K.P., VINCZE, L., VEKEMANS, B., SOMOGYI, A., DRAKOPOULOS, M. & ADAMS, F. (2003): Micro-heterogeneity study of trace elements in USGS, MPI-DING and NIST glass reference materials by means of synchrotron micro-XRF. *J. Anal. Atom. Spectrom*. **18**, 350-357.

KLEMME, S., PROWATKE, S., MÜNKER, C., MAGEE, C., LAHAYE, Y., ZACK, T., KASEMANN, A., CABATO, E.J. & KAESER B. (2008): Synthesis and preliminary characterization of new silicate, phosphate and titanite reference glasses. *Geostand. Geoanalyt. Res*. **32**, 39-54. (GeoReM 2789)

KOŠLER, J. (2008): Laser ablation sampling strategies for concentration and isotope ratio analyses by ICP–MS. *In* Laser Ablation ICP–MS in the Earth Sciences: Current Practices and Outstanding Issues (P. Sylvester, *ed*.). *Mineral. Assoc. Can. Short Course Series* **40**, 79-92.

KROSLAKOVA, I. & GÜNTHER, D. (2007): Elemental fractionation in laser ablation–inductively coupled plasma–mass spectrometry: evidence for mass load induced matrix effects in the ICP during ablation of a silicate glass. *J. Anal. At. Spectrom.* **22**, 51-62.

LUVIZOTTO, G.L., ZACK, T., MEYER, H.P., LUDWIG, T., TRIEBOLD, S., KRONZ, A., MÜNKER, C., STOCKLI, D.F., PROWATKE, S., KLEMME, S., JACOB, D.E. & VON EYNATTEN, H. (2008): Rutile crystals as potential trace element and isotope mineral standards for microanalysis. *Chem. Geol*., doi: 10.1016/j.chemgeo.2008.04.012 (GeoReM 2842)

MERTZ-KRAUS, R., BRACHERT, T.C., JOCHUM, K.P., REUTER, M. & STOLL, B. (2008): Late Miocene heavy winter rain events in the Eastern Mediterranean inferred from LA-ICP-MS analyses on coral growth increments. *Palaeogeography, Palaeoclimatology, Palaeoecology,* submitted

MOZNA, V., PISONERO, J., HOLA, M., KANICKY, V. & GÜNTHER, D. (2006), Quantitative analysis of Fe-based samples using ultraviolet nanosecond and femtosecond laser ablation-ICP–MS. *J. Anal. At. Spectrom*. **21**, 1194-1201. (GeoReM 2470)

MUNGALL, J.E., ANDREWS, D.R.A., CABRI, L.J., SYLVESTER, P.J. & TUBRETT, M. (2005): Partitioning of Cu, Ni, Au, and platinum-group elements between monosulfide solid solution and sulfide melt under controlled oxygen and sulfur fugacities. *Geochim. Cosmochim. Acta* **69**, 4349-4360.

MUNKSGAARD, N.C., ANTWERTINGER, Y. & PARRY, D.L. (2004): Laser ablation ICP–MS analysis of Faviidae corals for environmental monitoring of a tropical estuary. *Environ. Chem.* **1**, 188-196. (GeoReM 1150)

NORMAN, M.D., GARCIA, M.O. & BENNETT, V.C. (2004): Rhenium and chalcophile elements in basaltic glasses from Ko'olau and Moloka'i volcanoes: Magmatic outgassing and composition of the Hawaiian plume. *Geochim. Cosmochim. Acta* **68**, 3761-3777. (GeoReM 684)

ODEGARD, M., SKAR, O., SCHIELLERUP, H. & PEARSON, N.J. (2005): Preparation of a synthetic titanite glass calibration material for *in situ* microanalysis by direct fusion in graphit electrodes: a preliminary characterization by EPMA and LA–ICP–MS. *Geostand. Geoanal. Res*. **29**, 197-209. (GeoReM 647)

PAUL, B., WOODHEAD, J.D. & HERGT J.M. (2005): Improved *in situ* isotope analysis of low-Pb materials using LA–MC–ICP–MS with parallel ion counter and Faraday detection. *J. Anal. At. Spectrom*. **20**, 1350-1357. (GeoReM 911)

PEARCE, N.J.G., PERKINS, W.T., WESTGATE, J.A., GORTON, M.P., JACKSON, S.E., NEAL, C.R. & CHENERY, S.P. (1997): A compilation of new and published major and trace element data for NIST SRM 610 and NIST SRM 612 glass reference materials. *Geostand. Newslett*. **21**, 115-144. (GeoReM 23)

PEARSON, N.J., GRIFFIN, W.L. & O'REILLY, S.Y. (2008): Mass fractionation correction in laser ablation multiple-collector ICP–MS: implications for overlap corrections and precise and accurate *in situ* isotope ratio measurement. *In* Laser Ablation ICP–MS in the Earth Sciences: Current Practices and Outstanding Issues (P. Sylvester, *ed*.). *Mineral. Assoc. Can. Short Course Series* **40**, 93-116.

RACZEK, I., JOCHUM, K.P. & HOFMANN, A.W. (2003): Neodymium and strontium isotope data for USGS reference materials BCR-1, BCR-2, BHVO-1, BHVO-2, AGV-1, AGV-2, DTS-1, DTS-2, GSP-1, GSP-2 and eight MPI-DING reference glasses. *Geostand. Newslett*. **27**, 173-179. (GeoReM 12)

ROCHOLL, A. (1998): Major and trace element composition and homogeneity of microbeam reference material: basalt glass USGS BCR-2G. *Geo-*

*standards Newsletter* **22**, 33-45. (GeoReM 431)

ROCHOLL, A.B.E., SIMON, K., JOCHUM, K.P., BRUHN, F., GEHANN, R., KRAMAR, U., LUECKE, W., MOLZAHN, M., PERNICKA, E., SEUFERT, M., SPETTEL, B. & STUMMEIER, J. (1997): Chemical characterization of NIST silicate glass reference material SRM 610 by ICP-MS, TIMS, LIMS, SSMS, INAA, AAS and PIXE. *Geostand. Newslett.* **21**, 101-114. (GeoReM 72)

ROSNER, M. & MEIXNER, A. (2004): Boron isotopic composition and concentration of ten geological reference materials. *Geostand. Geoanal. Res*. **28**, 431-441. (GeoReM 275)

SIMONETTI, A., HEAMAN, L.M. & CHACKO, T.. (2008): Use of discrete-dynode secondary electron multipliers with Faradays – a '*reduced volume*' approach for *in situ* U–Pb dating of accessory minerals within petrographic thin section by LA–MC–ICP–MS. *In* Laser Ablation ICP–MS in the Earth Sciences: Current Practices and Outstanding Issues (P. Sylvester, *ed*.). *Mineral. Assoc. Can. Short Course Series* **40**, 241-264.

STOLL, B., JOCHUM, K.P., HERWIG, K., AMINI, M., FLANZ, M., KREUZBURG, B., KUZMIN, D., WILLBOLD, M. & ENZWEILER, J. (2008): An automated iridium-strip heater for LA–ICP–MS bulk analysis of geological samples. *Geostand. Geoanalyt. Res*. **32**, 5-26 (GeoReM 2767)

SOUDERS, A.K. & SYLVESTER, P.J. (2008): Improved *in situ* measurements of lead isotopes in silicate glasses by LA-MC-ICP-MS using multiple ion counters. *J. Anal. Atom. Spectrom*. **23**, 535-543 (GeoReM 2853)

TIEPOLO M., BOUMAN, C. VANNUCCI, R. & SCHWIETERS, J. (2006): Laser ablation multicollector ICP–MS determination of $\delta^{11}B$ in geological samples. *Applied Geochemistry* **21**, 788-801. (GeoReM 654)

TREJOS, T. & ALMIRALL, J.R. (2004): Effect of fractionation on the forensic elemental analysis of glass using laser ablation inductively coupled plasma mass spectrometry. *Anal. Chem*. **76**, 1236-1242. (GeoReM 671)

USGS (1996): *Microbeam standard Columbia River basalt (Glass) BCR-2G*. United States Geological Survey Special Bulletin (Reference Materials Project), US Geological Survey, preliminary report, 10pp.

USGS (2004): *Geochemical reference materials and certificates.* http://minerals.cr.usgs.gov/geo_chem_stand/

WIEDENBECK, M., ALLÉ, P., CORFU, F., GRIFFIN, W.L., MEIER, M., OBERLI, F., VON QUANDT, A., RODDICK, J.C. & SPIEGEL, W. (1995): Three natural zircon standards for U–Th–Pb, Lu–Hf, trace element and REE analyses. *Geostand. Newslett*. **19**, 1-23. (GeoReM 78)

WIEDENBECK, M., HANCHAR, J.M., PECK, W.H., SYLVESTER, P., VALLEY, J., WHITEHOUSE, M., KRONZ, A., MORISHITA, Y., NASDALA, L., FIEBIG, J., FRANCHI, I., GIRARD, J.-P., GREENWOOD, R.C., HINTON, R., KITA, N., MASON, P.R.D., NORMAN, M., OGASAWARA, M., PICCOLI, P.M., RHEDE, D., SATOH, H., SCHULZ-DOBRICK, B., SKAR, O., SPICUZZA, M.J., TERADA, K., TINDLE, A., TOGASHI, S., VENNEMANN, T., XIE, Q. & ZHENG, Y.-F. (2004): Further characterisation of the 91500 zircon crystal. *Geostand. Geoanal. Res*. **28**, 9-39. (GeoReM 104)

WILSON, S.A., RIDLEY, W.I. & KOENIG, A.E. (2002): Development of sulfide calibration standards for the laser ablation inductively coupled plasma mass spectrometry technique. J. *Anal. At. Spectrom.* **17**, 406-409. (GeoReM 2770)

WOHLGEMUTH-UEBERWASSER, C.C., BALLHAUS, C., BERNDT, J., STOTTER NÉE PALIULIONYTE, V. & MEISEL, T. (2007): Synthesis of PGE sulfide standards for laser ablation inductively coupled plasma mass spectrometry (LA–ICP–MS). *Contrib. Mineral. Petrol*. **154**, 607-617. (GeoReM 2769)

WOODHEAD, J.D. & HERGT, J.M. (2005): A preliminary appraisal of seven natural zircon reference materials for *in situ* Hf isotope determination. *Geostand. Geoanal. Res*. 29, 183-195. (GeoReM 646)

WYNDHAM, T., MCCULLOCH, M., FALLON, S. & ALIBERT, C. (2004): High resolution coral records of rare earth elements in coastal seawater: biogeochemical cycling and a new environmental proxy. *Geochim. Cosmochim. Acta* **68**, 2067-2080.

YU, Z., NORMAN, M.D. & ROBINSON, P. (2003): Major and trace element analysis of silicate rocks by XRF and laser ablation ICP–MS using lithium borate fused glasses: Matrix effects, instrument response and results for international reference materials. *Geostand. Newslett*. **27**, 67-89. (GeoReM 68)

# CHAPTER 11: CALIBRATION STRATEGIES FOR ELEMENTAL ANALYSIS BY LA–ICP–MS

Simon E. Jackson
ARC National Key Centre for Geochemical Evolution and Metallogeny of Continents (GEMOC),
Macquarie University, NSW 2109, Australia

Current address: Geological Survey of Canada, Natural Resources Canada,
601 Booth Street, Ottawa, ON, K1A 0E8, Canada
E-mail: sijackso@NRCan.gc.ca

## INTRODUCTION

It was once thought likely that calibration would prove to be a fatal weakness of LA techniques for elemental analysis because different optical and mechanical, and thus ablation, properties of different materials might render satisfactory calibration virtually impossible. At a minimum, it seemed likely to require development of an array of suitable reference materials; ***i.e.,*** matrix matched to sample, homogeneous and well characterized at the trace element level. In practice, matrix effects have not proven to be as severe as once expected and calibration is thus relatively straightforward in most cases. A procedure that combines calibration of analyses by ablation of an external standard (usually a synthetic glass) and correction of matrix effects by internal standardization, using an element of known concentration in the sample and standard, has proven to provide remarkably accurate analyses for many elements in many sample matrices without matrix matching.

By contrast to the simplicity of the calibration procedure, there are probably few geochemical analytical techniques for which data reduction is such a critical, time-consuming and interactive process as for LA–ICP–MS. This is because laser ablation sampling occurs on spatial and time scales where transient signals related to sample heterogeneity (zoning, inclusions, *etc*.) are commonly resolvable. These time-resolved signals provide a wealth of information on the distribution of elements within the ablation volume, but require appropriate processing to generate meaningful results.

This chapter first describes the most commonly used calibration procedures for *in situ* elemental analysis of geological samples, building on the list of those reviewed by Günther *et al.* (1999). It then describes variations that have been employed for specific applications (***e.g.,*** analysis of fluid inclusions, C-based matrices, and sulfide minerals) and reports on available, commonly used standard reference materials. It also discusses inaccuracies introduced as a result of non-stoichiometric processes, generally termed 'elemental fractionation', which occur during laser ablation analysis, and discusses the need for matrix matching in LA–ICP–MS. Finally, it outlines approaches to data reduction, and discusses data reduction algorithms, including those that have been used to correct errors that occur as a result of elemental fractionation effects. Calibration of isotopic ratios by LA–(MC)–ICP–MS is not discussed here; this is reviewed by Pearson *et al*. (2008) and in other chapters of this volume.

## CALIBRATION STRATEGIES

The ICP–MS has long since been recognized as a relatively unstable instrument that requires frequent recalibration of its response. It is also well established that the disparate chemical, physical and optical properties of geological materials result in markedly different responses during laser ablation; that is, the amount and physical form of the ablation products will generally be different even if the same ablation conditions are used. The amount of material transported to the ICP is commonly termed the 'ablation yield'.

Quantification of LA–ICP–MS data therefore involves two major operations: calibration of the (changing) mass response of the ICP–MS and correction for the difference in ablation yield between the sample and calibration standard. A third component of a robust calibration protocol, that is often overlooked but will be considered later in this chapter, is correction of the non-stoichiometric effects that are an inherent aspect of laser sampling. These effects are a product of differing volatility of the elements, which result in certain elements preferentially fractionating, during ablation, into either the vapor or the liquid (or, in some cases, the solid) phase. These are differentially transported from the sample to ICP

Mineralogical Association of Canada Short Course 40, Vancouver, B.C., p. 169-188.

and also differentially volatilized in the ICP (Guillong & Günther 2002, Kuhn & Günther 2004, 2005), resulting in the widely observed effect of elemental fractionation.

Calibration of the mass response of the ICP–MS is generally achieved via analysis of a standard reference material. Analyses of the standards are generally repeated on a regular basis (hourly) to take into account the changing mass response of the ICP–MS. The signal, background corrected, from all or part of an ablation of a sample, is then compared to that of the standard and a correction applied for differences in ablation yield of the standard and sample. Instrument background signals are generally obtained from measurement of a 'gas blank' (*i.e.,* the ICP–MS signal with no ablation), usually acquired immediately prior to initiating ablation (*e.g.,* Fig. 11-1). It can be argued that a truly representative blank can only be obtained by ablating a solid (*e.g.,* a high purity material containing none of the elements of interest) because of potential matrix suppression of background signals, release (by acoustic shock) of particles deposited in the cell and transfer tubing during prior ablations, and desorption of volatile elements from the sample cell window. For example, the latter may explain the significant Hg signals that can sometimes be observed when firing the laser into an empty sample cell. In practice, this approach to background correction has not been adopted because of the impracticality of finding suitable blanks and the minimal effect it will generally have on the results.

Laser ablation signals for geological samples are generally selectively integrated, *i.e.*, the time segment of the time-resolved signals that is deemed most representative (*e.g.,* free of surface contamination, inclusions, *etc*.) is integrated. An ablation yield correction is then generally applied, most commonly using internal standardization. Internal standardization corrects primarily for differences in mass of material that is ablated, transported and ionized in the ICP. These differences result not only from different ablation characteristics of different materials but also different ablation conditions (*e.g.,* spot size) that may be used for different analyses. The magnitude of the ablation yield correction can be extremely large. For example, Jackson (2001) showed that, even using the same ablation conditions, ablation yield can vary by up to several hundred percent between materials that absorb a particular laser wavelength weakly and strongly. The mathematics of this correction is described by Longerich *et al.* (1996) and is summarized later in this chapter.

Six calibration strategies for LA–ICP–MS analysis have been described:

1) external calibration alone, using ablation of a solid reference standard,
2) external calibration using ablation of a solid reference standard, in conjunction with internal standardization
3) external calibration using aspirated solutions in conjunction with internal standardization,
4) external calibration using ablation of a liquid reference standard, in conjunction with internal standardization,

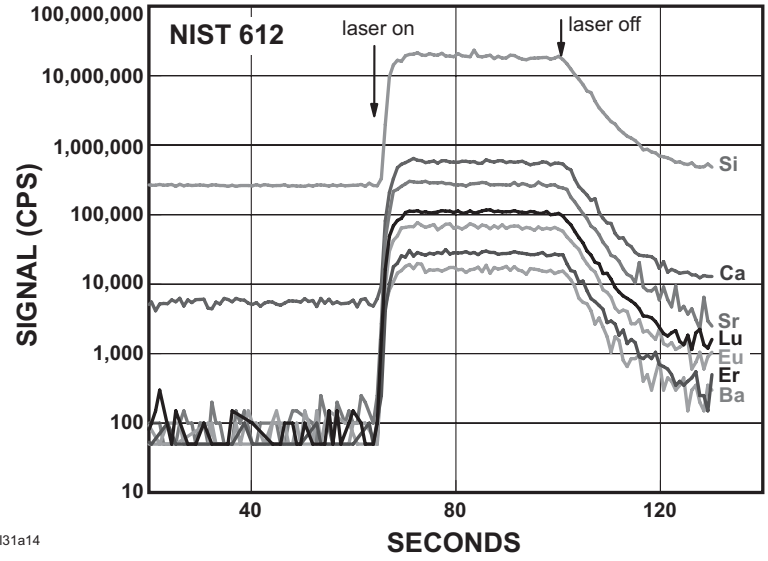


FIG. 11-1. Time resolved LA–ICP–MS signals for selected elements from an analysis of NIST 612 glass.

5) external calibration using normalization of total measured concentrations to 100%,
6) isotope dilution calibration.

***1. External calibration using ablation of a solid reference standard only:*** External calibration alone has been used for preliminary investigations of sample compositions. However, because of the large differences in ablation yield that result from variations in absorptivity of laser light by different target matrices, together with fluctuations in laser output and other analytical variables, it requires reference materials that are closely matrix-matched, both chemically and physically, to the samples and very closely replicated ablation conditions. Even then, it is barely more than a semi-quantitative technique.

***2. External calibration using ablation of a solid reference standard plus internal standardization:*** In contrast to protocol 1, the use of internal standards produces a much more robust calibration method by allowing a correction to be applied for differing ablation yield between sample and reference material (*e.g.,* Jackson *et al.* 1992). For analysis of solids in their natural state, a 'naturally occurring' internal standard must be used. The internal standard is, therefore, generally a major constituent, the concentration of which can be determined from independent analysis (*e.g.,* electron microprobe) or, in some instances, that can be calculated with sufficient accuracy from known stoichiometry of the material (*e.g.*, some geological minerals). Internal standardization has been critical to the development of the technique of LA–ICP–MS since it allows calibration using a standard that is not matrix-matched with the sample. Indeed, by far the most commonly used primary standards in LA–ICP–MS analysis of geological matrices are the NIST SRM 610/611 and 612/613 glasses, which have a matrix unlike almost any naturally occurring geological material.

Internal standardization also corrects, to some extent, for matrix suppression/enhancement effects and signal drift in the ICP–MS. This is of most importance for bulk sampling techniques where vigorous ablation can result in heavy loading of the ICP; for most microanalytical analyses, the sampled mass is so small that ICP–MS-related sample-loading matrix effects are small. It should be noted, however, that the major elements of most rock-forming minerals are of low atomic mass compared to the trace elements commonly being determined. As a result, frequent recalibration is required and mass-dependent drift corrections have to be applied during data processing (see below), because matrix effects and drift in ICP–MS are mass-dependent.

For bulk sampling applications (pressed powders or fused glasses) internal standards can potentially be added during preparation of the sample. An internal standard in the mid-mass range (*e.g.,* In) has been employed (Perkins *et al.* 1993) or multiple internal standards spanning the mass range can potentially be added to correct for differential instrumental drift and matrix effects across the mass range (Eggins 2003). However, the practical limitations of the latter approach include finding suitable internal standards that span the mass range and the lack of support in current data reduction software packages.

***3. Calibration using aspirated solutions plus internal standardization:*** External calibration using nebulized solution standards of known elemental composition has been widely reported (*e.g.,* Chenery & Cook 1993, Cromwell & Arrowsmith 1995, Moenke-Blankenburg *et al.* 1992). In this procedure, the carrier gas flow from the sample cell is combined with an aerosol generated by solution nebulization, either with or without desolvation. This allows the user to analyze sequentially either a nebulized solution standard or the solid sample by laser ablation. When ablation of the sample is performed, a blank solution is aspirated to maintain consistent conditions in the ICP. Internal standardization is essential.

This calibration procedure offers complete flexibility in the composition of the reference material. However, nebulization of a 'blank' solution during ablation nullifies the key advantages of dry plasma (laser only) operation by introducing solvents and their inherent contaminants (*e.g.,* Pb) that raise backgrounds and increase poly-atomic interferences. Although desolvation can be used to reduce solvent-related poly-atomic ions signals, desolvating nebulization systems have been shown to provide anomalous, non-quantitative transmission for some elements, notably Cu (Halicz & Günther 2004). Additionally, the different particle size distributions of laser- and nebulization-generated aerosols are likely to exacerbate differences in matrix effects in the ICP for sample and standard. The drawbacks outlined above, together with the ease with which accurate results can be obtained using ablation of solid reference materials, have limited the application of calibration using solutions.

***4. External calibration using ablation of a liquid reference standard plus internal standardization:*** A novel variation on protocol 2 is to use direct ablation of a liquid standard for calibration. The first application of this method for calibrating LA–ICP–MS analyses was in calibrating fluid inclusion analyses (Moissette *et al.* 1996, Günther *et al.* 1998), but it has also been shown to be a viable procedure for calibrating analyses of solid samples (Günther *et al.* 1997). In these studies, the liquid standard was placed in a microwell and covered with a thin seal (parafilm or Sellotape) through which small holes were ablated to access the liquid standard. Again, internal standardization is essential to correct for the different ablation efficiencies of the liquid standard and solid sample. Excellent accuracy was reported by Günther *et al.* (1997) for analyses of NIST SRMs 610 and 612.

The major advantage of this technique is that it provides full flexibility in the composition of the standard, thus lending itself to applications where solid standards (*e.g.,* NIST glasses) are not suitable. It has therefore been applied in several applications of LA–ICP–MS to analysis of carbon-based matrices, such as diamond (Jackson *et al.*1999, Rege *et al.* 2005) and bitumen (Mossman *et al.* 2001), where the only viable internal standard is C, which is not present in the NIST glasses at accurately measurable concentrations. These applications are discussed further below.

Direct liquid ablation also provides a means of gaining *quantitative* analyses of fluid inclusions in minerals (microscopic bubbles of fluid trapped during crystallization of a mineral). The method pioneered by Günther *et al.* (1998) involves calibrating analyses using direct liquid ablation of synthetic brines. Internal standardization was achieved using Na (or Cl) concentrations derived from microthermometric estimations of salinity of the inclusions, together with major cation ratios determined from the LA–ICP–MS signal. Other approaches to calibration of fluid inclusion analyses are discussed by Pettke (2008).

***5. External calibration using normalization of totals to 100%:*** An alternative procedure to normalizing the concentrations using a single internal standard element is that of normalizing the total element concentrations to 100% abundance (Halicz & Günther 2004, Guillong *et al.* 2005). In this procedure, all concentrations (converted m/m to weight percent oxides for rock-forming minerals and silicate glasses) are calculated and then normalized to 100%. Provided that the concentration of components that cannot be measured (*e.g.,* $H_2O$) is negligible (or can be assumed), this method corrects for the different sensitivities obtained for sample and calibration material as a result of differing ablation yield *without prior quantitative knowledge of the chemistry of the sample*. The major analytical drawback is the implicit requirement that *all* elements present in significant concentrations be known and accurately determined.

***6. Isotope dilution calibration:*** To overcome the requirement for suitable standards and to eliminate sample–standard matrix effects, several studies have employed isotope dilution (ID) to calibrate LA–ICP–MS analyses. Three approaches that have been described are:

*i) addition of an isotopically enriched spike solution to a fused glass or pressed powder sample preparation*. Reid *et al.* (1999) applied ID to the determination of Zr and Hf concentrations in a variety of geological certified reference materials. Enriched isotopes were added to the powders as solutions prior to flux-free fusion using an Ir strip heater. Precise LA–ICP–MS Zr and Hf values were obtained (*ca*. 1% and *ca*. 4% RSD respectively), with counting statistics the major limiting factor. Concentrations agreed favorably with literature data. Tibi & Heumann (2003) successfully applied a similar approach to determination of 7 elements in a variety of sample matrices, including two sediment samples, prepared as pressed powder pellets. The major advantage of these techniques is that, provided that isotopic equilibration is achieved between sample and spike, signal drift, matrix effects and analyte losses during fusion are corrected.

*ii) addition of an isotopically enriched solid spike to a pressed powdered sample*. In order to reduce sample preparation time associated with spiking powders with solutions, Fernández *et al*. (2008) developed a procedure in which a solid ID spike was mixed with sample powders which were then pressed into a pellet. Accurate data and precision generally better than 10% (1 RSD) were shown for two sediment and two soil reference materials.

*iii) on-line nebulization of an enriched isotopic tracer solution into the ablation cell*. Pickhardt *et al*. (2006) described an ID method for LA–ICP–MS determination of U directly in a solid (NIST SRM 612 glass) without the need for homogenization of

sample and spike. In this procedure, an enriched isotopic tracer solution was nebulized directly into the laser sample cell using a low flow (10 µl/min) nebulizer. Data collection involved three measurements: (1) laser ablation of the sample while nebulizing 2% $HNO_3$, (2) laser ablation of the sample while nebulizing the enriched isotope tracer solution and (3) nebulization of the enriched isotope tracer with no ablation. In addition to the analyte of interest, measurements were also made of the isotope ratio of an internal standard element (Th) for correction of sensitivity differences between solution and laser ablation analyses. Although incomplete homogenization of the sample and spike does not allow correction of errors derived from the ablation processes (Fernández *et al.* 2008), the on-line spiking procedure does open up the possibility of using isotope dilution to calibrate *in situ* mineral and glass analyses.

In practice, external calibration using ablation of a solid reference standard, in conjunction with internal standardization (protocol 2), has received by far the greatest usage, except in a few important applications (*e.g.,* fluid inclusion analysis). This is, probably, largely because of its simplicity, particularly when compared to direct liquid ablation, its full multi-element applicability, compared to isotope dilution methods, and its well established efficacy. Normalization of totals to 100% may well receive more widespread usage as its acceptance grows and if and when it is directly supported in the available LA–ICP–MS data reduction software packages.

### Choice of internal standard

For the calibration methods that involve internal standardization, correct choice of internal standard is a critical consideration. The internal standard must be an element that meets the following conditions:

1) it is homogeneously distributed in the ablation volume,
2) it is present in the sample *and standard* at sufficient concentrations for accurate determination by LA–ICP–MS, *and* for independent determination or estimation based on mineral stoichiometry,
3) it should have a concentration in the sample and standard that it is not too large for determination by ICP–MS (*cf.* Na and Al in the NIST glasses under some analytical conditions),
4) it should have the same fractionation behavior (see below) as the analytes.

Calcium is one of the best internal standards for the determination of lithophile elements due to its percent level abundance in many minerals (and the NIST SRM 600 series glasses that are often used for calibration), its three low abundance, isobaric interference-free isotopes (amu 42, 43, 44) and its similar fractionation behavior to many petrogenetically important elements (see below). Silicon is not generally as suitable as Ca because its fractionation behavior is significantly different to most of these elements (see below).

## CALIBRATION STANDARDS

Calibration standards for LA–ICP–MS are discussed in detail by Jochum & Stoll (2008). Some salient points regarding the application of some of the more commonly used standards for LA–ICP–MS are presented below.

### NIST SRM glasses

Although originally developed for calibration and control of techniques for the *bulk* analysis of glass only, by far the most widely used standards for calibration of LA–ICP–MS analyses of geological materials are the NIST SRM 600 series glasses (Kane 1998). These can be obtained from the National Institute of Standards and Technology (formerly National Bureau of Standards, NBS), Gaithersburg, Maryland, USA (www.nist.gov). These four materials, which are available in 3 mm (SRMs 610, 612, 614 and 616) and 1 mm thickness wafers (SRMs 611, 613, 615, 617) are synthetic soda lime glasses, composed predominantly of $SiO_2$, $Al_2O_3$, CaO and $Na_2O$, which have been spiked with 61 trace elements at nominal concentrations of 500 ppm, 50 ppm, 1 ppm and 0.02 ppm respectively (Kane 1998). The most widely used working values for the two most commonly used glasses (NIST 612 and 610) are those proposed, on the basis of new and compiled data, by Pearce *et al.* (1997) and, for NIST 610 only, by Rocholl *et al.* (1997). A more recent and continually updated compilation of published data, including 'preferred values' for these glasses can now be accessed on-line via the GeoREM web site (http://georem.mpch-mainz.gwdg.de) (Jochum *et al.* 2005a).

The NIST glasses have been used to calibrate analyses of a huge array of geological minerals effectively (silicates, oxides, carbonates, fluorides, tungstates, phosphates, *etc*.) and natural and synthetic glasses. By performing LA–ICP–MS analyses on samples that have been analyzed

independently, it is now well established that calibration using these glasses provides accurate data for many elements in sample matrices ranging from dark, strongly UV-absorbing materials (*e.g.,* titanite) to colorless, weakly UV-absorbing materials (*e.g.,* fluorite)(see Fig. 11-2). However, despite their widespread application, they are not universally appropriate for several reasons:

*(a) Mg, K, Fe and Ti* – the NIST 600 series glasses have only trace levels of the important 'major elements', Mg, K, Ti and Fe. These low concentrations, combined with high background ($^{39}$K) or the low isotopic abundance of their most analytically appropriate isotopes ($^{25}$Mg, 10%; $^{47}$Ti, 7.3%; $^{49}$Ti, 5.5%; $^{57}$Fe, 2.14%), make them challenging to determine precisely, should they be needed for internal standardization purposes (*e.g.,* Mg for olivine analysis, Ti for phlogopite analysis, *etc.*). This is especially true for NIST 612 which is the preferred standard when measuring samples with very low concentrations because of the reduced potential for contamination/memory effects.

More critically, the trace level concentrations of Ti, Mn and Fe, the main elements that impart color to geological minerals, mean that the NIST glasses ablate quite differently to many rock-forming minerals and igneous glasses. This means

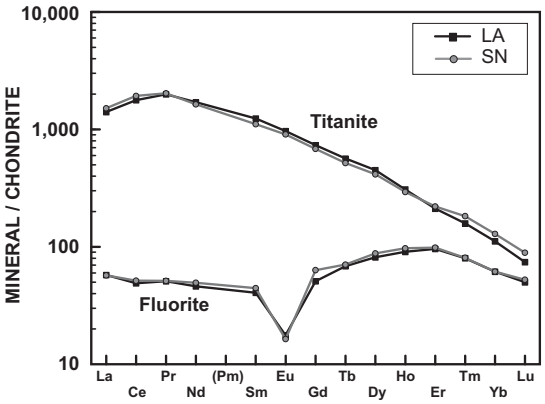


FIG. 11-2. Chondrite-normalized REE patterns for two minerals with extreme differences in absorption efficiency, titanite and fluorite. Each mineral was analyzed by LA–ICP–MS (LA) using non-matrix-matched calibration with NIST glasses. Titanite data (S. Jackson, unpublished data) are the mean of ten 10 μm spot analyses, fluorite data (C. Collins, Masters thesis, Memorial University of Newfoundland) are the mean of 3 spot analyses. Also shown are solution nebulization-ICP–MS (SN) after digestion of a sample aliquot. SN data for titanite from Jackson *et al.* (1992), SN data for fluorite from C. Collins (*ibid*). In both cases, SN data fall within the natural range of LA data.

that the NIST glasses can exhibit substantially different elemental fractionation behavior than many common geological matrices, resulting in degraded precision and accuracy for some elements (see below).

(b) *Heterogeneity* – Eggins & Shelley (2002) have reported significant heterogeneity for at least 25 of the trace elements in the NIST glasses. The heterogeneity is manifested largely as domains that are significantly depleted, mainly in volatile and siderophile elements, Ag, As, Au, B, Bi, Cd, Cr, Cs, Mo, Pb, Re, Sb, Se, Te, Tl and W, and enrichments in Cu and, sometimes, Cd, Fe and Mn. Many of these elements show >10% variability. These domains occur both close to the wafer rims and in irregular streaks in the interior of the disks. When determining these elements, monitoring the behavior of particularly loss-prone elements, such as Tl, is advised (Eggins & Shelley 2002).

(c) *Characterization* – There are a few elements in these glasses that have been characterized only poorly or not at all (*e.g.,* Te).

(d) *PGE* – The NIST glasses were not spiked with PGE. Although low ppm levels of some of these elements (Rh, Pd, Pt) have been reported to occur in these glasses (Sylvester & Eggins 1997), they cannot be used for calibrating the full group of PGE. Also, there are issues with large spectral interferences (*e.g.*, $^{63}$Cu$^{40}$Ar on $^{103}$Rh, $^{106}$Cd on $^{106}$Pd) and inhomogeneous domains within the wafers (Sylvester & Eggins 1997).

(e) *Analysis of sulfides and metals* – Sulfide minerals and native metals (*e.g.,* Au) are composed largely of chalcophile and siderophile elements. During laser ablation analysis, these elements are subject to severe fractionation (Fryer *et al.* 1995, see below), which is matrix-dependent. The NIST glasses are not therefore ideally suited to analysis of sulfide minerals and metals. Additionally, the ideal universal internal standard for analyzing sulfide minerals, S, is not present in the NIST glasses at precisely measurable levels.

(f) *Carbon-based matrices* – Most carbon-based matrices (*e.g.,* diamond, coal) require the use of C as the internal standard. Because of the very low C content of the NIST glasses, together with the high gas background for C in ICP–MS, resulting from entrainment of air into the ICP, impurities in the Ar supply and degassing of plastic gas supply tubing, these glasses are not appropriate as primary standards.

The limitations listed above have led to numerous efforts to develop alternative primary

standard reference materials for analysis of geological materials. Some of these materials and two specific applications for which the NIST glasses are not appropriate for primary calibration are discussed below. However, despite these limitations, the NIST glasses remain an invaluable resource for microbeam techniques and will probably remain the primary reference material for analysis of geological materials for some time to come.

**Other Primary Standards**

To simulate the matrix of many geological materials better, the USGS has produced a series of four synthetic glass reference materials for calibration of microbeam analyses (Guillong *et al.* 2005). These standards, which have nominal trace concentrations for more than 50 trace elements of 0, 5, 50 and 500 ppm, differ from the NIST glasses most notably in their matrix composition, which is similar to that of basalt. They are, therefore, dark in color and have much higher absorptivity of UV laser radiation than the NIST glasses (particularly for longer wavelengths, *e.g.,* 266 nm). They therefore represent a much closer matrix to many geological materials (*e.g.,* mafic minerals and glasses).

A large number of publications describe methodologies for preparation of mineral and glass standards matrix-matched to specific mineral compositions; *e.g.,* calcite (Pearce *et al.* 1992, Hathorne *et al.* 2008), apatite, clinopyroxene, and titanite (Klemme *et al.* 2008), quartz and rutile (Ødegård 1999), titanite (Ødegård *et al.* 2005). It should be noted that all of these materials are either pressed powders or glasses and thus, although chemically matched to the target minerals, they are not physically matched. It is well established that the physical properties of a material influence its ablation characteristics, as exhibited, for example, by cleavage controlled spalling of angular (rhombic) calcite fragments (*e.g.,* Jackson *et al.* 1992, Jackson 2001, Hathorne *et al.* 2008).

**Analysis of sulfides**

By comparison with the huge volume of LA–ICP–MS data for silicate minerals that is now in the literature, published data for sulfide minerals is remarkably scant. The corollary to this is that the paucity of publications on analysis of sulfides, is due, in part, to the lack of an off the shelf reference material well suited to analysis of sulfides. Ideally, this should be a sulfide mineral, or other S-rich material, in order to allow application to all sulfide mineral analyses using S as the internal standard. It should also possess a wide range of homogeneously distributed chalcophile and siderophile elements at ppm levels.

Natural sulfide minerals rarely contain the wide range of trace elements that geologists are interested in. Many are hydrothermal in origin and thus are typically extremely heterogeneous in their trace element distributions. Synthesizing, by fusion, homogeneous sulfide minerals with a wide range of trace elements has not yet been achieved due to the issues of incompatibility and the high volatility of many important chalcophile elements at the fusion temperatures of most sulfide minerals. Some success in synthesizing homogeneous standards for a limited range of elements, namely the PGE and Au, has been reported. A fused pyrrhotite SRM, referred to as Po41, and containing all six PGE and Au, has recently been produced at CANMET in Ottawa, Canada, (and calibrated at Memorial University of Newfoundland) in sufficient quantities for limited distribution (Sylvester *et al.* 2005). Pyrrhotite ($Fe_{(1-x)}S$) was used because some (up to nearly 20%) of the Fe sites in this mineral's structure are missing, creating omission defects that can be filled with other elements. Other procedures have been reported for synthesis of PGE-only sulfide standards (*e.g.,* Wohlgemuth-Ueberwasser *et al.* 2007).

In order to increase the range of elements present in a sulfide matrix, Wilson *et al.* (2002) produced for distribution a synthetic sulfide standard by chemical precipitation of amorphous Cu, Fe, Zn sulfide containing 21 chalcophilic elements (10–50 ppm), and available as a powder (PS-1) or pressed pellet (MASS-1, formerly MS-1). Unfortunately, analyses of this material in the GEMOC laboratories have shown a tendency for spalling of particulate material during ablation. Sylvester *et al.* (2005) have also noted that Au is somewhat heterogeneously distributed and the percent level concentrations of Cu and Zn in the matrix produce substantial argide interferences on Rh and Pd.

Other approaches for standardizing multi-element LA–ICP–MS analyses of sulfidic materials have been proposed. Norman *et al.* (2003) produced a sulfide glass prepared by Li-borate fusion of a mixture of CANMET sulfide ore reference materials and successfully used this to analyze glasses prepared from other ore standards. Perkins *et al.* (1997) proposed the use of pressed pellets of

sulfide minerals that were spiked with various trace elements or use of metal standards (*e.g.,* brass) for calibration of sulfide mineral analyses.

In the GEMOC laboratory, we have developed a dual standard calibration procedure for standardizing multi-element LA–ICP–MS analyses of sulfides (*e.g.,* Aulbach *et al.* 2004). The sample is first calibrated against a synthetic NiS button (PGE-A) and then a NIST glass. PGE-A was prepared by Ingo Horn at Memorial University of Newfoundland by spiking a standard NiS fire assay charge with stock solutions of the PGE and a range of other chalcophile elements. The charge was fused and the molten NiS was poured directly into water to achieve instantaneous quenching. While many of the trace elements added to the charge were not collected efficiently by the NiS and/or were heterogeneously distributed, the PGE and several other trace elements were (Cu, As, Se, Te, Bi). In the dual standardization procedure, the sample is first calibrated against PGE-A using S (or another suitable element) as the internal standard. This allows determination of the concentration of at least one element in the sample that can then be used as in internal standard to calibrate additional elements using one of the NIST glasses as the standard.

**Analysis of diamond and other carbon-based samples**

There has been growing interest in recent years in *in situ* analysis of carbon-based geological matrices; *e.g.,* diamonds, bitumen, oil inclusions. These require the use of C as the internal standard, which makes use of the NIST glasses inappropriate as their C content is too low for precise measurement.

The choice of solid standards for analysis of C-based materials containing a wide range of elements at analytically appropriate and well characterized concentrations is limited. Thus, Jackson *et al.* (1999) employed direct liquid ablation of synthetic oil standards to calibrate LA–ICP–MS analyses of diamond. The oil reference material (S-21, Conostan) was drawn into a glass capillary tube and sampled through a hole ablated in the wall of the tube. Strong stable signals were generated (Fig. 11-3) and good accuracy obtained for elements in fibrous diamonds previously determined by other techniques. Comparable data were achieved using a synthetic aqueous standard into which was dissolved sucrose to produce a solution with 7.5 wt.% C for internal standardization (Jackson, unpublished data). The latter allowed much greater flexibility in the composition of the standards used, but suffered from clogging of the hole through which the laser was fired by crystallizing sucrose.

Mossman *et al.* (2001) used the oil calibration procedure in a study of bitumen from the natural nuclear fission reactors at Oklo and Bangcombe, Gabon. Quantitative LA–ICP–MS analyses of bitumen were demonstrated by analysis of NIST SRM 1632B (bituminous coal). This material was not appropriate as a primary calibration standard because of significant heterogeneity on the scale of laser sampling, limited list of certified elements and very low concentrations of several important analytes (e.g, sub ppm for many of the REE)

Although calibration by direct liquid ablation is a viable technique for analysis of samples with

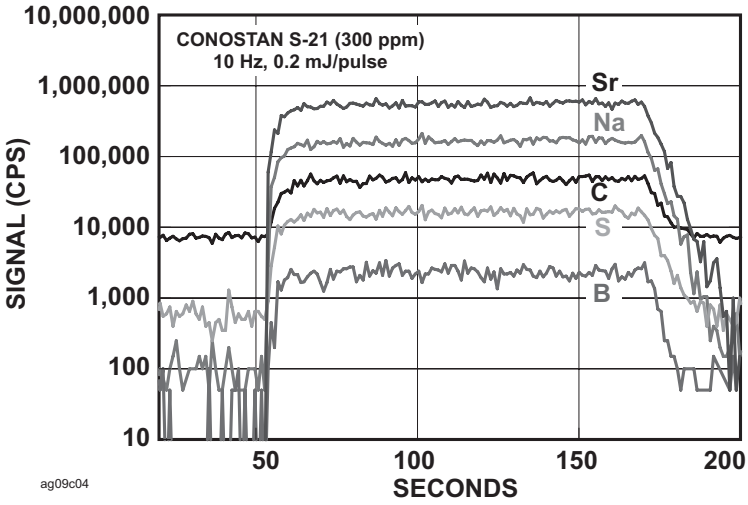


FIG. 11-3. Time resolved LA–ICP–MS signals for selected elements from an analysis of synthetic oil standard, Conostan S-21 (300 ppm), by direct liquid ablation.

matrices for which no suitable solid standard exists, Rege *et al.* (2005), in their demonstration of quantitative analysis of diamonds by LA–ICP–MS, pointed out several shortcomings of the technique:

1) the continuous volatilization of oil adds to C backgrounds,
2) preparing micro-wells or capillaries for each analytical session is time-consuming,
3) the oil standards used were found to degrade over time,
4) the oil standards did not contain all of the elements of interest.

Thus, a dual standard calibration procedure was required, whereby the oil standard was used to calibrate the elements for which it was spiked. Then, to extend the list of elements calibrated, the data for one of these measured elements was used as the internal standard for calibration against a NIST glass standard. However, this led to significant matrix-related calibration errors for elements with high ionization potential due to C-enhanced ionization efficiency in the ICP when analyzing the C-based matrices.

In response to these limitations, Rege *et al.* (2005) prepared a solid C-based standard by pressing into pellet-form a cellulose powder that had been cleaned and then doped with a multi-element solution. Despite markedly different ablation characteristics for the diamond and cellulose, analysis of two diamond samples gave results that were in agreement with values determined by other techniques, with the heterogeneity of the diamond being the major limiting factor on the precision of the results. The cellulose calibration procedure was thus more convenient, and provided better accuracy and precision, than the oil calibration method.

### Secondary standards

A number of important reference materials have been developed for distribution as secondary standards for microbeam analysis. These materials are fused glasses of geological materials. Because of the very low concentrations of some elements (*e.g.,* HREE) in these materials, they are not ideally suited as primary calibration standards. They are, however, invaluable as secondary standards that are analyzed as unknowns for quality control purposes. These include an extensively used group of fused glasses prepared by the USGS from basaltic rock powders – BCR-2G, BHVO-2, BIR-2G. More recently, a group of eight silicate glasses, covering a wider compositional range, has been prepared as *in situ* microanalytical standards. These so-called MPI-DING glasses, which are available on application, were prepared by directly fusing and stirring 50–100 g each of basalt, andesite, komatiite, peridotite, rhyolite, and quartz diorite and have been certified for up to 74 major and trace elements (Jochum *et al.* 2000, Jochum *et al.* 2006) (http://www.mpch-mainz.mpg.de/~geo/ICPMS_group/MPI_DING.html). The isotopic composition of H, Li, B, O, Ca, Sr, Nd, Hf and Pb have also been determined.

## ACCURACY AND THE NEED FOR MATRIX MATCHING

The ongoing development of new matrix-matched microbeam standards (as discussed in the previous section) suggests that there is a general belief that matrix-matched standards are required for accurate analysis. For example, Ødegård (1999) and Klemme *et al.* (2008) discussed the problems of using NIST glasses for calibration of geological matrices, and suggested that use of non-matrix-matched calibration using NIST glasses can pose problems because of the large differences in chemical composition of these materials compared to many geological matrices. Yet, there is now substantial literature reporting on the accuracy of LA–ICP–MS data for a considerable array of minerals and glasses. The large majority of these studies utilized a NIST glass reference material and internal standardization using a major element for calibration. Despite the lack of matrix matching of sample and reference standard, most of these studies report generally accurate results, *i.e.,* results that are within error of the independently determined concentrations for the samples. Indeed, it is the general matrix intolerance of LA–ICP–MS and the consequent simplicity and flexibility of calibration that is one of the main reasons that the technique has flourished.

While the need for matrix-matched standards to verify analytical methodologies is not in question, their *requirement* for calibration warrants further scrutiny because the conditions under which matrix matching is truly required for accurately calibrating LA–ICP–MS analyses are not universally understood.

The NIST glasses have been shown to calibrate effectively not only glasses of widely varied composition (*e.g.,* Jochum *et al.* 2000, 2005b, 2006, Eggins 2003) but also a huge array of silicate minerals (*e.g.,* Jackson *et al.* 1992, Ødegård 1999, Ødegård *et al.* 2005, Klemme *et al.* 2008),

oxides (*e.g.,* Jackson *et al.* 1992, Ødegård 1999), carbonates (Feng 1994), phosphates (Klemme *et al.* 2008), and other materials. In general, this mode of calibration provides accurate results, even without matrix matching of sample and reference standard, *provided that* the internal standard(s) and analytes exhibit similar elemental fractionation characteristics.

**Elemental fractionation**

It has long been recognized that not all elements exhibit the same behavior during laser ablation analysis; that is, elements can fractionate relative to each other, resulting in signal intensities that are not representative of the target material. There is now an extensive literature on the cause of these non-stoichiometric processes (see, for example, Guillong & Günther 2002, Kuhn & Günther 2004, 2005, and references therein).

Fryer *et al.* (1995) first characterized the relative fractionation behavior of a wide range of elements by calculating fractionation indices (Fig. 11-4), where the fractionation index (FI) is a comparative measure of the amount of fractionation that occurs relative to Ca. This showed that different element groups, namely the lithophile, siderophile, and chalcophile elements of Goldschmidt (1923), have generally similar FIs. While the fractionation behavior has been correlated to a number of different properties of the elements, *e.g.,* ionization potential (Chen 1999) and element melting and boiling points (Outridge *et al.* 1997), Jackson (2001) demonstrated that FI correlates strongly with condensation temperature (see Fig. 11-4). This ties in well with the demonstration that fractionation occurs, in part, due to two different processes controlled by volatility: (1) differential transport of nanoparticles (condensed vapor) and microparticles (quenched liquid droplets) into which different elements selectively partition on the basis of volatility, and, (2) differential volatilization of elements during incomplete vaporization of the microparticles in the ICP (Kuhn & Günther 2004).

The *relative* values of FI are remarkably independent of matrix and operating conditions. However, the absolute degree to which fractionation occurs during an ablation is highly dependent on numerous factors including laser-operating

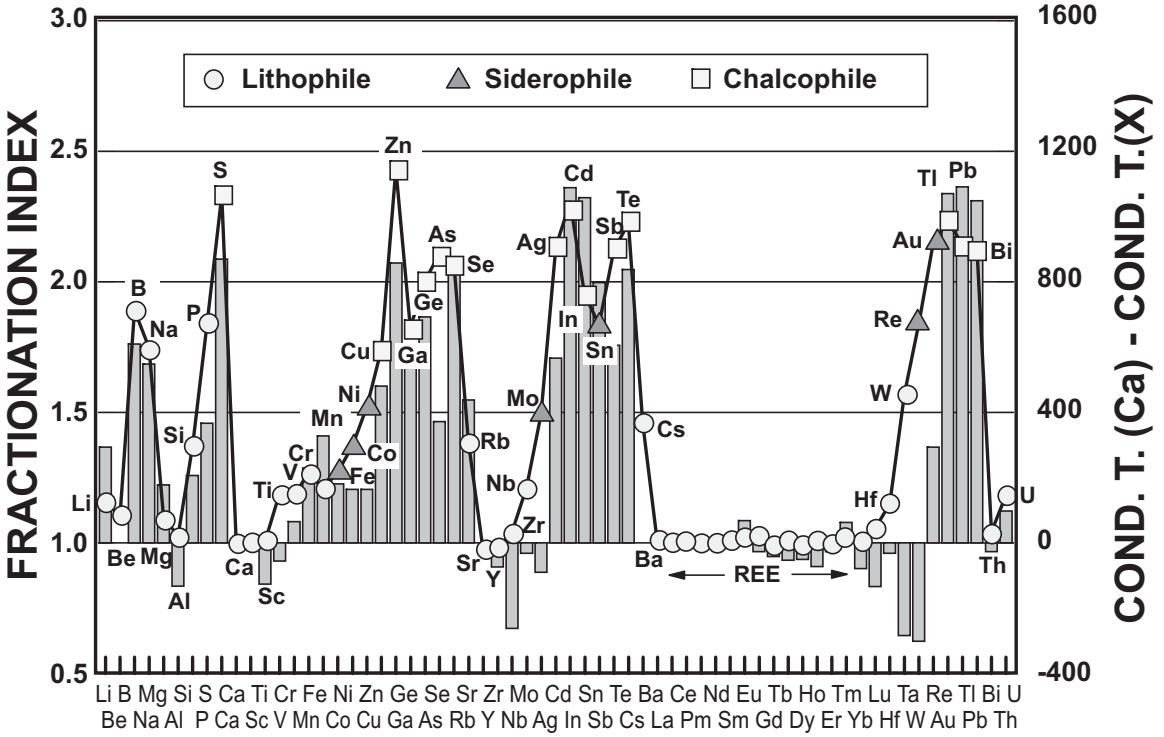


FIG. 11-4. Fractionation indices for 62 elements relative to Ca (modified from Fryer 1995 and Jackson 2001). Symbols categorize the elements according to the classification of the elements of Goldschmidt (1923). Bars represent the condensation temperature (data from Newsom 1995, Wasson 1985) relative to that of Ca. Condensation temperature is defined as the temperature at which 50% of the element would be condensed from a system with a bulk solar system composition at $10^{-4}$ atmospheres.

conditions (*e.g.,* spot size, pulse energy, pulse width) and sample matrix (Günther *et al.* 1999). Furthermore, fractionation can be a dynamic process, where measured ratios for elements during a spot ablation show a systematic change due, at least in part, to progressively changing particle size distribution. The rates at which these ratios can change are also highly matrix-dependent. It should be noted that a steady stream of large particles entering the ICP, such as is produced during line scan ablation, will still produce a steady state fractionation due to incomplete vaporization in the ICP even though it will not result in dynamic fractionation during the course of the analysis.

This discussion has two very important implications:

1) Where an element has a different FI than the internal standard element being used, the wrong ratio will be measured and inaccurate results can be expected unless fractionation is the same for sample and standard. The latter will generally be true only where matrices, ablation conditions and signal integration times are closely matched. This is the approach that has been widely adopted for U–Pb dating of zircons by LA–ICP–MS due to the strong fractionation of Pb and U (see Fig. 11-4).
2) Where an element has a similar FI to the internal standard element being used, accurate results can be expected, regardless of whether matrices, ablation conditions and signal integration times are closely matched.

The magnitude of the fractionation error will depend strongly on what type of laser is used (wavelength and pulse width), ablation conditions and the magnitude of the matrix difference between sample and standard. It has been shown that errors in measured concentrations due to elemental fraction are progressively less severe with (1) increasingly short wavelength UV lasers (Guillong *et al.* 2003), as all matrices tend to absorb with similar efficiency (tending to 100%), and (2) shorter pulse width lasers as intensity of fractionation is reduced (*e.g.,* Horn & von Blanckenburg 2007).

Figure 11-4 is thus an invaluable tool for optimizing calibration strategies. For example, the alkaline earth elements, the rare earth elements, and the actinide elements share very similar FIs with Mg, Al, Ca, which are, therefore, the most appropriate internal standards. However, Si, which has a significantly different fractionation behavior to these elements, is the best internal standard for calibrating the transition metals. Accurate determination of chalcophile elements in silicate matrices is difficult because none of the other typical major elements of many silicate materials have similar fractionation behavior. Figure 11-4 was also the inspiration for development of a multi-internal standard correction procedure for elemental fractionation described below.

**A case study on analysis of gold**

To demonstrate the concepts presented above, data are presented from a study in which a large number of native Au samples were analyzed using a Royal Canadian Mint Au standard, FAU-8. To extend the list of elements that could be quantified, NIST 610 was also used for calibration. Royal Canadian Mint Au standard, FAU-7, was analyzed many times for quality control purposes. This well characterized sample was thus analyzed using matrix-matched and non-matrix-matched calibration. Note that metallic Au has physical properties (density, reflectivity, thermal conductivity, absorption, *etc*.) that are about as different from those of NIST glasses as any geological sample.

Figure 11-5 shows the concentrations calculated for sample FAU-7, using both FAU-8 and NIST 610 for calibration, and Ag as the internal standard, versus the certified concentrations. For elements, As, Pb, and Bi, with very similar FIs to Ag (see Fig. 11-4), both standards provide indistinguishable and accurate results. For the other elements, there are very substantial errors in the non-matrix matched values. Figure 11-6 shows the percentage error in the non-matrix matched values

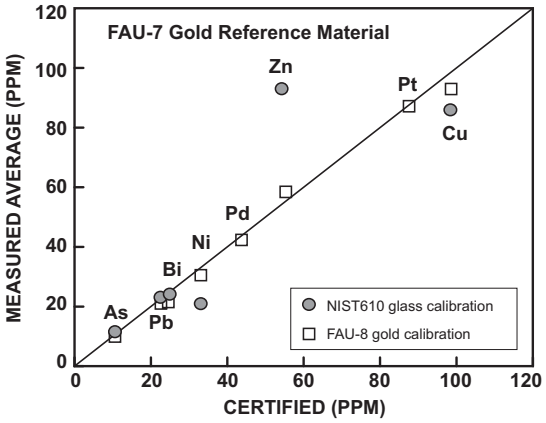


FIG. 11-5. LA–ICP–MS analyses of FAU-7 gold (mean of 21 analyses in ppm) calibrated against FAU-8 gold reference material and NIST 610 glass versus certified value (Royal Canadian Mint). The 1:1 line is shown for reference.

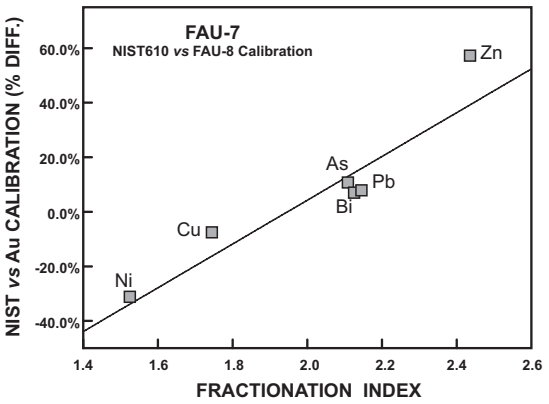


FIG. 11-6. Percentage difference between mean LA–ICP–MS analyses of FAU-7 gold calibrated against FAU-8 gold reference material and against NIST 610 glass versus fractionation index (from Fryer *et al.* 1995). Solid line is the least-squares regression of the data.

as a function of the FI of the elements taken from Fryer *et al.* (1995). The approximately linear relationship indicates that, in non-matrix-matched calibration, any errors will be approximately proportional to the difference in the FI of the analytes and the internal standard employed. This relationship is used below to develop a multi-internal standard procedure for correction of elemental fractionation.

## DATA REDUCTION

A critical aspect of producing meaningful, quantitative analyses using LA–ICP–MS is data reduction. This is because, unlike solution-based and some *in situ* analytical techniques, which generate essentially steady state signals, laser ablation is a dynamic sampling process. This means that the ablation surface can propagate successively through a variety of sources of chemical heterogeneity; *e.g.,* surface contamination, chemical zoning, inclusions, fractures, cleavages, zones of alteration, mineral boundaries, *etc.*, on a time scale that can readily be resolved using a fast data acquisition protocol (*i.e.,* one mass sweep per second or faster). The dynamic nature of the sampling is thus a tremendous strength of the technique because (a) it gives rise to transient (time-resolved) signals that, using appropriate software, can be viewed and selectively integrated for the most representative segment of the ablation signal (and background signal), often allowing meaningful results to be gleaned even from complex sample volumes; and (b) the time-resolved signals provide important clues as to how elements are hosted in the sample; *e.g.,* substituted in the crystal lattice, in metamict zones, as micro-inclusions, on cleavage planes, *etc.*, (see Fig. 11-7).

Following selective integration, background corrected ablation signals must be converted to concentrations (or ages) by referencing to a standard. For elemental concentration measurements, corrections must be applied for differing ablation yields, usually via internal standardization. Corrections must also be applied for mass-dependent drift in sensitivity during the course of the analytical session and, ideally, for elemental fractionation. A variety of different computer programs that have been developed for reducing data from LA–ICP–MS analysis are described in the appendices of this volume.

### Calculation of concentrations

Longerich *et al.* (1996) presented the equation for calculation of the concentrations of an analyte in LA–ICP–MS when calibrating against an external standard and using internal standardization. Derivation of the equation is briefly summarized below.

The concentration of an analyte element in the sample ($CAN_{SAM}$) is given by the count rate for the analyte ($RAN_{SAM}$) in the sample divided by the normalized sensitivity (S), as follows:

$$C_{AN_{SAM}} = \frac{R_{AN_{SAM}}}{S} \qquad (1)$$

where S is determined on a calibration standard (CAL), corrected for the weight of sample ablated/transported/ionized, and all count rates are background corrected. When using naturally occurring internal standards, the concentration of an analyte in a sample ($CAN_{SAM}$) is:

$$C_{AN_{SAM}} = C_{AN_{CAL}} \frac{R_{AN_{SAM}}}{R_{AN_{CAL}}} \left( \frac{C_{IS_{SAM}}}{R_{IS_{SAM}}} \frac{R_{IS_{CAL}}}{C_{IS_{CAL}}} \right) \qquad (2)$$

where:

$RAN_{CAL}$ is the count rate of the analyte in the calibration material,

$RAN_{SAM}$ is the count rate of the analyte in the sample,

$RIS_{CAL}$ is the count rate of the internal standard in the calibration material,

$RIS_{SAM}$ is the count rate of the internal standard in the sample,

$CAN_{CAL}$ is the concentration of the analyte in the calibration material,

$CIS_{CAL}$ is the concentration of the internal standard in the calibration material, and

$CIS_{SAM}$ is the concentration of the internal standard in the sample.

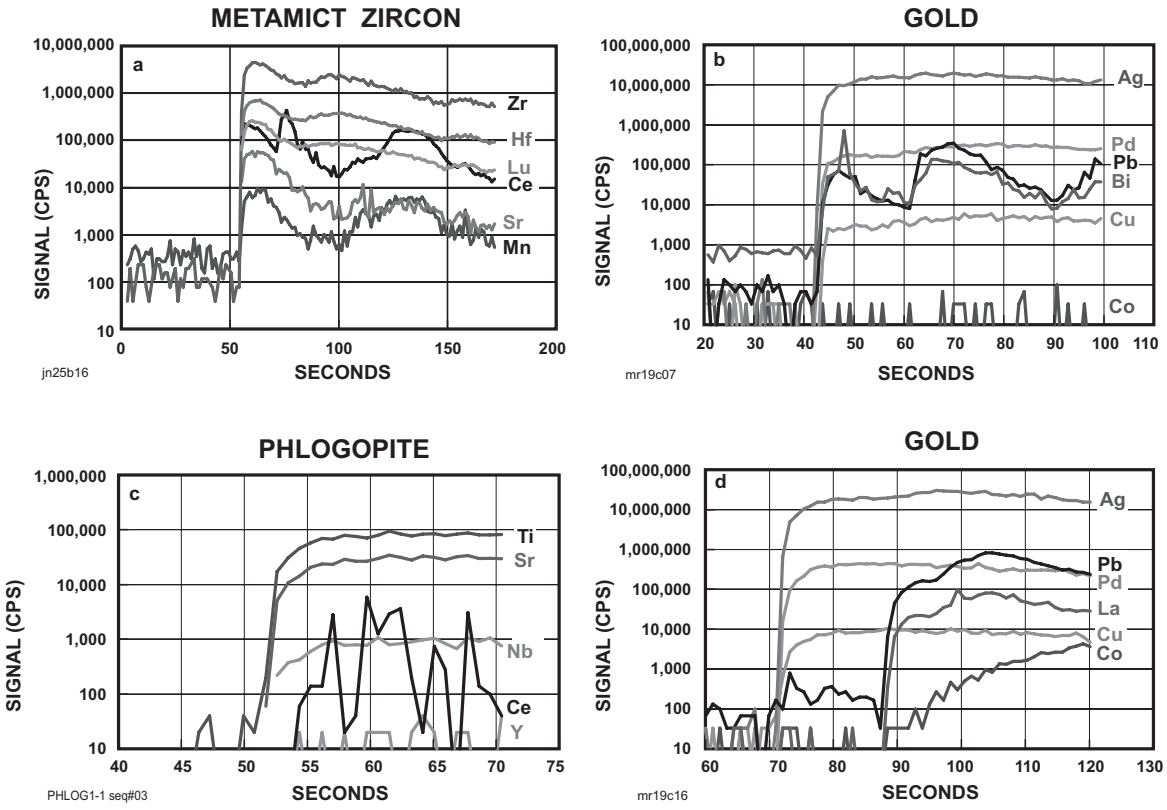


FIG. 11-7. Examples of how complex time-resolved LA–ICP–MS signals, typical of many geological media, provide information on how elements are bound: (**a**) zircon showing extremely heterogeneous distribution of Ce and Mn as a result of concentration in high-U (signal not shown), radiation-damaged zones; (**b**) decoupling of elemental behavior as indicated by strong (order of magnitude) oscillatory zoning of Pb and Bi on a 10s μm scale, and homogeneous distribution of Pd and Cu in native gold; (**c**) dramatic variability in Ce intensity due to cleavage plane-localized LREE enrichment in phlogopite; (**d**) sudden intense increase in signals for Pb and LREE (La) during ablation of a grain of gold mounted in a polished epoxy block is interpreted as a surface (lower) enrichment. This interpretation is based on the concomitant rise of the signal for Co, which was determined to be relatively enriched in the epoxy mount.

It should be noted that, in most natural minerals, the major elements that are suitable as an internal standard are of low atomic mass compared to most trace elements being determined. This potentially compromises their effectiveness in making instrumental matrix and drift corrections since sensitivity (S) in ICP–MS analysis is prone to mass-dependent matrix effects and drift (*i.e.,* the sensitivity of each analyte may change during the course of a run of several analyses relative to the internal standard). Given the general absence of high mass analytes that can be used for internal standardization, it is generally assumed that this mass-dependent drift occurs linearly with time (or analysis number). By bracketing analyses of samples by analyses of standards, an estimate of the sensitivity ratios of analytes to internal standard for the calibration standard can be calculated for the time (or position in a run) of each analysis. This is achieved by reorganizing the above equation as follows:

$$C_{AN_{SAM}} = R_{AN_{SAM}} \frac{C_{IS_{SAM}}}{R_{IS_{SAM}}} \left( \frac{C_{AN_{CAL}}}{R_{AN_{CAL}}} \frac{R_{IS_{CAL}}}{C_{IS_{CAL}}} \right)_{Interpolated} \quad (3)$$

Evident from this equation is that any error in the estimation of the concentration of the internal standard in the sample ($C_{IS_{SAM}}$) will result in an *equivalent* error in the calculated concentration of *all* the analytes.

### Correction procedures for elemental fractionation

A large amount of research effort has gone into development of hardware and analytical protocols aimed at reducing elemental fractionation. Currently, a major area of research is in the development of femtosecond laser ablation systems,

which are producing significant reductions in elemental and isotopic fractionation (*e.g.,* Horn & von Blanckenburg 2007). However, femtosecond lasers are complex and expensive, and are not currently turn-key instruments that will be adopted widely by cost-conscious purchasers. A substantial amount of effort has also gone into the development of reference materials that allow elimination of elemental fractionation errors via matrix matching. However, the number of materials developed is still minor relative to the vast array of geological matrices.

By contrast, remarkably little effort has gone into development of computational algorithms for correction of elemental fractionation; yet, effective algorithms would substantially reduce the need for hardware and reference material 'fixes' to the elemental fractionation problem. The following sections discuss the most widely used algorithm for calculation of elemental concentrations (the mean count rate method) and three post-analytical data-processing procedures that have been developed for correcting elemental fractionation (note that a procedure developed specifically for correcting Pb/U ratios for geochronological investigations (Horn *et al.* 2000) is not discussed here).

**Signal selection and the mean count rate method**

LA–ICP–MS signals are generally processed using software that allows the users to integrate the signals selectively for an ablation so as to obtain the most representative parts of an ablation signal (*i.e.,* avoid artifacts related to inclusions, *etc*.). The main data reduction packages available today utilize algorithms that were developed prior to the full significance of elemental fractionation being recognized and calculate concentrations based on the 'mean count rates' during the chosen integration intervals. However, it is evident from equation (3) above that the calculated concentration of an element is dependent on the ratios $RAN_{SAM}/RIS_{SAM}$ and $RIS_{CAL}/RAN_{CAL}$. Since, for two elements with dissimilar FI, these ratios will generally change during an analysis, and may change differently for sample and standard, inaccuracies will result unless matrices, ablation conditions and signal integration intervals are closely matched. Three mathematical procedures that have been developed to correct for the effects of fractionation are described below.

**Intercept method**

The intercept method is based on the premise that 'true' inter-element ratios in LA–ICP–MS are those measured at the beginning of a spot ablation and that, with progressive fractionation, ratios evolve away from the true ratio.

In an excimer LA–ICP–MS investigation of scheelite chemistry, Sylvester & Ghaderi (1997) used the NIST 610 glass standard to calibrate analyses of scheelite ($CaWO_4$). Although this study used deep UV laser radiation (193 nm), which is considered to produce less inter-element fractionation than other commonly employed wavelengths (*e.g.,* Guillong *et al.* 2003) , it was noted that W fractionated "rather strongly" relative to the internal standard, Ca, during ablation of NIST610. A correction procedure was proposed that assumed that the true analyte/internal standard intensity ratios occurred near the beginning of the ablations (t = ≈11 s after initiation of ablation, to avoid initial instability in the signals). For each element, a least squares regression of the analyte/internal standard intensity ratio *versus* time data was performed to determine this initial ratio. This constrained the ratio more tightly than simply using measured ratios at time t = 11 s. The calculated intensity ratios at t = 11 s were then used to calculate concentrations. This method resulted in measured W concentrations that agreed within error with electron microprobe data.

**Slope method**

Chen (1999) developed a procedure that utilized internal standard normalized fractionation factors (ISNFF) that were calculated for each element for both the sample and standard to correct concentrations (*C*) for elemental fractionation using the following equation:

$$C_{correct} = C_{measured} \, x \, ISNFF_{standard} / ISNFF_{sample} \quad (4)$$

The ISNFF, calculated for each element, was a function of the slope of the analyte/internal standard intensity ratio with ablation time relationship, which was shown to be approximately linear over the duration of a typical ablation. Significantly improved accuracy was demonstrated for several elements when analyzing fused rock glasses using NIST SRM 613 for calibration.

**Multi-internal standard correction procedure**

A limitation of the procedures described above is that they can only be applied when analyzing relatively homogeneous materials. Any small scale compositional heterogeneity within the ablation volume can result in an erroneous intercept or slope determination. Trace elements, in

particular, are commonly distributed heterogeneously in geological materials. An additional concern with the intercept procedure of Sylvester & Ghaderi (1997), particularly for longer wavelength laser ablation systems (*e.g.,* 266 nm), is that the proportion of large particles produced is generally greatest at the start of a spot ablation and reduces with ablation time (Guillong & Günther 2002). Incomplete volatilization of these particles in the ICP results in ICP-induced fractionation that is most severe at the *beginning* of an ablation (this effect was reduced by the choice of t = 11 s by Sylvester & Ghaderi 1997).

A new procedure for correcting laser ablation data that circumvents these problems is described here. The procedure can be illustrated using the Au data presented above. As demonstrated, there is a general relationship between accuracy and fractionation index (FI) when non-matrix-matched calibration is used. The data used to construct Figure 11-6, which shows that there is an approximately linear relationship between percentage error of the analyses and FI, can be inverted and the concentration of Ag calculated using each of the other elements as the internal standard. These concentrations produce a semi-linear relationship with FI (Fig. 11-8). This relationship provides a simple means of correcting fractionation-related errors. If two or more major elements with different FI are used separately for internal standardization, different results will be attained. The calculated concentrations will be a function of the difference in FI of the internal standards. This allows construction of a line which can be used to calculate what the concentration of an analyte would be if an element with the same FI as the analyte had been used to calculate concentrations.

As an example, Jackson (2001) presented data for 213 nm LA–ICP–MS analyses of basaltic glass reference material, BCR-2G, using NIST SRM 612 as the external standard and Ca for internal standardization. While most elements agreed with reference values to better than 10%, large errors (>15%) were shown for shown for two trace elements, Pb and Zn, both of which have FI significantly different from that of Ca (Fryer *et al.* 1995). Figure 11-9 shows the concentrations of Zn calculated using Ca and Si as internal standards plotted against the FI of Fryer *et al.* (1995). By projecting the trend of these points to the FI of Zn (2.43), the corrected concentration of Zn can be calculated. This concentration, $C_{AN_{CORR}}$ (point A on Fig. 11-9), equals the concentration of the analyte calculated using internal standard 1 ($C_{AN_{IS1}}$ – point B, using Ca as internal standard 1) minus FG.

Now:

$$FG = DE \times CF/CD \quad (5)$$

Thus:

$$C_{AN_{CORR}} = C_{AN_{IS1}} - DE \times CF/CD \quad (6)$$

The generic form of this equation is as follows:

$$C_{AN_{CORR}} = C_{AN_{IS1}} - \left(C_{AN_{IS1}} - C_{AN_{IS2}}\right)\frac{\left(FI_{AN} - FI_{IS1}\right)}{\left(FI_{IS2} - FI_{IS1}\right)} \quad (7)$$

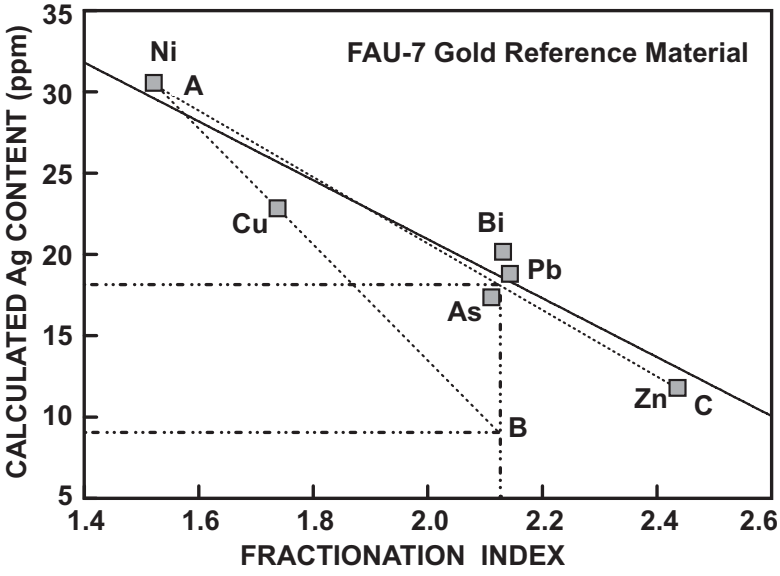


FIG. 11-8. Calculated concentrations of Ag in FAU-7 Au using NIST 610 for calibration and Ni, Cu, Zn, As, Pb and Bi for internal standardization. Solid line is the least-squares regression of the data.

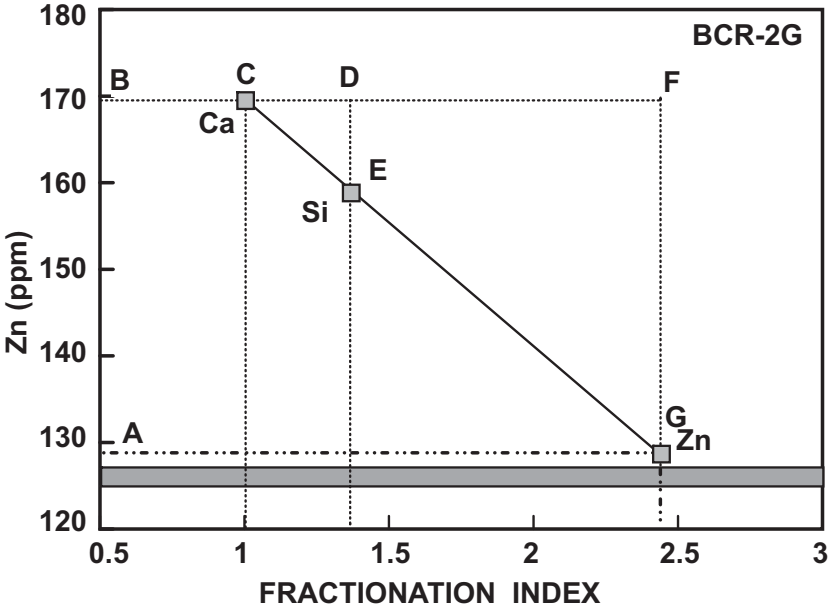


FIG. 11-9. Demonstration of the multi internal standard procedure for correction of errors induced by elemental fractionation when a matrix matched standard is not employed. The data show determinations of Zn in BCR-2G using NIST 612 for calibration and Ca and Si as internal standards (test data from Jackson 2001). The grey box shows the range of preferred values for Zn in BCR-2G from GeoREM and the material provider (USGS).

where:

$C_{AN_{CORR}}$ = the corrected concentration of an analyte,

$C_{AN_{IS1}}$ = the concentration of an analyte calculated using internal standard 1,

$C_{AN_{IS2}}$ = the concentration of an analyte calculated using internal standard 2,

$FI_{AN}$ = the fractionation index of the analyte,

$FI_{IS1}$ = the fractionation index of internal standard 1,

$FI_{IS2}$ = the fractionation index of internal standard 2.

The corrected concentration of Zn in this example is 129 ppm, which compares very favorably with published values for Zn in BCR-2G (125–127 ppm). The advantages of this procedure are that it is not predicated on near-linear analyte/ internal standard intensity ratios and it relies only on data for major elements, which are almost invariably more homogeneously distributed within geological materials than the trace elements, and can generally be measured very precisely because of their high abundance.

The disadvantages are that it requires accurate information on two or more major elements, which must have a substantially different FI. For rock-forming minerals, these will normally exist because most will contain one or more of Ca, Mg or Al, which have FI close to 1, and one or more of Si, Na, P, which have substantially higher FI. However, this condition will not always be met (*e.g.,* analysis of diamond, many oxide minerals). Also, because the difference in FI between the major elements can be relatively small, any errors in the measurements can propagate into much larger errors when a two point calibration is extrapolated to elements with much larger (or smaller) FI. For example, it is evident from Figure 11-8 that, if Cu and Ni are used as internal standards, the extrapolated line AB would result in an estimate of the concentration of Ag (FI = 2.13) in sample FAU-7 (certified value of 20.3 ppm) of approximately 9 ppm, which has a similar margin of error as using Ni as the internal standard and larger than when using Cu. However, if Ni and Zn, two elements with large differences in FI are used (line AC), the corrected concentration of Ag (18 ppm) is substantially more accurate than the estimates based on either of the internal standards alone (31 and 12 ppm respectively).

Analysis of sulfide minerals is one area where this method may be particularly applicable because there are few available matrix-matched standards and these minerals commonly contain two elements with large differences in FI (*e.g.,* Fe and S). This is a topic of ongoing research.

## CONCLUSIONS

Excellent results for geological matrices can generally be achieved by LA–ICP–MS using non-matrix matched calibration, particularly when using shorter wavelength lasers (213 nm and 193 nm), which minimize inter-matrix elemental fractionation differences. Where elements share the same fractionation index as the internal standard, accurate data (*i.e.,* within error of independently determined values) can be generated even when there are extreme differences in the matrices of the sample and standard. Because the precision (2 SD) of LA–ICP–MS elemental analyses, when all sources of error are propagated, is typically of the order of several (≥5) percent, it is not clear whether matrix-matched calibration provides any improvement in accuracy over non-matrix-matched

calibration for these elements. In practice, this is a moot point since ±5% accuracy provided by non-matrix matched calibration is quite sufficient for most geological applications. However, much larger errors can occur for elements that have a substantial difference in fractionation index from the internal standard employed. A range of solutions to this problem exist. Considerable effort is currently going into generation of new matrix-matched calibration materials and development of advanced, femtosecond ablation sources. It is proposed here that further research is warranted into development of mathematical algorithms for correction of elemental fractionation-induced errors.

## ACKNOWLEDGEMENTS

The author has had the good fortune to work with numerous exceptional analytical geochemists from whose knowledge he has benefited immensely. In particular, the author wishes to acknowledge the major contributions of Henry Longerich, Brian Fryer, and Detlef Günther to his knowledge of analytical geochemistry and laser ablation, without which this work would not have been possible.

The author would like to thank Paul Sylvester and Detlef Günther for reviews that significantly improved the manuscript. A. Sharma assisted with the Au study.

## REFERENCES

AULBACH, S., GRIFFIN, W.L., PEARSON, N.J., O'REILLY, S.Y., KIVI, K. & DOYLE, B.J. (2004): Mantle formation and evolution, Slave Craton: constraints from HSE abundances and Re–Os isotope systematics of sulfide inclusions in mantle xenocrysts. *Chem. Geol.* **208**, 61– 88.

CHEN, Z. (1999): Inter-element fractionation and correction in laser ablation inductively coupled plasma mass spectrometry. *J. Analyt. Atom. Spectrom.* **14**, 1823–1828.

CHENERY, S. & COOK, J.M. (1993): Determination of rare earth elements in single mineral grains by laser ablation microprobe–inductively coupled plasma mass spectrometry – preliminary study. *J. Analyt. Atom. Spectrom.* **8**, 299-303.

CROMWELL, E.F. & ARROWSMITH P. (1995): Semiquantitative analysis with laser ablation inductively coupled plasma mass spectrometry. *Analyt. Chem.* **67**, 131-138.

EGGINS, S.M. (2003): Laser ablation ICP–MS analysis of geological materials prepared as lithium borate glasses. *Geostand. Newslett.: J. Geostand. & Geoanalys.* **27**, 147-162.

EGGINS, S.M. & SHELLEY, J.M.G. (2002): Compositional heterogeneity in NIST SRM 610-617 glasses. *Geostand. Newslett.: J. Geostand. & Geoanal.* **26**, 269-286.

FENG, R. (1994): *In situ* trace element determination of carbonates by laser probe inductively coupled plasma mass spectrometry using nonmatrix matched standardization. *Geochim. Cosmochim. Acta* **58**, 1615-1623.

FERNÁNDEZ, B., CLAVERIE, F., PÉCHEYRAN, C. & DONARD, O.F.X. (2008): Solid-spiking isotope dilution laser ablation ICP–MS for the direct and simultaneous determination of trace elements in soils and sediments. *J. Analyt. Atom. Spectrom.* **23**, 367-377.

FRYER, B.J., JACKSON, S.E. & LONGERICH, H.P. (1995): The design, operation and role of the laser-ablation microprobe coupled with an inductively coupled plasma–mass spectrometer (LAM–ICP–MS) in the earth sciences. *Can. Mineral.* **33**, 303-312.

GOLDSCHMIDT, V.M. (1923): Geochemische Verteilungsgesetze der Elemente (I). *Vidensk. Skrifter. I. Mat.-Naturv. Klasse*.

GUILLONG, M. & GÜNTHER, D. (2002): Effect of particle size distribution on ICP-induced elemental fractionation in laser-ablation–inductively coupled plasma–mass spectrometry. *J. Analyt. Atom. Spectrom.* **17**, 831-837.

GUILLONG, M., HORN, I. & GÜNTHER, D. (2003): A comparison of 266 nm, 213 nm and 193 nm produced from a single solid state Nd:YAG laser for laser ablation ICP–MS. *J. Analyt. Atom. Spectrom.***18**, 1224-1230.

GUILLONG, M., HAMETNER, K., REUSSER, E., WILSON, S.A. & GÜNTHER, D. (2005): Preliminary characterization of new glass reference materials (GSA-1G, GSC-1G, GSD-1G and GSE-1G) by laser ablation–inductively coupled plasma–mass spectrometry using 193 nm, 213 nm and 266 nm wavelengths. *Geostand. & Geoanalyt. Res.* **29**, 315-331.

GÜNTHER, D., FRISCHKNECHT, R., MÜSCHENBORN, H.-J. & HEINRICH, C.A. (1997): Direct liquid ablation: a new calibration strategy for laser ablation–ICP–MS microanalysis of solids and liquids. *Fresenius J. Analyt. Chem.* **359**, 390-393.

GÜNTHER, D., AUDÉTAT, A, FRISCHKNECHT, R. & HEINRICH, C.A. (1998): Quantitative analysis of major, minor and trace elements in fluid inclusions using laser ablation–inductively coupled plasma mass

spectrometry. *J. Analyt. Atom. Spectrom.* **13**, 263-270.

GÜNTHER, D., JACKSON, S.E. & LONGERICH, H.P. (1999): Laser ablation and arc/spark solid sample introduction into inductively coupled plasma mass spectrometers. *Spectrochim. Acta B* **54**, 381-409.

HALICZ, L. & GÜNTHER, D. (2004): Quantitative analysis of silicates using LA–ICP–MS with liquid calibration. *J. Analyt. Atom. Spectrom.* **19**, 1539-1545.

HATHORNE, E.C., JAMES, R.H., SAVAGE, P. & ALARD, O. (2008): Physical and chemical characteristics of particles produced by laser ablation of biogenic calcium carbonate. *J. Analyt. Atom. Spectrom.* **23**, 240-243.

HORN, I. & VON BLANCKENBURG, F. (2007): Investigation on elemental and isotopic fractionation during 196 nm femtosecond laser ablation multiple collector inductively coupled plasma mass spectrometry. *Spectrochim. Acta B* **62**, 410-422.

HORN, I, RUDNICK, R.L. & MCDONOUGH, W.F. (2000): Precise elemental and isotope ratio determination by simultaneous solution nebulization and laser ablation–ICP–MS: application to U–Pb geochronology. *Chem. Geol*. **164**, 281-301.

JACKSON, S.E. (2001): The application of Nd:YAG lasers in LA–ICP–MS, in, *Laser Ablation–ICP–Mass Spectrometry in the Earth Sciences: Principles and Applications* (Sylvester, P.J., Ed.), Mineralogical Association of Canada (MAC) Short Course Series **29**, 29-45.

JACKSON, S.E., LONGERICH, H.P., DUNNING, G.R. & FRYER, B.J. (1992): The application of laser ablation microprobe–inductively coupled plasma–mass spectrometry (LAM–ICP–MS) to in situ trace element determinations in minerals. *Can. Mineral*. **30**, 1049-1064.

JACKSON, S.E, DAVIES, R.M., GRIFFIN, W.L., O'REILLY, S.Y. & DOYLE, B. (1999): Quantitative LAM–ICPMS analysis of trace elements in diamonds. *Journal Conference Abstracts, V.M. Goldschmidt Conference IX, Boston, Mass*., 135.

JOCHUM, K.P. & STOLL, B. (2008): Reference materials for elemental and isotopic analyses by LA–(MC)–ICP–MS: successes and outstanding needs. *In* Laser Ablation ICP–MS in the Earth Sciences: Current Practices and Outstanding Issues (P. Sylvester, *ed*.). *Mineral. Assoc. Can. Short Course Series* **40**, 147-168.

JOCHUM, K.P., DINGWELL, D.B., ROCHOLL A., STOLL, B., HOFMANN, A.W., BECKER, J.S., BESMEHN, A., BESSETTE, D., DIETZE, H.-J., DULSKI, P., ERZINGER, J., HELLEBRAND, E., HOPPE, P., HORN, I., JANSSENS, K., JENNER, G.A., KLEIN, M., MCDONOUGH, W.F., MAETZ, M., MEZGER, K., MÜNKER, C., NIKOGOSIAN, I.K., PICKHARDT, C., RACZEK, I., RHEDE, D., SEUFERT, H.M., SIMAKIN, S.G., SOBOLEV, A.V., SPETTEL, B., STRAUB, S. M., VINCZE, L., WALLIANOS, A., WECKWERTH, G., WEYER, S., WOLF, D. & ZIMMER, M. (2000): The preparation and preliminary characterisation of eight geological MPI-DING reference glasses for in-situ microanalysis. *Geostand. Newslett.: J. Geostand. & Geoanalys.* **24**, 87-133.

JOCHUM, K.P., NOHL, U., HERWIG, K., LAMMEL, E., STOLL, B. & HOFFMAN, A.W. (2005a): GeoReM: a new geochemical data base for reference materials and isotopic standards: *Geostand. Geoanalyt. Res.* **29**, 333-338.

JOCHUM, K.P., WILLBOLD, M., RACZEK, I., STOLL, B. & HERWIG, K. (2005b): Chemical characterisation of the USGS reference glasses GSA-1G, GSC-1G, GSD-1G, GSE-1G, BCR-2G, BHVO-2G and BIR-1G using EPMA, ID–TIMS, ID–ICP–MS and LA–ICP–MS. *Geostand. Geoanalyt. Res.* **29**, 285-302.

JOCHUM, K.P., STOLL, B., HERWIG, K., WILLBOLD, M., HOFMANN, A.W., AMINI, M., AARBURG S., ABOUCHAMI, W., HELLEBRAND, E., MOCEK, B., RACZEK, I., STRACKE, A., ALARD, O., BOUMAN, C., BECKER, S., DÜCKING, M., BRÄTZ, H., KLEMD, R., DE BRUIN, D., CANIL, D., CORNELL, D., DE HOOG J.C.M., DALPÉ, C., DANYUSHEVSKY, L.V., EISENHAUER, A., GAO, Y., SNOW, J.E., GROSCHOPF, N., GÜNTHER, D., LATKOCZY, C., GUILLONG, M., HAURI, E.H., HÖFER, H.E., LAHAYE, Y., HORZ, K., JACOB, D.E., KASEMANN ,S., KENT, A.J.R., ZACK, T., LUDWIG, T., MASON, P.R.D., MEIXNER, A., ROSNER, M., MISAWA, K., NASH, B.P., PFÄNDER, J.A., PREMO, W.R., SUN, W.D., TIEPOLO, M., VANNUCCI, R., VENNEMANN, T., WAYNE, D. & WOODHEAD, J.D. (2006): MPI-DING reference glasses for *in situ* microanalysis: New reference values for element concentrations and isotope ratios. *Geochem. Geophys. Geosyst.* **7**, 44 pp.

KANE, J.S. (1998): A history of the development and certification of NIST glass SRMs 610-617. *Geostand. Newslett: J. Geostand. & Geoanalys.* **22**, 7-13.

KLEMME, S., PROWATKE, S., MÜNKE, C., MAGEE, C.W., LAHAYE, Y., ZACK, T., KASEMANN, S.A., CABATO, E.J.A. & KAESER, B. (2008): Synthesis and preliminary characterisation of new phosphate and titanite reference glasses. *Geostand. Geoanalyt. Res.*

**32**, 39-54.

KUHN, H.-R. & GÜNTHER, D. (2004): Laser ablation–ICP–MS: particle size dependent elemental composition studies on filter-collected and online measured aerosols from glass. *J. Analyt. Atom. Spectrom.* **19**, 1158-1164.

KUHN, H.-R. & GÜNTHER, D. (2005): The agglomeration state of nano-second laser-generated aerosol particles entering the ICP. *Analyt. Bioanal. Chem.* **383**, 434-441.

LONGERICH, H.P., JACKSON, S.E. & GÜNTHER, D. (1996): Laser Ablation–Inductively Coupled Plasma–Mass Spectrometric transient signal data acquisition and analyte concentration calculation. *J. Analyt. Atom. Spectrom.* **11**, 899-904.

MOENKE-BLANKENBURG, L., SCHUMANN T., GÜNTHER, D., KUSS, H.-M. & PAUL M. (1992): Quantitative analysis of glass using inductively coupled plasma atomic emission and mass spectrometry, laser micro-analysis inductively coupled plasma atomic emission spectrometry and laser ablation inductively coupled plasma mass spectrometry. *J. Analyt. Atom. Spectrom.***7**, 251-254.

MOISSETTE, A. , SHEPHERD, T.J. & CHENERY, S.R. (1996): Calibration strategies for the elemental analysis of individual aqueous fluid inclusions by laser ablation inductively coupled plasma mass spectrometry. *J. Analyt. Atom. Spectrom.* **11**, 177-185.

MOSSMAN, D.J., JACKSON, S.E. & GAUTHIER-LAFAYE, F. (2001): Trace element and isotopic analysis by laser ablation ICP–MS of ore deposit bitumens: a test case with uranium ores from Oklo, Gabon. *Energy Sources* **23**, 809-822.

NEWSOM, H.E. (1995): Composition of the solar system, planets, meteorites, and major terrestrial reservoirs. *In* A Handbook of Physical Constants: Global Earth Physics (Vol.1) (Ahrens, T.J., *ed.*), American Geophysical Union, 159-189.

NORMAN, M., ROBINSON, P. & CLARK, D. (2003): Major- and trace-element analysis of sulfide ores by laser-ablation ICP−MS, solution ICP−MS, and XRF: new data on international reference materials. *Can. Mineral*. **41**, 293-305.

ØDEGÅRD, M. (1999): Preparation of synthetic calibration materials for use in the microanalysis of oxide minerals by direct fusion in high-purity graphite electrodes: preliminary results for quartz and rutile. *Geostand. Newslett.: J. Geostand. & Geoanalys.* **23**, 173-186.

ØDEGÅRD, M., SKÅR, Ø, SCHIELLERUP, H. & PEARSON, N.J. (2005): Preparation of synthetic calibration materials for use in the microanalysis of oxide minerals by direct fusion in high-purity graphite electrodes: preliminary results for quartz and rutile. *Geostand. & Geoanalyt. Res.* **29**, 197-209.

OUTRIDGE, P.M., DOHERTY, W. & GREGOIRE, D.C. (1997): Ablative and transport fractionation of trace elements during laser sampling of glass and copper. *Spectrochim. Acta B* **52**, 2093-2102.

PEARCE, N.J.G., PERKINS, W.T. & FUGE, R. (1992): Developments in the quantitative and semiquantitative determination of trace elements in carbonates by laser ablation inductively coupled plasma mass spectrometry. *J. Analyt. Atom. Spectrom* **.7**, 595-598.

PEARCE, N.J.G., PERKINS, W.T., WESTGATE, J.A., GORTON, M.P., JACKSON, S.E., NEAL, C.R. & CHENERY, S.P. (1997): A compilation of new and published major and trace element data for NIST SRM 610 and NIST SRM 612 glass standard reference materials. *Geostand. Newslett.: J. Geostand. & Geoanalys.* **21**, 115-144.

PEARSON, N.J., GRIFFIN, W.L. & O'REILLY, S.Y. (2008): Mass fractionation correction in laser ablation multiple-collector ICP–MS: implications for overlap corrections and precise and accurate *in situ* isotope ratio measurement. *In* Laser Ablation ICP–MS in the Earth Sciences: Current Practices and Outstanding Issues (P. Sylvester, *ed.*). *Mineral. Assoc. Can. Short Course Series* **40**, 93-116.

PERKINS, W.T. PEARCE, N.G.J. & JEFFRIES, T.E. (1993): Laser ablation inductively coupled plasma mass spectrometry: A new technique for the determination of trace and ultra-trace elements in silicates. *Geochim. Cosmochim. Acta* **57**, 475-482.

PERKINS, W.T. PEARCE, N.G.J. & WESTGATE, J.A. (1997): The development of laser ablation ICP–MS and calibration strategies: examples from the analysis oftrace elements in volcanic glass shards and sulfide minerals: *Geostand. Newslett.: J. Geostand. & Geoanalys.* **21**, 175-190.

PETTKE, T. (2008): Analytical protocols for element concentration and isotope ratio measurements in fluid inclusions by LA–(MC–)ICP–MS. *In* Laser Ablation ICP–MS in the Earth Sciences: Current Practices and Outstanding Issues (P. Sylvester, *ed.*). *Mineral. Assoc. Can. Short Course Series* **40**, 189-217.

PICKHARDT, C., IZMER, A.V., ZORIY, M.V., SCHAUMLÖFFEL, D. & BECKER, J.S. (2006): On-line isotope dilution in laser ablation inductively coupled

plasma mass spectrometry using a microflow nebulizer inserted in the laser ablation chamber. *Internat. J. Mass Spectrom.* **248**, 136-141.

REGE, S., JACKSON, S., GRIFFIN, W.L., DAVIES, R.M., PEARSON, N.J. & O'REILLY, S.Y. (2005): Quantitative trace element analysis of diamond by laser ablation inductively coupled plasma mass spectrometry. *J. Analyt. Atom. Spectrom.* **20**, 601-611.

REID, J.E., HORN, I., LONGERICH, H.P., FORSYTHE, L. & JENNER, G.A. (1999): Determination of Zr and Hf in a flux-free fusion of whole rock samples using laser ablation inductively coupled plasma–mass spectrometry (LA–ICP–MS) with isotope dilution calibration. *Geostand. Newslett.: J. Geostand. & Geoanalys.* **23**, 149-155.

ROCHOLL, A., SIMON, K., JOCHUM, K.P., BRUHN, F., GEHANN, R., KRAMAR, U., LUECKE, W., MOLZAHN, M., PERNICKA, E., SEUFERT, H.M., SPETTEL, B. & STUMMEIER, J. (1997): Chemical characterisation of NIST silicate glass certified reference material SRM 610 by ICP–MS, TIMS, LIMS, SSMS, INAA, AAS and PIXE. *Geostand. Newslett.: J. Geostand. & Geoanalys.* **21**, 101-114.

SYLVESTER, P.J. & EGGINS, S.M. (1997): Analysis of Re, Au, Pd, Pt and Rh in NIST glass certified reference materials and natural basalt glasses by laser ablation ICP–MS. *Geostand. Newslett.: J. Geostand. & Geoanalys.* **21**, 215-229.

SYLVESTER, P.J. & GHADERI, M. (1997): Trace element analysis of scheelite by excimer laser ablation inductively coupled plasma–mass spectrometry (ELA–ICP–MS) using a synthetic silicate glass standard. *Chem. Geol.* **141**, 49-65.

SYLVESTER, P.J., CABRI, L.J., TUBRETT, M.N., PEREGOEDOVA, A., MCMAHON, G. & LAFLAMME, J.H.G. (2005): Synthesis and evaluation of a fused pyrrhotite standard reference material for platinum group element and gold analysis by laser ablation–ICPMS. *10th Internat. Platinum Symp.*, 16-20.

TIBI, M. & HEUMANN, K.G. (2003): Isotope dilution mass spectrometry as a calibration method for the analysis of trace elements in powder samples by LA–ICP–MS. *J. Analyt. Atom. Spectrom.* **18**, 1076-1081.

WASSON, J.T. (1985): Meteorites: their record of early solar-system history: W.H. Freeman, New York, 267 pp.

WILSON, S.A., RIDLEY, W.I. & KOENIG, A.E. (2002): Development of sulfide calibration standards for the laser ablation inductively–coupled plasma mass spectrometry technique: *J. Analyt. Atom. Spectrom.* **17**, 406-409.

WOHLGEMUTH-UEBERWASSER, C.C., BALLHAUS, C., BERNDT, J., STOTTER NÉE PALIULIONYTE, V. & MEISEL, T. (2007): Synthesis of PGE sulfide standards for laser ablation inductively coupled plasma mass spectrometry (LA–ICP–MS). *Contrib. Mineral. Petrol.* **154**, 607-617.

# CHAPTER 12: ANALYTICAL PROTOCOLS FOR ELEMENT CONCENTRATION AND ISOTOPE RATIO MEASUREMENTS IN FLUID INCLUSIONS BY LA–(MC–)ICP–MS

Thomas Pettke
University of Bern, Institute of Geological Sciences,
Baltzerstrasse 1+3,
CH–3012 Bern, Switzerland
E-mail: pettke@geo.unibe.ch

## INTRODUCTION

Fluids are significant agents for transfer of chemical constituents and heat in the Earth. The only direct samples of ancient fluid flow are provided by fluid inclusions in minerals (*e.g.*, Roedder 1984). Successively entrapped fluid generations monitor evolution and are thus unique windows on fluid-assisted geological processes of the past.

The term fluid encompasses all phases that are not solid at the P–T–X (composition) conditions of the process of interest, including aqueous or carbonic solutions, silicate or sulfide or carbonate melts to name only a few geologically relevant ones. At earth surface conditions, we observe a vast diversity of physically and chemically distinct fluid phases. It decreases conspicuously with increasing P and T when various systems reach their critical endpoints, *e.g.,* the basalt–water system at *ca.* 5–6 GPa and 1000–1050°C where aqueous fluid and silicate melt become indistinguishable because the miscibility gap disappears (Kessel *et al.* 2005). Common to all these fluid systems is the observation that element solubilities tend to increase with increasing P and T. The chemical compositions of fluids provide key information to constraining fluid-mediated chemical cycling in the Earth.

Laser ablation (LA–) ICP–MS has become the most versatile *in situ* analytical technique to determine the elemental composition of many materials, and is the method of choice for the analysis of heterogeneous phase mixtures such as fluid inclusions in minerals. Historically, crush-leach techniques were first explored to characterize the metal contents dissolved in fluid inclusions, more than 40 years ago (Czamanske *et al.* 1963). Methods refinement has subsequently allowed the determination of the bulk aqueous fluid element and isotopic compositions present in fluid inclusions (*e.g.,* Bottrell *et al.* 1988, Banks *et al.* 1991, Pettke & Diamond 1995). However, these data only provided the composition of the mixture of various fluid stages present in the sample. Obviously, better sampling resolution is required to resolve properly different fluid stages commonly trapped in a given sample in order to refine our understanding of fluid-mediated processes in the Earth.

The *in situ* analysis of solutes from individual fluid inclusions was originally explored using destructive methods, *e.g.*, laser ablation (Tsui & Holland 1979, Bennett & Grant 1980, Deloule & Eloy 1982) or secondary ion mass spectrometry (SIMS; Nambu & Sato 1981). These early investigations detected the presence of metal ions in individual fluid inclusions, importantly also of ore metals for samples from hydrothermal ore deposits. In efforts to control the analysis of an individual fluid inclusion better and to detect its solute contents better, the analytical approaches have been varied significantly, from non-destructive techniques such as proton-induced X-ray emission (PIXE; Horn & Traxel 1987) to laser ablation connected to various detection devices, such as optical emission spectroscopy (OES; *e.g.,* Ramsey *et al.* 1992, Wilkinson *et al.* 1994; laser-induced breakdown spectroscopy, LIBS, Boiron *et al.* 1991) or inductively coupled plasma mass spectrometry (ICP–MS; Shepherd & Chenery 1995). SIMS was also further explored but the severe matrix-dependence of SIMS analysis combined with very long analysis times (*i.e.*, very slow ablation rate), limited penetration depth into the sample and very expensive instrumentation impeded its broader methods development (*e.g.*, Diamond *et al.* 1991). Further methods developments towards the quantification of solute contents in fluid inclusions then demonstrated that laser ablation combined with quadrupole ICP–MS (ICP–QMS) is most promising, with low UV laser wavelengths (*e.g.,* 193 nm ArF Excimer laser systems) and energy-homogenized beam profiles being most suitable for the controlled ablation of individual quartz-hosted fluid inclusions (Günther *et al.* 1998). The work by Günther *et al.* (1998) has established the analytical

Mineralogical Association of Canada Short Course 40, Vancouver, B.C., p. 189–217.

protocol for fluid inclusions, resulting in the first fluid chemical characterization of a Sn-ore forming system (Audétat *et al.* 1998). This was followed by a series of other applications to magmatic–hydrothermal fluids (*e.g.,* Heinrich *et al.* 1999, Ulrich *et al.* 2002, Audétat & Pettke 2003, Rusk *et al.* 2004, Stoffel *et al.* 2004, Landtwing *et al.* 2005, Hanley *et al.* 2005a, Banks *et al.* 2007, Klemm *et al.* 2007, 2008), metamorphic ore fluids (*e.g.,* Klemm *et al.* 2004) or basinal fluid migration (*e.g.,* Lüders *et al.* 2005). Applications to fluid inclusions have become broader as the LA–ICP–MS technique has become more accepted, *e.g.,* the first applications to experimental determination of fluid metal solubility (for Au: Loucks & Mavrogenes 1999, Simon *et al.* 2005; for PGE: Hanley *et al.* 2005b; for Sn: Duc-Tin *et al.* 2007; or even for transition metals such as Fe: Simon *et al.* 2004), or the analysis of metamorphic high-P fluid inclusions both from nature (*e.g.,* Scambelluri *et al.* 2004) and from experiment (*e.g.,* Spandler *et al.* 2007). The fundamental principles of the LA–ICP–MS analytical approach of Günther *et al.* (1998) for fluid inclusions has since remained largely unchanged; however, methods refinements have continuously improved the techniques. Cross-check against synthetic fluid inclusions of known composition has demonstrated that accurate fluid element concentrations can be obtained by LA–ICP–MS (Heinrich *et al.* 2003, Allan *et al.* 2005).

Halter *et al.* (2002) have expanded the LA–ICP–MS technique towards the analysis of individual, heterogeneous inclusions in any host phase, where the analysis of quartz-hosted fluid inclusions represents a specialized application. These authors published the mathematical procedures for signal deconvolution into pure host and pure inclusion including rigorous uncertainty estimation in great detail. This most general approach to the problem of signal quantification for entire inclusions drilled out of their host mineral has then been documented to be accurate at useful analytical precision based on melt inclusions from volcanic and shallow plutonic rocks (Pettke *et al.* 2004, Halter *et al.* 2004). This novel approach does not render homogenization efforts of melt inclusions obsolete, however, since reversed crystallization sequences and the temperature and mode of disappearance of the bubble provides essential petrologic information (*e.g.*, Bodnar & Student 2006). An update on approaches and methods for the analysis of individual, polyphase, entire, unexposed melt inclusions by LA–ICP–MS has recently been presented by Pettke (2006), and Mason *et al.* (2008) reports on latest developments in the field of melt inclusion analysis.

LA–ICP–MS has a key advantage, in that it allows independent optimization of two fundamentally different processes, (i) sample ablation and (ii) ion production, analyte filtering and signal recording in an ICP–MS. This is an enormous advantage over most other *in situ* analytical techniques (*e.g.,* SIMS or LIBS) where ion production or light emission is directly related to sample ablation. This dual optimization potential opens up the possibility for considerably reducing matrix effects on analyte signals. An instrument optimization strategy particularly focused on matrix-"insensitive" LA–ICP–MS chemical analysis of geological materials has been discussed by Pettke (2006). Following such a strategy, the need for matrix-matched calibration, which is essential for SIMS analysis and strongly recommended for electron probe microanalysis (EPMA), can be relaxed for LA–ICP–MS. This is the fundamental and, to date, unique analytical characteristic allowing for the bulk chemical analysis of heterogeneous phase mixtures such as fluid or crystallized melt inclusions in minerals. It must be appreciated, however, that the extent to which matrix effects can be minimized also strongly depends on the LA–ICP–MS setup considered (see Sylvester, 2008, for a detailed assessment).

Data reported in the literature are the outcome of the highly complex interplay between sample characteristics, laser ablation of fluid inclusions, ion production and signal recording. Each LA–ICP–MS instrumental set-up has its characteristic set of specifications, and these differ considerably between different set-ups. To generalize conclusions for LA–ICP–MS analysis is therefore not only delicate but also potentially misleading. It is therefore mandatory that instrumental parameters and settings, data reduction schemes, as well as sample characteristics, be reported in great detail so that results can be reproduced in other laboratories possessing closely similar analytical equipment. The large amount of precise data that can be produced in a short time may often belie potential problems in accuracy. Only critical assessment of data quality by every analyst and, more importantly even, also by every data user will help advance our understanding of how routine analytical procedures by LA–ICP–MS should best be done, which in turn will greatly increase comparability of published data sets.

This contribution focuses on the handwork of performing meaningful fluid inclusion analyses, reports on recent methods developments and refinements and will document relevant details of the analytical strategies. Essential characteristics of the special sample type "fluid inclusions" are outlined first. Relevant instrumental parameters and settings are discussed in detail, in order to achieve matrix-"independence" of analyte calibration, to maximize analyte sensitivities and to reduce element sensitivities selectively as may be required for quantification of fluid inclusion element concentrations. The various types of spectral interferences particularly relevant to fluid inclusion analysis are characterized.

In a second section, I elaborate on how to select, analyze and quantify a series of individual fluid inclusions belonging to a compositionally uniform fluid inclusion assemblage. Selection criteria for fluid inclusions suitable for LA–ICP–MS analysis are reported. The preferred technique of fluid inclusion ablation is then developed. Strategies for the most representative recording of fast transient signals produced from polyphase fluid inclusions for single detector (*i.e.,* sequential data recording) mass spectrometers are evaluated. The data reduction scheme for obtaining element concentration data of fluid inclusions is then discussed step by step, and the data are evaluated with respect to precision and accuracy. Procedures to improve significantly on limits of detection (LOD) for individual fluid inclusion analysis are described.

In a third section, I report the analytical strategy for Pb isotopic ratios of individual fluid inclusions using LA–MC–ICP–MS and address the figures of merit currently obtained. The chapter then concludes with a detailed assessment of the statistical relevance of concentration and isotope ratio data sets obtained for fluid inclusions.

The new procedures for elemental and isotopic analysis of individual fluid inclusions reported herein shall aid in achieving accurate data at useful external reproducibility. For fluid inclusion assemblages, average solute concentrations with ±5% 1 SD (standard deviation) uncertainties can be achieved. Uncertainties on inclusion to inclusion reproducibility of a natural fluid inclusion assemblage (n=11) approached 0.07% 2 SD for $^{208}Pb/^{206}Pb$ and $^{207}Pb/^{206}Pb$ ratios and 0.14% 2 SD for Pb isotope ratios normalized to mass 204, respectively, and these isotope ratio data are accurate.

## FLUID INCLUSIONS: CHARACTERISTICS RELEVANT FOR THEIR LA–ICP–MS ANALYSIS

Fluid inclusions are commonly trapped as a single phase at elevated temperatures and pressures (exceptions are heterogeneous entrapment in a two or more phase stability volume; *e.g.,* Roedder 1984). Key to the usefulness of fluid inclusions (and melt inclusions) is that after entrapment, the inclusions behaved as a chemically closed system, *i.e.,* individual fluid inclusions do not lose or gain chemical components[1].

Figure 12-1a shows a typical fluid inclusion assemblage. As can be seen, an individual fluid inclusion consists of several phases. After formation, daughter minerals crystallize and other phases (*e.g.,* a vapor bubble) unmix from the initially homogeneous phase while the fluid inclusion cools to room temperature. It is this polyphase sample of confined volume that we wish to analyze altogether in order to reconstitute the bulk chemical composition of the fluid inclusion at the time of entrapment. It is therefore crucial not to lose any fraction of the fluid inclusion content (solids or liquids or gases) and to analyze all the different phases present within an inclusion quantitatively. Partial ablation of a fluid inclusion will inevitably provide measurements that return data of which only a few element concentrations may be deemed correct, at best.

Fluid or melt inclusion assemblages (Goldstein & Reynolds 1994), per definition, are a series of fluid inclusions entrapped at the same time in a host mineral. Petrographically, geometric features are employed to argue for coeval entrapment of fluid inclusions, *e.g.*, the entrapment of fluid inclusions along a host mineral growth zone or a fracture plane. We distinguish homogeneous entrapment and heterogeneous entrapment. Homogeneous entrapment implies that a compositionally uniform single phase fluid was entrapped. Heterogeneous entrapment implies that two coexisting fluid types (*i.e.*, chemically distinct fluids) were coevally entrapped, forming, for example, a boiling assemblage where liquid and vapor inclusions coexist. Throughout this chapter, I refer to homogeneously entrapped fluid inclusion

[1] Discussion of the real case where post-entrapment modification of fluid inclusion contents may have occurred (e.g., Sterner & Bodnar 1989, Audétat & Günther 1999, Bodnar 2003, Klemm et al. 2007) is beyond the scope of this paper.

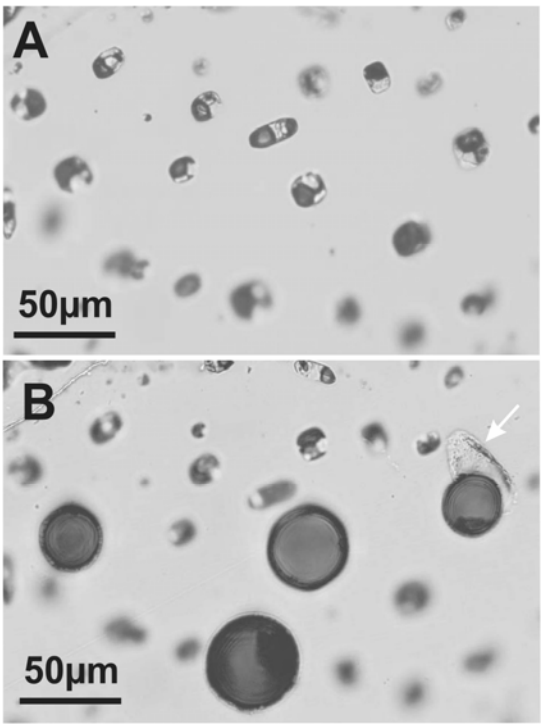


FIG. 12-1. **a)** Brine fluid inclusion assemblage in quartz from a stockwork vein of a porphyry-Cu deposit, Rosia Poieni, Romania (focused below sample surface). Note the uniform phase proportions between individual inclusions, petrographically indicating that they are compositionally identical. **b)** Sample after analysis of 4 inclusions from this assemblage (focused on sample surface), demonstrating the highly controlled laser ablation of individual fluid inclusions with the GeoLas system used. This is the ideal case.

assemblages unless stated explicitly otherwise.

Let us take the fracture as an example of how inclusions formed. The fracture was filled with a one-phase fluid and then started to heal, thereby forming a series of individual fluid inclusions, each trapping a fraction of the homogeneous fluid that filled the fracture. Ideally, individual fluid inclusions have been isolated (*i.e.*, sealed) while the fluid was still in the one phase field. Each individual fluid inclusion therefore represents an isolated sample of this homogeneous fluid, and all individual fluid inclusions of an assemblage are thus compositionally identical. Evidence of this can be seen petrographically by identical phase proportions at room temperature (illustrated in Fig. 12-1a), and it can be corroborated by consistent microthermometric results. The analysis of a series of fluid inclusions belonging to a fluid inclusion assemblage therefore allows for repetitive analysis of a compositionally uniform sample (identical to analyzing several spots on a homogeneous solid). Consequently, the fluid composition is best characterized as the average plus external uncertainty of the individually analyzed fluid inclusions from the homogeneously entrapped assemblage. This provides the most robust characterization of element compositions in the fluid at the time of entrapment, *i.e.,* at a given stage of fluid evolution in the system of interest. The main analytical challenge is therefore to determine the composition of a homogeneous fluid phase based on the analysis of a series of micro-samples of a confined, heterogeneous phase mixture of *a priori* unknown mass proportions.

Note that even apparently simple aqueous or aqueo-carbonic (Fig. 12-2a) or vapor fluid inclusions (Fig. 12-2b) may contain a major proportion of some trace elements concentrated in a tiny daughter mineral that may be too small for microscopic detection or simply hidden by the large vapor bubble. It is therefore mandatory that the entire fluid inclusion is ablated in a controlled manner and analyzed completely.

## SPECIFIC LA–ICP–MS INSTRUMENTAL REQUIREMENTS FOR FLUID INCLUSION ANALYSIS

Before turning to relevant aspects of the handwork of fluid inclusion analysis by LA–ICP–MS, the analytical setup used for obtaining most of the data shown here will be characterized first. This is essential as each analytical setup has its advantages and drawbacks; hence, the problems to be solved determine which setup will most likely provide the overall best analytical performance. The system at the University of Bern consists of a GeoLas Pro 2006 (Lambda Physik, Germany) pulsed 193 nm ArF excimer laser system coupled with an ELAN DRC-e ICP quadrupole mass spectrometer (Perkin Elmer, Canada). Typical settings for fluid inclusion analysis using this setup are reported in Table 12-1. The GeoLas Pro system is operated exclusively in manual mode. Energy densities on the sample surface are homogeneous irrespective of ablation crater size, adjustable to between 4 and 200 µm. Crater sizes below 8 µm and above 120 µm are generally not relevant for fluid inclusion analysis, since complete ablation of the entire fluid inclusion is a prerequisite for obtaining relevant compositional data, and inclusions larger than *ca.* 50 µm do not return improved LODs (see below).

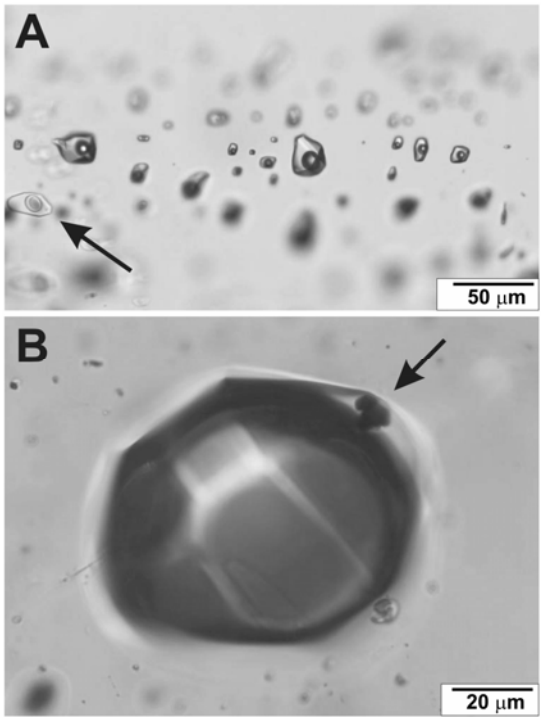


FIG. 12-2. **a)** Assemblage of three-phase $CO_2$-rich inclusions from auriferous quartz veins, Brusson, NW Italy (Diamond 1990, Pettke *et al.* 2000a). Note the flat inclusion (black arrow) that shows menisci of $CO_{2,\ liquid}$ and $CO_{2,\ vapor}$ in aqueous solution. **b)** Large vapor inclusion with a thin rim of aqueous liquid wetting the inclusion walls and containing opaque daughter crystals (black arrow, in focus). It is obvious that such tiny daughter crystals can escape petrographic recognition when they are beneath the vapor bubble or out of focus during petrographic inspection.

The principle for fluid inclusion analysis by LA–ICP–MS is simple. A polished sample thick section is placed in an ablation cell, together with an external standard material. A laser beam is used to completely drill out individual fluid inclusions; the liberated material forms an aerosol that is carried by the aerosol carrier gas into the ICP where ions are produced. Cations are then analyzed according to their mass to charge (m/z) ratios on a detection device. Measurement data are read out as transient (*i.e.,* time resolved) signal intensities, preferably in counts or volts, depending on the type of detector used. These machine data are then converted off-line into element ratio, element concentration or isotope ratio data employing various data reduction protocols.

In summary, accurate LA–ICP–MS measurements of geological materials including multiphase inclusions should obviously follow the

TABLE 12-1: LA–ICP–MS INSTRUMENT AND DATA ACQUISITION PARAMETERS

| **GeoLasPro 193 nm ArF excimer laser (Compex 102 Pro)** | |
|---|---|
| Laser fluence on sample | 24 J/cm$^2$, homogeneous energy distribution |
| Pulse duration | 15 ns |
| Repetition rate | 10 Hz |
| Pit sizes | Between 8 and 90 μm |
| Ablation cell volume | 7 cm$^3$ |
| Ablation cell gas flows | 1.0 L min$^{-1}$ He, 0.008 L mi n$^{-1}$ $H_2$ |

| **ELAN DRC-e quadrupole ICP–MS** | |
|---|---|
| Nebulizer gas flow | 0.83 L min$^{-1}$ Ar |
| Auxiliary gas flow | 0.70 L min$^{-1}$ Ar |
| Cool gas flow | 16.0 L min$^{-1}$ Ar |
| rf power | 1450 kV |
| rPa value | 0 |
| rPq value | 0.25 |
| Detector mode | Dual (cross-calibrated pulse / analog modes) |
| Quadrupole settling time | 3 ms |
| Detector housing vacuum | 4.5 – 6.5 *10$^{-6}$ Torr during analysis |
| Oxide production rate | Tuned to <0.5% ThO |
| Robust plasma conditions | Tuned to S(U) = S(Th) |

| **Data acquisition parameters** | |
|---|---|
| Sweeps per reading | 1 |
| Readings per replicate | 600 |
| Replicates | 1 |
| Dwell time per isotope | 10 ms, except for $^{29}$Si = 8 ms |
| Points per peak | 1 per measurement |
| Isotope sequence analyzed in jump routine | $^{23}$Na, $^{197}$Au, $^{29}$Si, $^{197}$Au, $^{35}$Cl, $^{197}$Au, $^{39}$K, $^{197}$Au, $^{55}$Mn, $^{197}$Au, $^{57}$Fe, $^{197}$Au, $^{65C}$u, $^{197}$Au, $^{88}$Sr, $^{197}$Au, $^{95}$Mo, $^{197}$Au, $^{207}$Pb, $^{197}$Au |

Note: S stands for sensitivity

philosophy of keeping all parameters as uniform as possible in order to minimize the potential for complications. A series of relevant parameters to be considered was provided by Pettke (2006) and are briefly summarized as follows:

- Best possible visualization of sample on TV screen during laser ablation sampling
- Sufficient laser energy density on sample at appropriate wavelength to controllably ablate all matrices of interest
- Homogenized energy density across tunable ablation crater sizes, to minimize ablation energy dependent changes in aerosol production and to maximize control of the ablation process notably for bulk inclusion analysis.
- Robust plasma conditions, to maximize matrix independence of analytical conditions (external calibration)
- Maximize analytical signal to noise ratios, and not only sensitivity
- Constant and low backgrounds to minimize LOD
- Representative recording of short transient signals as commonly produced from ablation of inclusions
- Proper analyte selection for minimizing polyatomic interference problems

**Step 1: Laser ablation of fluid inclusions**

For liberation of the fluid inclusion content, a monochromatic, collimated, coherent, pulsed laser beam is used. Wavelengths in the low UV are preferred nowadays, because the absorption of light generally increases with decreasing wavelength for silicate and oxide phases commonly hosting fluid inclusions. Laser beams in Q-switched mode (*i.e.,* pulsed) are preferred, as they allow for establishing the desired ablation rate at constant energy density on the sample surface, they reduce (nanosecond lasers) or eliminate (femtosecond lasers) negative interactions between aerosol expanding above the ablation spot and incoming laser light, and sample heating around the ablation spot is minimized. Laser systems delivering a homogeneous energy distribution across the entire ablation spot are strongly preferred, because they allow for choosing the appropriate beam size for fluid inclusion ablation at constant energy density (thus eliminating any energy–density-related fractionation at the ablation site). They also enhance the control of the fluid inclusion ablation process by minimizing cracking of the host mineral and associated catastrophic liberation of the fluid inclusion contents during ablation.

Laser ablation of fluid inclusions, as for other samples, is also best done in a He atmosphere because sample deposition around the craters is greatly reduced when using He instead of Ar as ablation chamber gas (Eggins *et al.* 1998, Günther & Heinrich 1999). This in turn maximizes the fraction of ablated material that can be transported to the ICP.

**Aerosol transport system**

The aerosol transport system encompasses the ablation chamber (or ablation cell) and the transport tubing to the injector tube. The ablation chamber must accommodate the sample and reference material(s) and should be characterized by minimal washout times. The latter translates into higher signal to background intensity ratios for the transient signal interval of a given fluid inclusion ablation, resulting in improved LODs. Interestingly, the length of the tubing connecting the ablation chamber to the torch has a subordinate influence on the overall shape of the transient signal (Venable & Holcombe 2001) – signal dispersion is almost exclusively dominated by gas flow conditions inside the ablation chamber (*e.g.,* Günther 2001). For fluid inclusions, we commonly use either a 1 $cm^3$ or a *ca.* 7 $cm^3$ ablation chamber with optimized washout times (documented in Fig. 12-3).

Prior to the ICP torch, the "Nebulizer Ar gas stream" needs to be admixed to the aerosol-in-He gas stream, because mixed He–Ar aerosol carrier gas is required to maintain a stable plasma. The connector used to admix the Ar delivered by the "Nebulizer gas flow" consists in our case of a simple y-piece where the aerosol-bearing He is blown into the Ar flow using a syringe needle, and the mixture then flows into the torch (Fig. 12-4). This setup ensures perfect mixture between Ar and the aerosol-bearing He but has the disadvantage that it is prone to particle accumulation, particles that may then cause signal spikes in subsequent analyses that must be eliminated for quantification (more below).

**Step 2: Ion production and recording**

In principle, all the sample material reaching the ICP should be completely converted to singly charged cations, and all these cations should be recorded on the detection device. Obviously, reality is very far from this ideal. It is therefore the challenge for the analyst to optimize the ICP–MS

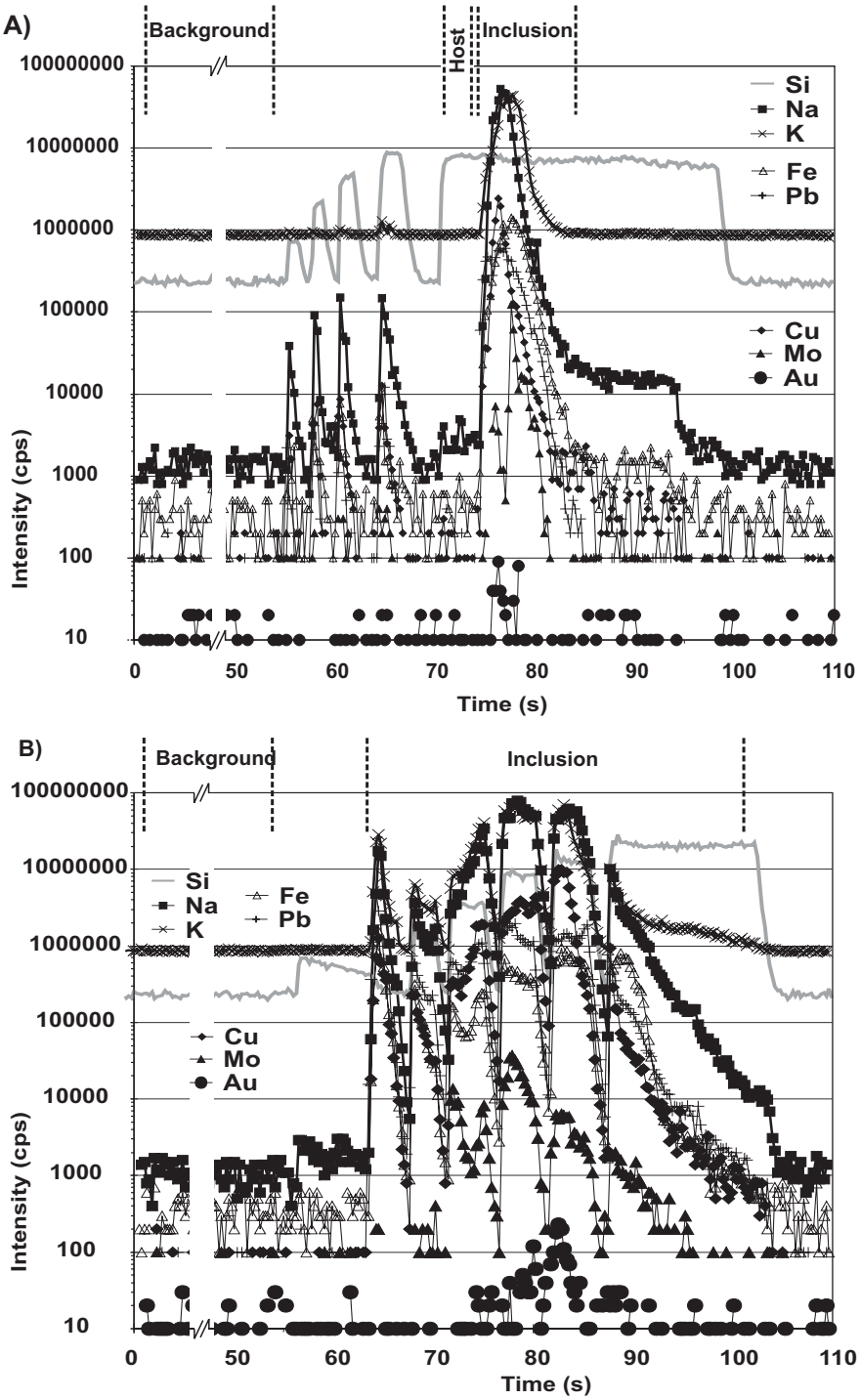


FIG. 12-3. Transient LA–ICP–MS signals of individual fluid inclusions, with signal count rates shown in logarithmic scale. Background, Host and Inclusion refer to the respective signal intervals used for quantification. **a)** Signal of a polyphase brine inclusion resulting from the straight ablation method (inclusion 14fre11, Table 12-3). Note the surface contamination (these are deposits from previous fluid inclusion ablations nearby in this case) at every crater size increase. **b)** Signal of a polyphase brine inclusion produced by the stepwise fluid inclusion opening procedure (inclusion from Bingham Cu–Au±Mo porphyry vein). For this inclusion, a host quartz signal needs to be measured separately nearby. (Continued on next page.)

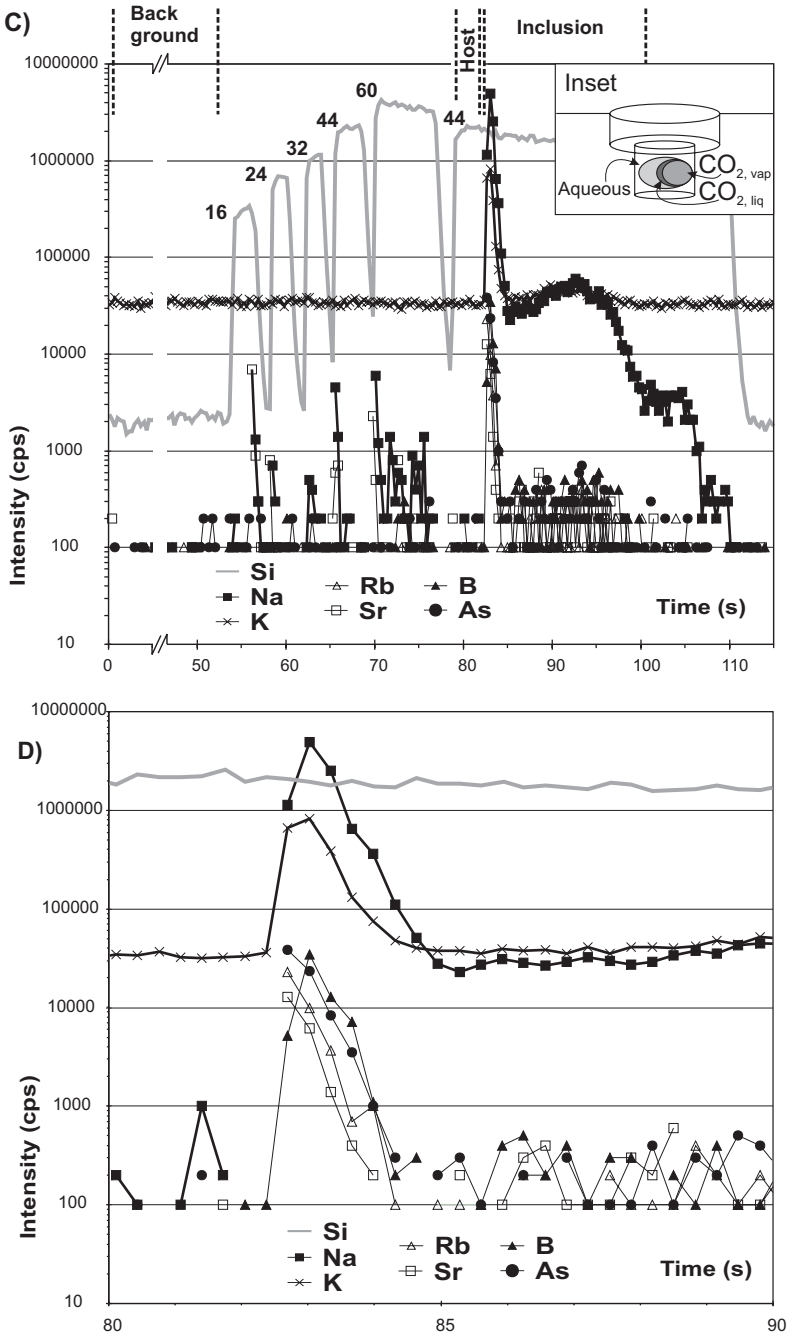


FIG. 12-3 (contd.). Transient LA–ICP–MS signals of individual fluid inclusions, with signal count rates shown in logarithmic scale. Background, Host and Inclusion refer to the respective signal intervals used for quantification. **c)** Characteristic swan-shaped signal for the analysis of a three-phase $CO_2$-rich fluid inclusion released by straight ablation, after having step-wise increased the pit size (labeled next to the grey Si signal) to a larger diameter than that finally used for fluid inclusion ablation (see inset). This technique can be employed to remove host material lying above deeper inclusions in order to minimizing negative side effects encountered for craters with a high depth to diameter ratio (exceeding *ca.* 2), such as signal tailing. Note the extremely fast transient signal maximum at fluid inclusion opening (see enlargement of signal shown in **d)** that probably results from increased internal pressure in response to heating induced by laser light reaching the inclusion before opening. This analysis has been acquired without $H_2$-mode. Also note for figures **a)** to **c)** the fast signal decay after the laser was switched off, documenting a washout time of about 3 s.

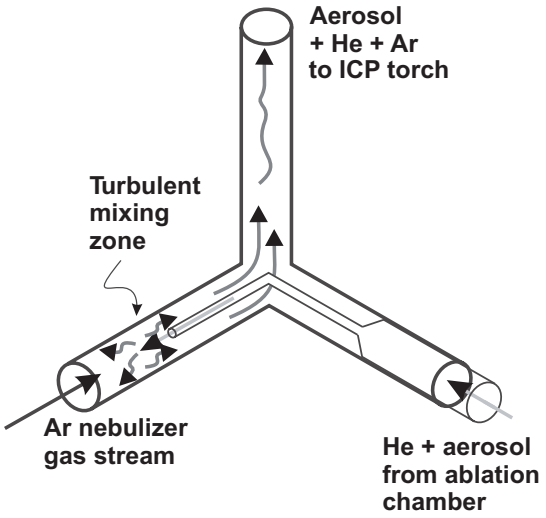


FIG. 12-4. Drawing of the Y piece used to mix the aerosol_in-He stream with the nebulizer Ar gas stream prior to entering the torch.

instrumental part such that the cations recorded on the detector are representative for the sample analyzed. This sounds simple, but it is far from trivial.

***Optimization of the ICP–MS parameters:*** The simple function of the ICP is to convert the aerosol particles to atoms and to ionize these. In practice, most recent research has demonstrated that this is currently the instrumental weak point in LA–ICP–MS analysis in general (*e.g.,* Günther & Hattendorf 2005). Most well known in LA–ICP–MS are problems collectively referred to as elemental fractionation, *i.e.*, changes of element responses (*i.e.,* element sensitivity ratios) with changing LA–ICP–MS analytical conditions (*e.g.,* Longerich *et al.* 1996a), and, for isotopic ratio analysis, mass bias. Elemental fractionation historically has been assigned to processes occurring at the laser ablation site (*e.g.,* Fryer *et al.* 1995, Mank & Mason 1999), and only recently has it become apparent that plasma processes are equally – if not dominantly – responsible for elemental fractionation (*e.g.,* Guillong & Günther 2002).

This insight has encouraged Günther & Hattendorf (2005) to establish optimization criteria for "**robust plasma conditions**"; simply speaking, conditions where ion production in the ICP is uniform and as complete as possible. At such ICP conditions, fractionation effects resulting from incomplete ionization are minimized. Pettke (2006) has summarized the aspects relevant for the analysis of polyphase inclusions in detail and introduced this approach as a means of minimizing matrix-dependency of external calibration. Briefly, the ICP–MS is optimized daily for maximum signal to noise ratios (and not only sensitivity) across the entire mass range of interest, at low element oxide production levels commonly monitored using the ThO production rate. These settings are then tested for equal sensitivity of Th and U, two elements with nearly equal first ionization energies, mass, and abundance of major isotopes. The SRM 610 and 612 glasses from NIST are ideal for this as they possess largely equal U and Th concentrations; thus, the $^{238}U/^{232}Th$ intensity ratio should be one. Günther & Hattendorf (2005) demonstrated that ICP–MS optimizations based on maximum sensitivity and ThO/Th < 0.5% may return U/Th sensitivity ratios much higher than one, indicative of non-uniform aerosol ionization. Analyzing samples with such an ICP–MS setting would therefore require matrix- and crater size-matched external standardization, conditions at which such fractionation processes would be closely comparable between sample and external standard and thus cancel. A matched external calibration approach grossly limits the versatility of LA–ICP–MS analysis, however, and it is not practical for the analysis of polyphase fluid inclusions in complex silicate host minerals. Capillaries containing aqueous solutions compositionally similar to the inclusions to be analyzed have been proposed as an improved external calibration strategy (*e.g.,* Stoffel *et al.* 2004). While the standard matrix more closely approaches the sample when compared to the use of SRM 61X glasses, there are caveats regarding some aspects of this approach. Experiments in our lab have revealed that element sensitivity ratios obtained from the ablation of solutions in capillaries may vary as a function of the focusing depth of the laser beam (*i.e.*, the z-axis). Capillaries are commonly thicker than *ca.* 50 µm; hence, using a crater size similar to that employed for fluid inclusion ablation returns a crater aspect ratio (depth to diameter ratio) that exceeds one, conditions at which fractionation at the laser ablation site may become relevant. The content of capillaries is also not sampled completely for calibration (capillaries are simply too large in volume), thus not allowing for complete sampling of the solution as required for fluid inclusion analysis (more below). Finally, the bulk mass analyzed during complete inclusion ablation corresponds to largely equal proportions of matrix mineral and inclusion content (*e.g.,* Halter *et al.*

2002, Pettke 2006); hence, the analyzed aerosol represents a mixture of silicate, water and salts for which external calibration based on SRM 61X glasses returns accurate fluid inclusion data (*e.g.,* Heinrich *et al.* 2003).

That matrix-independent external calibration can be achieved through careful ICP optimization has been demonstrated in the literature, *e.g.,* for silicate minerals by Jackson *et al.* (1992), for aqueous fluid inclusions (Günther *et al.* 1998, Heinrich *et al.* 2003), oxides (*e.g.,* Heinrich *et al.* 2003), carbonates (*e.g.,* Eggins *et al.* 2003) and even for Fe, Ni, Co and Cu in some sulfides (chalcopyrite, pyrrhotite and millerite; Halter *et al.* 2004). Having fit for purpose instrumentation and following ICP–MS optimization criteria to establish robust plasma conditions (Günther & Hattendorf 2005) for minimizing matrix dependence will provide the versatility needed for the analysis of polyphase inclusions in minerals (Pettke 2006).

***Analyte sensitivities:*** It has long been recognized that sensitivity in dry aerosol mode LA–ICP–MS (50 μm crater size) is about three orders of magnitude lower than what can be achieved in solution mode ICP–MS (*e.g.*, Günther *et al.* 1997). Consequently, LODs are also significantly higher than in solution mode, despite overall much lower gas background intensities. Sensitivity enhancement is therefore central to improving the detection capability in LA–ICP–MS. Commonly such sensitivity enhancement can be achieved for LA–ICP–MS with a few modifications such as the use of He in the ablation chamber (*e.g.,* Eggins *et al.* 1998) or the reduction of the interface pressure (Günther *et al.* 1997). Recently, Guillong & Heinrich (2007a) demonstrated an up to 7-fold, element-specific increase in sensitivity through the addition of small amounts of $H_2$ to the aerosol carrier gas on their GeoLas 193 nm LA–ICP–MS system (Elan 6100 DRC). Not only the analyte signals but also the gas backgrounds are variably affected by the above modifications. The sum of these effects will determine whether an improvement in signal to noise ratio can be achieved on a given LA–ICP–MS instrumental setup, potentially significantly lowering the LODs and improving the external reproducibility of ultra-trace element measurements. Implementing $H_2$ addition to the aerosol carrier gas following Guillong & Heinrich (2007a), sensitivities achieved on our Elan DRCe QMS are reported in Table 12-2. Since gas backgrounds deteriorate for only a subset of m/z commonly used for analysis, an improvement in LOD results also for most elements commonly analyzed in fluid inclusions.

TABLE 12-2: ELEMENT SENSITIVITIES

| | Mass analyzed | Sensitivity (cps per μg $g^{-1}$) |
|---|---|---|
| Na | 23 | 1400 |
| Si | 29 | 520 |
| K | 39 | 2400 |
| Mn | 55 | 3300 |
| Fe | 57 | 3600 |
| Cu | 65 | 2700 |
| Sr | 88 | 4800 |
| Mo | 95 | 4000 |
| Pb | 208 | 6700 |
| Au | 197 | 3400 |

Analytical conditions as in Table 12-1
Pit size = 44 μm
Reference material: SRM 612

For fluid inclusion analysis, we aim at analyzing for major to trace elements (*i.e.,* from tens of wt.% to ng $g^{-1}$ concentrations). In order to cope with such an extreme range in signal intensities, even cross-calibrated dual detector systems providing up to 9 orders of magnitude linear dynamic range may become insufficient for some applications. Among the major elements in fluid inclusions, Na is often the major constituent (recall that the bulk salinity of fluid inclusions is commonly expressed as wt.% equivalent NaCl). Element-specific mass resolution (as can be calibrated in an Elan ICP–QMS) can selectively lower the sensitivity on a given isotope (*e.g.*, Heinrich *et al.* 2003). These authors presented the analysis of 1 ng $g^{-1}$ U in halite as an example, a situation where a linear dynamic range of the detector exceeding 9 orders of magnitude would have been required to solve this analytical challenge. This becomes more of a concern notably because sensitivities in laser ablation mode are getting better and because major elements are commonly used as the internal standard elements for signal quantification (more below).

The range in signal count rates required to analyze an individual inclusion for major (up to several tens of wt.%; Table 12-3), minor and trace elements (down to tens of ng $g^{-1}$ possible in the best case) can also be reduced by using element-specific bandpass filtering as available in dynamic reaction cell (DRC) technology implemented in some Elan ICP–QMS instruments (see Tanner & Baranov 1999, for the theory of operation). This approach is

TABLE 12-3: ELEMENT CONCENTRATION DATA OF INDIVIDUAL FLUID INCLUSIONS OF ONE FLUID INCLUSION ASSEMBLAGE FROM A PORPHYRY STAGE QUARTZ VEIN OF GRANISLE

| Shot number | Ablation quality | Ablation mode SW; straight | Au signal visible Y=yes; N=no† | FI size µm | Na µg/g | K µg/g | Mn µg/g | Fe µg/g | Cu µg/g | Sr µg/g | Mo µg/g | Pb µg/g | Au µg/g |
|---|---|---|---|---|---|---|---|---|---|---|---|---|---|
| 14frc03 | ++(+) | STRAIGHT | N | 26 | 107300 | 116200 | 13400 | 133300 | 9100 | 290 | 390 | 1870 | <0.028 |
| 14frc04 | +++ | STRAIGHT | Y | 22 | 117400 | 110800 | 12600 | 115900 | *12100* | 240 | 340 | 1680 | 0.069 |
| 14frc06 | +++ | STRAIGHT | Y | 25 | 110500 | 121400 | 12700 | 122400 | 6800 | 230 | 300 | 1680 | 0.054 |
| 14frc07 | ++(+) | STRAIGHT | Y | 25 | 129100 | 99400 | 10700 | 101000 | 6600 | 210 | 310 | 1510 | 0.024 |
| 14frc08 | +++ | STRAIGHT | N | 18 | 112300 | 117300 | 13900 | 120600 | 5600 | 280 | 380 | 1850 | <0.072 |
| 14frc09 | +++ | STRAIGHT | N | 25 | 136300 | 82900 | 10000 | 99600 | 5000 | 200 | 210 | 1290 | <0.066 |
| 14fre10 | +++ | SW | Y | 25 | 128000 | 99700 | 11200 | 102900 | 7400 | 240 | 280 | 1370 | *0.087* |
| 14fre11 | +++ | STRAIGHT | Y | 20 | 112200 | 116100 | 12600 | 123200 | 7800 | 260 | 350 | 1520 | 0.064 |
| 14fre12 | +++ | STRAIGHT | Y | 32 | 121300 | 109800 | 11700 | 109000 | *18500* | 210 | 310 | 1500 | 0.053 |
| 14fre13 | +++ | STRAIGHT | Y | 25 | 116500 | 110400 | 12200 | 118700 | 3400 | 250 | 310 | 1500 | *0.100* |
| 14fre14 | +++ | SW | Y | 25 | 128800 | 99700 | 10100 | 102200 | 3600 | 210 | 250 | 1280 | 0.026 |
| 15frb03 | +++ | SW | Y | 20 | 114700 | 124300 | 12000 | 111200 | 7800 | 250 | 290 | 1380 | 0.041 |
| 15frb04 | +++ | STRAIGHT | Y | 20 | 112100 | 128400 | 11900 | 113600 | *20000* | 260 | 330 | 1530 | 0.039 |
| 15frb05 | ++(+) | STRAIGHT | Y | 28 | 127900 | 108700 | 10200 | 96300 | 6400 | 220 | 260 | 1320 | 0.054 |
| 15frb06 | +++ | STRAIGHT | Y | 15 | 101200 | 143300 | 13600 | 124000 | 6500 | 290 | 230 | 1770 | 0.068 |
| 15frb07 | +++ | STRAIGHT | Y | 25 | 112500 | 128300 | 11900 | 112800 | *21400* | 240 | 350 | 1450 | 0.056 |
| 15frb08 | +++ | SW | Y | 35 | 125300 | 117000 | 10500 | 95000 | 3900 | 190 | 260 | 1250 | 0.040 |
| 15frb09 | +++ | STRAIGHT | N | 18 | 130500 | 108800 | 10200 | 90600 | 4200 | 220 | 270 | 1340 | <0.058 |
| 15frb10 | +++ | STRAIGHT | N | 15 | 103900 | 134200 | 14300 | 125000 | 5900 | 270 | 230 | 1800 | <0.089 |
| *14frc05* | ++ | *STRAIGHT* | *Y* | *24* | *59300* | *198900* | *19700* | *165400* | *16500* | *270* | *370* | *2210* | *0.052* |
| | | | | **average** | 118305 | 114600 | 11900 | 111400 | 6000 | 240 | 300 | 1520 | 0.049 |
| | | | | **1 stdev** | 9966 | 14000 | 1300 | 12000 | 1700 | 30 | 50 | 200 | 0.015 |
| | | | | **1 sterr** | 2286 | 3212 | 298 | 2753 | 439 | 7 | 11 | 46 | 0.004 |
| | | | | **1 stdev %** | 8% | 12% | 11% | 11% | 28% | 13% | 17% | 13% | 31% |
| | | | | **1 sterr %** | 1.9% | 2.8% | 2.5% | 2.5% | 7.3% | 2.9% | 3.8% | 3.0% | 8.8% |

Sample used is GI-13-17. Equivalent NaCl concentration used as the internal standard for signal quantification is 55 wt.%. Isotopes analyzed are listed in Table 12.1

Values *in italic* are deemed outliers and thus have not been used for statistical calculations (as explained in text)

+++ indicates perfect ablation of fluid inclusion

++(+) indicates good ablation of fluid inclusion with a very minor problem (e.g., signal tailing because the fluid inclusion was deep)

++ indicates acceptable ablation, with problems such as surficial quartz breakout or unclear signal boundary because an underlying inclusion was hit before the first signal ended

STRAIGHT indicates straight ablation (see Fig. 3a, c and text for explanations)

SW indicates stepwise opening (see Fig. 3b and text for explanations)

† indicates whether a gold signal is visible in the transient signal plot (Y) or not (N)

<value I indicates that the concentration value is below the LOD, calculated using the 3 σ criterion (Longerich et al., 1996) as explained in text

more versatile as it does not require a separate calibration of an element-specific resolution. All that is required is to optimize the RPa and RPq values to achieve the desired element-specific reduction in sensitivity, *i.e.,* bandpass filtering. The analysis of the external calibration and sample material at these conditions will then allow for the use of the major element as the internal standard, such as Na for trace elements in halite (see Heinrich *et al.* 2003). Another approach to avoid problems created from too intense analyte signals could be to optimize the ion extraction lenses such that the sensitivities of low m/z elements (*i.e.,* the common major elements) are suppressed – however, this suppresses the sensitivities of low m/z trace elements alike; hence, it is not considered to be a method of choice.

***Spectral interferences*** also plague LA–ICP–MS analysis. However, they are less of a problem than in many other spectrometric detection devices. Since we always have *all the matrix all the time* during analysis, matrix-related interferences are most problematic, and their effects are possibly often underestimated.

Isobaric interferences are considered to be "easy" types of interferences. Sometimes, they can easily be avoided by proper isotope selection (and often accepting significantly elevated LODs, *e.g.,* for Ca). If not feasible, isobaric overlap can be corrected for mathematically provided that the interfering cation is part of a stable isotope pair (*e.g.,* $^{106}$Cd on $^{106}$Pd as derived from in-run measured $^{110}$Cd). For cases where the interferent is far subordinate in intensity, a simple subtraction of interferent count rate may be tolerable. For cases where the interferent signal is a considerable fraction of the total signal, notably in the low mass range or for highly accurate isotope ratio measurements, the mathematical interference subtraction must be based on a mass-bias corrected interferent isotope ratio (see below).

Gas interferences from plasma gas and entrained air (*e.g.,* adsorbed on ablation chamber and aerosol transport system or entrained into the atmospheric pressure ICP) are accounted for by background subtraction (*e.g.,* $^{12}C^{16}O^{1}H$ or $^{13}C^{16}O$ or $^{14}N^{15}N$ on $^{29}$Si). Finally, care has to be taken to avoid doubly charged ions (recall that the mass filter of an ICP–MS resolves ions according to their mass/charge ratio), notably since second ionization potentials of some elements are lower than the first ionization potentials of other elements, *e.g.,* doubly charged light rare earth elements (LREE) producing interferences on Ga, Ge, As or Se. For LREE-enriched fluid, as can be expected for some pegmatites or for LREE-rich accessory minerals, interferences of $^{150}Nd^{2+}$ (10.73 eV 2$^{nd}$ ionization potential) and $^{150}Sm^{2+}$ (11.07 eV 2$^{nd}$ ionization potential) may render the analysis of $^{75}$As (9.79 eV 1$^{st}$ ionization potential) problematic. Similarly, trace $^{45}$Sc in zircon cannot be analyzed using low resolution mass spectrometry because of the $^{90}Zr^{2+}$ overlap. Using the $H_2$ admixture to the aerosol carrier gas described above also results in an increased $M^{2+}$ production rate (*e.g.,* $Ca^{2+}$ from 0.6% to *ca.* 1.2% on our system; similar to that reported by Guillong & Heinrich 2007a). This should be taken into consideration for analyte selection especially when using the $H_2$ mode.

Problematic interferences are polyatomic ions that form by combination of elements abundant in the plasma gas with elements abundant in the analyzed matrix. Element oxides also belong to this group simply because oxygen is the most abundant element in silicates. Metal argides ($(M^{40}Ar)^{+}$) are always a concern, *e.g.,* $^{55}Mn^{40}Ar$ on $^{95}$Mo for magmatic–hydrothermal fluids where Mn is a major cation, or $^{65}Cu^{40}Ar$ on $^{105}$Pd for magmatic–hydrothermal fluids or Cu-rich sulfides, or $^{12}C^{12}C$, $^{12}C^{13}C$, $^{13}C^{13}C$ on $^{24,25,26}$Mg in aqueo-carbonic fluids or carbonates. Importantly, these types of interferences are not only produced from sample– gas interaction but equally so from standard–gas interaction, *e.g.,* $^{63}$Cu should not be calibrated using the SRM 612 glass because of the $^{23}Na^{40}Ar$ polyatomic interference resulting from the >13 wt.% $Na_2O$ in these reference materials plus plasma Ar.

Interferences can commonly be resolved analytically with the appropriate equipment, *e.g.,* higher mass resolution as available for some magnetic sector field instruments (*e.g.,* Moens *et al.* 1995) or dynamic reaction cell or collision cell ICP–MS technologies (*e.g.,* Tanner & Baranov 1999, Mason 2001). These techniques, offering advantages and new drawbacks in combination with laser ablation (*e.g.,* Shibuya *et al.* 1998, Hattendorf & Günther 2000, Latkoczy & Günther 2002), are beyond the scope of this chapter, and the reader is referred to the literature for more information. For multi-element fluid inclusion analysis, however, only a few contributions have been published using these instruments (*e.g.,* Günther *et al.* 2001, Allan *et al.* 2005). Note that operating high-resolution sector field instruments at high mass resolution results in a very substantial loss in sensitivity that may corrupt

the anticipated benefit of the approach.

For multi-isotope elements where the presence of interferences on the isotope of choice for analysis cannot be excluded, test analyses recording more than one isotope of this element are a simple evaluation. For example, $^{95}$Mo is about 1.6 times as abundant as $^{97}$Mo, yet , $^{95}$Mo may suffer from $(^{55}Mn^{40}Ar)^+$ interference for the trace analysis of Mo in magmatic–hydrothermal fluids where MnO abundances may be several wt.%. Recording both $^{95}$Mo and $^{97}$Mo for a series of individual inclusion shots will then reveal whether the $(^{55}Mn^{40}Ar)^+$ interference is relevant at the given ICP–MS operating conditions. It needs to be considered, however, that analyzing more than one isotope per element will decrease the duty cycle per element (*i.e.*, the time fraction per sweep spent for the measurement of a given analyte signal) and, thus, potentially deteriorate the analytical quality for short transient signals.

## HOW TO SELECT, ANALYZE AND QUANTIFY A SERIES OF INDIVIDUAL FLUID INCLUSIONS

Having discussed fundamental parameters and aspects relevant for the analysis of individual, polyphase fluid inclusions, let us now focus on some practical aspects on how to perform such analyses and factors that should be taken into consideration during data reduction. Real data sets are used to assess figures of merit for fluid inclusion analysis.

### Selection criteria for fluid inclusions suitable for LA–ICP–MS analysis

Sample preparation involves selection of "optimum" fluid inclusions from fluid inclusion assemblages (Figs. 12-1 and 12-5) for analysis. This is done prior to the laser ablation measurement session, and suitable inclusions are mapped so that they can be easily found for LA–ICP–MS analysis. Such fluid inclusions need to fulfill as many criteria as possible from the following list (see Fig. 12-5 for an example):

- Size should be between 5 and *ca.* 80 µm, preferably between 15 and 50 µm. Larger inclusions do not return higher signal to noise ratios, except for vapor inclusions, because the ablation rate is largely host mineral controlled; hence, LODs cannot be further lowered.
- Spherical inclusions (round, isometric shape) are best to maximize the inclusion signal size per unit time.
- Minimum depth should be *ca.* 20 µm (for small inclusions) to 40 µm (for large inclusions) to avoid surface contamination of the fluid inclusion signal (Fig. 12-3a).
- Maximum depth should not exceed *ca.* 60 µm. Signals from deeper inclusions tend to tail significantly, thereby reducing the signal to noise ratio and, consequently, returning elevated LODs. Moreover, there is the danger for ablation-induced element fractionation for such deep inclusions.
- Spatial isolation of individual inclusions is required, so that one selected inclusion can be ablated without liberating material from neighboring inclusions (Figs. 12-1b, 12-5).
- The sample section must be at least *ca.* 100 µm thick, preferably even thicker (*i.e.*, >3 times the depth of inclusions to be analyzed) to avoid inclusion rupture through the *lower* surface of the section. On the other hand, the section needs to be thin enough to allow for transmitted light inspection and localization of the fluid inclusions to be analyzed.

Among the above criteria, the minimum size of inclusions that may return useful data is most difficult to generalize. Important is the bulk dissolved load of these fluid inclusions; the more dilute the fluid is, the larger will be the minimal inclusion size for obtaining useful data. Because of the sequential data recording and the highly transient signal structure, only a few key elements can be determined reliably in very small inclusions. Shallow inclusions are not as suitable for analysis as they are prone to surface contamination and tend to explode. For a 10 µm inclusion at a preferred depth of >20 µm, the aspect ratio of the final ablation crater may easily exceed 3; hence, laser ablation-induced fractionation may become a problem. An increase in beam size is often not recommended because the mixed inclusion plus host signal may become dominated by host contribution, thus increasing the uncertainty on the determination of fluid element concentrations (Halter *et al.* 2002).

### The technique of fluid inclusion ablation

Various techniques for improving the control on the fluid inclusion ablation process have been proposed, all aiming at the liberation of the entire fluid inclusion content without any losses, an endeavor which is far from trivial. In my view, the best technique for controlled ablation of the entire fluid inclusion content is **straight ablation**. In this

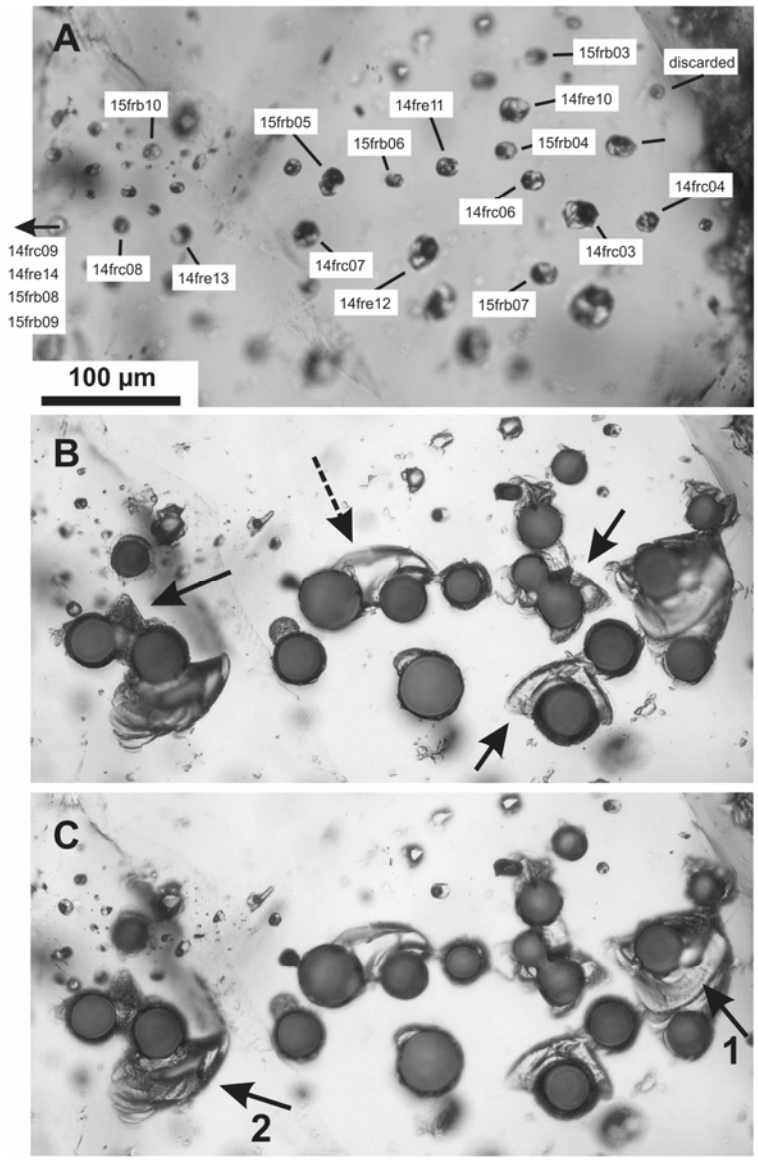


FIG. 12-5. **a)** Brine fluid inclusion assemblage, the LA–ICP–MS results of which are tabulated in Table 12-3. The labels are the shot numbers. The analysis of the shallow inclusion labeled "discarded" has not been saved because its signal contained surface contamination from previous ablations. Because of surface contamination resulting from deposits of ablated fluid inclusions, the sample has been surface-cleaned after the 14frc and 14fre shots and analyzed again the day after (*i.e.*, the 15frb series).

**b)** Same sample after the analyses, focused on the surface. Surficial breakout of quartz at crater rims occurred often on this sample (black arrows). In one case (dashed black arrow), a crack formed, but the quartz chip is still in place.

**c)** Same image as **b)** but focused 10 µm below the sample surface. Note that at a depth of 10 µm, all craters are round and sharply defined. Arrow 1 points to a deeper quartz breakout for shot 14frc05, causing loss of parts of the NaCl crystal (see text for explanation). This analysis has thus been rejected for average element concentration calculations (set in italics in Table 12-3). Arrow 2 indicates a similarly deep breakout of quartz. This analysis was a good one, however, because the analyzed fluid inclusion was deeper in the sample and thus not affected by this quartz breakout. Also note for **b)** and **c)** the inclusions near ablation pits may change their appearance without modifying their bulk chemical compositions (Lambrecht *et al.* 2008).

approach, the beam size is set to slightly larger than the maximum diameter of the fluid inclusion *before* the inclusion is opened, and the entire inclusion is then ablated at constant beam size (Fig. 12-3a). Admittedly, such an ablation procedure does not always work well, notably for quartz-hosted fluid inclusions or inclusions hosted by minerals possessing a good cleavage, where rupture of inclusions during ablation is sometimes observed. In order to minimize the uncontrolled release of liquid and daughter minerals, a stepwise procedure for opening fluid inclusions has been proposed, by which the fluid inclusion is pierced with a small crater size and, once open, the fluid inclusion is then ablated entirely by enlarging the beam size to slightly larger than the size of the fluid inclusion (Fig. 12-3b; see also Fig. 1 in Günther *et al.* 1998). This procedure indeed minimizes loss of inclusions due to rupturing but, unfortunately, has 3 serious drawbacks. First, a manually controlled crater size selection is required, yet most of the commercially available laser ablation systems are equipped with a motorized change in crater size that is too slow for the stepwise opening procedure. The next, more important drawback is surface contamination that inevitably will contaminate the fluid inclusion signal during stepwise opening. Figure 12-3a illustrates a signal from an inclusion of the assemblage illustrated in figure 12-5 obtained by fast manual stepwise opening to the final crater size

*before* the inclusion is opened. The signals for some trace elements (*e.g.*, Pb, Na, and Cu) regularly observed at each beam size increase before the fluid inclusion is opened are real and represent surface contamination resulting in this case from previously ablated inclusions nearby. Surface contamination may also originate from material smeared during sample polishing, *e.g.*, sulfides or native gold intimately intergrown with the vein quartz. The latter often cannot be removed even by most careful cleaning with organic solvents or inorganic acids prior to laser-ablation analysis. One could envision using a few, low energy, large diameter cleaning laser pulses to remove surface contamination, but our experience has shown that even such low energy laser pulses may decrepitate inclusions. Surface cleaning shots generally work well for deeper inclusions (30–50 μm depth), but these inclusions can equally well be shot with a straight ablation procedure (with or without stepwise opening before the inclusion is hit) which itself avoids surface contamination for the fluid inclusion signal (Fig. 12-3a). Finally, every fluid inclusion has a confined mass that will be analyzed over a longer time interval when using the stepwise opening procedure. This will return lower signal to background intensity ratios that translate into elevated LODs when compared to straight ablation (as also acknowledged by Günther 2001). An elegant, custom-made approach for "stepwise" opening of crater size to final size has been presented by Guillong & Heinrich (2007b) who used an iris diaphragm with which ablation can be initiated at *ca.* 8 μm and the crater size increased fast and continuously to the final crater size to allow for straight ablation of the fluid inclusion.

Why rupture of fluid inclusions occurs, sometimes very often, during laser ablation cannot be answered satisfactorily to date. Processes contributing to the problem are:

1) Incomplete laser light absorbance by the host phase, allowing for energy transfer into the fluid inclusion (*e.g.*, Lambrecht *et al.* 2008), and even to the sample holder below (as already reported by Günther 2001). Consequently, inclusion contents are heated up and may partially or totally homogenize, resulting in an increased internal pressure. The transient signals obtained invariably from aqueo-carbonic fluid inclusions testify to this process (Fig. 12-3c, d).
2) Most of the inclusions analyzed in quartz formed in former cracks. It can be speculated that quartz precipitating during crack healing may have slightly different trace element compositions which may cause the quartz structure to be more prone to laser light-induced stress along healed fracture interfaces. During the analysis of quartz cements in our lab, cracking predominantly occurs along the interface between the detrital grain surface and the quartz cement.
3) Quartz may have a stressed mineral structure, for example as revealed by undulatory extinction. Experience shows that such quartz generally does not ablate as uniformly as non-stressed quartz.
4) For minerals with very good cleavage (*e.g.*, carbonates), the features alluded to above will more likely result in rupture of the fluid inclusion before it can be ablated in a controlled manner. Nonetheless, even fluid inclusions hosted by minerals with excellent cleavage such as calcite can be analyzed well (Bodnar, pers. comm. 2008). This illustrates that it is best practice to explore the ablation behavior of a given sample suite before engaging into extensive sample preparation for fluid inclusion analysis.

Active focusing (*e.g.*, Hirata & Nesbitt 1995) during fluid inclusion ablation also helps to ablate the entire fluid inclusion content completely. The laser beam optics of the GeoLas system are such that the laser beam imaged onto the sample surface is slightly conical. For this system, actively focusing the beam during laser ablation of fluid inclusions helps keeping the laser fluence on the ablation spot constant, minimizes deposition of inclusion material onto crater walls and will aid in completely sampling the fluid inclusion contents.

**Representative recording of fast transient signals**

Since the beginning of fluid inclusion analysis it has been observed that the external reproducibility of average element concentrations for fluid inclusion assemblages was conspicuously worse for some elements (notably some of the metals) when compared to classical "ionic" elements of the alkali and alkali-earth series such as Na, K, Rb, Sr or Cs. The external reproducibility of both these element groups for fluid inclusions is up to an order of magnitude worse than that typically achieved for the repetitive measurement of a homogeneous solid. Some of these poorly reproducible elements can actually be expected to reside in either the vapor bubble or in tiny precipitates (referred to as daughter crystals; *e.g.*,

Fig. 12-2b) that may be extremely enriched in rare elements. In fact, thermodynamic equilibrium modeling (McKibben 2007) predicts that many metals in solution at the time of fluid inclusion entrapment could be expected to precipitate when the fluid inclusion cools to ambient temperatures (unless these metals remain in solution in a metastable state). Tiny gold particles are one extreme example of such highly enriched daughter crystals. Signals produced from such small phases are highly transient, notably for fast washout ablation chambers as required for the analysis of inclusions in minerals at minimized LODs. Pettke *et al.* (2000b) have illustrated and discussed causes and effects of non-representative recording of fast transient signals by sequential analyte detection in detail. A key result of this work is that very fast recording protocols (10 ms dwell time per isotope is now commonly used) are required for multi-element fluid inclusion analysis. However, this compromises LODs because shorter dwell times (keeping all other parameters constant) translate into higher LODs (more below). Large volume aerosol transport systems would extend the signal produced from a given inclusion (recall that the mass for analysis is fixed), thereby maximizing representative recording of the transient signal and, potentially, allowing for longer dwell times. Importantly, however, it would also result in lower signal to noise ratios, translating into higher LODs. Signal smearing is therefore not considered to be a viable alternative for the analysis of commonly available fluid inclusion types.

To solve the above dilemma, Pettke & Klemm (in prep.) have developed what they call a "**jump routine**" where elements prone to occur as nuggets or in tiny precipitates in fluid inclusions are analyzed more often during one sweep than elements residing in solution (*e.g.,* the alkali and alkali-earth metals). The data-recording scheme follows the idea that the element prone to precipitation (in this example Au) is recorded every other time, resulting in a sweep sequence such as Na, Au, Si, Au, K, Au, Mn, Au, Fe, Au, Cu, Au, Sr, Au, Mo, Au, Pb, Au employed here. For this given example, the sweep time (one sequential measurement at 10 ms of all isotopes listed above; 3 ms quadrupole settling time) is 234 ms, of which Au is measured for 90 ms (9 times 10 ms). This results in a duty cycle for Au of 38.5%, significantly higher than the duty cycle of 7.7% achieved for the conventional Na, Si, K, Mn, Fe, Cu, Sr, Mo, Au, Pb routine at equal dwell times. More importantly, the maximum time elapsing without measuring for Au is reduced to 16 ms in the jump routine which strongly minimizes the likelihood of missing a significant fraction of a highly transient gold signal. Obviously, the probability of accurately recording the highly transient Au signal is dramatically improved when using the jump routine as opposed to the conventional routine where periods of 117 ms elapse without measuring for Au. This is impressively demonstrated in Table 12-3 by the uncertainties on average element concentrations for Mo and Au, both potentially precipitating elements in this sample. Although Mo is *ca.* 6000 times more abundant than Au, its external analytical uncertainty is only twice as good as that of Au. In fact, the analytical precision on the average Au concentration of this assemblage of $0.049 \pm 0.015$ μg $g^{-1}$ (1 standard deviation) is remarkable for such a low content.

Sector field instruments provide a flat top peak and, therefore, would be much more appropriate for such a jump routine than a QMS with its slightly skewed Gaussian peak shape. However, data acquisition speed is limited by the still rather long (of the order of 50–100 ms) spectrometer settling time after a magnet field change. Therefore, unless the element of interest and the internal standard element required for signal quantification (more below) can be measured at one magnet setting, a sector field instrument will not be advantageous relative to fast quadrupole mass filters.

**Signal quantification strategies**

This section addresses the steps required to quantify element concentration data from instrument signal readouts obtained from the controlled ablation of an individual fluid inclusion, and addresses the inherent uncertainties. In brief, following representative data recording for the measurement of a series of individual fluid inclusions, signal quantification involves sequentially the following steps:

a) Integration of background interval and signal interval count rates for inclusion and pure host mineral sections for each analysis (Fig. 12-3), and background correction of inclusion and host signals
b) Subtraction of host mineral contribution from the inclusion signal
c) Drift correction based on the bracketing external standard measurements

d) Calculation of element concentration ratios based on the external standard
e) Conversion of these element concentration ratios into absolute element concentrations based on a known element concentration in the fluid inclusion
f) Filtering of the apparent element concentrations by the inclusion-specific LODs, to obtain the significant element concentration data for an individual fluid inclusion.

This procedure is identical to that described in Heinrich *et al.* (2003; summarized in their Fig. 10).

The basic relationship of LA–ICP–MS signal quantification (Longerich *et al.* 1996b) is

$$C_i(sam)/C_{IS}(sam) = C_i(std)/C_{IS}(std) * (I_i(sam)*I_{IS}(std))/(I_{IS}(sam)*I_i(std)) * (S_i(sam)*S_{IS}(std))/(S_{IS}(sam)*S_i(std)) \quad (1)$$

where *C* is the concentration of the subscripted element *i* or internal standard *IS* in the material in brackets (*sam* is sample, *std* is external standard material), *I* refers to the background-corrected intensities (count rate; in counts per second, cps) and *S* denotes sensitivity. The sensitivity ratios $S_i(sam)/S_i(std)$ are identical for all elements including the IS element. Therefore, although $S_i(sam)/S_i(std)$ is unknown, the sensitivity term cancels, and the concentrations of all elements in the sample ($C_i$) can be calculated when $C_{IS}(sam)$ and the concentrations of all elements in the external standard ($C_i(std)$) are known.

We will now go from (a) through (f) in more detail. The raw count data are best read out from the instrument as counts per second (cps) because count rates already account for potentially different dwell times employed for analysis.

(a) Each measurement is ideally integrated for 3 signal intervals: gas background (prior to laser ablation), host mineral and inclusion plus host (Fig. 12-3). Each of these signal intervals needs to be filtered carefully for signal spikes. These are positive outliers, confined to one sweep and at least one order of magnitude larger than the neighboring count rates for this isotope. Signal spikes may originate from electronic spikes or, more likely, may represent a highly transient signal originating from a large (a few μm in size) particle flushed to the plasma that may be unrelated to the sample currently measured (*i.e.*, cross-contamination from previous ablations). Background-corrected count rates are now calculated for the host and the inclusion plus host signal intervals.

(b) The next step is subtraction of host mineral contribution from the mixed inclusion plus host signal. The mass proportions of pure host and pure inclusion in the mixed inclusion plus host signal are unknown *a priori*. The simplest approach for this host mineral correction is to assume that one element is exclusively present in the host mineral. For low-P fluid inclusions in quartz, Si is such an element. Element/Si count rate ratios are determined for the host mineral signal interval (*e.g.*, the host mineral possesses $10^{-5}$ cps Li normalized to one cps Si signal). The Si count rate in the inclusion plus host interval, assumed to originate exclusively from the host mineral ablated with the inclusion, is then multiplied by these element-specific host mineral count rate ratios to determine the total count rate of host mineral contribution. As an example let us assume we had 1000000 cps Si in our inclusion plus host signal interval. Having $10^{-5}$ cps Li per cps Si in the host mineral interval then translates into 10 cps Li host mineral contribution to the inclusion plus host signal interval, and these 10 cps Li are then subtracted from the inclusion plus host signal count rate for Li. This returns the host mineral-corrected count rate for Li, *i.e.*, the Li count rate of the pure inclusion signal. For the general case where all elements are variably present in both the host mineral and the inclusion, an iterative calculation scheme is required to deconvolve the mixed host plus inclusion signal into pure inclusion and pure host signal (Halter *et al.* 2002). Uncertainties resulting from host mineral correction have been discussed in great detail in Halter *et al.* (2002) who provided a rigorous mathematic uncertainty quantification for individual melt inclusions analyzed in bulk. These authors illustrated that for elements enriched in the host mineral, inclusion data are inevitably associated with a larger uncertainty, primarily resulting from host mineral correction of the analytical inclusion signal.

(c) The bracketing external standard measurements are then used to effect an instrumental drift correction using reference materials such as SRM 610 or SRM 612 from NIST. This results in an ablation-specific set of analyte sensitivities for the external standard (reference) material.

(d) The drift-corrected element sensitivities (*i.e.*, cps per μg $g^{-1}$ element) calculated for each inclusion analysis individually are then used to derive element concentration ratios for the background- and host mineral-corrected fluid inclusion signals.

(e) Microthermometrically determined bulk salinity expressed as $NaCl_{equiv}$ may be used to derive the Na concentration in the fluid inclusion, by employing a "salt correction". This is a two step approach. (i) Element concentrations are calculated assuming that the $NaCl_{equiv}$ value is pure NaCl. This returns apparent concentrations for all other elements in the fluid inclusion, based on which one can identify those salt cations present in significant concentrations (*e.g.,* > 5% of the $NaCl_{equiv}$ value). (ii) Employ the empirical formulation for the salt correction discussed in Heinrich *et al.* (2003), to obtain "salt-corrected" element concentration data for the inclusion. This procedure corrects the microthermometrically determined $NaCl_{equiv}$ values for the presence of Cl-complexed cations other than Na. Heinrich *et al.* (2003) demonstrated that this correction scheme returns significantly more accurate element concentration data than would be obtained without accounting for the presence of metal chlorides other than NaCl when microthermometrically determined $NaCl_{equiv}$ values are used as the internal standard. Using microthermometrically determined Cl is an alternative internal standard. However, Cl measurement as a $^{35}Cl^+$ ion suffers from low sensitivity and polyatomic interference problems. We are currently exploring the quality of $^{35}Cl^+$ measurements by LA–ICP–MS using Cl bearing silicates. Future testing using synthetic fluid inclusions of known bulk Cl content will then reveal which approach of internal standardization (*i.e.*, Na or Cl as derived from microthermometry) returns more accurate results.

Heinrich *et al.* (2003) have convincingly demonstrated that neither absolute nor volume-normalized signal intensities have any direct relation to absolute element concentrations within individual fluid inclusions. Consequently, attempts to derive element concentration data without the use of an internal standard may not even provide the correct order of magnitude. It is also worth emphasizing that these highly transient fluid inclusion signals return element concentration data that are by no means erratic but that are externally well reproducible (see Table 12-3).

There are cases where accurate $NaCl_{equiv}$ data cannot be estimated from microthermometry, *e.g.,* for vapor-dominated inclusions where phase transitions in the aqueous phase cannot be observed reliably (*e.g.*, Fig. 12-2b), for $CO_2$-bearing inclusions that show clathrate melting in the absence of a free $CO_2$ phase, or for non-saline inclusions as can be produced in experiment (*e.g.*, Spandler *et al.* 2007). Here, an internal standard may be determined based on experimental data, *e.g.,* vapor salinities from the NaCl–$H_2O$ phase diagram, or may be derived from element concentration data for the host mineral and experimental fluid–mineral element partition coefficients applicable to P and T of entrapment. Another approach chosen by Scambelluri *et al.* (2004) rests on mass balance considerations. These authors quantified the Li and B contents of antigorite dehydration fluid by estimating the bulk chlorinity of the dehydration fluid based on Cl contents of antigorite serpentinite and resulting dehydrated olivine–orthopyroxene rocks, and assuming that Na is exclusively present as NaCl in these fluid inclusions.

Note, importantly, that element concentration ratios of individual fluid inclusions are uniquely defined after having performed steps (a) to (d) above, *i.e.,* for cases where no reliable internal standard is available. For many geoscientific applications (*e.g.*, Landtwing *et al.* 2005, Klemm *et al.* 2007), these already are extremely useful data.

(f) Finally, the LODs are calculated for each element in every inclusion individually according to the formula (Longerich *et al.* 1996b)

$$\mathrm{LOD} = \frac{3 * \mathrm{stdev}\, I_i(\mathrm{bkg})}{S_i * \left(1/N(\mathrm{bkg}) + 1/N(\mathrm{an})\right)^{0.5}} \qquad (2)$$

where *stdev* stands for standard deviation, $I_i(bkg)$ refers to the intensity of the gas background for element *i*, $S_i$ denotes the sensitivity of element *i* (as determined on the external standard), and *N* refers to the number of measurements (*i.e.,* sweeps) integrated for the background and analyte (*an*) signal interval, respectively. The above example returns the element concentration threshold value above which calculated element concentrations are real with 99% confidence.

**Ways of improving on LODs**

The LOD is a concentration threshold value above which a calculated concentration is deemed true, and this threshold value varies as a function of statistical parameters employed to derive it. For LA–ICP–MS signals, the variability of the background measurement around its mean intensity matters most (note the factor 3 in equation 2). The LODs are strongly element-dependent, because the analyzed isotopes are variably abundant in nature and instrument sensitivities vary greatly for different elements (*e.g.,* Table 12-2). High signal to

background intensity ratios are also essential. The improvements in element sensitivities achieved through the use of $H_2$ in the aerosol carrier gas have been introduced above. The various parameters influencing the LODs specifically for fluid inclusion analysis are addressed now, and ways to optimize each of these in order to minimize LODs are highlighted. Importantly, improving LODs also improves the quality of low element concentration data, because analytical uncertainties stemming from counting statistics are reduced (more below).

For fluid inclusion analysis, a key parameter influencing the LODs is the shape of the transient signal produced from inclusion ablation. Since an individual fluid inclusion provides a confined mass for analysis, it is intuitive that the faster we drill though the entire inclusion and the faster we record it, the higher are the signal to background ratios for the analytes. Recall, however, that controlled and complete ablation of the fluid inclusion content must be ensured; catastrophic ablation, although fast, is no option. The aerosol transport system is also essential in that a slow washout will smear the transient fluid inclusion signal and thus lower its signal to noise ratios for the analytes. The aerosol transport system employed here has a washout time of *ca.* 3s which is well suited for fluid inclusion analysis (Fig. 12-3).

Moreover, given the confined mass of sample for fluid inclusion analysis, inclusion size, shape and depth in the sample add to the observed LOD variability between different inclusions. Spherical inclusions are best, and an optimum depth is between *ca.* 20 and 50 µm (shallower for smaller inclusions) to allow for straight ablation. The stepwise opening signal shown in Fig. 12-3b has been modeled as a straight ablation signal (not shown), for which the LODs are improved by up to *ca.* 35%; hence, it is obvious that stepwise opening should be avoided also when optimizing LODs.

The fluid inclusion bulk salinity is also important, because the more dilute the fluid in the inclusion (fluid inclusion salinity in nature varies by more than two orders of magnitude) the greater is the fraction of $H_2O$ or $CO_2$, and these pass by unmeasured. As can be seen from Fig. 12-3, controlled ablation of a fluid inclusion produces a signal the transient shape of which is largely controlled by the laser ablation rate of the host mineral that determines the speed with which laser ablation drills "through the inclusion". Consequently, dilute fluid inclusions simply provide less analytes per unit time. This lowers the signal to noise ratio, translating into elevated LODs. The fact that the ablation rate of a fluid inclusion is largely controlled by the ablation rate of the host mineral for controlled inclusion ablation also explains why inclusions larger than about 50 µm will not result in improved LODs (except for vapor inclusions).

The fluid inclusion bulk density affects the LODs in a way similar to that of bulk salinity. The bulk density for aqueous inclusions determines the fraction of the entire fluid inclusion that is liquid at room temperature. For a vapor inclusion the liquid fraction may be for example 5%, and even if the salinity of this liquid is high, the total mass of solutes for this inclusion will be low. Consequently, LODs are elevated. In other words, a dense, spherical fluid inclusion of 20 µm diameter containing 50 wt.% NaCl equivalent has about 2 ng material that can be analyzed. The best LODs obtained for such inclusions in a multi-element menu is *ca.* 0.01 µg $g^{-1}$, translating into 0.05 fg required for the significant analysis of such well detectable elements. In my experience, best LODs can be achieved for *ca.* 30 µm spherical fluid inclusions about 30 µm beneath the sample surface using straight ablation.

Next, the dwell time affects the LOD significantly. Increasing the dwell time reduces the variability of the background measurement around its mean; hence, LODs are lowered according to equation 2 above. For fluid inclusion analysis, however, an increase in dwell times deteriorates the temporal resolution of the fast transient signal to the point where representative recording in sequential mode may no longer be possible (addressed above). It is here, where the jump routine provides an additional benefit. Not only does the jump routine ensure representative sampling of the jumped analyte, it also increases significantly its dwell time per sweep. For our example, Au has a summed dwell time of 90 ms per sweep. With this long dwell time, the standard deviation of the background count rate for Au improved by about a factor of 4, and this significantly reduces the resulting LOD. Thanks to this additional benefit of the jump routine, the significant quantification of Au in the example reported in Table 12-3 has become possible.

Sometimes, a short, tiny but significant signal identified graphically (*e.g.,* Fig. 12-3b) may not survive LOD filtering, because treating this short, tiny signal using average count rates as determined across the entire signal interval (defined based on *e.g.,* Na) will “dilute” this short, tiny signal to the

point that it may no longer survive the >99% confidence filtering. For such signals, a semi-quantitative concentration can be derived by relaxing the statistical limit for the LOD from 3 $SD_{bkg}$ to 2 or 1 $SD_{bkg}$ (referred to as the limit of quantification by Günther *et al.* 1998).

Finally, LODs are useful numbers only when reported for known LA–ICP–MS parameters, fluid inclusion size, bulk density and bulk salinity, and LOD filtering criteria employed.

## PRECISE AND ACCURATE ISOTOPE RATIO MEASUREMENTS USING LA–MC–ICP–MS: ACHIEVEMENTS AND PROSPECTS

Constraints on the source of fluids help identify provenance of components, thus constraining processes of chemical and heat transfer in the Earth. A prime tool for this is radiogenic isotopes, notably because different sources often possess quite variable signatures and, for heavier isotopes, mass-dependent fractionation during geological processes does not modify the isotopic signatures (unlike for classical light stable isotopes, *e.g.,* H, C, O, Li, B). Therefore, accurate data at moderate precision may often resolve potential source components. Pettke *et al.* (2003) reported a reconnaissance study measuring Pb isotope ratios in individual fluid inclusions using laser ablation–multiple collector–ICP–MS (LA–MC–ICP–MS). The precision achieved in this study exceeded that obtainable with single-collector instruments, motivating a more in depth evaluation of this technique. Today, accurate Pb isotope data including quantification of mass 204 can be obtained with 2 SD uncertainties on inclusion to inclusion reproducibility from assemblages of 0.05 ($^{208}Pb/^{206}Pb$ and $^{207}Pb/^{206}Pb$ ratios) and 0.4% (Pb isotope ratios normalized to mass 204), respectively (Fig. 12-6; Pettke *et al.* 2008). Natural fluid inclusions that contain more Pb and are larger than those analyzed in figure 12-6 can be measured even more precisely for Pb isotope ratios normalized to mass 204, achieving 0.15% 2 SD uncertainties. This section briefly summarizes the key aspects of this method development.

All data have been acquired with a GeoLas 193 nm ArF excimer laser system combined with either the Nu Plasma or the Nu Plasma 1700 MC–ICP–MS instruments (for machine parameters see Pettke *et al.*, in prep.). Self-made synthetic fluid inclusions of known Pb isotopic compositions (SRM 981 from NIST) have been used to establish the LA–MC–ICP–MS analytical protocol for fast

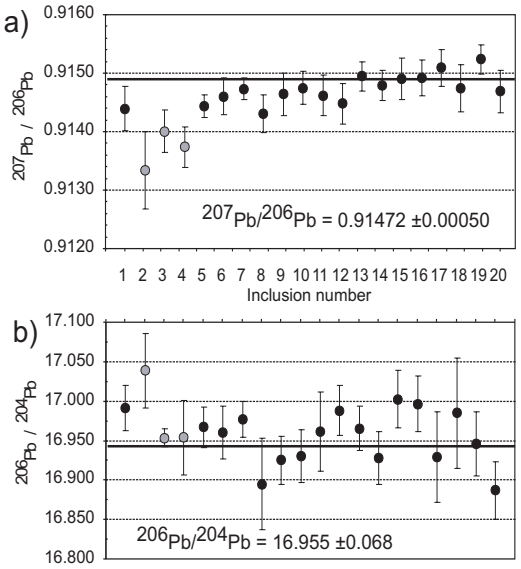


FIG. 12-6. External reproducibility of Pb isotope ratio determinations of individual synthetic fluid inclusions, with an external uncertainty quoted at the 2 SD level, **a)** for $^{207}Pb/^{206}Pb$ ratios and **b)** for $^{206}Pb/^{204}Pb$ ratios. The thick solid line represents the SRM 981 Pb isotope reference value (Baker *et al.* 2004). The three grey data points are deemed outliers (due to poorly controlled ablation; inclusion number 3 even exploded) and are thus not used for statistics. Note that the uncertainty for the example shown in Fig. 12-6b is higher than that quoted in text because the synthetic fluid inclusions have lower Pb concentrations than some of the natural inclusions we have analyzed so far.

transient signals as produced from the ablation of individual fluid inclusions. These inclusions contained *ca.* 5000 µg $g^{-1}$ Pb which compares well with Pb concentrations typically measured in magmatic–hydrothermal brine inclusions (*e.g.,* Audétat *et al.* 2000, Landtwing *et al.* 2005, Klemm *et al.* 2007). For an egg-shaped fluid inclusion with longest dimension of 30 µm, the amount of Pb available for analysis is of the order of 0.3 ng. This is considerably less than the amounts consumed for precise MC–ICP–MS isotope analysis of Pb in solution mode (isotopic ratios of ±100 ppm precision can be obtained on amounts of Pb as low as *ca.* 5–10 ng; Baker *et al.* 2004).

Controlled ablation of individual fluid inclusions ensured, masses 200, 202, 203, 204, 205, 206, 207 and 208 were recorded simultaneously on Faraday detectors and read out in 0.2 s intervals (sweeps), employing the instrument's transient software capabilities (Fig. 12-7). Since Pb does not possess a stable isotope pair, Tl was admixed via desolvated nebulisation to the LA aerosol up-torch

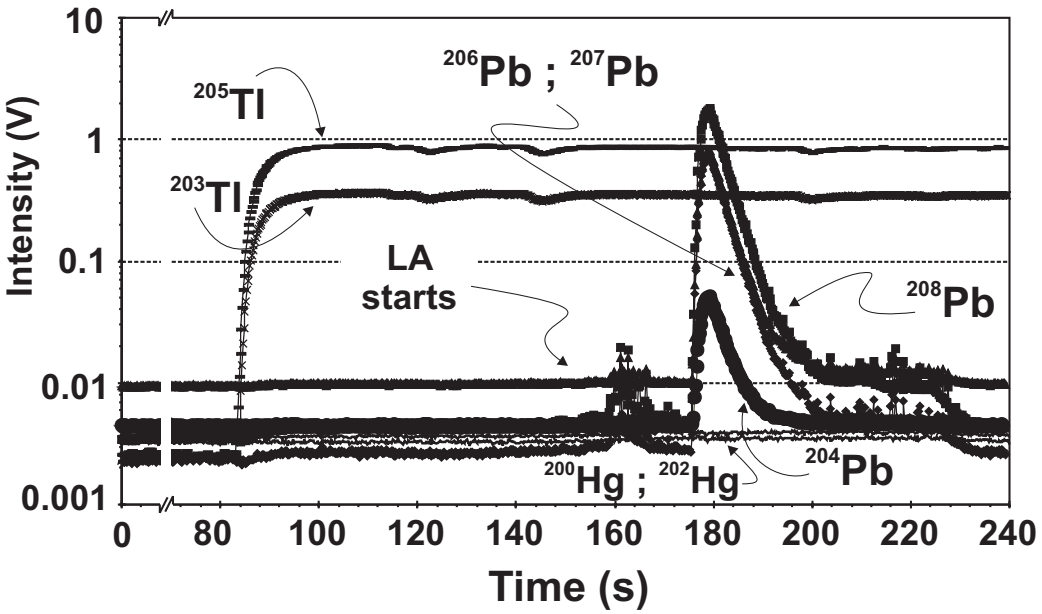


FIG. 12-7. Transient Pb isotope signal of a synthetic fluid inclusion. The Tl signal rising before laser ablation (LA) starts is from a desolvated Tl solution and is used for within-run mass bias correction. Once the Tl signal is stable, the laser ablation starts, and ablation of the fluid inclusion superimposes a Pb signal onto the Tl signal. Note that for quartz-hosted fluid inclusions, a host mineral correction is not required for Pb isotopic ratio analysis since quartz contains virtually no Pb.

for use in within-run correction of mass bias (*e.g.*, Longerich *et al.* 1987). Raw data have been corrected for background contributions first (gas background measured on peak prior to laser ablation). Background-corrected intensities were corrected for interferences, of which $^{204}$Hg on $^{204}$Pb was the only significant one. The measured $^{205}$Tl/$^{203}$Tl isotope ratio was used to predict the mass-biased $^{202}$Hg/$^{204}$Hg ratio of interfering mercury, and the $^{204}$Hg on $^{204}$Pb interference was corrected successfully this way. Other interferences have been shown to be insignificant at the analytical accuracy obtained, even on SRM 610 glass. These Hg interference-corrected Pb isotope ratios were then corrected for mass bias based on the within-run measured $^{205}$Tl/$^{203}$Tl using procedures of Woodhead (2002) and Baxter *et al.* (2006). For more details and justification of this procedure, the reader is referred to Pettke *et al.* (in prep.). The 2 SD uncertainty on the external reproducibility of SRM 610 ablations during a one day analytical session converged to ± 130 ppm for $^{208}$Pb/$^{206}$Pb and $^{207}$Pb/$^{206}$Pb ratios and to ± 420 ppm for Pb isotope ratios normalized to mass 204, or ± 22 and ± 73 ppm, respectively, at the 2 SE uncertainty level (n=36), irrespective of whether line scan or single spot ablations (90 µm crater size) were acquired.

Detailed inspection of the transient fluid inclusion signals revealed evolving isotope ratios that are ascribed to fractionation occuring during the process of fluid inclusion ablation (Pettke *et al.* (in prep.). This fractionation does not affect analytical accuracy, however, given controlled ablation of the entire fluid inclusion and integration of the entire transient signal.

Magmatic–hydrothermal fluid inclusions typically contain a few to several thousand µg g$^{-1}$ Pb (Table 12-3), translating into about 0.2–1 ng of Pb available for the analysis of individual ellipsoidal inclusions 40x40x30 µm in size. Acceptably reproducible results (±1 ‰ and 5 ‰, respectively) were obtained for inclusions containing as little as 0.1 ng Pb with the current setup using Faraday detectors, demonstrating the potential of our analytical protocol for low amount fast transient signals.

## FIGURES OF MERIT

The type of geochemical problem defines the type and precision of the data set required to resolve the issues. More importantly, it is the statistics employed that influence the analytical uncertainty cited on a given measurement, and it is crucial to define which contributions are relevant when determining an overall analytical uncertainty. Finally, the data-recording scheme (*e.g.*, multiple collector *vs.* single collector data recording) also significantly influences which statistical parameters are most relevant.

**Analytical precision**

For LA–ICP–MS analysis in general, two fundamentally different results are obtained:

a) The analytical uncertainty associated with data obtained for an individual analysis is referred to as internal or within-run or shot precision.
b) The uncertainty obtained on the average of a series of individual analyses of a homogeneous material (*e.g.,* a series of fluid inclusions from a homogeneously entrapped assemblage), is referred to as external or run-to-run or shot-to-shot precision or, specifically, inclusion-to-inclusion precision.

LA–ICP–MS analysis of fluid inclusions inevitably produces highly transient signals (Figs. 12-3 and 12-7), a signal structure that is explicitly avoided in all other *in situ* analytical techniques. For the analysis of a series of fluid inclusions belonging to a fluid inclusion assemblage, the following considerations are thus relevant:

***(a) Internal precision:*** The assessment of the analytical uncertainty for element concentration data of individual fluid inclusions acquired by sequential data recording (*i.e.,* single collector instruments) is extremely difficult because several contributions – interrelated or independent – contribute to the overall uncertainty. Among all these, important contributions are:

- Counting statistics uncertainties, which are especially important for low intensity signals.
- Variability in signal intensities within the transient signal interval (Fig. 12-3).

While the former uncertainty can be calculated from data acquired, the latter is impossible to quantify for fast transient signals as produced from fluid inclusion ablation. Moreover, analytical uncertainties stemming from systematic contributions (*e.g.,* short term variability resulting from plasma flicker) are not considered here. Consequently, if there is an uncertainty on individual fluid inclusion analysis to be reported, then it is a minimum uncertainty provided by counting statistics that dominates the overall internal precision unless instrumental background intensities are large.

For the determination of isotope ratios by simultaneous measurements as provided by multiple collector instruments, common use is to calculate the final isotope ratios for each sweep (*i.e.,* time slice or data readout) and then calculate the variability around the mean (*i.e.,* the standard error of the mean) isotope ratio for the entire analyte signal. While this procedure is robust for signals of constant intensity (because each sweep is measured with equal precision), it may not be the method of choice for fast transient signals from fluid inclusions (Fig. 12-7). Examining figure 12-7 it appears intuitive that an average weighted on the basis of signal intensities per sweep would probably be a better representation of the average isotope ratios measured for an inclusion signal. Therefore, the Pb isotope data set of 20 fluid inclusions has been reduced in two modes (Pettke *et al.*, in prep.):

i) The Pb isotope ratios have been calculated based on corrected signal intensities for each sweep individually, and the final result corresponds to the mean of the sweeps in the signal.
ii) The isotope ratio has been calculated based on the corrected isotope intensities summed across the entire signal interval.

While each reading (sweep) is weighed equally in approach (i), irrespective of signal intensity, the high intensity readings are more significant in defining the average Pb isotope ratio of an individual fluid inclusion in approach (ii). Indeed, the external reproducibility obtained for data reduced in mode (ii) is better (Pettke *et al.*, in prep.), thus illustrating the effect of overrating the low intensity measurements near the signal tails in mode (i). This result illustrates that intensity-weighted mean data more accurately determine the isotope ratios of fast transient signals measured by MC–ICP–MS.

***(b) External precision*** is a much more robust assessment of the overall analytical reproducibility, for both single and multiple collector data recordings. The external precision is best determined for fluid inclusions belonging to compositionally homogeneous assemblages (Figs. 12-1 and 12-5). Such an external reproducibility can be obtained by calculating either simple averages and associated uncertainties (*i.e.,* individual inclusion analyses are weighted equally), or uncertainty-weighted averages (where precise determinations exert a larger influence on the average concentrations than do imprecise determinations; see Pettke *et al.* 2004 for an example). Uncertainty-weighted average data sets are preferred notably for element concentrations close to their LODs, because such concentrations have grossly variable analytical precisions primarily resulting from counting statistics. The current example of 20 fluid inclusions analyzed for element

concentrations individually (Table 12-3) demonstrates that for elements residing dominantly in the aqueous solution during analysis, external uncertainties on average element concentration data of ±5% (1 standard deviation) can be achieved (in this case, all elements except Au are far above their respective LODs, rendering an uncertainty-weighted averaging based on counting statistics uncertainties unnecessary). Such precise data demonstrate that these inclusions indeed represent individual samples of a compositionally uniform fluid, and that their individual LA–ICP–MS analysis was controlled and complete. Table 12-3 also reports one fluid inclusion analysis (14frc05, set in italics; see also Fig. 12-5) that has not been used for average data calculation. This inclusion reveals a deficit in Na and excesses in all other major cation concentrations, which is indicative of loss of at least some of the NaCl daughter crystal during analysis (given microthermometric uniformity of analyzed inclusions). If this occurs, signal intensity ratios of element/Na are elevated, however, the signal of Na is equaled to the internal standard element concentration during data reduction, and this returns excesses for those elements completely sampled during analysis. This example demonstrates that average fluid element concentrations determined for fluid inclusion assemblages (homogeneous entrapment) provide the most accurate data, notably also because outliers can be identified and excluded from further consideration (as already stressed by Pettke *et al.* 2004).

The external uncertainty of data obtained for a fluid inclusion assemblage (homogeneous entrapment) could also be expressed as the standard error of the mean of N analyses, *i.e.,* the variability of data around the mean value. This method of uncertainty quantification returns lower values when compared to the standard deviation because the standard deviation is divided by the square root of N analyses to obtain the standard error of the mean. For our example of 20 inclusions in Table 12-3, it can be seen that the standard error of the mean is a factor of 4–5 lower than the corresponding standard deviation. It is thus essential that the type of uncertainty cited is defined.

**Analytical accuracy**

Analytical accuracy is best demonstrated through the analysis of synthetic fluid inclusions of known composition or by analyzing a fluid inclusion assemblage using various, independent analytical techniques. Extensive tests demonstrate that accurate fluid inclusion compositional (Heinrich *et al.* 2003, Allan *et al.* 2005) and Pb isotopic (Pettke *et al.* 2008) data can be obtained at useful precision.

First of all, representative and complete sampling and signal recording of the content of individual fluid inclusions is a prerequisite for potentially obtaining accurate data – this is why I put so much emphasis on these issues above. The best indication for the absence of such analytical problems for fluid inclusions of unknown composition is the quality of the external reproducibility obtained for assemblages. The data reported in Table 12-3, by themselves, document this.

Accuracy to date is limited most significantly by the accuracy with which the concentration of the internal standard element can be derived, *e.g.,* from microthermometric data, as documented in Heinrich *et al.* (2003). These authors concluded that the farther the bulk fluid composition deviates from the binary $H_2O$–NaCl system, the larger is the probable error associated with the determination of the Na concentration to be used as the internal standard element.

It is also obvious that the quality with which the IS signal is recorded directly translates on all element concentrations calculated based on this IS. This is nicely demonstrated for the inclusion analysis 14frc05 (Table 12-3) discussed above, where a part of the NaCl daughter crystal has been lost during analysis. This also implies that the use of Cl for internal standardization is limited to relatively high fluid salinities, since the low sensitivity of $Cl^+$ plus the elevated background on mass 35 will return high enough signal to noise ratios for calibration only for high fluid Cl concentrations. Moreover, our own tests (unpublished data) have revealed serious interference problems on mass 35 notably at low signal intensities, the exact nature of which is currently under investigation.

For fluids that contain significant amounts of non-chlorine complexed species (*e.g.,* sulfuric or fluoro- or hydrated silicate species) the use of an internal standard other than microthermometrically determined Na concentration may be preferable. It is here where much progress in the accuracy of signal quantification for fluid inclusions can be expected in the near future.

Recall that the analytical accuracy on element concentration ratios is uniquely defined by the use

of external standardization alone (plus all instrument-related uncertainty contributions). As a consequence, analytical accuracy on element concentration ratios will be limited at least for some elements by the accuracy with which these element concentrations are known for the external standard material employed for analysis (*e.g.,* SRM 612 and SRM 610 glasses in our case). In fact, some of the relevant fluid elements are only poorly constrained in the SRM 61X glasses, and some of the most commonly used values are demonstrably wrong (for a detailed assessment see Spandler *et al.* 2008, and in prep.; Jochum 2008).

Note that when averaging individual fluid inclusion data from assemblages, there may be a bias towards elevated element concentrations for elements near their LOD, because analyses below the LOD are obviously omitted for averaging. In such cases, the average element concentration data should be regarded as maximum element concentrations.

In summary, the most severe limitation for LA–ICP–MS inclusion analysis is the knowledge of the absolutely necessary internal standard constraint. This is most commonly an element concentration, but for some applications it can also be an element concentration ratio (*e.g.,* Halter *et al.* 2002, Pettke 2006). For aqueous fluid inclusions, a more accurate multi-component description of the liquidus surface of ice and the final dissolution of hydrohalite or halite would be highly desirable, but equations of state for fluids with >3 components have so far not been derived. The data presented here demonstrate that a LA–ICP–MS analytical setup dedicated for the analysis of inclusions in minerals can provide data at an external precision that may well exceed the accuracy currently achievable for element concentration data.

## ACKNOWLEDGEMENTS

I would like to thank Carl Spandler and Janos Kodolanyi for sharing their time and experience on our new LA–ICP–MS facility and the many interesting and stimulating ideas and discussions on LA–ICP–MS issues. In the group of Chris Heinrich at ETHZ I had great opportunities and ample exposure to excellent LA–ICP–MS fluid inclusion projects for which I am very grateful to you, Chris. Leonhard Klemm kindly provided the sample GI-13-17 that he originally received from Steve Kesler. I also thank Detlef Günther for many great contributions he made to the topic I cover here. I am indebted to Bob Bodnar and Paul Mason for very helpful reviews, allowing me to refine some of my statements, and to Paul Sylvester for his efforts in editorial handling. Continued funding by the Swiss National Science Foundation (current project PP002–106569) and funding of a LA–ICP–MS technical upgrade by the Berne University Research Foundation are greatly acknowledged.

## REFERENCES

ALLAN, M.M., YARDLEY, B.W.D., FORBES, L.J., SHMULOVICH, K.I., BANKS, D.A. & SHEPHERD, T.J. (2005): Validation of LA–ICP–MS fluid inclusion analysis with synthetic fluid inclusions. *Am. Mineral.* **90**, 1767-1775.

AUDÉTAT, A. & GÜNTHER, D. (1999): Mobility and $H_2O$ loss from fluid inclusions in natural quartz crystals. *Contrib. Min. Petrol.* **137**, 1-14.

AUDÉTAT, A. & PETTKE, T. (2003): The magmatic–hydrothermal evolution of two barren granites: A melt and fluid inclusion study of the Rito del Medio and Canada Pinabete plutons in northern New Mexico (USA). *Geochim. Cosmochim. Acta* **67**, 97-121.

AUDÉTAT, A., GÜNTHER, D. & HEINRICH, C.A. (1998): Formation of a magmatic–hydrothermal ore deposit: Insights with LA–ICP–MS analysis of fluid inclusions. *Science* **279**, 2091-2094.

AUDÉTAT, A., GÜNTHER, D. & HEINRICH, C.A. (2000): Magmatic–hydrothermal evolution in a fractionating granite: A microchemical study of the Sn–W–F-mineralized Mole Granite (Australia). *Geochim. Cosmochim. Acta* **64**, 3373-3393.

BAKER, J., PEATE, D., WAIGHT, T. & MEYZEN, C. (2004): Pb isotopic analysis of standards and samples using a $^{207}Pb$–$^{204}Pb$ double spike and thallium to correct for mass bias with a double-focusing MC–ICP–MS. *Chem. Geol.* **211**, 275-303.

BANKS, D.A., DAVIES, G.R., YARDLEY, B.W.D., MCCAIG, A.M. & GRANT, N.T. (1991): The chemistry of brines from an Alpine thrust system in the Central Pyrenees: An application of fluid inclusion analysis to the study of fluid behaviour in orogenesis. *Geochim. Cosmochim. Acta* **55**, 1021-1030.

BANKS, D.A., RICE, C., STEELE, G., BOYCE, A. & FALLICK, T. (2007): The formation of the world's largest silver deposit, Cerro Rico, Bolivia. Abstract. Biennial Conference ECROFI XIX, Bern, Switzerland, 17-20 July, p. 72.

BAXTER, D.C., RODUSHKIN, I., ENGSTROM, E. & MALINOVSKY, D. (2006): Revised exponential model for mass bias correction using an internal standard for isotope abundance ratio measurements by multi-collector inductively coupled plasma mass spectrometry. *J. Analyt. Atom. Spectrom.* **21**(4), 427-430.

BENNETT, J.N. & GRANT, J.N. (1980): Analysis of fluid inclusions using a pulsed laser micro-probe. *Mineral. Mag.* **43**, 945-947.

BODNAR, R.J. (2003): Reequilibration of fluid inclusions. *In* Fluid inclusions: Analysis and data interpretation (I. Samson, A. Anderson & D. Marshall, eds.). *Mineral. Assoc. Can. Short Course Series Volume* **32**, 213-231.

BODNAR, R.J. & STUDENT, J.J. (2006): Melt inclusions in plutonic rocks: petrography and microthermometry. *In* Melt Inclusions in Plutonic Rocks (J. D. Webster, ed.). *Mineral. Assoc. Can. Short Course Series Volume* **36**, 1-25.

BOIRON M.C., DUBESSY J., ANDRE N., BRIAND A., LACOUR J.L., MAUCHIEN P. & MERMET J.M. (1991): Analysis of mono-atomic ions in individual fluid inclusions by laser-produced plasma emission-spectroscopy. *Geochim. Cosmochim. Acta* **55**, 917-923.

BOTTRELL, S.H., YARDLEY, B.W.D. & BUCKLEY, F. (1988): A modified crush-leach method for the analysis of fluid inclusion electrolytes. *Bull. Minéral.* **111**, 279-290.

CZAMANSKE, G.K., ROEDDER, E. & BURNS, F.C. (1963): Neutron activation analysis of fluid inclusions for copper, manganese, and zinc. *Science* **140**, 401-403.

DELOULE, E. & ELOY, J.F. (1982): Improvements of laser probe mass-spectrometry for the chemical analysis of fluid inclusions in ores. *Chem. Geol.* **37**, 191-202.

DIAMOND, L.W. (1990): Fluid inclusion evidence for P–V–T–X evolution of hydrothermal solutions in late-Alpine gold–quartz veins at Brusson, northwest Italian Alps. *Am. J. Sci.* **290**, 912-958.

DIAMOND, L.W., JACKMAN, J.A. & CHAROY, B. (1991): Cation ratios of fluid inclusions in a gold–quartz vein at Brusson, Val d'Ayas, northwestern Italian Alps: Comparison of bulk crush-leach results with SIMS analyses of individual inclusions. *Chem. Geol.* **90**, 71-78.

DUC-TIN, Q., AUDÉTAT, A. & KEPPLER, H. (2007): Solubility of tin in (Cl, F)-bearing aqueous fluids at 700 degrees C, 140 MPa: A LA–ICP–MS study on synthetic fluid inclusions. *Geochim. Cosmochim. Acta* **71**, 3323-3335.

EGGINS, S.M., KINSLEY, L.P.J. & SHELLEY, J.M.G. (1998): Deposition and element fractionation processes during atmospheric pressure laser sampling for analysis by ICP–MS. *Applied Surface Science* **129**, 278-286.

EGGINS, S.M., DE DECKKER, P. & MARSHALL, J. (2003): Mg/Ca variation in planktonic foraminifera tests: implications for reconstructing palaeo-seawater temperature and habitat migration. *Earth Planet. Sci. Lett.* **212**, 291-306.

FRYER, B.J., JACKSON, S.E. & LONGERICH, H.P. (1995): Design, operation and role of the laser-ablation microprobe coupled with an inductively-coupled plasma–mass-spectrometer (LAM–ICP–MS) in the Earth sciences. *Can. Mineral.* **33**, 303-312.

GOLDSTEIN R.H. & REYNOLDS T.J. (1994): Systematics of fluid inclusions in diagenetic minerals. *Society for Sedimentary Geology Short Course* **31**, 199p.

GUILLONG, M. & GÜNTHER, D. (2002): Effect of particle size distribution on ICP-induced elemental fractionation in laser ablation-inductively coupled plasma–mass spectrometry. *J. Analyt. Atom. Spectrom.* **17**, 831-837.

GUILLONG, M. & HEINRICH, C.A. (2007a): Sensitivity enhancement in laser ablation ICP–MS using small amounts of hydrogen in the carrier gas. *J. Anal. At. Spectrom.* **22**, 1488-1494.

GUILLONG, M. & HEINRICH, C.A. (2007b): LA–ICP–MS analysis of inclusions: Improved ablation and detection. Biennial Conference ECROFI XIX, Bern, Switzerland, 17-20 July, p. 82.

GÜNTHER, D. (2001): Quantitative fluid inclusion analysis using a 193 nm excimer laser-ablation system coupled to ICP–MS. *In* Laser Ablation in the Earth Sciences (P. Sylvester, ed.). *Minera.l Assoc. Canada Short Course Series Volume* **29**, 47-62.

GÜNTHER, D. & HATTENDORF, B. (2005): Solid sample analysis using laser ablation inductively coupled plasma mass spectrometry. *TRAC - Trends in Analytical Chemistry* **24**, 255-265.

GÜNTHER, D. & HEINRICH, C.A. (1999): Enhanced sensitivity in laser ablation-ICP mass spectrometry using helium-argon mixtures as aerosol carrier – plenary lecture. *J. Analyt. Atom. Spectrom.* **14**, 1363-1368.

GÜNTHER, D., FRISCHKNECHT, R., HEINRICH, C.A. & KAHLERT, H.J. (1997): Capabilities of an Argon Fluoride 193 nm excimer laser for laser ablation inductively coupled plasma mass spectrometry microanalysis of geological materials. *J. Analyt. Atom. Spectrom.* **12**, 939-944.

GÜNTHER, D., AUDÉTAT, A., FRISCHKNECHT, R. & HEINRICH, C.A. (1998): Quantitative analysis of major, minor and trace elements in fluid inclusions using laser ablation inductively coupled plasma mass spectrometry. *J. Analyt. Atom. Spectrom.* **13**, 263-270.

GÜNTHER, D., HATTENDORF, B. & AUDÉTAT, A. (2001): Multi-element analysis of melt and fluid inclusions with improved detection capabilities for Ca and Fe using laser ablation with a dynamic reaction cell ICP–MS. *J. Analyt. Atom. Spectrom.* **16**, 1085-1090.

HALTER, W.E., PETTKE, T., HEINRICH, C.A. & ROTHEN-RUTISHAUSER, B. (2002): Major to trace element analysis of melt inclusions by laser-ablation ICP–MS: methods of quantification. *Chem. Geol.* **183**, 63-86.

HALTER, W.E., PETTKE, T. & HEINRICH, C.A. (2004): Laser-ablation ICP–MS analysis of silicate and sulfide melt inclusions in an andesitic complex I: analytical approach and data evaluation. *Contrib. Min. Petrol.* **147**, 385-396.

HANLEY, J.J., MUNGALL, J.E., PETTKE, T., SPOONER, E.T.C. & BRAY, C.J. (2005a): Ore metal redistribution by hydrocarbon–brine and hydrocarbon–halide melt phases, North Range footwall of the Sudbury Igneous Complex, Ontario, Canada. *Mineralium Deposita* **40**, 237-256.

HANLEY, J.J., PETTKE, T., MUNGALL, J.E. & SPOONER, E.T.C. (2005b): The solubility of platinum and gold in NaCl brines at 1.5 kbar, 600 to 800 degrees C: A laser ablation ICP–MS pilot study of synthetic fluid inclusions. *Geochim. Cosmochim. Acta* **69**(10), 2593-2611.

HATTENDORF, B. & GÜNTHER, D. (2000): Characteristics and capabilities of an ICP–MS with a dynamic reaction cell for dry aerosols and laser ablation. *J. Analyt. Atom. Spectrom.* **15**, 1125-1131.

HEINRICH C.A., GÜNTHER D., AUDETAT A., ULRICH T., & FRISCHKNECHT R. (1999): Metal fractionation between magmatic brine and vapor, determined by microanalysis of fluid inclusions. *Geology* **27**, 755-758.

HEINRICH, C.A., PETTKE, T., HALTER, W.E., AIGNER-TORRES, M., AUDÉTAT, A., GÜNTHER, D., HATTENDORF, B., BLEINER, D., GUILLONG, M. & HORN, I. (2003): Quantitative multi-element analysis of minerals, fluid and melt inclusions by laser-ablation inductively-coupled-plasma mass-spectrometry. *Geochim. Cosmochim. Acta* **67**, 3473-3497.

HIRATA, T. & NESBITT, R.W. (1995): U–Pb isotope geochronology of zircon – evaluation of the laser probe-inductively coupled plasma-mass spectrometry technique. *Geochim. Cosmochim. Acta* **59**, 2491-2500.

HORN, E.E. & TRAXEL, K. (1987): Investigations of individual fluid inclusions with the Heidelberg proton microprobe – A nondestructive analytical method. *Chem. Geol.* **61**, 29-35.

JACKSON, S.E., LONGERICH, H.P., DUNNING, G.R. & FRYER, B.J. (1992): The application of laser-ablation microprobe – inductively coupled plasma – mass-spectrometry (LAM–ICP–MS) to in situ trace-element determinations in minerals. *Can. Mineral.* **30**, 1049-1064.

JOCHUM, K.P. & STOLL, B. (2008): Reference materials for elemental and isotopic analyses by LA–(MC)–ICP–MS: successes and outstanding needs. *In* Laser Ablation ICP–MS in the Earth Sciences: Current Practices and Outstanding Issues (P. Sylvester, *ed.*). *Mineral. Assoc. Can. Short Course Series* **40**, 147-168.

KESSEL, R., ULMER, P., PETTKE, T., SCHMIDT, M.W. & THOMPSON, A.B. (2005): The water–basalt system at 4 to 6 GPa: Phase relations and second critical endpoint in a K-free eclogite at 700 to 1400 degrees C. *Earth Planet. Sci. Lett.* **237**, 873-892.

KLEMM, L., PETTKE, T., GRAESER, S., MULLIS, J. & KOUZMANOV, K. (2004): Fluid mixing as the cause of sulphide precipitation at Albrunpass, Binn Valley, Central Alps. *Schweiz. Mineral. Petrogr. Mitt.* **84**, 189-212.

KLEMM, L. M., PETTKE, T., HEINRICH, C.A. & CAMPOS, E. (2007): Hydrothermal evolution of the El Teniente deposit, Chile: Porphyry Cu–Mo

ore deposition from low-salinity magmatic fluids. *Econ. Geol.* 102, 1021-1045.

KLEMM, L.M., PETTKE, T. & HEINRICH, C.A. (2008): Fluid and source magma evolution of the Questa porphyry Mo deposit, New Mexico, USA. *Mineralium Deposita,* in press.

LAMBRECHT, G., DIAMOND, L.W. & PETTKE, T. (2008): Modification of gas speciation in quartz-hosted fluid inclusions by stray laser radiation during LA–ICP–MS analysis. *Am. Mineral*. **93**, 1187-1190.

LANDTWING, M.R., PETTKE, T., HALTER, W.E., HEINRICH, C.A., REDMOND, P.B., EINAUDI, M.T. & KUNZE, K. (2005): Copper deposition during quartz dissolution by cooling magmatic–hydrothermal fluids: The Bingham porphyry. *Earth Planet. Sci. Lett.* **235**, 229-243.

LATKOCZY, C. & GÜNTHER, D. (2002): Enhanced sensitivity in inductively coupled plasma sector field mass spectrometry for direct solid analysis using laser ablation (LA–ICP–SFMS). *J. Analyt. Atom. Spectrom.* **17**, 1264-1270.

LONGERICH, H.P., FRYER, B.J. & STRONG D.F. (1987): Determination of lead isotope ratios by inductively coupled plasma–mass spectrometry (ICP–MS). *Spectrochim. Acta Part B-Atom. Spectrosc.* **42**, 39-48.

LONGERICH, H.P., GÜNTHER, D. & JACKSON, S.E. (1996a): Elemental fractionation in laser ablation inductively coupled plasma mass spectrometry. *Fres. J. Analyt. Chem.* **355**, 538-542.

LONGERICH, H.P., JACKSON, S.E. & GÜNTHER, D. (1996b): Laser ablation inductively coupled plasma mass spectrometric transient signal data acquisition and analyte concentration calculation. *J. Analyt. Atom. Spectrom.* **11**, 899-904.

LOUCKS, R.R. & MAVROGENES, J.A. (1999): Gold solubility in supercritical hydrothermal brines measured in synthetic fluid inclusions. *Science* **284**, 2159-2163.

LÜDERS, V., REUTEL, C., HOTH, P., BANKS, D.A., MINGRAM, B. & PETTKE, T. (2005): Fluid and gas migration in the North German Basin: fluid inclusion and stable isotope constraints. *Intl. J. Earth Sci.* **94**, 990-1009.

MANK A.J.G. & MASON P.R.D. (1999): A critical assessment of laser ablation ICP–MS as an analytical tool for depth analysis in silica-based glass samples. *J. Analyt. Atom. Spectrom.* **14**, 1143-1153.

MASON, P. (2001): Expanding the capabilities of laser-ablation ICP–MS with collision and reaction cells. *In* Laser Ablation in the Earth Sciences (P. Sylvester, ed.). *Mineral. Assoc. Can. Short Course Series Volume* **29**, 63-82.

MASON, P.R.D., NIKOGOSIAN, I.K. & VAN BERGEN, M. (2008): Major and trace element analysis of melt inclusions by laser ablation ICP–MS. *In* Laser Ablation ICP–MS in the Earth Sciences: Current Practices and Outstanding Issues (P. Sylvester, *ed*.). *Mineral. Assoc. Can. Short Course Series* **40**, 219-239.

MCKIBBEN, M.A. (2007): Effect of host mineral species on post-trapping changes in fluid inclusion composition – an equilibrium modeling approach. GSA Annual Meeting, 28-31 October 2007, Denver, USA.

MOENS, L., VANHAECKE, F., RIONDATO, J. & DAMS, R. (1995): Some figures of merit of a new double focusing inductively-coupled plasma–mass spectrometer. *J. Anal. At. Spectrom.* **10**, 569-574.

NAMBU M. & SATO T. (1981) The analysis of fluid inclusions in The microgram range with an ion microanalyzer. *Bull. Minéral.* **104**, 827-833.

PETTKE, T. (2006): *In situ* laser-ablation ICPMS analysis of melt inclusions and prospects for constraining subduction zone magmatism. *In* Melt Inclusions in Plutonic Rocks (J. D. Webster, ed.). *Mineral. Assoc. Can. Short Course Series Volume* **36**, 51-80.

PETTKE, T. & DIAMOND, L.W. (1995): Rb–Sr isotopic analysis of fluid inclusions in quartz: Evaluation of bulk extraction procedures and geochronometer systematics using synthetic fluid inclusions. *Geochim. Cosmochim. Acta* **59**, 4009-4027.

PETTKE, T. & KLEMM, L.M. (in prep.): A novel analyte jumping routine for the representative recording of fast transient signals in LA–ICP–MS. *J. Analyt. Atom. Spectrom.*, to be submitted.

PETTKE, T., DIAMOND, L.W. & KRAMERS, J.D. (2000a): Mesothermal gold lodes in the north-western Alps: A review of genetic constraints from radiogenic isotopes. *Eur. J. Mineral.* **12**, 213-230.

PETTKE, T., HEINRICH, C.A., CIOCAN, A.C. & GÜNTHER, D. (2000b): Quadrupole mass spectrometry and optical emission spectroscopy: detection capabilities and representative sampling of short transient signals from laser-ablation. *J.*

*Analyt. Atom. Spectrom.* **15**, 1149-1155.

PETTKE, T., WIECHERT, U.H., AUDÉTAT, A., GÜNTHER, D. & HEINRICH, C.A. (2003): Can accurate Pb isotopic compositions be determined on single fluid inclusions? *Geochim. Cosmochim. Acta* **67**, A378-A378.

PETTKE, T., HALTER, W.E., WEBSTER, J.D., AIGNER-TORRES, M. & HEINRICH, C.A. (2004): Accurate quantification of melt inclusion chemistry by LA–ICPMS: a comparison with EMP and SIMS and advantages and possible limitations of these methods. *Lithos* **78**, 333-361.

PETTKE, T., OBERLI, F., AUDÉTAT, A., WIECHERT, U.H., HARRIS, C.R. & HEINRICH, C.A. (2008): Precise and accurate lead isotopic analysis of fast transient signals by laser-ablation MC–ICP–MS. Abstract. 18th Annual Goldschmidt Conference, July 13-18, Vancouver, Canada.

PETTKE, T., OBERLI, F., AUDÉTAT, A., WIECHERT, U.H., HARRIS, C.R. & HEINRICH, C.A. (in prep.): Precise and accurate lead isotopic analysis of fast transient signals by laser-ablation MC–ICP–MS. *J. Analyt. Atom. Spectrom.*, to be submitted.

RAMSEY, M.H., COLES, B.J., WILKINSON, J.J. & RANKIN, A.H. (1992): Single fluid inclusion analysis by laser ablation inductively coupled llasma atomic emission spectrometry – quantification and validation. *J. Analyt. Atom. Spectrom.* **7**, 587-593.

ROEDDER, E. (1984): Fluid Inclusions. *In* Reviews in Mineralogy (P. H. Ribbe, ed.) *Mineral. Soc. Am.,* **12**, 646p.

RUSK, B.G., REED, M.H., DILLES, J.H., KLEMM, L.M. & HEINRICH, C.A. (2004): Compositions of magmatic hydrothermal fluids determined by LA–ICP–MS of fluid inclusions from the porphyry copper–molybdenum deposit at Butte, MT. *Chem. Geol.* **210**, 173-199.

SCAMBELLURI, M., MUNTENER, O., OTTOLINI, L., PETTKE, T.T. & VANNUCCI, R. (2004): The fate of B, Cl and Li in the subducted oceanic mantle and in the antigorite breakdown fluids. *Earth Planet. Sci. Lett.* **222**, 217-234.

SHEPHERD, T.J. & CHENERY, S.R. (1995): Laser-ablation ICP–MS elemental analysis of individual fluid inclusions – an evaluation study. *Geochim. Cosmochim. Acta* **59**, 3997-4007.

SHIBUYA, E.K., SARKIS, J.E.S., ENZWEILER, J., JORGE, A.P.S. & FIGUEIREDO, A.M.G. (1998): Determination of platinum group elements and gold in geological materials using an ultraviolet laser ablation high-resolution inductively coupled plasma mass spectrometric technique. *J. Analyt. Atom. Spectrom.* **13**(9), 941-944.

SIMON, A.C., PETTKE, T., CANDELA, P.A., PICCOLI, P.M. & HEINRICH, C.A. (2004): Magnetite solubility and iron transport in magmatic–hydrothermal environments. *Geochim. Cosmochim. Acta* **68**, 4905-4914.

SIMON, A.C., FRANK, M.R., PETTKE, T., CANDELA, P.A., PICCOLI, P.M. & HEINRICH, C.A. (2005): Gold partitioning in melt–vapor–brine systems. *Geochim. Cosmochim. Acta* **69**, 3321-3335.

SPANDLER, C., MAVROGENES, J. & HERMANN, J. (2007): Experimental constraints on element mobility from subducted sediments using high-P synthetic fluid/melt inclusions. *Chem. Geol.* **239**, 228-249.

SPANDLER, C., PETTKE, T., BERGER, A. & MAGEE, C. (2008): New constraints on the high-field-strength element concentration of NIST SRM 610 and 612 glasses. Abstract. 18th Annual Goldschmidt Conference, July 13-18, Vancouver, Canada.

SPANDLER, C., PETTKE, T., BERGER, A., ULMER, P. & MAGEE, C. (in preparation): Reference element concentrations of NIST SRM 610 and 612 glasses: Consistency evaluation and new constraints on high field strength element data.

STERNER, S.M. & BODNAR, R.J. (1989): Synthetic fluid inclusions.7. Re-equilibration of fluid inclusions in quartz during laboratory-simulated metamorphic burial and uplift. *J. Metam. Geol.* **7**, 243-260.

STOFFELL, B., WILKINSON, J.J. & JEFFRIES, T.E. (2004): Metal transport and deposition in hydrothermal veins revealed by 213nm UV laser ablation microanalysis of single fluid inclusions. *Am. J. Sci.* **304**, 533-557.

SYLVESTER, P.J. (2008): Matrix effects in laser ablation–ICP–MS. *In* Laser Ablation ICP–MS in the Earth Sciences: Current Practices and Outstanding Issues (P. Sylvester, *ed*.). *Mineral. Assoc. Can. Short Course Series* **40**, 67-78.

TANNER, S.D. & BARANOV, V.I. (1999): Theory, design, and operation of a dynamic reaction cell for ICP–MS. *Atom. Spectrosc.* **20**, 45-52.

TSUI, T.F. & HOLLAND, H.D. (1979): Analysis of fluid inclusions by laser microprobe. *Econ. Geol.* **74**, 1647-1653.

ULRICH, T., GÜNTHER, D. & HEINRICH, C.A. (2002): Evolution of a porphyry Cu–Au deposit, based on LA–ICP–MS analysis of fluid inclusions: Bajo de la Alumbrera, Argentina. *Econ. Geol.* **97**, 1888-1920.

VENABLE, J. & HOLCOMBE, J.A. (2001): Peak broadening from an electrothermal vaporization sample introduction source into an inductively coupled plasma. *Spectrochim. Acta Part B-Atom. Spectrosc.* **56**, 1431-1440.

WILKINSON, J.J., RANKIN, A.H., MULSHAW, S.C., NOLAN, J. & RAMSEY, M.H. (1994): Laser ablation–ICP–AES for the determination of metals in fluid inclusions – an application to the study of magmatic ore fluids. *Geochim. Cosmochim. Acta* **58**, 1133-1146.

WOODHEAD, J. (2002): A simple method for obtaining highly accurate Pb isotope data by MC–ICP–MS. *J. Analyt. Atom. Spectrom.* **17**, 1381-1385.

# CHAPTER 13: MAJOR AND TRACE ELEMENT ANALYSIS OF MELT INCLUSIONS BY LASER ABLATION ICP–MS

Paul R.D. Mason, Igor K. Nikogosian and Manfred J. van Bergen
Department of Earth Sciences,
Utrecht University, Budapestlaan 4,
3584 CD Utrecht,
The Netherlands
mason@geo.uu.nl

## INTRODUCTION

Melt inclusions (MI) in mineral phenocrysts are a potential source of information about the elemental and isotopic composition of magmatic melts that cannot otherwise be readily sampled. The analysis of MI has drawn much attention among petrologists, volcanologists and planetary scientists over the last 20 years, since they typically indicate far more heterogeneity in magmatic phase compositions than can be identified from the analysis of minerals and bulk rock samples alone (see excellent reviews by Roedder 1984, Schiano 2003, Lowenstern 2003, Davidson *et al.* 2007). This recent explosion in MI studies has largely been stimulated by improved knowledge of processes responsible for MI entrapment and preservation, but advances in microanalytical techniques have also been a major driving force. The analysis of silicate and sulfide MI is a major application area of laser ablation ICP–MS (*e.g.,* Audétat 2000, Halter *et al.* 2002a, Heinrich *et al.* 2003, Sylvester 2005, Pettke 2006, Halter & Heinrich 2006). The introduction of high spatial resolution UV lasers and high sensitivity mass spectrometers has enabled the technique to compete with other more established methods and laser ablation ICP–MS now forms an important part of many MI investigations (*e.g.,* Taylor *et al.* 1997, Kamenetsky *et al.* 1998, Spandler *et al.* 2000, de Hoog *et al.* 2001, Audétat & Pettke 2003, Danyushevsky *et al.* 2003, Halter *et al.* 2004a, Sun *et al.* 2004, Heinrich *et al.* 2005, Lukaìcs *et al.* 2005, Bleiner *et al.* 2006, Beaudoin *et al.* 2007, Zajacz *et al.* 2007).

Most melt inclusion studies involve the analysis of silicate glasses, a sample matrix ideally suited to laser ablation sampling. Glasses are routinely used as calibration standards and in inter-laboratory comparison studies where the accuracy and precision of laser ablation ICP–MS has been clearly demonstrated (*e.g.,* Jochum & Stoll 2008). An important strength of using laser ablation ICP–MS is its relative speed and ability to measure many elements in both glassy and crystallized inclusions at different depths within the host mineral (Halter *et al.* 2002a, Pettke *et al.* 2004). However, due to their size, common lack of exposure at the mineral surface and potentially complex crystallinity, the analysis of MI in minerals is not as simple a task as might be initially apparent. Key considerations in a MI study are the dimensions, depth within the sample, composition and crystallinity of the inclusions, as well as the type of host mineral, potential for post-entrapment modification, type of magmatic system in question and the elements to be measured in relation to the nature of the scientific problem to be addressed. Melt inclusion analysis is one of the few applications of laser ablation ICP–MS where the resolution of mixing between two different components (MI and host) can be an important consideration. A number of other analytical techniques are generally required in a MI study. This can be for sample preparation reasons such as the need to rehomogenize crystalline inclusions, for the determination of an internal standard element, or to determine elements and species that cannot be readily measured by laser ablation ICP–MS. Accompanying instrumental techniques and sample preparation methods can be extensive and laser ablation is typically only a small part of the total work required in characterizing a MI population. Finally, there is no single laser ablation ICP–MS method that can be applied in all MI studies. The success of a particular analytical protocol might not be directly transferable from lab to lab due to important differences in instrumental specifications.

In this chapter we initially discuss what is represented by a MI. We then summarize a number of different analytical techniques for MI analysis and review recent developments in the use of laser ablation ICP–MS to measure MI chemistry. We show which types of inclusions can be measured

Mineralogical Association of Canada Short Course 40, Vancouver, B.C., p. 219–239.

and give an indication of expected levels of analytical accuracy and precision. The potential for isotope ratio measurements using laser ablation multiple collector ICP–MS is also briefly discussed. We outline a number of problems that can be encountered in a typical MI study and discuss anticipated future developments for MI analysis using laser ablation techniques.

**Information recorded by melt inclusions**

Melt inclusions represent small amounts of melt which become entrapped in minerals during crystal growth or recrystallization (Roedder 1979, Sobolev 1996, Schiano 2003, Lowenstern 2003, Faure & Schiano 2005). Assuming that MI remain as closed systems since the time of their formation (discussed below) they can record stages of magma generation and evolution which are inaccessible from more established macroscale mineral and bulk rock studies. Studies of MI have four main applications in petrology:

1. In basaltic systems MI can provide accurate data concerning the chemical and physical characteristics of the primary melt, including elemental and isotopic composition, temperature, oxygen fugacity and volatile content. These data can be used to reconstruct the nature of the mantle source and melting conditions.
2. In many basic and more evolved rocks, the variability of melt compositions recorded in inclusions gives important constraints on magma chamber processes such as crystal fractionation, magma mixing, recharge and assimilation as well as the behavior of volatiles ($H_2O$, $CO_2$ *etc.*) which influence eruption conditions.
3. A comparison of trapped melts with their host minerals enables the estimation of mineral-melt partition coefficients ($K_D$).
4. A combination of melt and fluid inclusion data in magmatic–hydrothermal systems gives constraints on ore deposit formation (*e.g.,* Audétat *et al.* 2000, Campos *et al.* 2002, Kamenetsky *et al.* 2004)

Melt inclusions can be described using the terms 'assemblage' and 'population' (discussed in Pettke *et al.* 2004). An assemblage is defined as a group of inclusions that were trapped coevally during mineral growth and record a distinct magmatic composition, whereas a population covers all MI in a single mineral grain and can include numerous assemblages and individual MI of exotic composition (*e.g.,* Sobolev *et al.* 2000, Danyushevsky *et al.* 2003). In any MI study it is thus necessary to measure sufficient numbers of inclusions to sample the total number of assemblages present. Thus a rapid analytical technique such as laser ablation ICP–MS is highly desirable, especially if it can be applied to multiple inclusions at different positions and depths within a host mineral (Halter *et al.* 2002a).

Melt inclusions are typically less than 300 μm in diameter, but most are in the size range of only a few tens of micrometres. Inclusions can form co-genetically with the host phase (primary inclusions) or can be secondary, where there is no relationship between the trapped melt and growth of the host phase. Secondary inclusions are typically concentrated along healed fractures that cut across growth zones or cleavage planes in the crystal. Primary inclusions are created during crystal growth. They are formed along the growth front as cavities are sealed by subsequent growth steps (*e.g.,* Roedder 1984, Renner *et al.* 2002, Faure & Schiano 2005).

Following incorporation into a mineral a MI becomes isolated from the surrounding magmatic system with which it was originally in equilibrium. Consequently it can undergo physical and chemical modification, largely influenced by the composition of the host phenocryst. New minerals can crystallize within the inclusion and immiscible fluids can separate from the melt. It is widely assumed that volatile species remain in the melt or fluid phase during ascent through the magmatic–volcanic system. Most magmatic phenocrysts are incompressible relative to the trapped melt, so that after entrapment the inclusion volume is nearly constant (for more detailed discussion, see Roedder 1984 or Schiano 2003). The relatively high degree of contraction of the glass then results in the formation of small gas cavities or 'bubbles' in the free space inside the inclusion (Fig. 13-1a-e).

If the MI is allowed to cool slowly it can crystallize, a process termed post-entrapment crystallization (PEC). New minerals or 'daughter minerals' can either nucleate and crystallize from the trapped melt or can form due to devitrification of the quenched glass inclusion (Fig. 13-1a). Distinguishing between these processes is not always easy, but devitrification can be identified by the formation of fibrous, dendritic or spherulitic aggregate textures that grow into the glass from the outer surface (Fig. 13-1b). In the case of crystallization from the trapped melt, the melt will be initially saturated in the host phase and this will

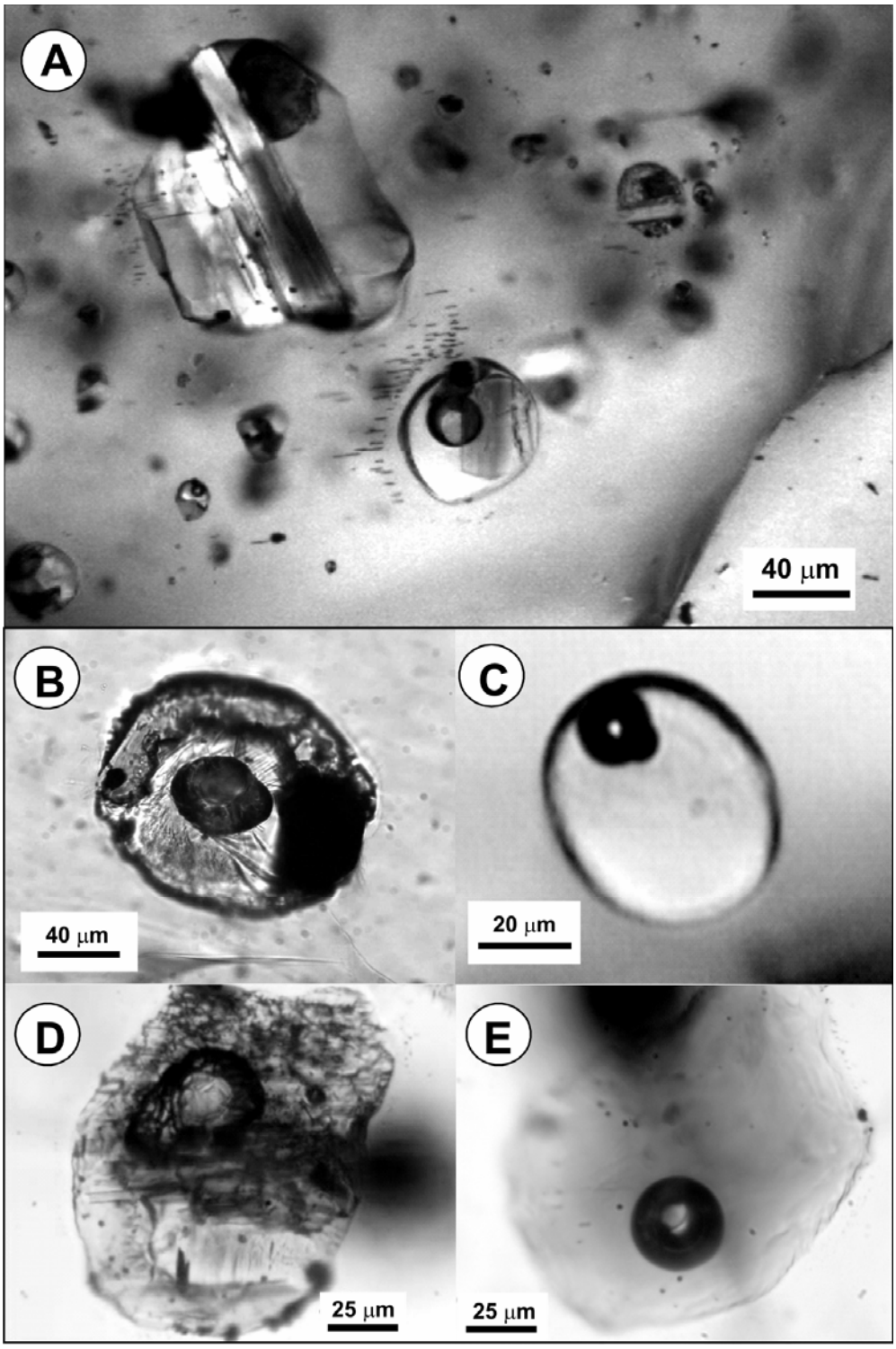


FIG. 13-1. Example of olivine-hosted melt inclusions sampled from Italy, the Canary Islands and the Azores. **A,** an assemblage of MI in olivine from Vesuvius, Italy showing the diversity of size and degree of crystallinity; **B,** a crystalline MI from the Canary Islands, **C,** a natural glassy MI from the Canary Islands, **D**, crystalline melt inclusion from the Azores before homogenization, **E**, the same MI shown in (D) after partial homogenization. Note that it was impossible to dissolved the high $P_{CO2}$ fluid back into the melt during heating experiments at atmosphere pressure.

usually crystallize on the walls of the inclusion, reducing its apparent size. New phases will then crystallize in the inclusion as the melt evolves along a path of closed system differentiation. These minerals tend to nucleate as new clusters of crystals within the inclusion (Fig. 13-1a,b). An additional complexity is that heterogeneous entrapment may occur (Roedder 1984) where previously crystallized phases are incorporated into the mineral together with the melt. These are typically distinguished from daughter minerals on the basis of volume relationships between the trapped phases and the MI. If MI do not contain daughter minerals or other trapped phases they are often termed 'glassy' (Fig. 13-1c). In summary, a MI can be either a homogeneous glass or a collection of phases and thus requires detailed petrographic investigation prior to attempting chemical analysis. A single host mineral can contain both glassy and crystallized MI reflecting multiple stages of crystallization and entrapment of melts of variable composition (Fig. 13-1a).

Following entrapment MI may also react with the host phase and diffusive re-equilibration may occur with the external melt, which may have evolved in composition. The degree of re-equilibration of the element in question increases as the rate of volume diffusion through the host mineral increases (see discussion in Danyushevsky *et al.* 2002). This is in turn related to the mineral/melt partition coefficient. The inclusion size (volume/surface area ratio) and the distance between the MI and an external crystal face of the host mineral also play a role. The type of host mineral will thus exert a strong control on which elements in the MI can be used for petrological interpretation. Fortunately, diffusive re-equilibration is insignificant for elements that are incompatible in the host mineral (Qin *et al.* 1992), although the validity of this assumption has recently been called into question (Spandler *et al.* 2007).

Melt inclusions in magmatic systems can either have a silicate or sulfide composition. Many studies have concentrated on silicate MI and basaltic systems, with olivine being the most commonly investigated host mineral. Olivine does not readily incorporate many trace elements of wider petrological interest (*e.g.,* rare earth elements (REE), high field strength elements (HFSE), large ion lithophile elements (LILE)) into its crystal structure which reduces the possibility for post-entrapment modification and reduces the influence of the host phase as a potential contaminant during analysis. It is also typically one of the first phases to crystallize, recording a very early stage of magmatic differentiation and trapping melts that are close to equilibrium with the most primitive compositions. In more felsic magmatic systems, quartz is an ideal host mineral since it also has a low $K_D$ for most elements, resulting in close to closed system behavior for the MI. However, other more compositionally diverse host minerals have also been studied including pyroxene, amphibole and plagioclase (*e.g.,* Halter *et al.* 2002b, Halter *et al.* 2004b), apatite (Audétat & Pettke 2006, Guzmics *et al.* in press) and spinel (Kamenetsky *et al.* 2002).

## REVIEW OF TECHNIQUES FOR STUDYING MELT INCLUSIONS

The accurate and precise chemical analysis of a MI is a challenging task. Since MI are so diverse in character and composition, many microanalytical instrumental techniques have been developed for this purpose. We discuss the most commonly used techniques below and evaluate their capabilities using a hypothetical sample containing a varied assemblage of MI inside a single host mineral, shown schematically in Figure 13-2a. Inclusion 1 is apparently glassy and is exposed at the surface of the host mineral by polishing. Although this inclusion would appear ideal for direct analysis it can only be used if the absence of daughter minerals was identified prior to exposure during polishing. For the purpose of this discussion, let us assume that this was indeed the case. Although large in lateral extent inclusion 1 has a limited depth before the underlying host is encountered, limiting the potential analysis volume at depth. Inclusion 2 is also exposed at the surface, where it appears glassy, but it contains daughter minerals at depth. Part of this inclusion has been lost during polishing and the shrinkage bubble is no longer observed. The remaining two inclusions are intact and can thus be properly petrographically assessed. The third inclusion is glassy with a small shrinkage bubble, while the fourth is a larger, partially crystallized, unexposed MI at depth. Note that both crystalline and glassy inclusions can occur together in the same host mineral reflecting a non-uniform post-entrapment history or variable melt composition during successive entrapments.

### Electron and ion beam techniques: EMPA and SIMS

Electron microprobe microanalysis (EMPA) was the first widely used technique for determining

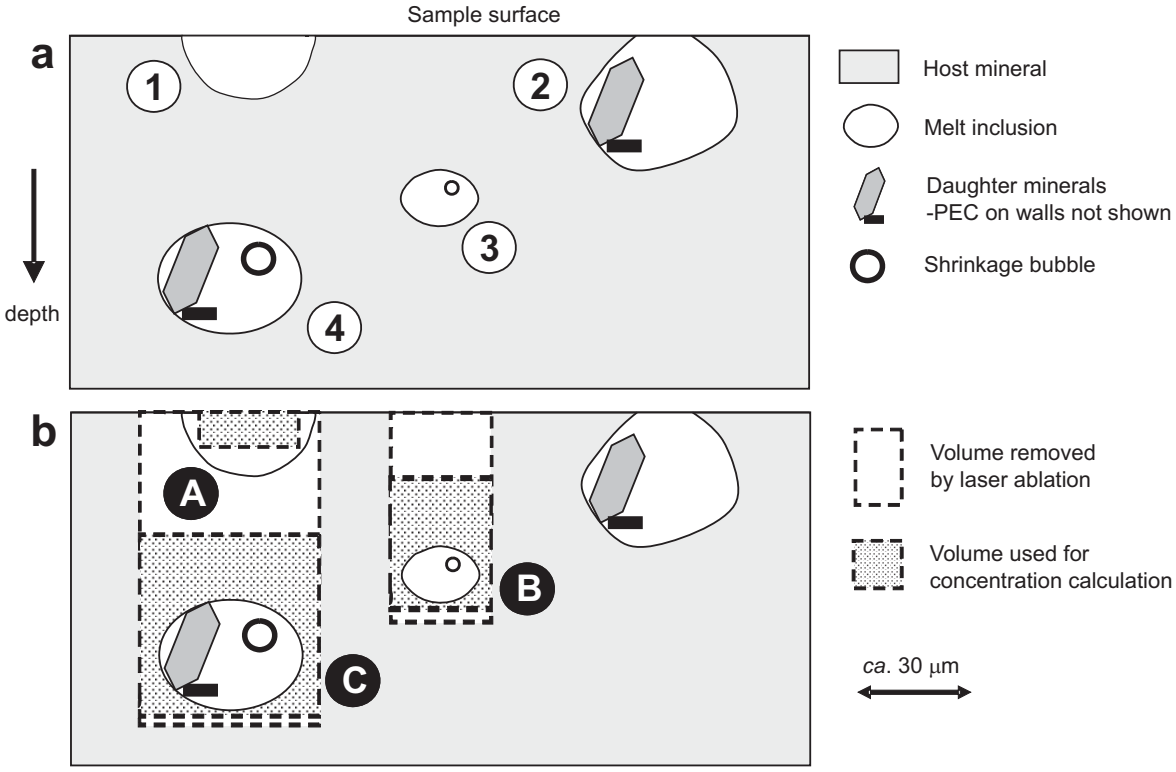


FIG. 13-2. Schematic diagram to show (**a**) the distribution and nature of a typical melt inclusion population, (**b**) the volumes of sample analyzed during laser ablation sampling.

major and minor element concentrations in MI and it remains an essential tool (*e.g.,* Métrich *et al.* 1999), due to ease of use and capability for high levels of spatial resolution of <5 μm (Table 13-1). A drawback of this technique is that damage to hydrous silica-rich glasses can arise from interaction with the electron beam, resulting in preferential loss from the analysis volume of alkali metal cations. This damage from EMPA can additionally compromise subsequent analysis by other microbeam techniques (Humphreys *et al.* 2006). For electron beam analysis MI must be exposed in a highly polished thin section or grain mount (such as inclusion 1 in Fig. 13-2a), which limits the volume of individual MI as well as the total number of MI that can be exposed in the host phenocryst at any one time. The same constraint applies to secondary ionization mass spectrometry (SIMS or ion probe), which enables the analysis of many trace elements and volatile species (*e.g.,* Sobolev & Shimizu 1993, Sobolev 1996, Hauri *et al.* 2002). SIMS gives low detection limits (Table 13-1) and has successfully been used to analyze inclusions on a scale of *ca*. 20 μm. Calibration requires a set of well characterized standard glasses, since matrix effects and interferences can be significant, but for many elements it has been shown to be a highly accurate and precise method. Stable and radiogenic isotope analysis is also possible by SIMS (*e.g.,* Gurenko & Chaussidon 1997, Layne *et al.* 2004). The limited volume of glass exposed to the electron or ion beam, means that this sampled part of the MI must be representative for the original trapped melt. This condition can be fulfilled for many quenched glassy MI, providing the effect of PEC of the host mineral on the walls of the MI can be accounted for. Inclusion 1 in Figure 13-2a could thus be accurately measured by EMPA or SIMS (providing that no daughter minerals were lost during polishing), whereas inclusion 2 would give significantly different results due to the incorporation of elements in the daughter minerals crystallized at depth. For crystallized or devitrified MI it is essential first to re-heat the inclusions experimentally to the temperature at which they were trapped in order to reverse the phase changes that occurred during cooling (discussed in detail in Danyushevsky *et al.* 2002, schematically represented in Fig. 13-3). This can be done by heating the MI and observing

TABLE 13-1. TECHNIQUES FOR CHEMICAL ANALYSIS OF MELT INCLUSIONS WITH TYPICAL PERFORMANCE SPECIFICATIONS AND SAMPLE PREPARATION REQUIREMENTS

| Technique | elements/isotopes | spatial resolution | detection limits | preparation required |
|---|---|---|---|---|
| EMPA | major and minor elements | 1-5 μm | ca. 500 μg $g^{-1}$ | exposed polished sections |
| SIMS | trace elements, isotopes | 20 μm | < 1 μg $g^{-1}$ | exposed polished sections |
| PIXE | trace elements (ideally for *m/z* >40) | 1-2 μm | ca. 1 μg $g^{-1}$ | exposed polished sections |
| PIGE | Light elements *e.g.* Li, Be, B, F up to Si | 1-2 μm | | exposed polished sections |
| FTIR | $H_2O$ and $CO_2$ | *ca*. 10 μm | 1-10 μg $g^{-1}$ | exposed or unexposed in doubly polished section |
| Confocal micro-Raman | $H_2O$ | 1–2 μm | 0.1 wt.% | unexposed MI in transparent minerals |
| μ-SXRF | trace elements | 15 μm | < 1 μg $g^{-1}$ | exposed polished sections |
| μ-XANES | Speciation, structural parameters | 20-50 μm | *ca*. 500 μg $g^{-1}$ | exposed polished sections |
| Laser ablation ICP-MS | major and trace elements, isotopes | 20-80 μm | < 1 μg $g^{-1}$ | exposed or unexposed MI in polished section |

phase changes under the microscope. Initially, on heating, any crystallized phases and the shrinkage bubble will be reduced in size (Fig. 13-3). At a certain temperature the daughter minerals will completely melt but the bubble will still be present. On further heating the overgrowth on the walls of the host phenocryst will melt. Finally at the exact temperature on which the shrinkage bubble stops reducing in size or disappears the MI can be quenched into a homogeneous glass, close in composition to the original trapped melt. This ideal rehomogenization process as shown in Figure 13-3 cannot always be achieved and although the MI may reach a glassy state, a sizeable shrinkage bubble can remain (Fig. 13-1e). This can occur for many reasons, such as decrepitation (explosive expansion) of the MI or due to a high gas partial pressure in the bubble as the result of post-entrapment exsolution of $CO_2$ (Nikogosian *et al.* 2002). It is also important to note that re-equilibration will not necessarily give the original composition of the MI as experimental parameters (especially pressure) may be different to the original magmatic setting (see more detailed discussion in Pettke 2006). The heating stage technique (Fig. 13-3, originally developed by Sobolev *et al.* 1980) is preferable since it allows direct monitoring of phase changes during the experiment, but reheating can also be performed using a quenching furnace under controlled oxygen fugacity (Schiano 2003). Over-heating or under-heating of the MI can result in extra addition or a decreasing proportion of host mineral from the inclusion walls into the rehomogenized glass. For olivine this does not affect most trace element ratios, but large errors could be introduced for other more compositionally diverse host minerals (Pettke *et al.* 2004). In Figure 13-2a, inclusions 3 and 4 could be rehomogenized and then exposed at the mineral surface by careful polishing. Inclusion 2 could not be rehomogenized, not only because it is exposed at the surface, but also since the shrinkage bubble as well as potential daughter minerals on the inclusion wall are missing.

At the present time a combination of EMPA and SIMS is the approach of choice in many laboratories for the chemical investigation of MI. This is due to the very good levels of accuracy and precision can be achieved at the highest levels of spatial resolution, with minimal destruction of the sample. Another advantage of EMPA is that a rapid

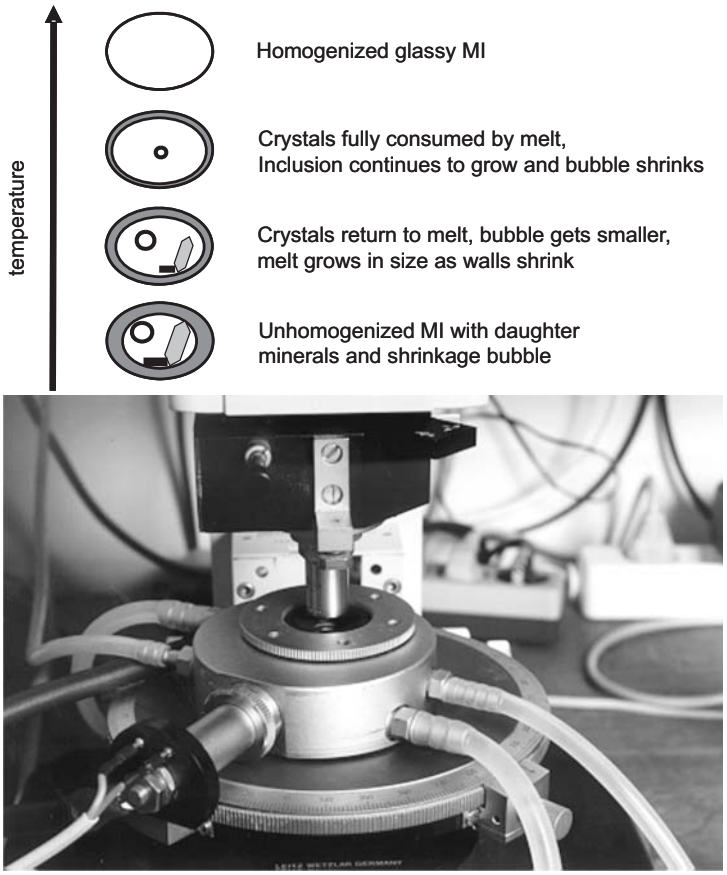


FIG. 13-3. Schematic diagram to show the steps taken to rehomogenize a crystalline melt inclusion using a heating stage (after Danyushevsky *et al.* 2002). The rim of the host mineral crystallized onto the inclusion wall becomes progressively smaller with heating until it disappears at the temperature when the shrinkage bubble is no longer observed. The lower part of the figure shows the Vernadsky institute High-T (1600°C) heating/quenching stage.

mineralogical survey can initially be conducted to assess the possible presence of multiple assemblages of phenocrysts in bulk samples (*e.g.,* as a result of magma mixing). It is important to note here that determination of the host mineral composition is essential, regardless of the techniques used, as it provides information concerning the stage of magma evolution during entrapment of the inclusion. EMPA is clearly the most appropriate technique for this purpose. A drawback of this combination of methods is the more laborious sample preparation that is required, mainly due to the rehomogenization experiments necessary for crystallized inclusions, but also due to the careful polishing required to bring inclusions to the sample surface.

**Nuclear microprobe**

Other techniques have also been developed for the trace element analysis of MI including the nuclear microprobe (Table 13-1). This instrument can be used for proton induced X-ray emission or proton induced γ-ray emission analysis (PIXE or PIGE, *e.g.,* Sie 1997, Ryan *et al.* 2001, Campos *et al.* 2002, Kamenetsky *et al.* 2004). Nuclear microprobe techniques have an advantage that they have a relatively large penetration depth of up to 40 μm. This allows the analysis of the entire inclusion volume, including phases formed during PEC (Ryan *et al.* 2001), providing that the inclusion is sufficiently small. Thus inclusion 2, as well as inclusion 1 in Figure 13-2a, could potentially be accurately measured without the need for rehomogenization experiments. However, it is important to note that the potential existence of daughter minerals in the volume of this second inclusion that was lost to polishing could lead to error in the total measurement. Detection limits for the nuclear microprobe are on the order of 0.2–1 $\mu g\ g^{-1}$, which could be a limitation for some elements and when working with more trace element depleted melts, typical of basaltic systems.

**Spectroscopic methods**

Fourier transform infra-red vibrational spectroscopy (FTIR) has been widely used to quantify the amounts and speciation of $H_2O$ and $CO_2$ in silicate MI (*e.g.,* Stolper 1982, Wysoczanski

*et al.* 2006, Table 13-1). The IR beam is usually directed through a sample slice that is polished on both surfaces to reveal the MI to be studied, but more recently a technique has been developed that enables the measurement of unexposed inclusions (Nichols & Wysoczanski 2007). Confocal micro-Raman spectroscopy has also recently been developed to measure $H_2O$ in melt inclusions (Thomas 2000, Zajacz *et al.* 2005, Behrens *et al.* 2006). It is a non-destructive technique that can be used on unexposed MI, providing that the host mineral is transparent. These techniques could be used on inclusions 1, 3 and 4 shown in Figure 13-2a, but results might be affected by the precipitation of hydrous phases such as amphibole amongst the daughter minerals. Unfortunately they only provide limited chemical and no isotopic information.

Micro-Synchrotron X-ray fluorescence (μ-SXRF) and micro-X-Ray Absorption Near Edge Structure (μ -XANES) have also been applied to MI analysis. Both techniques are non-destructive and μ-SXRF which uses photons for excitation gives good detection limits (Kramar *et al.* 2007). Micro-XANES provides information on speciation (*e.g.*, Fe oxidation state) as well as local structural information such as inter-atomic distances and coordination number (Mosbah *et al.* 1999, Bonnin-Mosbah 2001, Métrich *et al.* 2006). Both techniques are relatively new in MI analysis and have not yet been widely used but offer great potential. Sample thickness must be accurately constrained for μ-SXRF and the techniques are best suited to exposed homogeneous inclusions.

**Laser ablation ICP–MS**

The use of laser ablation ICP–MS for MI analysis was first demonstrated by Taylor *et al.* (1997) following the development of UV ablation systems with a sufficiently accurate and reproducible high spatial resolution sampling capability. This study focussed on exposed glassy inclusions (similar to inclusion 1 in Fig. 13-2a) in quartz using Ti as an internal standard, previously measured by EMPA. External precision (1σ) was typically <10% RSD for a number of trace elements including REE, LILE and HFSE. Laser ablation craters were made within the boundaries of the MI and the signal was integrated to calculate concentration by avoiding inclusion of the host mineral. This is shown schematically for analysis volume A in Figure 13-2b. However, since the host mineral quartz in the study of Taylor *et al.* (1997) did not contain significant amounts of either the internal standard element or the trace elements of interest, the inadvertent ablation of the host did not significantly affect the results. Several more recent studies have used a similar approach with glassy (de Hoog *et al.* 2001, Danyushevsky *et al.* 2003, Lukaìcs *et al.* 2005) or experimentally rehomogenized MI (Kamenetsky *et al.* 1998, Spandler *et al.* 2000, Mustard *et al.* 2006), exposed at the mineral surface. In the case of the glassy MI a correction is necessary for PEC of additional host on the walls of the inclusion, but this can be relatively easily modelled (de Hoog *et al.* 2001, Lukaìcs *et al.* 2005). Sr isotope ratios have been measured in glassy and rehomogenized MI using similar methodology where only the exposed MI is ablated (Jackson & Hart 2006), and the capability for Pb isotope ratio measurement has also been demonstrated (Jochum *et al.* 2004, 2005).

A new approach for MI analysis by laser ablation ICP–MS was developed by Halter *et al.* (2002a) and has been used or expanded in a number of more recent publications (Audétat & Pettke 2003, Halter *et al.* 2004a,b, Pettke *et al.* 2004, Zajacz & Halter 2007). The technique involves ablating the entire MI including the surrounding rim of host mineral, shown for inclusions 3 and 4 (Fig. 13-2a) as analysis volumes B and C (Fig. 13-2b). The analytical signal must then be deconvoluted into a signal for the pure host and a signal for the pure MI. This can be quantified providing that changes in the relative sensitivity factor (RSF) of the ICP–MS and changes in the relative ablation rates of MI and host can be monitored. Instrumental RSF is usually corrected by measuring a reference element or 'internal standard', a method which works well if only the MI is ablated, or if the host mineral does not contain significant amounts of the internal standard, as discussed above. The internal standard cannot correct for RSF when its abundance changes due variation in the relative amounts of host and MI in the ablated volume. To avoid this problem Halter *et al.* (2002a) showed that normalization to a fixed oxide total of 100% (or less if volatiles, *e.g.*, $H_2O$, which cannot be measured, are taken into account) can correct for RSF whereas an internal standard is used for subtracting the fraction of the host mineral from the mixed inclusion plus host signal in order to obtain the pure MI composition. There are four different approaches for this second step of internal standardization, described in Halter *et al.* (2002a), using:

1) a constant internal standard for the MI (assumed),

2) estimation of an internal standard from whole rock differentiation trends,
3) estimation of an internal standard using an element ratio taken from mineral-melt distribution coefficients, measured elsewhere in the same mineral or magmatic system,
4) measuring the volume of the ablated inclusion and total amount of ablated material.

Options (1) or (2) gave the most accurate results (Halter *et al.* 2002a). A major advantage of this newer technique is that crystallized or devitrified MI can be measured without prior rehomogenization. Furthermore, the entire MI is consumed, maximizing the ablated volume and therefore providing lower detection limits. Ablation of MI in minerals which contain significant concentrations of the elements to be measured in the MI, as well as the chosen internal standard, also becomes possible.

More recently, this technique has been further refined to avoid the need for prior knowledge of an internal standard element (Zajacz & Halter 2007). Melt inclusions were measured in co-precipitated phases and quantitative results were obtained by modelling a liquid line of descent to estimate the correct bulk composition. This approach works successfully, provided that the mineral phases used were co-precipitated. Since many rocks are affected by magma mixing, co-precipitation should be confirmed by the presence of intergrowth textures that contain adequate numbers of MI.

In summary, laser ablation ICP–MS provides the possibility to measure either portions of glassy or rehomogenized MI (inclusion 1 in Fig. 13-2a and analysis volume A in Fig. 2b), or the entire MI whether or not it is glassy, devitrified or crystallized when unexposed at the sample surface (inclusions 3 and 4, corresponding to analysis volumes B and C in Fig. 13-2). We discuss the relative merits of these different approaches below.

## LASER ABLATION ICP–MS: INSTRUMENTAL CONSTRAINTS AND CONSIDERATIONS

Inclusions have a limited size and their analysis requires accurate targeting during ablation or complete resolution of MI and host contributions to a mixed analytical signal. These requirements mean that the optimization of methodology and/or the type of laser ablation ICP–MS instrumentation available can have a major impact on MI analysis. We summarize the most significant analytical considerations below.

### Laser ablation system

A clear prerequisite to accurate MI analysis is the ability to view a sample clearly and at sufficient magnification (Fig. 13-1). The most ideal laser ablation systems for MI analysis are those built around a petrographic microscope, with both transmitted and reflected light sources through the viewing optics. However, since a detailed petrographic investigation should have been carried out prior to attempting laser ablation analysis, it is usually sufficient just to be able to identify the location and outer walls of the MI. The diameter of the ablation crater should be readily adjustable over a range of sizes that match the dimensions of the MI assemblage (Fig. 13-2b). In the case of exposed inclusions, the dimensions of the LA crater should be maximized within the inclusion volume, to ensure high precision measurements, good accuracy and sufficient detection power. For unexposed MI, the crater diameter should be somewhat larger than the inclusion so that the entire MI, including all daughter minerals can be ablated. With many laser ablation systems it is important first to check that the ablation crater has the same dimensions at depth as it does close to the surface. Crater shape is controlled by the optics of the laser ablation system and related to the laser irradiance (power density). Low irradiance for example (*e.g.,* <0.1 GW $cm^{-2}$ for 193 nm) can lead to an ablation crater that has a sharply decreasing diameter with depth (*e.g.,* Eggins *et al.* 1998, Mank & Mason 1999). An additional complexity is that crater diameter also controls power density in some laser ablation systems without homogenized energy density distribution across different scales.

As a general rule, short wavelength and short pulse length lasers in the deep UV are preferential for MI analysis since they lead to more reproducible ablation rates of a wider range of materials (Longerich 2008, Horn 2008), as well as more representative particle aerosols and a smaller average aerosol particle size and more limited particle size distribution (Günther & Koch 2008). This results in more precise measurements that can be more accurately calibrated against silicate glass reference materials (*e.g.,* NIST SRM 600 series glasses, Jackson 2008). However, the importance of laser wavelength depends upon the type of host mineral. It is especially critical to use the deep UV (193 or 157 nm) for the ablation of unexposed MI in quartz, which is poorly absorbing above 200 nm. Most published MI studies, reviewed in this chapter, have employed 193 nm ArF excimer lasers

but it is also possible to ablate exposed MI or unexposed MI at 213 and 266 nm successfully (Taylor *et al.* 1997), especially for more absorbing olivine, pyroxene and amphibole hosts.

Inaccuracy caused by elemental fractionation can be minimized by ablating craters of relatively low depth/diameter aspect ratio and by utilizing a deep UV or short pulse laser ablation system that provides an aerosol dominated by relatively small particles (reviewed in Pettke 2006). During depth analysis by laser ablation ICP–MS there is the possibility for mixing of ablated material within the crater that reduces or even completely obscures depth resolution (Mason & Mank 2001). However, since MI are usually higher in concentration than the host for most elements of interest, and since common host minerals such as quartz and olivine have very low mineral–melt partition coefficients, this problem is usually avoided. It is not recommended to measure elements in the MI that are of comparable or higher concentration in the host.

The 'sample chamber' or 'ablation cell' should be rapidly purged by the carrier gas (see discussion in Bleiner & Chen 2008). Minimizing the volume of the sample introduction system helps to reduce dilution of the ablated particles, reduce mixing between host and MI signals and enhances detection limits, while reducing the total temporal extent of measurable signal. Helium is used routinely as an ablation medium, especially for 193 nm laser ablation, due to enhanced sensitivity during ICP–MS detection. Most modern ablation cell designs are not a limiting factor for MI analysis.

## ICP–MS instrumentation

The appropriate optimization (or selection) of the mass spectrometer can potentially be much more important for MI analysis than the laser ablation system. Prior to any microanalytical study the ICP–MS should first be correctly optimized to ensure robust plasma conditions and good short to medium term stability. In general the instrument should be set up to give low $ThO^+/Th^+$ of <0.5 and Th/U of as close to 1 as possible while ablating NIST SRM 612 or 610 glass (Günther & Hattendorf 2005). The most important considerations for the ICP–MS are outlined below.

***Ability to measure both accurately and precisely all elements of interest.*** If normalization of the analytical result to 100% is to be used to correct for instrument-relative sensitivity factor, all major elements in both host and MI must be determined. Many more isotopes are therefore likely to be measured than in standard trace element mineral analysis. Isotopes that have been selected for concentration calculation or isotope ratio measurement should ideally be free of spectral interferences. The most problematic elements in silicate MI are Si that suffers interference by C, O, N and H-based polyatomic ions on all three $^{28}Si$, $^{29}Si$ and $^{30}Si$ isotopes, and K with $^{38}Ar^1H^+$. Although the high abundance of Si and K in MI and host minerals typically gives acceptable signal/background ratios, these interferences should be minimized during instrument tuning. The alkali metals, Na, K and Li can also suffer from sustained high background levels in some ICP–MS instruments due to contamination and memory problems, especially if these elements are routinely introduced at high concentration. Mg can be affected at *m/z* 24 by $^{48}Ca^{2+}$ but this problem is only significant in a very Ca-rich matrix or if the ratio of $M^{2+}/M^+$ is poorly optimized. Interference attenuation or avoidance is possible using collision and reaction cells (Günther *et al.* 2001, Mason 2001) but these techniques can also create new interferences through reaction with the collision gas. For example using $H_2$ as a reaction gas efficiently attenuates $^{12}C^{16}O^+$ allowing the measurement of $^{28}Si$ interference-free, but $^{29}Si$ can then be difficult to measure due to the formation of $^{12}C^{16}O^1H^+$. The resolution of spectral interferences using sector field instrumentation is possible but is only currently applied for isotope ratio measurements due to the significant drop in sensitivity in high resolution mode and the relatively poor duty cycle of sector field mass spectrometers (discussed below). Although spectral interference may initially appear a problem for major element analysis of MI it can usually be reduced to insignificant levels through careful optimization of instrument parameters. A potentially more serious problem is the extent of the linear dynamic range of the detection system. Many modern ICP–MS instruments can provide linearity to over eight orders of magnitude by employing detectors that can operate in both analog and pulse-counting modes, with a stable cross-calibration. This must be carefully checked to ensure that major and trace elements can be detected simultaneously.

***Efficient as possible duty cycle.*** Sequential measurement, in quadrupole ICP–MS, results in partial loss of information during ablation of the

sample (discussed in Pettke *et al.* 2000, Pettke 2008). The proportion of time spent measuring the analytical signal as opposed to jumping between masses or waiting for electronics to reset should be maximized. This can be achieved by selecting appropriate dwell and settling times. Since many MI are small, laser ablation is rapidly destructive. Many elements are typically measured and this can result in a measurement time that is too short to ensure adequate counting statistics. Daughter phases can be a few micrometres in extent and could be rapidly consumed and lost from the integrated result if the duty cycle is inefficient. Simultaneous measurement, which solves this problem, is possible using alternative time of flight (TOF) or sector field mass spectrometers. Unfortunately, TOF instruments do not give as good detection limits as quadrupole mass spectrometers (*e.g.,* Balcerzak 2003) and sector field ICP–MS only has sufficient mass dispersion required for simultaneous measurement in isotope analysis. A combination of scanning using magnetic and electric field potentials has improved the duty cycle of SF–ICP–MS but it remains a slower technique than that provided by quadrupole instruments.

***High sensitivity and low background count rates.*** Improvements in signal/noise enable measurement of smaller MI more readily, and given the small size of many MI this is highly beneficial. Li, Be and B are often difficult to determine due to the steep mass response curve of many ICP–MS instruments that results in relatively poor detection limits and can lead to significant intra-run instrumental drift. Melt inclusion analysis is one of the few ICP–MS application areas where a further decrease in instrumental detection limits could yield major improvements and expansion of applications. This is particularly critical for isotope ratio studies in order to enable the measurement of low abundance isotopes and utilize stable Faraday detectors in MC–ICP–MS.

## Standards

The most widely used calibration standards are the NIST SRM 600 series glasses (Jackson 2008), which are homogeneous for most elements, well characterized or certified for a wide range of trace elements and which have been used successfully to give accurate results in the majority of published LA–ICP–MS MI studies. Secondary standards such as basaltic glasses from the USGS or the MPI-DING glasses (Jochum & Stoll 2008) are highly suited for assessing accuracy as they often have a close composition to MI samples.

## Comparison of methodologies for melt inclusion analysis

The steps required to perform a MI analysis using either exposed or unexposed inclusions are outlined schematically in Figure 13-4. The first point to note from the figure is that laser ablation ICP–MS typically forms only a small part of a much broader MI study, with over 90% of the work carried out prior to using the laser ablation technique. Detailed petrography and sample preparation is required before trace element or isotope measurements can be performed. Other analytical techniques such as EMPA can provide essential supporting data and the use of a heating stage may be important, depending upon the type of inclusions to be studied and the type of laser ablation ICP–MS methodology used. The steps necessary for exposed MI are shown to the left of Figure 13-4, resulting in laser ablation method 1 that relies on quantification of the glass at the sample surface with the use of an internal standard. Unexposed MI can be dealt with using either laser ablation method 1, following polishing, or method 2 by ablating the whole inclusion plus daughter minerals and host as necessary (Fig. 13-4). Laser ablation method 2 clearly involves the fewest analytical steps with consequence for high throughput, especially when coupled with the fact that inclusions can be measured at multiple depths within a sample without need for repeated polishing.

We tested laser ablation method 1 using two exposed silicate MI in olivine from Etna, Italy. The MI, which were initially crystalline and completely enclosed in the host, were rehomogenized and quenched to glass using a heating stage (design of Sobolev *et al.* 1980) at the Free University, Amsterdam. The sample was then polished to expose the MI at the crystal surface. Electron microprobe analysis was carried out at Utrecht University using methods described in de Hoog *et al.* (2001) and ion probe (SIMS) analysis was performed at the Institute of Microelectronics, Yaroslavl′, Russia using standard techniques (Sobolev 1996). Laser ablation ICP–MS sampling (conditions given in Table 13-2), was carried out after all other techniques were completed. The ablation craters were 40 μm in diameter and approximately 25–30 seconds of analysis was collected for each MI before the underlying olivine

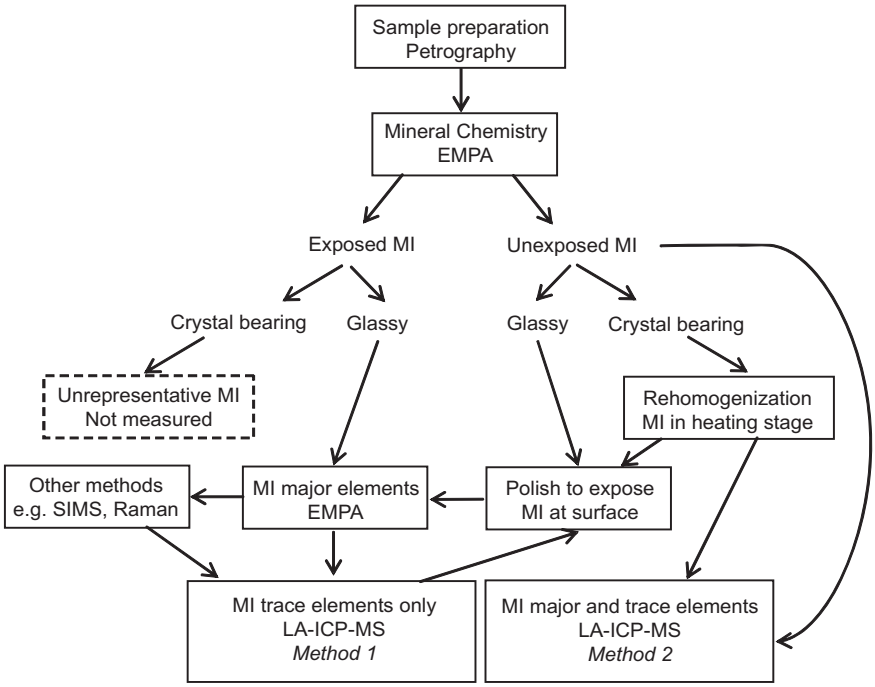


FIG. 13-4. Flow diagram to show the steps performed in a typical melt inclusion study.

TABLE 13-2. INSTRUMENT OPERATING PARAMETERS

| **ICP-MS Instrument** | **Platform ICP** (Micromass) |
|---|---|
| Cool gas flow | 13.0 l $min^{-1}$ |
| Intermediate gas flow | 1.10 l $min^{-1}$ |
| Carrier gas flow | 0.40 l $min^{-1}$ Ar and 0.45 l $min^{-1}$ He mixed after the ablation cell |
| RF power | 1100 W |
| Sampling cone | Al sampler with 1.0 mm orifice |
| Skimmer cone | Ni skimmer with 0.7 mm orifice |
| Extraction lens potential | -100 V |
| Hexapole gases | 4.0 l $min^{-1}$ He and 1.0 l $min^{-1}$ $H_2$ |
| Hexapole bias | -3.0 V |
| Dwell time | 10 ms |

| **Excimer laser** | **GeoLas 200Q (Lambda Physik)** |
|---|---|
| Output energy | 200 mJ at 193 nm |
| Pulse duration | 15 ns |
| Energy density at substrate | 10 $Jcm^{-2}$ |
| Pulse repetition rate | 5 Hz |

was ablated at a depth of approximately 25–30 μm. The MI part of the analytical signal was identified using Ni concentrations, and Ti was used as an internal standard element with NIST SRM 612 as the calibration standard using the preferred values of Pearce *et al.* (1997). Accuracy of the laser ablation ICP–MS technique for MI analysis was tested using a secondary standard of USGS basaltic glass BCR-2G at the beginning and end of each analytical run. All elements were measured to within 8% of the GeoReM preferred values (Jochum & Stoll 2008, data not shown here). Identical MI were measured by EMPA, SIMS and laser ablation ICP–MS (Figure 13-5). Agreement between the different techniques was excellent for most elements and was within 1σ standard deviation for the major elements Na, Al, K (LA–ICP–MS *vs.* EMPA) and the trace elements REE, Hf, Zr, Sr, Y, Ba and Cs (LA–ICP–MS *vs.* SIMS). Poorer agreement with deviations of up to 50% was found for Pb, Th, Nb and U which are all lower in the SIMS than the laser ablation data. The results from this short experiment confirm previous studies that more thoroughly compare laser ablation ICP–MS and SIMS/EMPA for exposed MI analysis (de Hoog *et al.* 2001, Pettke *et al.* 2004). A similar result with generally good agreement but anomalous results for a few elements, including Th and U was found in the extensive comparative study of Pettke *et al.*

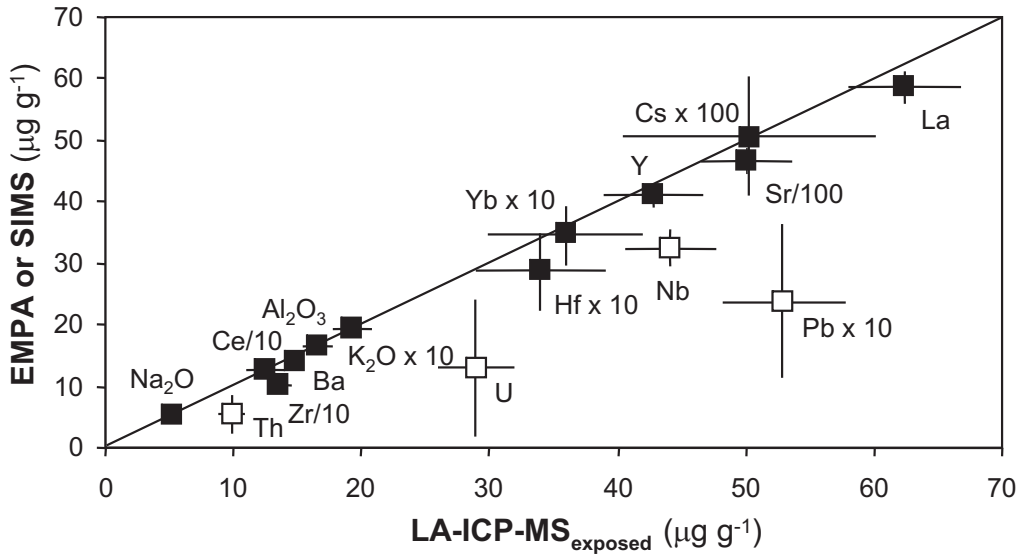


FIG. 13-5. Comparison of concentration data determined for 16 elements in the same exposed melt inclusions (n=2) measured by both laser ablation ICP–MS and EMPA or SIMS. Error bars on the laser ablation data represent the average 1σ internal precision calculated for the two measurements using the methods outlined in Halter *et al.* (2002a). Internal precision (1σ) on the EMPA or SIMS data gives error bars that are often smaller than the symbol size. Analytical details are given in the text. Accuracy of the laser ablation data were independently tested by ablating basaltic glass BCR2-G (Jochum & Stoll 2008) and all elements were measured to within 8% of the GeoReM preferred values. Open symbols show elements for which the two techniques do not agree well.

(2004). These authors attributed the difference in Th and U to the relatively low total counts measured for these elements by SIMS, corresponding to poor 1σ precision, a process which may also have led to the poor agreement for Pb, Th, Nb and U in our more limited comparison. We can conclude from these studies that laser ablation ICP-MS can provide sufficiently accurate and precise results for many elements in exposed silicate MI. The main disadvantage of method 1 is the time-consuming nature of the work and the loss of many MI during polishing.

We have also tested laser ablation method 2 for the analysis of unexposed rehomogenized MI using two inclusions in the same olivine crystal as tested for method 1 above. The MI diameters were approximately 90 and 80 μm prior to ablation, and a large 120 μm diameter crater was thus ablated in both cases to ensure complete removal of the MI with the surrounding host. Raw intensity results for one of these inclusions are shown in Figure 13-6 using the analytical conditions given in Table 13-2. The ablation rate was approximately 100 nm per pulse, which, coupled with a pulse repetition rate of 5 Hz represented a depth of approximately 60 μm for the MI shown in Figure 13-6. Olivine has a very similar ablation rate to NIST SRM 612 glass (Nobbe & Mason 2005) at 193 nm, and the extent of the MI with depth in this case was thus 100–120 μm. The host olivine was ablated at depth for a further 80 μm into the sample, the total depth of the crater being 220 μm. At this depth of almost twice the crater diameter, a flat bottom crater profile can no longer be sustained by the GeoLas 200Q laser ablation system used in this experiment. This is reflected in the recorded intensities, which show continued sampling of the MI after apparently passing the boundary from MI into olivine. In an extreme case the MI ablation might stop due to the conical shape of the laser beam imaged onto the sample. The apparent contamination of the underlying olivine with MI can also be partially a function of inefficient particle extraction and mixing within the crater (Mason & Mank 2001). It is thus generally not a good idea to calculate the concentration of elements in the host mineral using the second integration volume indicated on Figure 13-6 unless these effects can be excluded.

The results for these MI were calculated using the methodology described by Halter *et al.* (2002a). We calculated mass ratios of 0.17 and 0.20 using the Na/Si ratio which was significantly different between host and MI and was one of the least variable element ratios in MI previously measured in exposed MI from this sample. The use of other element ratios such as Ti/Al or Zr/Nb using data

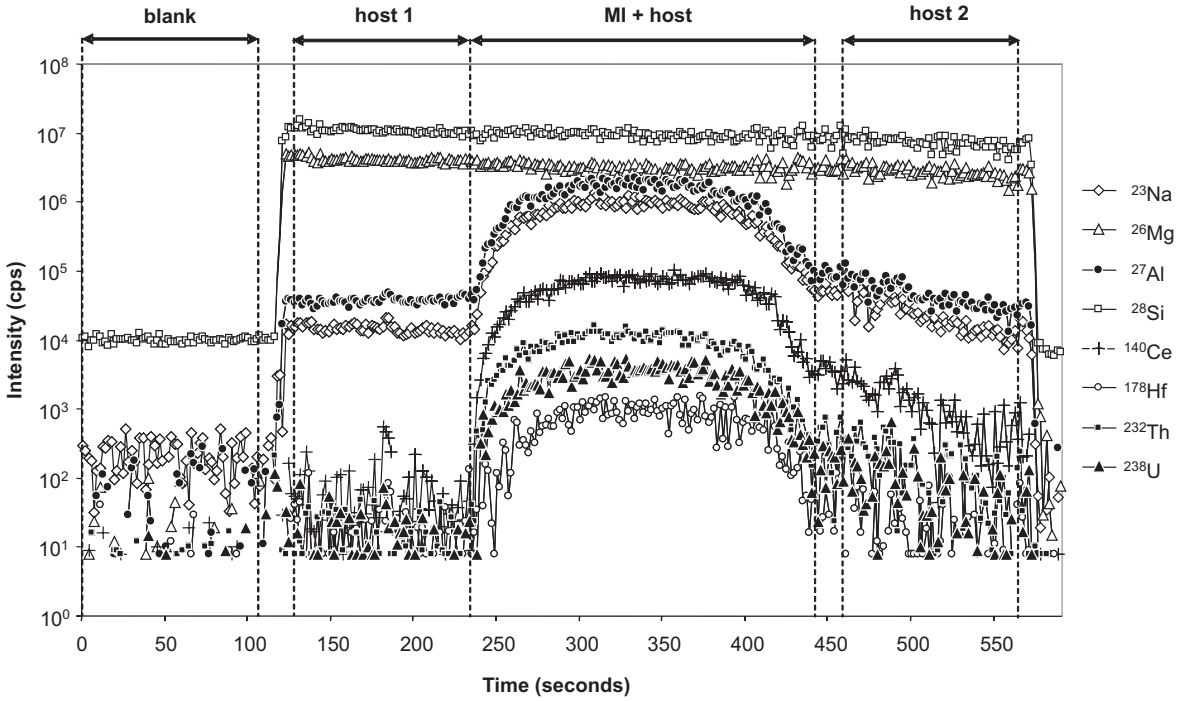


FIG. 13-6. Raw intensities measured for 8 isotopes during the ablation of an unexposed rehomogenized silicate MI in a host olivine mineral. Analytical details are given in the text. Note that interval 2 for the host mineral shows an elevated Ce and U signal due to continued contribution from the MI, and thus host interval 1 must be used for correction during data reduction.

obtained from exposed MI in the same sample gave comparable results. Concentrations were then calculated using the following relationship from Halter *et al.* (2002a):

$$C_i^{INCL} = C_i^{HOST} - \frac{(C_i^{HOST} - C_i^{MIX})}{x} \qquad (1)$$

where $C_i^{INCL}$, $C_i^{MIX}$ and $C_i^{HOST}$ are the concentrations of an element i in the inclusion, mix and host respectively, and x is the mass ratio that was derived as described above. The correction for instrumental RSF was applied by summation of the total signal to 98% (based on EMP totals for exposed MI). The results are shown in Figure 13-7. Agreement between data for exposed and unexposed MI falls within 1σ error for all elements. Uncertainties on the unexposed MI results were calculated as described in detail by Halter *et al.* (2002a). The internal precision of the data obtained by method 2 is clearly poorer than that obtained by method 1, due to the additional uncertainly introduced by the subtraction of the host mineral contribution to the mixed signal. However, external precision calculated for the analysis of a series of MI in a single population, or where possible on multiple analyses of a single large MI, typically gives 1σ uncertainties that are comparable with the external precision of method 1 or with external error on the EMPA/SIMS techniques (see discussion in Pettke 2006). The poor internal precision of method 2 means that method 1 is preferable for the analysis of limited numbers of anomalous inclusions that can often be found in MI populations (*e.g.*, Danyushevsky *et al.* 2003).

Summation of the total signal to correct for RSF requires accurate measurement of all major elements. In some of our analytical measurements it was not possible to accurately determine Fe, due to the $^{56}Fe$ isotope exceeding the linear dynamic range of the ICP–MS and variable interference from $^{40}Ar^{16}O^{1}H^{+}$ or another unidentified polyatomic ion that precluded accurate measurement of $^{57}Fe$. An alternative method would therefore be to initially optimize the mass ratio, followed by a step of internal standardization using a single major element, previously determined for other MI in the same olivine by EMPA. We tested this method with the Na/Si ratio, followed by Ti normalization, which gave results within error of the summation plus mass ratio correction.

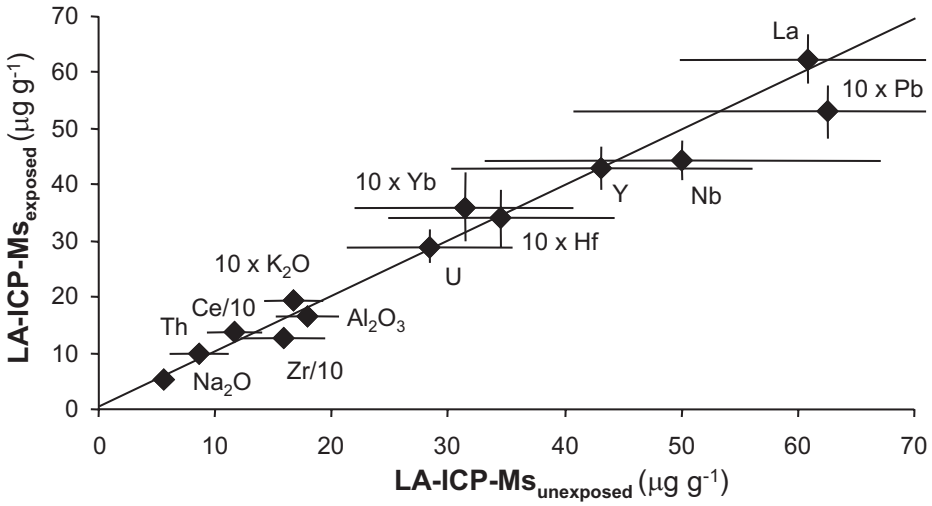


FIG. 13-7. Comparison of concentration data determined by laser ablation ICP–MS for exposed (n=2) and unexposed (n=2) melt inclusions in the same olivine phenocryst. Analytical details are given in the text.

The results we present above are for a best case scenario where a large rehomogenized MI has been ablated at depth in olivine. Many MI are smaller, resulting in elevated detection limits, poorer accuracy and lower precision due to the smaller ablated mass per unit time and shorter measurement times. Many MI are inhomogeneous due to their crystallinity and in these cases continued ablation into the underlying host and a sufficiently large diameter for the ablation crater are essential to ensure that all phases are sampled. Despite potential difficulties, the application of this technique, with acceptable levels of accuracy and precision, has been proven for heterogeneous MI in the more rigorous study of Pettke et al (2004)..

The methods we have illustrated so far give sufficiently accurate and precise data for use in petrological studies, but there are several application areas where high accuracy may not be required. Laser ablation has sufficient precision, regardless of accuracy to provide a very rapid confirmation of different assemblages within a MI population. This could be important to ascertain before embarking on a more exhaustive MI study. Here we show an example where the presence of different MI populations is suspected from changes in host mineral composition in two different volcanic centers from the K-rich volcanic region of central Italy (Figure 13-8). In each case, MI analyzed in primitive olivine with high- and low-Ca concentrations show clear differences in key incompatible trace element ratios such as Rb/Ba, Th/U or Ce/Pb, providing evidence for multiple parental melts. This link between differences in mineral and MI chemistry has been explored in a number of recent studies (Elburg *et al.* 2006, Kamenetsky *et al.* 2006, Elburg *et al.* 2007). Based on results such as these it is clear that laser ablation ICP–MS could be an important stand-alone survey tool for ratio determination.

## SUMMARY AND FUTURE DEVELOPMENTS

Laser ablation ICP–MS is both an accurate and precise technique for MI analysis that can be used for ablating either exposed or unexposed inclusions. Careful preparation or calibration using complimentary analytical techniques is often required, including EMPA to determine an internal standard concentration, and heating stage experiments for rehomogenization of crystalline inclusions. Unexposed crystalline inclusions can be measured directly but care must be taken to ensure ablation of the whole inclusion and the accurate implementation of correction procedures. Internal precision is poorer for the analysis of unexposed *versus* exposed MI, and thus the latter technique (method 1 in our discussion) may be preferable in some studies, such as for the characterization of rare anomalous inclusions. Laser ablation can also be rapidly applied as a stand-alone technique for determining trace element ratios rather than element concentrations. It could be very useful as an initial survey tool before starting a more detailed MI study.

The most important positive and negative aspects of laser ablation, in comparison with other microanalytical techniques such as SIMS/EMPA are outlined below.

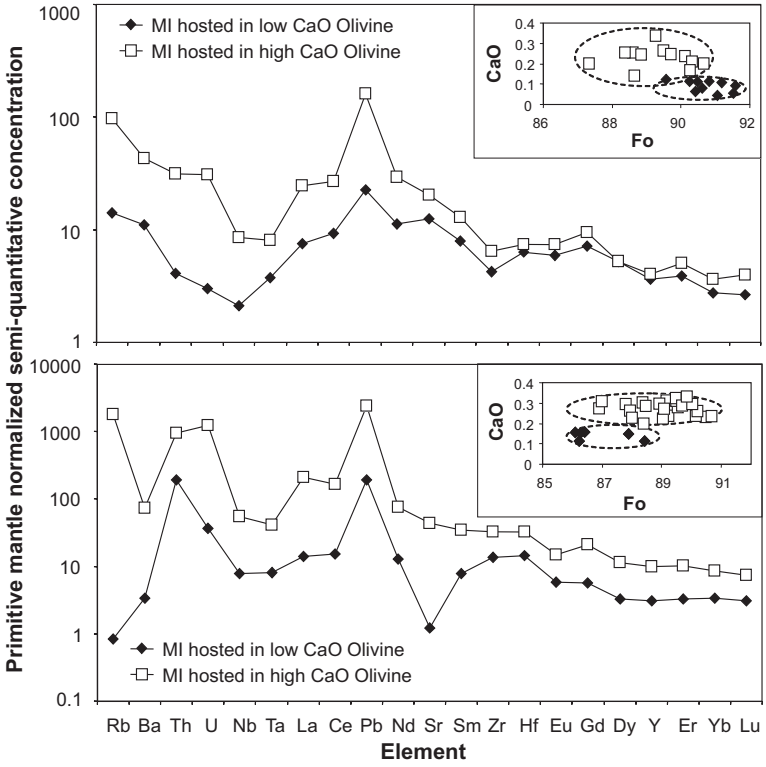


FIG. 13-8. Variation in trace element ratios within different melt inclusion assemblages belonging to a MI population. Note that these trace element data are semi-quantitative as they have not been corrected using an internal standard. The inset shows the forsterite content *vs*. CaO concentration in olivine from the same sample determined by EMPA.

***Strengths of laser ablation ICP–MS***

1. Melt inclusions can be effectively rehomogenized by the laser during the complete ablation of unexposed inclusions. This enables more MI to be measured in a sample, more quickly and avoids rehomogenization experiments which may suffer problems such as decrepitation or may not be available in many labs. In addition, some MI cannot be rehomogenized due to crucial differences between experimental conditions and those experienced during trapping.
2. Sampling at different depths is possible by LA without the need for polishing, resulting in access to a greater proportion of the total number of MI in a single phenocryst than by other methods. Additional benefits include the possibility to measure metals (*e.g.,* chalcophile elements) that are dissolved in the bubble which are not easily soluble in the melt phase (Zajacz & Halter 2007).

***Weaknesses of laser ablation ICP–MS***

1. Laser ablation is destructive and MI are often completely consumed during laser ablation sampling. This leaves little or no sample left in all but the largest inclusions, and thus complimentary studies must be performed prior to ablation.
2. Either knowledge of an internal standard is required, or a detailed study of many inclusions, preferably in several host phases should be attempted in order to obtain accurate results. This is especially important in studies which attempt to measure mineral–melt partitioning behavior or where data are to be used in numerical modeling. Trace element ratios or isotope ratios are not affected by this problem for cases where the trace elements under consideration are not contained in the host.
3. LA cannot be used to determine the concentration of volatile molecular species ($H_2O$, $CO_2$), cannot measure F and is poor for determining Cl and S due to the high first ionization energy, coupled with significant spectral interferences. A combination of a laser ablation study with FTIR or confocal micro-Raman spectroscopy could be used to provide a more comprehensive dataset and solve this problem.
4. For most currently available laser ablation systems and depending upon the scientific goal, inclusion size should be at least 20–30 μm in diameter. Many MI are smaller than this and the detection capability of most ICP–MS instruments is still not sufficient to make as robust measurements as is desirable.

**Future developments**

We anticipate that the application of laser ablation ICP–MS will continue to grow in MI studies. However, since MI contain many elements and molecular species across a large range of concentrations, we also expect it to remain a component part of studies that employ a number of different analytical techniques (*e.g.,* Wysoczanski *et al.* 2006), rather than being a stand-alone method. Potentially one of the most exciting future developments will be for isotope ratio measurements, which are not easy to perform using currently available analytical techniques (Davidson *et al.* 2007). Further improvements in (MC–)ICP–MS sensitivity and matrix-independent laser ablation, could open up many new research directions and potentially revolutionize the field of petrology.

**ACKNOWLEDGEMENTS**

We thank Thomas Pettke and Leonid Danyushevsky for thorough and detailed reviews. This research was supported by the Netherlands Research Centre for Integrated Solid Earth Science (ISES) through grants 2.2.3b, 2.2.3c and 6.2.12. The Utrecht laser ablation ICP–MS laboratory has received funding from the Netherlands Organization of Scientific Research (NWO).

**REFERENCES**

AUDÉTAT, A. (2000): Quantitative analysis of melt and fluid inclusions by LA–ICP–MS: Practical aspects and selected results. *Acta Petrologica Sinica* **16**, 715.

AUDÉTAT, A., & PETTKE, T. (2003): The magmatic–hydrothermal evolution of two barren granites: A melt and fluid inclusion study of the Rito del Medio and Canada Pinabete plutons in northern New Mexico (USA). *Geochim. Cosmochim. Acta* **67,** 97-121.

AUDÉTAT, A. & PETTKE, T. (2006): Evolution of a porphyry-Cu mineralized magma system at Santa Rita, New Mexico (USA). *Journal Of Petrology,* **47**, 2021-2046.

AUDÉTAT A., GUNTHER D., AND HEINRICH C.A. (2000) Magmatic-hydrothermal evolution in a fractionating granite: a microchemical study of the Sn-W-F-mineralized Mole Granite (Australia). *Geochim. Cosmochim. Acta* **64**, 3373-3393.

BALCERZAK, M. (2003): An overview of analytical applications of time of flight-mass spectrometric (TOF–MS) analyzers and an inductively coupled plasma–TOF–MS technique. *Analyt. Sci.* **19**, 979-989.

BEAUDOIN, Y., SCOTT, S.D., GORTON, M.P., ZAJACZ, Z., HALTER, W. (2007): Pb and other ore metals in modern seafloor tectonic environments: Evidence from melt inclusions. *Marine Geol.* **242**, 271-289.

BEHRENS, H. ROUX, J. NEUVILLE D.R. & SIEMANN, M. (2006): Quantification of dissolved $H_2O$ in silicate glasses using confocal microRaman spectroscopy, *Chem. Geol.* **229**, 96–112.

BLEINER, D & CHEN, Z. (2008): Computer modeling of laser ablation elemental microanalysis. *In* Laser Ablation ICP–MS in the Earth Sciences: Current Practices and Outstanding Issues (P. Sylvester, *ed*.). *Mineral. Assoc. Can. Short Course Series* **40**, 35-52.

BLEINER, D., MACRÌ, M., GASSER, P., SAUTTER, V., & MARAS, A. (2006): FIB, TEM and LA–ICPMS investigations on melt inclusions in Martian meteorites – Analytical capabilities and geochemical insights. *Talanta* **68**, 1623-1631.

BONNIN-MOSBAH, M., SIMIONOVICI, A.S., MÉTRICH, N., DURAUD, J.-P., MASSARE, D. & DILLMANN, P. (2001): Iron oxidation states in silicate glass fragments and glass inclusions with a XANES micro-probe. *J. Non-Crystalline Solids,* 288, 103-113**.**

CAMPOS, E., TOURET, J.L.R., NIKOGOSIAN, I.K., DELGADO, J. & MORALES, P. (2002): Overheated, Cu-bearing magmas in Zaldivar Porphyry Copper Deposit, Northern Chile: Geodynamic evidence. *Tectonophys.* **345**. 229-251.

DANYUSHEVSKY L.V., MCNEILL A.W., SOBOLEV, A.V. (2002): Experimental and petrological studies of melt inclusions in phenocrysts from mantle-derived magmas: an overview of techniques, advantages and complications. *Chem. Geol.* **183**, 5 –24.

DANYUSHEVSKY, L.V., PERFIT, M.R., EGGINS, S.M. & FALLOON, T.J. (2003): Crustal origin for coupled 'ultra-depleted' and 'plagioclase' signatures in MORB olivine-hosted melt inclusions: Evidence from the Siqueiros Transform Fault, East Pacific Rise. *Contrib. Mineral. Petrol.* **144**, 619-637.

DAVIDSON, J.P., MORGAN, D.J., CHARLIER, B.L.A., HARLOU, R. & HORA, J.M. (2007): Microsampling and isotopic analysis of igneous

rocks: Implications for the study of magmatic systems. *Ann. Rev. Earth Planet. Sci.* **35**, 273-311.

DE HOOG, J.C.M., MASON, P.R.D. & VAN BERGEN, M.J. (2001): Sulfur and chalcophile elements in subduction zones: Constraints from a laser ablation ICP–MS study of melt inclusions from Galunggung volcano, Indonesia. *Geochim. Cosmochim. Acta* **65**, 3147-3164.

EGGINS, S., KINSLEY, L.P.J. & SHELLEY, J.M.G. (1998): Deposition and elemental fractionation processes during atmospheric pressure laser sampling for analysis by ICP–MS. *Appl. Surf. Sci.* **129**, 278-286.

ELBURG, M., KAMENETSKY, V.S., NIKOGOSIAN, I., FODEN, J. & SOBOLEV, A.V. (2006): Coexisting high- and low-calcium melts identified by mineral and melt inclusion studies of subduction-influenced syn-collisional magma from south Sulawesi, Indonesia. *J. Petrol.* **47**, 2433-2462.

ELBURG, M., KAMENETSKY, V.S., FODEN, J. & SOBOLEV, A.V. (2007): The origin of medium-K ankaramitic arc magmas from Lombok (Sunda arc, Indonesia): Mineral and melt inclusion evidence. *Chem. Geol.* **240**, 260-279.

FAURE, F. & SCHIANO, P. (2005): Experimental investigation of equilibration conditions during forsterite growth and melt inclusion formation. *Earth Planet. Sci. Lett.* **236**, 882– 898

GÜNTHER, D. & HATTENDORF, B. (2005): Solid sample analysis using laser ablation inductively coupled plasma mass spectrometry. *Trends Analyt. Chem.* **24**, 255-265.

GÜNTHER, D., HATTENDORF, B. & AUDÉTAT, A. (2001): Multi-element analysis of melt and fluid inclusions with improved detection capabilities for Ca and Fe using laser ablation with a dynamic reaction cell ICP–MS. *J. Analyt. Atom. Spectrom.* **16**, 1085-1090.

GÜNTHER, D. & KOCH, J. (2008): Formation of aerosols generated by laser ablation and their impact on elemental fractionation in LA–ICP–MS. *In* Laser Ablation ICP–MS in the Earth Sciences: Current Practices and Outstanding Issues (P. Sylvester, *ed.*). *Mineral. Assoc. Can. Short Course Series* **40**, 19-34.

GURENKO, A.A., & CHAUSSIDON, M. (1997): Boron concentrations and isotopic composition of the icelandic mantle: Evidence from glass inclusions in olivine. *Chem. Geol.* **135**, 21-34.

GUZMICS, T., ZAJACZ, Z., KODOLÁNYI, J., HALTER, W. & SZABÓ, C. (in press): LA–ICP–MS study of apatite- and K feldspar-hosted primary carbonatite melt inclusions in clinopyroxenite xenoliths from lamprophyres, Hungary: Implications for significance of carbonatite melts in the Earth's mantle. *Geochim. Cosmochim. Acta,* in Press.

HALTER, W.E. & HEINRICH, C.A. (2006): Magmatic processes and volatile phase generation in porphyry-type environments: A laser ablation–ICP–MS study of silicate and sulfide melt inclusions. *Mineral. Assoc. Can. Short Course* **36**, 151-164.

HALTER, W.E., PETTKE, T., HEINRICH, C.A. & ROTHEN-RUTISHAUSER, B. (2002a): Major to trace element analysis of melt inclusions by laser ablation ICP–MS: Methods of quantification. *Chem. Geol.* **183**, 63-86.

HALTER, W.E., PETTKE, T. & HEINRICH, C.A. (2002b) The origin of Cu/Au ratios in porphyry-type ore deposits. *Science* **296**, 1844-1846.

HALTER, W.E., HEINRICH, C.A. & PETTKE, T. (2004a): Laser ablation ICP–MS analysis of silicate and sulfide melt inclusions in an andesitic complex II: Evidence for magma mixing and magma chamber evolution. *Contrib. Mineral. Petrol.* **147**, 397-412.

HALTER, W.E., PETTKE, T. & HEINRICH, C.A. (2004b): Laser ablation ICP–MS analysis of silicate and sulfide melt inclusions in an andesitic complex I: Analytical approach and data evaluation. *Contrib. Mineral. Petrol.* **147**, 385-396.

HAURI, E. WANG, J. DIXON, J.E. KING, P.L. MANDEVILLE C. & NEWMAN, S. (2002): SIMS analysis of volatiles in silicate glasses 1. Calibration, matrix effects and comparisons with FTIR, *Chem. Geol.* **183**, 99–114.

HEINRICH, C.A., PETTKE, T., HALTER, W.E., AIGNER-TORRES, M., AUDÉTAT, A., GÜNTHER, D., HATTENDORF, B., BLEINER, D., GUILLONG, M. & HORN, I. (2003): Quantitative multi-element analysis of minerals, fluid and melt inclusions by laser-ablation inductively-coupled-plasma mass-spectrometry. *Geochim. Cosmochim. Acta* **67**, 3473-3496.

HEINRICH, C.A., HALTER, W., LANDTWING, M.R. & PETTKE, T. (2005): The formation of economic porphyry copper (-gold) deposits: Constraints from microanalysis of fluid and melt inclusions.

*Geol. Soc. Special Publ.* **248**, 247-263.

HORN, I. (2008): Comparison of femtosecond and nanosecond laser interactions with geologic matrices and their influence on accuracy and precision of LA–ICP–MS data. *In* Laser Ablation ICP–MS in the Earth Sciences: Current Practices and Outstanding Issues (P. Sylvester, *ed*.). *Mineral. Assoc. Can. Short Course Series* **40**, 53-65.

HUMPHREYS, M.C.S., KEARNS, S.L. & BLUNDY, J.D. (2006): SIMS investigation of electron-beam damage to hydrous, rhyolitic glasses: Implications for melt inclusion analysis. *Am. Mineral.* **91**, 667-679.

JACKSON, S.E. (2008): Calibration strategies for elemental analysis by LA–ICP–MS *In* Laser Ablation ICP–MS in the Earth Sciences: Current Practices and Outstanding Issues (P. Sylvester, *ed*.). *Mineral. Assoc. Can. Short Course Series* **40**, 169-188.

JACKSON, M.G. & HART, S.R. (2006): Strontium isotopes in melt inclusions from Samoan basalts: Implications for heterogeneity in the Samoan plume. *Earth Planet. Sci. Lett.* **245**, 260-277.

JOCHUM, K.P. & STOLL, B. (2008): Reference materials for elemental and isotopic analyses by LA–(MC)–ICP–MS: successes and outstanding needs. *In* Laser Ablation ICP–MS in the Earth Sciences: Current Practices and Outstanding Issues (P. Sylvester, *ed*.). *Mineral. Assoc. Can. Short Course Series* **40**, 147-168.

JOCHUM, K.P., STOLL, B., HERWIG, K. & HOFMANN, A.W. (2004): Pb isotopes and trace elements in melt inclusions from Hawaiian basalts using LA–ICPMS and SR–XRF. *Geochim. Cosmochim. Acta* 68/11S:A564 (Abstr.)

JOCHUM, K.P., STOLL, B., HERWIG, K., AMINI, M., ABOUCHAMI, W. & HOFMANN, A.W. (2005): Lead isotope ratio measurements in geological glasses by laser ablation–sector field–ICP mass spectrometry (LA–SF–ICPMS). *Internat. J. Mass Spectrom.* **242**, 281-289.

KAMENETSKY, V.S., EGGINS, S.M., CRAWFORD, A.J., GREEN, D.H., GASPARON, M. & FALLOON, T.J. (1998): Calcic melt inclusions in primitive olivine at 43°N MAR: evidence for melt-rock reaction/melting involving clinopyroxene-rich lithologies during MORB generation. *Earth Planet. Scie. Lett.* **160**, 115-132.

KAMENETSKY, V.S., SOBOLEV, A.V., EGGINS, S.M., CRAWFORD, A.J. & ARCULUS, R.J. (2002): Olivine-enriched melt inclusions in chromites from low-Ca boninites, Cape Vogel, Papua New Guinea: Evidence for ultramafic primary magma, refractory mantle source and enriched components. *Chem. Geol.* **183**, 287-303.

KAMENETSKY, V.S., NAUMOV, V.B., DAVIDSON, P., VAN ACHTERBERGH, E. & RYAN, C.G. (2004): Immiscibility between silicate magmas and aqueous fluids: A melt inclusion pursuit into the magmatic-hydrothermal transition in the Omsukchan Granite (NE Russia). *Chem. Geol.* **210**, 73-90.

KAMENETSKY, V.S., ELBURG, M., ARCULUS, R. & THOMAS, R. (2006): Magmatic origin of low-Ca olivine in subduction-related magmas: Co-existence of contrasting magmas. *Chem. Geol.* **233**, 346-357.

KRAMAR, U., HARTING, M., RICKERS, K. & STÜBEN, D. (2007): μ-Synchrotron radiation excited X-ray fluorescence microprobe trace element studies on spherules of the Cretaceous/Tertiary boundary transitions of NE-Mexico and Haiti samples. *Spectrochim. Acta B* **62**, 824-835.

LAYNE, G.D., GODON, A., WEBSTER, J.D., BACH, W. (2004): Secondary ion mass spectrometry for the determination of δ37Cl Part I. Ion microprobe analysis of glasses and fluids. *Chem. Geol.* **207**, 277-289.

LONGERICH, H. (2008): Laser ablation–inductively coupled plasma–mass spectrometry (LA–ICP–MS); an introduction. *In* Laser Ablation ICP–MS in the Earth Sciences: Current Practices and Outstanding Issues (P. Sylvester, *ed*.). *Mineral. Assoc. Can. Short Course Series* **40**, 1-18.

LOWENSTERN, J.B. (2003): Melt Inclusions Come of Age: Volatiles, Volcanoes, and Sorby's Legacy. 1-21. *In*: B. De Vivo and R.J. Bodnar (*eds*.) Melt Inclusions in Volcanic Systems: Methods, Applications and Problems. Developments in Volcanology **5**, Elsevier Press, Amsterdam.

LUKAÌCS, R., HARANGI, S., NTAFLOS, T. & MASON, P.R.D. (2005): Silicate melt inclusions in the phenocrysts of the Szomolya Ignimbrite, Bukkalja Volcanic Field (Northern Hungary): Implications for magma chamber processes. *Chem. Geol.* **223**, 46-67.

MANK, A.J.G. & MASON, P.R.D. (1999): A critical assessment of laser ablation ICP–MS as an analytical tool for depth analysis in silica-based

glass samples. *J. Analyt. Atom. Spectrom.* **14**, 1143-1153.

MASON, P.R.D. (2001): Expanding the capabilities of laser ablation ICP–MS using collision and reaction cells. In: Sylvester P (ed*) Laser ablation ICP–MS in the Earth Sciences. Principles and Applications. Mineral. Assoc. Can. Short Course* **29**, 63-83.

MASON, P.R.D. & MANK, A.J.G. (2001): Depth-resolved analysis in multi-layered glass and metal materials using laser ablation inductively coupled plasma mass spectrometry (LA–ICP–MS). *J. Analyt. Atom. Spectrom.* **16**, 1381-1388.

MÉTRICH, N., SCHIANO, P., CLOCCHIATTI R. & MAURY, R.C. (1999): Transfer of sulfur in subduction settings: an example from Batan Island (Luzon volcanic arc, Philippines). *Earth Planet. Sci. Lett.* **167**, 1–14.

MÉTRICH, N., SUSINI, J., FOY, E., FARGES, F., MASSARE, D., SYLLA, L., LEQUIEN, S. & BONNIN MOSBAH, M. (2006): Redox state of iron in peralkaline rhyolitic glass/melt: X-ray absorption micro-spectroscopy experiments at high temperature. *Chem. Geol.* **231**, 350-363**.**

MOSBAH, M., DURAUD, J.P., MÉTRICH, N., WU, Z., DELANEY, J.S. & SAN MIGUEL, A. (1999): Micro-XANES with synchrotron radiation: A complementary tool of micro-PIXE and micro-SXRF for the determination of oxidation state of elements. Application to geological materials. *Nuclear Instruments & Methods in Physics Research B:* **158**, 214-220

MUSTARD, R., ULRICH, T., KAMENETSKY, V.S. & MERNAGH, T. (2006): Gold and metal enrichment in natural granitic melts during fractional crystallization. *Geology* **34**, 85-88.

NICHOLS, A.R.L. & WYSOCZANSKI, R.J. (2007): Using micro-FTIR spectroscopy to measure volatile contents in small and unexposed inclusions hosted in olivine crystals. *Chem. Geol.* **242**, 371-384.

NIKOGOSIAN I.K., ELLIOTT, T. & TOURET, J.L.R. (2002): Melt evolution beneath thick lithosphere: A magmatic inclusions study of La Palma, Canary Islands. *Chem. Geol.* **183**, 171-195

NOBBE, G. & MASON, P.R.D. (2005): Correlation between ablation rate and measured signal in laser ablation ICP–MS. *ICP Information Newslett.* **30**, 1006-1008.

PEARCE, N.J.G., PERKINS, W.T., WESTGATE, J.A., GORTON, M.P., JACKSON, S.E., NEAL, C.R. & CHENERY, S.P. (1997): A compilation of new and published major and trace element data for NIST SRM 610 and NIST SRM 612 glass reference materials. *Geostand. Newslett.* **21**, 115-144.

PETTKE, T. (2006): *In situ* laser ablation ICP–MS analysis of melt inclusions and prospects for constraining subduction zone magmatism. *Mineral. Assoc. Can. Short Course Volume* **36**, 51-80.

PETTKE, T. (2008): Analytical protocols for element concentration and isotope ratio measurements in fluid inclusions by LA–(MC–)ICP–MS. *In* Laser Ablation ICP–MS in the Earth Sciences: Current Practices and Outstanding Issues (P. Sylvester, *ed.*). *Mineral. Assoc. Can. Short Course Series* **40**, 189-217.

PETTKE, T., HEINRICH, C.A., CIOCAN, A.C. & GÜNTHER, D. (2000): Quadrupole mass spectrometry and optical emission spectroscopy: detection capabilities and representative sampling of short transient signals from laser ablation. *J. Analyt. Atom. Spectrom.* **15**, 1149-1155.

PETTKE, T., HALTER, W.E., WEBSTER, J.D., AIGNER-TORRES, M. & HEINRICH, C.A. (2004): Accurate quantification of melt inclusion chemistry by LA–ICPMS: A comparison with EMP and SIMS and advantages and possible limitations of these methods. *Lithos* **78**, 333-361.

QIN, Z., LU, F. & ANDERSON, J.A.T. (1992): Diffuse re-equilibration of melt and fluid inclusions. *Am. Mineral.* **77**, 565-576.

RENNER, J., EVANS, B. & HIRTH, G. (2002): Grain growth and inclusion formation in partially molten carbonate rocks. *Contrib. Mineral. Petrol.* **142**, 501-514.

ROEDDER, E. (1979) Origin and significance of magmatic inclusions. *Bull. Minéral.* **102**, 487-510.

ROEDDER, E. (1984): Fluid Inclusions. *Rev. Mineral.* **12**, Mineral. Soc. America, pp 645.

RYAN, C.G., VAN ACHTERBERGH, E., GRIFFIN, W.L., PEARSON, N.J., O'REILLY, S.Y. & KIVI, K. (2001): Nuclear microprobe analysis of melt inclusions in minerals: Windows on metasomatic processes in the earth's mantle. *Nuclear Instruments & Methods in Physics Research, Section B:* **181**, 578-585.

SCHIANO, P. (2003): Primitive mantle magmas recorded as silicate melt inclusions in igneous

minerals. *Earth Sci. Rev.* **63,** 121–144.

SIE, S.H. (1997): Nuclear microprobe in geological applications: Where do we go from here? *Nuclear Instruments and Methods in Physics Research, Section B*, **130,** 592-607.

SOBOLEV, A.V. (1996) Melt Inclusions in Minerals as a Source of Principle Petrological Information. *Petrology* **4**, 209–220.

SOBOLEV, A.V. & SHIMIZU, N. (1993): Ultra-depleted primary melt included in olivine from the Mid-Atlantic Ridge. *Nature*, **363**, 151-154.

SOBOLEV, A.V., BARSUKOV, V.L., NEVSOROV V.N. & SLUTSKY, A.B. (1980): The formation conditions of the high-magnesian olivines from the monomineralic faction of Lunar 24 regolith. *Proc. 11th Lunar Planet Sci. Conf.,* 105-116.

SOBOLEV, A.V., HOFMANN, A.W. & NIKOGOSIAN, I.K. (2000): Recycled oceanic crust observed in 'ghost' plagioclase within the source of Mauna Loa lavas. *Nature*, **404**, 986-990.

SPANDLER, C.J., EGGINS, S.M., ARCULUS, R.J. & MAVROGENES, J.A. (2000): Using melt inclusions to determine parent-magma compositions of layered intrusions: Application to the Greenhills Complex (New Zealand), a platinum group minerals-bearing, island-arc intrusion. *Geology*, **28**, 991-994.

SPANDLER, C., O'NEILL, H.ST.C. & KAMENETSKY, V.S. (2007): Survival times of anomalous melt inclusions from element diffusion in olivine and chromite. *Nature,* **447**, 303-306.

STOLPER, E. (1982) Water in silicate glasses: an infrared spectroscopic study, *Contrib. Mineral. Petrol.* **81**, 1–17.

SUN, W., BENNETT, V.C. & KAMENETSKY, V.S. (2004): The mechanism of Re enrichment in arc magmas: Evidence from Lau Basin basaltic glasses and primitive melt inclusions. *Earth and Planetary Science Letters,* **222**, 101-114.

SYLVESTER, P.J. (2005): Laser ablation ICP–MS developments and trends for 2003. *Geostand. Geoanalyt, Res.* **29**, 41-51.

TAYLOR, R.P., JACKSON, S.E., LONGERICH, H.P. & WEBSTER, J.D. (1997): *In situ* trace-element analysis of individual silicate melt inclusions by laser ablation microprobe–inductively coupled plasma–mass spectrometry (LAM–ICP–MS). *Geochim. Cosmochim. Acta* **61**, 2559-2567.

THOMAS, R. (2000): Determination of water contents of granite melt inclusions by confocal laser Raman microprobe spectroscopy, *Am. Mineral.* **85**, 868–872.

WYSOCZANSKI, R.J. WRIGHT, I.C. GAMBLE, J.A. HAURI, E.H. LUHR, J.F. EGGINS S.M. & HANDLER M.R. (2006): Volatile contents of Kermadec Arc–Havre Trough pillow glasses; fingerprinting slab-derived aqueous fluids in the mantle sources of arc and back-arc lavas, *J. Volcanol. Geotherm. Res.* **152**, 51–73.

ZAJACZ, Z. & HALTER, W. (2007): LA–ICPMS analyses of silicate melt inclusions in co-precipitated minerals: Quantification, data analysis and mineral/melt partitioning. *Geochim. Cosmochim. Acta* **71**, 1021-1040.

ZAJACZ Z., HALTER W., MALFAIT W.J., BACHMANN O., BODNAR R.J., HIRSCHMANN M.M., MANDEVILLE C.W., MORIZET Y., MUNTENER O., ULMER P., & WEBSTER J.D. (2005): A composition-independent quantitative determination of the water content in silicate glasses and silicate melt inclusions by confocal Raman spectroscopy. *Contrib. Mineral. Petrol.* **150**, 631-642.

ZAJACZ, Z., KOVÁCS, I., SZABÓ, C., HALTER, W. & PETTKE, T. (2007): Evolution of mafic alkaline melts crystallized in the uppermost lithospheric mantle: A melt inclusion study of olivine-clinopyroxenite xenoliths, Northern Hungary. *J. Petrol.* **48**, 853-883.

# CHAPTER 14: USE OF DISCRETE-DYNODE SECONDARY ELECTRON MULTIPLIERS WITH FARADAYS – A '*REDUCED VOLUME*' APPROACH FOR *IN SITU* U–Pb DATING OF ACCESSORY MINERALS WITHIN PETROGRAPHIC THIN SECTION BY LA–MC–ICP–MS

Antonio Simonetti, Larry M. Heaman & Thomas Chacko
Department of Earth and Atmospheric Sciences, University of Alberta,
1–26 Earth Sciences Building,
Edmonton, Alberta T6G 2E3 Canada
E-mail: antonio.simonetti@ualberta.ca

## INTRODUCTION

Recent U–Pb isotope studies of accessory minerals (*e.g.*, zircon, monazite, titanite) using laser ablation multicollector inductively coupled plasma mass spectrometry (LA–MC–ICP–MS) have made significant advances in generating precise and accurate age data (*e.g.,* Horstwood *et al*. 2003, Simonetti *et al*. 2005, 2006). In particular, the advent of MC–ICP–MS instruments housing multiple ion counting devices (electron multipliers) have provided improvement with regards to the quality of the Pb–Pb or Pb–U isotope data relative to spatial resolution (*i.e.*, lower total volume of sample material consumed). For example, Willigers *et al*. (2002) and Paul *et al*. (2005) conducted *in situ* common Pb isotope measurements by LA–MC–ICP–MS involving a combination of multiple Faraday detectors and one or two electron multipliers, respectively; the latter measured either the $^{204}$Pb or $^{202}$Hg ion beams. In contrast, Souders & Sylvester (2008a, 2008b) reported on LA–MC–ICP–MS investigations of the common Pb isotope ratios for silicate glasses using a multiple electron multiplier detection system involving five channeltrons housed within a Finnigan Neptune MC–ICP–MS instrument.

The studies of Simonetti *et al*. (2005, 2006) employed MC–ICP–MS instrumentation (NuPlasma from Nu Instruments, Wrexham, UK) housing an innovative collector block containing a combination of twelve Faraday collectors and three discrete-dynode electron multipliers. The three electron multipliers housed within the 'U–Pb collector block' of the NuPlasma instrument at the University of Alberta permit acquisition of low $^{207, 206, 204}$Pb ion signals (between ~1 and ~30 millivolts – Faraday bucket ion signal equivalent) with high precision and consequently laser ablation analyses consume relatively small sample volumes. Figure 14-1 compares the precision *versus* sample consumption of the protocol described here to those of other analytical methods including other LA–(+/–MC)–ICP–MS configurations, sensitive high resolution ion microprobe (SHRIMP), and isotope dilution thermal ionization mass spectrometry (ID–TIMS). A typical 30-second laser ablation analysis of zircon at a fluence of ~2 J/cm$^2$ (~0.03 mJ pulse energy), 20–40 μm diameter, and 4 Hz repetition rate produces a pit depth between ~5 and ~10 μm (Fig. 14-2); this is markedly less than the thickness of a standard petrographic thin section (~30 μm). The U–Pb date of 1835.7 ± 4.7 Ma (2σ; Fig. 14-2d) obtained by the repeated laser ablation analysis (n = 10) of a single zircon from a petrographic thin section of sample LH94-15 (Fig. 14-2; Simonetti *et al*. 2006) is indistinguishable from its ID–TIMS age

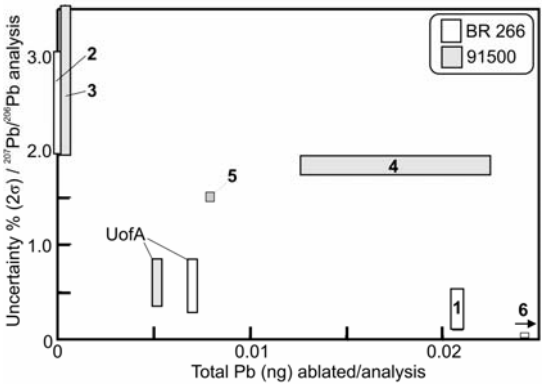


FIG. 14-1. Comparative plot illustrating the typical uncertainty (internal precision, 2σ) associated with the $^{207}$Pb/$^{206}$Pb measurement *versus* the total amount of Pb (ng) ablated for international zircon standards BR266 and 91500 using various laser ablation–ICP–MS instrument configurations and SHRIMP analysis. 1, MC–ICP–MS (all Faraday bucket configuration: Simonetti *et al*. unpublished BR266 data); 2, SHRIMP (Stern 2001); 3, LA–quadrupole (Cox *et al*. 2003); 4, LA–quadrupole (Jackson *et al*. 2004); 5, LA–quadrupole (Jeffries *et al*. 2003); 6, range of ~3 to 11 ng of total Pb by ID–TIMS (Stern 2001); UofA = Pb consumed using the protocol described here. Diagram taken from Simonetti *et al*. (2005).

Mineralogical Association of Canada Short Course 40, Vancouver, B.C., p. 241–264.

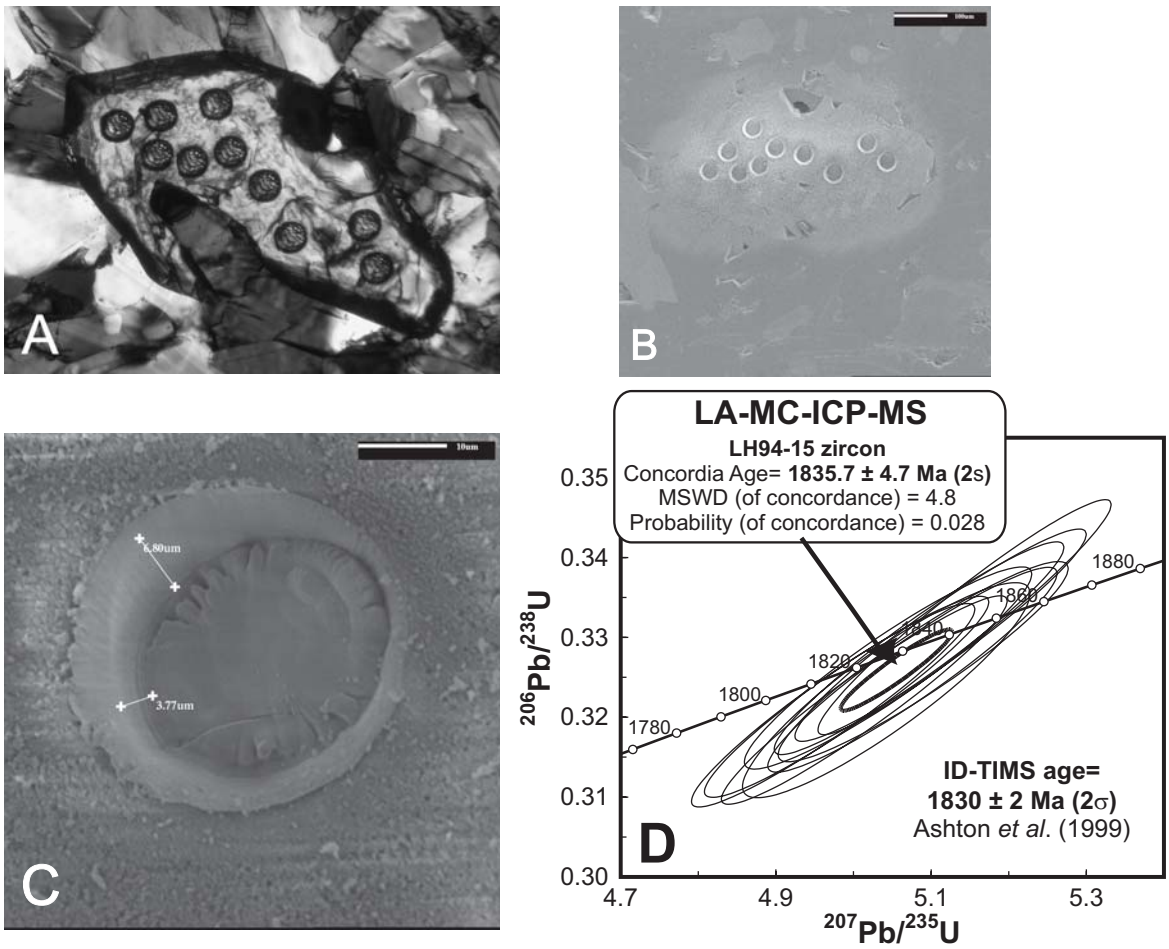


FIG. 14-2. **A**, Photomicrograph of a petrographic thin section of enderbite sample LH94-15 (source of internal zircon standard LH94-15). The photo displays the locations of the 40 μm analysis spots within a large zircon crystal, which is surrounded predominantly by pyroxene, plagioclase, biotite and quartz; **B**, Topographic scanning electron microprobe (SEM) photo of same LH94-15 zircon grain shown in A; **C**, enlarged view of one of the 40 μm laser pits indicating a depth of between ~4 to ~7 microns; **D**, Concordia plot indicating an age of 1835.7 ± 4.7 Ma (2σ) obtained with the 10 laser ablation analyses shown in A. This date is indistinguishable from the ID–TIMS age of 1830 ± 2 Ma (2σ; Ashton *et al*. 1999).

of 1830 ± 2 Ma (2σ; Ashton *et al*. 1999).

The advantages of dating accessory minerals *in situ* within petrographic thin section by LA–MC–ICP–MS cannot be overstated. This approach greatly reduces both sample preparation and analysis time relative to that needed for other geochronological methods. For example, in a typical 8-hour analytical session, 3 to 5 thin sections with 10–20 spots per section can be analyzed using the protocol outlined in Simonetti *et al*. (2006). This '*reduced volume*' *in situ* dating technique also provides the opportunity to link age information directly for a particular sample with deformational fabrics or fine scale textures (*e.g.,* Banerjee *et al*. 2007), and pressure–temperature data derived from electron microprobe analysis of minerals in the same thin section (*e.g.,* Laberge & Pattison 2007). Thirdly, the LA–MC–ICP–MS methodology generates data at significantly lower cost (by a factor of 2 to 4) than is possible with ID–TIMS or SHRIMP.

In this chapter, we describe in detail the instrumentation and important calibration procedures involved in obtaining high quality and accurate geochronological information using the LA–MC–ICP–MS analytical protocol outlined in Simonetti *et al*. (2006). We demonstrate the accuracy of the analytical protocol with several examples of LA–MC–ICP–MS age data obtained on petrographic thin sections for samples also dated by ID–TIMS. As a follow up to our earlier study (Simonetti *et al*. 2006) involving the use of the

standard 30 $cm^3$ ablation cell, here we conduct analogous U–Pb dating experiments with thin sections using the 33 $cm^3$ SuperCell™ (also manufactured by New Wave Research). Both ablation cells have similar volumes; however, the geometry and flow characteristics of the SuperCell™ have been specifically designed to enable rapid evacuation of ablated particles in a large cell format (Fig. 14-3). Another important reason for using the SuperCell™ is its capacity to house thin sections and mounts containing matrix-matched external standards simultaneously (Fig. 14-3). This feature permits the use of the 'standard sample' bracketing technique for monitoring the Pb *versus* U laser-induced elemental fractionation (LIEF) without the need to open the ablation cell (hence results in fewer perturbations to plasma conditions during an analytical session and increased productivity).

**MC–ICP–MS and laser ablation instrumentation**

A summary of instrument parameters used for both the laser ablation system and MC–ICP–MS instrument is listed in Table 14-1. This collector configuration allows for simultaneous acquisition of ion signals ranging from mass $^{203}Tl$ to $^{238}U$, with the $^{207}Pb$, $^{206}Pb$, and $^{204}Pb$ ($+^{204}Hg$) ion beams measured on the three electron multipliers (Table 14-2; Simonetti *et al*. 2005). The NuPlasma MC–ICP–MS is coupled to a frequency quintupled ($\lambda$ = 213 nm) Nd:YAG laser ablation system (New Wave Research, USA) and comparative tests were conducted using both 'standard' and 'SuperCell™' ablation cassettes.

***Discrete-dynode electron multipliers.*** The information relative to the ETP electron multipliers presented in this section is summarized from resource material available at the SGE Analytical

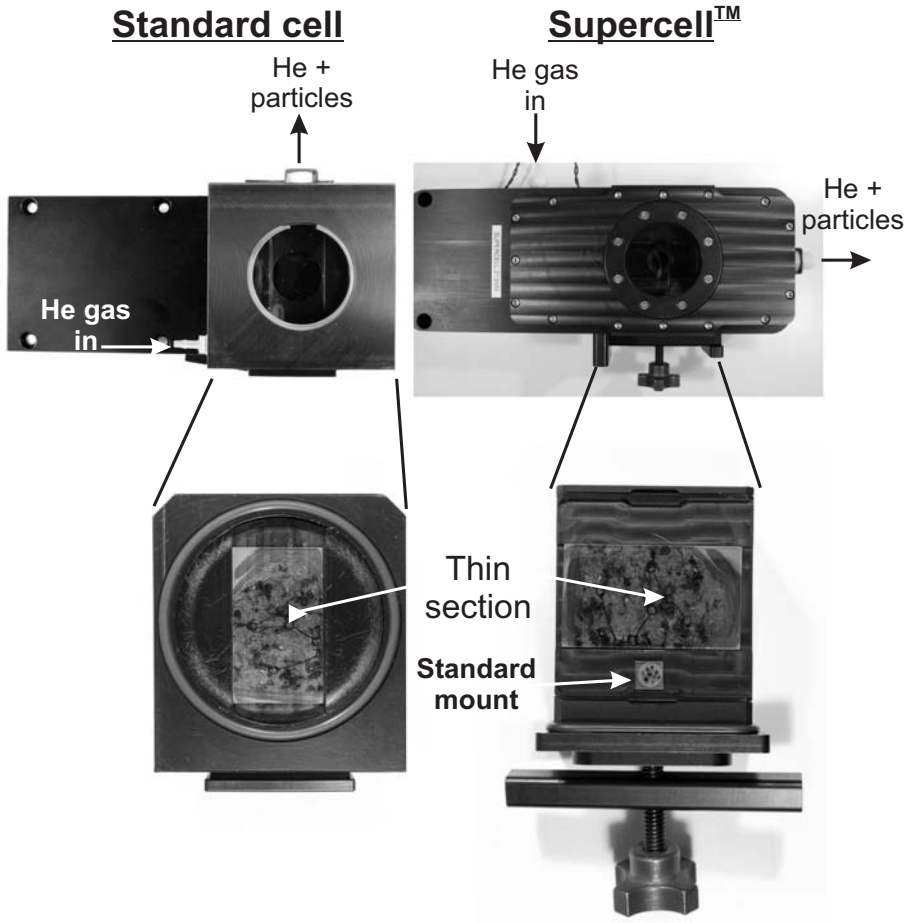


FIG. 14-3. Comparative photographs of the standard ablation cell and Supercell and their corresponding sample holder cassettes from New Wave Research. The larger volume, geometric design of the Supercell allows for the simultaneous insertion of mounts containing standard grains adjacent to the thin section.

TABLE 14-1. OPERATING CONDITIONS AND INSTRUMENT SETTINGS

| **ICP** | | **Laser** | |
|---|---|---|---|
| MC-ICP-MS | | | |
| Model | Nu plasma from Nu instruments | Model | UP213 Nd:YAG – New Wave Research with aperture imaging system |
| Forward power | 1300 W | Wavelength | 213 nm |
| Reflected power | ≤10 W | Max. output energy | 3 mJ per pulse @ 20 Hz using a 160 μm spot size |
| Cool gas flow rate | 13 $Lmin^{-1}$ (Ar) | Pulse width | 3 ns |
| Auxiliary gas flow rate | 1 $Lmin^{-1}$(Ar) | Energy density | 2 -3 $J/cm^2$ |
| Sample transport: | | Focus | Fixed at sample surface |
| Ablation cell | 1 $Lmin^{-1}$(He) | Repetition rate | 4 Hz |
| DSN-100 | Membrane – 2.70 to 3.50 $Lmin^{-1}$ (Ar) heated to 110ºC | Spot size | Single spot analysis – 12, 40 μm |
| | Spray chamber – 0.30 $Lmin^{-1}$(Ar) heated to 110ºC | Ablation cell | 30 $cm^3$ standard cell & 33 $cm^3$ Supercell™ |
| Nebuliser - DSN | Glass Expansion micromist (borosilicate glass) – 100 $\mu Lmin^{-1}$ equipped with Teflon PTFE adaptor & PFA Teflon tubing (1.3 mm OD x 0.25 mm ID) | | |
| Sampler cone | Ni with 1.15 mm orifice | | |
| Skimmer cone | Ni with 0.6 mm orifice | | |

Conditions and instrument settings are identical for experiments using both the standard and Supercell™ laser ablation cells.

Chemistry Ltd. website (http://www.sge.com). The purpose of an electron multiplier is to detect every ion of the selected mass that has passed through the energy (mass) filter of a mass spectrometer. The basic physical process that allows an electron multiplier to operate is referred to as *secondary electron emission*. When an ion or electron strikes a surface it can cause electrons located within the outer layers of atoms to be released. The number of secondary electrons released depends on the type of incident primary particle, its energy, and characteristic of the incident surface. In general, there are two basic types of electron multipliers commonly used in mass spectrometric analysis: these are *discrete-dynode* (Fig. 14-4) and *continuous-dynode* electron multipliers. The three discrete-dynode electron multipliers contained within the 'U–Pb' collector block of the NuPlasma instrument are manufactured by ETP Electron Multipliers (a division of THE SGE Group). Discrete-dynode electron multipliers amplify the secondary electron emission process by using an array of electrodes referred to as dynodes. Ions hitting the first dynode cause secondary electrons to be emitted from the

TABLE 14-2. CONFIGURATION OF THE 'U-PB COLLECTOR BLOCK' USED FOR LASER ABLATION EXPERIMENTS

| **EX-H** | H6 | H5 | H4 | H3 | H2 | H1 | AX | L1 | L2 | **IC0** | **IC1** | **L3** | **IC2** | **EX-L** |
|---|---|---|---|---|---|---|---|---|---|---|---|---|---|---|
| **Faraday** | Far. | Far. | Far. | Far. | Far. | Far. | Far. | Far. | Far. | **Discrete dynode EM** | **Discrete dynode EM** | **Faraday** | **Discrete dynode EM** | **Faraday** |
| $^{238}U$ | $^{235}U$ | ---- | ---- | ---- | ---- | ---- | ---- | ---- | ---- | $^{207}Pb$ | $^{206}Pb$ | $^{205}Tl$ | $^{204}Pb$ + ($^{204}Hg$) | $^{203}Tl$ |

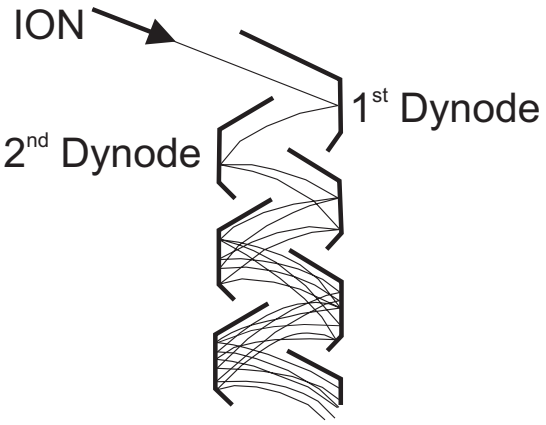


FIG. 14-4. Illustration depicts the ion optics of an ETP discrete-dynode electron multiplier showing the electron gain at each successive dynode. This electron cascading process can result in 'gains' up to $10^8$ being achieved with ~21 dynodes (diagram taken from ETP's website at www.etpsci.com).

surface. The optics of the dynodes focuses these secondary electrons onto the next dynode of the array (Fig. 14-4), which in turn emits even more secondary electrons from its surface than the first dynode. Consequently, a cascade of electrons is produced between successive dynodes, with each dynode increasing the number of electrons in the cascade by a factor of 2 to 3; this process is allowed to continue until the cascade of electrons reaches the output electrode where the signal is extracted. A typical discrete-dynode electron multiplier has between 12 and 24 dynodes and is used with an operating 'gain' of between $10^4$ and $10^8$. For a new (unused) electron multiplier, the gain is achieved with a lower applied voltage (~1800 volts). With time and usage, the surfaces of the dynodes slowly become covered with contaminants from the high vacuum system, which results in a decrease of their secondary electron emission capacity (and consequently drop in 'gain'). Thus, the operating high voltage applied to the electron multipliers must be periodically increased in order to maintain the required multiplier gain. In previous investigations Richter *et al*. (2001) and Hoffmann *et al*. (2005) have conducted detailed investigations of the analytical performances (*e.g.*, linearity, relative yield, stability) of the same ETP electron multipliers employed here primarily for the purpose of U–Th disequilibrium series research using several types of MC–TIMS and MC–ICP–MS instruments. Several of the electron multiplier calibration procedures described here (*e.g.*, determining optimal operating voltage and electron multiplier–Faraday detector calibration) are identical to those reported in both Richter *et al*. (2001) and Hoffmann *et al*. (2005).

The NuPlasma MC–ICP–MS instrument equipped with the U–Pb collector block contains slits that permit passage of ions to the three discrete-dynode electron (ETP) multipliers (labeled IC0, IC1 and IC2), which lie on the low mass side between the last four Faraday collectors (Table 14-2). A small double ESA assembly that deflects the two outer ion beams into off-axes ETP multipliers is located behind the Faraday collector block. In contrast, the central ion beam passes through a slit in the middle part of the Faraday block. There is a small deflection imposed onto the central ion beam to ensure that the multiplier does not lie directly in line with its central channel. The latter offers a simple, but effective means of protecting the ion counters from excessive beams (typically $>10^7$ cps; counts per second) that may be incident on the devices. The multipliers can safely measure signals up to several million counts per second; however, ion signals were kept below 2 x $10^6$ cps in almost all of the laser ablation analyses of zircon so as to prolong the longevity of the ETP detectors. The linearity and stability of the ion counters are better than 0.2% during any one analytical session, whereas dark noise is 0.1 cps or less.

***Discrete-dynode–Faraday calibration: measurement of $^{206}Pb/^{238}U$ values.*** As stated earlier, with progressive use, electron multipliers experience degradation in 'gain' and this is compensated by periodic augmentation of the operating voltage. The frequency of the latter procedure is strictly dependent on the use of the electron multipliers; however it is typically in the order of several months. The relative gains ('linearity') between the three electron multipliers (relative to size of the different Pb ion signals) are measured before each analytical session. If these fall below values of 70% and 80% for IC0, IC1 and IC2, respectively, then the operating voltage is increased in order to yield relative gains of ~80% for IC0 and IC1, and ~90% for IC2 (as recommended by Nu Instruments Ltd.). The optimal operating voltage for each electron multiplier is determined by examining the relationship between high voltage and the relative yield (*i.e.*, absolute ion signal), similar to the procedure outlined in Richter *et al*. (2001). A ~1 ppb solution (2% $HNO_3$) containing the NIST

SRM 981 Pb standard is aspirated continuously and the absolute count rates are recorded at different operating voltage settings for IC0, IC1, and IC2 sequentially. Typical electron multiplier percent yield curves are shown in Fig. 14-5 and these are characterized by 'horizontal operating plateaus' at higher voltage settings for each ion counter. As outlined by Richter *et al*. (2001), the optimal high voltage setting is the area corresponding to the initial segment of the horizontal plateau, or just past the 'knee' of the curve (Fig. 14-5).

The relative gain between IC0 and IC1 (measure $^{207}$Pb and $^{206}$Pb ion signals, respectively; Table 14-2) has been demonstrated to be extremely linear over a wide range of absolute count rates (Simonetti *et al*. 2005). However, the electron multipliers can become 'non-linear' after prolonged use and at higher operating voltages, the 'linearity' associated with the gain of any individual electron multiplier is lost. Therefore, it is imperative to monitor relative gains of the electron multipliers especially when operating at higher amplifier voltage. The electron multipliers within the NuPlasma instrument at the University of Alberta have experienced extensive use since October 2003 and after four years are now at operating voltages of –2675, –2600, and –2075 for IC0, IC1, and IC2, respectively (starting operating voltages were approximately –2000).

It is also extremely important to monitor the relative gain between electron multiplier IC1 and Faraday collector EX–H, which measure the $^{206}$Pb and $^{238}$U ion signals, respectively (Table 14-2). Obviously, an accurate assessment of the relative gain between these two detectors is crucial for determining $^{206}$Pb/$^{238}$U values and hence the degree of concordance of mineral standards and unknowns (by comparing the Pb/U and $^{207}$Pb/$^{206}$Pb values). In other words, the relationship (if any) between the absolute $^{206}$Pb ion signal recorded on IC1 and calculated $^{206}$Pb/$^{238}$U has to be determined; the calibration procedure described below is conducted subsequent the adjustment and increase of the operating voltages for each electron multiplier as described above.

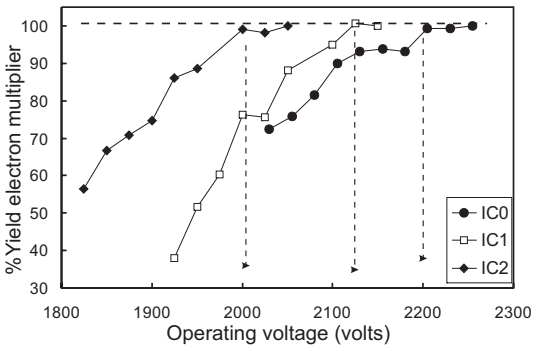


FIG. 14-5. Diagram illustrating the typical %yield for electron multipliers IC0, IC1, and IC2 *versus* the operating voltage setting. The dashed arrows respresent the optimal operating voltage setting located at the initial segment of the 'horizontal operating plateau'.

There are two possible methods for investigating the relationship between the absolute $^{206}$Pb ion signal and measured $^{206}$Pb/$^{238}$U values. One approach is to prepare gravimetric solutions with variable concentrations of Pb and U such that the $^{206}$Pb ion signal recorded spans the typical range of signal intensities measured in unknown zircons (*i.e.*, between >1 x $10^5$ and <2 x $10^6$ cps). This approach is similar to that described by Hoffmann *et al*. (2005). An alternative method would involve repeated laser ablation analysis of a well characterized internal zircon standard that yields concordant ages but contains variable Pb and U contents. However, in practice the latter option is currently not feasible because well established, international zircon standards (*e.g.*, BR266, 91500) are characterized by relatively homogeneous Pb and U abundances; thus we have investigated the electron multiplier IC1–EX-H Faraday calibration using the first option.

A 100 ml gravimetric 'shelf' solution (in 2% $HNO_3$) was established containing Pb (NIST SRM 981) – natural U – Tl (NIST SRM 997) with concentrations of 2 ppb, 25 ppb, and 2 ppb, respectively. The solutions were analyzed using an introduction set up identical to that employed for laser ablation analysis; *i.e.*, laser ablation cell sample-out line (flushed with He gas) is 'Y'–connected to DSN-100 (desolvating nebulizer, Nu Instruments) sample-out line (Simonetti *et al*. 2005). This gravimetric 'shelf' solution was subsequently diluted in different proportions in order to vary the absolute $^{206}$Pb ion signal. The measured $^{206}$Pb/$^{238}$U values were then recorded and the results are shown in Figure 14-6. The measured $^{206}$Pb/$^{238}$U values (Fig. 14-6a) and deviation relative to the stoichiometric value of the solution (Fig. 14-6b) are plotted as a function of the absolute $^{206}$Pb ion signal. The data in both plots define well constrained arrays ($r^2$ ~0.97) that can be described by logarithmic equations. Of importance, the deviation is confined to <3% for $^{206}$Pb ion signal intensities between ~2.5 x $10^5$ and 1.5 x $10^6$ cps,

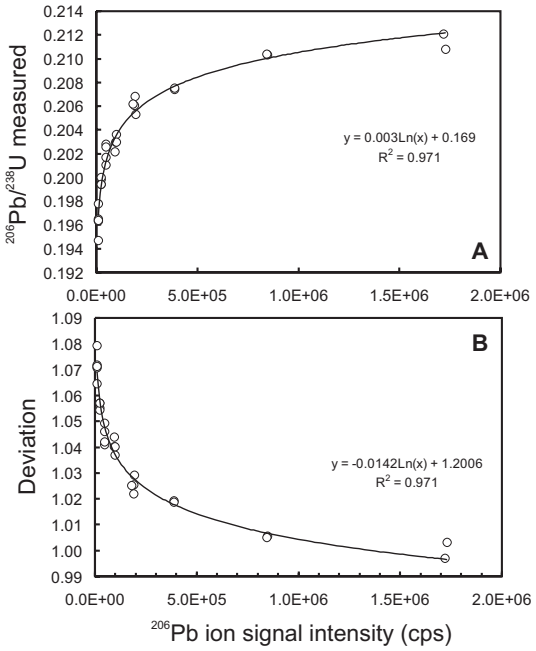


FIG. 14-6. Plots of measured $^{206}Pb/^{238}U$ values (**A**) and deviation factor relative to stoichiometric value (**B**) *versus* $^{206}Pb$ ion signal intensity in counts per second (cps) obtained for solution mode analyses of a gravimetric shelf solution containing natural U, Pb (NIST SRM 981) and Tl (NIST SRM 997). The same solution was analyzed consecutively with repeated dilutions using 2%$HNO_3$.

with an increase occurring particularly at extremely low $^{206}Pb$ ion signal (<5 x $10^4$ cps). The equation defined in Fig. 14-6b can then be inserted into an off-line excel data reduction spreadsheet as a correction factor for the $^{206}Pb/^{238}U$ values (and $^{207}Pb/^{235}U$) as a function of the absolute $^{206}Pb$ ion signal. However, as explained in the Simonetti *et al*. (2005) study, the $^{207}Pb/^{235}U$ values reported are not those measured due to the very small $^{235}U$ ion signals but instead are calculated by multiplying the $^{207}Pb/^{206}Pb$ and $^{206}Pb/^{238}U$ (both mass bias and blank corrected), and the natural $^{238}U/^{235}U$ value of 137.88 (Steiger & Jäger 1975).

***Standard ablation cell versus the 'SuperCell™'– Ion signal decay + 'washout' and 'sensitivity'.*** Other important features to investigate are the signal 'decay' (relative to Faraday collector EX-H) and particle 'wash-out' times associated with the measurement of the $^{238}U$ ion signal. This evaluation is critical for certain LA–MC–ICP–MS geochronological applications, such as dating a large population of detrital zircon (*e.g.*, Lemieux *et al*. 2007). For such 'high volume' sample applications, it is important to determine the minimum amount of time required to wait in between individual analyses in order to avoid cross-contamination.

In recent years, use of the standard laser ablation cell with the UP213 system at the University of Alberta was slightly modified in that 1-inch diameter clear plastic inserts were placed within the central hole of the sample mount holder. This is done primarily to eliminate the 'dead' volume located beneath an epoxy mount or thin section being analyzed and hence reduce re-equilibration time (for plasma conditions) subsequent sample exchanges. This practice also increased sensitivity by a factor of at least 2, such that the sensitivity of the standard cell is similar to that obtained with the SuperCell™ design (discussed later; see Fig. 14-8). Thus, the comparative tests described below between the standard and SuperCell™ ablation cassettes were conducted with the 1-inch plastic inserts placed in the former.

Figure 14-7 displays the results of combined 'wash-out' + 'decay' patterns recorded on Faraday collector EX-H (Fig. 14-7a) and electron multiplier IC1 (Fig. 14-7b) subsequent to the standard 30 seconds of laser ablation analysis for various zircon standards (with variable U contents). The in-house zircon standard LH94-15 was ablated using the SuperCell™, whereas the remaining zircon standards were analyzed using the standard laser cell. The analyses of LH94-15 yielded a 4-fold variation in $^{238}U$ ion signal intensities (Fig. 14-7a) with the decay (+ washout) times averaging ~15 seconds. Decay times for ablation runs of zircon standards BR266 (Stern & Amelin 2003) and 91500 (Wiedenbeck *et al*. 1995) using the standard laser ablation cell also yielded comparable decay (+ washout) times of ~15 seconds; this despite the fact that 3 to 10 times more $^{238}U$ ion signal (*i.e.*, >0.2 volts) was recorded during the ablation of BR266 using a 40 μm spot size (Fig. 14-7). Decay (+ washout) patterns for the $^{206}Pb$ ion signals measured on IC1 were also similar for both types of ablation cells and accomplished in <10 seconds (Fig. 14-7b); thus a little faster than that observed for $^{238}U$ (Fig. 14-7a). Thus, the results shown in Fig. 14-7 indicate that both types of laser ablation cells are characterized by similar washout times. Moreover, 15 seconds is much shorter than the total amount of time taken in between consecutive zircon analyses (~1 minute). The latter is the time required to displace the cell to the position of the subsequent

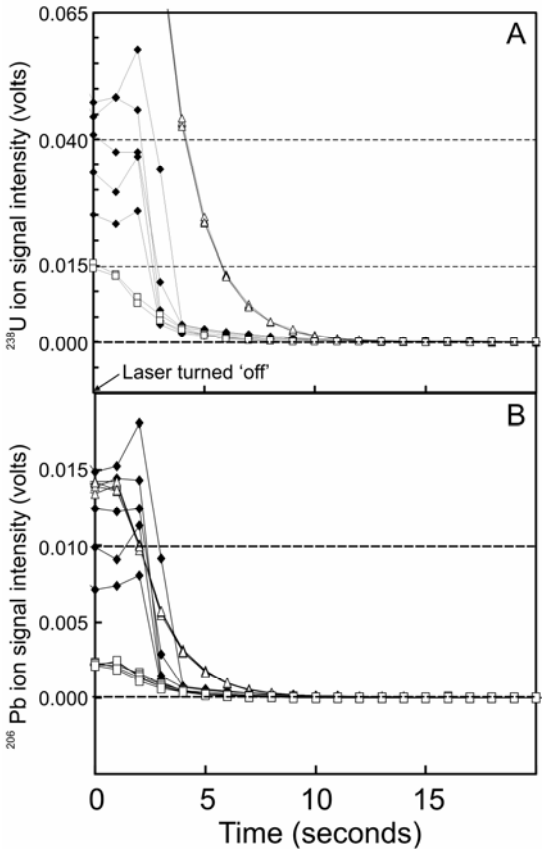


FIG. 14-7. Diagram illustrates the variation in $^{238}$U (**A**) and $^{206}$Pb (**B**) ion signals *versus* time (seconds) measured on Faraday bucket EX-H and electron multiplier IC1, respectively, subsequent to switching 'off' the laser unit following the completion of a 30-second ablation analysis of various zircon standards. Filled diamonds = ablation runs of internal zircon standard LH94-15 using the SuperCell™; Open triangles = ablation runs of international zircon standard BR266 using the standard cell; Open squares = ablation runs of international zircon standard 91500 using the standard cell.

grain to be analyzed and precisely locate the analysis spot within the grain with the aid of either back-scattered electron or cathodoluminescent images.

The 'sensitivity' or ion signal yield was also investigated for both the standard ablation cassette and SuperCell™ with repeated measurements of zircon standard BR266 analyzed using identical instrument conditions. Despite having conducted the tests during different analytical sessions, any bias with regards to differing sensitivity resulting from other instrument parameters (*e.g.*, cones, quartz torch assembly) is eliminated by normalization of the $^{238}$U and $^{206}$Pb to equivalent $^{205}$Tl ion signals (Fig. 14-8). The latter is introduced via the desolvating nebuliser (DSN-100) in solution mode and thus independent of the laser ablation conditions. The laser ablation results shown in Fig. 14-8 indicate that the SuperCell™ yields slightly higher ion signals for both Pb and U compared to the standard cell. However, compared to the standard cell laser ablation runs, the analyses conducted with the SuperCell are characterized by slightly less stable ion signals, in particular during the last 5 seconds of analysis (Fig. 14-8). Despite this feature, the results from the laser ablation runs obtained with the SuperCell™ in general yield measured Pb/Pb and Pb/U values with similar internal precision relative to those obtained with the standard cell (examples provided in 'Results' section below). Given the overall similarity in performances relative to ion signal yield and ion signal decay (+washout) times for the standard and SuperCell™ cassettes, both were utilized in conducting the laser ablation analysis of unknown accessory minerals within petrographic thin sections.

**Petrographic examination, measurement protocol and data reduction**

Prior to any analytical session, the petrographic thin sections to be investigated are carefully examined. This serves both to locate the accessory minerals and evaluate the paragenesis of the grains in the context of deformational fabrics and other salient features in the section. Petrographic examination is typically followed by backscattered

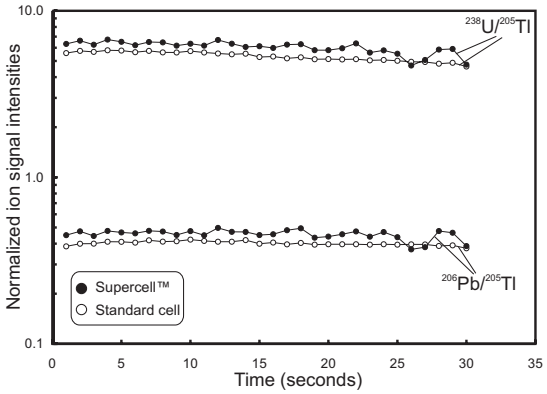


FIG. 14-8. A plot of log $^{206}$Pb/$^{205}$Tl and $^{238}$U/$^{205}$Tl values *versus* time (seconds) for ablation runs of BR266 (*i.e.*, same epoxy mount) using both the standard ablation cell and SuperCell™ and identical instrument conditions. The curves represent average values of three individual measurements.

electron imaging of the selected grains by electron microprobe. This step highlights compositional zonation or metamict areas within the grains and thereby enables optimal citing of spots for isotopic analysis. The carbon coat required for BSE imaging is subsequently removed and areas containing accessory minerals to be analyzed are circled with a marker pen (Fig. 14-9).

The following description of the LA–MC–ICP–MS analytical protocol is summarized from more detailed descriptions in Simonetti *et al*. (2005, 2006). At the start of each analytical session, the Faraday-ion counter bias is determined using a mixed 0.4 ppb standard solution of Pb (NIST SRM 981) and Tl (NIST SRM 997). The Faraday-multiplier calibration is calculated using a two sequence acquisition cycle, where the $^{207}Pb/^{206}Pb$ (= 0.914585; Todt *et al*. 1996) is measured on the IC1 (ion counter #1)–L3 (Faraday) combination. The IC0 (ion counter #0) and IC2 (ion counter #2) calibrations are determined against the IC1 bias using the measured $^{207}Pb/^{206}Pb$ and $^{206}Pb/^{204}Pb$ (=16.9356; Todt *et al*. 1996) values, respectively. This approach is similar to that adopted in previous isotopic studies involving MC–ICP–MS instruments equipped with multiple ion-counting devices (Taylor *et al*. 2003). A routine U–Pb analysis consists of a 30 second blank measurement (He + Ar gases + 2%$HNO_3$ acid) prior to the commencement of the laser ablation. Background levels of $^{206}Pb$ and $^{207}Pb$ are typically less than 200 cps each, and the combined $^{204}Pb+^{204}Hg$ background ion signal is generally <1000 cps; these background ion signal intensities are extremely stable and reproducible during the course of an analytical session. The ablated particles are transported into the sample-out line (Saint-Gobain Tygon® tubing) with a He carrier gas and mixed with nebulized Tl via a 'Y'-connection located just prior to the torch box. The simultaneous introduction of laser-induced and dried solution aerosols was developed several years ago as an alternative calibration method for various laser ablation-ICP–MS instruments (*e.g.*, Chenery & Cook 1993, Günther *et al*. 1997). A NIST SRM 997 Tl isotopic standard solution (1 ppb in 2% $HNO_3$) is nebulized using a DSN-100 desolvating introduction system (Nu Instruments, UK) and aspirated (free aspiration mode) into the

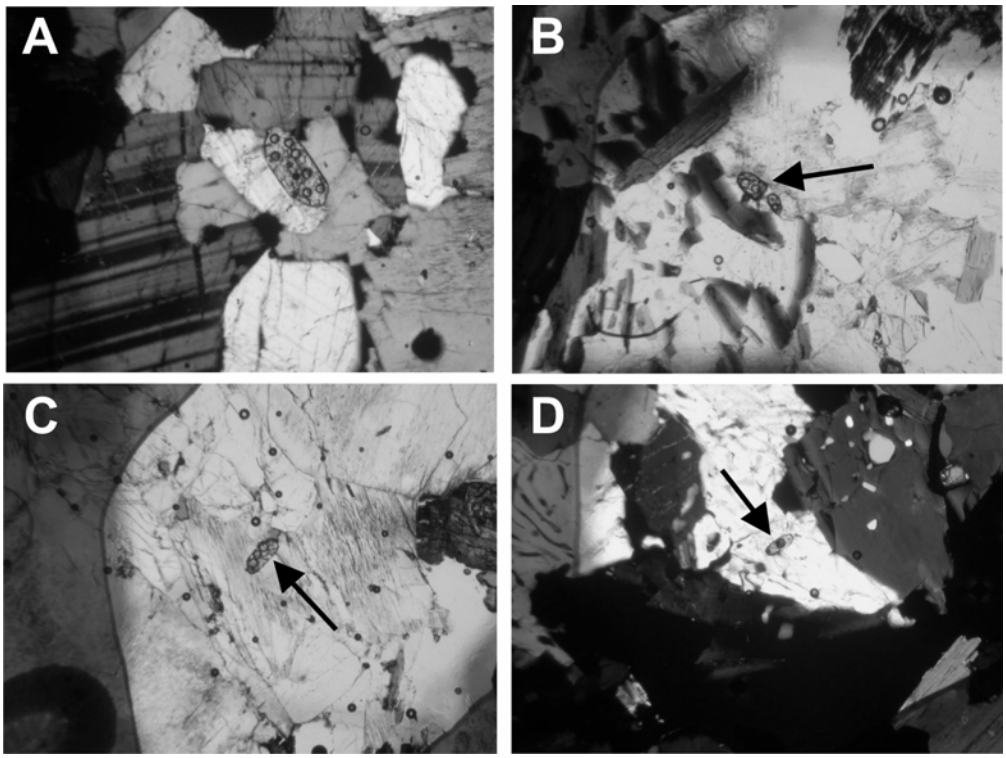


FIG. 14-9. Photomicrographs of areas delineated with a blue marker pen containing zircon in petrographic thin section of sample 243-336E (see main text for petrographic description). The zircon grains contain laser ablation pits of 40 μm in diameter and the corresponding U–Pb isotope data are shown in Figure 14-11 and listed in Table 14-3 for zircon grains labeled #1 (**A**), #2 (**B**), #3 (**C**), and #4 (**D**). Please note that zircon #2 (B) and #4 (D) indicate inherited ages of *ca*. 2.5 Ga.

ICP source during the laser ablation run. Both the spray chamber and desolvating membrane of the DSN-100 are heated to 110ºC, with the Ar (Argon) flow rate set to 0.3 L $min^{-1}$ and 2.7–3.2 L $min^{-1}$ for the spray chamber and desolvating membrane, respectively. The measured Pb/U values are positively correlated with the membrane gas flow rate (Simonetti *et al*. 2005), and this is an expected result since varying the mixture of He and Ar within the main sample-out tube will most certainly change the plasma characteristics (*e.g.*, Eggins *et al*. 1998, Horn *et al*. 2000). The measured $^{205}Tl/^{203}Tl$ value is used to correct the measured Pb isotope ratios for instrumental mass bias using the reference value of 2.3871 (Dunstan 1980). The analytical protocol adopted here involving a Tl-doping method for monitoring of instrumental mass bias yields 2σ relative standard deviations that are 0.3 to 1% ($^{207}Pb/^{206}Pb$) and 1 to 3% ($^{206}Pb/^{238}U$ and $^{207}Pb/^{235}U$). Figure 14-10 illustrates the average and typical external reproducibility (2σ level) obtained for the $^{207}Pb/^{206}Pb$ ratio during repeated measurement of the in-house external zircon standard LH94-15 (described below) using the Tl-doped protocol described here during an analytical session. Simonetti *et al*. (2005) investigated the external reproducibility for both Tl-doped and non-Tl-doped (*i.e.*, mass bias controlled solely by external matrix-matched standard) methods and these yielded 0.5% to 0.34% (2σ level), respectively; this is entirely in agreement with the external reproducibility (0.32%; 2σ level) obtained for the analyses shown in Fig. 14-10. Moreover, the average $^{207}Pb/^{206}Pb$ of 0.11191 ± 0.00036 shown in Fig. 14-10 is within uncertainty to the ID–TIMS value (0.111869; Ashton *et al*. 1999) and validates the analytical method employed here.

Correction for LIEF (laser induced element fractionation) during a single laser ablation session of unknowns using the Tl-doping method was achieved by analysis of the matrix-matched 'external' standards of zircon (BR266 – Stern & Amelin 2003; 91500 – Wiedenbeck *et al*. 1995; LH94–15 – Ashton *et al*. 1999), and monazite (Western Australia and Madagascar – Heaman *et al*., unpublished ID–TIMS data). The measured Pb/U values for the unknowns are compared to those obtained for their respective standards (ablated using identical run conditions) at the start of an analytical session, and normalization (= measured value/'true' value) factors are determined. Analytical uncertainties associated with the $^{207}Pb/^{206}Pb$ and Pb/U values for individual analyses were propagated relative to the external reproducibility obtained for the external zircon standard and followed the procedure outlined in Horstwood *et al*. (2003). Subsequent to the study by Simonetti *et al*. (2006), the uncertainty associated with the common Pb correction based on the calculation of the absolute count rate of $^{204}Pb$ (cps; Simonetti *et al*. 2005) is propagated as part of the total error associated with the $^{207}Pb/^{206}Pb$ values. This error propagation is significant primarily when accessory minerals are characterized by a high amount of common Pb, or yield relatively low Pb ion signals (*e.g.*, young zircon <200 Ma old). A more detailed discussion of the error propagation associated with the common Pb correction is given in Horstwood *et al*. (2008). As outlined in Simonetti *et al*. (2005), the true amount of common $^{204}Pb$

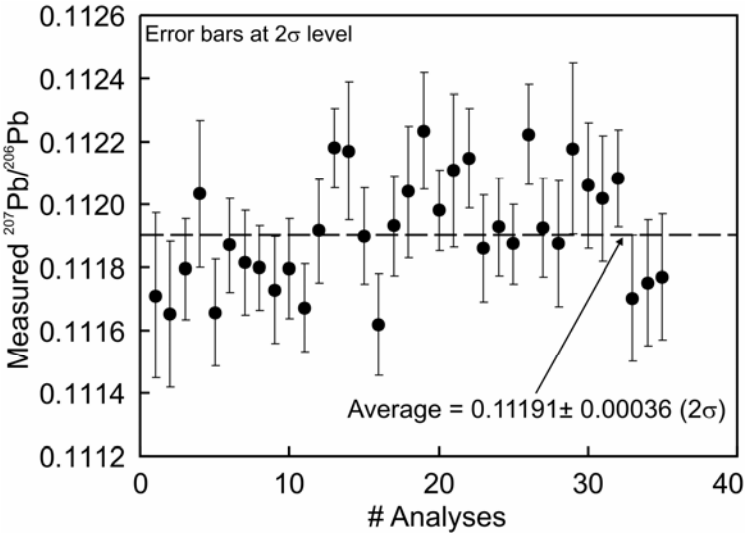


FIG. 14-10. Plot of measured $^{207}Pb/^{206}Pb$ *versus* analysis number (n= 35) for repeated laser ablation measurements of the in-house LH94-15 zircon standard during a single analytical session (~9 hours) using the Tl-doped method to monitor instrumental mass bias. The average $^{207}Pb/^{206}Pb$ value of 0.11191 ± 0.00036 (2σ) is indistinguishable compared to the accepted ID–TIMS value of 0.111869 ± 0.00006 (2σ; Ashton *et al*. 1999).

present within the zircon (or monazite) as opposed to $^{204}$Hg possibly produced during the ablation process is evaluated off-line by graphical means using a plot of total 204 ion signal intensity *versus* the measured $^{207}$Pb/$^{206}$Pb ratio. In theory, if the 204 ion signal is derived entirely from common Pb *intrinsic* to the zircon, then one should obtain a horizontal line on such a plot. A negative correlation between the total 204 ion signal and measured $^{207}$Pb/$^{206}$Pb diagram most likely indicates the presence of $^{204}$Hg produced during the ablation process (unless of course a common Pb-bearing mineral inclusion was ablated during the analysis). In the case of the latter situation, the true amount of $^{204}$Pb intrinsic to the mineral is taken to be zero.

The data presented in the 'Results' section have been obtained using all of the calibration procedures and data reduction protocols outlined in this paper and those described in Simonetti *et al*. (2005, 2006). The correlation coefficients ('rho' values) for the Pb/U ratios were calculated according to the equations defined in Ludwig (2003).

## RESULTS

### Background

U–Pb geochronology of uranium-bearing accessory minerals is based on the radioactive decay schemes of the two unstable uranium nuclides, $^{238}$U (decay constant = 1.55125 x $10^{-10}$ $yr^{-1}$) and $^{235}$U (decay constant = 9.8485 x $10^{-10}$ $yr^{-1}$; both constants from Jaffey *et al*., 1971); these decay through a series of intermediate daughter products to the stable daughter isotopes of $^{206}$Pb and $^{207}$Pb, respectively. Thus, two independent apparent ages (dates) can be obtained from each geochronometer, *i.e.*, $^{206}$Pb/$^{238}$U and $^{207}$Pb/$^{235}$U, for every isotopic analysis of a U-bearing accessory mineral (*e.g.*, zircon, monazite, titanite, baddeleyite, perovskite). If the mineral being analyzed has remained 'closed' with regards to either gain or loss of parent and/or daughter isotopes since its time of formation, then the two Pb/U chronometers shall yield identical ages. This is then referred to as a 'concordant' analysis or age. A plot of $^{206}$Pb/$^{238}$U *vs*. $^{207}$Pb/$^{235}$U is referred to as a 'concordia' diagram and illustrates the 'concordia' curve; the latter represents the locus of identical or '*concordant*' Pb/U ages throughout geologic time (*e.g.*, Fig. 14-11). Analyses of accessory minerals that have undergone gain or loss of either Pb and/or U typically do not yield concordant analyses (*i.e.*, plot on the concordia curve) but rather define colinear arrays on the

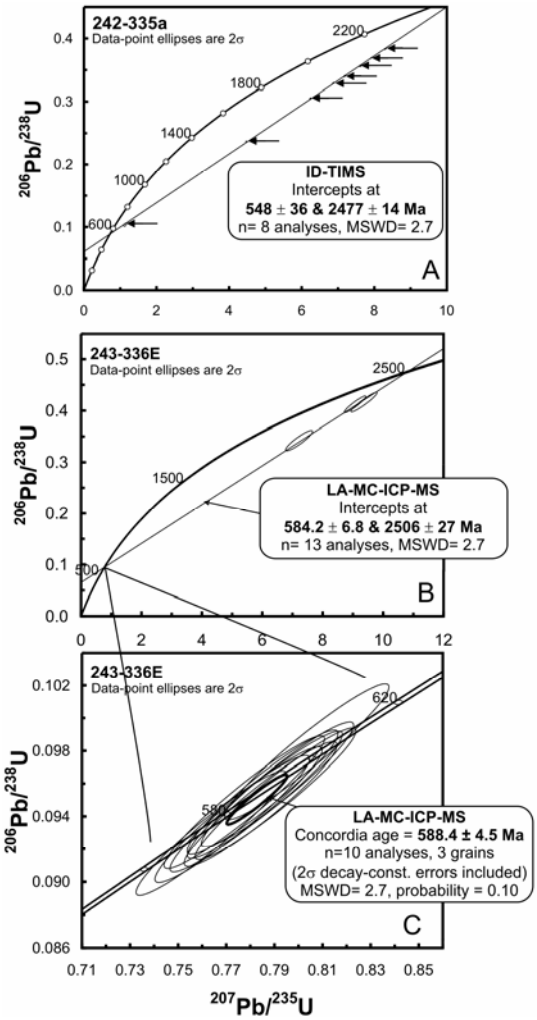


FIG. 14-11. Concordia plots that contain the U–Pb age results for (**A**) sample 242-335A (ID–TIMS results) with arrows indicating position of individual analyses (Table 14-3); (**B**) sample 243-336E obtained by LA–MC–ICP–MS; and (**C**) enlarged view of lower intercept region from plot shown in B. These concordia plots and those shown in subsequent diagrams were constructed with Isoplot version 3.00 (Ludwig 2003).

concordia plot; these analyses are referred to as '*discordant*' and the best-fit line through these data is called a '*discordia*' or mixing line (*e.g.*, Fig. 14-11a, b). Both the upper and lower intercepts between the discordia line and the concordia curve are interpreted to represent ages of geological events, such as time of magma emplacement and much later metamorphic event (*e.g.*, Fig. 14-11a, b). In subsequent sections, several ages or dates are also reported as '*weighted mean*' $^{207}$Pb/$^{206}$Pb or $^{206}$Pb/$^{238}$U ages as calculated by Isoplot version 3.0

(Ludwig, 2003); this algorithm takes into account the scatter (MSWD – mean square weighted deviation). If the latter is not much greater than 1, then the weighted mean is determined by weighting each data point by its inverse variance and associated uncertainty. In contrast, a 'concordia age' is the most probable age for an analysis (or weighted mean) on a concordia diagram, where the true location of the analysis is assumed to fall precisely on the concordia curve (Ludwig, 2003).

***Zircon – Cardamom Hills Massif, southern India***

Samples 243-336E and 247-339C are from the 'Cardamom Hills' massif, one of the large charnockite massifs of the southern Indian granulite terrain. The massif is characterized by at least three different types of charnockite that formed at different times and have variable major- and trace-element compositions.

Sample 243-336E is a late stage felsic dyke that clearly cross-cuts the foliation in one of the charnockite/enderbite units. The dyke is coarse grained and consists of perthitic alkali feldspar, quartz, subordinate plagioclase, biotite and retrogressed orthopyroxene. Accessory minerals include coarse grained zircon and abundant Th-rich, U-poor monazite. The U–Pb ID–TIMS results for eight small multi-grain and single zircon grains (Table 14-3) in a broadly similar charnockite (242-335A) from nearby outcrops define a discordia line that is interpreted to indicate that the rocks which host the dyke formed at *ca*. 2.5 Ga and experienced a Pan-African overprint at *ca*. 550 Ma (Fig. 14-11a).

A petrographic thin section of sample 243-336E was analyzed using the standard laser ablation cell and the Pb/U LIEF was monitored and bracketed by repeated analysis of the in-house zircon standard LH94-15 (Ashton *et al*. 1999; Fig. 14-2). The LA–MC–ICP–MS U–Pb dating results for 4 zircon grains analyzed at 40 micrometres spatial resolution are listed in Table 14-3 and shown in Fig. 14-11b. These four analyses plot along an identical mixing line with overlapping upper and lower intercept ages compared to the ID–TIMS data for charnockite 242-335A (Fig. 14-11a). In addition, 10 analyses from three zircon grains in sample 243-336E yielded a precise concordant age of 588.4 ± 4.5 Ma (2σ; Fig. 14-11c), which we interpret to be the crystallization age of the felsic dyke.

Sample 247-339C is a very coarse grained patch or pod (partial melt?) hosted within the finer grained charnockite. It comprises alkali feldspar, quartz, and plagioclase along with large grains of orthopyroxene, which in some cases have rims of hornblende; accessory minerals include apatite, Fe-Ti oxides and zircon. U–Pb ID–TIMS analysis of three zircon fractions from a nearby charnockite of similar major- and trace-element composition (188-281a, b) to the host charnockite of sample 247-339C yielded a discordia line with an upper intercept ~820 Ma and a lower intercept ~520 Ma (Table 14-3; Fig. 14-12a).

A petrographic thin section of sample 247-339C was analyzed using the SuperCell™ laser ablation cassette. As mentioned earlier, one advantage of this cell compared to the standard ablation cassette is the capacity to house zircon standards mounted on glass slides simultaneously and placed adjacent to the thin section to be analyzed (in the central area). The Pb–U 'LIEF' was monitored by intermittent analysis of the in-house zircon standard LH94-15 grains mounted on a glass slide (~0.5 cm x ~0.5 cm). The LA–MC–ICP–MS results for 17 analyses of 6 zircon grains

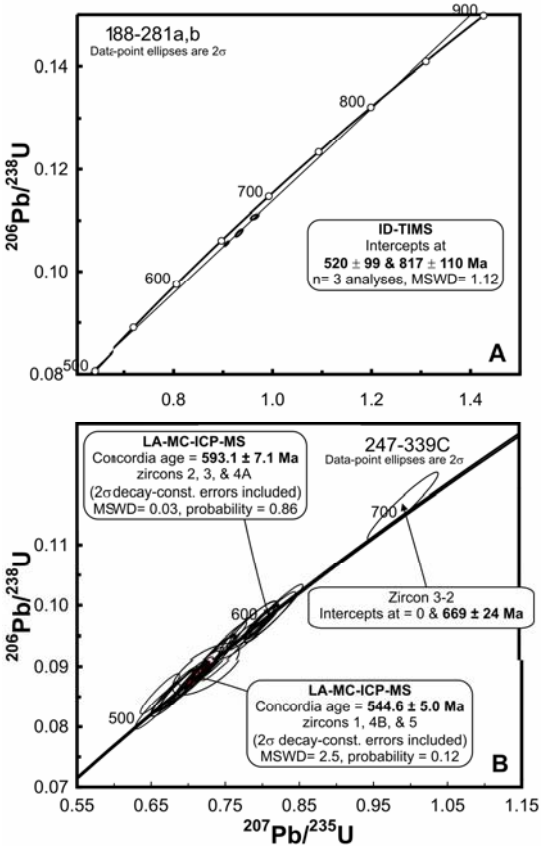


FIG. 14-12. Concordia plots illustrating the U–Pb age results for (A) sample 188-281a, b (by ID–TIMS); (B) LA–MC–ICP–MS results for sample 247-339C.

TABLE 14-3. U-PB RESULTS FOR ZIRCON AND MONAZITE

| Anal.# | Spot size (μm) | $^{206}$Pb cps | $^{206}$Pb/$^{204}$Pb | $^{207}$Pb/$^{206}$Pb | 2σ uncert. | $^{207}$Pb/$^{235}$U | 2σ uncert. | $^{206}$Pb/$^{238}$U | 2σ uncert. | 'rho' | $^{207}$Pb/$^{206}$Pb Age (Ma) | $^{207}$Pb/$^{206}$Pb 2σ uncert. | $^{206}$Pb/$^{238}$U Age (Ma) | $^{206}$Pb/$^{238}$U 2σ uncert. | % Disc. |
|---|---|---|---|---|---|---|---|---|---|---|---|---|---|---|---|
| 243-336E | | | | | | | | | | | | | | | |
| zircon 4-1 | 40 | 167683 | 3422 | 0.16321 | 0.00194 | 9.3659 | 0.3556 | 0.4164 | 0.0156 | 0.950 | 2489 | ±20 | 2244 | ±84 | 9.8 |
| zircon 2-2 | 40 | 544941 | 16513 | 0.15951 | 0.00174 | 9.0678 | 0.2942 | 0.4121 | 0.0133 | 0.943 | 2450 | ±18 | 2225 | ±72 | 9.2 |
| zircon 2-1 | 40 | 327641 | 7446 | 0.15345 | 0.00320 | 7.2177 | 0.3653 | 0.3420 | 0.0161 | 0.912 | 2385 | ±35 | 1896 | ±89 | 20.5 |
| zircon 1-1 | 40 | 294897 | infinite | 0.06001 | 0.00063 | 0.7861 | 0.0263 | 0.0953 | 0.0032 | 0.951 | 604 | ±23 | 587 | ±20 | 2.8 |
| zircon 1-2 | 40 | 280451 | infinite | 0.05969 | 0.00063 | 0.7782 | 0.0259 | 0.0944 | 0.0031 | 0.950 | 592 | ±23 | 582 | ±19 | 1.8 |
| zircon 1-3 | 40 | 442333 | infinite | 0.05942 | 0.00063 | 0.7775 | 0.0273 | 0.0949 | 0.0033 | 0.954 | 583 | ±23 | 584 | ±20 | -0.3 |
| zircon 1-4 | 40 | 482446 | infinite | 0.05947 | 0.00062 | 0.7637 | 0.0255 | 0.0930 | 0.0031 | 0.952 | 584 | ±22 | 573 | ±19 | 1.9 |
| zircon 1-5 | 40 | 394251 | infinite | 0.05986 | 0.00064 | 0.7913 | 0.0259 | 0.0959 | 0.0031 | 0.947 | 598 | ±23 | 591 | ±19 | 1.3 |
| zircon 1-6 | 40 | 389059 | infinite | 0.05969 | 0.00063 | 0.7851 | 0.0256 | 0.0955 | 0.0031 | 0.948 | 592 | ±23 | 588 | ±19 | 0.8 |
| zircon 1-7 | 40 | 291868 | infinite | 0.05983 | 0.00065 | 0.7843 | 0.0260 | 0.0947 | 0.0031 | 0.947 | 598 | ±23 | 584 | ±19 | 2.3 |
| zircon 3-1 | 40 | 553897 | infinite | 0.05957 | 0.00062 | 0.8034 | 0.0280 | 0.0979 | 0.0034 | 0.955 | 588 | ±23 | 602 | ±21 | -2.5 |
| zircon 3-2 | 40 | 455179 | infinite | 0.05976 | 0.00062 | 0.7905 | 0.0273 | 0.0954 | 0.0033 | 0.955 | 595 | ±22 | 587 | ±20 | 1.3 |
| zircon 3-3 | 40 | 307897 | infinite | 0.05972 | 0.00064 | 0.7725 | 0.0263 | 0.0938 | 0.0032 | 0.950 | 594 | ±23 | 578 | ±20 | 2.6 |
| 247-339C | | | | | | | | | | | | | | | |
| zircon 2-1 | 40 | 230297 | infinite | 0.06024 | 0.00067 | 0.8138 | 0.0284 | 0.0981 | 0.0034 | 0.949 | 612 | ±24 | 603 | ±21 | 1.5 |
| zircon 2-2 | 40 | 193247 | 32208 | 0.05956 | 0.00079 | 0.7893 | 0.0274 | 0.0967 | 0.0032 | 0.924 | 588 | ±29 | 595 | ±20 | -1.3 |
| zircon 3-1 | 40 | 226262 | infinite | 0.06036 | 0.00069 | 0.8190 | 0.0321 | 0.0988 | 0.0038 | 0.958 | 616 | ±25 | 607 | ±24 | 1.5 |
| zircon 4A-1 | 40 | 182137 | 18214 | 0.05939 | 0.00106 | 0.7845 | 0.0333 | 0.0960 | 0.0038 | 0.908 | 581 | ±39 | 591 | ±23 | -1.6 |
| zircon 4A-2 | 40 | 1005883 | infinite | 0.05961 | 0.00062 | 0.7571 | 0.0317 | 0.0925 | 0.0039 | 0.969 | 590 | ±22 | 570 | ±24 | 3.3 |
| zircon 4B-1 | 40 | 808141 | infinite | 0.05852 | 0.00060 | 0.7356 | 0.0262 | 0.0913 | 0.0032 | 0.959 | 549 | ±22 | 563 | ±20 | -2.6 |
| zircon 4B-2 | 40 | 899776 | 449888 | 0.05845 | 0.00059 | 0.7440 | 0.0316 | 0.0925 | 0.0039 | 0.971 | 547 | ±22 | 570 | ±24 | -4.3 |
| zircon 4B-3 | 40 | 942588 | 188518 | 0.05852 | 0.00060 | 0.7303 | 0.0288 | 0.0906 | 0.0036 | 0.966 | 549 | ±22 | 559 | ±22 | -1.8 |
| zircon 4B-4 | 40 | 507954 | 126988 | 0.05840 | 0.00061 | 0.7068 | 0.0247 | 0.0879 | 0.0031 | 0.955 | 545 | ±23 | 543 | ±19 | 0.4 |
| zircon 5-1 | 40 | 113735 | 28434 | 0.05789 | 0.00084 | 0.6822 | 0.0265 | 0.0856 | 0.0032 | 0.928 | 526 | ±32 | 530 | ±20 | -0.8 |
| zircon 5-2 | 40 | 139044 | infinite | 0.05886 | 0.00072 | 0.7371 | 0.0254 | 0.0913 | 0.0031 | 0.936 | 562 | ±27 | 563 | ±19 | -0.2 |
| zircon 1-1 | 40 | 167479 | infinite | 0.05833 | 0.00065 | 0.6936 | 0.0264 | 0.0871 | 0.0033 | 0.956 | 542 | ±25 | 538 | ±20 | 0.7 |
| zircon 1-2 | 40 | 165637 | infinite | 0.05797 | 0.00067 | 0.7159 | 0.0285 | 0.0890 | 0.0035 | 0.958 | 528 | ±25 | 549 | ±22 | -4.0 |
| zircon 1-3 | 40 | 121963 | infinite | 0.05785 | 0.00067 | 0.6893 | 0.0250 | 0.0864 | 0.0031 | 0.949 | 524 | ±25 | 534 | ±19 | -1.9 |
| zircon 1-4 | 40 | 172343 | infinite | 0.05850 | 0.00067 | 0.7158 | 0.0243 | 0.0890 | 0.0030 | 0.942 | 548 | ±25 | 549 | ±18 | -0.2 |
| zircon 3-2 | 40 | 864436 | 9196 | 0.06209 | 0.00072 | 0.9932 | 0.0390 | 0.1164 | 0.0045 | 0.956 | 677 | ±25 | 710 | ±28 | -4.9 |
| 242-335A (TIMS) | | | | | | | | | | | | | | | |
| 1z, col. abr. | | | | 0.07935 | 0.00194 | 1.13100 | 0.0312 | 0.10337 | 0.0021 | 0.508 | 1181 | ±48 | 634 | 13 | 46.3 |
| 2z, col. abr. | | | | 0.13677 | 0.00018 | 4.46800 | 0.0138 | 0.23693 | 0.0007 | 0.905 | 2187 | ±2 | 1371 | 4 | 37.3 |
| 3z, col. abr. | | | | 0.15529 | 0.00024 | 7.62443 | 0.0242 | 0.35610 | 0.0011 | 0.876 | 2405 | ±3 | 1964 | 6 | 18.4 |
| 4z, col. abr. | | | | 0.15552 | 0.00011 | 7.91027 | 0.0231 | 0.36890 | 0.0011 | 0.973 | 2408 | ±1 | 2024 | 6 | 15.9 |
| 5z, col. abr. | | | | 0.15725 | 0.00012 | 8.31274 | 0.0238 | 0.38340 | 0.0011 | 0.964 | 2426 | ±1 | 2092 | 6 | 13.8 |
| 6z, col. abr. | | | | 0.15321 | 0.00033 | 7.18704 | 0.0277 | 0.34023 | 0.0012 | 0.827 | 2382 | ±4 | 1888 | 6 | 20.8 |
| 7z, col. abr. | | | | 0.51270 | 0.00032 | 6.86820 | 0.0191 | 0.32929 | 0.0009 | 0.975 | 4278 | ±1 | 1835 | 5 | 57.1 |
| 8z, col. abr. | | | | 0.14804 | 0.00012 | 6.23494 | 0.0173 | 0.30546 | 0.0009 | 0.959 | 2323 | ±1 | 1718 | 5 | 26.0 |
| 1z, col. abr. | | | | 0.07935 | 0.00194 | 1.13100 | 0.0312 | 0.10337 | 0.0021 | 0.508 | 1181 | ±48 | 634 | 13 | 46.3 |

TABLE 14-3 (CONTINUED). U-PB RESULTS FOR ZIRCON AND MONAZITE

| Anal.# | Spot size (μm) | $^{206}$Pb cps | $^{206}$Pb/$^{204}$Pb | $^{207}$Pb/$^{206}$Pb | 2σ uncert. | $^{207}$Pb/$^{235}$U | 2σ uncert. | $^{206}$Pb/$^{238}$U | 2σ uncert. | 'rho' | $^{207}$Pb/$^{206}$Pb Age (Ma) | 2σ uncert. | $^{206}$Pb/$^{238}$U Age (Ma) | 2σ uncert. | % Disc. |
|---|---|---|---|---|---|---|---|---|---|---|---|---|---|---|---|
| 188-281a (TIMS) | | | | | | | | | | | | | | | |
| 1z, lt. pink | | | | 0.06314 | 0.00032 | 0.9640 | 0.0064 | 0.1107 | 0.0004 | 0.63 | 713 | ±11 | 677 | 3 | 5.0 |
| 2z, col. | | | | 0.06235 | 0.00013 | 0.9074 | 0.0041 | 0.1055 | 0.0004 | 0.882 | 686 | ±5 | 647 | 3 | 5.7 |
| 188-281b (TIMS) | | | | | | | | | | | | | | | |
| 1z, col abr | | | | 0.06283 | 0.00023 | 0.9323 | 0.006 | 0.1076 | 0.0006 | 0.824 | 702 | ±8 | 659 | 4 | 6.2 |
| GJ1-32 (Fig. 14-10) | | | | | | | | | | | | | | | |
| 1 | 40 | 429248 | 28617 | 0.06040 | 0.00082 | 0.8253 | 0.0326 | 0.0992 | 0.0038 | 0.939 | 618 | ±29 | 610 | ±23 | 1.4 |
| 2 | 40 | 456445 | infinite | 0.06040 | 0.00065 | 0.8209 | 0.0349 | 0.0983 | 0.0042 | 0.968 | 618 | ±23 | 604 | ±26 | 2.2 |
| 3 | 40 | 458752 | 24145 | 0.05964 | 0.00089 | 0.8214 | 0.0311 | 0.1000 | 0.0036 | 0.920 | 590 | ±32 | 614 | ±22 | -4.0 |
| 4 | 40 | 495851 | infinite | 0.06048 | 0.00062 | 0.8314 | 0.0320 | 0.1003 | 0.0039 | 0.965 | 621 | ±22 | 616 | ±24 | 0.7 |
| 5 | 40 | 482876 | infinite | 0.06015 | 0.00063 | 0.8338 | 0.0281 | 0.1006 | 0.0034 | 0.952 | 609 | ±23 | 618 | ±21 | -1.5 |
| 6 | 40 | 408628 | 58375 | 0.06016 | 0.00067 | 0.8026 | 0.0303 | 0.0967 | 0.0036 | 0.956 | 609 | ±24 | 595 | ±22 | 2.3 |
| 7 | 40 | 436632 | 33587 | 0.05976 | 0.00077 | 0.7795 | 0.0306 | 0.0942 | 0.0036 | 0.945 | 595 | ±28 | 580 | ±22 | 2.4 |
| 9 | 40 | 368644 | infinite | 0.06033 | 0.00063 | 0.8012 | 0.0283 | 0.0965 | 0.0034 | 0.957 | 615 | ±22 | 594 | ±21 | 3.5 |
| 11 | 40 | 426769 | 47419 | 0.05988 | 0.00070 | 0.7930 | 0.0298 | 0.0961 | 0.0036 | 0.951 | 599 | ±25 | 592 | ±22 | 1.3 |
| 12 | 40 | 443445 | 88689 | 0.06023 | 0.00064 | 0.7992 | 0.0291 | 0.0963 | 0.0035 | 0.957 | 612 | ±23 | 593 | ±21 | 3.1 |
| 14 | 40 | 394255 | 49282 | 0.05991 | 0.00069 | 0.7916 | 0.0282 | 0.0958 | 0.0034 | 0.947 | 600 | ±25 | 590 | ±21 | 1.8 |
| 15 | 40 | 360321 | 45040 | 0.06002 | 0.00071 | 0.7881 | 0.0263 | 0.0951 | 0.0031 | 0.936 | 604 | ±26 | 586 | ±19 | 3.1 |
| GJ1-32 Fig. 14-11b) | | | | | | | | | | | | | | | |
| 1 | 40 | 434524 | 108631 | 0.06017 | 0.00063 | 0.7995 | 0.0311 | 0.0965 | 0.0037 | 0.963 | 610 | ±23 | 594 | ±23 | 2.6 |
| 2 | 40 | 440443 | infinite | 0.06020 | 0.00062 | 0.7856 | 0.0262 | 0.0948 | 0.0032 | 0.952 | 611 | ±22 | 584 | ±19 | 4.4 |
| 3 | 40 | 418573 | 41857 | 0.05988 | 0.00072 | 0.7722 | 0.0272 | 0.0937 | 0.0032 | 0.941 | 599 | ±26 | 577 | ±20 | 3.7 |
| 4 | 40 | 442918 | infinite | 0.06021 | 0.00063 | 0.8251 | 0.0303 | 0.0994 | 0.0036 | 0.960 | 611 | ±22 | 611 | ±22 | 0.0 |
| 5 | 40 | 443444 | infinite | 0.06026 | 0.00063 | 0.8139 | 0.0320 | 0.0980 | 0.0038 | 0.965 | 613 | ±22 | 603 | ±24 | 1.7 |
| 6 | 40 | 444410 | 24689 | 0.05987 | 0.00088 | 0.8201 | 0.0269 | 0.0995 | 0.0031 | 0.896 | 599 | ±32 | 612 | ±19 | -2.1 |
| 7 | 40 | 446688 | infinite | 0.06002 | 0.00062 | 0.7988 | 0.0253 | 0.0965 | 0.0030 | 0.946 | 604 | ±23 | 594 | ±19 | 1.7 |
| 8 | 40 | 437755 | 54719 | 0.06014 | 0.00068 | 0.8062 | 0.0272 | 0.0973 | 0.0032 | 0.943 | 609 | ±24 | 599 | ±20 | 1.7 |
| 9 | 40 | 460438 | infinite | 0.05998 | 0.00063 | 0.8032 | 0.0262 | 0.0972 | 0.0032 | 0.948 | 603 | ±23 | 598 | ±19 | 0.8 |
| 10 | 40 | 461895 | 230948 | 0.06017 | 0.00062 | 0.8254 | 0.0269 | 0.0996 | 0.0032 | 0.950 | 610 | ±22 | 612 | ±20 | -0.4 |
| 11 | 40 | 450208 | 225104 | 0.06009 | 0.00062 | 0.8072 | 0.0258 | 0.0978 | 0.0031 | 0.947 | 607 | ±22 | 602 | ±19 | 0.9 |

TABLE 14-3 (CONTINUED). U-PB RESULTS FOR ZIRCON AND MONAZITE

| Anal.# | Spot size (μm) | $^{206}$Pb cps | $^{206}$Pb/$^{204}$Pb | $^{207}$Pb/$^{206}$Pb | 2σ uncert. | $^{207}$Pb/$^{235}$U | 2σ uncert. | $^{206}$Pb/$^{238}$U | 2σ uncert. | 'rho' | $^{207}$Pb/$^{206}$Pb Age (Ma) | 2σ uncert | $^{206}$Pb/$^{238}$U Age (Ma) | 2σ uncert | % Disc |
|---|---|---|---|---|---|---|---|---|---|---|---|---|---|---|---|
| LH98-239 | | | | | | | | | | | | | | | |
| zircon 1-1 | 40 | 132724 | infinite | 0.08520 | 0.00092 | 2.7099 | 0.1297 | 0.2310 | 0.0110 | 0.974 | 1320 | ±21 | 1340 | ±64 | -1.5 |
| zircon 2-1 | 40 | 152020 | infinite | 0.08437 | 0.00093 | 2.6198 | 0.0942 | 0.2243 | 0.0080 | 0.952 | 1301 | ±22 | 1304 | ±46 | -0.2 |
| zircon 2-2 | 40 | 150613 | infinite | 0.08425 | 0.00088 | 2.6076 | 0.1046 | 0.2249 | 0.0090 | 0.966 | 1298 | ±20 | 1308 | ±52 | -0.7 |
| zircon 3-1 | 40 | 311900 | infinite | 0.08437 | 0.00090 | 2.5980 | 0.0943 | 0.2237 | 0.0081 | 0.957 | 1301 | ±21 | 1301 | ±47 | 0.0 |
| zircon 3-2 | 40 | 355591 | infinite | 0.08388 | 0.00087 | 2.5326 | 0.0931 | 0.2192 | 0.0080 | 0.960 | 1290 | ±20 | 1278 | ±47 | 0.9 |
| zircon 4-2 | 40 | 55005 | infinite | 0.08353 | 0.00098 | 2.5948 | 0.0978 | 0.2253 | 0.0084 | 0.951 | 1282 | ±23 | 1310 | ±49 | -2.2 |
| zircon 4-b1 | 40 | 189233 | infinite | 0.08436 | 0.00090 | 2.6223 | 0.1065 | 0.2259 | 0.0091 | 0.966 | 1301 | ±21 | 1313 | ±53 | -0.9 |
| zircon 5-1 | 40 | 57627 | infinite | 0.08500 | 0.00126 | 2.5781 | 0.1032 | 0.2204 | 0.0085 | 0.930 | 1316 | ±29 | 1284 | ±49 | 2.4 |
| zircon 5-2 | 40 | 269343 | 7696 | 0.08443 | 0.00121 | 2.6280 | 0.1084 | 0.2258 | 0.0076 | 0.914 | 1302 | ±28 | 1312 | ±44 | -0.8 |
| zircon 5-3 | 40 | 203445 | infinite | 0.08474 | 0.00090 | 2.6903 | 0.0930 | 0.2308 | 0.0079 | 0.953 | 1310 | ±21 | 1339 | ±46 | -2.2 |
| zircon 6-2 | 40 | 92428 | infinite | 0.08449 | 0.00096 | 2.6547 | 0.1063 | 0.2272 | 0.0090 | 0.960 | 1304 | ±22 | 1320 | ±52 | -1.2 |
| zircon 6-3 | 40 | 90320 | infinite | 0.08482 | 0.00095 | 2.6519 | 0.0980 | 0.2259 | 0.0083 | 0.954 | 1311 | ±22 | 1313 | ±48 | -0.1 |
| zircon 7-1 | 40 | 210122 | infinite | 0.08485 | 0.00091 | 2.6601 | 0.0891 | 0.2276 | 0.0076 | 0.948 | 1312 | ±21 | 1322 | ±44 | -0.8 |
| zircon 7-2 | 40 | 100709 | infinite | 0.08491 | 0.00100 | 2.6143 | 0.0891 | 0.2192 | 0.0073 | 0.940 | 1313 | ±23 | 1278 | ±43 | 2.7 |
| zircon 1-2 | 40 | 1392378 | infinite | 0.08379 | 0.00086 | 2.7149 | 0.1282 | 0.2356 | 0.0111 | 0.976 | 1288 | ±20 | 1364 | ±64 | -5.9 |
| zircon 4b-2 | 40 | 109384 | infinite | 0.08471 | 0.00096 | 2.7833 | 0.0961 | 0.2369 | 0.0081 | 0.945 | 1309 | ±22 | 1371 | ±47 | -4.7 |
| zircon 6-1 | 40 | 223788 | infinite | 0.08463 | 0.00090 | 2.7376 | 0.1027 | 0.2346 | 0.0088 | 0.959 | 1307 | ±21 | 1359 | ±51 | -4.0 |
| zircon 4-1 | 40 | 536435 | infinite | 0.08440 | 0.00092 | 2.7180 | 0.1105 | 0.2339 | 0.0095 | 0.964 | 1302 | ±21 | 1355 | ±55 | -4.1 |
| LH98-239 (TIMS) | | | | | | | | | | | | | | | |
| 1 | | | 3998 | 0.08468 | 0.00014 | 2.5929 | 0.0108 | 0.2221 | 0.0008 | 0.918 | 1308.1 | ±3 | 1292.9 | ±4 | 1.3 |
| 2 | | | 15571 | 0.08445 | 0.00012 | 2.5814 | 0.0102 | 0.2217 | 0.0008 | 0.925 | 1302.9 | ±3 | 1290.9 | ±4 | 1.0 |
| ST-3a-mnz | | | | | | | | | | | | | | | |
| Grain 1-4 | 12 | 1117737 | infinite | 0.15309 | 0.00157 | 8.9391 | 0.27 | 0.42358 | 0.016 | 0.977 | 2381 | ±17 | 2279 | ±71 | 5.2 |
| Grain 1-5 | 12 | 2016729 | infinite | 0.15424 | 0.00155 | 9.3149 | 0.28 | 0.43821 | 0.014 | 0.954 | 2394 | ±17 | 2345 | ±65 | 2.5 |
| Grain 1-6 | 12 | 1728835 | infinite | 0.15329 | 0.00154 | 9.2486 | 0.28 | 0.43787 | 0.016 | 0.967 | 2383 | ±17 | 2343 | ±70 | 2.1 |
| Grain 1-7 | 12 | 1722542 | infinite | 0.15336 | 0.00154 | 9.2437 | 0.28 | 0.43744 | 0.015 | 0.963 | 2384 | ±17 | 2341 | ±68 | 2.2 |
| Grain 1-9 | 12 | 1350243 | infinite | 0.15331 | 0.00155 | 9.4298 | 0.28 | 0.44623 | 0.015 | 0.953 | 2383 | ±17 | 2380 | ±65 | 0.2 |
| Grain 2-3 | 12 | 1262285 | infinite | 0.15315 | 0.00159 | 9.1431 | 0.27 | 0.43313 | 0.020 | 0.652 | 2381 | ±18 | 2322 | ±89 | 3.1 |
| Grain 2-4 | 12 | 1546549 | infinite | 0.15272 | 0.00154 | 9.2401 | 0.28 | 0.43878 | 0.014 | 0.947 | 2377 | ±17 | 2347 | ±62 | 1.6 |
| Grain 3-4 | 12 | 1998724 | infinite | 0.16114 | 0.00165 | 10.0697 | 0.30 | 0.45327 | 0.015 | 0.953 | 2468 | ±17 | 2412 | ±67 | 2.8 |
| Grain 3-6 | 12 | 1800729 | infinite | 0.16254 | 0.00166 | 10.3013 | 0.31 | 0.45956 | 0.014 | 0.945 | 2482 | ±17 | 2440 | ±63 | 2.2 |
| Grain 3-7 | 12 | 2284983 | infinite | 0.16162 | 0.00167 | 10.2972 | 0.31 | 0.46196 | 0.014 | 0.942 | 2473 | ±17 | 2450 | ±63 | 1.2 |
| Grain 3-9 | 12 | 1385241 | infinite | 0.15328 | 0.00156 | 9.2990 | 0.28 | 0.44015 | 0.014 | 0.945 | 2383 | ±17 | 2353 | ±61 | 1.6 |
| Grain 3-10 | 12 | 1280531 | infinite | 0.15320 | 0.00156 | 9.4299 | 0.28 | 0.44662 | 0.018 | 0.737 | 2382 | ±17 | 2382 | ±81 | 0.1 |
| Grain 4-4 | 12 | 1422891 | infinite | 0.16259 | 0.00167 | 10.2183 | 0.31 | 0.45653 | 0.014 | 0.946 | 2483 | ±17 | 2426 | ±64 | 2.8 |
| Grain 4-5 | 12 | 1402247 | infinite | 0.16353 | 0.00166 | 10.3015 | 0.31 | 0.45680 | 0.016 | 0.958 | 2492 | ±17 | 2427 | ±69 | 3.2 |
| Grain 4-6 | 12 | 1320995 | infinite | 0.16294 | 0.00165 | 10.0907 | 0.30 | 0.44803 | 0.014 | 0.948 | 2486 | ±17 | 2388 | ±63 | 4.8 |
| Grain 4-7 | 12 | 1627700 | infinite | 0.15430 | 0.00159 | 8.9641 | 0.27 | 0.42149 | 0.015 | 0.959 | 2394 | ±18 | 2269 | ±66 | 6.3 |

within one petrographic thin section of sample 247-339C are listed in Table 14-3 and shown in Fig. 14-12b. The data can be separated into three distinct age groups: zircon samples 1, 4B and 5 define the youngest concordant age at 544.6 ±5.0 Ma (2σ), whereas zircon samples 2, 3, and 4A yield a concordant age at 598.1 ±8.0 Ma (2σ); the core analysis (3-2) of zircon #3 yields an inherited age of 669 ±24 Ma (2σ). Anchoring the ID–TIMS data for sample 188-281a, b to the more precise lower intercept age of 544.6 ± 5 Ma obtained by LA–MC–ICP–MS yields an upper intercept age of 850 ± 20 Ma. This upper intercept date most probably represents the magma crystallization age of the host charnockite or its granitoid protolith. The 544.6 ± 5.0 Ma date represents the time at which the coarse grained melt patch/pod formed, and the 598.1 ± 8 Ma and *ca*. 670 Ma age populations most probably reflect the ages of zircon inherited from the host charnockite. Of interest, the *ca*. 590 Ma age component in the host charnockite determined at this location was also documented in a previous geochronological study conducted on this charnockite massif (Miller *et al*., 1996). Thus, combining the laser ablation and ID–TIMS data, there is evidence for four major events in the Cardamom massif at *ca*. 2500 Ma, 850 Ma, 590 Ma and 545 Ma.

During the same analytical session, a second glass mount (~0.5 cm x ~0.5 cm) containing zircon fragments from aliquot GJ-1-32 (obtained from Macquarie University) was placed adjacent to the mount bearing the LH94-15 grains. Eight ID–TIMS analyses of four separate GJ-1-32 fragments by F. Corfu (University of Oslo) yielded a weighted mean $^{207}Pb/^{206}Pb$ age of 608.53 ±0.37 Ma (2σ; Jackson *et al*. 2004). ID–TIMS analysis of five GJ-1-32 zircon fragments conducted at the University of Alberta yield a weighted mean $^{207}Pb/^{206}Pb$ age of 606.7 ±2.3 Ma (2σ). Repeated laser ablation analysis (n=12) of GJ1-32 zircon grains using a 40 micrometre spot size yielded a weighted mean $^{207}Pb/^{206}Pb$ age of 608.8 ± 7.0 Ma (2σ; Fig. 14-13). The ID–TIMS and LA–MC–ICP–MS ages obtained in this study are indistinguishable within their associated uncertainties, and also overlap the ID–TIMS age for GJ–1 zircon reported by Jackson *et al*. (2004).

***Zircon: Voisey's Bay Granite.*** Sample LH98-239 is a medium grained clinopyroxene-fayalite granite from the Voisey's Bay intrusion, Labrador. In decreasing abundance, it consists of perthitic alkali feldspar, plagioclase, quartz, amphibole, clinopyroxene, fayalitic olivine and ulvospinel with subordinate zircon, pyrite, apatite and secondary biotite. Clinopyroxene and olivine typically form irregular clusters commonly surrounded by amphibole. Zircon is an abundant accessory mineral in this sample, has high Th/U (0.79), and forms relatively large euhedral oscillatory zoned crystals intergrown with a variety of minerals.

ID–TIMS analyses were conducted at the University of Alberta on two small multi-grain zircon fractions from sample LH98-239 and these

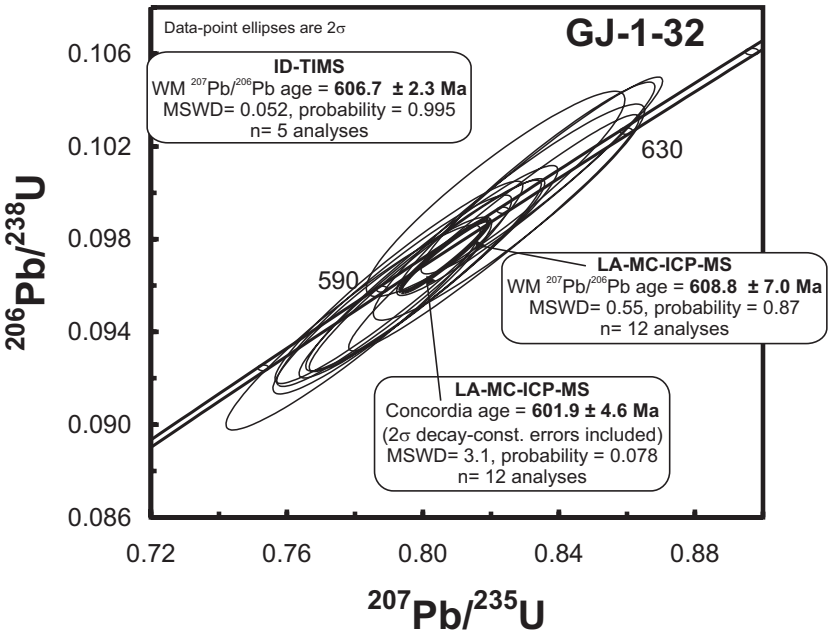


FIG. 14-13. Concordia plot containing the U–Pb dating results for zircon GJ1-32 obtained by LA–MC–ICP–MS using a 40 micrometre spot size. WM= weighted mean.

yielded a weighted mean $^{207}Pb/^{206}Pb$ age of 1305.3 ±2.2 Ma (2σ , Fig. 14-14a). LA–MC–ICP–MS analyses were conducted on one petrographic thin section of sample LH98-239 using the SuperCell™. The Pb–U LIEF was monitored by intermittent analysis of the in-house zircon standard LH94-15 located on a glass slide mount adjacent to the LH98-239 thin section. Figure 14-14a and Table 14-3 illustrate the U–Pb data obtained by LA–MC–ICP–MS analysis for a total of 18 analyses on 7 zircon samples. The 14 most concordant analyses yield a weighted mean $^{207}Pb/^{206}Pb$ age of 1304.1 ±5.7 Ma (2σ) or 'concordia age' of 1306.2 ± 6.2 Ma (2σ; Fig. 14-14a). The two LA–MC–ICP–MS and ID–TIMS ages are identical and once again corroborate the accuracy of the methodology employed in our lab. Of particular interest, the inset in Fig. 14-14a displays a high resolution back-scattered electron image of the petrological context in the immediate vicinity of euhedral zircon grain #6. The elongate, zircon crystal contains an appendage of pyrite; all are hosted by a larger ulvospinel grain that has exsolved to a trellis-textured intergrowth of magnetite and ilmenite. The fact that the U–Pb results from grain #6 are identical to those of the remaining zircon grains within the sample strongly suggests a genetic relationship between the sulfide mineralization and granite magmatism. This ability to document the textural context of the dated mineral highlights one of the principal advantages of the U–Pb protocol outlined here.

As with the previous sample, a glass slide mount containing zircon grains from sample GJ1-32

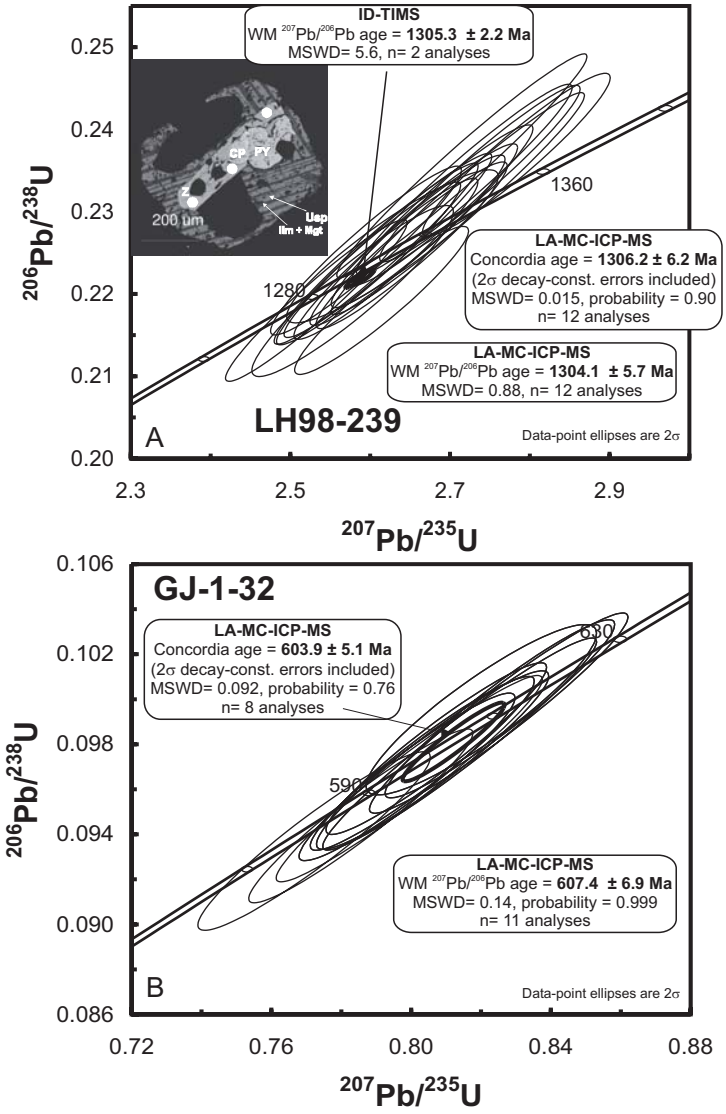


FIG. 14-14. Concordia plots illustrating the U–Pb age data for sample LH98-239, a clinopyroxene-fayalite granite from Voisey's Bay (**A**) obtained by ID–TIMS and LA–MC–ICP–MS, and (**B**) age results for GJ1-32 zircons using a spot size of 40 microns. Inset in (**A**) is a back-scattered electron image of the area within the petrographic thin section that surrounds zircon grain #6; z= zircon, CP= chalcopyrite, PY= pyrite, Usp= ulvospinel, Ilm= ilmenite, Mgt= magnetite. White circles represent locations of the laser ablation sites. WM= weighted mean. (**B**) Age results for GJ-1-32 zircons using a spot size of 40 microns.

was placed adjacent to the LH94-15 in-house zircon standard. Eleven laser ablation analyses using a 40 micron spot size yielded a weighted mean $^{207}Pb/^{206}Pb$ age of 607.4 ±6.9 Ma (2σ ; Fig. 14-14b). Once again, this result is indistinguishable from the LA–MC–ICP–MS data obtained during an earlier analytical session (Fig. 14-13) and ID–TIMS ages obtained at the University of Alberta and Macquarie University (Jackson *et al*. 2004).

***Monazite: Queen Maud Block*** In a recent study, Schultz *et al*. (2007) report *in situ* U–Pb ages obtained on monazite and zircon in petrographic thin sections obtained by LA–MC–ICP–MS using the protocol described here. Granitoid and metasedimentary samples from the main lithologies of the Queen Maud block, located on the northwestern margin of the Rae province (Arctic Canada), were analyzed in order to understand better the tectonic history of northwestern Laurentia. In particular, monazite grains from three metasedimentary samples were investigated in order to delineate the timing of regional metamorphism.

U–Pb data for monazite from a sample of garnet-bearing migmatite leucosome (ST-3a) were obtained with the standard ablation cell, and are illustrated in Fig. 14-15 and listed in Table 14-3 (from Schultz *et al*. 2007). The Pb *versus* U LIEF was monitored using the Western Australia monazite standard (2842.9 ± 0.3 Ma; Heaman *et al*. unpublished ID–TIMS data). The data for sample ST-3a define a two-part history; cores from two monazite grains are characterized by patchy compositional zonation and mantled by compositionally homogeneous rims (Fig. 14-15). Laser ablation–MC–ICP–MS analyses of the cores conducted using a 12 μm spot size yielded a weighted mean $^{207}Pb/^{206}Pb$ age of 2481 ±7 Ma (2σ), which is coeval with the 2460 to 2500 Ma zircon ages obtained on granitoid rocks from the Queen Maud block. In contrast, LA–MC–ICP–MS analyses of rims (n=3) and homogeneous grains (n=10) yield a weighted mean $^{207}Pb/^{206}Pb$ age of 2385 ±5 Ma (Fig. 14-15). The *ca*. 2.5 Ga is

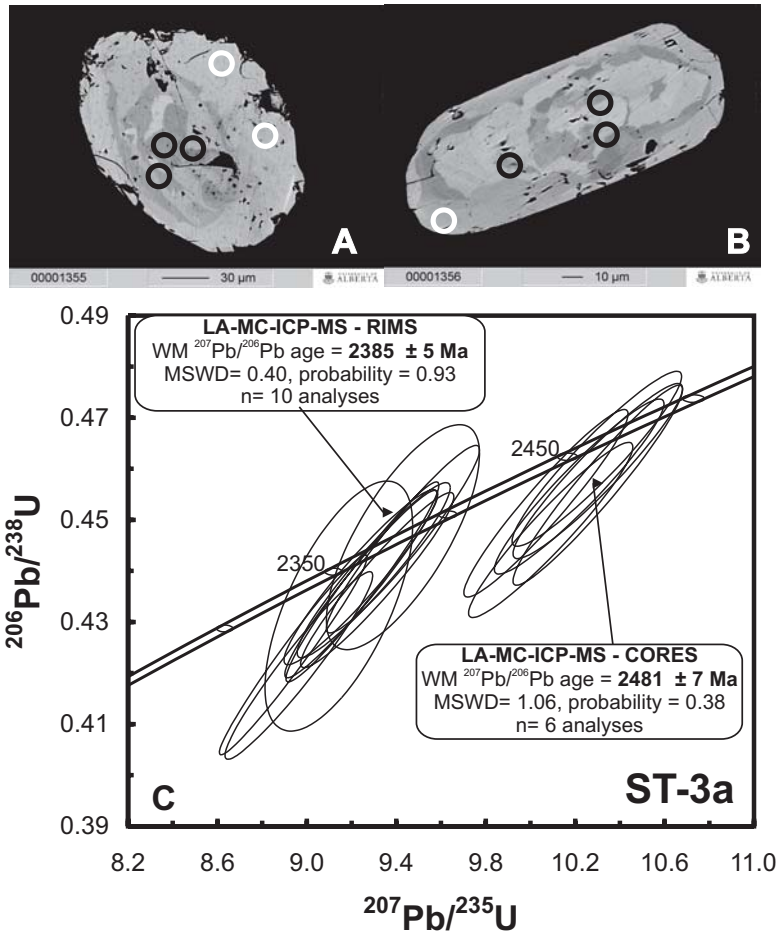


FIG. 14-15. (**A**) Back-scattered electron images of grain #3 and grain #4 (**B**) from sample ST-3a with locations of 12 μm ablation spots delineated; black open circles = core, white open circles = rim. (**C**) Concordia diagram that clearly illustrates the distinct age differences between cores and rims (diagram modified from Schultz *et al*., 2007).

interpreted as an igneous crystallization event, whereas the *ca*. 2.39 Ga most likely represents the timing of granulite-facies metamorphism since monazite with these ages occurs in melt leucosomes. Given the rather thin (~10 to 30 μm) nature of the metamorphic rims within the compositionally zoned monazite grains (Fig. 14-15), LA–MC–ICP–MS analysis of such grains in raster mode over a larger area would have resulted in geologically meaningless 'mixed' U–Pb ages (between ~2500 and ~2390 Ma). Hence, this study again demonstrates the importance of the 'reduced volume' approach.

***Perovskite: Ice River Complex.*** Perovskite ($CaTiSiO_3$) is a useful mineral for dating mantle-derived melts of mafic or ultramafic (*e.g.,* kimberlite) and alkaline (*e.g.,* ijolite; Fig. 14-16) affinities since it occurs as a magmatic phase and is not known to record inheritance. Its occurrence in rocks of economic importance such as kimberlite has provided the impetus for geochronological investigations of perovskite using conventional isotope dilution methods (*e.g.,* Heaman & Kjarsgaard 2000) or SHRIMP analysis (*e.g.,* Kinney *et al*. 1997). However, successful dating of perovskite hinges upon the correction of the common Pb component. Recently, Cox & Wilton (2006) accurately dated perovskite from the Oka carbonatite by LA–ICP–MS using the 'Tera-Wasserburg' technique. This method involves calculating a regression line through uncorrected data on a measured $^{207}Pb/^{206}Pb$ *vs*. measured $^{238}U/^{206}Pb$ plot, *i.e.*, Tera-Wasserburg diagram (*e.g.*, Fig. 14-17a). The y-intercept value represents the $^{207}Pb/^{206}Pb$ ratio of the common Pb component; whereas the $^{207}Pb/^{206}Pb$ value of the radiogenic component is given by the age defined by the lower intersection of the regression line and the concordia curve. Both the radiogenic and common Pb $^{207}Pb/^{206}Pb$ values are used in the formula below to calculate the proportion of common Pb ($f$) for each analysis (after Compston *et al*. 1984):

$$f = \frac{\left(^{207}Pb/^{206}Pb_{measured} - {}^{207}Pb/^{206}Pb_{radiogenic}\right)}{\left(^{207}Pb/^{206}Pb_{common} - {}^{207}Pb/^{206}Pb_{radiogenic}\right)}$$

The latter approach was also adopted by Simonetti *et al*. (2006) to date titanite by LA–MC–ICP–MS successfully in petrographic thin section (*e.g.,* Banerjee *et al*. 2007), another accessory mineral that is characterized by a significant amount of common Pb. The reader is referred to the studies cited above for a detailed description of both the perovskite and titanite dating protocols using the 'Tera-Wasserburg' method.

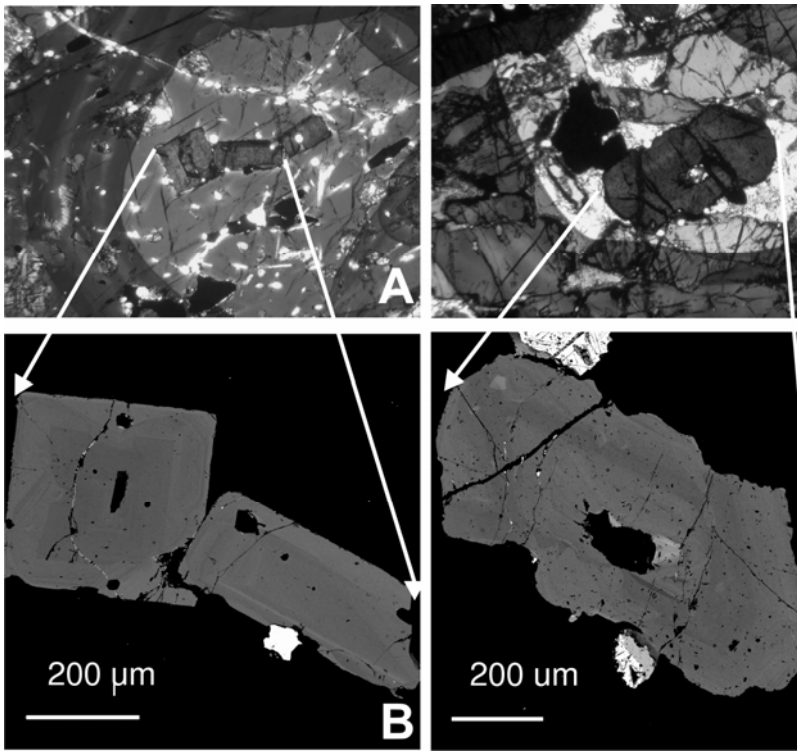


FIG. 14-16. Photomicrographs and back scattered electron images of perovskite grains taken from the petrographic thin section of sample I92-30 and subsequently analyzed by LA–MC–ICP–MS. **A**) and **B**) are pictures for grains labeled 2b and 2c in Table 14-4, whereas **C**) and **D**) represent images for grain 5 (Table 14-4).

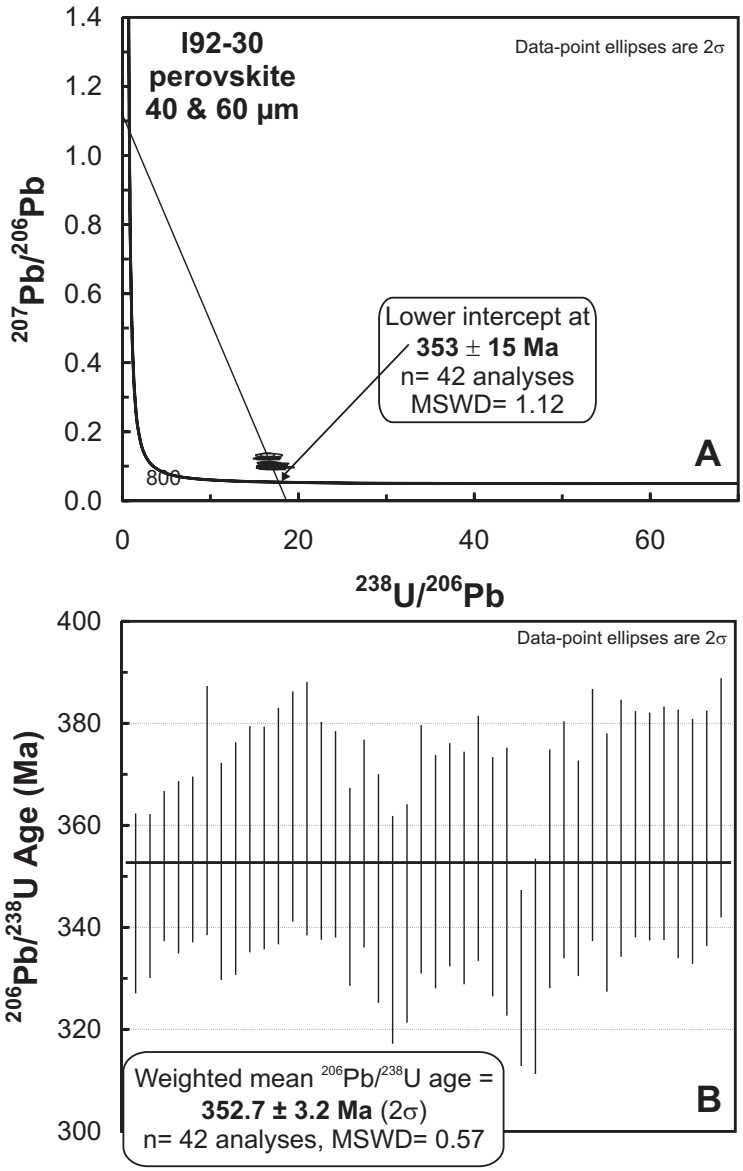


FIG. 14-17. **A**) Tera-Wassserburg plot illustrating the results obtained by LA–MC–ICP–MS for perovskite from the petrographic thin section of sample I92-30. **B**) Diagram depicting the individual, common Pb-corrected $^{206}Pb/^{238}U$ ages obtained for LA–MC–ICP–MS analyses of perovskite from sample I92-30 and corresponding calculated weighted mean age of 352.7 ± 3.2 Ma (2σ).

This analytical protocol was used to date perovskite within a sample of melteigite (Melanocratic end member of the ijolite series) from the Early Carboniferous Ice River ultramafic alkaline complex, British Columbia (Locock 1994, Pell & Höy 1989). The Ice River Complex is an arcuate shaped, zoned alkaline ultramafic intrusion covering an area ~30 km$^2$ and consists of two intrusive suites (from Pell & Höy 1989): an early, layered (feldspar-free) ijolite, jacupirangite, and urtite that is cored by a carbonatite plug and cut by carbonatite dykes; this was later intruded by a series of zoned syenite bodies associated with zeolitic and feldspathic carbonatite.

Six perovskite crystals from a petrographic thin section of sample I92-30, a perovskite-kaersutite-bearing melteigite (Fig. 14-16), were ablated predominantly at 40 µm for U–Pb age determination (Table 14-4; Fig. 14-17). The perovskite grains were ablated using the standard laser ablation cell and the Pb *vs*. U LIEF was monitored with repeated analysis of a perovskite external standard. The latter was also obtained from the Ice River Complex but from ijolite sample IR-6 (collected by T.D. Peterson, GSC Ottawa), which is characterized by abundant nepheline, clinopyroxene, perovskite with minor titanite, melanite garnet, apatite and ilmenite (pers. comm. from B. Kjarsgaard, GSC Ottawa). The external perovskite standard from sample IR-6 was dated by ID–TIMS

TABLE 14-4. U-PB LASER ABLATION DATA FOR ICE RIVER PEROVSKITE

| Anal. # | Spot size (μm) | $^{206}$Pb cps | $^{207}$Pb/ $^{206}$Pb | 2σ uncert. | $^{206}$Pb/ $^{238}$U meas. | 2σ uncert. | % Rad. Pb | $^{206}$Pb/ $^{238}$U corr. | 2σ uncert. | $^{206}$Pb/ $^{238}$U Age (Ma) | 2σ uncert. |
|---|---|---|---|---|---|---|---|---|---|---|---|
| Gr 1 -1 | 60 | 282691 | 0.0574 | 0.0029 | 0.0995 | 0.0011 | 95.7 | 0.0549 | 0.0028 | 345 | 18 |
| Gr 1 -2 | 60 | 318103 | 0.0575 | 0.0027 | 0.0972 | 0.0010 | 95.9 | 0.0552 | 0.0026 | 346 | 16 |
| Gr 1 -3 | 60 | 338572 | 0.0607 | 0.0025 | 0.1331 | 0.0043 | 92.5 | 0.0561 | 0.0023 | 352 | 15 |
| Gr 1b -4 | 60 | 311926 | 0.0586 | 0.0028 | 0.0987 | 0.0010 | 95.8 | 0.0561 | 0.0027 | 352 | 17 |
| Gr 1b -5 | 60 | 296524 | 0.0587 | 0.0027 | 0.0968 | 0.0010 | 95.9 | 0.0563 | 0.0026 | 353 | 16 |
| Gr 2a -6 | 40 | 156959 | 0.0603 | 0.0041 | 0.0960 | 0.0010 | 96.0 | 0.0579 | 0.0039 | 363 | 24 |
| Gr 2a -7 | 40 | 156225 | 0.0584 | 0.0035 | 0.0982 | 0.0011 | 95.8 | 0.0560 | 0.0034 | 351 | 21 |
| Gr 2a -8 | 40 | 170053 | 0.0590 | 0.0038 | 0.1017 | 0.0012 | 95.5 | 0.0564 | 0.0036 | 353 | 23 |
| Gr 2b -9 | 40 | 156842 | 0.0595 | 0.0037 | 0.0982 | 0.0011 | 95.8 | 0.0570 | 0.0035 | 357 | 22 |
| Gr 2b -10 | 40 | 160258 | 0.0596 | 0.0036 | 0.0989 | 0.0010 | 95.7 | 0.0570 | 0.0035 | 358 | 22 |
| Gr 2b -11 | 40 | 164301 | 0.0600 | 0.0039 | 0.0999 | 0.0011 | 95.7 | 0.0574 | 0.0037 | 360 | 23 |
| Gr 2c -12 | 40 | 171447 | 0.0607 | 0.0038 | 0.1001 | 0.0011 | 95.6 | 0.0580 | 0.0036 | 364 | 23 |
| Gr 2c-13 | 40 | 147706 | 0.0603 | 0.0041 | 0.0951 | 0.0010 | 96.1 | 0.0580 | 0.0040 | 363 | 25 |
| Gr 3a-14 | 40 | 158686 | 0.0596 | 0.0035 | 0.0960 | 0.0010 | 96.0 | 0.0573 | 0.0034 | 359 | 21 |
| Gr 3a-15 | 40 | 153350 | 0.0603 | 0.0034 | 0.1094 | 0.0032 | 94.8 | 0.0571 | 0.0032 | 358 | 20 |
| Gr 3a-16 | 40 | 214423 | 0.0575 | 0.0032 | 0.0910 | 0.0010 | 96.5 | 0.0555 | 0.0031 | 348 | 19 |
| Gr 3a-17 | 40 | 217238 | 0.0599 | 0.0034 | 0.1075 | 0.0011 | 94.9 | 0.0568 | 0.0033 | 356 | 20 |
| Gr 3b-18 | 40 | 246560 | 0.0583 | 0.0038 | 0.1059 | 0.0012 | 95.1 | 0.0554 | 0.0036 | 348 | 22 |
| Gr 3b-19 | 40 | 186671 | 0.0570 | 0.0037 | 0.1075 | 0.0012 | 94.9 | 0.0541 | 0.0036 | 340 | 22 |
| Gr 3b-20 | 40 | 173684 | 0.0573 | 0.0036 | 0.1041 | 0.0017 | 95.3 | 0.0546 | 0.0034 | 343 | 21 |
| Gr 4a-21 | 40 | 159137 | 0.0604 | 0.0041 | 0.1201 | 0.0013 | 93.8 | 0.0567 | 0.0039 | 355 | 24 |
| Gr 4a-22 | 40 | 167574 | 0.0584 | 0.0038 | 0.0978 | 0.0011 | 95.8 | 0.0559 | 0.0036 | 351 | 23 |
| Gr 4a-23 | 40 | 161580 | 0.0590 | 0.0036 | 0.0993 | 0.0011 | 95.7 | 0.0565 | 0.0035 | 354 | 22 |
| Gr 4a-24 | 40 | 189951 | 0.0584 | 0.0038 | 0.0956 | 0.0010 | 96.1 | 0.0561 | 0.0036 | 352 | 23 |
| Gr 4a-25 | 40 | 157063 | 0.0597 | 0.0040 | 0.1008 | 0.0014 | 95.6 | 0.0570 | 0.0038 | 357 | 24 |
| Gr 4b-26 | 40 | 150064 | 0.0582 | 0.0039 | 0.0985 | 0.0010 | 95.8 | 0.0558 | 0.0037 | 350 | 23 |
| Gr 4b-27 | 40 | 166885 | 0.0600 | 0.0045 | 0.1316 | 0.0041 | 92.7 | 0.0556 | 0.0042 | 349 | 26 |
| Gr 4c-28 | 40 | 151734 | 0.0548 | 0.0029 | 0.0970 | 0.0012 | 95.9 | 0.0525 | 0.0027 | 330 | 17 |
| Gr 4c-29 | 40 | 164872 | 0.0551 | 0.0035 | 0.0965 | 0.0011 | 96.0 | 0.0529 | 0.0034 | 332 | 21 |
| Gr 5-30 | 40 | 160266 | 0.0586 | 0.0039 | 0.1002 | 0.0011 | 95.6 | 0.0560 | 0.0037 | 351 | 23 |
| Gr 5-31 | 40 | 160920 | 0.0600 | 0.0039 | 0.1071 | 0.0014 | 95.0 | 0.0570 | 0.0037 | 357 | 23 |
| Gr 5-32 | 40 | 177411 | 0.0588 | 0.0035 | 0.1037 | 0.0011 | 95.3 | 0.0561 | 0.0034 | 352 | 21 |
| Gr 5-33 | 40 | 157318 | 0.0617 | 0.0042 | 0.1220 | 0.0021 | 93.6 | 0.0578 | 0.0039 | 362 | 25 |
| Gr 5-34 | 40 | 173758 | 0.0603 | 0.0043 | 0.1247 | 0.0014 | 93.3 | 0.0562 | 0.0040 | 353 | 25 |
| Gr 5-35 | 40 | 152028 | 0.0597 | 0.0042 | 0.0960 | 0.0011 | 96.0 | 0.0573 | 0.0040 | 359 | 25 |
| Gr 6a-36 | 40 | 158165 | 0.0599 | 0.0037 | 0.0971 | 0.0010 | 95.9 | 0.0575 | 0.0035 | 360 | 22 |
| Gr 6a-37 | 40 | 171996 | 0.0595 | 0.0037 | 0.0917 | 0.0010 | 96.4 | 0.0574 | 0.0036 | 360 | 22 |
| Gr 6a-38 | 40 | 163006 | 0.0602 | 0.0038 | 0.1011 | 0.0011 | 95.5 | 0.0575 | 0.0037 | 360 | 23 |
| Gr 6a -39 | 40 | 166792 | 0.0597 | 0.0041 | 0.0993 | 0.0017 | 95.7 | 0.0572 | 0.0039 | 358 | 24 |
| Gr 6a -40 | 40 | 179446 | 0.0601 | 0.0040 | 0.1099 | 0.0014 | 94.7 | 0.0569 | 0.0038 | 357 | 24 |
| Gr 6b -41 | 40 | 166895 | 0.0597 | 0.0038 | 0.0965 | 0.0010 | 96.0 | 0.0573 | 0.0037 | 359 | 23 |
| Gr 6b -42 | 40 | 162029 | 0.0608 | 0.0039 | 0.0962 | 0.0010 | 96.0 | 0.0583 | 0.0037 | 365 | 23 |

and has yielded an age of 356.4 ± 1.1 Ma (2σ; n= 8 analyses; Heaman *et al*., in prep.). A total of 42 laser ablation analyses of perovskite from sample I92-30 define a lower intercept of 353 ± 15 Ma (2σ; Fig. 14-17a) and a weighted mean $^{206}Pb/^{238}U$ age of 352.7 ± 3.2 Ma (2σ; Fig. 14-17b). This date corroborates the ID–TIMS age results obtained on the IR-6 external perovskite standard (356.4 ± 1.1 Ma) and that of 356.2 ± 5.9 Ma (2σ) based on analyses of mineral separates of pyrochlore, perovskite, and schorlomite from various intrusive phases of the Ice River Complex (Locock 1994).

## SUMMARY

The U–Pb protocol described here involving the use of a unique collector array consisting of a combination of three discrete-dynode electron multipliers and twelve Faraday collectors provides distinct advantages for U–Pb dating of accessory mineral phases by LA–MC–ICP–MS. These are:

1. Measurement of the $^{207}Pb$, $^{206}Pb$, and $^{204}Pb$ ion signals using the three electron multipliers allows for the laser ablation of a number of accessory phases to be conducted at low fluence and hence consumes much less sample volume without lowering the precision of the $^{207}Pb/^{206}Pb$ analyses. This '*reduced volume*' approach readily allows for the U–Pb dating of accessory phases including zircon, monazite, titanite and perovskite within standard petrographic thin sections. The capacity to date accessory minerals precisely and accurately in their petrological context is invaluable for resolving a wide range of geological questions.
2. The typical 2σ uncertainty associated with measurement of the $^{207}Pb/^{206}Pb$ value with our LA–MC–ICP–MS protocol is lower than that typically obtained by SHRIMP. The 2σ uncertainty associated with the calculated weighted mean $^{207}Pb/^{206}Pb$ age approaches that obtained by ID–TIMS. Thus, the analytical protocol described here is certainly more cost-effective than either of these two methods.
3. The comparative laser ablation tests conducted using either the standard or SuperCell™ ablation cells seem to yield similar performances relative to sensitivity, signal 'washout', and overall quality of the U–Pb data. The important advantage of the SuperCell™ relative to the standard laser ablation cell is its capacity to incorporate glass mounts containing matrix-matched standards simultaneously. This enables more frequent monitoring of the Pb *versus* U laser induced element fractionation during a single analytical session and also increases sample through-put.
4. When using a combination of discrete-dynode electron multipliers and Faraday collectors for U–Pb age dating by LA–MC–ICP–MS, high quality data is achievable when the ion-counting devices are properly calibrated relative to one another, and against the Faraday bucket recording the $^{238}U$ ion signal.

## ACKNOWLEDGEMENTS

The radiogenic isotope facility at the University of Alberta is partly supported by a NSERC MRS grant. We thank Jason Cameron, GuangCheng Chen, Gayle Hatchard, Mark Labbe, Don Resultay, and Judy Schultz for technical assistance. We are extremely grateful to Andrew Locock for providing sample I92-30 from his MSc thesis collection and discussions relating to the dating of common Pb–bearing accessory minerals. We thank Adam Kent and an anonymous reviewer for providing constructive comments.

## REFERENCES

ASHTON, K.E., HEAMAN, L.M., LEWRY, J.F., HARTLAUB, R.P. & SHI, R. (1999): Age and origin of the Jan Lake Complex ; a glimpse at the buried Archean craton of the Trans-Hudson orogen. *Can. J. Earth Sci.* **36**, 105-208.

BANERJEE, N.R., SIMONETTI, A., FURNES, H., MUELENBACHS, K., STAUDIGEL, H., HEAMAN, L. & VAN KRANENDONK, M.J. (2007): Direct dating of Archean microbial ichnofossils. *Geology* **35**, 487-490.

CHENERY, S. & COOK, J.M. (1993): Determination of rare earth elements in single mineral grains by laser ablation microprobe-inductively coupled plasma mass spectrometry-preliminary study. *J. Anal. At. Spectrom.* **8**, 299-303.

COMPSTON, W., WILLIAMS, I.S. & MEYER, C.E. (1984): U–Pb geochronology of zircons from lunar breccia 73217 using a sensitive high mass-resolution ion microprobe. *J. Geophys. Res*. **B89**, 525-534.

COX, R.A. & WILTON, D.H.C. (2006): U–Pb dating of perovskite by LA–ICP–MS: An example from the Oka carbonatite, Quebec, Canada. *Chem. Geol*. **235**, 21-32.

COX, R.A., WILTON, D.H.C. & KOŠLER, J. (2003): Laser-ablation U–Th–Pb *in situ* dating of zircon

and allanite: An example from the October Harbour granite, central coastal Labrador, Canada. *Can. Mineral.* **41**, 273-291.

DUNSTAN, L.P., GRAMCH, J.W., BARNES, I.L. & PURDY, W.C. (1980): Absolute isotopic abundance and the atomic weight of a reference sample of thallium. *J. Res. National Bureau of Standards* **85**, 1-10.

EGGINS, S.M., KINSLEY, L.P.J. & SHELLEY, J.M.G. (1998): Deposition and element fractionation processes during atmospheric pressure laser sampling for analysis by ICP–MS. *Appl. Surf. Sci.* **127-129**, 278-286.

GÜNTHER, D., COUSIN, H., MAGYAR, B. & LEOPOLD, I. (1997): Calibration studies on dried aerosols for laser ablation-inductively coupled plasma mass spectrometry. *J. Anal. At. Spectrom.* **12**, 165-170.

HEAMAN, L.M. & KJARSGAARD, B.A. (2000): Timing of eastern North American kimberlite magmatism; continental extension of the Great Meteor Hotspot track? *Earth Planet. Sci. Lett*. **178**, 253-268.

HOFFMANN, D.L., RICHARDS, D.A., ELLIOT, T.R., SMART, P.L., COATH, C.D. & HAWKESWORTH, C.J. (2005): Characterization of secondary electron multiplier nonlinearity using MC–ICPMS. *Int. J. Mass Spectrom.* **244**, 97-108.

HORN, I., RUDNICK, R.L. & MCDONOUGH, W.F. (2000): Precise elemental and isotope ratio determination by simultaneous solution nebulization and laser ablation–ICP–MS: application to U–Pb geochronology. *Chem. Geol.* **164**, 281-301.

HORSTWOOD, M.S.A. (2008): Data reduction strategies, uncertainty assessment and resolution of LA–(MC–)ICP–MS isotope data. *In* Laser Ablation ICP–MS in the Earth Sciences: Current Practices and Outstanding Issues (P. Sylvester, *ed*.). *Mineral. Assoc. Can. Short Course Series* **40**, 283-303.

HORSTWOOD, M.S.A., FOSTER, G.L., PARRISH, R.R., NOBLE, S.R. & NOWELL, G.M. (2003): Common-Pb corrected *in situ* U–Pb accessory mineral geochronology by LA–MC–ICP–MS. *J. Anal. At. Spectrom.* **18**, 837-846.

JACKSON, S.E., PEARSON, N.J., GRIFFIN, W.L. & BELOUSOVA, E.A. (2004): The application of laser ablation-inductively coupled plasma–mass spectrometry to *in situ* U–Pb geochronology. *Chem. Geol.* **211**, 47-69.

JAFFEY, A.H., FLYNN, K.F., GLENDENIN, L.E., BENTLEY, W.C. & ESSLING, A.M. (1971): Precision measurement of half-lives and specific activities of 235U and 238U. *Physical Rev*. **4**, 1889-1906.

JEFFRIES, T.E., FERNANDEZ-SUAREZ, J., CORFU, F. & Gabriel Gutierrez, A. (2003): Advances in U–Pb geochronology using a frequency quintupled Nd:YAG based laser ablation system ($\lambda$ = 213) and quadrupole based ICP–MS. *J. Anal. At. Spectrom.* **18**, 847-855.

KINNEY, P.D., GRIFFIN, B.J., HEAMAN, L.M., BRAKHFOGEL, F.F. & SPETSIUS, Z.V. (1997): SHRIMP U–Pb ages of perovskite from Yakutian kimberlites. *Russ. Geol. Geophys*. **38**, 97-105.

LABERGE, J.D. & PATTISON, D.R.M. (2007): Geology of the western margin of the Grand Forks complex, southern British Columbia: high-grade Cretaceous metamorphism followed by early Tertiary extension of the Granby fault. *Can. J. Earth Sci.* **44**, 199-228.

LEMIEUX, Y., THOMPSON, R.J., ERDMER, P., SIMONETTI, A. & CREASER, R.A. (2007): Detrital zircon geochronology and provenance of Late Proterozoic and mid-Paleozoic successions outboard of the miogeocline, southeastern Canadian Cordillera. *Can. J. Earth Sci.* **44**, 1675-1693.

LOCOCK, A.J. (1994): Aspects of the geochemistry and mineralogy of the Ice River Alkaline Intrusive Complex, Yoho National Park, British Columbia. University of Alberta, MSc thesis, 163 pages.

LUDWIG, K.R. (2003): User's manual for Isoplot 3.00: A geochronological toolkit for Microsoft Excel. *Berkeley Geochronology Center Special Publication* No. **4**, 70 pages.

MILLER, J.S., SANTOSH, M., PRESSLEY, R.A., CLEMENTS, A.S. & ROGERS, J.J.W. (1996): A Pan-African thermal event in southern India. *J. Southeast Asian Earth Sci.* **14**, 127-136.

PAUL, B., WOODHEAD, J.D. & HERGT, J. (2005): Improved *in situ* isotope analysis of low-Pb materials using LA–MC–ICP–MS with parallel ion counter and Faraday detection. *J. Anal. At. Spectrom*. **20**, 1350-1357.

PELL, J. & HÖY, T. (1989): Carbonatites in a continental margin environment – the Canadian Cordillera. *In* Carbonatites: Genesis and Evolution (K. Bell, *ed*.). Unwin Hyman, London,

200-220.

RICHTER, S., GOLDBERG, S.A., MASON, P.B., TRAINA, A.J. & SCHWIETERS, J.B. (2001): Linearity tests for secondary electron multipliers used in isotope ratio mass spectrometry. *Int. J. Mass Spectrom.* **206**, 105-127.

SCHULTZ, M.E.J., CHACKO, T., HEAMAN, L.M., SANDEMAN, H.A., SIMONETTI, A. & CREASER, R.A. (2007): Queen Maud Block: A newly recognized Paleoproterozoic (2.4–2.5 Ga) terrane in northwest Laurentia. *Geology* **35**, 707-710.

SIMONETTI, A., HEAMAN, L.M., HARTLAUB, R.P., CREASER, R.A., MACHATTIE, T.G. & BÖHM, C. (2005): U–Pb zircon dating by laser ablation–MC–ICP–MS using a new multiple ion counting Faraday collector array. *J. Anal. At. Spectrom.* **20**, 677-686.

SIMONETTI, A., HEAMAN, L.M., CHACKO, T. & BANERJEE, N.R. (2006): *In situ* petrographic thin section U–Pb dating of zircon, monazite, and titanite using laser ablation–MC–ICP–MS. *Int. J. Mass Spectrom.* **253**, 87-97.

SOUDERS, A.K. & SYLVESTER, P.J. (2008): Use of multiple channeltron ion counters for LA–MC–ICP–MS analysis of common lead isotopes in silicate glasses. *In* Laser Ablation ICP–MS in the Earth Sciences: Current Practices and Outstanding Issues (P. Sylvester, *ed.*). *Mineral. Assoc. Can. Short Course Series* **40**, 265-281.

SOUDERS, A.K. & SYLVESTER, P.J. (2008b): Improved *in situ* measurements of lead isotopes in silicate glasses by LA–MC–ICPMS using multiple ion counters. *J. Anal. At. Spectrom*. **23**, 535-543.

STEIGER, R.H. & JÄGER, E. (1975): Subcommission on geochronology: convention on the use of decay constants in geo- and cosmochronology. *Earth Planet. Sci. Lett.* **36**, 359-362.

STERN, R.A. (2001): A new isotopic and trace element standard for the ion microprobe: preliminary thermal ionization mass spectrometry (TIMS) U–Pb and electron microprobe data. *Geol. Surv. Canada, Current Research* 2001-F1.

STERN, R.A. & AMELIN, Y. (2003): Assessment of errors in SIMS zircon U–Pb geochronology using a natural zircon standard and NIST SRM 610 glass. *Chem. Geol.* **197**, 111-142.

TAYLOR, R.N., WARNEKE, T., MILTON, J.A., CROUDACE, I.W., WARWICK, P.E. & NESBITT, R.W. (2003): Multiple ion counting determination of plutonium isotope ratios using multi-collector ICP–MS. *J. Ana. At. Spectrom.* **18**, 480-484.

TODT, W., CLIFF, R.A., HANSER, A. & HOFMANN, A.W. (1996): Evaluation of a $^{202}Pb$–$^{205}Pb$ double spike for high-precision lead isotope analysis. In : Earth Processes. Reading the Isotope Code. Geophysical Monograph **95**. Ed. A. Basu, American Geophysical Union, Washington, 429-437.

WIEDENBECK, M., ALLÉ, P., CORFU, F., GRIFFIN, W.L., MEIER, M., OBERLI, F., VON QUADT, A., RODDICK, J.C. & SPIEGEL, W. (1995): Three natural zircon standards for U–Th–Pb, Lu–Hf, trace element and REE analyses. *Geostand. Newsl.* **19**, 1-23.

WILLIGERS, B.J.A., BAKER, J.A., KROGSTAD, E.J. & PEATE, D.W. (2002): Precise and accurate *in situ* Pb–Pb dating of apatite, monazite, and sphene by laser ablation multiple-collector ICP–MS. *Geochim. Cosmochim. Acta* **66**, 1051-1066.

# CHAPTER 15: USE OF MULTIPLE CHANNELTRON ION COUNTERS FOR LA–MC–ICP–MS ANALYSIS OF COMMON LEAD ISOTOPES IN SILICATE GLASSES

A. Kate Souders and Paul J. Sylvester
Micro-Analysis Facility, INCO Innovation Center (MAF-IIC)
*and* Department of Earth Sciences, Memorial University,
St. John's, Newfoundland A1B 3X5 Canada
kates@esd.mun.ca

## INTRODUCTION

One of the most significant developments in laser ablation–inductively coupled plasma–mass spectrometry (LA–ICP–MS) over the past decade has been the growth of *in situ*, high precision isotope ratio analyses of geological materials using multicollector (MC) magnetic sector instruments. A variety of isotopic systems have been investigated including B (*e.g.*, Tiepolo *et al.* 2006), Mg (*e.g.*, Norman *et al.* 2006), Si (*e.g.*, Chmeleff *et al.* 2008), S (*e.g.*, Mason *et al.* 2006), Fe and Cu (*e.g.*, Graham *et al.* 2004) Rb–Sr (*e.g.*, Woodhead *et al.* 2005), Sm–Nd (*e.g.*, McFarlane & McCulloch 2008), Lu–Hf (*e.g.*, Iizuka & Hirata 2005), Re–Os (*e.g.*, Pearson *et al.* 2002), U–Pb (*e.g.*, Simonetti *et al.* 2008) and U-series (*e.g.*, Eggins *et al.* 2005). Most of these studies have focused on isotopes that are sufficiently abundant in the sample (*e.g.*, Mg in olivine; S, Fe and Cu in sulfides, Nd in monazite; Hf in zircon) such that Faraday detectors can be used for ion collection.

There are many advantages of Faraday collection such as efficiency and uniform response (see Longerich 2008 for further discussion) but their precision is severely compromised by resistor noise at low signal intensities, as are found during *in situ* analysis of isotopes of minor to trace elements in minerals and glasses. In these cases, discrete-dynode, secondary electron multipliers (SEMs) or continuous-dynode, channel electron multipliers (CEMs or Channeltrons®) may be employed. Figure 15-1, for instance, illustrates the improved precision that can be attained on a $^{208}$Pb signal of ~40,000 cps using a Channeltron ion counter (1.5% RSD) compared to Faraday detector (6.7% RSD).

In this short course volume, Simonetti *et al.* (2008) describe the use of SEMs in conjunction with Faradays for LA–MC–ICP–MS U–Pb geochronology. Here, we report on LA–MC–ICP–MS analyses for silicate glass standard reference materials (SRMs) using Channeltrons. Our results on these SRMs have already been reported elsewhere (Souders & Sylvester 2008) but here we give more details on the analytical procedures used and principles behind them. The use of Channeltrons for LA–MC–ICP–MS is a relatively new development. Tiepolo *et al.* (2006) used Channeltrons for *in situ* B isotope measurements by LA–MC–ICP–MS. Cocherie & Robert (2008) reported combined Channeltron–Faraday measurements for LA–MC–ICP–MS U–Pb zircon geochronology.

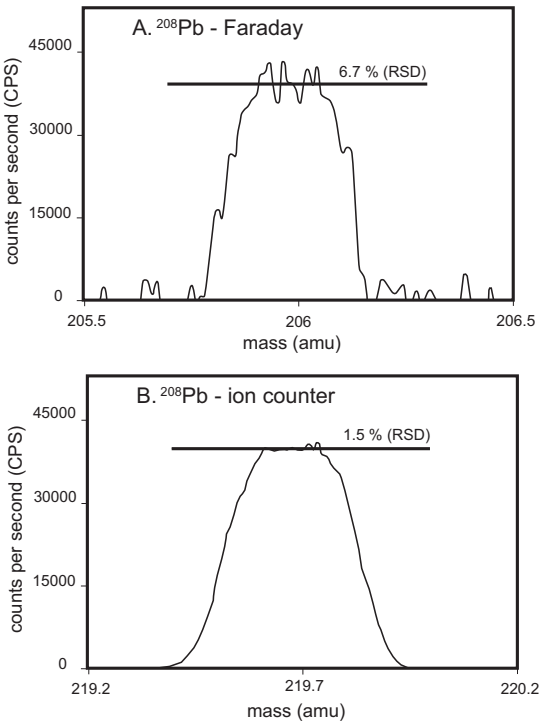


FIG. 15-1. Peak shapes of $^{208}$Pb from a SRM 981standard solution of 0.5 ppb total Pb concentration measured on a (**A**) Faraday detector and a (**B**) Channeltron ion counter. The x-axis corresponds to the mass range over which the peak was measured with the center value representing the axial mass of the collector array. The noise level for the plateau of the $^{208}$Pb signal collected in the Faraday detector (6.71 % RSD, 1-σ) is over four times that of the noise level for the plateau of the $^{208}$Pb signal collected in the ion counter (1.5 % RSD, 1-σ).

Mineralogical Association of Canada Short Course 40, Vancouver, B.C., p. 265–281.

## PRINICPLES OF MULTI-ION COUNTING WITH ELECTRON MULTIPLIERS

Ion counting and the use of electron multipliers have been incorporated into mass spectrometry for almost 50 years to detect and measure ions of low to moderate intensity ion beams, that is, less than $10^6$ counts per second (cps). The physical process that allows electron multipliers, or ion counters, to operate is secondary ion emission. The general principle of secondary electron emission is that a particle or ion impacts a high voltage surface, or dynode, causing the release of secondary electrons from the outer layers of atoms. The number of electrons produced by an impact is dependant on the type of particle hitting the surface (*i.e.,* positive ion, negative ion, electron, *etc.*), the angle of contact between the particle and the surface, the mass and energy of the incoming particles and the condition of the surface. The electrons produced by this initial collision are directed down the detector by an electric potential gradient, generating even more secondary electrons each time a collision occurs between an electron and the dynode surface inside the detector. This amplification process is quite effective: some 10 thousand to 100 million electrons are produced from each ion. Eventually the electrons reach an output device at the end of the ion counter, where a resultant pulse is produced that is processed using digital electronics.

A schematic of a Channeltron continuous-dynode electron multiplier is shown in Figure 15-2. They consist of curved Pb silicate glass tubes that have the ability to detect both positive and negative ions, electrons and photons. A potential between ~2000 and 3200 V is applied to the top or input end of the CEM and decreases steadily to ground state at the output end of the detector. Secondary electrons generated at the input end of the detector

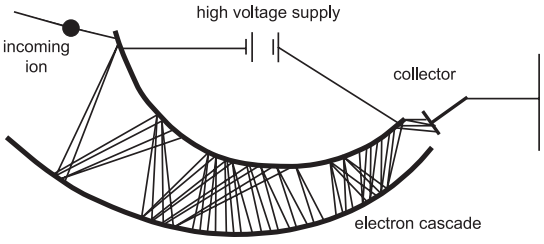


FIG. 15-2. Example of a continuous-dynode electron multiplier (modified from Turner *et al.* 1998). Secondary electrons are produced when ions impact the high voltage surfaces while traveling down the channel.

are driven down the channel to a collector by the potential gradient generating even more secondary electrons each time the particles come in contact with the inner surface walls of the detector (Burle Technologies Inc. 2003). SEMs operate on the same principle as CEMs, but consist of discrete dynode plates (see Simonetti *et al.* 2008) rather than a continuous dynode.

Electron gains, or the output current divided by the input current, are a function of the application, the voltage applied to the detector and the length of the dynode surface within the detector. The voltage applied to each detector has an effect on the impact energy of ions arriving at the detector, which in turn influences the electron gain of the detector. In order to maintain normal gains, it is important to make sure the operational voltage of the ion counter is set properly. It is also important to understand that ion counter gains change or "drift" with exposure to ion currents over time, even within a single analytical session of a few hours. The challenge for isotope ratio measurements using multiple ion counters (MICs) is that each Channeltron will see different count rates, which are largely a function of the relative abundances of the isotopes measured, and thus the cross-calibration normalization factors for the different gains between the detectors or "yields" will drift as well. If the drift is linear over time, however, it may be corrected using a standard–sample–standard bracketing technique assuming that the standard and sample drift in an analogous fashion (Tiepolo *et al.* 2006, Souders & Sylvester 2008, Cocherie & Robert 2008). Drift may also be corrected by normalization to the invariant ratio of an isotope pair that is analyzed at the same time as the unknown isotope ratio (*e.g.*, Pearson *et al.* 2008). Possible concerns about differences in drift between the sample and an external reference material are eliminated if the invariant pair is of the same chemical element as the unknown isotope ratio pair (*e.g.*, $^{179}Hf/^{177}Hf$ for $^{176}Hf/^{177}Hf$).

Linearity of the ion counters can become compromised by the accuracy of pulse pile up or "dead time" corrections at count rates exceeding approximately 300,000 cps. Thus it is recommended to adjust LA parameters (beam size, fluence, repetition rate) so that analytical work can be carried out at count rates below these levels. This is an unusual (but welcome) case in microbeam-based geoanalysis where the analytical protocols for optimal data quality are in concert with the desire of the geologist to reveal fine scale heterogeneities in

minerals by reducing the analytical volume as much as possible.

Tiepolo *et al.* (2006) have indicated that a "burn-in" period is needed for the stabilization of the gain factors for new Channeltrons. They suggested that Channeltrons become increasingly stable after exposure to more than 1.5 billion counts and have an operation voltage higher than 2300 V. Over months to years (depending on use), the surface of the detector where electron multiplication takes place will begin to degrade due to contamination from the vacuum system and as a result of ion impacts. The operational voltage of the detector will need to be increased in order to keep the impact energy of arriving particles constant and to maintain normal electron gains. Thus it is advantageous to keep count rates low (<300,000 cps) not only to limit detector drift and potential dead time correction errors, but also in order to prolong the life-span of the ion counters before replacement becomes necessary.

## PROCEDURES FOR LA–MC–ICP–MS ANALYSES OF PB ISOTOPES USING MULTIPLE CHANNELTRONS

### Instrumentation

*In situ* Pb isotope measurements described in this chapter were performed on a Thermo Finnigan NEPTUNE double focusing multi-collector (MC)–ICP–MS equipped with nine Faraday detectors and eight Channeltron ion counters. The ion counters are identical in size to the Faraday detectors and can be attached to the high or low mass side of a Faraday cup within the collector array (Schwieters *et al.* 2004). A generalized schematic of the NEPTUNE MC–ICP–MS is shown in Figure 15-3. Normal instrument operating parameters and the collector configuration used in this study are provided in Tables 15-1 and 15-2, respectively. Five ion counters are attached to the low mass side of Faraday cup L4. They are used for the static, concurrent measurement of $^{202}$Hg, $^{204}$(Hg + Pb), $^{206}$Pb, $^{207}$Pb and $^{208}$Pb. The $^{202}$Hg measurement is used to correct for the isobaric interference of $^{204}$Hg on $^{204}$Pb. Hg is a ubiquitous laboratory contaminant, present in the gas supplies for the ICP–MS and from other environmental sources that can coat surfaces of instrument components and sample mounts. It also can be a constituent of the sample matrix itself. To reduce levels of Hg in the Ar gas, an activated charcoal filter made by Frontier GeoSciences Inc. is placed in the gas line to the ICP torch. The dry sorbent in the trap collects the vapor phase Hg present in both elemental and oxidized forms.

It is possible to monitor $^{235}$U (simultaneously with the Pb isotopes) in an ion counter attached to a high mass Faraday cup due to the mass dispersion provided by the dynamic zoom optics of the NEPTUNE system and the variable multi-collector array. In this chapter however $^{235}$U data are not discussed because we are concerned only with describing Pb isotope analyses in silicate glass SRMs of known composition. But the reader should keep in mind that $^{235}$U data would be valuable for Pb isotope investigations of minerals or glasses of unknown composition in which Pb isotope ratios have been modified by the in-growth of radiogenic

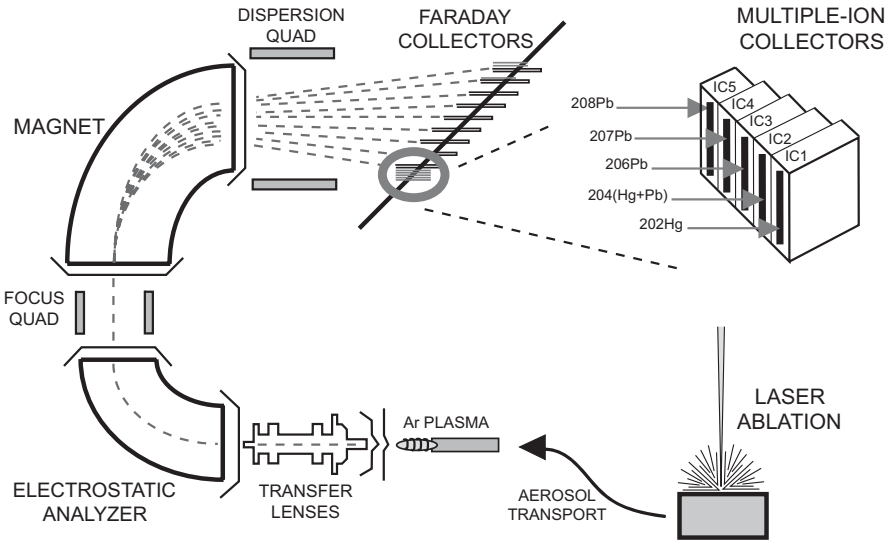


FIG. 15-3. Generalized illustration of the Finnigan NEPTUNE multi-collector inductively coupled plasma mass spectrometer.

TABLE 15-1 TYPICAL OPERATING CONDITIONS FOR THE FINNIGAN NEPTUNE MC–ICP–MS AND GEOLAS LASER ABLATION SYSTEM

| | |
|---|---|
| **Finnigan Neptune MC-ICPMS** | |
| Operation power | 1200 W |
| HV | 10 kV |
| Cool gas flow | 16 l $min^{-1}$ |
| Auxiliary gas flow | 0.7 l $min^{-1}$ |
| Carrier gas (Ar) flow rate | 0.9 l $min^{-1}$ |
| Cones | Ni (H skimmer cone) |
| **GeoLas laser ablation system** | |
| Lambda Physik Compex Pro 110 ArF excimer | 193 nm |
| Laser fluence | ~5 J $cm^{-2}$ |
| Spot size | 40 - 99 μm |
| Repetition rate | 10 Hz |
| He gas to cell | 1.2 l $min^{-1}$ |

Pb via the decay of U after crystallization, or in U-rich phases such as zircon measured for U–Pb geochronology.

A GeoLas laser ablation system is linked to the MC–ICP–MS for *in situ* analyses. This system includes a Lambda Physik ComPex Pro 110 ArF excimer laser operating at a wavelength of 193 nm and a pulse width of 20 ns. Typical operating conditions for the GeoLas system are included in Table 15-1. A laser fluence of approximately 5 J/$cm^2$ and a repetition rate of 10 Hz were used for all glass analyses. The spot size of the analyses ranged from 40 to 99 μm depending on the total Pb concentrations of the glasses. Samples were ablated in He gas, which reduces sample re-deposition and elemental fractionation while increasing sensitivity for 193 nm ablation (Eggins *et al.* 1998, Günther & Heinrich 1999). Hg was filtered from the He using Au-coated glass wool placed on the He gas line feeding the ablation cell.

**Long term settings of Channeltrons**

The dead time for each ion counter on our instrument is set to 70 ns at the recommendation of the manufacturer due to the tendency for Channeltrons to produce double pulses, the second arriving 30–40 ns after the main pulse (Tiepolo *et al.* 2006). The dark noise and operation voltage for each ion counter are checked every few months. The typical dark noise measurement for a single ion counter has not exceeded 0.0060 cps. A plateau calibration curve (cps *vs.* voltage) is constructed to determine the operation voltage for each ion counter using a PCL script within the NEPTUNE operating software. This procedure is performed in solution mode for each ion counter individually. The calibration curve is constructed by focusing the ion beam into one ion counter while the operation voltage of that ion counter is increased in 20 V increments. The output signal for each step is recorded in counts per second. The operation voltage for each ion counter is determined by observing the point, or bend in the curve where the change in signal intensity (cps) no longer significantly increases with a corresponding increase in the detector voltage. The operation voltage can be different for each ion counter so a plateau calibration curve must be constructed for each individual ion counter. Operation voltages for the Channeltrons in our laboratory were set at ~2100 V when they were new and had reached ~3000 V when they first needed to be replaced.

**Sample preparation**

Sample preparation for LA–MC–ICP–MS is relatively straightforward. In the case here, small separates of the silicate glass SRMs were mounted in 10 or 25 mm rings using epoxy resin. Once the epoxy had cured, the mount was ground to a flat surface and polished using diamond abrasive, exposing a cross-section of each glass. The mounts

TABLE 15-2 FINNIGAN NEPTUNE COLLECTOR ASSIGNMENTS FOR PB ISOTOPE ANALYSIS

| **Collector**[a] | **IC1** | **IC2** | **IC3** | **IC4** | **IC5** | **L4** | **L3** | **L2** | **L1** | **C** | **H1** | **H2** | **H3** | **IC6** | **H4** | **IC7** | **IC8** |
|---|---|---|---|---|---|---|---|---|---|---|---|---|---|---|---|---|---|
| Ion Counters | | | | | | | | | | | | | | | | | |
| isotope | $^{202}$Hg | $^{204}$(Hg +Pb) | $^{206}$Pb | $^{207}$Pb | $^{208}$Pb | | | | | 219.68 | | | | $^{235}$U | | | |
| Faraday | | | | | | | | | | | | | | | | | |
| isotope | | | | | | $^{200}$Hg | $^{202}$Hg | $^{204}$(Hg +Pb) | | | $^{206}$Pb | $^{207}$Pb | $^{208}$Pb | | | | |

[a] L4 to L1, C, and H1 to H4 are Faraday cups. IC1 to IC5 are ion counters fixed to Faraday cup L4. IC6 is an ion counter fixed to Faraday cup H3. IC7 and IC8 are ion counters fixed to Faraday cup H4.

fit inside circular cavities of the polycarbonate holders fashioned for the laser ablation cell.

The SRMs discussed here are USGS BCR2-G and MPI-DING T1-G, ATHO-G, KL2-G and ML3B-G, made by fusion of natural rocks. BCR2-G, KL2-G and ML3B-G all have basaltic compositions whereas T1-G is quartz diorite and ATHO-G is rhyolite. Each glass has well defined Pb isotope ratios and chemical composition, with total Pb concentrations ranging from ~1 to 11 ppm (Jochum *et al.* 2000, Jochum *et al.* 2005a, Jochum *et al.* 2006a).

**Tasks for set-up of an analytical session of isotope ratio measurements**

Figure 15-4 is a flow chart documenting the step by step tasks that an analyst needs to do each day that LA–MC–ICP–MS analyses are to be carried out. To begin, great care must be given to eliminate any potential contamination from the ambient environment on the surfaces of components of the ICP–MS instrument (ablation cell, transfer tubing, torch, cones, *etc.*) and the samples themselves. This is particularly true of Pb and other "sticky" metals that are ubiquitous contaminants in laboratory settings. It is true that laboratory contaminants can be removed from the surface of sample mounts by "pre-ablation" for a few seconds before the "analytical ablation" is carried out but since this only disperses contaminants into the sample introduction system where they may be released during subsequent analyses, we emphasize careful cleaning instead.

Our epoxy mounts are cleaned in an ultrasonic bath for approximately 15 min with double distilled water, deionized and purified (to 18 MΩ $cm^{-1}$) by a Milli-Q water system. The surface of each mount is then scrubbed with double distilled, ~8 N $HNO_3$ followed by a Milli-Q water rinse. The mount is left to dry in a positive pressure air box prior to loading into the laser ablation sample cell. The ICP torch, injector, quartz shield, glass T-piece used to mix the He and Ar gases, and sampler and skimmer cones are all cleaned prior to each analytical session as well. Torch parts and glassware are soaked in a ~0.5 N $HNO_3$ bath and subsequently rinsed with double distilled ~8 N $HNO_3$ followed by a Milli-Q water rinse. Residue from prior ablations was removed from both the sample and skimmer cones with a cotton-topped applicator and each cone was rinsed with deionized water prior to installation on the instrument.

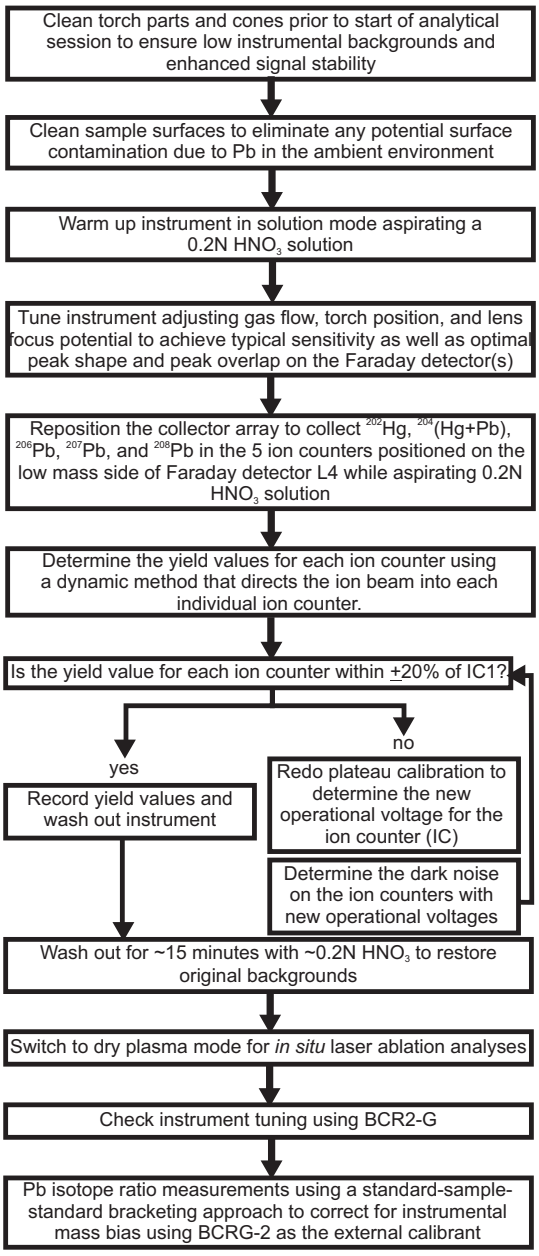


FIG. 15-4. Flow chart describing the daily analytical set-up for Pb isotope analyses using multiple ion counters.

The next steps in the daily set-up involve instrument tuning and determinations of yields (cross-calibration normalization factors) for the Channeltrons, which are both done in solution mode prior to *in situ* laser analyses. On the NEPTUNE, after a typical 30 to 45 minute warm-up period, gas flow, torch position, and lens focus potentials are all first adjusted for maximum sensitivity as well as optimal peak shape and peak overlap using the Faraday detectors (Table 15-2) and aspirating a 10

ppb Pb NBS 981 solution. Typical sensitivity is 28 mV or ~1,750,000 cps (1 mV is ~62,500 cps) per ppb $^{208}$Pb. Following a brief wash-out with dilute $HNO_3$, the collector array is repositioned for the collection of $^{202}$Hg, $^{204}$(Hg + Pb), $^{206}$Pb, $^{207}$Pb, and $^{208}$Pb in the 5 MICs attached to the low mass end of Faraday cup L4 (Table 15-2).

Determination of the ion counter yields is shown schematically in Figure 15-5. This process is similar to determining the gain for a Faraday collector but instead of an electronic pulse being sent through each detector, the relative yield of each ion counter is determined by a dynamic peak jumping method which sequentially places a reference signal of ~100,000 cps into each of the 8 ion counters by changing the mass setting for the center Faraday cup. The relative yield value for each ion counter is determined in solution mode to maximize signal stability and attain the best precision. The dynamic cycle is repeated 10 times using an integration time of 4.194 s. The relative yield value for each ion counter to be used in the analytical session (IC1–IC5 in the case of Pb isotopes) is then determined by normalizing the average of the measured signal intensities for each ion counter to the average response of IC1. If the relative yield values are not within 80% of IC1, the operation voltage on the ion counter is adjusted.

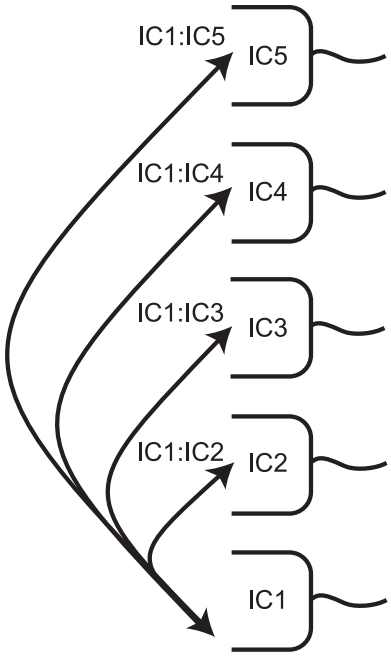


FIG. 15-5. Illustration depicting how the yield cross-calibration factors for each ion counter are determined. An ion beam of ~100 000 counts is directed into each individual ion counter 10 times over the course of the yield calibration. The beam intensity is measured using an ~8 s integration time. To determine the yield factor, the measured beam intensities of ion counters 2–5 (IC2–IC5) are recorded and normalized to the measured ion beam intensity of ion counter 1 (IC1).

After another brief wash-out period, the instrument is switched to laser ablation mode and rechecked for sensitivity on a known reference material and, if necessary, retuned. Under dry plasma conditions a typical sensitivity of 23,000 cps per ppm $^{208}$Pb for *in situ* analyses of BCR2-G (~11 ppm total Pb) with a 40 μm laser spot is achieved using our instrumentation. Signal intensities during *in situ* analysis are typically less then ~5 mV, or ~312,500 cps, in all ion counters (for BCR2-G with a 40 μm spot, ~230,000 cps $^{208}$Pb is typical). Ion counter backgrounds are usually less than 1000 cps for all the Pb isotopes.

**Analytical routine**

The duration of each standard and sample analysis in our experiments is ~120 seconds or 120 cycles using an integration time of ~1 sec/cycle. The first 30 seconds (cycles) are used to measure the background count rates with the laser off followed by 60 seconds of laser ablation monitoring of the $^{202}$Hg, $^{204}$Pb, $^{206}$Pb, $^{207}$Pb and $^{208}$Pb isotopes followed by a 30 second wash-out.

Standard–sample–standard bracketing is employed to correct for instrumental mass fractionation in the Ar plasma and other components of the ICP (*e.g.*, the transfer lenses), as well as for detector drift. The Pb isotopic system does not have an invariant isotopic pair that can be used to monitor fractionation and drift. Also, the configuration of ion counters on our instrument does not allow us to monitor mass bias and drift relative to an aspirated Tl tracer solution of known isotopic composition or measured $^{202}$Hg/$^{200}$Hg using the MICs in static mode (Pearson *et al.* 2008). For bracketing, the Pb isotope measurement of every three unknown samples is preceded and followed by three measurements of the bracketing standard, BCR2-G. Souders & Sylvester (2008) discussed the suitability of BCR2-G as a bracketing standard for *in situ* Pb isotope measurements including its homogeneity (which, on the micrometre scale, is better than 1% for Pb isotope ratios with $^{204}$Pb and as good as 0.15% for $^{207}$Pb/$^{206}$Pb), and gave the calibration values used for Pb isotope ratios in this material.

On-line corrections for yield, dark noise and dead time are performed using the NEPTUNE software prior to downloading the measured mass

intensities into an Excel spreadsheet for off-line subtraction of mean gas background intensities from the time-resolved signal intensities for each isotope, $^{204}$Hg interference corrections on $^{204}$Pb (described below), Pb isotope ratio calculations, and instrumental mass bias corrections based on the exponential mass bias law (Albarede *et al.* 2004). Pb isotope ratios determined for the set of three BCR2-G standards run before and after each set of 3 unknown samples are averaged together. The Pb isotope ratios for the unknowns are linearly interpolated, anchored by the average value of the three standards.

As noted above, bracketing with an external standard can be carried out by simple interpolation only if drift in the measured isotopic ratios of the standard are linear over the course of an analytical session, and there are no differences in mass bias between the standard matrix and the sample matrix. Figure 15-6 illustrates how the Channeltrons used for $^{206}$Pb (IC3) and $^{208}$Pb (IC5) drifted for BCR2-G, ML3B-G, KL2-G and ATHO-G SRMs over the course of two experiments separated by five months in our laboratory. $^{208}$Pb is about twice as abundant as $^{206}$Pb in the SRMs and thus the efficiency of IC5 decreases more rapidly than IC3 as it is exposed to greater total counts over time than IC3. The $^{208}$Pb/$^{206}$Pb ratio decreases accordingly but in a linear fashion that is consistent for all four SRM glasses. It is particularly noteworthy that ATHO-G, a rhyolite glass, exhibits similar drift behavior as BCR2-G, ML3B-G and KL2-G, which are basalt glasses. This gives us some confidence that BCR2-G can be effectively used as a bracketing standard for Pb isotope measurements in unknown glasses of basalt to rhyolite composition. Note that the total drift of the Channeltrons was much greater in the later experiment (May 2007) than in the

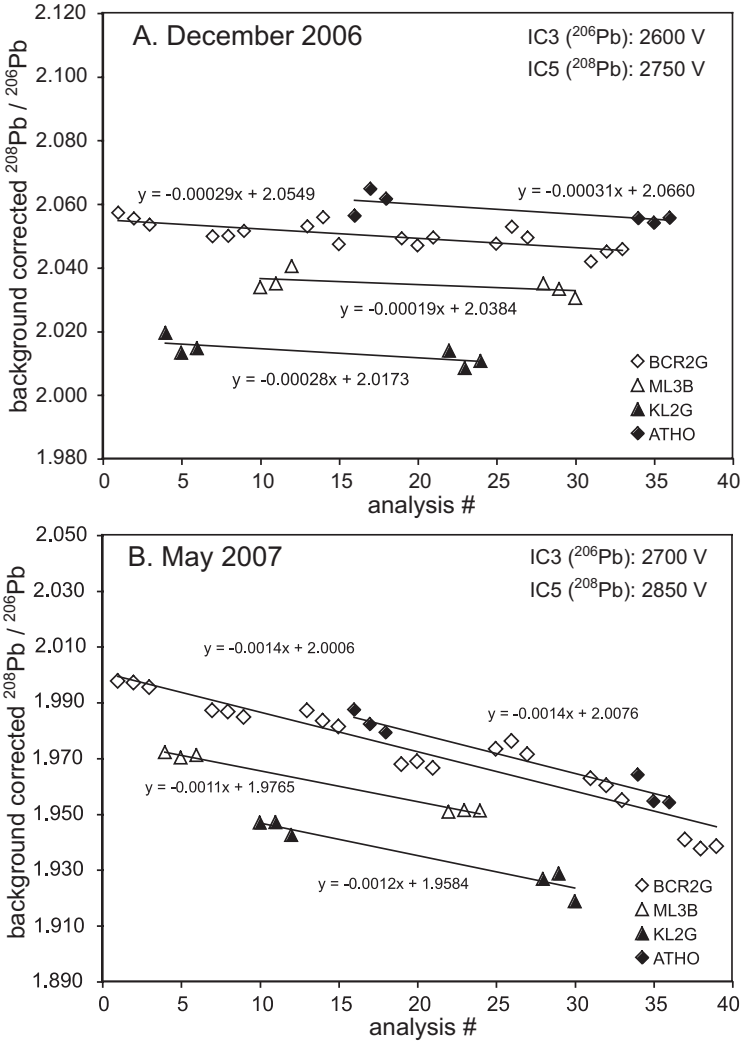


FIG. 15-6. Decrease in the measured (uncorrected) $^{208}$Pb/$^{206}$Pb ratio within sequences of analyses consisting of 4 different silicate glass SRMs performed in (**A**) December 2006 and (**B**) May 2007, the latter with collector voltages set somewhat higher. The decrease is due largely to drift in ion counter yields. The slopes of the linear regressions fit to the drift are similar for all materials, independent of composition, indicating that BCR2-G may be used effectively as the bracketing standard for the other silicate glasses. The time intervals covered by the December 2006 and May 2007 experiments are 85 and 90 minutes, respectively.

earlier one (December 2006). This may reflect the fact that the operation voltage settings for the ion counters had not been recently calibrated before the May 2007 experiment, in contrast to the December 2006 experiment.

**Interference corrections for Hg on $^{204}$Pb**

The main motivation for using multicollector ICP–MS instruments for measurements of Pb isotope ratios rather than single collector instruments is the potential to determine ratios involving the minor $^{204}$Pb isotope much more precisely. The ability to measure Pb isotope ratios involving $^{204}$Pb is particularly difficult in Pb-poor samples due to its low relative abundance (~1.4% of all common Pb) and the isobaric interference from $^{204}$Hg mentioned above. The interference from $^{204}$Hg is potentially very significant for laser analyses where target materials contain more than ~10 ppm Hg, and even for materials with less Hg where Pb concentrations are very low (< 5 ppm total Pb).

We have explored two methods for interference corrections for $^{204}$Hg on $^{204}$Pb, which are detailed in Figure 15-7 and in Souders & Sylvester (2008). In Method 1, which is very similar to the off-line 204-correction procedure presented in Horstwood *et al.* (2003) and Paul *et al.* (2005), gas background subtraction removes the $^{204}$Pb and $^{204}$Hg in the gas from the $^{204}$(Hg + Pb) measurement, and any residual $^{204}$Hg derived from the sample itself is calculated from the $^{204}$Hg/$^{202}$Hg and the background corrected $^{202}$Hg measurement in the sample. $^{204}$Hg/$^{202}$Hg is ideally calculated from the relative natural abundances of the Hg isotopes and a mass bias factor (β) determined from the observed $^{202}$Hg/$^{200}$Hg, measured in the gas background at the start of a day's laser ablation session using a cup configuration in which $^{200}$Hg is collected in IC1 and $^{202}$Hg in IC2. With our instrumentation, however, we could not measure $^{202}$Hg/$^{200}$Hg in the ion counters accurately (possibly due to an isobaric interference on $^{202}$Hg). We thus had to simply assume that $^{204}$Hg/$^{202}$Hg had the natural ratio recommended by IUPAC (Rosman & Taylor 1997).

In Method 2, the $^{204}$Hg/$^{202}$Hg of the gas background is determined from measurements of $^{202}$Hg, $^{204}$(Hg+Pb) and $^{208}$Pb made with the laser off prior to each analysis. For each gas background measurement cycle, $^{204}$Pb is calculated from the measured $^{208}$Pb and $^{208}$Pb/$^{204}$Pb, assuming that the actual isotopic composition of Pb in the gas is given by the $^{208}$Pb/$^{204}$Pb for modern Pb ($^{208}$Pb/$^{204}$Pb = 38.63 ±0.98; Stacey & Kramers 1975). The $^{204}$Hg in the gas is then determined by subtraction of the calculated $^{204}$Pb from the measured $^{204}$(Hg + Pb), and a calculated $^{204}$Hg/$^{202}$Hg in the gas is derived using the measured $^{202}$Hg in the gas. With both $^{204}$Pb and $^{204}$Hg/$^{202}$Hg in the gas now established, the $^{204}$Pb for each laser ablation measurement cycle is determined by subtracting $^{204}$Hg from the measured $^{204}$(Hg + Pb) using the measured $^{202}$Hg during laser ablation and the average $^{204}$Hg/$^{202}$Hg for the gas background. The resulting $^{204}$Pb is then background corrected using the average $^{204}$Pb calculated for the gas background.

Souders & Sylvester (2008) tested both methods and found that Method 2 gave somewhat more precise results for their data sets. They also showed that while within-run fluctuations in the mass bias factor (β) calculated from $^{202}$Hg/$^{200}$Hg in Method 1 will have little effect on the accuracy of the final Pb isotope results for most natural silicate glasses, which have $^{204}$Hg/$^{204}$Pb ratios of less than 0.5, data quality will be degraded for minerals (notably some sulfides) with $^{204}$Hg/$^{204}$Pb intensities greater than ~2 (Fig. 15-8). Therefore Method 2 is preferred for determining Pb isotope ratios from LA–MC–ICP–MS data.

**ION COUNTER LINEARITY**

The linearity of each of ion counters IC2–IC5 as a function of count rate is shown for both solution and laser analysis in Figures 15-9 and 15-10, respectively. In the solution experiment, a series of SRM 981 dissolutions with total Pb concentrations from 0.025 to 0.1 ppb were analyzed. Signal intensities varied from a few hundred counts per second for $^{204}$Pb to ~120,000 cps for $^{208}$Pb (Fig. 9A–D). All results are well correlated ($r^2$ >0.99) showing a linear increase in count rate with increasing Pb concentration. The laser linearity test was performed by ablating BCR2-G for 60 seconds and varying the total volume of material ablated by changing the diameter of the laser spot while keeping the laser energy (3 J/cm$^2$) and laser repetition rate (10 Hz) constant. Pb count rates ranged from ~300 cps (20 μm spot) to ~4000 cps (109 μm spot) for $^{204}$Pb, to ~7000 cps (20 μm spot) to ~130,000 cps (109 μm spot) for $^{208}$Pb (Fig. 10A–D). This is associated calculated laser pit volumes of ~18,000 μm$^3$ to ~575,000 μm$^3$ respectively. Again, the results are well correlated ($r^2$ > 0.99) with count rates increasing linearly with increasing spot size.

The co-linearity of the ion counters as a function of count rate is illustrated for both solution

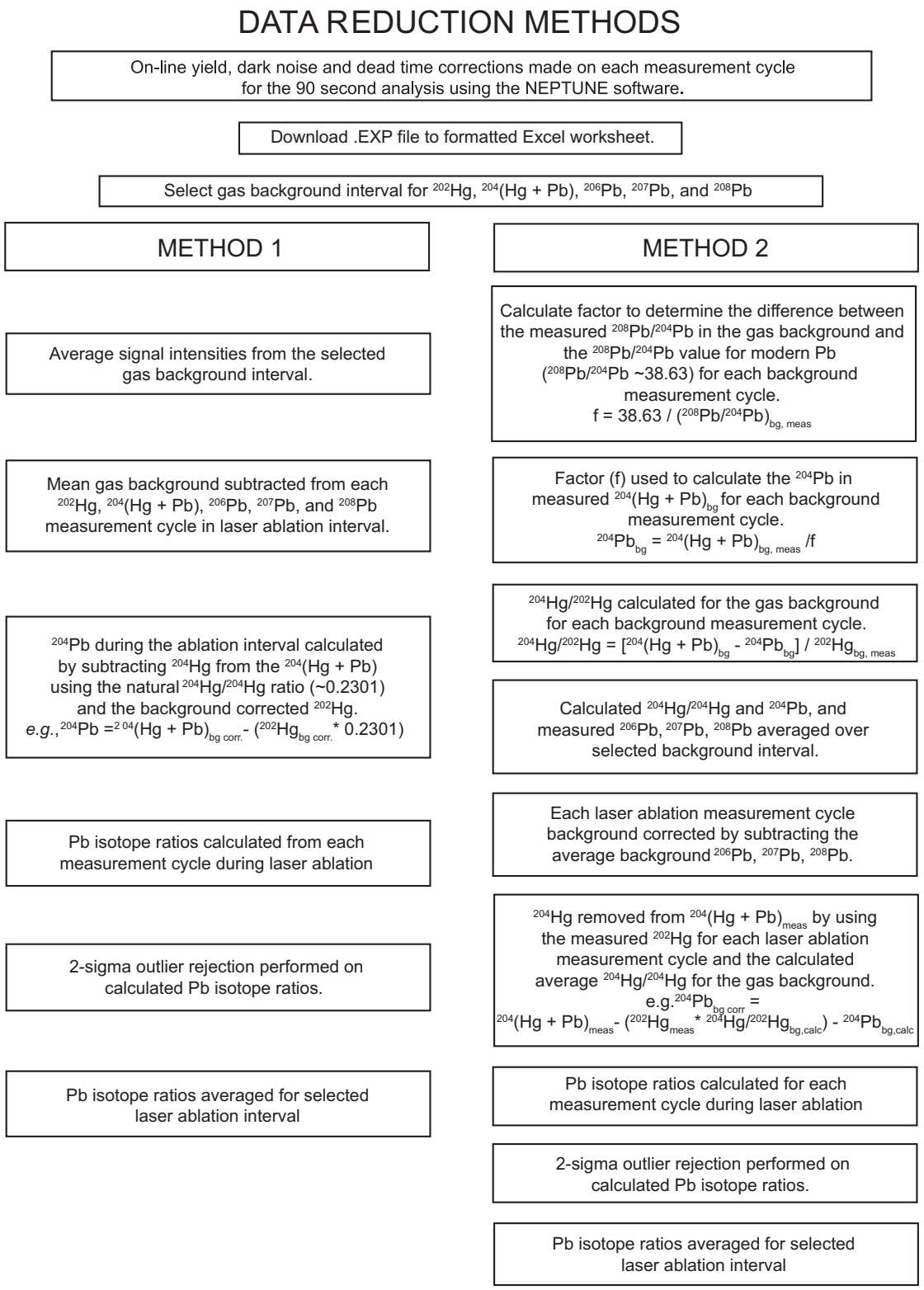


FIG. 15-7. Comparison of the two data reduction strategies presented in this chapter. Method 2 is the reduction method favored by the authors and used for routine daily Pb isotope analyses using multiple ion counters.

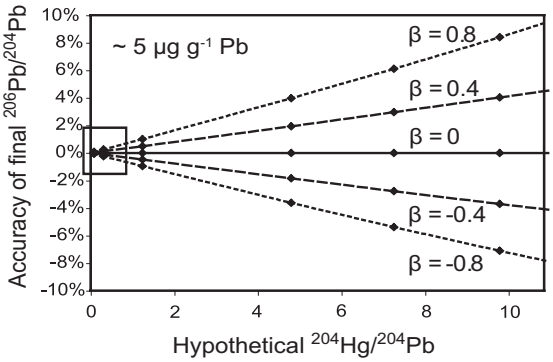


FIG. 15-8. Plot of accuracy of the final $^{206}Pb/^{204}Pb$ as a function of hypothetical $^{204}Hg/^{204}Pb$ and various mass bias factors (β) for a material of approximately 5 µg $g^{-1}$ Pb. The box highlights the typical Hg/Pb ratios for silicate glasses used in our study, which is < 0.5. (From Souders & Sylvester 2008).

(Fig. 9E–H) and laser ablation (Fig. 10E–H) analyses using $^{208}Pb/^{204}Pb$ (IC5/IC2) and $^{207}Pb/^{206}Pb$ (IC4/IC3) ratios. The figures plot the data both before (E–F) and after (G–H) mass bias corrections were applied and are shown relative to the preferred values of each of SRM 981 (Baker *et al.* 2004) and BCR2-G (http://georem.mpch–mainz.gwdg.de). The results of the solution and laser analyses show that within the range of Pb concentrations and amounts of ablated material that were evaluated, the mass bias corrected Pb isotope ratios match the preferred values to better than ~0.2% for the solution data and to within ~0.7 to 1% for the laser data. The somewhat better accuracy for the solution data compared to the laser data reflect additional sources of error in laser analyses beyond ion counter co-linearity. These additional errors are probably associated with the generation, transport and vaporization of laser-derived aerosols.

## ACCURACY AND PRECISION OF SILICATE GLASS ANALYSES

Souders & Sylvester (2008) reported Pb isotope ratios for the silicate glass SRMs T1-G (11.6 ppm total Pb), ATHO-G (5.67 ppm total Pb), KL2-G (2.07 ppm total Pb) and ML3B-G (1.38 ppm total Pb), measured using the methods discussed in this chapter (Fig. 15-11). Results for T1-G and ATHO-G agree, on average, with the preferred values to within 0.10% and 0.15%, respectively, using 40 µm laser ablation spots. For KL2-G and ML3B-G, measured mean $^{208,207,206}Pb/^{204}Pb$ ratios are within 0.75% of the accepted values using 69 µm spots, whereas measured mean $^{207}Pb/^{206}Pb$ and $^{208}Pb/^{206}Pb$ ratios are within 0.45% of preferred values. For the glasses with the lowest concentrations of Pb, Method 2 for the Hg interference correction produces somewhat more accurate and precise results than Method 1.

Figure 15-12 provides a comparison between the external precision of $^{207}Pb/^{206}Pb$ and $^{208}Pb/^{204}Pb$ ratios determined by Souders & Sylvester (2008) with the combined SEM–Faraday, LA–MC–ICP–MS measurements of Paul *et al.* (2005) and Simonetti *et al.* (2005) and the single SEM collector, LA– sector field (SF)–ICP–MS data of Jochum *et al.* (2005b) and Jochum *et al.* (2006b). For laser spot sizes between 90 to 120 µm, the external precision of the multi-Channeltron LA–MC–ICP–MS measurements of Souders & Sylvester (2008) for both the $^{207}Pb/^{206}Pb$ and $^{208}Pb/^{204}Pb$ ratios in the SRMs with the lowest Pb concentrations, KL2-G and ML3B-G, show a distinct improvement when compared to the measurements made with the combined SEM–Faraday LA–MC–ICP–MS and single SEM–collector LA–SF–ICP–MS methods. For 40 and 50 µm spots on the SRMs with somewhat more Pb, ATHO-G and T1-G, there is improvement in the precision on $^{208}Pb/^{204}Pb$ ratios for the data of Souders & Sylvester (2008) compared to the single SEM collector data, but not in the precision on $^{207}Pb/^{206}Pb$ ratios. The results attest to the particular improvement in external precision that can be achieved for Pb isotope ratios involving $^{204}Pb$ when ion counters are used to collect all 4 Pb isotopes in Pb-poor samples. With multicollector cup configurations that include Faraday detectors, it is necessary to produce a signal of at least ~5mV (~310,000 cps) to preserve acceptable levels of precision.

Souders & Sylvester (2008) compared the theoretical and observed limits of precision for the multiple Channeltron measurements for Pb isotopes using the observed internal precision for the silicate SRMs glasses that they analyzed, plotted as a function of total $^{208}Pb$ intensity (Fig. 15-13). Theoretical limits of precision are governed by Poisson counting statistics, detector dark noise, the uncertainty on the measurement of the blank, and uncertainties associated with ion counter gains and the correction for the isobaric interference of $^{204}Hg$ on the 204 mass. Theoretical precision degrades rapidly at total $^{208}Pb$ intensities of less than 1 mV (~62,500 cps). The minimum theoretical limits of precision for Pb isotope ratios measured using multiple Channeltrons are approached at lower total $^{208}Pb$ count rates than for Faraday–SEM cup

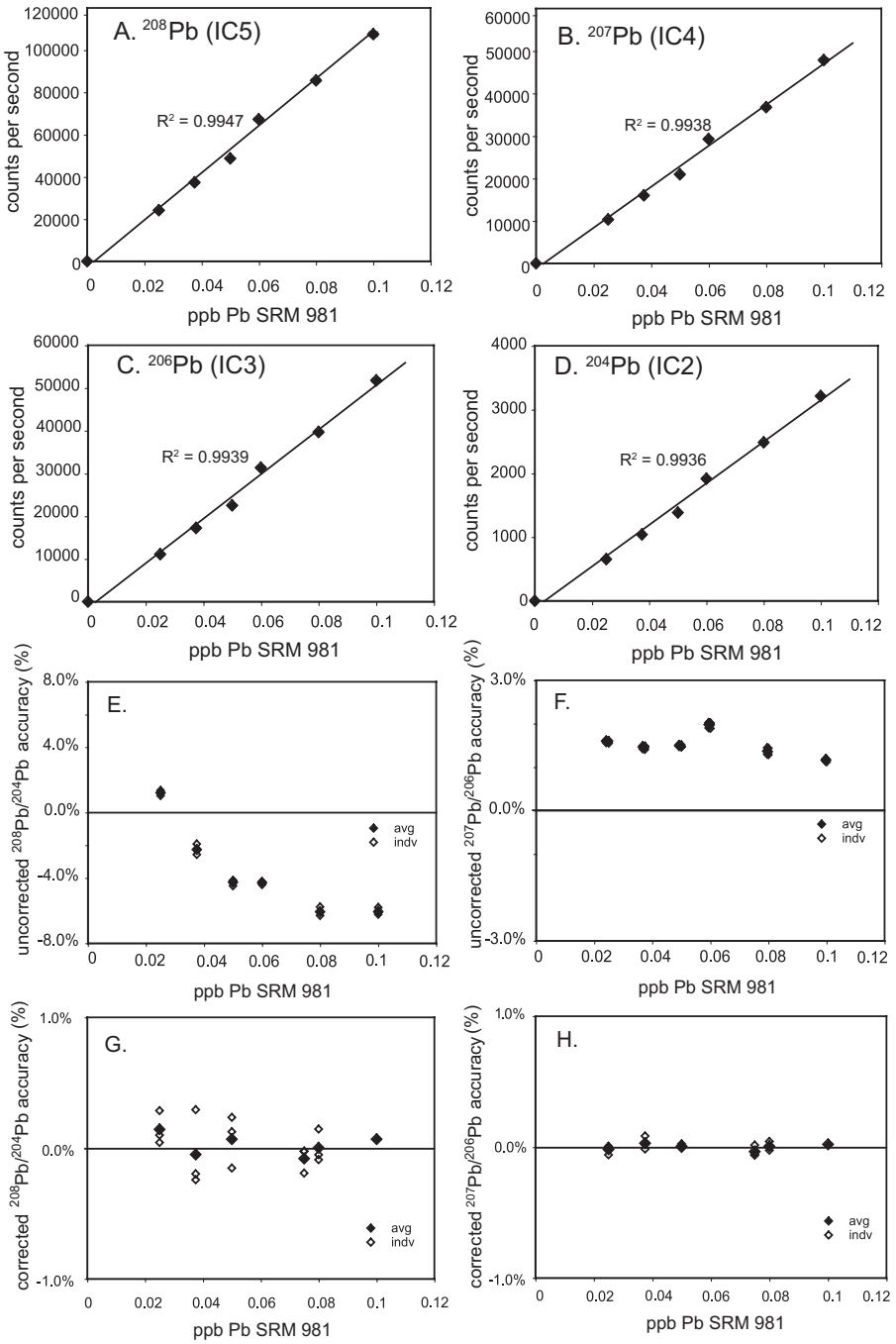


FIG. 15-9. Channeltron linearity in solution mode. (**A–D**) Graphs showing the linear increase in measured intensities (cps) for each Pb isotope as the total Pb concentration of a SRM 981 standard solution is increased. A concentrated 'mother' solution was diluted with varying amounts of ~0.2% $HNO_3$ to make all solutions used in the experiment. Each point represents the average background corrected count rate of 3 analyses of the same SRM 981 solution. (**E–H**) Plots displaying the accuracy of the measured, uncorrected $^{208}Pb/^{204}Pb$ (**E**) and $^{207}Pb/^{206}Pb$ (**F**) ratios, and the mass bias corrected $^{208}Pb/^{204}Pb$ (**G**) and $^{207}Pb/^{206}Pb$ (**H**) ratios for various total Pb concentrations of standard solution SRM 981. Solid diamonds represent the accuracy of the average of three Pb isotope ratio measurements of the same SRM 981 solution. The unfilled diamonds are the accuracy of each individual measurement of the same standard solution. The preferred values for SRM 981 from Baker *et al.* (2004) were used to calculate the mass bias corrected Pb isotope ratios used in plots G and H, the accuracy results in plots E–H.

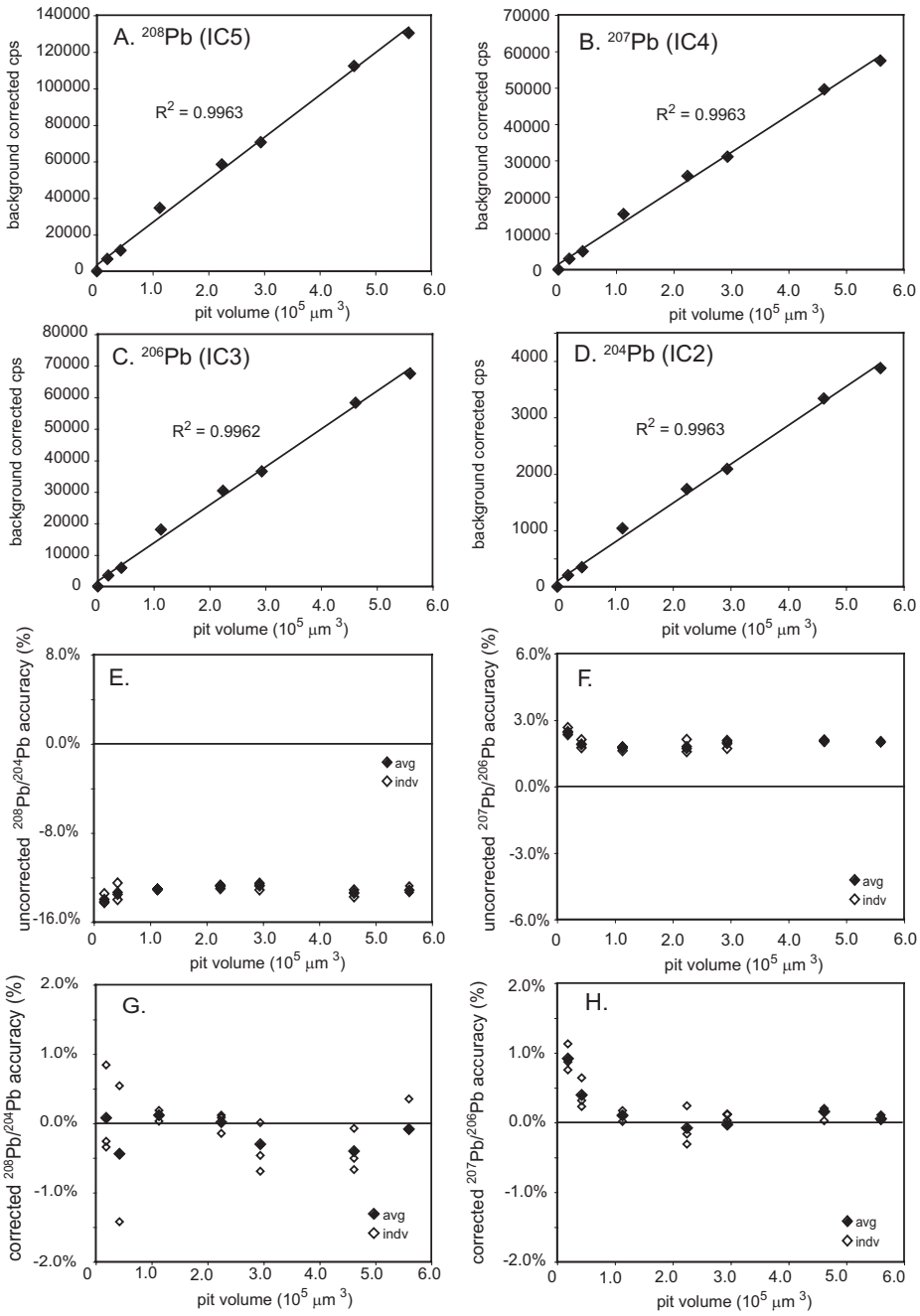


FIG. 15-10. Channeltron linearity in laser ablation mode. (**A–D**) Plots of background corrected count rates for each Pb isotope over a range of laser ablation pit volumes. Variation in the volume of material ablated was produced by adjusting the laser spot size while keeping the laser energy (3 J/cm$^2$) and repetition rate (10 Hz) constant. Each point represents the average background corrected count rate of three 60 second laser analyses of BCR2-G at a single spot size. The volume of material ablated was estimated using a drill rate of ~1 μm/sec. (**E–H**) Plots showing the accuracy of the background corrected $^{208}$Pb/$^{204}$Pb and $^{207}$Pb/$^{206}$Pb ratios (**E–F**) and the mass bias corrected $^{208}$Pb/$^{204}$Pb and $^{207}$Pb/$^{206}$Pb ratios (**G–H**) for an increasing range of laser ablation pit volumes. Solid diamonds represent the accuracy of the average of three Pb isotope ratio measurements performed under the same laser ablation conditions. The unfilled diamonds represent each individual analysis. Method 2 outlined in this paper and the preferred values for BCR2-G given in GeoREM (http://georem.mpch-mainz.gwdg.de/) were used to calculate the mass bias corrected Pb isotope ratios used in plots G and H, the accuracy results in plots E–H.

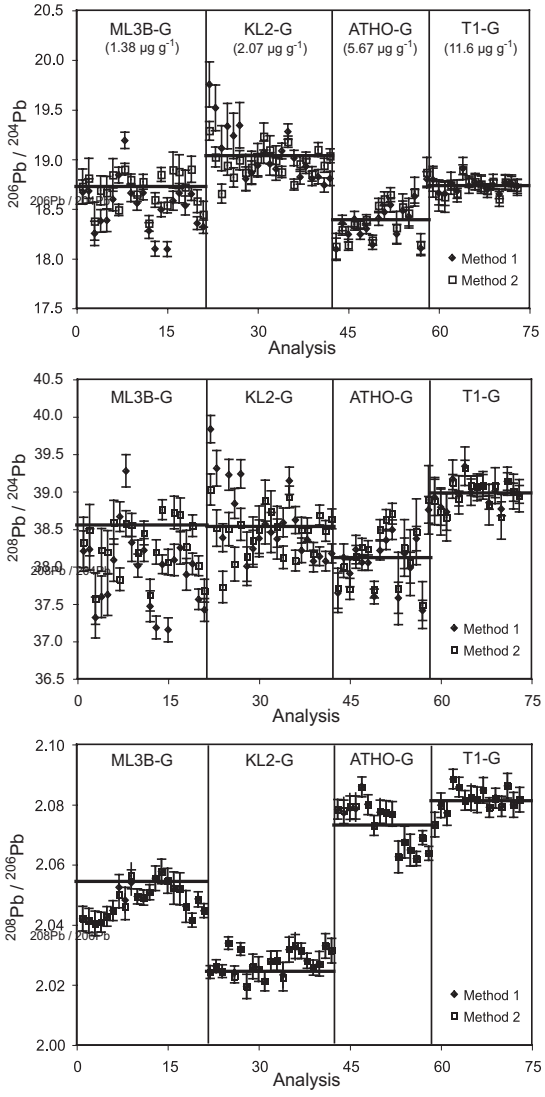


FIG. 15-11. LA–MC–ICPMS analysis of Pb isotope ratios in silicate glass SRMs ML3B–G, KL2-G, ATHO-G and T1-G, arranged from left to right in order of increasing Pb concentration. Solid horizontal lines indicate the preferred Pb isotopic values for each glass given in GeoREM (http://georem.mpch-mainz.gwdg.de/). Pb isotope ratios for each analysis are calculated using both Method 1 (filled diamonds) and Method 2 (unfilled squares). There is general agreement between the Method 1 and 2 results and the preferred values for the glasses with higher Pb concentrations (ATHO-G and T1-G) for the $^{206}Pb/^{204}Pb$, $^{208}Pb/^{204}Pb$ and $^{208}Pb/^{206}Pb$. There is more scatter and larger discrepancies between the two methods for the two glasses with lower concentrations (ML3B-G and KL2-G) but, in general, Method 2 produces more accurate and precise results than Method 1. (From Souders & Sylvester 2008).

configurations (*e.g.,* Paul *et al.* 2005). This is because the uncertainty budget of the multiple Channeltron method is dominated by uncertainties in the ion counter gains, which are large only at very low $^{208}Pb$ count rates. Internal precision of measured Pb isotope ratios in the silicate glass SRMs plot well above the theoretical curves. This reflects additional errors not included in the theoretical calculations, including possible matrix effects associated with the laser-produced aerosols, spot to spot heterogeneity in the Pb isotopic composition of the BCR2-G calibrant and fluctuations in mass bias factors over short time scales (*i.e.,* between individual analyses).

Kent (2008) has recently compared analytical uncertainties for LA–MC–ICP–MS measurements of Pb isotope ratios using a combined Faraday-SEM detector array (with the discrete-dynode ion counters used for $^{204}Pb$, $^{202}Hg$ and $^{200}Hg$) to those made using solely Faraday cups. He found that at signal intensities of 5 mV or ~310,000 cps for $^{204}Pb$, the precision on measurements using an ion counter for $^{204}Pb$ are significantly better than those using a Faraday cup for $^{204}Pb$. However, the use of a parallel Faraday-SEM configuration introduces an additional error of ±0.3% (2s) associated with the measurement of differences in gain between the ion counters and Faraday cups, which is required for determination of $^{208,207,206}Pb/^{204}Pb$ ratios. Thus, Kent (2008) argued that improvements in the precision on $^{208,207,206}Pb/^{204}Pb$ ratios are realized with the combined Faraday-SEM detector array only when measuring intensities of less than 2 mV or ~130,000 cps $^{204}Pb$ in an ion counter.

Kent (2008) compared the precision on $^{208}Pb/^{204}Pb$ ratios as a function of Pb count rates, with measured intensities of $^{204}Pb$ as low as ~7000 cps in an ion counter, and ~4000 cps in a Faraday. At these very low intensities his data show uncertainties on $^{208}Pb/^{204}Pb$ of about ±0.8% (2σ) for the ion counter measurement and about ±10% (2σ) for the Faraday measurement. Our multiple Channeltron data for Pb isotope ratios cover an even lower range of $^{204}Pb$ intensities (~200 to 4000 cps) so we have compared our data to Kent's in Figure 15-14. The plot illustrates the potential improvements in precision that can be attained by employing multiple Channeltrons for LA–MC–ICP–MS in samples that have very low Pb concentrations, or require analysis at a very fine spatial resolution, and thus remove only very small aliquots of the target matrix during laser ablation. Particularly important applications in the earth

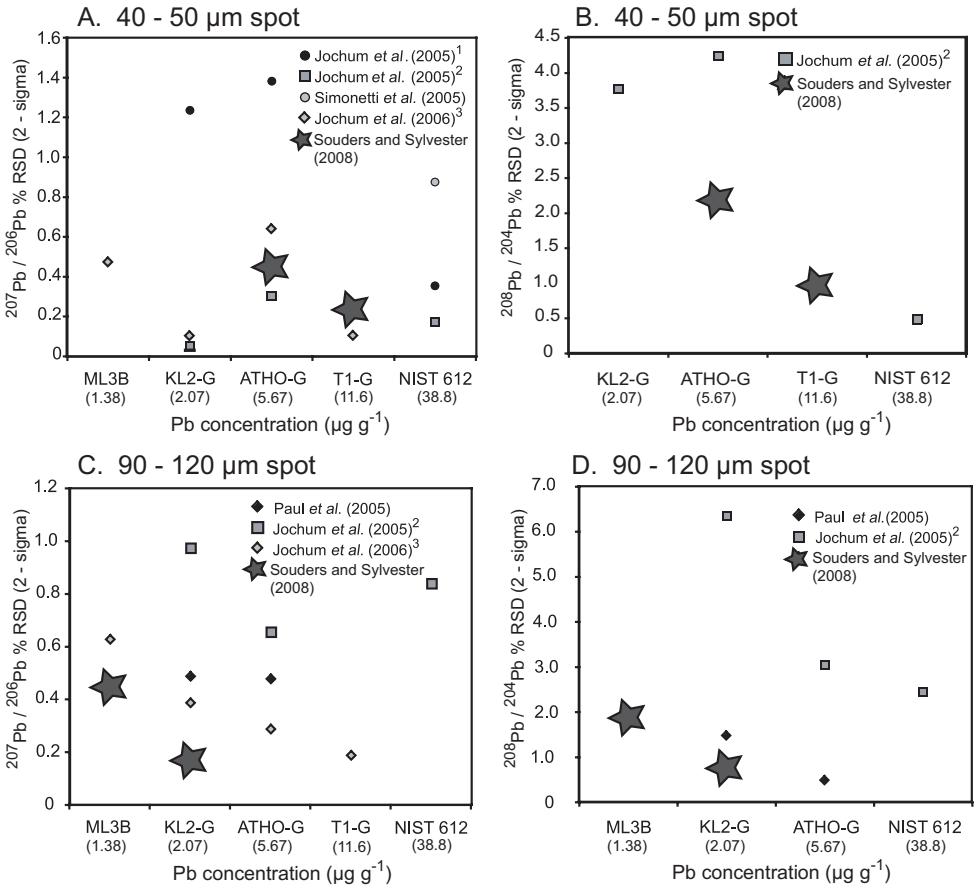


FIG. 15-12. Comparison of the external precision on $^{207}Pb/^{206}Pb$ and $^{208}Pb/^{204}Pb$ ratios in a silicate glass SRMs as a function of spot size in Souders & Sylvester (2008) and other LA–MC–ICP–MS and single collector LA–SF–ICP–MS investigations. (**A**) and (**B**) compare analyses using spot sizes ranging from 40 to 50 µm, and (**C**) and (**D**) compare the reproducibility of measurements using spot sizes between 90 and 120 µm. [1]Measurements using Escan mode. [2]Measurements using combined Escan and Bscan modes. [3]Only 193nm laser data considered.

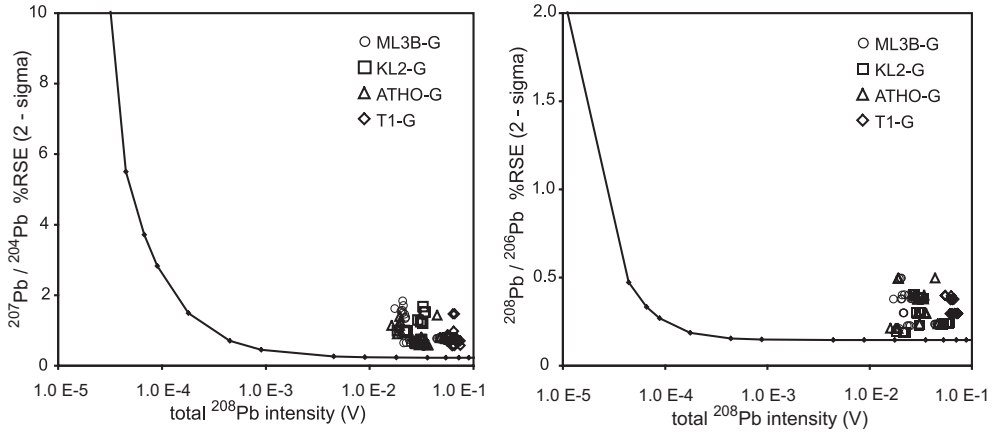


FIG. 15-13. Theoretical limits of precision, expressed as %RSE (2-sigma), for the measurement of Pb isotope ratios using MICs are defined by the solid line. The observed internal precision on the Pb isotope ratio measurements of Souders & Sylvester (2008) for the MPI-DING silicate glasses are also shown. Uncertainties due to counting statistics, dark noise, background subtraction, ion counter yield, and the $^{204}Hg$ correction on the 204 mass are all included in the calculation of the theoretical curves. (From Souders & Sylvester 2008).

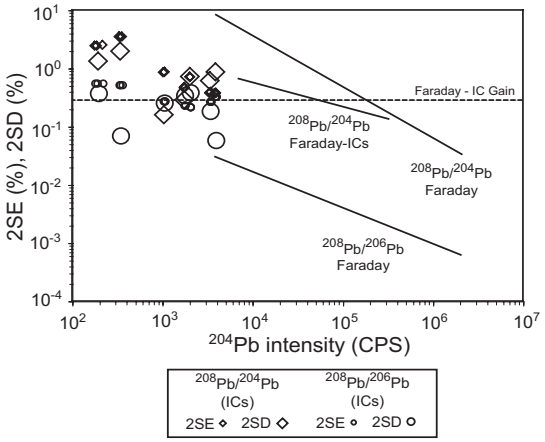


FIG. 15-14. Plot of observed measurement precision and $^{204}$Pb average signal intensity (cps) for replicate analyses of BCR2-G. Variations in the observed count rates were produced by changing the laser spot size. The points represent the 2SE (%) and 2SD (%) for mass bias corrected $^{208}$Pb/$^{204}$Pb and $^{208}$Pb/$^{206}$Pb ratios where all Pb isotopes of interest were measured on ion counters. The standard error of the mean (2SE (%)) was calculated for each individual analysis of BCR2-G consisting of 30 seconds of background measurement followed by 60 seconds of laser ablation followed by 30 seconds of wash-out. The standard deviation (2SD (%)) was calculated for the 3 replicate analyses for each laser spot size. The solid lines are the observed measurement precision trends for Pb isotope ratios using both Faraday–Faraday and Faraday–ion counter cup configurations from Kent (2008) for NIST 610 SRM and the dashed line is the analytical uncertainty for Faraday-ion counter cross calibration (gain). The uncertainty on the Faraday ion counter gain is the greatest source of error for measurements below this line. It is only a very low count rates that analytical precision is improved using multiple ion counters to measure Pb isotope ratios involving $^{204}$Pb.

sciences that may be developed in the coming years are *in situ* analyses of fluid inclusions (Pettke 2008) and melt inclusions (Mason *et al.* 2008).

## THE FUTURE

LA–MC–ICP–MS with Faraday cup collection has changed geoanalysis fundamentally in recent years by providing earth scientists with the ability to determine precise isotopic ratios of major and minor elements in minerals *in situ*. Whereas geologists were once trying to understand isotopic variations only on the scale of whole rock samples, they now are increasingly analyzing and modeling isotopic variations on the mineral scale, and debating the significance of those models, in ever more detail.

The development of ion counters for LA–MC–ICP–MS opens up the possibility of determining precise isotopic ratios of trace elements in minerals *in situ*, thereby expanding the data sets available to the Earth scientist significantly. We can look forward confidently to exciting new applications in accessory mineral geochronology and thermochronology, sedimentary provenance, and petrogenesis in the years to come. Proper use of LA–MC–ICP–MS instruments equipped with multiple Channeltron detectors will be an essential part of this development.

## ACKNOWLEDGEMENTS

K.P. Jochum kindly supplied the MPI-DING glasses for our studies. We thank Bence Paul for discussions on analytical uncertainties and Mike Tubrett, Rebecca Lam and Graham Layne for continuing advice and support in the laboratory. The research was supported by an NSERC Discovery grant to PJS.

## REFERENCES

ALBAREDE, F., TELOUK, P., BLICHERT-TOFT, J., BOYET, M., AGRANIER, A. & NELSON, B. (2004): Precise and accurate isotopic measurements using multiple-collector ICPMS. *Geochim. Cosmochim. Acta* **68**, 2725-2744.

BAKER, J., PEATE, D., WAIGHT, T. & MEYZEN, C. (2004): Pb isotopic analysis of standards and samples using a $^{207}$Pb–$^{204}$Pb double spike and thallium to correct for mass bias with a double-focusing MC–ICP–MS. *Chem. Geol.* **211**, 275-303.

BURLE TECHNOLOGIES, INC. (2003): Channeltron Electron Multiplier, Handbook for Mass Spectrometry Applications, 64 pp. (www.burle.com/cgi-bin/byteserver.pl/pdf/ ChannelBook.pdf)

CHMELEFF, J., HORN, I, STEINHOEFEL, G & VON BLANCKENBURG, F. (2008): *In situ* determination of precise stable Si isotope ratios by UV-femtosecond laser ablation high-resolution multi-collector ICP–MS. *Chem. Geol.* **249**, 155-166.

COCHERIE, A. & ROBERT, M. (2008): Laser ablation coupled with ICP–MS applied to U-Pb zircon geochronology: A review of recent advances. *Gondwana Research*, doi:10.1016/j.gr.2008.01.003.

EGGINS, S.M., KINSLEY, L.P.J. & SHELLEY, J.M.G. (1998): Deposition and element fractionation

processes during atomospheric pressure laser sampling for analysis by ICP–MS. *Appl. Surf. Sci.* **127-129**, 278-286.

EGGINS, S.M., GRUN, R., MCCULLOCH, M.T., PIKE, A.W.G., CHAPPELL, J., KINSLEY, L., MORTIMER, G., SHELLEY, M., MURRAY-WALLACE, C.V. & TAYLOR, L (2005): *In situ* U-series dating by laser ablation multi-collector ICPMS: new prospects for Quaternary geochronology. *Quat. Sci. Rev.* **24**, 2523-2538.

GEOREM, Max-Planck-Institute data base for geological and environmental reference materials, http://georem.mpch-mainz.gwdg.de/.

GRAHAM, S., PEARSON, N.J., JACKSON, S.E., GRIFFIN, W.L. & O'REILLY, S.Y. (2004): Tracing Cu and Fe from source to porphyry: *in situ* determination of Cu and Fe isotope ratios in sulfides from the Grasberg Cu–Au deposit. *Chem. Geol.* **207**, 147-169.

GÜNTHER, D. & HEINRICH, C.A. (1999): Enhanced sensitivity in laser ablation-ICP mass spectrometry using helium-argon mixtures as aerosol carrier. *J. Analyt. Atom. Spectrom.* **14**, 1363-1368.

HORSTWOOD, M.S.A., FOSTER, G.L., PARRISH, R.R., NOBLE, S.R. & NOWELL, G.M. (2003): Common Pb corrected *in situ* U-Pb accessory mineral geochronology by LA–MC–ICP–MS. *J. Analyt. Atom. Spectrom.* **18**, 837-846.

IIZUKA, T. & HIRATA, T. (2005): Improvements of precision and accuracy in *in situ* Hf isotope microanalysis of zircon using the laser ablation–MC–ICPMS technique. *Chem. Geol.* **220**, 121-137.

JOCHUM, K.P., DINGWELL, D.B., ROCHOLL, A., STOLL, B., HOFMANN, A.W., BECKER, S., BESMEHN, A., BESSETTE, D., DIETZE, H.-J., DULSKI, P., ERZINGER, J., HELLEBRAND, E., P. HOPPE, HORN, I., JANSSENS, K., JENNER, G.A., KLEIN, M., MCDONOUGH, W.F., MAETZ, M., MEZGER, K., MUNKER, C., NIKOGOSIAN, I.K., PICKHARDT, C., RACZEK, I., RHEDE, D., SEUFERT, H.M., SIMAKIN, S.G., SOBOLEV, A.V., SPETTEL, B., STRAUB, S., VINCZE, L., WALLIANOS, A., WECKWERTH, G., WEYER, S., WOLF, D. & ZIMMER, M. (2000): The preparation and preliminary characterization of eight geological MPI-DING reference glasses for *in situ* microanalysis. *Geostand. Newsl.* **24**, 87-133.

JOCHUM, K.P., PFANDER, J., WOODHEAD, J.D., WILLBOLD, M., STOLL, B., HERWIG, K., AMINI, M., ABOUCHAMI, W. & HOFMANN., A.W. (2005a): MPI-DING glasses: New geological reference materials for *in situ* Pb isotope analysis. *Geochem. Geophys. Geosyst.* **6**, DOI: 10.1029/2005GC000995, Q10008.

JOCHUM, K.P., STOLL, B., HERWIG, K., AMINI, M., ABOUCHAMI, W. & HOFMANN, A.W. (2005b): Lead isotope ratio measurements in geological glasses by laser ablation-sector field-ICP mass spectrometry (LA–SF–ICPMS). *Int. J. Mass Spectrometry* **242**, 281-289.

JOCHUM, K.P., STOLL, B., HERWIG, K., WILLBOLD, M., HOFMANN, A.W., AMINI, M., AARBURG, S., ABOUCHAMI, W., HELLEBRAND, E., MOCEK, B., RACZEK, I., STRACKE, A., ALARD, O., BOUMAN,C., BECKER, S., DUCKING, M., BRATZ, H., KLEMD, R., DE BRUIN, D., CANIL, D., CORNELL, D., DE HOOG, C., DALPE, C., DANYUSHEVSKY, L., EISENHAUER, A., GAO, Y., SNOW, J.E., GROSCHOPF, N., GUNTHER, D., LATKOCZY, C., GUILLONG, M., HAURI, E.H., HOFER, H.E., LAHAYE, Y., HORZ, K., JACOB, D.E., KASEMANN, S.A., KENT, A.J.R., LUDWIG, T., ZACK, T., MASON, P.R.D., MEIXNER, A., ROSNER, M., MISAWA, K., NASH, B.P., PFANDER, J., PREMO, W.R., SUN, W.D., TIEPOLO, M., VANNUCCI, R., VENNEMANN, T., WAYNE, D. & WOODHEAD, J.D. (2006a): MPI-DING reference glasses for *in situ* microanalysis: New reference values for element concentrations and isotope ratios. *Geochem. Geophys, Geosyst.*, **7**, DOI: 10.1029/2005GC001060.

JOCHUM, K.P., STOLL, B., HERWIG, K. & WILLBOLD, M. (2006b): Improvement of *in situ* Pb isotope analysis by LA–ICP–MS using a 193 nm Nd:YAG laser. *J. Analyt. Atom. Spectrom.* **21**, 666-675.

KENT, A.J.R. (2008): *In situ* analysis of Pb isotope ratios using laser ablation MC–ICP–MS: Controls on precision and accuracy and comparison between Faraday cup and ion counting systems. *J. Analyt. Atom. Spectrom.* 2008, DOI: 10.1039/b801046c.

LONGERICH, H. (2008): Laser ablation–inductively coupled plasma–mass spectrometry (LA–ICP–MS); an introduction. *In* Laser Ablation ICP–MS in the Earth Sciences: Current Practices and Outstanding Issues (P. Sylvester, *ed.*). *Mineral. Assoc. Can. Short Course Series* **40**, 1-18.

MASON, P.R.D., KOSLER, J., DE HOOG, J.C.M., SYLVESTER, P.J. & MEFFAN-MAIN, S. (2006): *In*

*situ* determination of sulfur isotopes in sulfur–rich materials by laser ablation multiple–collector inductively coupled plasma mass spectrometry (LA–MC–ICP–MS). *J. Analyt. Atom. Spectrom.* **21**, 177-186.

MASON, P.R.D., NIKOGOSIAN, I.K. & VAN BERGEN, M. (2008): Major and trace element analysis of melt inclusions by laser ablation ICP–MS. *In* Laser Ablation ICP–MS in the Earth Sciences: Current Practices and Outstanding Issues (P. Sylvester, *ed*.). *Mineral. Assoc. Can. Short Course Series* **40**, 219-239.

MCFARLANE, C. & MCCULLOCH, M. (2008): Sm–Nd and Sr isotope systematics in LREE-rich accessory minerals using LA–MC–ICP–MS. *In* Laser Ablation ICP–MS in the Earth Sciences: Current Practices and Outstanding Issues (P. Sylvester, *ed*.). *Mineral. Assoc. Can. Short Course Series* **40**, 117-133.

NORMAN, M., MCCULLOCH, M., O'NEILL, H. & YAXLEY, G. (2006). Magnesium isotopic analysis of olivine by laser ablation multi–collector ICP–MS: Composition dependent matrix effects and a comparison of the Earth and Moon. *J. Analyt. Atom. Spectrom.* **21**, 50-54.

PAUL, B., WOODHEAD, J.D. & HERGT, J. (2005): Improved *in situ* isotope analysis of low Pb materials using LA–MC–ICP–MS with parallel ion counter and Faraday detection. *J. Analyt. Atom. Spectrom.* **20**, 1350 - 1357.

PEARSON, N.J., ALARD, O., GRIFFIN, W.L., JACKSON, S.E. & O'REILLY, S.Y. (2002): *In situ* measurement of Re–Os isotopes in mantle sulfides by laser ablation multicollector inductively coupled plasma mass spectrometry: Analytical methods and preliminary results. *Geochim. Cosmochim. Acta*, **66**, 1037-1050.

PEARSON, N.J., GRIFFIN, W.L. & O'REILLY, S.Y. (2008): Mass fractionation correction in laser ablation multiple-collector ICP–MS: implications for overlap corrections and precise and accurate *in situ* isotope ratio measurement. *In* Laser Ablation ICP–MS in the Earth Sciences: Current Practices and Outstanding Issues (P. Sylvester, *ed*.). *Mineral. Assoc. Can. Short Course Series* **40**, 93-116.

PETTKE, T. (2008): Analytical protocols for element concentration and isotope ratio measurements in fluid inclusions by LA–(MC–)ICP–MS. *In* Laser Ablation ICP–MS in the Earth Sciences: Current Practices and Outstanding Issues (P. Sylvester, *ed*.). *Mineral. Assoc. Can. Short Course Series* **40**, 189-217.

ROSMAN, K.J.R. & TAYLOR, P.D.P. (1997): Isotopic compositions of the elements. *Pure Appl. Chem.* **70**, 217-236.

SCHWIETERS, J.B., BOUMAN,C., TUTTAS, C. & WIESER, M. (2004): A new tool for *in situ* isotopic analysis of small samples: multiple ion counting–ICPMS and TIMS. *Geochim. Cosmochim. Acta*, **68 (Suppl 1)**, A60.

SIMONETTI, A., HEAMAN, L.M., CHACKO, T. & BANERJEE, N.R. (2005): U–Pb zircon dating by laser ablation–MC–ICP–MS using a new multiple ion counting Faraday collector array. *J. Analyt. Atom. Spectrom.* **20**, 677–686.

SIMONETTI, A., HEAMAN, L.M. & CHACKO, T.. (2008): Use of discrete-dynode secondary electron multipliers with Faradays – a '*reduced volume*' approach for *in situ* U–Pb dating of accessory minerals within petrographic thin section by LA–MC–ICP–MS. *In* Laser Ablation ICP–MS in the Earth Sciences: Current Practices and Outstanding Issues (P. Sylvester, *ed*.). *Mineral. Assoc. Can. Short Course Series* **40**, 241-264.

SOUDERS, A.K. & SYLVESTER, P.J. (2008): Improved *in situ* measurements of lead isotopes in silicate glasses by LA–MC–ICPMS using multiple ion counters. *J. Analyt. Atom. Spectrom.* **23**, 535-543.

STACEY, J.S. & KRAMERS, J.D. (1975): Approximation of terrestrial lead isotope evolution by a two-stage model. *Earth Planet. Sci. Lett.*, **26**, 207-221.

TIEPOLO, M. BOUMAN C., VANNUCCI, R. & SCHWIETERS, J. (2006): Laser ablation multicollector ICPMS determination of $\delta\ ^{11}B$ in geological samples. *Appl. Geochem.* **21**, 788-801.

TURNER, P.J., MILLS, D.J., SHRODER, E., LAPITAJS, G., JUNG, G., IACONE, L.A., HAYDAR, D.A. & MONTASER, A. (1998): Instrumentation for low- and high-resolution ICPMS. *In* Inductively Coupled Plasma Mass Spectrometry (A. Montaser, *ed.*). Wiley-VCH, New York: 421-501.

WOODHEAD, J.D., SWEARER, S., HERGT, J. & MAAS, R. (2005): *In situ* Sr-isotope analysis of carbonates by LA–MC–ICP–MS: interference corrections, high spatial resolution and an example from otolith studies. *J. Analyt. Atom. Spectrom.* **20**, 22-27.

# CHAPTER 16: DATA REDUCTION STRATEGIES, UNCERTAINTY ASSESSMENT AND RESOLUTION OF LA–(MC–)ICP–MS ISOTOPE DATA

Matthew S.A. Horstwood,
NERC Isotope Geosciences Laboratory, British Geological Survey
Keyworth, Nottingham NG12 5GG, UK
Email: msah@nigl.nerc.ac.uk

## INTRODUCTION

Publications and interpretations based on isotope analyses of geological and biological materials by laser ablation ICP–MS (including multiple collector and single collector sector field) appear with ever increasing frequency in the scientific literature. The apparent ease and speed with which such data can be gathered lends itself to voluminous production where statistical manipulation and quantity of data can easily mask or become synonymous with quality. Consideration of data corrections and uncertainty estimation combined with known or possible geological/geochemical/analytical phenomena is crucial to interpreting data appropriately and comprehending the likely resolution of data.

With examples specific to U–Th–Pb geochronology and Hf and Sr isotope geochemistry, data reduction and uncertainty assessment principles are discussed in order to illustrate likely resolution limits of LA–ICP–MS data in these and other applications.

All data and concepts discussed are based on data acquired using 266 nm and 193 nm laser ablation systems coupled to MC–ICP–MS instruments and desolvating nebulizers for simultaneous introduction of monitor solutions (see page 284, Monitor Solutions).

## DATA REDUCTION

Having acquired ICP–MS data, either by single collector peak jumping or simultaneous multiple collector methodologies, corrections need to be applied, isotope ratios calculated and uncertainties assessed before the data can be interpreted. This data reduction can take many forms depending on the preference of the analyst, however transparency should be maintained throughout. In general, the less the data need reducing or correcting the fewer the uncertainties that will need propagating and the lower the overall uncertainty. Since the intentions of all are to produce data with the best possible uncertainties, elimination of correction components is therefore more beneficial than correction.

### Laser-Induced elemental fractionation

Laser-induced elemental fractionation (LIEF), where an elemental ratio changes over the course of an ablation, is a common occurrence during single spot static ablation (Fryer *et al*. 1995, Longerich *et al*. 1996) and has been extensively studied and documented for U–Pb geochronology (*e.g.*, Hirata & Nesbitt 1995, Horn *et al.* 2000, Košler *et al.* 2001). This fractionation is one of the fundamental limiting uncertainties in LA U–Pb geochronology and is a key area of research when trying to improve the precision of the technique.

The usual approach for U–Pb laser ablation analyses is to tolerate LIEF and to correct for this either by assuming that samples and reference materials behave the same, using the same time-slice of data for each (as used in many data processing packages; Horn *et al.* 2000) and assuming the normalization factors are equivalent, or to regress the fractionated response to some initial starting time at which fractionation relative to a standard is assumed to be zero (Sylvester & Ghaderi 1997). However, not all zircon grains are built the same and any variation of the slope and/or initial fractionation behavior can affect the accuracy of the determined result. This variation of the fractionation trend between zircon grains can be caused through differential U concentrations resulting in metamictization and/or differential absorption of the laser energy due to differences in the absorption characteristics (*e.g.*, color) of the grains. No single or set of reference material analyses will therefore appropriately normalize out this fractionation which may have its origin in factors other than laser-induced effects. The effect on the data will be most apparent when using external normalization only, where slight differences in matrix between samples and reference materials can cause differences in the required normalization on the order of a few

Mineralogical Association of Canada Short Course 40, Vancouver, B.C., p. 283–303.

percent. If selecting a time-slice of the fractionated trend rather than integrating the whole, this effect will be exacerbated and the difference in slope between the reference material and sample will change the apparent concordance of the resultant data point and may lead to selection of a time-slice which renders the data point concordant when in reality it is a truly discordant zircon. The interpretation of this data point will therefore be erroneous since any discordance may not have been along the zero age trajectory caused by LIEF but may instead have reflected a metamorphic event which caused Pb loss and now results in the upper intercept ($^{207}Pb/^{206}Pb$) age reflecting only a minimum and not a true age (see also p. 298, Effect of U–Pb age discordance and uncertainty on εHf).

When using the intercept method of Sylvester & Ghaderi (1997) these differences in slope and minor matrix effects are largely corrected out but potential differences in the initial normalization factors may still remain.

Due to the complex nature of these interactions and the resultant greater uncertainty, elimination of LIEF would appear to be beneficial. This can be achieved in two ways – keeping the aspect ratio (depth/diameter) of the ablation pit low (Mank & Mason 1999, Mason & Mank 2001) and/or using a laser with a shorter wavelength (Guillong *et al.* 2003) and/or pulse width (Horn 2008). Off the shelf 'turn-key' short wavelength and/or short pulse width 213–193nm UV laser ablation systems are now the norm in most laboratories interested in LA geochronology and are capable of excellent results. Laser ablation systems operating with very short femtosecond pulse widths are showing promising results by reducing or eliminating LIEF (see Horn 2008). In the absence of such technology a more practical solution for most laboratories is to limit the aspect ratio of the ablation crater such that LIEF is reduced to well within analytical uncertainty. Our data indicate that this is only achieved when the aspect ratio is <<1. A typical 213nm or 193nm UV laser system operating with a 25–5 ns pulse width ablates an average zircon at *ca.* 0.05–0.1μm/pulse using a laser fluence of 2–3J/cm$^2$. A 40 s ablation time (first 10 s discarded to allow inter-element ratios to stabilize) at 5Hz results in a crater depth of *ca.* 10–20μm. Using typical spot sizes of 25–50μm this equates to aspect ratios between 0.2–0.8. Figure 16-1a shows data acquired using just such parameters and indicates fractionation on the order of 8% is still present by the end of the analysis suggesting even smaller depth/diameter ratios are required to eliminate this fractionation altogether when using a static spot.

Using a dynamic ablation pattern (or raster) has been shown to eliminate LIEF in LA U–Pb geochronology (Figure 16-1b; Horstwood *et al.* 2003), apparently reducing significantly any remaining matrix differences and eliminating the need to propagate an additional uncertainty (see comparison of static and dynamic ablation in Košler *et al*. 2008). However, this benefit is offset by the production of larger ablated particles (Guillong & Günther 2001, Günther & Koch 2008, Košler *et al.* 2008) which ionize less efficiently in the plasma. However, at the current uncertainty levels of most published U–Pb studies (2–3% 2σ), this does not appear to be limiting. An advantage to the dynamic ablation approach appears to be that some degree of non-matrix-matched standardization can be achieved (Horstwood *et al.* 2006), reducing the effects of matrix differences between grains of very different chemistry and suggesting a possible way forward in dating less abundant accessory minerals for which homogeneous, accurately calibrated reference materials might not be currently available.

Currently then, an ablation protocol which eliminates LIEF whilst maintaining spatial resolution, precision of the analysis and stable plasma conditions appears the best way forward for improving the consistency and reliability of U–Pb analyses. In the meantime, the likely constraints imposed by the ablation protocol on the resolution of the data with respect to interpretation, should be considered.

**Monitor solutions**

Laser ablation applications typically use a purely dry plasma and sample standard bracketing protocols to tune the system and correct acquired data initially. Introducing a monitor solution either as a wet or desolvated aerosol can however help in elucidating any changes in the inter-element fractionation and mass bias of the plasma (Günther *et al.* 1997, O'Connor *et al.* 2006). Initial tuning of the instrument can also be performed more reliably using a stable solution signal rather than the inherently noisy laser ablation signal (Günther *et al.* 1997) and additionally effects related to variations in the plasma can be separated as distinct from those attributable to the ablation process. Using a monitor solution, many relevant corrections can be performed on-line during the analysis. In this way a more detailed illustration of the various phenomena

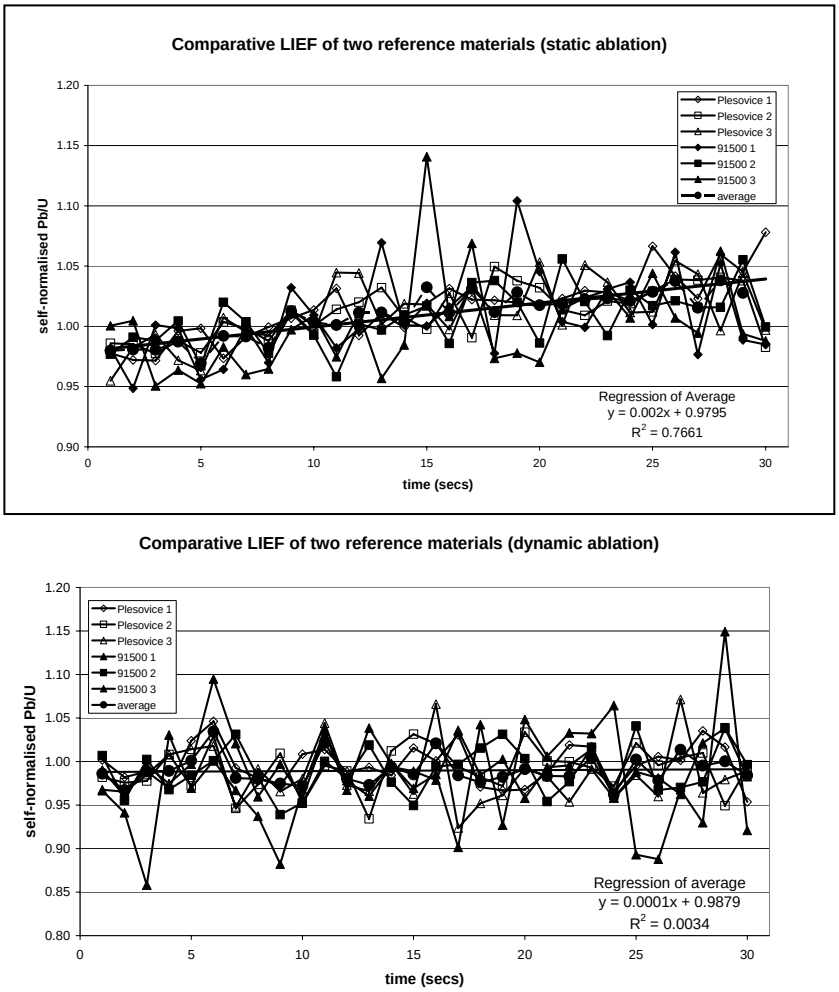


FIG. 16-1 – Comparative laser-induced inter-element fractionation (LIEF) during static ablation (upper diagram) and dynamic ablation (lower diagram).

occurring during each analysis and over the course of an analytical session can be gained. With greater control and understanding of these variables, data reduction procedures can be minimized or altered to cater for these changes and the overall uncertainty for the data reduced. After Longerich *et al.* (1987) demonstrated the utility of using the $^{205}Tl/^{203}Tl$ ratio to mass-bias correct Pb isotope samples, studies have reported the use of $^{235}U$ or $^{233}U$ combined with Tl to elucidate inter-element fractionation effects in the plasma and provide a means of correcting U–Pb data for instrumental mass bias in real time (Horn *et al.* 2000, Košler *et al.* 2001, Horstwood *et al.* 2003). Comparing these parameters before and during ablation of zircon and monazite using sub-50μm spot sizes and a desolvated solution, our data show that inter-element fractionation as monitored by the Tl/U ratio remains constant to within *ca.* 0.75% (2σ) and the $^{205}Tl/^{203}Tl$ mass bias is constant to *ca.* 0.2% (2σ), suggesting that matrix-induced changes to the plasma are minimal during these ablations.

Figure 16-2 illustrates this concept using LA U–Pb data acquired in a single session. The data show variation of the inter-element ratio within the plasma as monitored by a simultaneously aspirated $^{205}Tl/^{235}U$ desolvated solution as well as a similar variation in the measured $^{206}Pb/^{238}U$ of the ablated zircon reference material (Fig. 16-2a). Correction of the latter using the former reduces the uncertainty assigned to the Pb/U ratio from *ca.* 3.2% (2σ) to *ca.* 1% (2σ, Fig. 16-2b), indicating in this instance that much of the inter-element variation experienced during the session is due to plasma instability rather than being related to the ablation process. In essence the monitor solution is being used here as a direct drift correction rather than correcting the resulting data set by mathematical regression. Correcting or at least monitoring the plasma-induced inter-element fractionation (PIEF) in this way, also allows the true behavior of the ablation (*e.g.*, LIEF or lack thereof) to be ascertained. Although the solution behavior may not be an exact

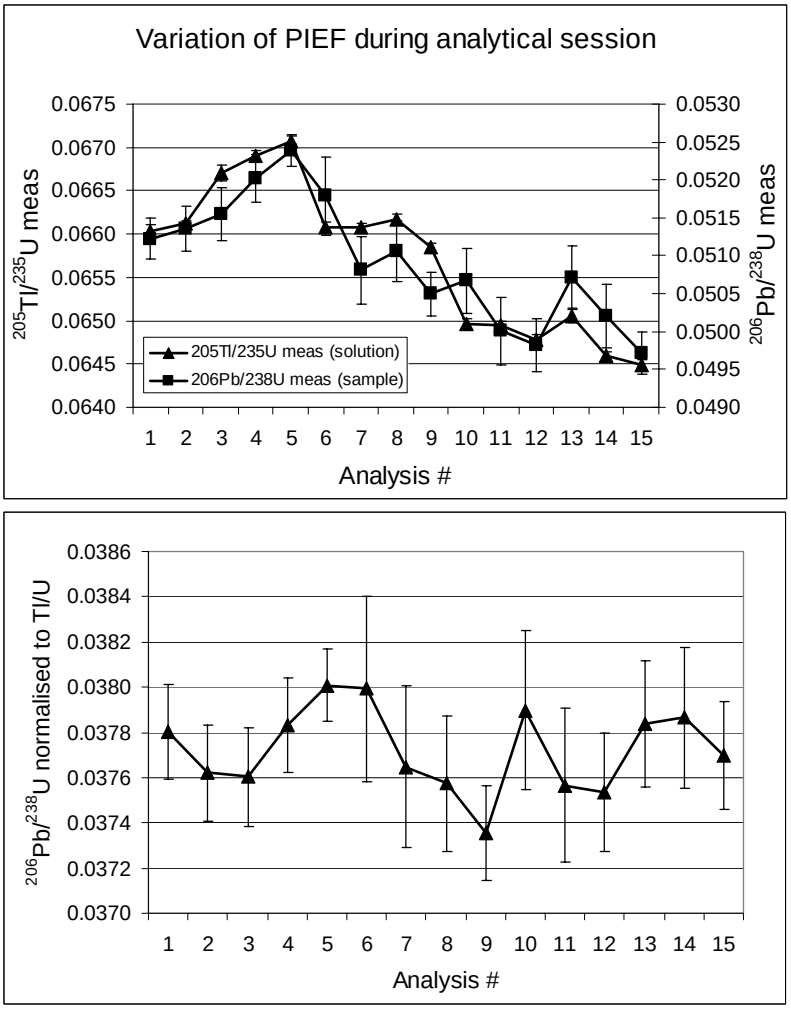


FIG. 16-2 – Variation of plasma-induced inter-element fractionation (PIEF) during an analytical session.

**above:** Measured ratios for both desolvated solution aspiration ($^{205}Tl/^{235}U$) and laser ablation ($^{206}Pb/^{238}U$) for a number of analyses. Ratio variation is *ca.* 3.2% 2σ.

**below:** $^{206}Pb/^{238}U$ of the same analyses after normalization to $^{205}Tl/^{235}U$. Ratio variation is *ca.* 1% 2σ.

match for that of the ablated material in the plasma, initial correction to the monitor solution provides a reasonable first pass correction that corrects out effects due to variation of the plasma environment, leaving only those effects directly attributable to the ablation and the ionization of the ablated material. Final normalization of the data set to an ablation reference material is still required but variations (*e.g.*, fundamental mass bias of the instrument) can be corrected on an integration by integration basis. In this way analytical uncertainty can potentially be improved with the uncertainty propagation for these corrections being effectively 'built in' to the final result since their variations are reflected in the analytical uncertainty of the on-line calculations.

A disadvantage of using a monitor solution is that backgrounds are generally increased due to the blank of the acid and spike solutions used, the background within the spray chamber or desolvator and the potential for intermittent spiking of the background. When analyzing very small Pb ion beams this can be a significant problem leading to inaccurate data. These disadvantages may however be offset by an increase in overall sensitivity (at least for U–Pb analyses) when utilizing a wet plasma (Gehrels *et al*. 2008).

**Complications when interpreting common Pb-affected data for accessory mineral geochronology**

Accessory minerals used in U–Pb geochronology commonly contain a modest to significant proportion of non-radiogenic Pb (common Pb) which is incorporated into the crystal lattice at the time of their crystallization. This is especially common with monazite (Parrish 1990) and ubiquitous for other phases such as allanite and titanite. This common Pb is generally considered to have a composition reflecting the average Pb isotope composition of the host rock which can be

determined through the analysis of syngenetic phases. Correction for this component of non-radiogenic Pb is essential in order to determine the true age of the mineral. Without knowledge of the common Pb composition, one method usually employed to determine this and derive the true age of the mineral is through a Tera-Wasserburg (1972) concordia diagram where correlations to high $^{207}Pb/^{206}Pb$ ratios are interpreted to represent the composition of the common Pb within the mineral. Regression of these data to determine an intercept age and uncertainty on the concordia curve (see Fig. 16-3a) then gives the age of the mineral without common Pb. This approach requires multiple analyses of the same phase in order to define a spread of U–Pb ratios to form the correlation. For individual data points therefore, it is not possible to use this approach unless a $^{207}Pb/^{206}Pb$ composition of the common Pb component is assumed.

Previous studies have advocated the use of on-line common Pb corrections (Horstwood *et al.* 2003, Storey *et al.* 2006), using the calculated $^{204}Pb$ signal and an assumed common Pb ratio (*e.g.*, that taken from the Stacey & Kramers (1975) Pb evolution curve at the apparent age of the sample) to correct the analysis directly. Although it is possible to achieve accurate results using this approach, particularly with older mineral grains, it also has its limitations, particularly with young samples where the age of the components contributing the common Pb can be quite variable. Figure 16-3 illustrates data from two monazite samples from the Himalaya, both of which contain appreciable common Pb. In Figure 16-3a data not corrected for common Pb suggest a correlation between the points with regression to 21 Ma and an upper intercept of *ca.* 4 Ga. However, alternative results and interpretations can be envisioned if the data are considered to represent two groups with similar common Pb compositions appropriate to the age of the mineral

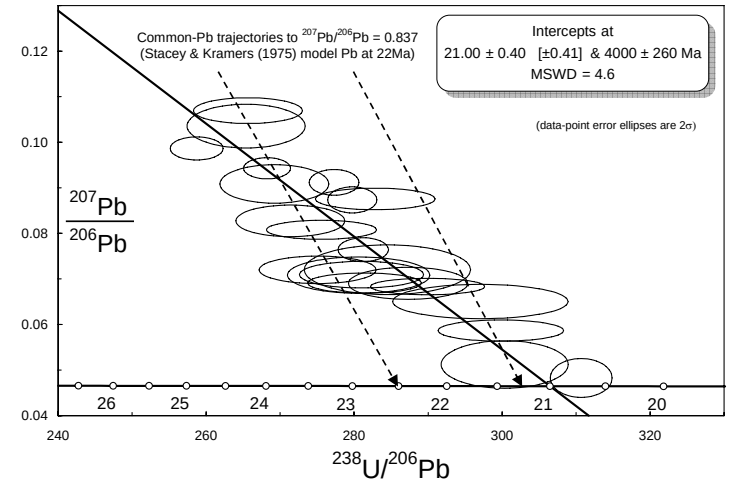


FIG. 16-3a – Tera-Wasserburg plot illustrating different common Pb interpretations for a *ca.* 20 Ma monazite sample. Dashed lines are possible common Pb regression trajectories for different parts of the data. Solid line is a linear regression of all the data using Isoplot (Ludwig 2008).

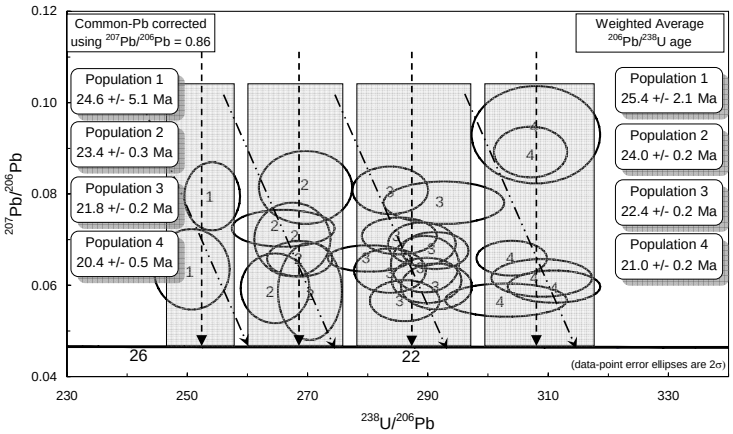


FIG. 16-3b – Monazite sample recording various growth events all with a 'not so common' common Pb composition. Ages on the left of the diagram are calculated using $^{207}Pb/^{206}Pb = 0.86$, ages on the right are the weighted average $^{206}Pb/^{238}U$ age of the data points constituting each population (data taken from Cottle 2007).

($^{207}Pb/^{206}Pb = 0.837$ from Stacey & Kramers (1975) Pb evolution curve at 22 Ma, dashed regressions in Fig. 16-3a). Without textural and/or chemical knowledge of the sample grains to provide evidence for the existence of two populations, the interpretation is ambiguous. Figure 16-3b illustrates another sample where careful chemical mapping and textural relationships have been maintained in thin section (in the manner advocated by Simonetti *et al.* 2008) such that correlations between equivalent analyses can be seen to define sub-vertical trends on a Tera-Wasserburg plot. Here then the data clearly do not fit a typical common Pb trend but instead suggest a 'not so common' Pb composition with a more vertical trajectory.

Clearly then the exact composition of the common Pb in a sample can be difficult to predict for on-line correction and as such, assessment and regression of multiple equivalent data points using a Tera-Wasserburg plot appears the best way to proceed unless the composition of the common Pb component within the sample can be independently determined, *e.g.*, through analyses of feldspar crystals. However, such a determined composition may still be at variance to that recorded in the accessory mineral phases and/or may have been subject to change or alteration. Regardless of whether the common Pb composition used for correction is measured or assumed, an uncertainty should be assigned and propagated into the final calculation. Mattinson (1987, Fig. 3) demonstrated that an absolute uncertainty in the value of the $^{207}Pb/^{204}Pb$ ratio of just 0.2 used for correction of common Pb, can cause uncertainty in the interpreted $^{207}Pb/^{206}Pb$ age of up to 100 Ma. Appropriate uncertainties for the $^{206}Pb/^{204}Pb$, $^{207}Pb/^{204}Pb$ and $^{208}Pb/^{204}Pb$ ratios can also be determined from Stacey & Kramers (1975).

Alternative correction mechanisms use $^{207}Pb$ or $^{208}Pb$ to estimate the amount of common Pb present in the analysis. However, both these approaches assume concordance of the U–Pb and/or Th–Pb systems respectively and so are fundamentally limited in their use. A more useful approach was described by Anderson (2002), who derived a mathematical correction for common Pb assuming that discordance is the result of the sum of Pb loss and common Pb components. The benefit of this approach is that it neither assumes concordance nor relies on the difficult measurement of $^{204}Pb$. An estimate of the time of lead loss is required but the error arising from uncertainty in this estimate is not limiting and the resulting biases are less than when using $^{207}Pb$ or $^{208}Pb$ to estimate the amount of common Pb.

Another complication is in the use of accessory phases containing common Pb as reference materials. Here, variable concentrations of common Pb will lead to variations of the measured $^{206}Pb/^{238}U$ ratio within and between ablations. If this common Pb is not homogeneously distributed throughout the crystal such that the measured $^{206}Pb/^{238}U$ ratio can be compared to the non-common Pb corrected reference value, this must first be corrected to determine a true Pb/U normalization factor by which to correct the unknown sample analyses. Inevitably, this must result in a larger uncertainty on the final result when compared to using a reference material without common Pb, due to the additional uncertainty of the correction.

Either way, using ICP–MS it is imperative to measure and correct for the $^{204}Hg$ component of the signal that is inherent to the Ar (and sometimes He) source gas used in plasma mass spectrometry. This is difficult and constitutes a limiting uncertainty in applying a common Pb correction since the amount of background $^{204}Hg$ far outweighs the amount of $^{204}Pb$ measured in most analyses (unless analyzing accessory minerals with appreciable common Pb, *e.g.*, titanite, allanite, apatite). Monitoring of the Hg-corrected $^{204}Pb$ component during ablation, with or without direct on-line correction of common Pb, is essential to be able to ascertain the level of common Pb which may be affecting an analysis. This is important even for zircon, where micro-inclusions and alteration can result in significant components of common Pb in the analysis. Although gold traps can help reduce Hg levels (Storey *et al.* 2006), as the technique evolves to using smaller and smaller ablation volumes this problem will continue to exist unless Hg contamination can be completely eliminated.

**Isobaric interference corrections**

The above concepts are not restricted to U–Pb isotope ratios. The same principles apply to any inter-element isotope system *e.g.*, Yb–Lu–Hf and Rb–Sr. In these instances however, the accurate determination of inter-element ratios is not generally being attempted, Yb, Lu and Rb having isotopes which interfere on one or more of the Hf or Sr isotopes of interest. Accurate on-line correction of these interferences can be achieved by first determining an adapted 'true' ratio for one of the isotope pairs of the interfering element (see full

description in Nowell *et al.* 2007 and discussion in McFarlane & McCulloch. 2008). In the case of Rb–Sr for example, the interference-free $^{85}$Rb peak is used to determine the amount of interfering $^{87}$Rb which must be stripped from $^{87}$Sr. The $^{87}$Rb/$^{85}$Rb ratio used for this calculation can either be previously determined by mass bias correction using Zr as an adjacent mass element (Waight *et al.* 2002) or using Sr itself in a series of experiments at the start of the analytical session where solution reference materials for Sr are doped with Rb to various levels and the adapted 'true' $^{87}$Rb/$^{85}$Rb mass bias-corrected ratio is calculated using the Sr mass bias assuming $^{86}$Sr/$^{88}$Sr = 0.1194. In this way an adapted $^{87}$Rb/$^{85}$Rb suitable for inversely correcting the Rb isotope ratio during ablation using the Sr mass bias determined at the time can be determined and accurate on-line interfering element corrections made (Nowell & Parrish 2001, Jackson & Hart 2006).

The same approach can be used for Hf isotope analyses of zircon where $^{176}$Yb and $^{176}$Lu interfere on $^{176}$Hf. Alternatively, a direct measure of the Yb mass bias at the time of ablation can be determined using $^{173}$Yb/$^{171}$Yb (or $^{173}$Yb/$^{172}$Yb, Woodhead *et al.* 2004). Indeed, Woodhead *et al.* (2004, Fig. 2b) illustrated that inaccurately determining the Yb mass bias by *ca.* 8% leads to an inaccuracy of 350 ppm on the measured $^{176}$Hf/$^{177}$Hf ratio. Although differential loading of the plasma on ablation can result in changes in mass bias and inter-element behavior (O'Connor *et al.* 2006), comparison of inter-element and mass bias stability of the plasma before and during ablation using a desolvated Tl/U solution, suggests that for the amount of material typically introduced during laser ablation U–Pb and Hf analyses, inter-element fractionation and mass bias behaviors are essentially constant (see page 284, Monitor solutions). This would suggest that the characterization of any difference between Hf and Yb mass bias using solution analyses could remain stable and consistent during laser ablation analysis. Pearson *et al.* (2008) discuss this example in detail and conclude similarly. The absolute levels of these biases local to ionizing ablation particles could however be different to those for desolvated solution particles. Inter-element fractionation for example, requires an additional normalization to an ablation reference material to achieve accurate inter-element data on unknown samples. Jackson & Günther (2003) further demonstrated that for volatile elements at least, isotopic fractionation of ablated particles can occur during incomplete vaporization and ionization in the plasma. However, our Hf isotope data and that of others (Vervoort *et al.* 2007, Dufrane *et al.* 2007), when compared to chemically purified reference zircon analyzed by solution MC–ICP–MS, including those with high REE contents (*e.g.*, zircon R33), indicates that for Hf isotope analysis of zircons compositions accurate to within *ca.* 100 ppm can be achieved by laser ablation MC–ICP–MS using Yb correction ratios determined by interferent-doped solution analyses. Clearly, it would currently appear prudent that each laboratory determines the most appropriate methodology for their set-up to achieve accurate results on high-Yb reference materials. Unfortunately, such reference materials are currently limited and/or do not possess the requisite Yb/Hf ratios to prove these corrections to the interference levels seen in some samples. However, the use of multiple standards is encouraged to demonstrate the efficacy of the correction routines at the time of analysis.

For the $^{176}$Lu interference correction (and for the Rb–Sr system) direct measurement of two interference-free Lu peaks is not possible since there are only 2 isotopes of Lu. In this case however, the $^{176}$Lu correction on $^{176}$Hf is so small that an accepted $^{176}$Lu/$^{175}$Lu ratio of 0.02653 (or other similar ratios in the literature, *e.g.*, De Bievre & Taylor 1993) can be used to determine the present day $^{176}$Hf/$^{177}$Hf of a zircon, even without allowing for the effect of mass bias on this ratio. However, in order to calculate the Hf isotope ratio at the time of crystallization, the Lu/Hf inter-element ratio must be determined accurately in order to correct for the amount of the $^{176}$Lu which will have decayed to $^{176}$Hf since crystallization. Here then we have an inter-element ratio which will be affected by both laser and plasma-induced elemental fractionation and must be normalized. In this instance, a dynamic ablation pattern or at least an ablation crater with limited aspect ratio will prove beneficial to eliminate any LIEF. A more pressing need however is to have an ablation reference material with a known and constant Lu/Hf ratio such that this normalization value can be determined. In a natural material such consistency is relatively unlikely and one of the factors currently limiting the total uncertainty on Hf isotope studies of zircon older than about 500 Ma. At present 91500 & BR266 appear to have Lu/Hf ratios consistent to within 10% (Woodhead & Hergt 2005) and would appear the best options for this purpose. The uncertainty on the Lu/Hf ratio of the reference

material, both in terms of the reproducibility experienced during the analytical session and on the reference value should also be propagated into the calculation of the initial Hf isotope uncertainty (see page 298, Example of uncertainty propagation strategy and also page 298, Effect of U–Pb age discordance and uncertainty on εHf).

## UNCERTAINTY ASSESSMENT

To assess the quality of a result for a population of data or a single data point an uncertainty is required, usually expressed at the level of 2σ (data point) or 95% confidence (population). Proper assessment of the uncertainty of a result is essential. To quote Ludwig (2003), "*… the age of a rock, mineral or process … is unusable in the absence of its uncertainty.*" "*...for most studies, the uncertainty of a date is no less significant than the date itself.*" All components of a calculation contribute uncertainties that must therefore be propagated into the final uncertainty. The uncertainty of the result will then reflect the confidence with which this result can be reproduced another time.

For each step of a calculation the uncertainty component must be quantified and its effect on the final result ascertained and propagated into the final uncertainty. This applies both to high precision methodologies of analysis and those of lower precision. Arguably this is even more important for laser ablation methodologies where the size of any correction can vary over orders of magnitude during a single analysis and therefore the associated propagated uncertainty will vary also.

One of the main mechanisms by which isotope results are assessed is through the use of the mean squared weighted deviation (MSWD). This statistical quantity represents the distribution of data points around a mean value taking into account the data point uncertainties. If MSWD =1 all scatter within the data can be accounted for as a result of the assigned analytical uncertainties. MSWD values <<1 indicate an overestimation of the data point uncertainties while MSWD values >1 suggest underestimation of the component uncertainties and/or excess scatter due to non-analytical causes, *e.g.*, real geological differences. (For a complete description of the MSWD term see Wendt & Carl 1991). The actual MSWD value for which the scatter of the data can be considered due to analytical factors alone is not restricted to a value of one but in fact varies according to the number of data points in the calculation (see Fig. 3 in Wendt & Carl 1991). So, to be 95% confident that the observed scatter of the data is due to analytical uncertainties alone when n=5, an acceptable MSWD range would be 0.2–2.2 but for n=25 this would be 0.6–1.5 (see Fig. 16-4). Critically, it should also be noted that MSWD = 1 need not indicate that no geological variation is present, but that any variation is not resolvable at the uncertainty level of the technique used (Kalsbeek 1992).

### Uncertainty propagation

This discussion only attempts to describe the principles by which uncertainty propagation is undertaken and assessed. For comprehensive information on uncertainty estimation and propagation see the EURACHEM/CITAC Guide to Quantifying Uncertainty in Analytical Measurement (http://www.measurementuncertainty.org/mu/guide/index.html). In order to aid clarity in the following discussion of uncertainty propagation, the definitions of some terms are given in the following paragraph, mostly taken from Section 2.4 of the EURACHEM Guide (in many cases word for word in order to ensure accuracy of representation).

The error of an analytical measurement is defined as the difference between a result and the known value. An error is therefore a single value which can in principle be applied as a correction for this offset. The uncertainty of a result is the range of values that could reasonably be attributed to the measurement, *i.e.*, the range within which the determined result is deemed to lie. Errors largely fall into two categories, random (internal) and systematic (external). Random errors are unpredictable "fluctuations in observations that

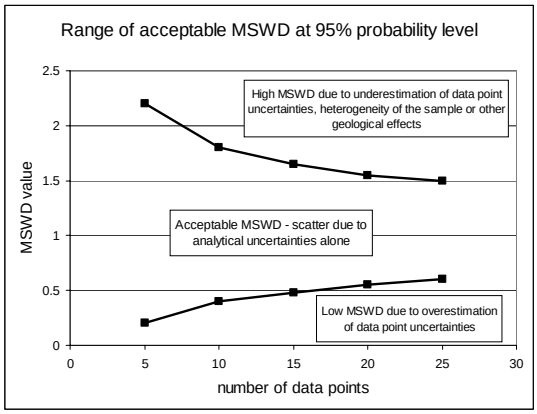


FIG. 16-4 – Range of acceptable MSWD values when scatter of data can be considered due to analytical causes alone (data distilled from Fig. 3. Wendt & Carl 1991).

yield different results each time an experiment is repeated, and thus require repeated experimentation to yield precise results" (Bevington & Robinson 2003). The random error of a result cannot be compensated for but can usually be reduced by increasing the number of observations. The experimental standard deviation of the mean of a series of observations is *not* the random error but a measure of the uncertainty of the mean due to some random effects. The exact value of the random error in the mean arising from these effects cannot be known (EURACHEM Guide). Systematic errors are "errors that will make our results different from the "true" values with reproducible discrepancies" (Bevington & Robinson 2003). They may be constant or may vary in a predictable way (*e.g.*, response effects of detectors) and are independent of the number of measurements made and cannot therefore be reduced by increasing the number of measurements (Taylor 1982, EURACHEM Guide). Systematic errors therefore lead to consistent unidirectional inaccuracies in a result. Systematic errors must therefore be identified and eliminated or their value estimated by assessing the determined results against known reference values.

During laser ablation ICP–MS measurements components of error are contributed at all levels. Some key components and whether they constitute the effect of random or systematic error are:

a) Measurement of the ratio of interest (random).
b) Measurement of the mass bias used for correction (random).
c) Detector response effects (*e.g.*, ion counter non-linearity, dead-time and gain) relative to a Faraday or other analog detector system (systematic).
d) Normalization factor as determined relative to a reference material over the course of the analytical session (random? See discussion below).
e) Reference value of the primary reference material (systematic).
f) Correction ratios used (*e.g.*, common Pb composition, $^{176}Yb/^{173}Yb$, Lu/Hf) (systematic).
g) Decay constants (systematic).

Uncertainties that must be quantified and their contribution to the final uncertainty assessed, therefore include:

1) Analytical uncertainty of the ratio of interest.
2) Analytical uncertainty of the mass bias measurement used for correction.
3) Reproducibility (quantified as a standard deviation) of detector response effects.
4) Reproducibility (standard deviation) of the normalization factor.
5) Ability to reproduce a given ratio relative to the size of the smallest isotope signal.
6) Uncertainty on the reference value of the primary reference material.
7) Uncertainty on the correction ratios used (*e.g.*, common Pb composition, $^{176}Yb/^{173}Yb$, Lu/Hf).
8) Uncertainties on decay constants.

Some debate exists in the LA U–Pb community as to whether the normalization factor constitutes a random or systematic error component. The normalization factor is largely a result of inter-element fractionation within the plasma and the value of this factor can be varied by changing the plasma conditions (*e.g.*, gas flows). In this way the factor can vary over the course of the analytical session and in detail probably at the analysis level. The normalization factor is therefore a non-constant offset which may appear reasonably stable on the time scale of a few analyses (or even hours) or may vary during and between analyses. Since the absolute value for the normalization factor is different for each analysis it is here considered more akin to a random than a systematic error. Therefore the uncertainty for this error is recommended to be propagated into each data point uncertainty. From a practical assessment point of view, this uncertainty limits the ability to know, at any one time, the exact value of the normalization factor and therefore also limits the ability to know the absolute age of the material analyzed. It is not viable therefore to discriminate data points different by much less than this uncertainty since any two consecutive analyses could have a normalization factor that is different by this amount (*i.e.*, *ca.* 2% in the case of Pb/U). Ireland & Williams (2003) also recommended propagation of the reproducibility of the Pb/U normalization factor, as determined by repeated measurement of the reference material, into the data point uncertainties of the unknown samples and secondary reference materials analyzed by secondary ionization mass spectrometry (SIMS). Any remaining error ('inaccuracy') of the result for the normalized secondary reference materials would then reflect additional systematic errors (*e.g.*, due to differences in signal strength and/or matrix between primary and secondary reference materials) the cause of which would need investigating and correcting and the uncertainty on this correction further propagating.

Uncertainties can be propagated using Equation 1:

$$\sigma_z = \sqrt{\left(\frac{\partial Z}{\partial A}\right)^2 .\sigma_A{}^2 + \left(\frac{\partial Z}{\partial B}\right)^2 .\sigma_B{}^2 + \left(\frac{\partial Z}{\partial C}\right)^2 .\sigma_C{}^2} \quad (1)$$

In this equation each differential term $(\partial)$ reflects the partial differential of function Z with respect to one variable, holding all others constant. The partial differentials are then multiplied by the absolute (not relative) uncertainties for each variable. The uncertainty on Z is equal to the square root of the sum of the squares of all these terms.

By example, the $^{207}Pb/^{235}U$ ratio is often calculated for laser ablation data as:

$$\frac{^{207}Pb}{^{235}U} = \frac{^{207}Pb}{^{206}Pb} * \frac{^{206}Pb}{^{238}U} * 137.88 \quad (2)$$

The uncertainty propagation for this using Equation 1 is:

$$\sigma_{^{206}Pb/_{^{235}U}} = \sqrt{\left(\frac{^{206}Pb}{^{238}U} * 137.88 * \sigma_{^{207}Pb/^{206}Pb}\right)^2 + \left(\frac{^{207}Pb}{^{206}Pb} * 137.88 * \sigma_{^{206}Pb/^{238}U}\right)} \quad (3)$$

However, for some simple forms of uncertainty propagation where corrections relate simply to addition or subtraction of components, *e.g.*, interfering element corrections, Equation 1 can be simplified as Equation 4.

$$\sigma_Z = \sqrt{\sigma_A{}^2 + \sigma_B{}^2 + \sigma_C{}^2} \quad (4)$$

where $\sigma_{A–C}$ are the various uncertainty components and must be expressed in relative terms (*i.e.*, as a percentage) and $\sigma_Z$ is the final propagated uncertainty. Where decay constant and age uncertainties are part of the required uncertainty expression, propagation is most practically carried out by running the $1\sigma$ limits through the calculation and propagating this empirically determined uncertainty envelope by quadratic addition with the other components of the uncertainty expression as calculated using Equation 1.

The uncertainties thereby defined for $^{206}Pb/^{238}U$ and $^{207}Pb/^{235}U$ are correlated because one is partially derived from the other using a constant $^{238}U/^{235}U$ ratio. This correlation is defined in Equation 5 following Schmitz & Schoene (2007).

$$\rho_{^{206}Pb/^{238}U - ^{207}Pb/^{235}U} = \frac{\sigma^2_{^{207}Pb/^{235}U} + \sigma^2_{^{206}Pb/^{238}U} - \sigma^2_{^{207}Pb/^{206}Pb}}{2 * \sigma_{^{207}Pb/^{235}U} * \sigma_{^{206}Pb/^{238}U}} \quad (5)$$

Making the assumption that the $^{207}Pb/^{235}U$ uncertainty results solely from quadratic addition of its two component uncertainties, the correlation coefficient can be simplified as the ratio of the two U–Pb uncertainties derived from rigorous uncertainty propagation (Equations 2 & 3).

$$\rho_{^{206}Pb/^{238}U - ^{207}Pb/^{235}U} = \frac{\sigma_{^{206}Pb/^{238}U}}{\sigma_{^{207}Pb/^{235}U}} \quad (6)$$

A fundamental limiting uncertainty is that of the reference material to which the result is being compared or normalized. A result for an unknown sample cannot have an uncertainty better than the reference material to which it is corrected since the uncertainty on the reference material provides the fundamental uncertainty from which the rest of the components are propagated.

Where backgrounds and detector noise are low and correction algorithms are insignificant, uncertainties for measurements taken on very linear and/or sensitive detection systems (*e.g.*, Faraday or ion-counting detectors) are limited only by counting statistics, *i.e.*, the square root of the total cumulative number of counts (N) set as a ratio against N (equation 7, expressed as a percentage).

$$\frac{\sqrt{N}}{N} * 100 \quad (7)$$

The same principles can however also be applied after all corrections to look at the uncertainty distribution relative to beam size. In this way a minimum uncertainty for an analytical protocol can be determined according to the correction algorithms employed and the size of the ion beam being analyzed. For example, Figure 16-5 illustrates the increase in reproducibility (expressed as $1\sigma$ %) of the $^{207}Pb/^{206}Pb$ ratio with decrease in $^{207}Pb$, as measured on multiple ion counters. The equation there defined can then be used in the uncertainty propagation of the $^{207}Pb/^{206}Pb$ ratio in conjunction with the analysis uncertainty.

The largest uncertainty component for those laser ablation protocols, where it exists, is that for calibration of the inter-element ratio. In both U–Pb and Lu–Hf isotope analysis the ability to reproduce the inter-element ratio consistently is limited to the percent level. In the case of Lu–Hf this

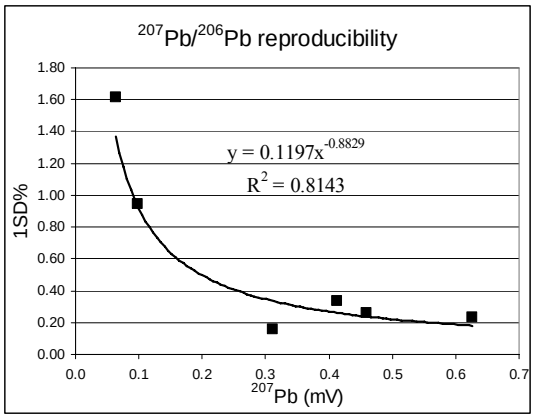


FIG. 16-5 – $^{207}Pb/^{206}Pb$ ratio reproducibility as determined using reference zircon and multiple ion counters, relative to the count rate of $^{207}Pb$. The determined relationship can then be used to propagate an appropriate level of uncertainty for each sample data point based upon the count rate of $^{207}Pb$ in the analysis.

uncertainty level can reach 10–20% (2σ) depending on the homogeneity of the reference material used, but only becomes a significant factor in the overall uncertainty of the epsilon Hf calculation when high REE concentrations are present and the sample is more than *ca.* 500 Ma. In geochronology studies, the Pb/U uncertainty can normally be reproduced to *ca.* 2% 2σ but relies on the assumption that all analyses of the calibration material are concordant (or equally discordant) and equivalent with no variations in Pb/U ratios due to small degrees of Pb loss, inheritance, *etc*. Since the Pb/U uncertainty represents the ability to quantify the Pb/U ratio accurately and therefore the age at any one time, this uncertainty must be propagated into each data point uncertainty and as such limits the age resolution of a single data point to at least this level. This uncertainty is based on reference material data collected with the sample data throughout the analytical session therefore this uncertainty is relevant at all times to all analyses within the session. Whether comparing data collected within or outside the same session therefore, this uncertainty should be propagated into the data point uncertainty for each analysis. The Pb/U uncertainty is therefore the most significant uncertainty that needs to be reduced to improve age resolution in laser ablation geochronology.

**Secondary and tertiary reference materials**

The limiting uncertainty for any laser ablation study is the ability for the technique to reproduce the data on the reference material used. For most LA studies 2–3 reference materials (or well characterized in-house materials) are generally required – the primary reference material to determine and quantify the value and uncertainty of any fundamental normalization and the secondary (and tertiary) to demonstrate accuracy (*i.e.*, elucidate any systematic error) after all corrections, with the different reference materials representing various levels of correction and/or count rates. These secondary and tertiary reference materials can then be used to assess the efficacy of the uncertainty propagation procedure through replicate measurements, *i.e.*, the ability to reproduce a result after all corrections, appropriate to the analytical routine at the time of analysis. Although reference materials with matrices appropriate for quantitative calibration of samples are scarce (Jochum & Stoll 2008), any one reference material can be used to assess the uncertainty level of a protocol through replicate measurements. This may indicate for example that an additional uncertainty needs propagating due to a difference in the mechanism of ablation for one reference material/in-house known, when compared to the primary.

Figure 16-6 shows εHf data after all corrections for two zircon reference materials. The first (Fig. 16-6a) has low REE concentrations requiring relatively minor correction of $^{176}Hf$ for the $^{176}Yb$ and $^{176}Lu$ isobaric interferences. Data in Figure 16-6a are very well constrained with a weighted mean εHf uncertainty of ±0.14 (95% conf., absolute) and an MSWD of 1.1. For a sample with high REE (Fig. 16-6b) however, and a $^{176}Hf/^{177}Hf$ correction >10 times greater than in Figure 16-6a, the resolution of the result decreases by a factor of three to ±0.41 epsilon units (95% conf., absolute) with an MSWD of 2.9 indicating a significant degree of excess scatter. In line with the conclusions of Vervoort *et al.* (2007) and Dufrane *et al.* (2007), assuming this material is indeed homogeneous, this suggests that an uncertainty estimate determined from analyses of more widely available low REE Hf LA reference materials significantly underestimates the level of propagation required for the higher REE containing materials. Concentrations of these REE may vary during the analysis and the correction routine needs to be responsive and capable of accurately correcting these potentially small scale variations.

In the example in Figure 16-7a data for zircon 91500 are used as a secondary U–Pb reference material and have been corrected with uncertainty

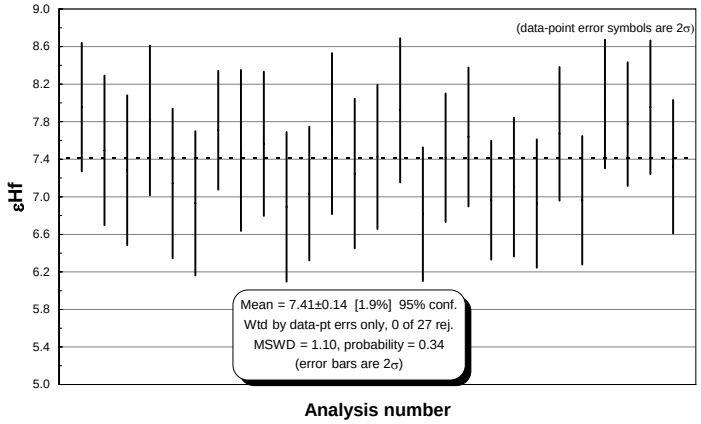


FIG. 16-6a – εHf data for a low REE Hf isotope reference material. Note MSWD ~1 indicating appropriate uncertainty propagation.

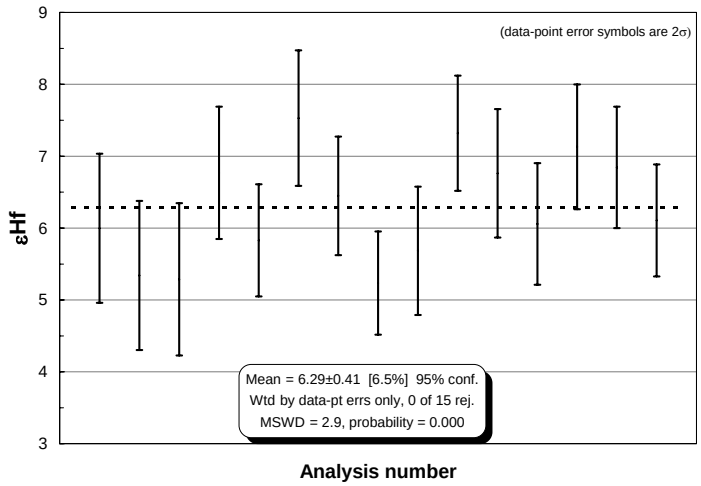


FIG. 16-6b – εHf data for a high REE Hf isotope reference material. Note MSWD >>1 indicating data point uncertainties require expansion (or reference material is not homogeneous)

propagated by quadratic addition for the uncertainty of the analysis and the reproducibility of the Plešovice primary reference material. The resulting statistics on a weighted average of the Pb–U age (MSWD = 0.98) suggests that this level of uncertainty propagation is appropriate and that the variation seen between data points is purely analytical. Should the MSWD prove to be >1, the data can be considered in a probability density plot. If the data are equivalent the distribution will be normal and fall on a single regression line on a linearized probability plot as in Figure 16-7b. If the data do reflect a normal distribution but result in an MSWD >>1 the data point uncertainties will need reconsidering, suggesting a component has been omitted from the uncertainty propagation. Should the data distribution not be normal, *e.g.*, bimodal, suggesting more than one data population in reality (*e.g.*, geological variation), the material is not clearly one by which to assess the appropriateness of the uncertainty propagation algorithm.

**Use of stable isotope ratios**

Interference corrections are often required to achieve the desired data by laser ablation – for example $^{176}$Yb and $^{176}$Lu corrections on $^{176}$Hf; $^{86}$Kr and $^{87}$Rb corrections on the equivalent sample Sr peaks; and $^{204}$Hg correction on $^{204}$Pb. Where stable isotope ratios are available within the isotope system of interest, interference free or otherwise, they should be calculated after mass bias correction and reported as a measure of data quality. In the Hf isotope system $^{180}$Hf/$^{177}$Hf and/or $^{178}$Hf/$^{177}$Hf should be reported so that data can be viewed with reference to the accuracy of these stable, largely interference-free ratios. Likewise in the Sr isotope system, the $^{84}$Sr/$^{86}$Sr should be reported. These data can then be scrutinized by the independent observer as a measure of the underlying robustness of the data when considering the effect and veracity of the interference correction routines employed for the $^{176}$Hf/$^{177}$Hf and $^{87}$Sr/$^{86}$Sr ratios. Reporting of stable isotope data provides a cross check for any

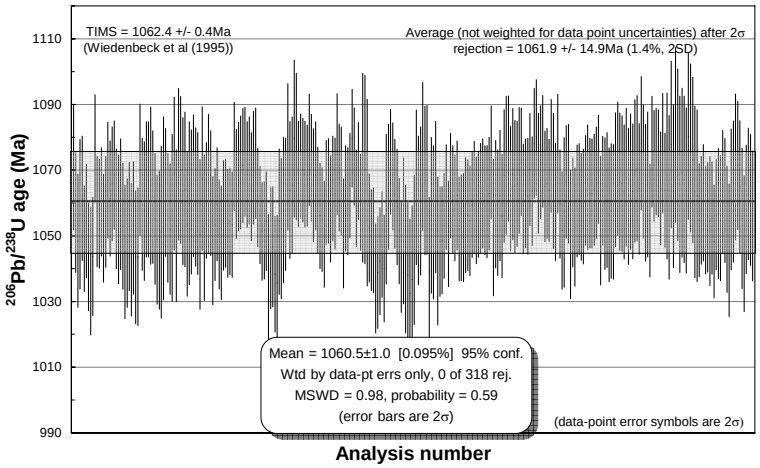


FIG. 16-7a – Pb/U age data (static ablation) for 91500 zircon normalized to Plešovice zircon. Data acquired over *ca.* 6 months. Grey box represents uncertainty of ±1.5% (2σ).

.

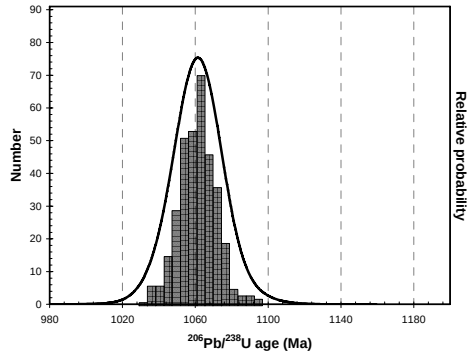


FIG. 16-7b – Data for Fig. 16-7a shown as normal distribution and linearized probability plots. Both plots indicate a single homogeneous population at the resolution of the input data point uncertainties

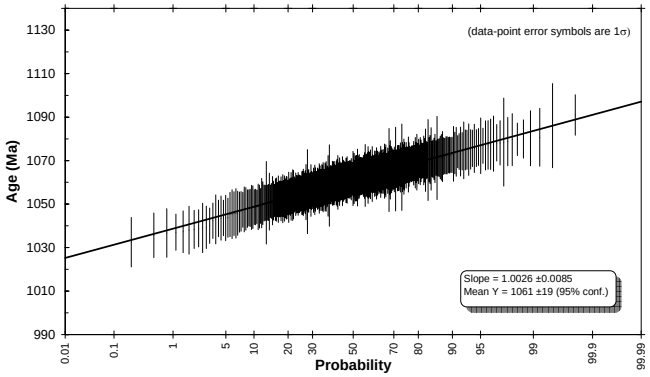


untoward analytical conditions including subtle interferences that may arise during laser ablation, a not uncommon occurrence, and provides the independent observer with confidence as to the quality of the data. Figure 16-8 illustrates the $^{178}Hf/^{177}Hf$ stable isotope data for a suite of zircon samples containing various levels of Hf, REE and zirconium from very high to very low. All data indicate a weighted mean $^{178}Hf/^{177}Hf$ of 1.46723 ±7 ppm (95% conf., MSWD = 0.53, n=117) with no data points rejected, indicating that relative to an expected ratio of 1.46715 (Patchett & Tatsumoto 1980) the underlying data are robust (since the $^{178}Hf$ peak requires no corrections except for mass bias).

**Representation of data**

Laser ablation ICP–MS is a lower precision technique than either solution mode ICP–MS or thermal ionization mass spectrometry (TIMS). Data produced by disaggregating an inherently

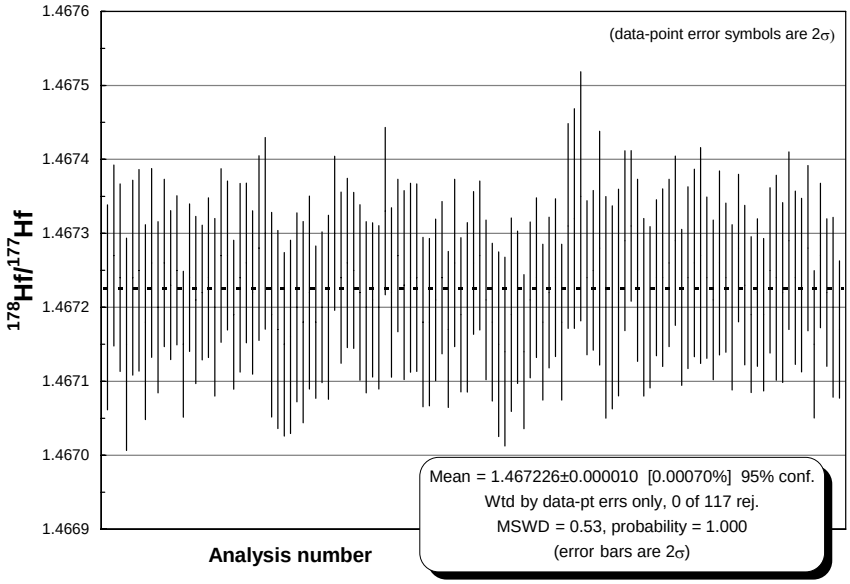


FIG. 16-8 – $^{178}Hf/^{177}Hf$ data for a range of Hf isotope reference materials with low to high REE interference corrections. Reporting of such stable isotope data along with the radiogenic data of interest is considered essential in order to illustrate the underlying data quality.

heterogeneous solid sample into particles of non-equal size which therefore ionize differently (however slightly) within the plasma, cannot be as precise as data produced by homogenizing (*i.e.*, dissolving) and purifying (after chemical separation) the sample material and aspirating it in a controlled fashion as a liquid aerosol (with or without desolvation) into the plasma as a stream of particles of much more equivalent size and composition. For these reasons (and provided sample/blank ratios are not limiting), solution measurement of dissolved samples purified through ion exchange chromatography, must be more precise than equivalent laser ablation methodologies. Due to the possibility for homogenization of multiple phases within the sample during dissolution, the question of which technique reflects the true value better is a separate one. However, the uncertainty on the result cannot be better for laser ablation than for an equivalent solution, not least because the initial calibration of a result obtained by laser ablation is often demonstrated with respect to instrument performance through solution analyses and as such this uncertainty provides a limiting uncertainty from which to propagate the laser ablation data. Equally, when attempting to determine an absolute result, protocols employing external normalization are limited in their uncertainty according to the uncertainty on the reference value used.

The laser ablation methodology which possibly comes closest to the uncertainty of its solution counterpart is the determination of Hf isotope ratios on zircon. Here, uncertainties of *ca.* 0.006% 2σ are quoted (Hawkesworth & Kemp 2006) for low REE reference materials whereas solution analysis of dissolved and separated aliquots may produce uncertainties of *ca.* 0.0015–0.0035% (2σ; Nowell *et al.* 2003). For U–Pb geochronology however, uncertainties of *ca.* 2% (2σ) are common for laser ablation compared to *ca.* 0.1% for TIMS methodologies, yet final age uncertainties of *ca.* 10x less can be mathematically achieved through the use of weighted mean statistics by virtue of the sheer number of data points (*e.g.*, see Sláma *et al.* 2008). The ability for a data point with a 2% uncertainty to resolve a 0.2% difference between itself and its neighbor is very limited. In U–Pb geochronology, instances of minor Pb loss or inheritance are common and small age differences arising from these sources become irresolvable at the 2% level. A limit of ultimate precision must therefore be admitted in all data with this level being dependent upon the uncertainty level of the data points which define it. According to Ludwig (2008), "…the real limit on accuracy for U/Pb dates is only a factor of two or so better than the analytical error of the individual analyses, rather than amenable to arbitrary improvement by increasing the number of analyses alone. This concept follows statistical

limitations on the ability to resolve complexity in the true age structure of a suite of analyses arising from open system behavior, presence of xenocrysts, or a variable and non-zero magma residence time."

Using a high-n dataset to calculate a weighted mean and uncertainty on the result does not therefore indicate the accuracy with which we know the true age but how precisely we know the result defined by that dataset. The statistics assume that all the data are equivalent and fit a normal distribution; this may be the case at the level of 2% data point uncertainties but fine details such as 0.1–0.2% shifts (0.5–1 Ma at 500 Ma) between data points representing Pb loss and/or inheritance will not be resolvable (Kalsbeek 1992) and the existence of such effects breaks the assumption of a single population with normal distribution. Their contribution to the weighted mean or concordia age calculation (Ludwig 2003) is however equivalent to the truly concordant data points and in this way can cause the weighted mean result to be biased. If a high-n data set has been collated the difference between the weighted mean age and the true age may be more than the weighted mean uncertainty. Bowring *et al.* (2006) compared micro-analytical and TIMS-derived data for a sample where minor Pb loss has resulted in slightly lower Pb/U ratios in the micro-analytical data, but which are masked by the data point uncertainties. Taking the weighted mean statistics on these two datasets, results in two ages with uncertainties that do not overlap. This is purely a function of the number of data points used in the weighted mean calculation and is not resolution of a real difference in age.

Therefore, not all data are necessarily the same and should not therefore be included in the same weighted mean calculation. This same argument applies to data at all levels of precision, including ID–TIMS, when dealing with high-n datasets in U–Th–Pb geochronology. Where the data set does conform to a single population with no Pb loss and/or inheritance effects (*e.g.*, for a reference material), the weighted average of the data set should conform to the result determined by high precision ID–TIMS methodologies and the determined uncertainty will represent the confidence in that value as the average value of the data set. However, the 'limit of interpretation' will still remain as a function limited by the data point uncertainties.

This same principle relates to all ablation data. An analog can be seen in the laser ablation Hf isotope data shown in Figure 16-8a where the weighted mean uncertainty of 27 data points is 0.14 epsilon units (= 0.0014% or 14 ppm!). Any suggestion that this uncertainty represents the confidence in the ability to resolve a result different by 0.003% is clearly errant and such a suggestion would not be made. Why then is this practice common when considering age resolution? At some point the limitation of any technique must be admitted and a technique with inherently higher precision capabilities must be used if the resolution of variations much smaller than the data point uncertainties is required.

To this end, when plotting data, fully propagated 2-sigma uncertainties should be represented. Use of 1-sigma uncertainties conveys undue weight to apparent differences between data points. Figure 16-9 illustrates this point. The smaller circles represent data points with 1sigma uncertainties, whilst the larger two data points are identical but with 2 sigma uncertainties. The data points with 1 sigma uncertainties could be argued to be significantly different at first inspection but once they are considered with 2 sigma uncertainties it can be seen that they are indistinguishable within this level of uncertainty. To aid objective evaluation of graphically presented data therefore, plotting at the 2sigma level of uncertainty is recommended.

An alternative representation of an uncertainty propagation protocol is given by Gehrels *et al.* (2008) where uncertainties on systematic errors are initially omitted to improve discrimination of sample populations before adding this uncertainty at the end.

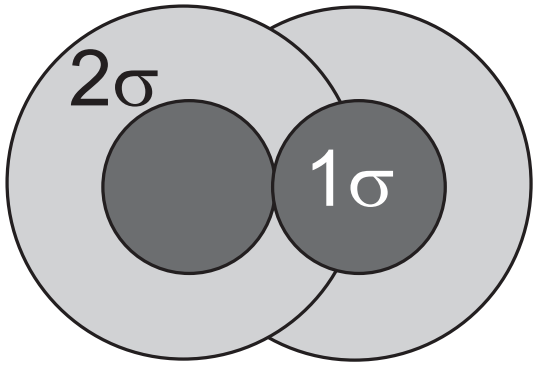


FIG. 16-9 –1σ *vs.* 2σ data point uncertainties illustrating the degree of overlap and therefore potential equivalence when considered at 2σ. At 1σ the potential for data points to be equivalent might not be recognized, leading to spurious interpretation of differences.

**Example of uncertainty propagation strategy**

The following example illustrates a strategy for the propagation of uncertainties which can be applied across a range of applications. In this example, laser ablation Hf isotope data are propagated by quadratic addition as shown in Equation 4, to calculate a value and uncertainty for epsilon Hf. Results are assessed to investigate whether the uncertainty propagation employed provides a realistic representation of the uncertainty expected for a single population.

**Example**

All data are normalized to the average of pure and Yb-doped JMC475 Hf solution reference material analyses (using a $^{176}Hf/^{177}Hf$ value of 0.282160, Patchett & Tatsumoto 1980) run to assess instrumental performance and to determine the Yb correction (as described in page 288, Isobaric interference corrections). Zircon reference material Mud Tank (U–Pb age 732 ±5Ma, Black & Gulson 1978, $^{176}Hf/^{177}Hf = 0.282507$, Woodhead & Hergt 2005) is used to assess accuracy of laser ablation $^{176}Hf/^{177}Hf$ results after normalization to the JMC475 results. Sample $^{176}Hf/^{177}Hf$ analytical uncertainties are propagated with the reproducibility of the Mud Tank reference material. Zircon 91500 is used as the primary standard for normalization of the Lu/Hf inter-element fractionation with reference to the values of Woodhead & Hergt (2005). Sample Lu/Hf uncertainties are propagated with the session reproducibility for the Lu/Hf ratio of 91500 or the variation of the Lu/Hf ratios known to occur in the reference material (whichever is greatest). Finally the 2σ age uncertainty is considered also, as determined by TIMS, SIMS or LA. The age uncertainty used should relate to the age quoted, *i.e.*, if only a single spot $^{206}Pb/^{238}U$ or $^{207}Pb/^{206}Pb$ age has been determined, the single spot uncertainty propagated with reference to the U–Pb standard, should be used. If a full multi-point concordia age determination has been used to calculate the age, this final age uncertainty should be used. In this way, some of the uncertainty as to the known age of the sample or analysis will be built into the uncertainty for epsilon Hf.

An example set of data used for these calculations is shown in Table 16-1. The resulting MSWD suggests that there may be a small component of overestimation in this propagation strategy.

**Effect of U–Pb age discordance and uncertainty on εHf**

The effect of the sample age uncertainty on the final epsilon Hf uncertainty should also be considered. Figure 16-10a plots data for four samples between 337 and 2000 Ma, with $^{176}Yb/^{177}Hf$ and $^{176}Lu/^{177}Hf$ ratios ranging from 0.0042–0.0407 and 0.00004–0.00049 respectively. Varying the age uncertainty from 1 to 20 Ma for these samples, while keeping all other variables constant, increases the uncertainty on the epsilon Hf value by *ca.* 50%. A bias in εHf can also be seen with respect to discordance. Quantification of discordance for detrital zircon samples is usually based on the percentage distance of the data point along a discordia through the origin to the upper intercept, in essence the percentage difference between the determined $^{207}Pb/^{206}Pb$ and $^{206}Pb/^{238}U$

TABLE 16-1. EXAMPLE ILLUSTRATING A STRATEGY FOR THE PROPAGATION OF UNCERTAINTIES.

| **Uncertainty component** | **$^{176}Hf/^{177}Hf$** | **2SD** |
|---|---|---|
| Yb doped and non-doped solution JMC475 | 0.282145 | 0.0039% |
| Mud Tank (after norm to JMC475) | 0.282509 | 0.0090% |
| Sample precision (after norm to JMC475) | 0.282495 | 0.0099% (2SE) |
| Total uncertainty after propagation | | 0.0139% (2σ) |
| | **$^{176}Lu/^{177}Hf$** | **2SD** |
| 91500 (including 2SD of Lu/Hf external variation) | 0.000313 | 9.6% |
| Sample (after norm to 91500 Lu/Hf) | 0.000145 | 0.36% (2SE) |
| Total uncertainty after propagation | | 9.6% (2σ) |
| | **Age** | **2SD** |
| TIMS, SIMS or LA age of sample | 337 Ma | 1 Ma |
| Epsilon Hf calculation of single data point | –2.13 | 1.44 |
| (*cf.* Epsilon Hf Population (uncertainty at 2SD) | –2.4 | 1.11) |
| (wtd mean of population (MSWD = 0.51, n = 20) | –2.37 | 0.34) |

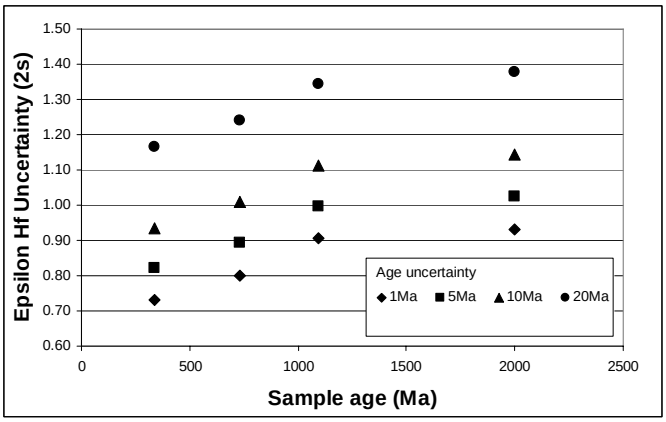


FIG. 16-10a – The effect of increased age uncertainty on calculated εHf uncertainty

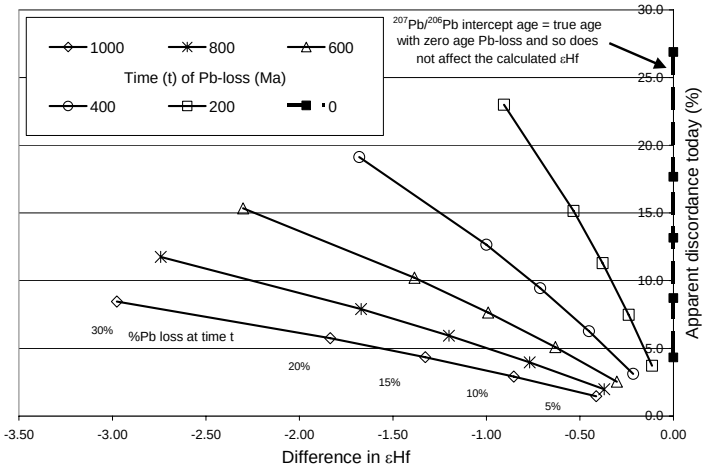


FIG. 16-10b – The difference in the calculated εHf between apparent ($^{207}Pb/^{206}Pb$ intercept) age and true age for a discordant 2 Ga zircon. The effect of different percentages of ancient Pb loss is illustrated. A detrital zircon with an apparent 5% discordance (*i.e.*, Pb loss trajectory through zero) at the present time, but which suffered up to *ca.* 15% Pb loss at 1 Ga, will result in a bias in the calculated εHf of *ca.* –1.3. Zircon grains affected only by modern day Pb loss or igneous populations whose true age can be determined through regression will not show this bias.

ages. If the apparent Pb loss from the grain was only a recent phenomenon, the Pb–Pb age represents the true age and there will be no bias in the determination of the εHf value from this grain regardless of the amount of Pb loss suffered. If however, Pb loss was an ancient phenomenon, the Pb–Pb age represents only a minimum age and even though the $^{206}Pb/^{238}U$ age might only be 5% discordant relative to the $^{207}Pb/^{206}Pb$ age, the true age of this grain will be older. In this instance, a Hf isotope determination on a 'relatively concordant' grain, could still represent a significant bias from the true εHf value. This is shown in Fig 16-10b which shows the variation of calculated εHf as a result of using the $^{207}Pb/^{206}Pb$ upper intercept age of a discordant zircon that has experienced ancient Pb loss. Relative to the true age of 2 Ga, the calculated εHf may show a bias of up to *ca.* 1.5 εHf for a 5% discordant grain resulting from *ca.* 17% Pb loss at 1 Ga. A similar grain that has only suffered 10% Pb loss at 1 Ga will appear 2.9% discordant, *i.e.*, pretty much concordant within the uncertainties of a large proportion of LA U–Pb data, but will still show a bias of 0.85 in the calculated εHf using the determined $^{207}Pb/^{206}Pb$ age. Note that this is still outside of the uncertainties reported for most LA Hf isotope data.

Considering the demonstrated effect of both the age uncertainty and discordance in the interpretation of εHf, a discordant data point not overlapping Concordia has a large uncertainty in determining both the true age and therefore the relevant age uncertainty and this should be reflected in both the calculation of epsilon Hf uncertainty (see Fig. 16-10a) and the potential for bias in the εHf value (Fig. 16-10b). In practice, due to the non-linear nature of the age equations, these uncertainties will be asymmetric. For Hf isotope determinations on detrital zircon, therefore, data point age uncertainties should be used in the calculation of individual epsilon Hf uncertainties for each analysis and these analyses are best conducted only on those data points well within uncertainty of the U–Pb concordia.

## SUMMARY

The approach outlined above highlights an empirical approach for assessing the uncertainty of laser ablation isotope data. Although focusing on the U/Pb, Hf and Sr isotope systems this approach is valid for other systems and has been used in assessing uncertainty contributions in other studies (*e.g.*, depleted uranium solution analysis of chemically separated urines, Parrish *et al.* 2008).

On-line monitoring and real-time correction of data helps elucidate competing phenomena, reduces off-line data reduction of data averages and includes relevant uncertainty components, while elimination of variable components of uncertainty (*e.g.*, LIEF) also limits the necessity for uncertainty propagation.

Secondary and tertiary reference materials or other 'knowns' can be used extensively to investigate the reproducibility of analytical protocols, accuracy and long term performance and in deriving the uncertainty propagation protocol required. Results from these secondary reference materials can then be used on a per-session basis to validate the data at the time. Quotation of stable isotope data is strongly encouraged, to indicate the underlying robustness of the fundamental corrections applied to all the data when inaccuracy of other ratios of interest might reflect poor performance of additional isobaric or other interference corrections performed at the time.

All data should be graphically presented and interpreted at the 2σ level and the limit of interpretation, reflected largely by the data point uncertainties, should be appreciated and respected without recourse to statistical manipulation of high-n datasets. The benefit of laser ablation resides in the ability to resolve different components to relatively high spatial resolution. However, it is a relatively low precision technique and these benefits are undermined when undue weight of interpretation is placed on data where precision has been statistically enhanced. Low precision data may reflect a normal distribution with MSWD values ~1 but can hide, and not resolve, small-scale variations which break the fundamental assumption of a normal distribution. These non-equivalent data can then result in inaccurate results when included in weighted mean statistical assessments. Higher precision methodologies should therefore be employed where a higher level of precision is required.

The effect of a component of uncertainty from one isotope system on the calculations and uncertainties of another should not be forgotten and can be a significant factor limiting the resolution of data and its interpretation.

## ACKNOWLEDGEMENTS

My many thanks go to visiting Professor Jon Patchett and my NIGL colleagues Steve Noble, John Cottle, Dan Condon and Randy Parrish for their comments and time in discussing and elucidating the various aspects in this paper. Many thanks are also due to Tom Anderson and George Gehrels for their constructive reviews.

## REFERENCES

ANDERSON, T. (2002): Correction of common lead in U–Pb analyses that do not report $^{204}$Pb. *Chem. Geol.*, **192**, 59-79

BEVINGTON, P.R. & ROBINSON, D.K. (2003): *Data reduction and error analysis for the physical sciences*. 3rd Edition. McGraw-Hill, New York.

BLACK, L.P. & GULSON, B.L. (1978): The age of the Mud Tank Carbonatite, Strangways range, Northern Territory. *BMR J. Austral. Geol. & Geophys.* **3**, 227–232.

BOWRING , S.A. , SCHOENE, B., CROWLEY , J.L, RAMEZANI, J. & CONDON, D.J. (2006): High-precision U-Pb geochronology and the stratigraphic record: progress and progress. 25-46. *In* Geochronology, Emerging Opportunities. (T. D. Olszewski, ed.) *The Paleontological Society Spec. Pub.***12**, New Haven, CT.

COTTLE, J.M. (2007): *Timing of crustal metamorphism, melting and exhumation of the Greater Himalayan, crust, Makalu-Kangshung-Kharta region, South Tibetan Himalaya*. PhD Thesis, University of Oxford.

DE BIEVRE, P. & TAYLOR, P.D.P. (1993): Table of the isotopic composition of the elements. *Int. J. Mass Spectrom. Ion Process.* **123**, 149.

DUFRANE S.A., VERVOORT, J.D. & HART, G.L., (2007): Uncertainty of Hf isotope analysis in zircon using LA-MC-ICPMS techniques: Full disclosure. 17th Annual V.M. Goldschmidt Conference, Cologne, Germany, August 2007, *Geochim. Cosmochim. Acta* **71**, A241.

EURACHEM/CITAC Guide (2000): Quantifying Uncertainty in Analytical Measurement. 2nd Edition. Eds S L R Ellison, M Rosslein, A Williams. ISBN 0 948926 15 5. LGC Information Services, Middlesex, UK. http://www.measurementuncertainty.org/mu/guide/index.html

FRYER, B.J., JACKSON, S.E. & LONGERICH, H.P. (1995): The design, operation and role of the laser ablation microprobe coupled with an inductively coupled plasma mass spectrometer (LAM-ICP-MS) in the earth sciences. *Can. Mineral.* **33**, 303-312

GEHRELS, G.E., VALENCIA, V.A. & RUIZ, J. (2008): Enhanced precision, accuracy, efficiency, and spatial resolution of U-Pb ages by laser ablation-multicollector-inductively couple plasma-mass spectrometry. *Geochem., Geophys., Geosystems* **9**.

GUILLONG, M. & GÜNTHER, D. (2002): Effect of particle size distribution on ICP-induced elemental fractionation in laser ablation-inductively coupled plasma-mass spectrometry. *J. Anaytl. Atom. Spectrom.* **17**, 831-837

GUILLONG, M., HORN, I. & GÜNTHER, D. (2003): A comparison of 266nm, 213nm and 193nm produced from a single solid state Nd:YAG laser for laser ablation ICP-MS. *J. Analyt. Atom. Spectrom.* **18**, 1224–1230

GÜNTHER, D. & KOCH, J. (2008): Formation of aerosols generated by laser ablation and their impact on elemental fractionation in LA–ICP–MS. *In* Laser Ablation ICP–MS in the Earth Sciences: Current Practices and Outstanding Issues (P. Sylvester, *ed.*). *Mineral. Assoc. Can. Short Course Series* **40**, 19-34.

GÜNTHER, D., COUSIN, H., MAGYAR, B. & LEOPOLD, I. (1997): Calibration studies on dried aerosols for laser ablation-inductively coupled plasma mass spectrometry. *J. Analyt. Atom. Spectrom.* **12**, 165-170

HAWKESWORTH, C.J. & KEMP, A.I.S. (2006): Using hafnium and oxygen isotopes in zircons to unravel the record of crustal evolution. *Chem. Geol.* **226**, 144–162.

HIRATA, T. & NESBITT, R.W. (1995): U-Pb isotope geology of zircon: Evaluation of the laser probe-inductively coupled plasma mass spectrometry technique. *Geochim. Cosmochim. Acta* **59**, 2491-2500.

HORN, I., MCDONOUGH, W.F. & RUDNICK, R.L. (2000): Precise elemental and isotope ratio determination by simultaneous solution nebulization and laser ablation ICP-MS: Application to U/Pb geochronology. *Chem. Geol.* **167**, 405-425

HORN, I. (2008): Comparison of femtosecond and nanosecond laser interactions with geologic matrices and their influence on accuracy and precision of LA–ICP–MS data. *In* Laser Ablation ICP–MS in the Earth Sciences: Current Practices and Outstanding Issues (P. Sylvester, *ed.*). *Mineral. Assoc. Can. Short Course Series* **40**, 53-65.

HORSTWOOD, M.S.A., FOSTER, G.L., PARRISH, NOBLE, S.R. & NOWELL, G.M. (2003): Common-Pb correction in-situ U-Pb accessory mineral geochronology by LA-MC-ICP-MS. *J. Analyt. Atom. Spectrom.* **18**, 837-846.

HORSTWOOD, M.S.A., PARRISH, R.R., CONDON, D.J. & PASHLEY, V. (2006): Laser ablation acquisition protocols and non-matrix matched standardization of U-Pb data. *Geochim. Cosmochim. Acta* **70**, Supplement 1, A264.

IRELAND, T.R. & WILLIAMS, I.S. (2003): Considerations in Zircon Geochronology by SIMS. *In* Zircon (Hanchar, J.M. & Hoskin, P.W.O. eds.) *Rev. Mineral. & Geochem.* **53**, 215-238.

JACKSON, M.G. & HART, S.R. (2006): Strontium isotopes in melt inclusions from Samoan basalts: Implications for heterogeneity in the Samoan plume. *Earth Planet. Sci. Lett.* **245**, 260–277

JACKSON, S.E. & GÜNTHER, D. (2003): The nature and source of laser induced isotopic fractionation in laser ablatio-multicollector-inductively couple plasma-mass spectrometry. *J. Analyt. Atom. Spectrom.* **18**, 205-212

JOCHUM, K.P. & STOLL, B. (2008): Reference materials for elemental and isotopic analyses by LA–(MC)–ICP–MS: successes and outstanding needs. *In* Laser Ablation ICP–MS in the Earth Sciences: Current Practices and Outstanding Issues (P. Sylvester, *ed.*). *Mineral. Assoc. Can. Short Course Series* **40**, 147-168.

KALSBEEK, F. (1992): The statistical distribution of the mean squared weighted deviation – Comment: Isochrons, errorchrons, and the use of MSWD-values. *Chem. Geol.* **94**, 241-243.

KOŠLER, J., TUBRETT, M & SYLVESTER, P.J. (2001): Application of laser ablation ICP-MS to-U-Th-Pb dating of monazite. *Geostand. Newslett.* **25**, 375-386.

KOŠLER, J. (2008): Laser ablation sampling strategies for concentration and isotope ratio analyses by ICP–MS. *In* Laser Ablation ICP–MS in the Earth Sciences: Current Practices and Outstanding Issues (P. Sylvester, *ed.*). *Mineral.*

*Assoc. Can. Short Course Series* **40**, 79-92.

LONGERICH, H.P, FRYER, B.J. & STRONG, D.F. (1987): Determination of lead isotope ratios by inductively coupled plasma mass spectrometry (ICP-MS). *Spectrochim. Acta* **42B**, 39-48.

LONGERICH, H.P, GÜNTHER, D. & JACKSON, S.E. (1996): Elemental fractionation in laser ablation inductively coupled plasma mass spectrometry. *Fres. Jour. Anal. Chem.* **355**, 538-542

LUDWIG, K.R. (2003): Mathematical-Statistical Treatment of data and errors for $^{230}$Th/U geochronology. *In* Uranium Series Geochemistry (Bourdon *et al.*, eds) Rev. Mineral. & Geochem., Mineral. Soc. Amer. **52**, 631-656.

LUDWIG, K.R. (2008): User's Manual for Isoplot 3.6, A Geochronological Toolkit for Microsoft Excel. Berkeley Geochronology Center Special Publication No. 4

MANK, A.J.G. & MASON, P.R.D. (1999): A critical assessment of laser ablation ICP-MS as an analytical tool for depth analysis in silica-based depth analysis. *J. Analyt. Atom. Spectrom.* **14**, 1143-1153.

MASON, P.R.D. & MANK, A.J.G. (2001): Depth-resolved analysis in multi-layered glass and metal materials using laser ablation inductively coupled plasma mass spectrometry (LA-ICP-MS) *J. Anal. At. Spectrom.*, **16**, 1381–1388.

MATTINSON, J.M. (1987): U-Pb ages of zircons: A basic examination of error propagation. *Chem. Geol.* **66**, 151-162.

MCFARLANE, C. & MCCULLOCH, M. (2008): Sm–Nd and Sr isotope systematics in LREE-rich accessory minerals using LA–MC–ICP–MS. *In* Laser Ablation ICP–MS in the Earth Sciences: Current Practices and Outstanding Issues (P. Sylvester, *ed*.). *Mineral. Assoc. Can. Short Course Series* **40**, 117-133.

NOWELL, G.M. & PARRISH, R.R. (2001): Simultaneous acquisition of isotope compositions and parent/daughter ratios by non-isotope dilution-mode plasma ionization multi-collector mass spectrometry (PIMMS). *In* Plasma Source Mass Spectrometry: The New Millenium (Holland, G. & Tanner, S.D.) *Royal Soc. Chem., Spec. Publ*. **267**, 298-310.

NOWELL, G.M., PEARSON, D.G., OTTLEY, C.J., SCHWIETERS, J & DOWALL, D. (2003): Long-term performance characteristics of a plasma ionization multi-collector mass spectrometer (PIMMS): The ThermoFinnigan Neptune. *In* Plasma source Mass Spectrometry: Applications and emerging technologies. (Holland, G. & Tanner, S.D. eds), *Royal Soc. Chem*. Cambridge, UK.

NOWELL, G.M., PEARSON, D.G., PARMAN, S.W., LUGUET, A. & HANSKI, E. (2007): Precise and accurate $^{186}$Os/$^{188}$Os and $^{187}$Os/$^{188}$Os measurements by Multi-Collector Plasma Ionisation Mass Spectrometry, part II: Laser ablation and its application to single-grain Pt-Os and Re-Os geochronology. *Chem. Geol*. **248**, 394–426.

O'CONNOR, C., SHARP, B.L. & EVANS, P. (2006): On-line additions of aqueous standards for calibration of laser ablation inductively coupled plasma mass spectrometry: theory and comparison of wet and dry plasma conditions. *J. Analyt. Atom. Spectrom.* **21**, 556-565.

PARRISH, R.R. (1990): U-Pb dating of monazite and its application to geological problems. *Can. J. Earth Sci*. **27**, 1431-1450.

PARRISH, R.R., HORSTWOOD, M., ARNASON, J.G., CHENERY, S., BREWER, T., LLOYD, N.S. & CARPENTER, D.O. (2008): Depleted uranium contamination by inhalation exposure and its detection after ~20 years: implications for health assessment. *Sci. Total. Env.* **390**, 58-68.

PATCHETT, P.J. & TATSUMOTO, M. (1980): A routine high-precision method for Lu-Hf isotope geochemistry and chronology. *Contrib. Min. Pet*. **75**, 263-267.

PEARSON, N.J., GRIFFIN, W.L. & O'REILLY, S.Y. (2008): Mass fractionation correction in laser ablation multiple-collector ICP–MS: implications for overlap corrections and precise and accurate *in situ* isotope ratio measurement. *In* Laser Ablation ICP–MS in the Earth Sciences: Current Practices and Outstanding Issues (P. Sylvester, *ed*.). *Mineral. Assoc. Can. Short Course Series* **40**, 93-116.

SCHMITZ, M.D. & SCHOENE, B. (2007): Derivation of isotope ratios, errors, and error correlations for U-Pb geochronology using $^{205}$Pb-$^{235}$U-($^{233}$U)-spiked isotope dilution thermal ionization mass spectrometric data. *Geochem., Geophys., Geosystems*, **8**, No.8.

SIMONETTI, A., HEAMAN, L.M. & CHACKO, T.. (2008): Use of discrete-dynode secondary electron multipliers with Faradays – a '*reduced volume*' approach for *in situ* U–Pb dating of accessory minerals within petrographic thin

section by LA–MC–ICP–MS. *In* Laser Ablation ICP–MS in the Earth Sciences: Current Practices and Outstanding Issues (P. Sylvester, *ed*.). *Mineral. Assoc. Can. Short Course Series* **40**, 241-264.

SLÁMA, J., KOŠLER, J., CONDON, D.J., CROWLEY, J.L., GERDES, A., HANCHAR, J.M., HORSTWOOD, M.S.A., MORRIS, G.A. & NASDALA, L., NORBERG, N., SCHALTEGGER, U., SCHOENE, B., TUBRETT, M.N., WHITEHOUSE, M.J. (2008): Plešovice zircon — A new natural reference material for U–Pb and Hf isotopic microanalysis. *Chem. Geol.* **249**, 1-35

STACEY, J.S. & KRAMERS, J.D. (1975): Approximation of terrestrial lead isotope evolution by a two-stage model. *Earth Planet. Sci. Lett.* **26**, 207-221.

STOREY, C.D., JEFFRIES, T.E. & SMITH, M. (2006): Common lead-corrected laser ablation ICP–MS U–Pb systematics and geochronology of titanite. *Chem. Geol.* **227**, 37– 52

SYLVESTER, P.J. & GHADERI, M. (1997): Trace element analysis of scheelite by excimer laser ablation inductively coupled plasma mass spectrometry (ELA-ICP-MS) using a synthetic silicate glass standard. *Chem. Geol.* **141**, 49-65.

TAYLOR, J.R. (1982): *An introduction to error analysis: the study of uncertainties in physical measurements.* University Science Books, CA, USA.

TERA, F. & WASSERBURG, G.J. (1972): U-Th-Pb systematics in three Apollo 14 basalts and the problem of initial Pb in lunar rocks. *Earth. Planet. Sci. Lett.* **17**, 281-304.

VERVOORT, J., DUFRANE, S. & HART, G., (2007): An assessment of the total uncertainty in Hf isotope analyses by LA-MC-ICPMS, *EOS Trans. AGU* **87**, Fall Meet. Suppl., Abstract V51B-0569.

WAIGHT, T., BAKER, J. & WILLIGERS, B. (2002): Rb isotope dilution analyses by MC-ICPMS using Zr to correct for mass fractionation: towards improved Rb–Sr geochronology? *Chem. Geol.* **186**, No.1-2, 99-116

WENDT, I. & CARL, C. (1991): The statistical distribution of the mean squared weighted deviation. *Chem. Geol.* **86**, 275-285.

WOODHEAD, J.D. & HERGT, J.M. (2005): A preliminary appraisal of seven natural zircon reference materials for in situ Hf isotope determination. *Geostandards & Geoanalytical Research* **29**, No.2 183-195.

WOODHEAD, J., HERGT, J., SHELLEY, M., EGGINS, S. & KEMP, R. (2004): Zircon Hf-isotope analysis with an excimer laser, depth profiling, ablation of complex geometries, and concomitant age estimation. *Chem. Geol.* **209**, 121-135

## APPENDIX A1: LAMTRACE DATA REDUCTION SOFTWARE FOR LA–ICP–MS

Simon E. Jackson
Geological Survey of Canada, Natural Resources Canada
601 Booth Street, Ottawa, ON, K1A 0E8
Canada
E-mail: sijackso@NRCan.gc.ca

### INTRODUCTION

The first widely used program developed specifically for calculating elemental concentrations and U–Pb age dates from LA–ICP–MS data for geological media was 'LAMTRACE'. Programming LAMTRACE commenced in about 1990 at Memorial University of Newfoundland, where the ICP–MS group was engaged in developing LA–ICP–MS as a technique for spatially resolved trace element analysis of geological materials. During this work, it quickly became clear that specialized software was required to handle the complex transient signals frequently generated as a result of the progressive laser sampling, during the course of an analysis, of various potential sources of significant chemical heterogeneity: surface contamination, elemental zoning, inclusions (both solid and liquid), fractures and mineral boundaries, *etc*. Achieving meaningful results from these complex signals requires software that allows examination and selective integration of transient signals.

LAMTRACE was born as a spreadsheet in LOTUS 1-2-3 (for DOS operating system), the pre-eminent spreadsheet software of the day, and was written initially for processing in-house data. However, the lack of any other data reduction software package for LA–ICP–MS data in the 1990s led to requests for LAMTRACE from other laboratories. It was migrated to the more contemporary LOTUS 1-2-3 version 5 for Windows (and more recently to version 9 for Windows) and numerous features were added to increase its flexibility and user friendliness. These upgrades included full automation using menu-activated macros, dialog boxes that guide the user through the operational procedure and writing of a detailed manual that includes a tutorial on optimal data acquisition parameters, handling elemental fractionation and other aspects of LA–ICP–MS. Thus, a 'commercial product'' developed out of an in-house spreadsheet. LAMTRACE has now been distributed to more than 25 laboratories worldwide.

### OPERATION

The transient nature of LA–ICP–MS signals requires that signals be acquired on a time-resolved basis with, ideally, at least one signal intensity measurement per isotope per second (more frequent for some applications). This results in the generation of large data sets that require data reduction software which allows signals (or signal ratios) to be viewed as a function of time and then selectively integrated in order to deal appropriately with a variety of complexities that may occur. The integrated background-corrected ablation signals must then be converted to concentrations (or ages) by referencing to a standard reference material. For elemental concentration measurements, a correction must be applied for differing ablation yield, using an internal standard element. Corrections must be applied for mass-dependent drift in sensitivity during the course of the analytical session. Automated detection limit filtering of results is an especially critical requirement in LA–ICP–MS because, unlike in many bulk analytical methods, detection limits can vary greatly from one analysis to the next as a function of ablation conditions (*e.g.*, spot size). Finally, quality control protocols must be applied to check that the instrumental parameters that affect accuracy, precision and detection limits are within acceptable ranges.

LAMTRACE was written in concert with the development at Memorial University of LA–ICP–MS data acquisition protocols (Jackson *et al.* 1992, Longerich *et al.* 1996) that have been widely adopted by the analytical community. Its functionality is a result of its development over many years in a research and production laboratory setting, where it was continually upgraded in response to the needs of both development and application scientists. Indeed, subsequent data reduction software packages require the use of the same data acquisition protocols and employ the same conceptual approach to data reduction as LAMTRACE (see Longerich *et al.*, 1996). This approach is achieved in LAMTRACE via a series of automated macro-

Mineralogical Association of Canada Short Course 40, Vancouver, B.C., p. 305–307.

driven operations accessed via self-explanatory menus. Thus, no operational knowledge of LOTUS 1-2-3 is required. The steps are as follows:

**Data formatting and pre-integration**

- reformatting of ICP–MS output files (11 ICP–MS instruments supported) and 'pre-integration' (integration of groups of a user-specified number of mass sweeps into single values) for smoothing purposes using LAMTRACE's sister program, 'CONVERT'.

**Calculation of element concentrations**

- graphical presentation of time-resolved signals for selected elements.
- interactive (or fully automated) selective integration of a pre-ablation background signal interval and an ablation signal interval for each analysis.
- calculation of trace element concentrations via external calibration against analyses of a standard bracketing the analyses of the unknown samples, coupled with internal standardization (using concentrations entered) and mass-dependent instrumental drift correction. Both detection limit-filtered (for presentation) and unfiltered (for statistical analysis) concentrations are calculated. Optional rounding of concentrations based on user-defined criteria.
- automated preparation of chondrite-normalized diagrams for each analysis, if required. These also show detection limits and, if required for comparative/QC purposes, literature values for any reference material that has been analysed.

**Chemical profiling**

- generation, if required, of time-resolved elemental concentration profiles (concentration versus ablation time, in graphical and tabular format) for depth profiling or line ablation applications.

**U–Pb dating**

- graphical presentation of time-resolved signals for selected elements and/or relevant Pb–Pb, Pb/U, Pb/Th ratios.
- interactive/automated selective integration of pre-ablation background signal interval and ablation signal interval (matched for analyses of samples and standard).
- calculation of $^{207}Pb/^{206}Pb$, $^{206}Pb/^{238}U$, $^{207}Pb/^{235}U$ and $^{208}Pb/^{232}Th$ ages (and errors) by external calibration against analyses of a mineral standard bracketing the analyses of the unknowns, coupled with mass-dependent instrumental drift correction.
- generation of U/Pb concordia plot.

**Quality control and reporting**

- generation of analytical run diagnostics plots documenting instrument sensitivity and backgrounds, mass-dependent drift, ablation yields and detection limits.
- automated printing of results and graphics, if required.
- exporting of results files, if required. Alternatively, results can be copied and pasted directly into other applications. U–Pb data are exported in the optimal format for further processing using IsoplotEx.

Due to the cumbersome data-exporting routines of the early ICP–MS instruments at Memorial University, ICP–MS data were normally exported only at the end of an analytical session. Thus, LAMTRACE was developed primarily for off-line data reduction that would usually be performed after data acquisition was completed.

## THE FUTURE

With the development of GLITTER (Griffin *et al.* 2008) and, more recently, several freeware packages for LA–ICP–MS data reduction, any thoughts of rewriting LAMTRACE in a more contemporary format or otherwise 'modernizing' it for continued commercial distribution were shelved. However, LAMTRACE is still a highly functional data-reduction package. It is, in particular, an invaluable research tool because all calculations and macro code are completely accessible and can be modified easily for new developments and applications by anyone with a reasonable knowledge of spreadsheet programming. Thus, LAMTRACE will be supported and developed for the foreseeable future. New features that are in an advanced state of programming into LAMTRACE include:

- a variety of element fractionation correction algorithms, some of which have been discussed in this volume (Jackson 2008).
- the capability of processing high precision LA–MC–ICP–MS data for isotope ratio measurements.
- capability of internal standardless analysis via normalization to 100% (oxides) (Halicz & Günther, 2004).

Options for dissemination of LAMTRACE in the near term include offering it as freeware. However, in the long term, the utility of LAMTRACE, even as freeware for research purposes, may be dictated by the availability of LOTUS 1-2-3. While still commercially available (http://www-306.ibm.com/software/lotus/products/smartsuite/), LOTUS SmartSuite's dramatic market decline could potentially result in its discontinuation at some point. There have been efforts by several parties to translate LAMTRACE into Microsoft Excel format. However, to the author's knowledge, these efforts have largely been unsuccessful due to lack of some critical functions in Excel. The author has received one report of a successful migration of LAMTRACE into Excel, but the user responsible continues to use the LOTUS version!

## REFERENCES

GRIFFIN, W.L., POWELL, W.J., PEARSON, N.J. & O'REILLY, S.Y. (2008): GLITTER: data reduction software for laser ablation ICP–MS. *In* Laser Ablation ICP–MS in the Earth Sciences: Current Practices and Outstanding Issues (P. Sylvester, *ed*.). *Mineral. Assoc. Can. Short Course Series* **40**, 308-311.

HALICZ, L. & GÜNTHER, D. (2004): Quantitative analysis of silicates using LA–ICP–MS with liquid calibration. *J. Analyt. Atom. Spectrom.* **19**, 1539-1545.

JACKSON, S.E. (2008): Calibration strategies for elemental analysis by LA–ICP–MS *In* Laser Ablation ICP–MS in the Earth Sciences: Current Practices and Outstanding Issues (P. Sylvester, *ed*.). *Mineral. Assoc. Can. Short Course Series* **40**, 169-188.

JACKSON, S.E., LONGERICH, H.P., DUNNING, G.R. & FRYER, B.J. (1992): The application of laser ablation microprobe–inductively coupled plasma–mass spectrometry (LAM–ICP–MS) to in situ trace element determinations in minerals. *Can. Mineral.* **30**, 1049-1064.

LONGERICH, H.P., JACKSON, S.E. & GÜNTHER, D. (1996): Laser ablation–inductively coupled plasma–mass spectrometric transient signal data acquisition and analyte concentration calculation. *J. Analyt. Atom. Spectrom.* **11**, 899-904.

## APPENDIX A2: GLITTER: DATA REDUCTION SOFTWARE FOR LASER ABLATION ICP–MS

W.L. Griffin, W.J. Powell, N.J. Pearson and S.Y. O'Reilly
GEMOC ARC National Key Centre, Department of Earth and Planetary Sciences,
Macquarie University, NSW 2109, Australia
E-mail: npearson@els.mq.edu.au

### INTRODUCTION

GLITTER is a data reduction software system developed by GEMOC. It provides real-time, on-line and user friendly treatment of quantitative chemical data produced during analysis of solid micro-samples by laser ablation microprobe–inductively coupled plasma–mass spectrometry (LAM–ICP–MS). With more than 10 years of development and upgrades it is a mature and stable software package. GLITTER gives the analyst immediate results and quality control information, and provides a unique interactive visual environment for data analysis and capture. These features have made GLITTER the leader in its field and it is now used in over 100 institutions and companies throughout the world.

The development of GLITTER (van Achterbergh *et al.*, 2001) provided the first real-time, on-line data reduction package and represented a significant improvement on spreadsheet-based routines. Prior to the development of GLITTER, data reduction could only be performed at the end of an analytical session (*e.g.*, LAMTRACE). This typically involved time-consuming off-line reduction procedures; most importantly it left the analyst 'flying blind' while the analyses were being performed. The feature that distinguishes GLITTER is that it is linked to the real-time data acquisition from the mass spectrometer and immediately provides the analyst with the elemental concentrations of the sampled material. However, GLITTER is more than a sophisticated set of numerical calculations. It embodies a holistic analytical strategy and protocols for *in situ* trace element analysis and isotope ratio measurements. These protocols include external standardization, internal standard normalization, time-resolved data collection, signal selection, instrumental drift and fractionation corrections.

GLITTER's features include:

- Automated importing of time-resolved signals from more than 10 ICP-MS platforms
- Automated graphing/pixel map of time-resolved signals
- Automated graphing/pixel map of time-resolved isotopic ratios
- Interactive/automated selection of optimal signal time intervals for integration
- Calculation of element concentrations using external calibration standard(s) and ablation yield correction using an internal standard
- Corrections for mass-dependent instrumental drift
- Detection limit filtering function
- Calculation of uncertainties for individual elements in each analysis
- Generation of chondrite-normalized spidergrams and other plots
- Chemical depth profiling
- Calculation of $^{207}Pb/^{206}Pb$, $^{206}Pb/^{238}U$ and $^{207}Pb/^{235}U$ ages and errors, using an external calibration
- Generation of interactive U/Pb Concordia plots
- Graphical analytical run diagnostics reports
- Printing of results and graphics
- Exporting of results in a simple spreadsheet format

A unique aspect of GLITTER is the graphical user interface, which provides for interactive selection of the relevant part of the signals, dynamically linked to graphical and tabular output and data reduction in real time; this allows inspection and evaluation of each result before the next analysis spot is chosen. GLITTER's unique pixel-row display of time-resolved signals provides an interface image that is easy to interpret visually and enables rapid selection of the best intervals for background and signal measurement, the easy identification of anomalous inclusions in the material being analyzed, and removal of data spikes. These features give the analyst total control during the course of the analytical session and immediate feedback on data quality.

GLITTER is written in the IDL programming language (www.ittvis.com/idl) and the current version of GLITTER (4.4.2) requires IDL version

Mineralogical Association of Canada Short Course 40, Vancouver, B.C., p. 308–311.

6.4 or higher. This version is compatible with Windows (2000, XP, Vista); Mac OS X and Linux versions are under development. GLITTER has also been updated to the latest generation instrument technologies and currently supports the following mass spectrometer platforms: Agilent 7500, Hewlett Packard HP4500, Perkin Elmer Elan (5100, 6000, 6100), VG-PQII/III, VG-Excell, Micromass Platform, ThermoFinnigan Element (I, II, XR), Varian 810/820-MS and output from PlasmaLab ICP-MS control software.

**Overview**

There are two workflow options for GLITTER: trace element analysis and isotope ratio measurement. In both of these modes of operation there are five main windows: the GLITTER or 'Main Window'; the 'Standards' window; the 'Review Signal Selection' window; the 'Plot Results' window; and the 'Options' window. All of these windows are dynamically linked such that any actions taken by the analyst will be automatically implemented in all windows. During routine operation the 'GLITTER Main Window', the 'Review Signal Selection' and the 'Plot Results' windows are open and visible (see Fig. A2-1), whereas the 'Standards' and 'Options' windows are only opened when user interaction is required or instigated.

The 'Main Window' displays the table of results, with options to show also lower limits of detection, one sigma uncertainties, signal and background intensities and run QC diagnostics (*e.g.*, % fractionation, ablation yield). The 'Review Signal Selection' window presents the time-resolved signals for individual samples in two formats. The fractionation with time and to display time-resolved isotope ratios. The upper panel is a pixel map display of the time-resolved signal of all of the isotopes in the selected analysis. Each row

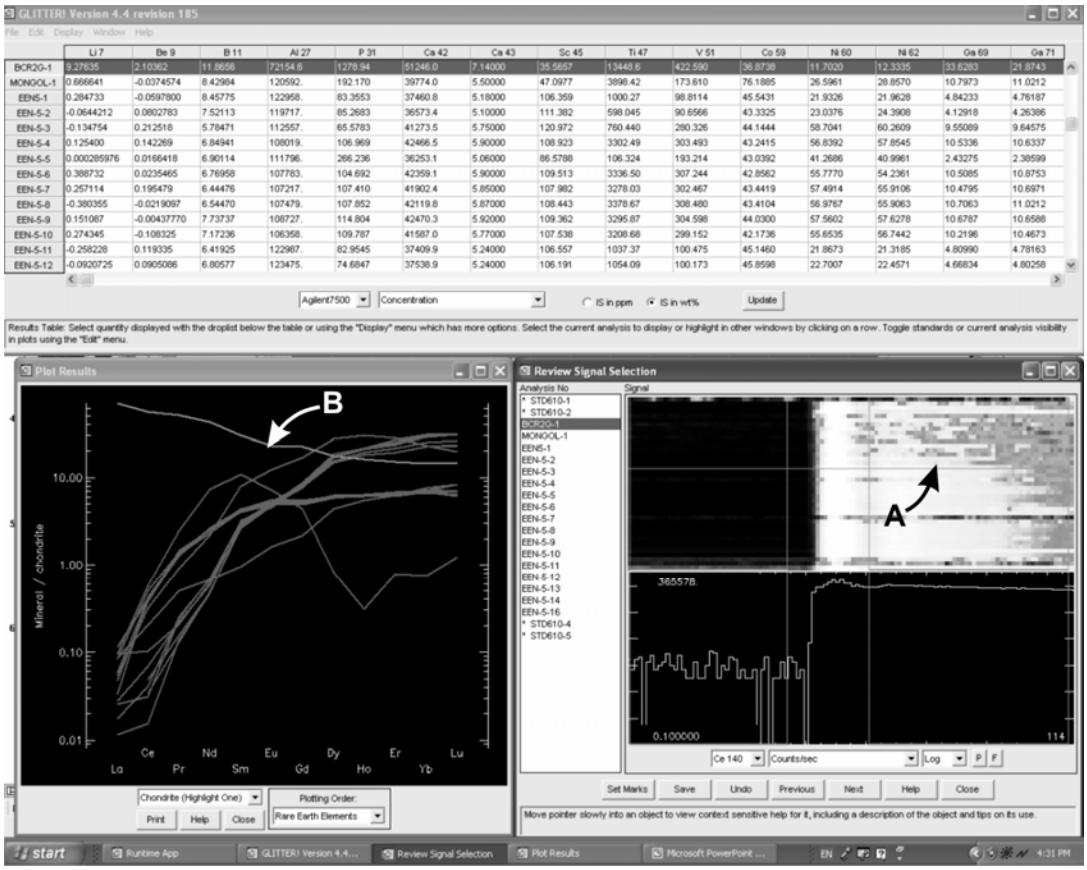


FIG. Ar-1: A GLITTER screen-shot showing the routine work environment for trace element analysis. The 'Main Window' at the top displays the element concentrations and is automatically linked to the signal integration intervals selected by the analyst in the 'Review Signal Selection' window. The 'Plot Results' window is similarly linked; the selected sample is highlighted (B) in the plot and is automatically updated to any changes in the integration interval.

represents an isotope and the color intensity represents the normalized signal intensity. The isotope selected for display in the lower panel is highlighted by a green horizontal line in the pixel map (labeled 'A' on Fig. A2-1). The main purpose lower panel of the display shows the signal for a single isotope selected by the user. Options here also include displaying the ratio of a selected isotope to internal standard to monitor elemental of the 'Review Signal Selection' window is to allow the analyst to select the signal and background integration intervals. This feature allows the analyst to identify heterogeneities and spikes in the data, and to adjust the markers accordingly. As the marker positions are shifted the table of results is automatically updated. Any changes to the marker positions are also updated in the graphs displayed in the 'Plot Results' window. The choice of plots in this window includes those for data presentation (*e.g.*, chondrite-normalized REE plots, spidergrams, X-Y plots) and assessing data quality (*e.g.*, fractio-ation, drift). In the Isotope Ratio mode, the plot options also include U/Pb Concordia plots.

The 'Standards' window allows the analyst to choose the internal standard and to enter values for the unknown samples (Fig. A2-2). There is also provision to enter different dwell times for individual isotopes if non-uniform counting times have been used to acquire the data. The 'Options' window allows the user a choice of methods to interpolate the drift between the groups of calibration standards, as well as enabling the user the capability to select the magnitude of the uncertainties on the 'true' values of the calibration standard and on the internal standard (Fig. A2-3).

The 'Isotope Ratio' mode of GLITTER was originally developed as an analytical protocol for the *in situ* U/Pb dating of zircon (Jackson *et al.* 2004). GLITTER calculates the age of an unknown zircon from its measured isotope ratios using an external calibration zircon standard of known age. There are several options available to correct for the potential fractionation of U and Pb during the ablation process, including direct linking of signal integration intervals between standards and samples or independent choice of signal intervals. GLITTER also provides estimates of the uncertainties on the ratio and age, and plots the data on a Concordia plot. In 'Isotope Ratio' mode, the dynamic linking of the various windows in GLITTER gives the analyst immediate information about the homogeneity of the zircon grain, as well as its age and concordance (Fig. A2-4). The 'Isotope Ratio' mode is not restricted to zircon, or even to U/Pb dating and can be used for any isotopic system provided an appropriate calibration standard is

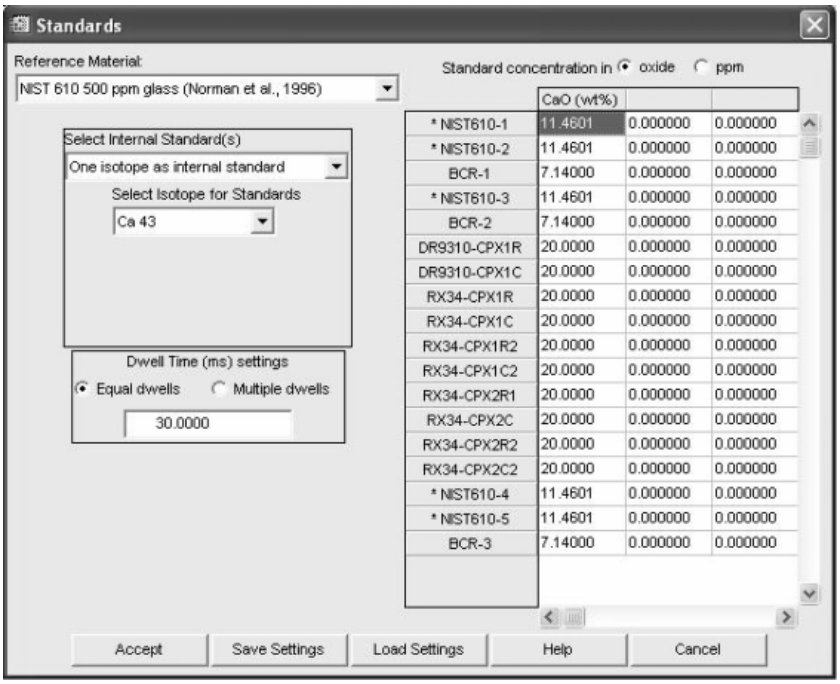


FIG. A2-2. The 'Standards' window is used by the analyst to choose the calibration standard and the internal standard, and to enter the value of the internal standard for each analysis.

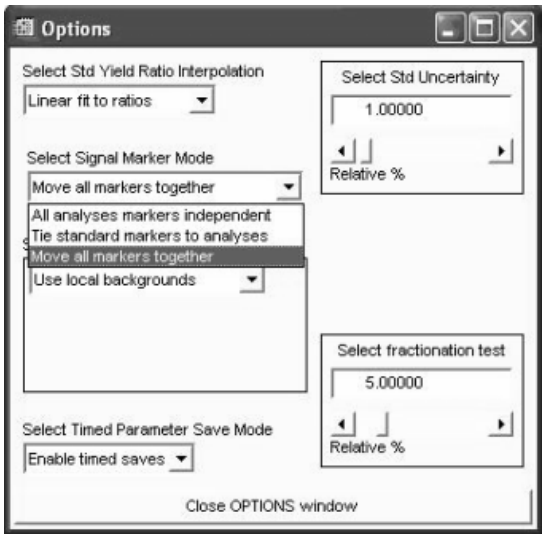


FIG. A2-3: The 'Options' window for the Isotope Ratio mode. This screen shot shows the three options available in the 'Select Signal Marker Mode' drop-down box to correct for fractionation.

available and the ratios of interest and their reference values have been incorporated into the relevant GLITTER files.

Data tables can be exported as ASCII text files and in formats that can be directly imported into Microsoft Excel.

More information about GLITTER can be found at www.glitter-gemoc.com.

## REFERENCES

JACKSON, S.E., PEARSON, N.J., BELOUSOVA, E. & GRIFFIN, W.L. (2004): The application of laser ablation-inductively coupled plasma-mass spectroetry (LA-ICP-MS) to in situ U-Pb geochronology. *Chem.Geol.***211**, 47-69.

VAN ACHTERBERGH, E., RYAN, C., JACKSON, S. & GRIFFIN, W. (2001): Appendix 3, Data reduction software for LA-ICP-MS. *In* Laser-Ablation-ICPMS in the Earth Sciences (P. Sylvester, ed.). *Mineral. Assoc. Can. Short Course Series* **29**, 239-243.

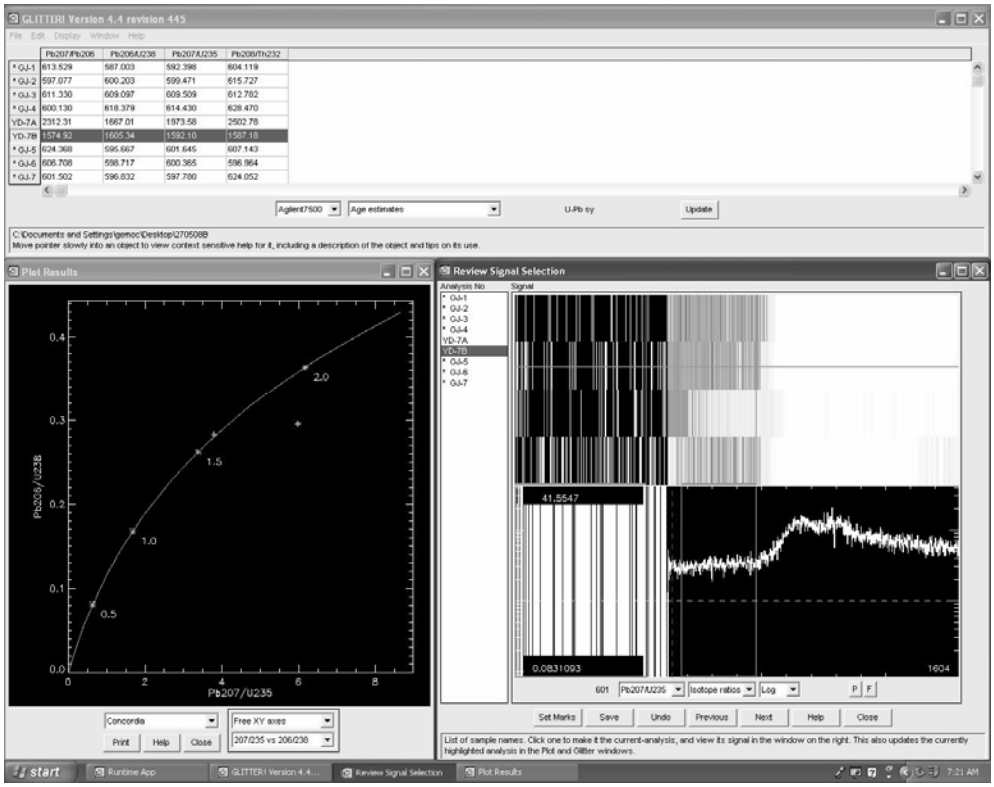


FIG. A2-4. A screen-shot of GLITTER in isotope ratio mode. In this example the 'Main Window" gives U-Pb age estimates, the 'Review Signal Selection' shows the variation of isotope ratios with time and the 'Plot Results' window displays a Concordia plot of $^{206}Pb/^{238}U$ vs $^{207}Pb/^{235}U$. The time-resolved plot of the $^{207}Pb/^{235}U$ ratio clearly shows an anomaly in this particular zircon grain. If the entire signal is integrated the data point plots away from the Concordia and towards common Pb. Selecting the portion of the signal before the anomaly moves the point close to the Concordia. The ability to do this evaluation on-line provides the analyst with a more powerful analytical tool.

## APPENDIX A3: COMPBCORR – SOFTWARE FOR COMMON LEAD CORRECTION OF U–TH–PB ANALYSES THAT DO NOT REPORT $^{204}$PB

Tom Andersen
Department of Geosciences, University of Oslo,
PO Box 1047 Blindern,
N-0316 Oslo, Norway
E-mail: tom.andersen@geo.uio.no

### INTRODUCTION

Common Pb is Pb of non-radiogenic origin incorporated into the crystal structure of a mineral. In U–Pb geochronology of zircon and other U-enriched minerals, common Pb may be a contaminant that needs to be corrected for, if an analysis is to be used for meaningful age calculation. In TIMS–ID, SIMS and MC–ICP–MS analysis, this is commonly done by measuring the non-radiogenic lead isotope $^{204}$Pb, and subtracting the corresponding amounts of the radiogenic isotopes $^{206}$Pb, $^{207}$Pb and $^{208}$Pb, given a model for the isotopic composition of common Pb. However, in LAM–ICP–MS analysis, mass 204 may be too heavily contaminated by $^{204}$Hg from the argon supply for this conventional method to be applicable, and some laboratories using quadrupole ICP–MS do not report $^{204}$Pb.

The algorithm implemented in ComPbCorr is based on general features of the isotope systematics of mixtures between radiogenic and non-radiogenic U–Th–Pb components. The theoretical background has been described in detail by Andersen (2002). The main point is that discordance in a U–Th–Pb system is either due to loss of Pb (or gain of U) after initial crystallization, to incorporation of common Pb, or to a combination of the two processes. Pb loss and contamination by common Pb leads to distinct shifts away from the concordia in a 3D conventional concordia diagram (along lines $t_1$–$t_2$ and $t_1$–$A$ in Fig. A3-1, respectively). If the composition of common Pb and the time of Pb-loss ($t_2$) are known or can be estimated, any discordant Pb composition can be modelled in terms its radiogenic and common Pb components and an additonal "Pb-loss component".

In Fig. A3-1, a present day Pb at *A'* contains a significant proportion of common Pb, and would give meaningless $^{206}$Pb/$^{238}$U, $^{207}$Pb/$^{235}$U, $^{208}$Pb/$^{232}$Th and $^{207}$Pb/$^{206}$Pb ages unless the common Pb component is removed. The present day composition of the radiogenic Pb component is at *B*, which lies on a Pb-loss line from concordant Pb at the time of initial crystallization ($t_1$) to the point on

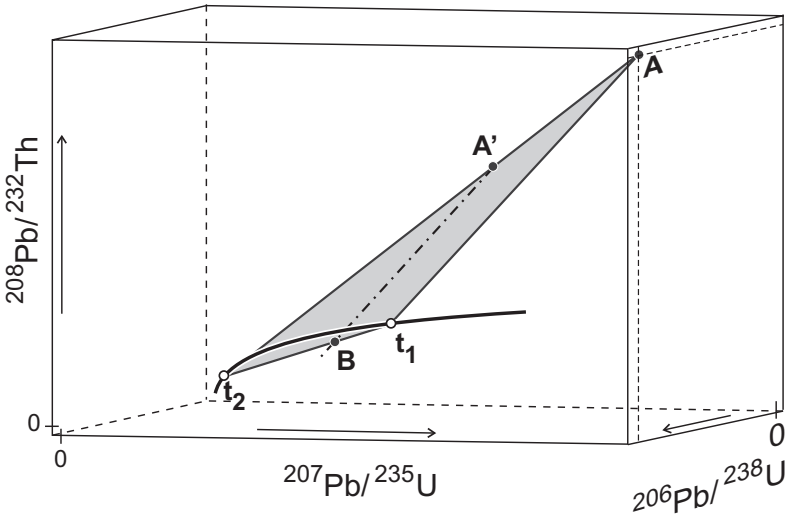


FIG. A3-1. U–Th–Pb systematics of a common Pb-bearing mineral (*e.g.* zircon) in a 3D concordia diagram. The concordia (heavy line) starts at the origin and terminates at the point where it pierces the arbitrarily chosen front surface of the diagram. The common Pb-bearing mineral crystallized at the time $t_1$, and lost Pb at $t_2$ ($t_2$<$t_1$). Its present day composition determined by analysis is at A', but if no loss of Pb had taken place, the composition would have been at A. The composition of the radiogenic component is at B, which is situated at a discordia line between points on the concordia at $t_1$ and $t_2$.

Mineralogical Association of Canada Short Course 40, Vancouver, B.C., p. 312–314.

the concordia representing the time of Pb loss ($t_2$). ComPbCorr uses a numeric algorithm to solve the mass balance equations of a discordant Pb, giving simultaneous estimates of the amounts of common and radiogenic Pb, the isotopic compostion of the radiogenic Pb component, the amount of Pb lost and the upper intercept age of the radiogenic Pb component ($t_1$). If $t_2 > 0$, $t_1$ will be greater than the common Pb corrected $^{207}Pb/^{206}Pb$ age of the mineral, and will represent the best estimate of initial crystallization. If $t_2 = 0$ the two ages will be identical.

The age of Pb-loss ($t_2$) is an input parameter that must be determined independently or be assumed. The method is sensitive to overestimates of $t_2$, which can cause a significant overestimate of $t_1$. Fortunately, the effect is not symmetric, and even a significant underestimate of $t_2$ may have trivial effects on $t_1$, unless the mineral is strongly discordant. For example, wrongly assuming $t_2 = 0$ for a mid-Proterozoic zircon which has lost less than 5% of its Pb at *ca*. 500 Ma will cause a systematic error in $t_1$ less than the uncertainty caused by analytical error. The systematic error induced by an erroneous $t_2$ increases with increasing Pb loss, and data from zircon grains whose common Pb corrected compositions are strongly discordant should be treated with care.

The main limitation of the program is that it cannot handle U–Th–Pb systems which have suffered more than one Pb-loss event, or whose U/Th ratio has been modified after initial crystallization. For such analyses, ComPbCorr can perform $^{207}Pb$ and $^{208}Pb$ corrections (Ludwig 2003), which assume that the radiogenic component is perfectly concordant in either the $^{207}Pb/^{235}U$–$^{206}Pb/^{238}U$ or $^{208}Pb/^{232}Th$–$^{206}Pb/^{238}U$ pairs, respectively. It should, however, be remembered that the assumption of $^{208}Pb/^{232}Th$ – $^{206}Pb/^{238}U$ concordance made in the $^{208}Pb$ correction method is highly questionable (Andersen 2002)

ComPbCorr comes as a template for Microsoft Excel, written mainly in VBA, but with the most calculation-intensive routines in compiled form (written in C) to speed up data processing. The software therefore consists of two files, the Excel template itself (*ComPbCorr.xlt*) and the library file *cfunc.dll*. The program has been developed and tested under Microsoft Excel 2003 on a Windows XP system.

Input parameters are the observed ratios $^{206}Pb/^{238}U$, $^{207}Pb/^{235}U$, $^{208}Pb/^{232}Th$ and $^{232}Th/^{238}U$. The user may set parameters such as the composition of common Pb, number of iterations, error limits for the calculation of concordance and time of Pb loss ($t_2$) from an interactive screen (Fig. A3-2). The program then performs the calculations and reports corrected isotope ratios and geochronological results derived from them. Uncertainties in derived ratios and ages are estimated by Monte

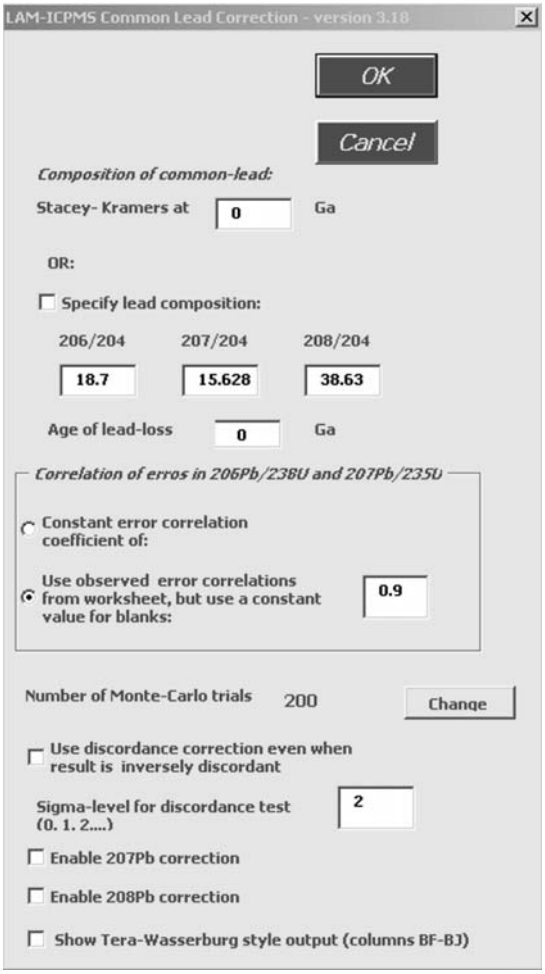


FIG. A3-2. Screenshot of the main control screen of ComPbCorr. The parameters that can be manipulated by the user are: (1) The composition of common Pb, which can either be measured from coexisting K-feldspar or based on the Stacey & Kramers (1975) global Pb model at a specified time. (2) The age of Pb loss ($t_2$), with a default value of zero. (3) The correlation coefficient of errors in the $^{206}Pb/^{238}U$ and $^{207}Pb/^{235}U$ ratios. (4) The number of Monte Carlo iterations to be used in the error analysis (defaults to 200, but should normally be set much higher – note that this slows down calculations). (5) Limits for concordance testing. (6) Optional extra output columns with $^{207}Pb/^{206}Pb$, $^{238}U/^{206}Pb$ ratios and errors.

Carlo routines based on a number of iterations to be determined by the user

ComPbCorr is available upon e-mail request to the author at: tom.andersen@geo.uio.no. The most recent version (at the time of writing) is 3.18, which was launched in 2007. The template and DLL file are packed in a zip-file together with some installation instructions. Installation under Windows XP and Windows Vista should be unproblematic.

**ACKNOWLEDGEMENTS**

ComPbCorr grew out of research carried out at the GEMOC Centre at Macquarie University, Australia, during visits in 2000 and 2001. Thanks are due to Macquarie University and the University of Oslo for financial support, and to colleagues at GEMOC for many inspiring discussions about LAM–ICPMS and common Pb problems, in particular to William L. Griffin, Suzanne O'Reilly and Elena Belousova.

**REFERENCES**

ANDERSEN, T. (2002): Correction of common lead in U–Pb analyses that do not report $^{204}$Pb. *Chem. Geol.* **192**, 59-79.

LUDWIG, K.R. (2003). *User's manual for Isoplot 3.00.* Berkeley Geochronology Center Special Publication No. **4**, 70 pp.

STACEY, J.S. & KRAMERS, J.D. (1975): Approximation of terrestrial lead isotope evolution by a two-stage model. *Earth Planet. Sci. Lett.* **26**, 207-221.

# APPENDIX A4: LAMDATE AND LAMTOOL: SPREADSHEET-BASED DATA REDUCTION FOR LASER ABLATION ICP–MS

Jan Košler[1], Libor Forst[2] & Jiří Sláma[1]
[1]Centre for Geobiology and Department of Earth Science, University of Bergen, Allegaten 41, N-5007 Bergen, Norway.
[2] Faculty of Mathematics and Physics, Charles University, Malostranské nám. 25, CZ-11800 Prague 1, Czech Republic
E-mail: jan.kosler@geo.uib.no

## INTRODUCTION

Reduction of data obtained by laser ablation inductively coupled plasma source mass spectrometry (LA–ICP–MS) requires that each analysis is visually inspected as time-resolved signal intensities of several isotopic species where the acquisition of "gas" blank is followed by collection of laser ablation signal. Following the blank subtraction, additional corrections for laser-induced elemental or isotopic fractionation, instrument mass discrimination and drift and ablation yield are often made before the final concentrations of isotopes or isotopic ratios are calculated using external calibration techniques or internal (spike) calibration. Given the speed of data acquisition that varies from a few milliseconds to several seconds per isotope, the reduction of signals measured over the time of several tens of seconds up to several minutes involves handling of large data sets. Most data acquisition and reduction strategies follow the procedure outlined in Jackson *et al.* (1992) and Longerich *et al*. (1996, 1997).

The nature of measurement by LA–ICP–MS only allows for data reduction to be done after the analysis is completed, *i.e.*, off-line. The available data reduction programs are either written in a programming code such as IDL (*Glitter*) or Matlab (*Sills*) or as a combination of macros (*e.g.*, Visual Basic) and spreadsheet functions in a spreadsheet editor (*e.g.*, *LAMTRACE* in Lotus 123 or *Lars-C* in MS Excel). Data reduction using a programming code is fast and computer memory efficient but it is often difficult for the user to implement changes in the code or to retrieve partial results from the calculation. The spreadsheet-based programs can be easily modified by the user but because all the partial results are generally stored in the same file, the routines are relatively slow and require large computer memory. As a result, only a limited number of analyses (*e.g.*, 30–50) can be processed simultaneously.

This paper provides a description of two MS Excel spreadsheet-based programs: *LamDate* was designed for reduction of LA–ICP–MS U–Pb data obtained on single collector instruments; and *LamTool* is used for the reduction of isotope ratio measurements from a multiple collector ICP–MS.

### LamDate

*LamDate* is a Visual Basic macro-driven program that runs in MS Excel (tested up to the version 2003) that can be used to reduce signal intensity data from LA single-collector ICP–MS U(Th)–Pb measurements of accessory minerals and to calculate their radiometric ages. It was developed by Jan Košler at Memorial University. The calculation follows the procedure described in Košler *et al.* (2002) for laser ablation analysis with simultaneous aspiration of a tracer solution and it is available in several versions for different accessory minerals. Handling, upload and combination of individual data files in an MS Excel workbook is controlled from a separate Visual Basic macro named *Convert&Import*. The main features of the program include:

- Available for data formats generated from ThermoFinnigan Element2/XR, HP/Agilent (ChemStation) and VG/Thermo (PQVision, PlasmaLab) platforms.
- Automated conversion of raw data files and integration of scans (sweeps).
- Automated upload of up to 50 converted files in an MS Excel workbook.
- Interactive selection of blank and laser signal intervals.
- Elimination of outliers in isotopic/elemental ratios (2 sigma test).
- Corrections for detector dead time, blank, laser-induced fractionation of Pb/U, instrument mass discrimination and optional correction for common Pb.

Mineralogical Association of Canada Short Course 40, Vancouver, B.C., p. 315–317.

- Calculation of Pb/U and Pb isotopic ratios, their uncertainties and corresponding radiometric ages.
- Output in format that can be read directly by IsoplotEx (the widely used Excel-based software of Ken Ludwig for generating concordia plots and additional calculations).
- Program is available as freeware from Memorial University (www.mun.ca/creait/maf/U-Th-Pb.php).
-

**LamTool**

*LamTool* is a Visual Basic macro-driven program that runs in MS Excel (tested up to the version 2003) that was originally developed from *LamDate* at the University of Bergen. It is primarily intended for handling and reduction of isotopic data obtained by LA multiple-collector ICP–MS but it can also be used for data from single-collector instruments and for solution measurements. The input format is a tab-delimited text file, such as the data export files generated from ThermoFinnigan Neptune software (*.exp files with isotope signal intensities in columns and individual readings in rows) but it is not specific to this platform and data obtained from other instruments (*e.g.* NuPlasma or GV Isoprobe) can also be imported.

The basic version of the *LamTool* MS Excel workbook contains three sheets. The "menu" sheet (Fig. A4-1a) is used to define the start and the end of a continuous array of raw data that are to be imported to the workbook and a choice of corrections and calibration parameters that are specific for a given isotopic system but common for all measurements in the workbook. The data are brought into the workbook as one measurement per sheet and pasted into data sheets that are generated as copies of the "template" during the data import, with an analysis identification/file name printed on the sheet tab. The "template" is created/modified by the user. It contains at least the selection of blank and laser signal intervals (Fig. A4-1b), but normally also a set of corrections that are specific to the analyzed isotopic system, propagation of analytical uncertainties and calculation of isotopic ratios. Creation and modification of the "template" requires the use of standard MS Excel functions. The "Results" sheet contains a summary of data that are copied from individual data sheets with an analysis identification/file name in the first column. The content of additional columns is defined by the user through references to cells in the data sheets that can be typed in the first row (*cf.* Fig. A4-1c). The main advantage of the *LamTool* is its flexibility and possibility for users to make changes in the calculations without the need to master a programming language. The main features of the program include:

- Automated upload of tab-delimited data (independent of the platform).
- Single analyses can be added to the workbook during measurement.
- Interactive selection of blank and laser signal intervals.
- User-defined calculations through standard MS Excel functions.
- Examples and templates are available for isotopic systems (Li, S, Fe, Sr, Hf, Pb and U–Pb dating) commonly studied in the Earth sciences.
- Results output is in an MS Excel table.
- Program is available as freeware from the University of Bergen (www.geo.uib.no/ceia).

**REFERENCES**

JACKSON, S.E., LONGERICH, H.P., DUNNING, G.R. & FRYER, B.J. (1992): The application of laser-ablation microprobe-inductively coupled plasma mass spectrometry LAM–ICP–MS to in situ trace element determinations in minerals. *Can. Mineral*. **30**, 1049-1064.

KOŠLER, J., FONNELAND, H., SYLVESTER, P., TUBRETT M. & PEDERSEN R.B. (2002): U–Pb dating of detrital zircons for sediment provenance studies – a comparison of laser ablation ICPMS and SIMS techniques. *Chem. Geol*. **182**, 605-618.

LONGERICH, H.P., JACKSON, S.E., & GÜNTHER, D. (1996): Laser ablation- inductively coupled plasma mass spectrometric transient signal data acquisition and analyte concentration calculation. *J. Analyt. Atom. Spectrom.* **11**, 899-904.

LONGERICH, H.P., JACKSON, S.E., & GÜNTHER, D. (1997): Laser ablation inductively coupled plasma mass spectrometric transient signal data acquisition and analyte concentration calculation: Errata. *J. Analyt. Atom. Spectrom.* **12**, 391.

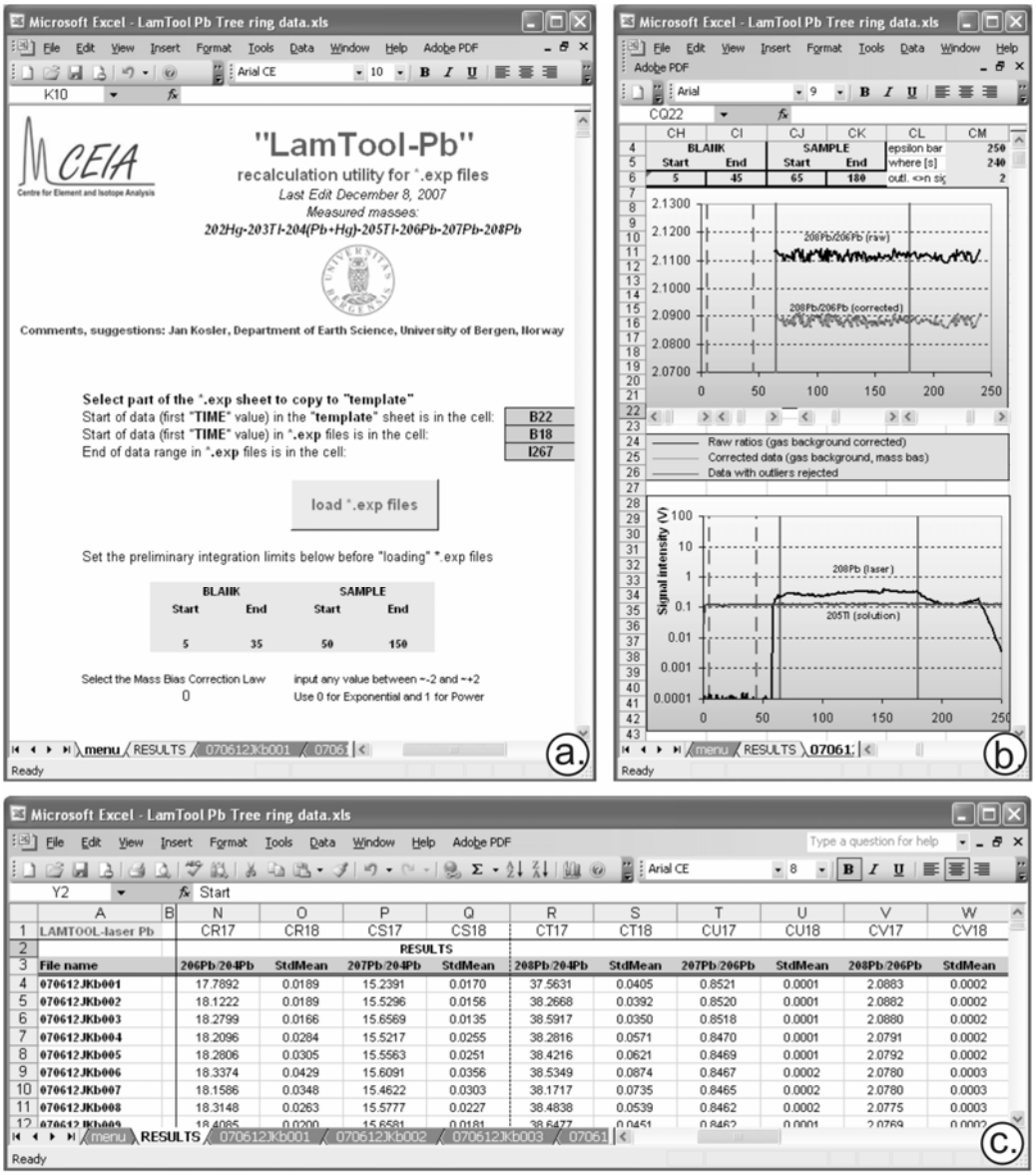


| | A | N | O | P | Q | R | S | T | U | V | W |
|---|---|---|---|---|---|---|---|---|---|---|---|
| 1 | LAMTOOL-laser Pb | CR17 | CR18 | CS17 | CS18 | CT17 | CT18 | CU17 | CU18 | CV17 | CV18 |
| 2 | | RESULTS | | | | | | | | | |
| 3 | File name | 206Pb/204Pb | StdMean | 207Pb/204Pb | StdMean | 208Pb/204Pb | StdMean | 207Pb/206Pb | StdMean | 208Pb/206Pb | StdMean |
| 4 | 070612JKb001 | 17.7892 | 0.0189 | 15.2391 | 0.0170 | 37.5631 | 0.0405 | 0.8521 | 0.0001 | 2.0883 | 0.0002 |
| 5 | 070612JKb002 | 18.1222 | 0.0189 | 15.5296 | 0.0156 | 38.2668 | 0.0392 | 0.8520 | 0.0001 | 2.0882 | 0.0002 |
| 6 | 070612JKb003 | 18.2799 | 0.0166 | 15.6569 | 0.0135 | 38.5917 | 0.0350 | 0.8518 | 0.0001 | 2.0880 | 0.0002 |
| 7 | 070612JKb004 | 18.2096 | 0.0284 | 15.5217 | 0.0255 | 38.2816 | 0.0571 | 0.8470 | 0.0001 | 2.0791 | 0.0002 |
| 8 | 070612JKb005 | 18.2806 | 0.0305 | 15.5563 | 0.0251 | 38.4216 | 0.0621 | 0.8469 | 0.0001 | 2.0792 | 0.0002 |
| 9 | 070612JKb006 | 18.3374 | 0.0429 | 15.6091 | 0.0356 | 38.5349 | 0.0874 | 0.8467 | 0.0002 | 2.0780 | 0.0003 |
| 10 | 070612JKb007 | 18.1586 | 0.0348 | 15.4622 | 0.0303 | 38.1717 | 0.0735 | 0.8465 | 0.0002 | 2.0780 | 0.0003 |
| 11 | 070612JKb008 | 18.3148 | 0.0263 | 15.5777 | 0.0227 | 38.4838 | 0.0539 | 0.8462 | 0.0002 | 2.0775 | 0.0003 |

FIG. A4-1. Screen shots of Pb isotopic data reduction in *LamTool* from laser ablation analysis of a tree ring with simultaneous aspiration of Tl solution. (**a**) the menu sheet with preliminary selection of signal intervals and selection of data array to be imported in the workbook, (**b**) selection of intervals in a data sheet showing measured and corrected isotopic ratios, ratio outliers and signal intensities of $^{206}$Pb (laser) and $^{205}$Tl (solution) in volts and (**c**) results page with references to data cells in the individual data sheets and calculated final Pb isotopic ratios and their uncertainties.

# APPENDIX A5: ANALYSIS MANAGEMENT SYSTEM (AMS) FOR REDUCTION OF LASER ABLATION ICP–MS DATA

S.R. Mutchler, L. Fedele and R.J. Bodnar
Department of Geosciences
Virginia Tech
Blacksburg, VA 24061
E-mail: rjb@vt.edu

## INTRODUCTION

This paper describes the Analysis Management System (AMS) software that has recently been developed to facilitate the reduction of data from laser ablation inductively coupled plasma–mass spectrometric (LA–ICP–MS) analysis of various materials. While the AMS software is applicable to analysis of any material, it was developed to address analytical and data reduction issues that are unique to the analysis of materials that are small (resulting in a short-lived signal) and/or heterogeneous at the scale (both spatial and temporal) of the analysis. Specifically, the AMS software is designed and optimized for reduction of data from fluid and melt inclusions in geologic samples (Roedder 1984).

In developing the AMS software, our goals were to develop an easy to use tool for reduction of LA–ICP–MS data from fluid and melt inclusions. To accomplish this we have automated many of the time-consuming steps commonly involved in LA–ICP–MS data reduction, such as normalization to 100% oxides. In addition, the AMS can provide more accurate and precise results by minimizing systematic errors, by allowing the use of multiple standards, and by incorporating an improved drift correction methodology.

The AMS software has the option to provide output as a single file that contains the ICP–MS data, the various options for data reduction, and the results, and is thus highly transportable. Moreover, AMS is a stand-alone software package that eliminates the need to purchase and learn to use commercial software. AMS software is written in Java and runs on Unix, Macintosh or Windows platforms. AMS is compatible with data formats used by most of the major ICP–MS manufacturers (*e.g.*, Perkin Elmer, Agilent, or any other instrument that has CSV-formatted output). AMS outputs the results in Excel, PDF, HTML or CSV formats. It is fully configurable by individual users and allows editing of XML text files to include, for example, additional standards or new mass conversion values. Importantly, the software incorporates well established algorithms for data analysis (Gunther *et al.* 1998, Halter *et al.* 2002, Heinrich *et al.* 2003, Longerich *et al.* 1996).

Both the software and source code are available on the Fluids Research Laboratory website at: http://www.geochem.geos.vt.edu/fluids/laICP–MS/ams.shtml. AMS software is a community project in which interested persons can submit requests to enhance the software or report bugs. AMS software is an Open Source application under GPL.

In the following sections we describe those features of the AMS software that make it unique or which represent improvement over existing LA–ICP–MS data reduction packages. This is accomplished by describing features for using multiple standards, applying drift corrections, visualizing fractionation patterns during the analysis and finally by providing working examples of the reduction of LA–ICP–MS data from fluid and melt inclusions.

## USE OF MULTIPLE STANDARDS AND DRIFT CORRECTION

AMS supports the use of multiple standards for a single analysis. In addition, AMS supports multiple standard runs (at different times) for each standard. A typical data reduction in AMS may include 6 or more spectra from 2 or more standards (*e.g.*, NIST 610, 612, *etc*.) that bracket (in time) the actual FI or MI analysis. The uncertainty in standard concentrations has been shown to be one of the largest sources of error in LA–ICP–MS analysis. If multiple standards (as a multi-point calibration) are used during the analysis of a sample with "known" element concentrations, such as the G-Probe-2 microprobe standard (Potts *et al.* 2008), the error in element abundance is commonly less than if only a single standard was used (Fig. A5-1).

If the FI or MI analysis is bracketed by standard runs, AMS can also correct for any

Mineralogical Association of Canada Short Course 40, Vancouver, B.C., p. 318–327.

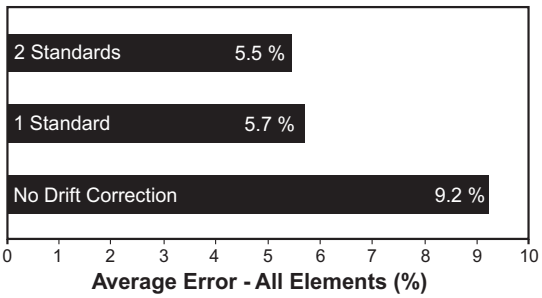


FIG. A5-1. Comparison of the average error in concentration (20 analyses) of 35 elements [Al, B, Ba, Ca, Ce, Cr, Cs, Cu, Eu, Fe, Gd, Hf, K, La, Mg, Mn, Na, Nb, Nd, Ni, Pb, Rb, Sc, Si, Sm, Sr, Ta, Tb, Th, Ti, U, V, Y, Zn, Zr] in the G-Probe-2 standard for data reduction involving only a single point standard with no drift correction (No Drift Correction), a single standard with drift correction (1 Standard), and two standards with drift correction (2 Standards).

instrumental drift (if present). AMS calculates the time-dependent drift in concentration for each element by calculating the element concentration using each standard run as a single point calibration. AMS then does a regression of element concentration *vs*. the time during the analytical sequence when the standard was analyzed. If the correlation ($R^2$) is greater than a user-specified value, AMS uses the regression value; otherwise AMS uses the concentration of the element calculated using the standard run closest in time (either before or after) to the analysis time. Analysis times are inferred from the ICP–MS data file time stamp.

An example of the method used for drift correction is shown in Figure A5-2 for Rb. Sample G-Probe-2 (Potts *et al.* 2008) was analyzed 20 times over a period of about 200 minutes, with the NIST 610 and 612 standards analyzed at the beginning, near the middle, and at the end of the session. Shown on the diagram are six concentrations for Rb in the G-Probe-2 sample that would have been obtained if only a single point calibration was used. For example, if the NIST 610 standard labeled "1" had been used as a single point standard, the concentration predicted for the unknown analyzed at time t=618 min would have been about 36.5 ppm. Similarly, if the NIST 610 standard labeled "6" had been used to determine the composition of Rb in the analysis conducted at 618 min, the estimated concentration would have been about 31.5 ppm. However, by analyzing multiple standards periodically during the entire analytical session and using these data to define a drift correction defined by the linear regression line through the standards data, a corrected concentration of approximately 34.6 ppm is obtained. The results show clearly that the use of only a single point reference standard, collected either before or after the analytical session, that did not take into account instrumental drift could lead to a less accurate result for the unknown.

## ELEMENTAL FRACTIONATION DURING ANALYSIS

Elemental fractionation can be a major issue during LA–ICP–MS analyses (Gunther & Hattendorf 2001). AMS provides a method to estimate the amount of fractionation for each element in a homogeneous sample volume through a series of fractionation plots (FP). When the option to generate the FP is on (see below), the signal region of interest (SROI) selected by the operator is divided into 10 slices and data reduction is performed on each slice. After the analysis the results are plotted as concentration vs. time, allowing a visual estimate of how SROI selection affects the outcomes of the calculations (Fig. A5-3).

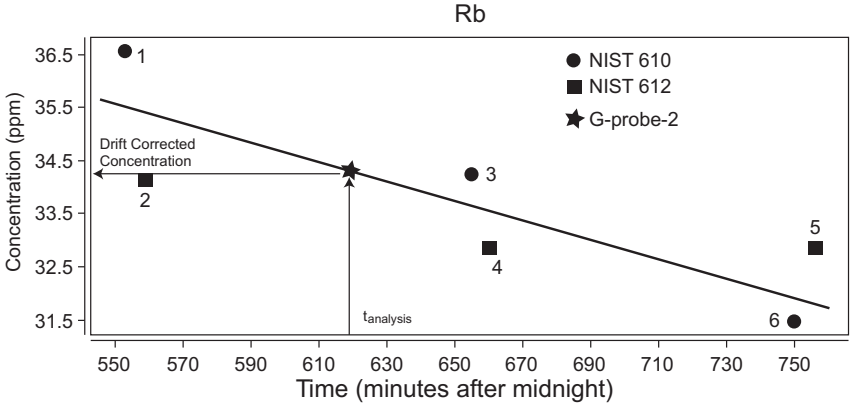


FIG. A5-2. Concentration of Rb in sample G-Probe-2 that would be obtained for the analysis conducted at ≈618 min using six single point standards (labeled 1 to 6), compared to the concentration that is obtained if the six single point standards are used to define an instrumental drift correction line.

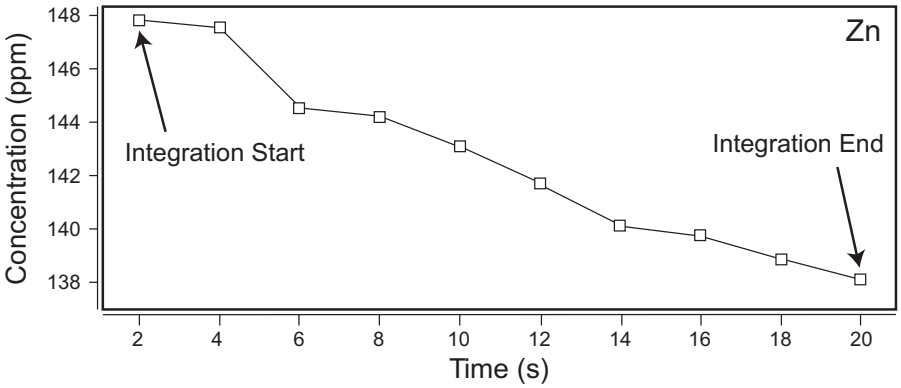


FIG. A5-3. Fractionation plot produced by AMS showing the concentration of zinc as a function of time in the signal region of interest.

The ideal output (*i.e.*, complete absence of fractionation) would be a flat line ($\Delta C/\Delta t = 0$) where the concentration ($C$) in each of the 10 slices is the same. Additional plots also display the standard/element signal ratios. The signal ratio plots show the stability (or lack thereof) of the intensity ratios during the analysis.

## FLUID INCLUSION ANALYSIS AND DATA REDUCTION

The logical steps followed during analysis of fluid and melt inclusions are shown in Figure A5-4. The analysis of fluid or melt inclusions starts with detailed petrographic examination of each sample to determine the relationship of the inclusions to the host mineral phase and to the petrogenesis of the sample (Bodnar 2003, Bodnar & Student 2006) (Fig. A5-4, box 1). After the fluid inclusions have been selected, the freezing point depression or the halite disappearance temperature of the inclusions is determined by microthermometry (Fig. A5-4, box 2). These temperatures are entered into AMS, which then uses published algorithms (Bodnar 1993, Bodnar *et al.* 1989, Sterner *et al.* 1988) to calculate an NaCl-equivalent bulk salinity of the inclusion (Fig. A5-4, box 3). The bulk salinity of the inclusion, in conjunction with elemental concentration ratios determined by LA–ICP–MS analysis, is used to calculate the absolute element concentrations in the inclusion.

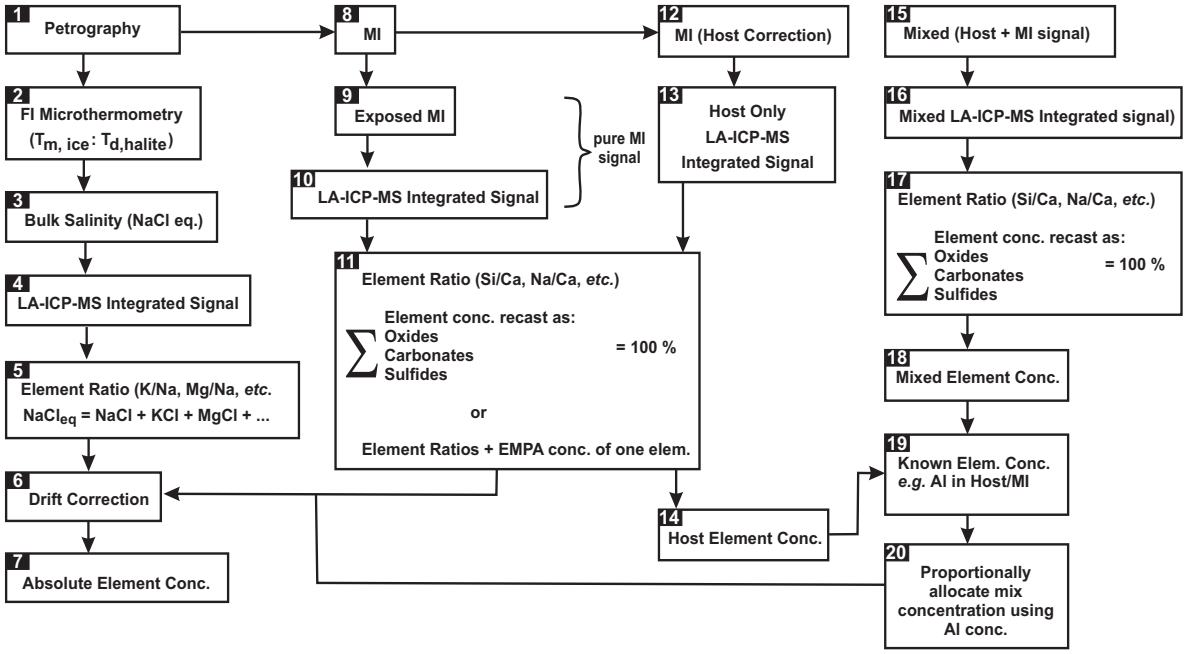


FIG. A5-4. Flow chart showing the sequence of tasks involved in the analysis and data reduction for fluid and melt inclusions using AMS software.

AMS uses the LA–ICP–MS signal from the FI (Fig. A5-4, box 4) and a known external standard (*e.g.*, NIST 610) to calculate elemental concentration ratios (Fig. A5-4, box 5). AMS uses the integrated signal areas after background subtraction for the FI and standard to determine elemental intensity ratios using equation (1) (from (Longerich *et al.* 1996). The use of an external standard eliminates the effects of element-specific instrumental sensitivity (Longerich *et al.* 1996).

$$\frac{C_{Ca}^{Sample}}{C_{Na}^{Sample}} = \frac{C_{Ca}^{Stand}}{C_{Na}^{Stand}} \times \frac{I_{Ca}^{Sample}}{I_{Na}^{Sample}} \times \frac{I_{Na}^{Stand}}{I_{Ca}^{Stand}} \qquad (1)$$

The absolute concentrations of individual elements in the inclusion are determined from the calculated element ratios and the bulk salinity obtained by microthermometry using mass balance constraints (Heinrich *et al.* 2003) (Fig. A5-4, box 7), with or without a drift correction (Fig. A5-4, box 6).

After the laser ablation ICP–MS spectra have been collected, one launches the options window in AMS (Fig. A5-5) to define the parameters used during the analysis, including which standards were used, how many standard analyses were conducted, and the method that will be used to calculate concentrations. In the example shown in Figure A5-5, four analyses of NIST 610 (two at the beginning of the session and two at the end) were used for the external standards. During microthermometry, the ice phase melted at –18ºC, and this value is entered in the "Method" section and used to calculate the bulk salinity. The host correction options shown in the lower left are not required for this fluid inclusion analysis because the host is quartz and we did not measure Si in the FI. The instrument settings used during the analysis included concentrations in counts, with a dwell time of 0.01 sec and drift correction confidence interval ($R^2$) of 0.9. In this example, the "Generate fractionation plots" option was not selected. At the conclusion of the data reduction process, the results window (see below) will be shown and the results will be written to an Excel file, as defined by the output options.

Once all the options have been set, the ICP–MS

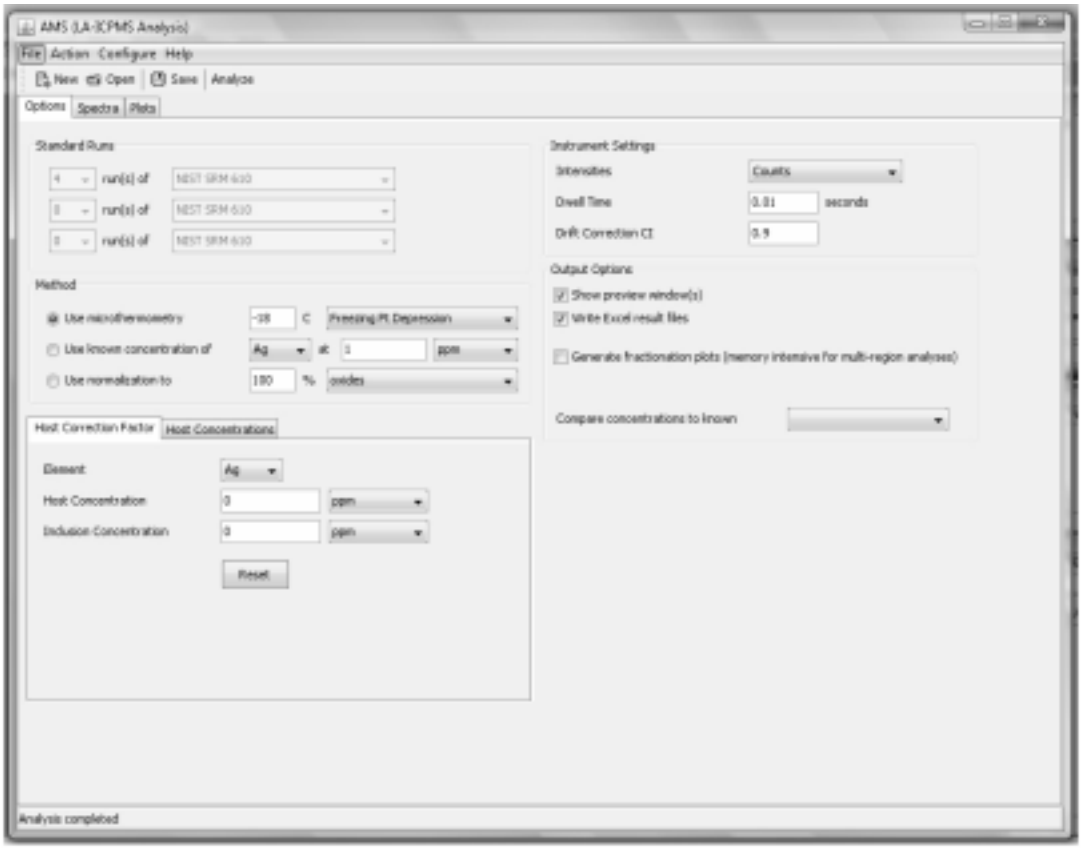


FIG. A5-5. Options Window to define the conditions that were used during data collection and methods to be used for data reduction in AMS.

data are loaded into AMS to define the signal regions of interest (SROI). The shaded region on the left of Figure A5-6 represents the SROI over which the background signal will be integrated to determine average background intensities. AMS automatically makes a "best guess" of the background and sample SROIs based on signal intensities from the current cycle compared to the average intensity for the three previous cycles.

However, these may be modified manually after visual inspection of the spectra. When the laser is turned on to begin the ablation process, the Si signal intensity increases significantly as the laser ablates through the quartz host overlying the fluid inclusion. After a few seconds the laser has ablated into the inclusion and the intensities of those elements contained in the inclusion (*i.e.*, Na, Ca, K, Sr, Ba, *etc*.) increase rapidly and then tail off as the material is quickly removed from the inclusion. The shaded region on the middle-right side of Figure A5-6 represents that portion of the signal that will be integrated to obtain signal intensities from the inclusion. As noted above, AMS selects this region automatically but the operator may adjust the limits of integration manually. The process of defining the SROIs is repeated for each analysis as well as for the standard runs.

Once the background and fluid inclusion signal integration ranges have been defined, clicking on the "Analyze" button produces the results window showing the elements measured; concentration of the elements in ppm (Con. (ppm)); limits of detection (LOD (ppm)); concentration in weight percent of the chloride salt containing the element (Weight %); counts per second above background for the sample (Sample (cps)); background counts per second for the sample (Bkg (cps)); counts per second above background for the standard (Std (cps)); background counts per second for the standard (Bkg (cps)) (Fig. A5-7). Additional information to identify the sample are included in the header of the results window. The results are

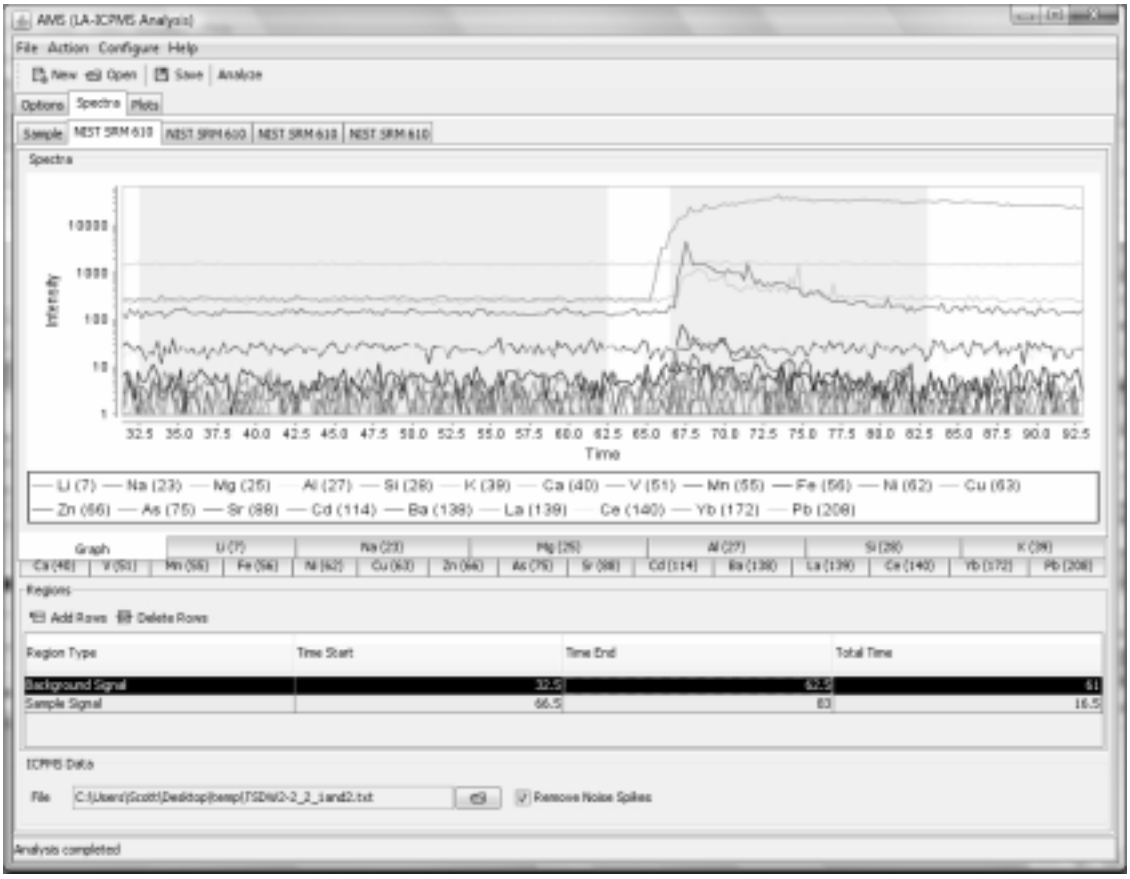


FIG. A5-6. ICP–MS time-resolved spectrum showing signal intensities during the analysis of a fluid inclusion. The relatively flat region on the left side is the background signal before the laser is turned on, the increase in intensity of Si at about 65 sec represents ablation of the host quartz above the inclusion, followed a few seconds later by the signal from the inclusion.

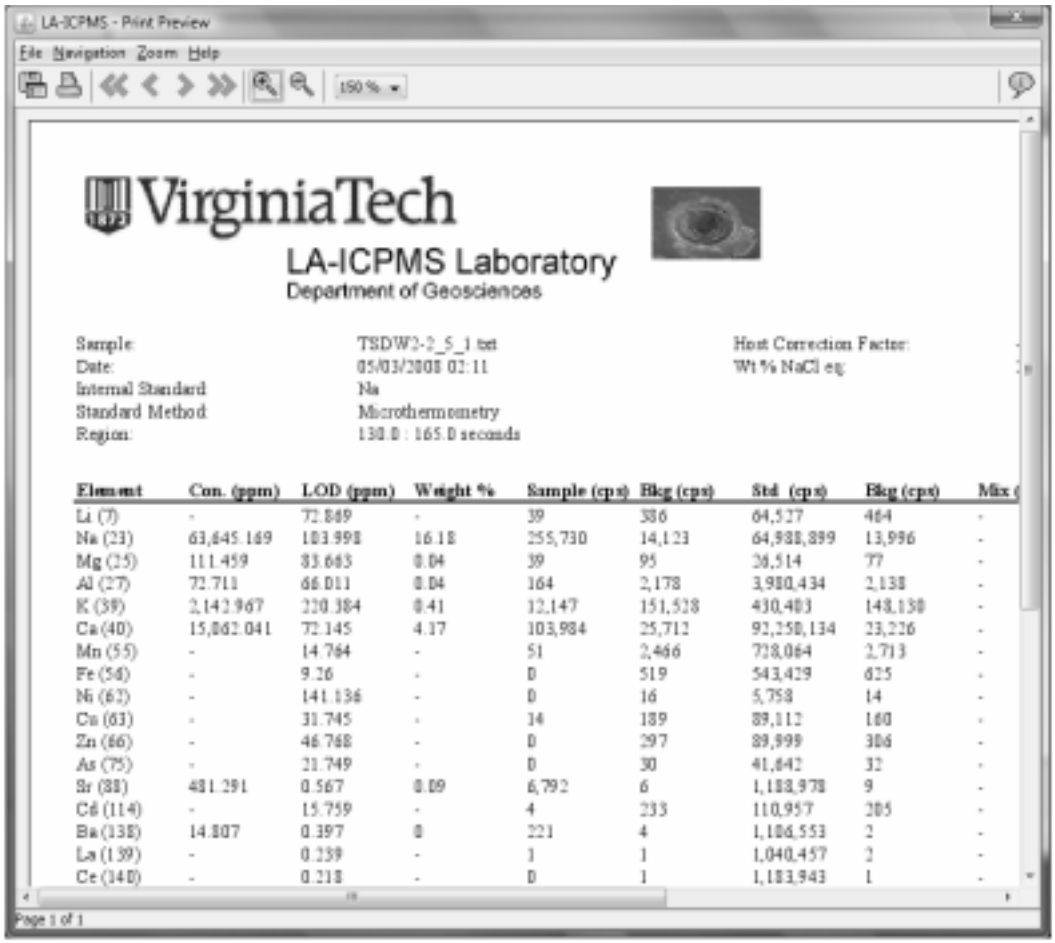


FIG. A5-7. Results window showing the composition of a fluid inclusion in quartz calculated with AMS. See text for description of each of the data columns.

available as PDF, Excel, CSV or HTML files and/or in hard copy.

The composition of the inclusion in this example calculated by AMS is 16.18 wt% NaCl, 4.17 wt% $CaCl_2$, 0.41 wt% KCl, and trace amounts of Mg, Al and Sr chlorides.

## MELT INCLUSION ANALYSIS AND DATA REDUCTION

One of the major advantages of AMS is in the interpretation of laser ablation ICP–MS spectra for melt inclusions. If the melt inclusion is homogeneous (*i.e.*, glassy) and exposed at the surface then the analysis and data reduction are straight forward and identical to the analysis of a solid phase. However, many melt inclusions are partly to completely crystallized and/or not exposed at the host crystal surface (Bodnar & Student 2006). In both cases it is necessary to use a laser spot that is somewhat larger than the melt inclusion, resulting in a mixed signal that includes signal from the MI as well as from the host. The mathematical process for separating the contributions of the MI and the host is conducted within AMS and requires no manual calculations.

The example below outlines the procedure for analyzing a glassy melt inclusion that is not exposed at the crystal surface. The laser diameter was set slightly less than the MI diameter so that when the laser ablated to the depth of the MI it would sample only MI material. As with analysis of fluid inclusions, the first step is to set the options in the options window. As described above for fluid inclusions, four analyses of the NIST 610 standard are used (two at the beginning of the session and two at the end) and the host material phase analysis will be normalized to 100% oxides. If the "Normalization to 100% oxides" option is selected, all elements that contribute significantly to the composition of the host must be included in the list

of elements measured. Next, the SROIs for the background and host are selected in the spectra window (Fig. A5-8). That portion of the signal collected before the laser has ablated to the depth of the MI is selected for the host SROI (shaded region between 45 and 55 seconds on Fig. A5-8), being careful to not include any of the mixed signal. Once the host SROI is selected the host concentration is calculated by clicking on the "Analyze" button at the top of the window.

Once the host composition has been determined, the next step is to set the host correction factor values on the options window (Fig. A5-9). In the example shown, the element aluminum is selected to determine the proportion of the mixed signal that comes from the melt inclusion (Halter *et al.* 2002). The concentration of Al in the host determined in the previous step (31.14 wt%) is entered into the "Host Concentration" box. To complete the host correction, the concentration of this same element (Al) in the melt inclusion must be known. This value can be obtained in various ways. If the MI are glassy, inclusions that are exposed at the host crystal surface can be analyzed by electron microprobe or LA–ICP–MS to determine the major element compositions. These values can then be used for analysis of buried MI. If the inclusions are buried and crystallized, obtaining the composition of one (or more) elements to use to reduce the data is more complicated. The preferred method is to homogenize a few inclusions from the same Melt Inclusion Assemblage and then analyze these

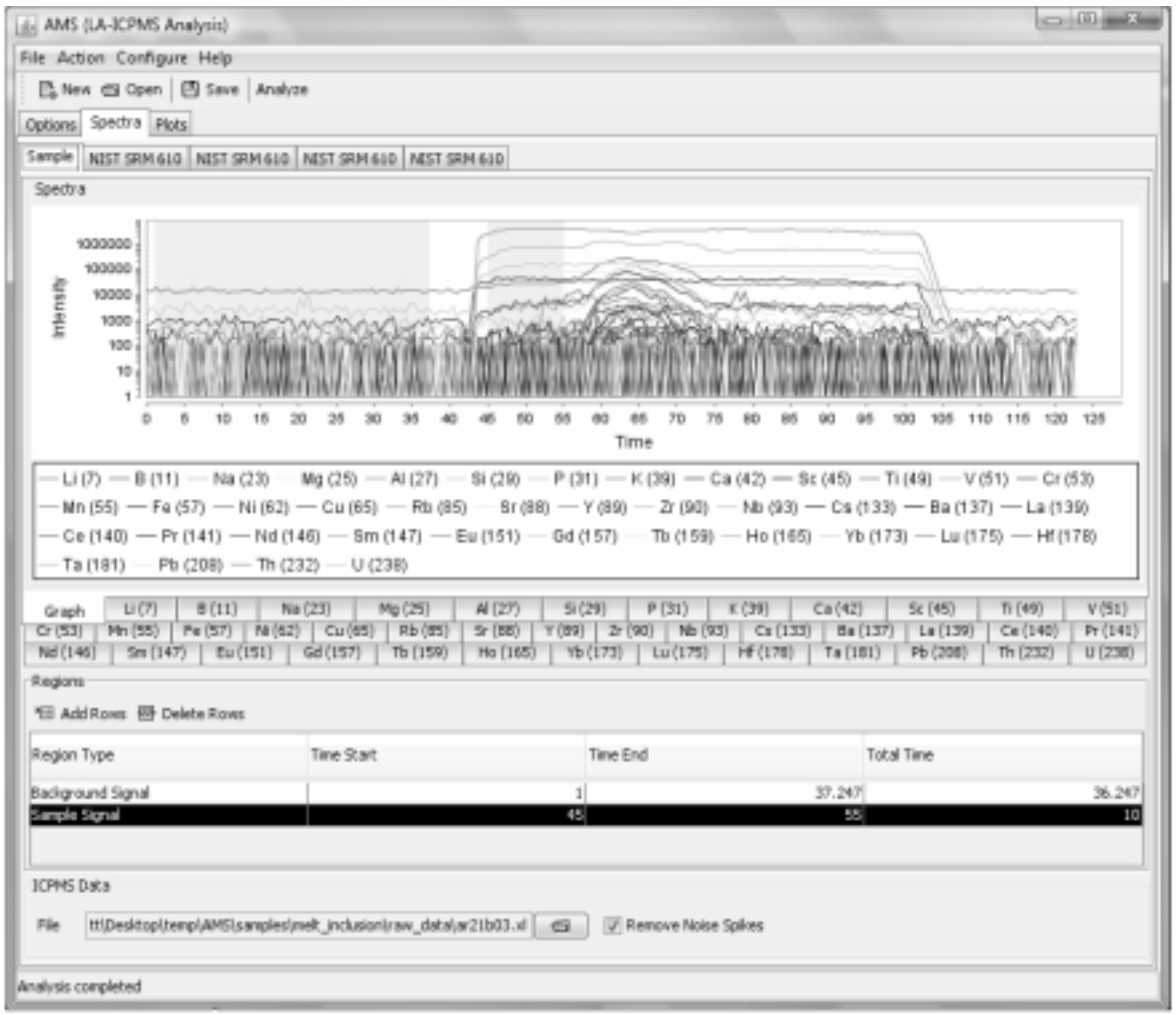


FIG. A5-8. ICP–MS time-resolved spectrum showing signal intensities during the analysis of a melt inclusion that is beneath the host mineral surface. The relatively flat region on the left side is the background signal before the laser is turned on. When the laser is turned on it begins to ablate the host phase only until it eventually reaches the buried melt inclusion. The region from 45–55 sec defines the host SROI in this example.


FIG. A5-9. Host correction window in AMS to enter the concentration of the element that will be used to deconvolve the mixed signal from the host and MI.

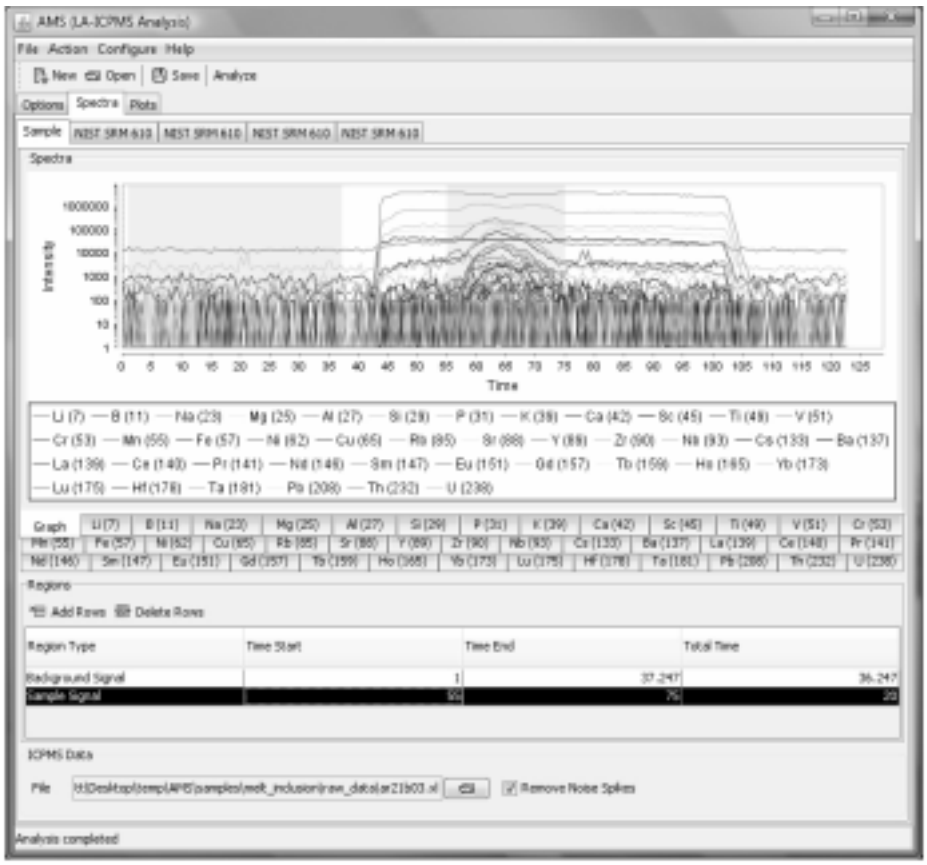


FIG. A5-10. ICP–MS time-resolved spectrum showing signal intensities during the analysis of a melt inclusion that is beneath the host mineral surface. The relatively flat region on the left side is the background signal before the laser is turned on. When the laser is turned on it begins to ablate the host phase only until it eventually reaches the buried melt inclusion. The region from 55–75 sec defines the mixed signal (host + MI) SROI in this example.

inclusions by electron microprobe or LA–ICP–MS to obtain concentration values that can be used to reduce data from the remaining inclusions. Alternatively, Halter *et al.* (2002) estimated the concentration of one or more elements in the MI based on whole rock analysis and assumptions concerning the relationship of the MI to the bulk rock composition. In the example here, the concentration of Al in the MI is estimated to be 17.26 wt% based on analyses of other MI in the same MIA that were exposed at the surface. Next, select the "Host Concentrations" tab and then click on "Use current results" to set the host concentrations – this uses the host concentrations determined in the previous steps.

Based on analyses of homogenized MI in this sample, we know that the MI contain about 4 wt% $H_2O$. Therefore, before analyzing the mixed signal region we return to the options window (*e.g.*, Figure A5-5) and enter "96" (rather than 100) in the box "Use normalization to" in the Methods subsection. The final step before the results can be calculated is to return to the spectra window and select the mixed signal region (Fig. A5-10). Finally, click on the "Analyze" button to complete the analysis. The results are then displayed in the results window (Fig. A5-11).

The first eight columns in the results window (Fig. A5-11) are the same as for the fluid inclusion analysis, except that in column 4, Weight % refers to weight percent oxide of the element.. Column 9 (Mix (ppm)) shows the concentration of the element in the mixed (host + MI) signal. Column 10 (Host (ppm)) shows the concentration of the element in the host. It is important to emphasize that the concentrations shown in columns 2 to 4 are the concentrations corrected for the host phase contribution. The host correction factor (0.53) indicates that 53% of the mixed signal was from the melt inclusion.

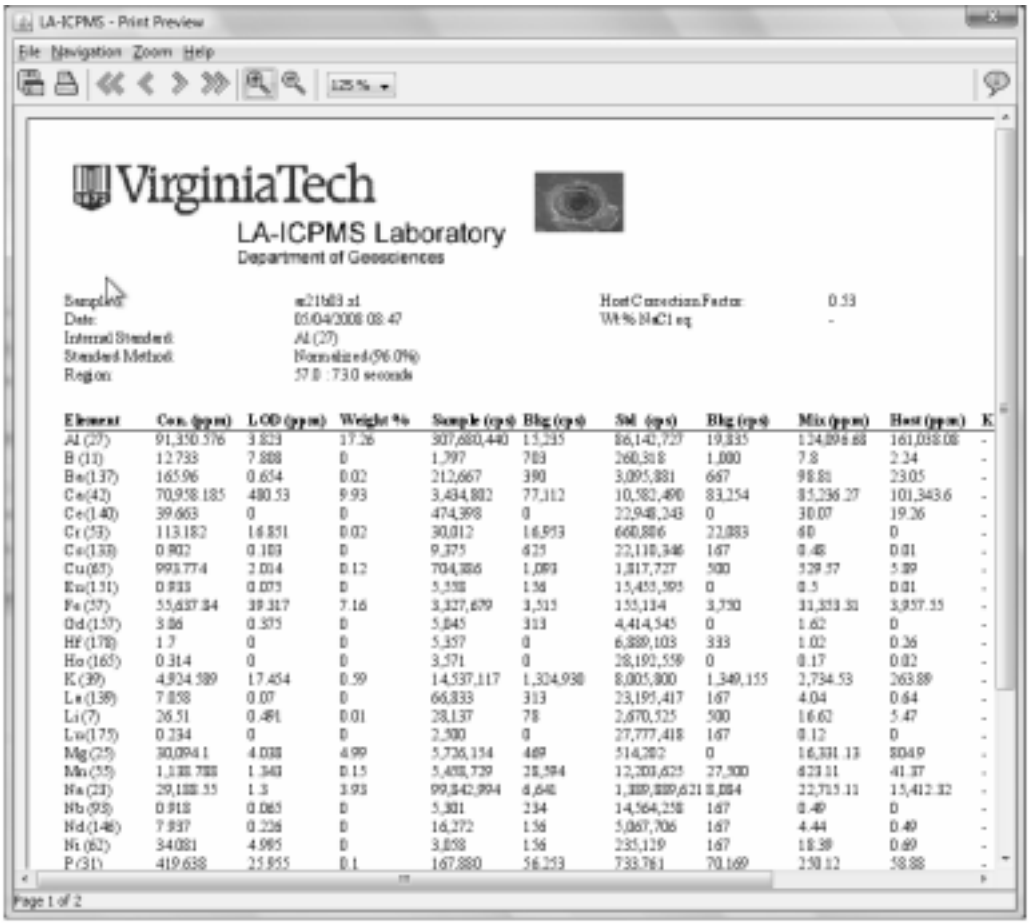


FIG. A5-11. Results window showing the composition of a buried melt inclusion calculated with AMS. See text for description of each of the data columns.

## SUMMARY

As described above, the AMS software automates many of the tedious tasks that previous were conducted graphically or manually, and greatly facilitates the reduction of LA–ICP–MS data. A video showing the data reduction steps described above for the melt inclusion is available at: http://www.geochem.geos.vt.edu/fluids/laICP–MS/ams.shtml.

## ACKNOWLEDGEMENTS

Funding for the laser ablation ICP–MS laboratory at Virginia Tech is provided by grants EAR0420849 and EAR0447237 from the NSF Earth Sciences Instrumentation and Facilities Program within the Directorate for Geosciences. The authors thank Marcel Guillong for his advice and assistance in developing AMS, and for his comments on an earlier version of this paper.

## REFERENCES

BODNAR, R.J. (1993): Revised equation and table for determining the freezing point depression of H2O–NaCl solutions. *Geochim. Cosmochim. Acta* **57**, 683-684.

BODNAR, R.J. (2003): Introduction to fluid inclusions. *In* Fluid Inclusions: Analysis and Interpretation (I. Samson, A. Anderson & D. Marshall, eds.). *Mineral. Assoc. Can. Short Course* **32**, 1-8.

BODNAR, R.J., STERNER, S.M. & HALL, D.L. (1989): SALTY: a FORTRAN program to calculate compositions of fluid inclusions in the system NaCl-KCl-H2O. *Computers &Geosciences* **15**, 19-41.

BODNAR, R.J. & STUDENT, J.J. (2006): Melt inclusions in plutonic rocks: Petrography and microthermometry. *In* Melt Inclusions in Plutonic Rocks (J.D. Webster, *ed.*), *Mineral. Assoc. Can. Short Course* **36**, 1-26.

GÜNTHER, D. & HATTENDORF, B. (2001): Elemental fractionation in LA–ICP–MS. *In* Laser ablation ICP–MS in the earth sciences: Principles and applications (P. Sylvester, *ed.*) *Mineral. Assoc. Can. Short Course* **29**, 83-92.

GÜNTHER, D., AUDÉTAT, A., FRISCHKNECHT, R. & HEINRICH, C.A. (1998): Quantitative analysis of major, minor and trace elements in fluid inclusions using laser ablation – inductively coupled plasma mass spectrometry. *J. Analyt. Atomic Spectroscopy* **13**, 263-270.

HALTER, W.E., PETTKE, T., HEINRICH, C.A. & ROTHEN-RUTISHAUSER, B. (2002): Major to trace element analysis of melt inclusions by laser-ablation ICP–MS: methods of quantification. *Chem. Geol.* **183**, 63-86.

HEINRICH, C.A., PETTKE, T., HALTER, W.E., AIGNER-TORRES, M., AUDETAT, A., GUNTHER, D., HATTENDORF, B., BLEINER, D., GUILLONG, M. & HORN, I. (2003): Quantitative multi-element analysis of minerals, fluid and melt inclusions by laser-ablation inductively-coupled-plasma mass-spectrometry. *Geochim. Cosmochim. Acta* **67**, 3473-3496.

LONGERICH, H.P., JACKSON, S.E. & GUNTHER, D. (1996): Laser ablation inductively coupled plasma mass spectrometric transient signal data acquisition and analyte concentration calculation. *J. Analyt. Atomic Spectroscopy* **11**, 899-904.

POTTS, P.J., THOMPSON, M., WILSON, S. & WEBB, P. (2008): G-Probe-2 – an international proficiency test for microprobe laboratories – report on round 2 / May 2005 (NKT-1G basaltic glass). *Geostandards & Geoanalyt. Res.* submitted.

ROEDDER, E., ed. (1984). *Fluid Inclusions*. Mineralogical Society of America, Washington, D.C., 644 p.

STERNER, S.M., HALL, D.L. & BODNAR, R.J. (1988). Synthetic fluid inclusions. V. Solubility relations in the system NaCl–KCl–H2O under vapor-saturated conditions. *Geochim. Cosmochim. Acta* **52**, 989-1006.

# APPENDIX A6: SILLS: A MATLAB-BASED PROGRAM FOR THE REDUCTION OF LASER ABLATION ICP–MS DATA OF HOMOGENEOUS MATERIALS AND INCLUSIONS

Marcel Guillong[1]
Dimitri L. Meier[1]
Murray M. Allan[2]
Christoph A. Heinrich[1]
Bruce W.D. Yardley[3]

[1] Department of Earth Sciences, Swiss Federal Institute of Technology, ETH Zürich, Switzerland
[2] Anglo American Exploration (Canada) Ltd., Vancouver, BC, Canada
[3] School of Earth and Environment, University of Leeds, Leeds, U.K.
E-mail: guillong@erdw.ethz.ch

## INTRODUCTION

This paper describes a software package named SILLS (Signal Integration for Laboratory Laser Systems) designed for data reduction and concentration calculation of transient Laser Ablation ICP–MS signals, written in MATLAB (The MathWorks, Inc.). The software is primarily designed for user friendly and flexible data reduction to obtain quantitative analyses of fluid, melt or mineral inclusions enclosed in mineral or glass host, but can also be used for homogeneous samples. The transient nature of these signals demands a dedicated data reduction procedure, particularly if signals from inclusions and their chemically distinct host minerals need to be separated quantitatively from each other (Heinrich *et al.* 2003, Longerich *et al.* 1996).

The program includes a convenient and versatile option to display raw transient signals from the ICP–MS. Inclusion analysis, in particular, requires the visualization of each inclusion signal and the possibility to select integration intervals for gas blank, host mineral and inclusions precisely and flexibly. In contrast to other data reduction approaches, SILLS yields quantitative analyses of host and inclusion for a range of possible data reduction approaches without error-prone copy–paste steps between spreadsheets.

The software was first developed and used by M. Allan at Leeds University (Allan *et al.* 2005) and later intensively redesigned, extended and tested in a collaborative effort at the Institute of Isotope Geochemistry and Mineral Resources at ETH Zürich. The SILLS data import is tested to work with files from Agilent and Perkin Elmer ICP–MS directly and with Thermo Element 2 data after a MATLAB-based convert script, editable for other instrument output files. The procedures and equations for concentration calculation are taken from the literature (Halter *et al.* 2002, Heinrich *et al.* 2003, Longerich *et al.* 1996) and are summarized in documents included with the software. All calculations are implemented according the most current knowledge, based on literature and in-house experience, but may still contain errors, thus requiring critical inspection of the results in every case. In particular, the calculation of uncertainties (Luo *et al.* 2007) on individual analyses and the calculation of limits of detection are undergoing continuous improvement, because no general applicable method has been published to date.

For further information about obtaining the software package and future updates, please visit http://www.igmr.ethz.ch/research/fluids/software.

## DESCRIPTION OF THE SOFTWARE

### MATLAB and some general considerations

MATLAB is a flexible, relatively easy programming language that is well suited for graphical interfaces. The scripts are easy for people with a basic programming background to understand. All the data are stored and calculated using variables with different levels and sublevels in structures and matrices that can be accessed in MATLAB. Therefore there is no defined limitation in number of measured elements, number of time slices in a measurement or number of measurements in a project. The software was tested for up to 64 elements and 54 measurements. However, with increasing data volume, the calculations might become slower. A typical saved project file with 4 standards and 16 samples, measuring 50 elements

Mineralogical Association of Canada Short Course 40, Vancouver, B.C., p. 328–333.

200 times per analysis is 2.5 Mb in size. A compiled standalone version is available for users without MATLAB.

It is possible to define parameters in no particular order. At any time, integration windows can be edited, a whole sample copied, the dwell times changed, and so on. The final results are calculated each time an output report is generated. At any time it is possible to save the project and continue working later.

**Main windows**

SILLS consists of two main windows: The main control window and the calculation manager. When SILLS is started, the main control window (Fig. A6-1) appears. From this window, all data files are selected (load standards and load unknowns), projects are saved and opened, and basic settings can be set: input format (cps or counts), time format (described in the drift correction section), the standard reference material (SRM, load from file or create new), the dwell time and the flicker noise. When standards are loaded (described in next section), the SRM is assigned, as well as the time when the analysis was stored on the computer (analysis time). Standards can be selected, plotted and deleted, unknowns can also be copied. When all essential files are loaded, the calculation manager window (described later in this report) can be opened.

**Graphical user interface for signal integration**

The graphic user interface for the definition of integration intervals is described using the analysis of a fluid inclusion as example. Every time a standard or sample is loaded from the main control window a figure (*e.g.*, Fig. A6-2) with the plotted transient signal appears. In this plot, the intervals of interest (IOI) are selected by click and drag with the computer mouse. The background (gas blank), up to three intervals for a signal (linked together to 1 signal) as well as up to two intervals for a possible host correction can be set either by click and drag or typing the time in seconds from the beginning of the signal. Intervals are visible in different colors. The definition of the IOIs is not limited to the time a signal is loaded, at any time IOIs can be changed or removed, reopening the window either from the main control window or the calculation manager. For comparison of several samples, multiple windows can remain open. To make this IOI selection as easy as possible a zoom tool and a custom selection of the visible elements is

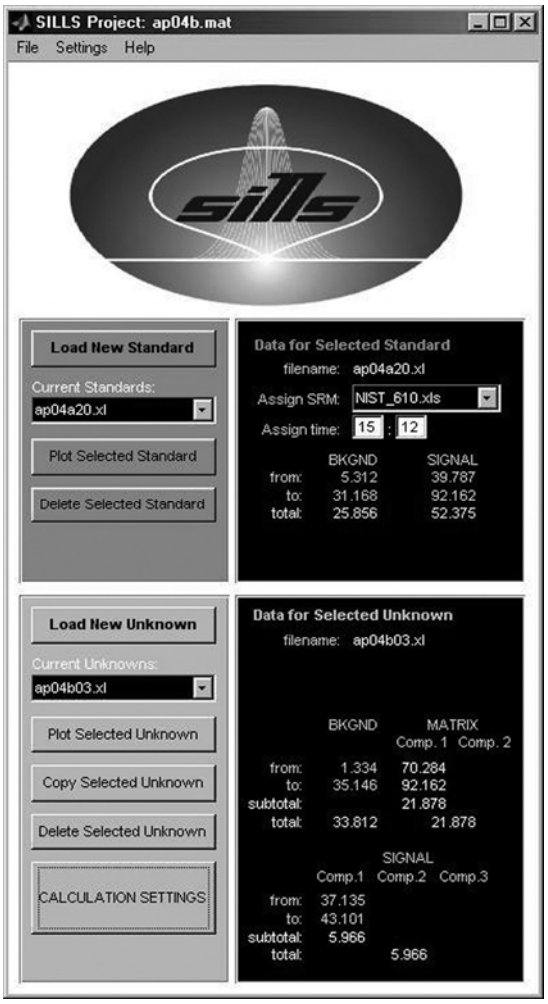


FIG. A6-1: The SILLS main window, used to handle project files, load measurements and standards and define basic settings.

implemented. By switching the display mode, background corrected count ratios (defined by the user) are plotted to help further to set the IOI. No matter which display mode is used and whatever elements are shown, the figures can be printed or saved as images in various raster or vector graphic formats. The spike/outlier detection can be accessed from the plots.

**Spike/outlier detection based on Grubbs test**

An algorithm to identify and correct possible spikes or outliers has been implemented in the software. The whole dataset with intensities above a selectable threshold (*e.g.*, 1000 cps) is tested for outlying points by the method described by Grubbs (Grubbs 1969). This test assumes a normal distribution, and compares the calculated statistic

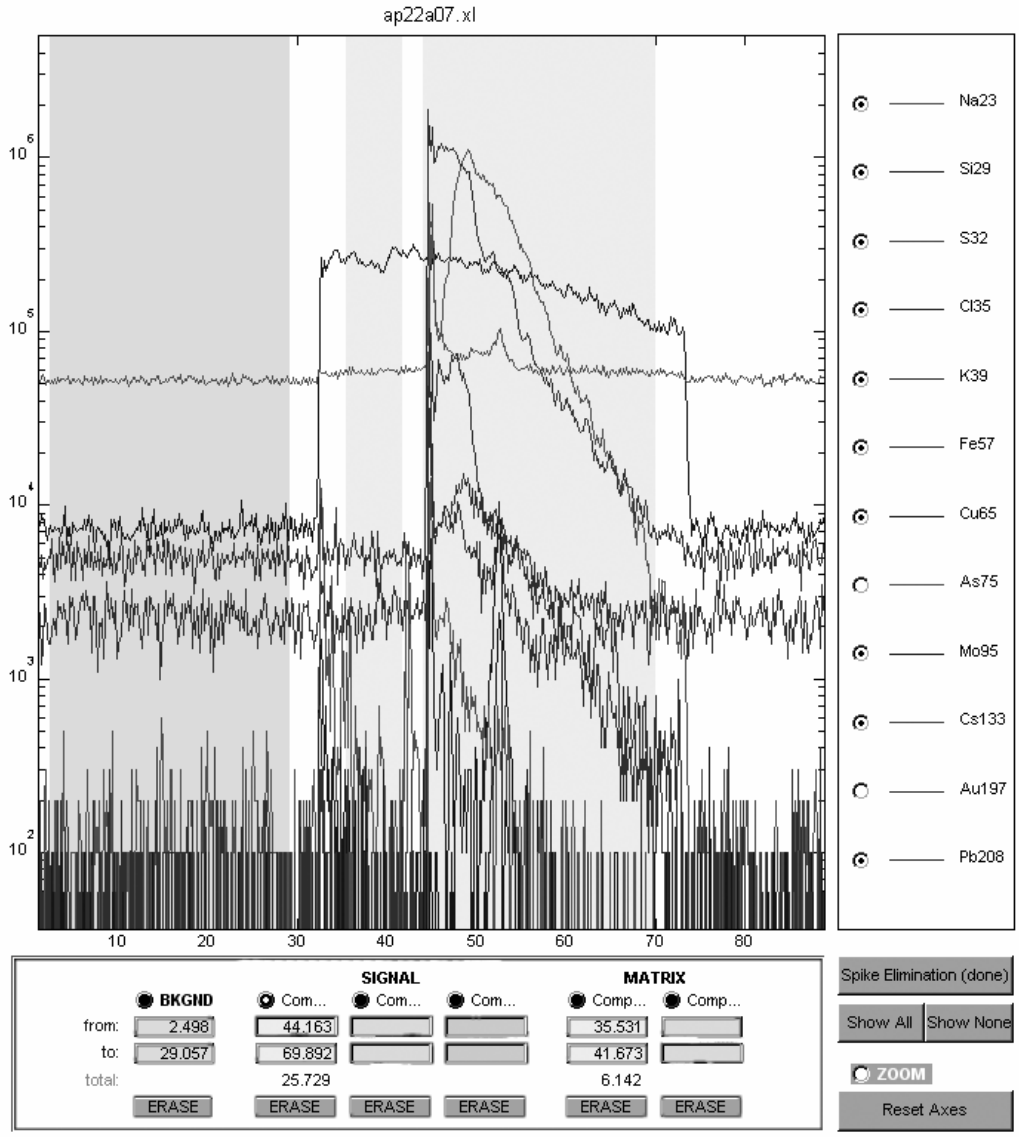


FIG. A6-2: Graphical user interface for definition of intervals of interest (IOI) in time-resolved signal intensity plots by click and drag, including a zoom function and spike elimination.

test value (STV, equation 1 below) with a tabled value depending on the number of measurements (7 in our case) and level of significance (1%, meaning the detected values are highly significant outliers):

$$STV = \frac{\left| x^* - \bar{x} \right|}{s} \qquad (1)$$

where $x^*$ is outlier suspected value, $\bar{x}$ is mean, calculated with all values in the series, and $s$ is standard deviation, calculated with all values in the series.

When outliers are detected, the software asks the user to confirm the spike and to confirm that the outlier should be replaced with the calculated, suggested value (mean of the measurements before and after the detected spike), or another user defined value, or to keep the original value. Once a spike is corrected, the original values can only be recovered by reloading the original data file, which will remain unchanged as SILLS continues to be used.

Modification of outlier data is a controversial practice questioned by many scientists, including the authors. The Grubbs test algorithm provides an objective method for spike identification, and the

user has to confirm the modification for every single detected spike. This does not make the practice scientifically or methodologically valid. The rejection of outliers is more acceptable when it is done based on an underlying model or when the possible source of the spike is confidently known, *e.g.*, contaminant particles accidentally mobilized into the ICP–MS from the transport or ablation system.

**Drift correction and quality control**

With SILLS, it is possible to correct for instrumental drift based on repeated analyses of standard reference material. So far only a linear drift correction based on changes in relative sensitivity is applied and visualized as shown in Figure A6-3. Times can be defined either using real clock analytical time or integer time points. It is possible to retrieve the analytical times from the file information. Using analytical times, the applied drift correction is closer to the real drift especially when there are breaks between the measurements of a run. For the visualization as shown in Figure A6-3, a drift correction standard that is assumed to have no drift can be chosen and the relative sensitivity of all measured elements can be plotted. The drift in relative sensitivity (compared to the drift correction standard) is plotted *vs*. the time for individual elements or for all elements in percent. This overview gives the user control over the quality of the standard measurements. Problems with standard measurements become visible in this overview.

After instrument warm up, the observed drift by repeated standard reference material analysis may be found to be completely random, and not linear. In this case, to apply no drift correction, the time format parameter can be set to one integer time step (everything is assumed to be measured at the same time) and the mean relative sensitivities from the repeated SRM analysis without drift correction are used for quantification.

**Quantification possibilities / calculation manager**

SILLS allows a set of quantification possibilities to fit most applications in LA–ICP–MS. The calculation manager window is shown in Figure A6-4. All unknown samples loaded show up in this window and they can be plotted, copied or deleted. A description can also be entered. In two rows, the parameter settings for the matrix (or host) and inclusion (or just the sample) are entered. Without a matrix (or host) correction for the inclusion, quantification is straightforward by selection of an internal standard concentration (either a known concentration of an element or a

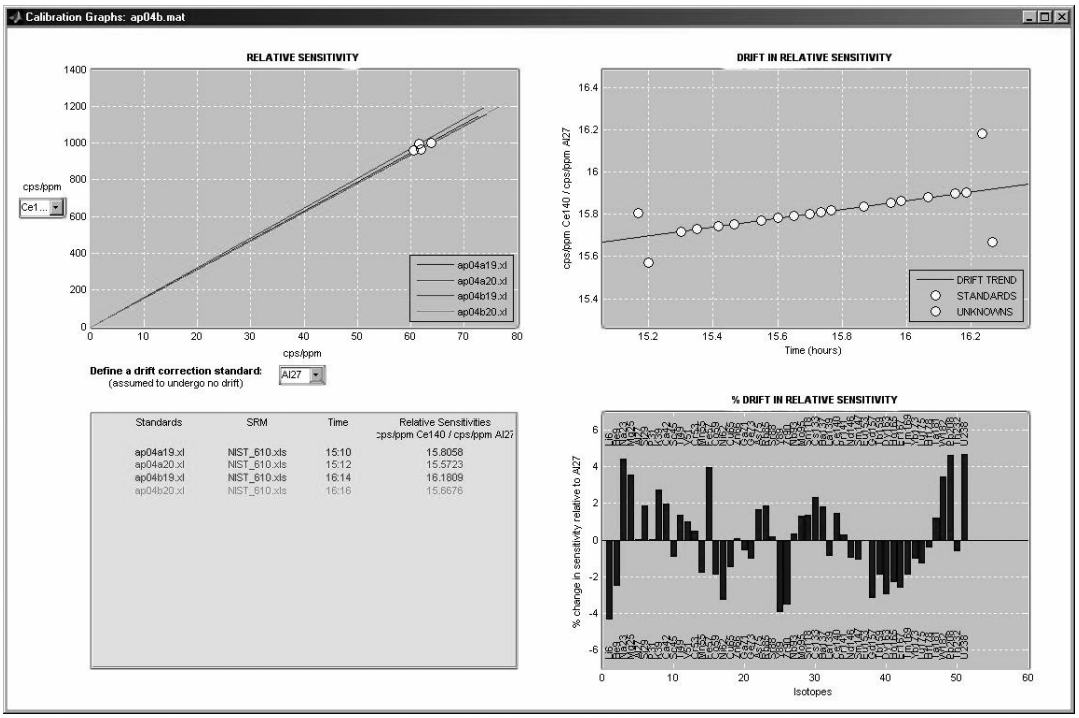


FIG. A6-3: Quality control window, including options for drift correction. See text for details.

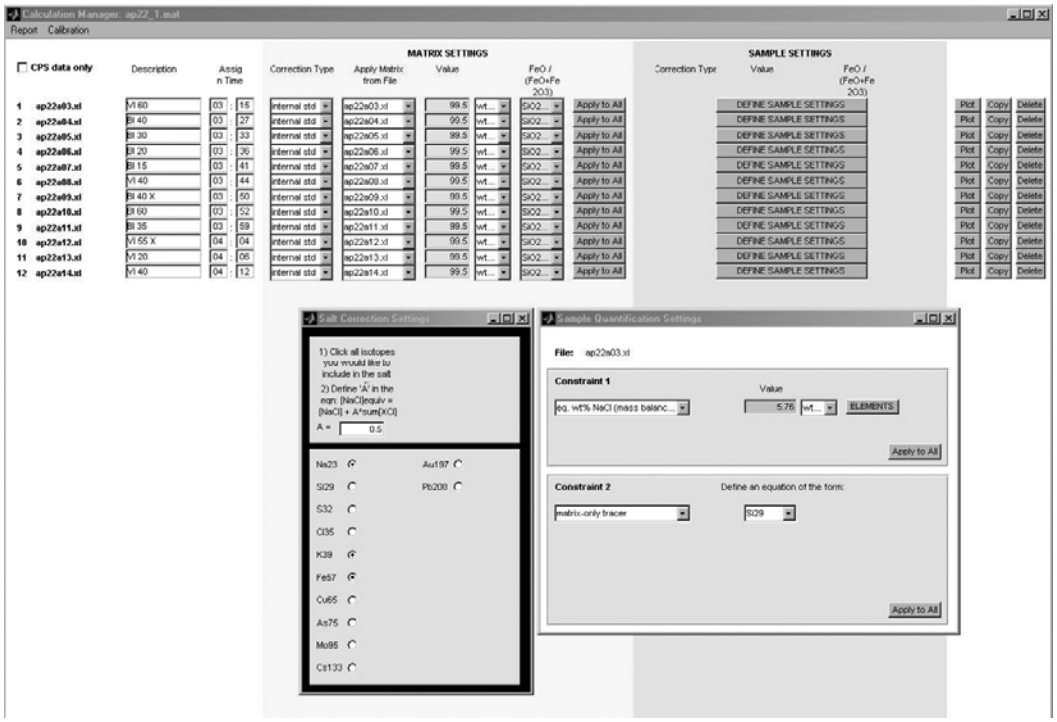


FIG. A6-4: Calculation manager window, including options for sample settings and the "salt correction" window.

calculation to the sum of all major oxides in wt.% (*e.g.*, 96 wt.% when a water content of 4% is known) with a defined FeO/(FeO+$Fe_2O_3$) ratio). The calculation to 100 wt.% oxide (Guillong *et al.* 2005) requires the measurement of all main cations and can have systematic errors due to unknown amounts of water, anions other than oxygen and other restrictions and has to be used with care. For fluid inclusions, the user can define a NaCl equivalent concentration and select the cations that are implemented in the correction (the "salt correction"), either by charge balance or mass balance (Heinrich *et al.* 2003).

If a matrix (or host) correction is applied, two more constraints are necessary for quantification:

1. For the host, an internal standard is needed (again with an element of known concentration or 100 wt% oxide);
2. For the inclusion, the user must know two separate concentration constraints. A special case is the assumption that one element is only present in the host and not in the inclusion is referred to as a "matrix only tracer". A second special case is often the assumption of 100 wt.% oxide instead of an individual element concentration. A third special case can be that not a single element concentration is known, but an equation (2) can be given:

$$\frac{X}{Y} = p\left(\frac{M}{N}\right)^2 + q\left(\frac{M}{N}\right) + r \qquad (2)$$

where X, Y, M and N are measured elements and p, q and r are constants. These two constraints allow calculation of the fraction of a mixed signal that is attributable to the inclusion and, consequently, also the concentrations in the inclusion.

It is possible either to define the host in the same measurement as the inclusion or in a separate measurement. The equations for quantification are from the literature (Günther *et al.* 1998, Halter *et al.* 2002, Heinrich *et al.* 2003, Longerich *et al.* 1996) and are summarized in a document that comes with the software. If the user only needs to determine gas blank corrected intensities or ratios (*e.g.*, isotope dating technique), without any concentration calculations, there is a box to check which allows all concentration calculations to be skipped.

**Report writing possibilities**

The output can be formatted according to the different needs or preferences of measurement and application type. There are several preferences selectable for the output report. In the menu of the calculation manager the user can define whether the

major elements are shown as wt.% oxides or as $\mu g\ g^{-1}$. There is also the possibility to set the limit of detection (LOD) filter factor, which will show data that are below the LOD calculated as suggested in the literature (Günther *et al.* 1998, Halter *et al.* 2002, Heinrich *et al.* 2003, Longerich *et al.* 1996). As soon as the option "create output report" in the calculation manager is selected, a preview of the sample concentrations appears, to check whether the results are plausible. At this stage many parameters (*e.g.*, concentrations in host and inclusion, limits of detection, gas blank count rate, gas blank corrected count rate for host and inclusion, ratios including the error and the details to the individual analysis) can be selected to be included in the final output report. Once selected, the report is created and saved as an Excel spreadsheet.

## SUMMARY AND AVAILABILITY

This software was specifically designed for inclusion analysis but can also be used for all other kind of applications (*e.g.*, homogeneous solids). It is intuitive and user friendly due to a graphical user interface, especially with respect to the choice of the integration of intervals of interest (IOI) by click and drag with the mouse. All necessary parameters can be controlled by the user.

A trial version and information about availability of the fully working version are given at: http://www.igmr.ethz.ch/research/fluids/software.

## ACKNOWLEDGEMENTS

We thank all users who helped with their feedback to improve the software. The intense discussions with Detlef Günther, Zoltan Zajacz, Jacob Hanley, Matthias Fricker, Elitsa Stefanova and Werner Halter are also acknowledged. Critical reading of this manuscript by Jacob Hanley, Paul Sylvester and Luca Fedele helped to improve the manuscript.

## REFERENCES

ALLAN, M.M., YARDLEY, B.W.D., FORBES, L.J., SHMULOVICH, K.I., BANKS, D.A. & SHEPHERD, T.J. (2005): Validation of LA–ICP–MS fluid inclusion analysis with synthetic fluid inclusions. *Am. Mineral*. **90**, 1767-1775.

GRUBBS, F.E. (1969): Procedures for Detecting Outlying Observations in Samples. *Technometrics* **11**, 1-21.

GUILLONG, M., HAMETNER, K., REUSSER, E., WILSON, S.A. & GÜNTHER, D. (2005): Preliminary characterisation of new glass reference materials (GSA-1G, GSC-1G, GSD-1G and GSE-1G) by laser ablation-inductively coupled plasma-mass spectrometry using 193 nm, 213 nm and 266 nm wavelengths. *Geostandards & Geoanalytical Research* **29**, 315-331.

GÜNTHER, D., AUDÉTAT, A., FRISCHKNECHT, R. & HEINRICH, C.A. (1998): Quantitative analysis of major, minor and trace elements in fluid inclusions using laser ablation inductively coupled plasma mass spectrometry. *J. Anal. At. Spectrom.* **13**, 263-270.

HALTER, W.E., PETTKE, T., HEINRICH, C.A. & ROTHEN-RUTISHAUSER, B. (2002): Major to trace element analysis of melt inclusions by laser-ablation ICP-MS: methods of quantification. *Chem. Geol.* **183**, 63-86.

HEINRICH, C.A., PETTKE, T., HALTER, W.E., AIGNER-TORRES, M., AUDETAT, A., GÜNTHER, D., HATTENDORF, B., BLEINER, D., GUILLONG, M. & HORN, I. (2003): Quantitative multi-element analysis of minerals, fluid and melt inclusions by laser-ablation inductively-coupled-plasma mass-spectrometry. *Geochim. Cosmochim. Acta* **67**, 3473-3497.

LONGERICH, H.P., JACKSON, S.E. & GÜNTHER, D. (1996): Laser ablation inductively coupled plasma mass spectrometric transient signal data acquisition and analyte concentration calculation. *J. Anal. At. Spectrom*. **11**, 899-904.

LUO, Y., GAO, S., LONGERICH, H.P., GÜNTHER, D., WUNDERLI, S., YUAN, H.L. & LIU, X.M. (2007): The uncertainty budget of the multi-element analysis of glasses using LA-ICP-MS. *J. Anal. At. Spectrom.* **22**, 122-130.

# APPENDIX A7: BRIEF INTRODUCTION TO THE WINDOWS PROGRAM PEPITA: DATA VISUALIZATION AND REDUCTION, OUTLIER REJECTION, CALCULATION OF TRACE ELEMENT RATIOS AND CONCENTRATIONS FROM LA–ICP–MS DATA

I. Dunkl[1], T. Mikes[1], K. Simon[2] & H. von Eynatten[1]

[1]Sedimentology & Environmental Geology, Geoscience Center, University of Göttingen
Goldschmidtstrasse 3, D–37077 Göttingen, Germany

[2]Geochemistry, Geoscience Center, University of Göttingen
E-mail: istvan.dunkl@geo.uni-goettingen.de

## INTRODUCTION

A key issue in the processing of time-resolved data sets produced by LA–ICP–MS, which is a highly sensitive analytical method, is the filtering out of noise from signal. Part of the scatter seen in the individual LA–ICP–MS measurements is related to the Poisson statistics of low count rates of ions or electrons recorded by the detector. However, noise in the signal is also added by the introduction of heterogeneous particles into the plasma and from the noise of the electronic devices. The importance of the treatment of spikes in the LA–ICP–MS measurement signals can not be neglected, especially when the average count rates are low (see *e.g.*, Barnet & Lewis 1994). Figure A7-1 demonstrates the effect of one single biased time slice on the calculated average. One should consider, however, that the spike/signal ratio can often be even higher than in the modeled example.

We have developed the program Pepita for the visualization, statistical evaluation and rejection of suspicious data in LA–ICP–MS. These tasks are all essential parts of the data reduction procedure. Pepita batch performs these tasks, and allows the user to select their own preferred degree of task automation *versus* manual processing. The purpose of this communication is to supply a simple and quick introduction to Pepita for the ICP–MS community, and also to stimulate further discussion on the statistical treatment procedures of time resolved LA–ICP–MS data.

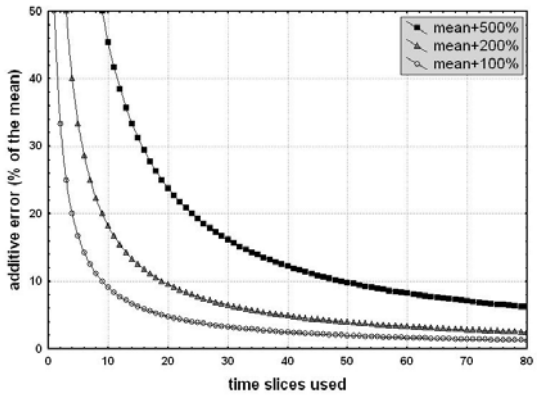


FIG. A7-1. Effect of a single unfiltered outlier on the calculated mean as a function of the number of time slices used. Three cases are shown, with the unfiltered outlier having 500%, 200% and 100% higher value than the mean of the remainder of the signal.

## CONCEPT AND STRUCTURE OF THE SOFTWARE

Pepita aims to be a user-friendly, fast and partly automated data reduction system. That is why the constants and settings (*e.g.*, standard composition, output file format) are stored in separate files. Pepita operates with a complex file system, but once installed, the program handles the files largely automatically, and thus external manipulation (cross-formatting, chopping, editing, *etc*.) is not necessary. The universal input filter of Pepita allows data files of any kind of format to be directly loaded, as long as the data are compactly arranged in a table-formatted, tab- or comma-separated text file, with the names of analytes being in one separate line.

We consider the visualization of both the true and derived signals in LA–ICP–MS to be very important. Thus the selection of time slices is done simply by mouse clicks. The whole selected data matrix is presented in a table. Results of simple, but robust outlier tests readily identify suspicious data by means of colour coding. The rejection can be performed according to the preferred criteria of the user. This step can be automated; all processed data files pass through the same noise filtering procedure in a strictly uniform and reproducible manner.

The output is designed to provide complete

Mineralogical Association of Canada Short Course 40, Vancouver, B.C., p. 334–340.

results. When using the full output, all details (files, internal standards, time slices selected, rejection method applied, *etc*.) will be registered into the output file. Thus, the entire process of data reduction becomes fully reproducible. The uniform structure of output files assists the user in subsequent trend analysis and data processing.

## PROGRAM DESCRIPTION

**Function:** Pepita is a Windows program that processes time-resolved raw data files (optimized for ICP–MS data) and calculates element concentrations using internal standards. The current version can handle data files with up to 6000 time slices and 100 analytes, with the possibility to visualize up to 50 analytes at once. Concentrations are calculated according to Longerich *et al.* (1996); the equations are shown in the Help window of the program.

**System:** Pepita has been tested successfully in Win2000, XP, Vista and MAC OSX (+Parallels Desktop) environments. There are no minimum hardware requirements (it will run on any computer capable of hosting Windows), but the plotting of curves is processor-intensive, so faster processors will result in a faster run.

**Files:** A variety of file types are used in Pepita. It is recommended to show file extensions in your system (*disable* the following option: My Computer / Tools / Folder Options / View / Hide file extensions for known file types).

***Setting files*** contain constants, the path to other files, graphical defaults, the preferred statistical test, the format of output, *etc*.

***Data files*** must contain one line with the names of analytes and an array with the count rates (cps) or counts for each time slice in each row. The user can specify the file format and can create individual input filters to specific data files.

***Standard composition files*** contain the element concentrations of the standard (in ppm). For each element present in the files, all common isotopes are included, thus any of them can be chosen for the element concentration calculation.

***Dwell time files*** contain the dwell times used for the detection of given masses (in ms).

***Standard measurement files*** contain cps data from the measurement of a reference material, obtained under the same conditions as for the unknowns.

***Blank files*** can be used if the blank values are stored in separate files (alternatively, blanks are simply extracted from the corresponding data files during signal processing).

**Help library:** Help items are available anytime while Pepita is running, with information on (i) the expected format of files used, (ii) equations used for calculations and (iii) the content of the exported results.

TABLE A7-1. FILE STRUCTURE OF PEPITA

| | | files stored | |
|---|---|---|---|
| **file types** | **extension** | **at installation** | **later, user determined** |
| Setting file (default) | .set | C:\Pepita-StartKit | anywhere ([1]) ([5]) |
| Setting file (user defined) | .set | --- | anywhere ([1]) |
| Standard composition files | .stc | C:\Pepita-StartKit | anywhere ([2]) ([4]) |
| Dwell time files | .dwe | C:\Pepita-StartKit | anywhere ([1]) ([2]) ([5]) |
| Standard measurement files | .stm | C:\Pepita-StartKit | anywhere ([1]) |
| Blank files | .blk | C:\Pepita-StartKit | anywhere ([1]) |
| Data (input) files | .csv .txt .xl | C:\Pepita-StartKit | anywhere ([3]) |
| Result (output) files | .txt | --- | anywhere ([3]) ([6]) |
| Quick results file (output only concentrations) | | --- | saved automatically into the directory of the data files |

([1]): can be stored together with data files, or assemble all of them into one separate directory; ([2]): path stored in the setting file; ([3]): after re-start Pepita offers automatically the formerly used directory; ([4]): recommended to assemble these files into one directory; ([5]): two files must be kept in the same directory: "dwell-usual-01.dwe" and "Pepita-default.set"; the path is stored by Pepita; ([6]): if the extension of the data files is .txt then save the result files into another subdirectory. For an easy and automatic start, and for studying the major functions of the program, every necessary file is collected in a "**Pepita-StartKit**" directory that must be in drive **C:**. After the training period with the software, the user can modify and create new setting files and place them and their own data files into another preferred path.

**Availability:** Pepita is distributed as a freeware and available from the homepage of the first author (ID), via the website of the University of Göttingen: www.sediment.uni-goettingen.de/staff/dunkl/software. Currently, it is under beta testing. Users having different data formats and isotope settings are kindly asked to report observed bugs, inconsistencies and suggestions for further development.

## GUIDED TOUR OF THE PROGRAM

The following tour is intended to illustrate how quickly and easily users can start using Pepita.

### Installation

1) Perform setup (the working directory is usually installed in "C:\Program Files").
2) Copy the "Pepita-StartKit" directory to C:\Pepita, which opens a default setting file at the first running. The user-defined personal setting files can be placed anywhere later, but the "C:\Pepita-StartKit" directory that contains the default setting, dwell time and standard composition files should remain in this place.

### Functions of Pepita, shown with the example files

Data processing is done in four steps, in four subsequent windows: (1) selection of files and constants, (2) selection of the time-resolved ablation interval for concentration calculations, (3) outlier tests and (4) output of results (Fig. A7-2).

***(1) Start Pepita.*** The program opens the default settings, an example data file and all necessary constants in different files.

***(1a) Press [Paste data from clipboard].*** Pepita allows a simple data input for a quick check by pasting a table from the clipboard. This function can be studied using the example file available in the Pepita-StartKit directory. Open the "Example-Copy-Paste.xls" file and follow the simple instructions.

***(1b) Press [Modify settings]***. The *Setting files* are essential elements of the system. Their content can be viewed in the settings window, and most parameters related to the data handling can be specified in this window. There is a default setting file (Pepita-default-h.set) but the user can define further personal settings and store them. At program start, Pepita automatically opens the default setting file. By pressing [Apply] once these settings are modified, the program will work with them until leaving it. (The settings can be stored [Save as], and

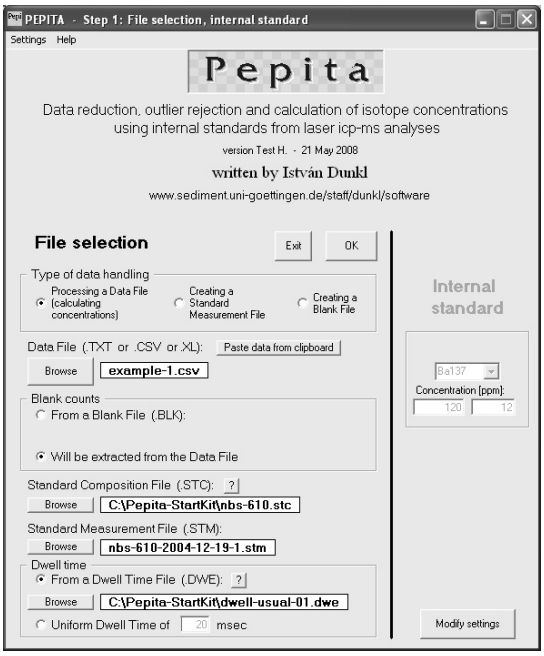


FIG. A7-2. The first window of Pepita allows the selection of files for calculation (data, standard composition, standard measurement, *etc*.). Pepita always opens a complete set of files automatically to facilitate testing, learning and regular usage of the program.

then re-loaded the next time they are needed in the menu of the File selection window: "Settings / Open setting file") (Fig A7-3).

***(1c) Press [Cancel] to close Settings window***

***(1d) Press [OK] on the File Selection window***

***(1e) Confirm the internal standard, press [Next Step]*** . The time selection window appears (Fig. A7-4); using left and right mouse clicks, respectively, the lower and upper limits of the time interval of choice are selected. The blank interval can be likewise marked by [Shift] and left and right mouse clicks (if the user has previously chosen this option in Window 1). At the left side of the window, the check boxes are used to switch the visualization of individual analytes on and off.

***(2a) Press [Append QUICK RESULTS].*** Pepita dumps the calculated concentrations into a simple text file, located in the directory from where the data file was loaded. The Quick Results file consists of a header and an array of the concentration values with one line per sample, without further details. Upon pressing this button, the Quick Results file will be created every time a data file is loaded from a new directory. If the file exists in the working directory, further results will be appended to its end.

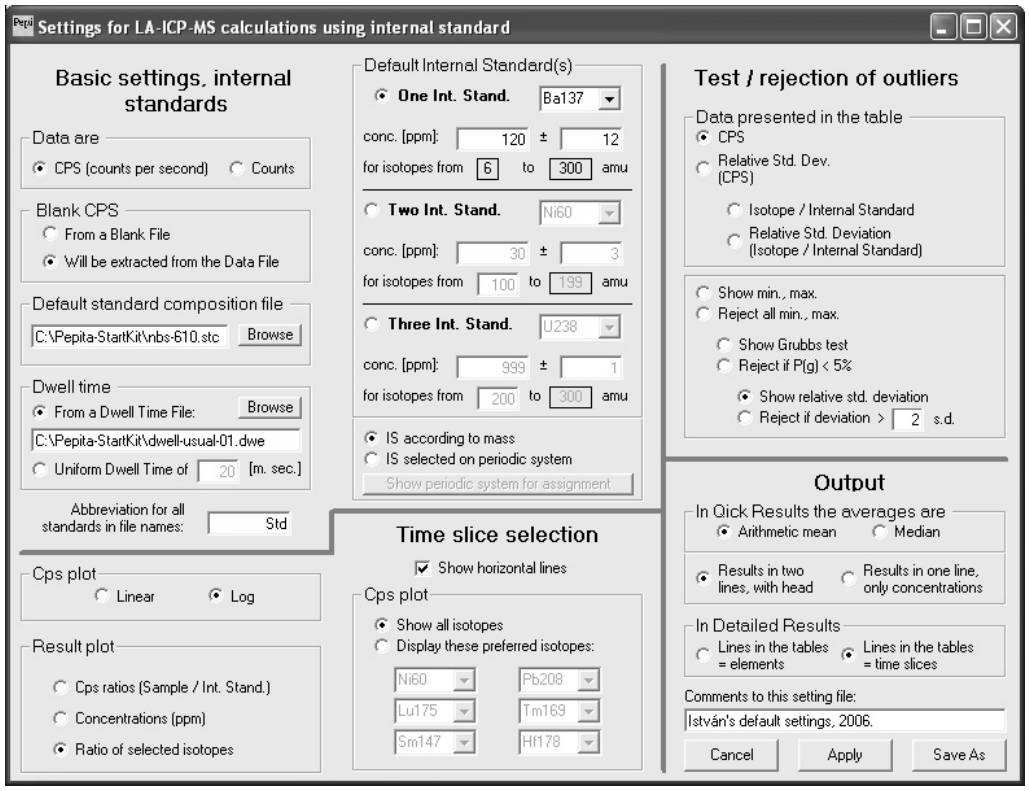


FIG. A7-3. The settings window of Pepita.

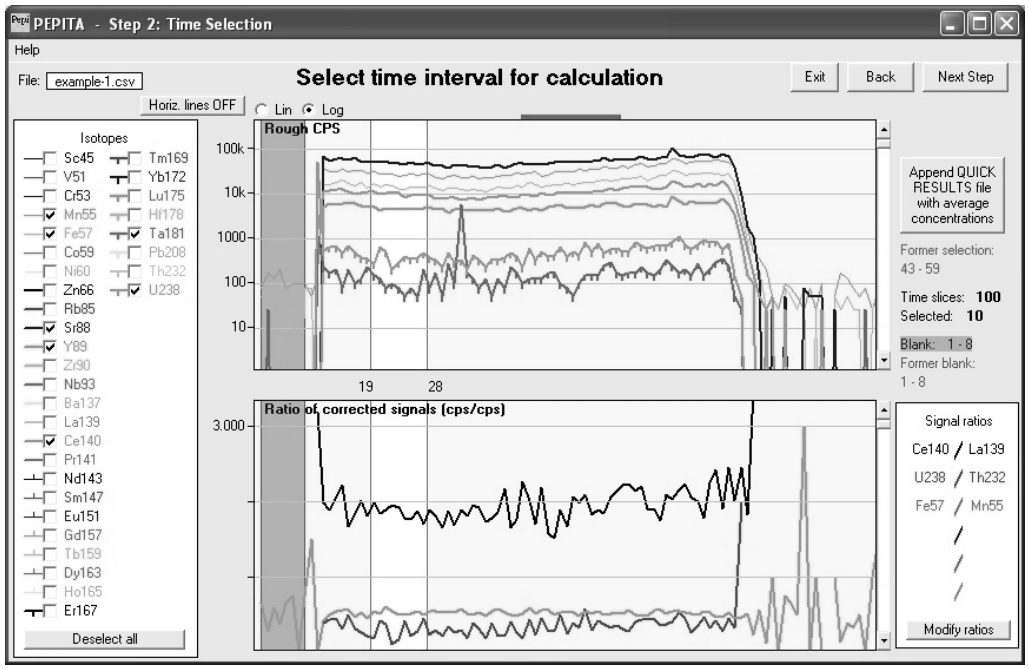


FIG. A7-4. The second step in data processing: selection of time interval for calculation of isotope ratios/concentrations (between 19 and 28 s in this example) and for blank (shown in initial interval in grey). The upper plot always shows the raw data, while the lower one can display (i) signal ratios (relative to a maximum of 3 internal standards), (ii) concentrations, calculated by internal standards or (iii) ratios of user-selected isotope pairs.

The file has a simple, tab-delimited table structure and can be opened by any spreadsheet calculating program.

***(2b) Press [Modify ratios].*** The user can select up to 6 pairs of analytes and plot their ratios. Click one of the analytes on the small field "Signal ratios" that appears in lower left of the window, and then replace it by another analyte by pulling it directly from the main list.

***(2c) Press [Plot ratios].*** These preferred isotope pairs are used throughout the program session unless changed, and can be stored in the Setting file anytime (by pressing [Modify settings / Save as]).

***(2d) Press [Next Step] on the second window.*** The third window (Fig. A7-5) presents the data in tabular form and shows the results of the outlier tests by means of colour coding. At top right corner of the window one of the four option buttons is used to determine what the table should display. It can present (i) the blank corrected cps values, (ii) their relative standard deviations, (iii) ratios of blank corrected cps values or (iv) the relative standard deviations thereof. In the table the internal standards are marked by light green background. By clicking an analyte in the left part of the window, a plot of its ratio to the internal standard element will appear in the window bottom. To the left of this plot, a very simple, robust homogeneity parameter occurs, showing the ratio of the first and the second signal halves. This allows quick inspection of the time-resolved trend of the isotope ratio curve and the identification of possible fractionation effects or sample inhomogeneity. The plot can also be useful for a rapid offline assessment of signal quality during instrument setup optimization.

Currently, three statistical tests are available for outlier analysis, based on: (i) minimum and maximum signals, (ii) the Grubbs test, indicating the probability that any given data point belongs to the remainder of the population, and (iii) the relative standard deviation of the signal. Rejection of outliers can be performed according to each of these tests automatically, or by manual user control. Once outlier rejection is done, the rejected cells will become grey. If a given time slice contains anomalous data, then it is rejected. Manual rejection (black background colour) can be performed simply by clicking the cells or column heads of the table. If necessary, rejection can be undone by clicking a cell, or by pressing [Reset All Rejection].

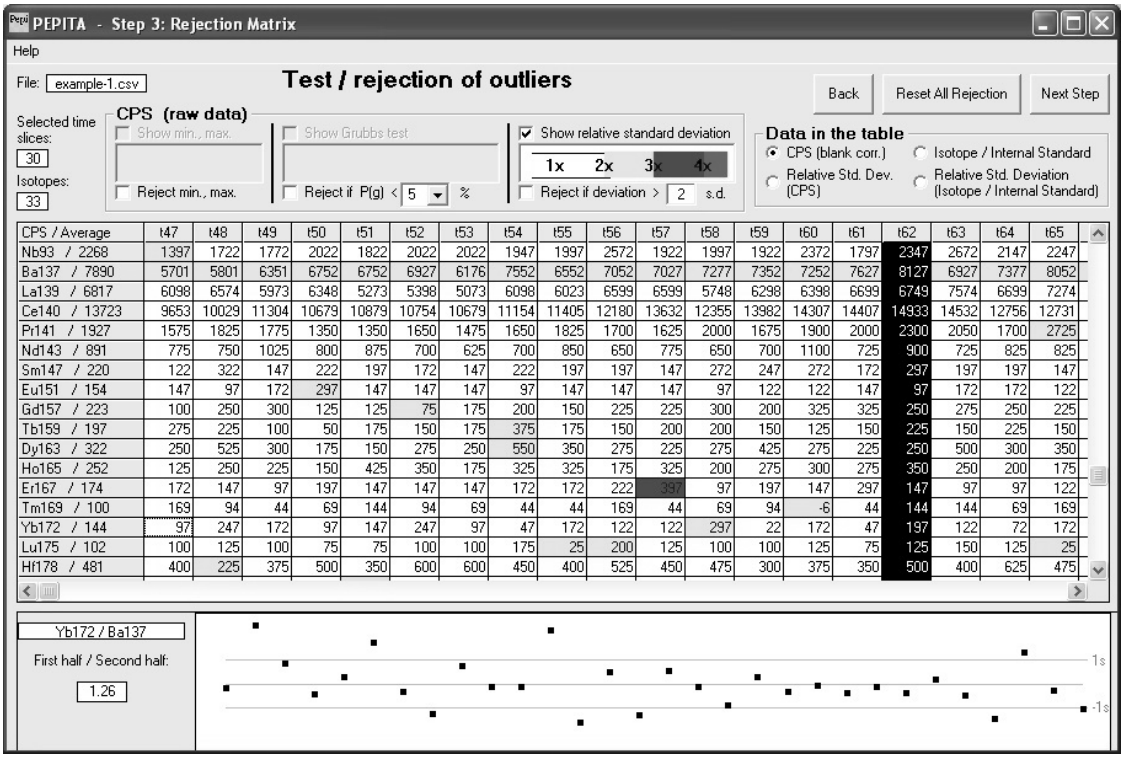


| CPS / Average | t47 | t48 | t49 | t50 | t51 | t52 | t53 | t54 | t55 | t56 | t57 | t58 | t59 | t60 | t61 | t62 | t63 | t64 | t65 |
|---|---|---|---|---|---|---|---|---|---|---|---|---|---|---|---|---|---|---|---|
| Nb93 / 2268 | 1397 | 1722 | 1772 | 2022 | 1822 | 2022 | 2022 | 1947 | 1997 | 2572 | 1922 | 1997 | 1922 | 2372 | 1797 | 2347 | 2672 | 2147 | 2247 |
| Ba137 / 7890 | 5701 | 5801 | 6351 | 6752 | 6752 | 6927 | 6176 | 7552 | 6552 | 7052 | 7027 | 7277 | 7352 | 7252 | 7627 | 8127 | 6927 | 7377 | 8052 |
| La139 / 6817 | 6098 | 6574 | 5973 | 6348 | 5273 | 5398 | 5073 | 6098 | 6023 | 6599 | 6599 | 5748 | 6298 | 6398 | 6699 | 6749 | 7574 | 6699 | 7274 |
| Ce140 / 13723 | 9653 | 10029 | 11304 | 10679 | 10879 | 10754 | 10679 | 11154 | 11405 | 12180 | 13632 | 12355 | 13982 | 14307 | 14407 | 14933 | 14532 | 12756 | 12731 |
| Pr141 / 1927 | 1575 | 1825 | 1775 | 1350 | 1350 | 1650 | 1475 | 1650 | 1825 | 1700 | 1625 | 2000 | 1675 | 1900 | 2000 | 2300 | 2050 | 1700 | 2725 |
| Nd143 / 891 | 775 | 750 | 1025 | 800 | 875 | 700 | 625 | 700 | 850 | 650 | 775 | 650 | 700 | 1100 | 725 | 900 | 725 | 825 | 825 |
| Sm147 / 220 | 122 | 322 | 147 | 222 | 197 | 172 | 147 | 222 | 197 | 197 | 147 | 272 | 247 | 272 | 172 | 297 | 197 | 197 | 147 |
| Eu151 / 154 | 147 | 97 | 172 | 297 | 147 | 147 | 147 | 97 | 147 | 147 | 147 | 97 | 122 | 122 | 147 | 97 | 172 | 172 | 122 |
| Gd157 / 223 | 100 | 250 | 300 | 125 | 125 | 75 | 175 | 200 | 150 | 225 | 225 | 300 | 200 | 325 | 325 | 250 | 275 | 250 | 225 |
| Tb159 / 197 | 275 | 225 | 100 | 50 | 175 | 150 | 175 | 375 | 175 | 150 | 200 | 200 | 150 | 125 | 150 | 225 | 150 | 225 | 150 |
| Dy163 / 322 | 250 | 525 | 300 | 175 | 150 | 275 | 250 | 550 | 350 | 275 | 225 | 275 | 425 | 275 | 225 | 250 | 500 | 300 | 350 |
| Ho165 / 252 | 125 | 250 | 225 | 150 | 425 | 350 | 175 | 325 | 325 | 175 | 325 | 200 | 275 | 300 | 275 | 350 | 250 | 200 | 175 |
| Er167 / 174 | 172 | 147 | 97 | 197 | 147 | 147 | 147 | 172 | 172 | 222 | 397 | 97 | 197 | 147 | 297 | 147 | 97 | 97 | 122 |
| Tm169 / 100 | 169 | 94 | 44 | 69 | 144 | 94 | 69 | 44 | 44 | 169 | 44 | 69 | 94 | -6 | 44 | 144 | 144 | 69 | 169 |
| Yb172 / 144 | 97 | 247 | 172 | 97 | 147 | 247 | 97 | 47 | 172 | 122 | 122 | 297 | 22 | 172 | 47 | 197 | 122 | 72 | 172 |
| Lu175 / 102 | 100 | 125 | 100 | 75 | 75 | 100 | 100 | 175 | 25 | 200 | 125 | 100 | 100 | 125 | 75 | 125 | 150 | 125 | 25 |
| Hf178 / 481 | 400 | 225 | 375 | 500 | 350 | 600 | 600 | 450 | 400 | 525 | 450 | 475 | 300 | 375 | 350 | 500 | 400 | 625 | 475 |

FIG. A7-5. The third step in data processing: visualization of extreme and suspicious data. Statistical parameters are calculated for every analyte considering all data from the selected time slices. Minimum and maximum values, the result of the Grubbs test, and the standard deviation can be marked by different colours. See text for further discussion.

***(3) Press [Next Step] on the third window***

In the Output Window the detailed results can be: (i) viewed in a simple table, (ii) saved into a file, (iii) copied to the clipboard, or (iv) the average concentrations and their standard errors can be written into the QUICK RESULTS file.

***(4a) Press [Show results] to see the structure of the full output***

The output files (Fig. A7-6) are Tab-delimited ASCII files and consist of four parts:

(i) Measurement conditions, including the analysis date, file names, internal standards and their concentrations, time slice selection, blank selection and rejections. A warning message will appear in case of incompatible file contents (*e.g.*, Pepita will not be able to calculate all expected results, if one or more isotopes are missing from the Standard Composition File or from the Standard Measurement File, *etc*.).

(ii) Average concentrations and statistical parameters for the isotopes including the median, mean concentration, standard deviation, standard error, limit of detection, relative error, average (blank corrected) signal counts, blank counts, time slices used.

(iii) Concentrations recorded by the time slices (in ppm).

(iv) Errors for the concentration measurements (in ppm).

***(4b) Press [Save as] to display the output file naming convention***

The output is saved into a file, with the file name containing the name of the input data file, the time slice intervals used, and the rejection method applied. An example of an output file name is **DataFileName_G5_t15_t22.txt** (G5 = Grubbs test applied to reject individual data less than 5% probability and time slices between 15 and 22 were considered). These output file names are generated automatically (user can modify them before saving). Hence, a data file from different processing cycles will result in output files of different names. After saving the results, there are several options to proceed (listed under "New Process"):

(i) the same data file can be re-processed by selecting another time interval or by

(ii) applying other rejection criterion, etc., or

(iii) another data file can be opened and processed using the same conditions as for the previous data file.

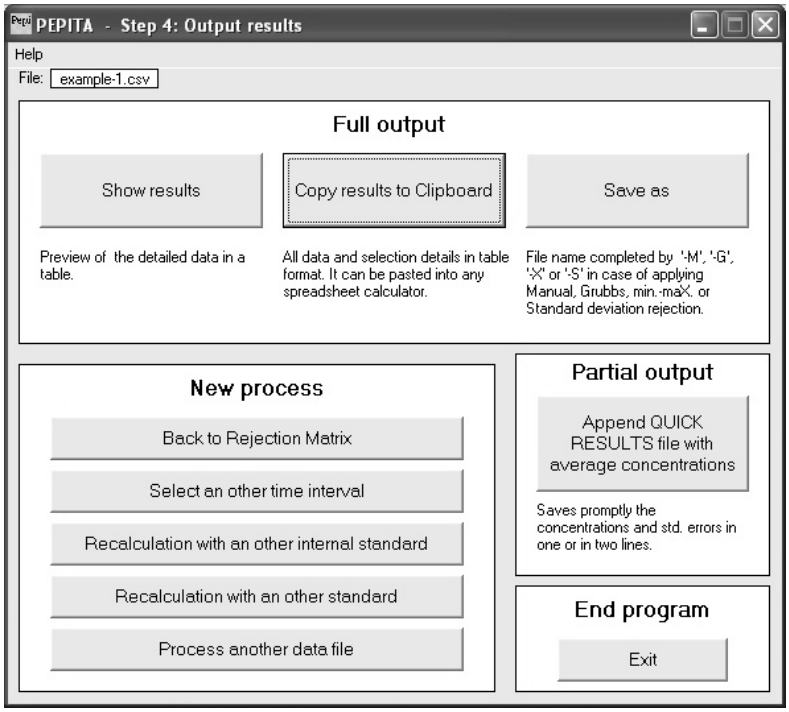


FIG. A7-6. The fourth step in data processing offers various options to save results and perform re-processing data files using different parameters.

**Creation of a standard measurement file and performing the concentration calculation for an unknown**

The routine usage of Pepita can be demonstrated by an example of the cross-evaluation of two NBS 610 data files supplied in the Pepita-StartKit directory. (i) Open the data file '**example-16-nbs610.xl**' (as a measurement of a standard reference material) and select the option 'Creating a Standard Measurement File', then process and save as a .stm file. (ii) Open '**example-17-nbs610.xl**' (as a data file of an unknown material), open the previously created '**example-16-nbs610_tXX-tXX.stm**' standard measurement file, set Ba, 429 ± 29 ppm as internal standard element (concentration in NBS 610), process and paste the results on the clipboard. The average concentrations can be compared with the recommended values of the reference material (see the content of **nbs-610.stc** standard composition file opened into Excel or another program).

**Customizing the input of Pepita for the format of user-defined data files**

After a proper study of the functions, the user can define input filter(s) for their own data files. Study the menu item "Set import for the format of the data files". This setting must be changed only at the beginning of a session with Pepita. We do not recommend changing the default setting before studying all functions of Pepita with the example files.

**REFERENCES**

BARNET, V. & LEWIS, T. (1994): *Outliers in Statistical Data*, 3rd ed.. John Wiley & Sons, Chichester, 584 p.

LONGERICH, H.P., JACKSON, S.E. & GÜNTHER, D. (1996): Laser ablation inductively coupled plasma mass spectrometric transient signal data acquisition and analyte concentration calculation. *J. Analyt. Atom. Spectrom.* **11**, 899-904.

# APPENDIX A8: LASER ABLATION DATA REDUCTION SOFTWARE FOR CONCENTRATION MEASUREMENTS – LARS-C

Antje Gebel
Institut für Endlagerforschung
TU Clausthal, Adolph-Roemer Str. 2A
Germany
E-mail: antje.gebel@tu-clausthal.de

## INTRODUCTION

The laboratory for Laser Ablation Inductively Coupled Plasma – Mass Spectrometry at the Institut für Mineralogie und mineralische Rohstoffe (IMMR) was established in 1996. Various methods for geochemical tasks, *e.g.* lead isotopes in Roman silver coins, trace element and U/Th-Pb analysis on single minerals, bulk rock analysis of $Li_2B_4O_7$ glass beads (Gebel 2000) as well as fluid inclusions in salt minerals (Ellendorf 1999) have been developed in the laboratory.

Data reduction of time-resolved laser ablation signals (Longerich *et al.*1996) was done manually with Microsoft Excel for Windows 95 because no commercial software was then available. This time-consuming process was automated step by step using the macro language Excel-VBA. Excel-VBA combines a powerful calculation program with a modern object-orientated programming language, which is relatively easy to learn. To improve speed, two Dynamic Link Libraries (DLLs) were programmed in Delphi 3: LADaten.dll, which converts raw data from the ICP–MS (Perkin Elmer ELAN 6000) to Excel; and LAPlot.dll, which is used to define the intervals of background and signal in the time-resolved spectra. The complete program, Lars-C, features multiple standardization, use of internal standards and visualization of transient signals. The results are output in an Excel workbook with cell references. Thus, various parameters, *e.g.*, concentration of internal standard, can be changed without running Lars-C again. This flexibility is the main advantage of this software.

Lars-C is freeware and available at http://www.immr.tu-clausthal.de/geoch/labs/icp-ms/lam.shtml.

## USING THE PROGRAM

For each measurement the user has to specify the internal standard, the calibration standard(s), type of measurement (sample or calibration standard) and concentration of the internal standard element. These settings can be changed easily in the resulting Excel workbook, which is very helpful in developing new methods. If two or more calibration standards are selected, calibration curves are calculated. The correlation coefficients can be used to check their quality. A list of all measured elements and known calibration standards is offered to the user by pull down menus. Calibration standards are administrated via an Excel worksheet and can be configured by the user.

The time resolved spectrum is used to define background and signal regions for each measurement (Fig. A8-1). The program finds the beginning of the ablation signal by calculating the largest difference between two data points of each measured element. The start position for most analyte elements minus 5 replicates is used as the end of the background whereas the same position plus 5 replicates is used for the beginning of the signal. The positions are marked on the x-axis of the diagram by vertical lines. The user can accept these settings or change them with the arrow buttons. Smooth signals are well recognized by the software but problems can arise from rapidly increasing intensities ("signal spikes") during ablation, produced by inclusions *etc*. In order to make minor irregularities visible, the y-axis can be varied from raw signal intensity to normalized data, and from linear to logarithmic scales. The selected settings are saved in the resulting Excel workbook for each measurement. Even after finishing the program, the user has the opportunity to change these settings by starting the dialog box from a worksheet in the resulting Excel workbook. A diagram with the respective measurement and the saved settings is shown and after changing them the results are recalculated immediately.

Mineralogical Association of Canada Short Course 40, Vancouver, B.C., p. 341–342

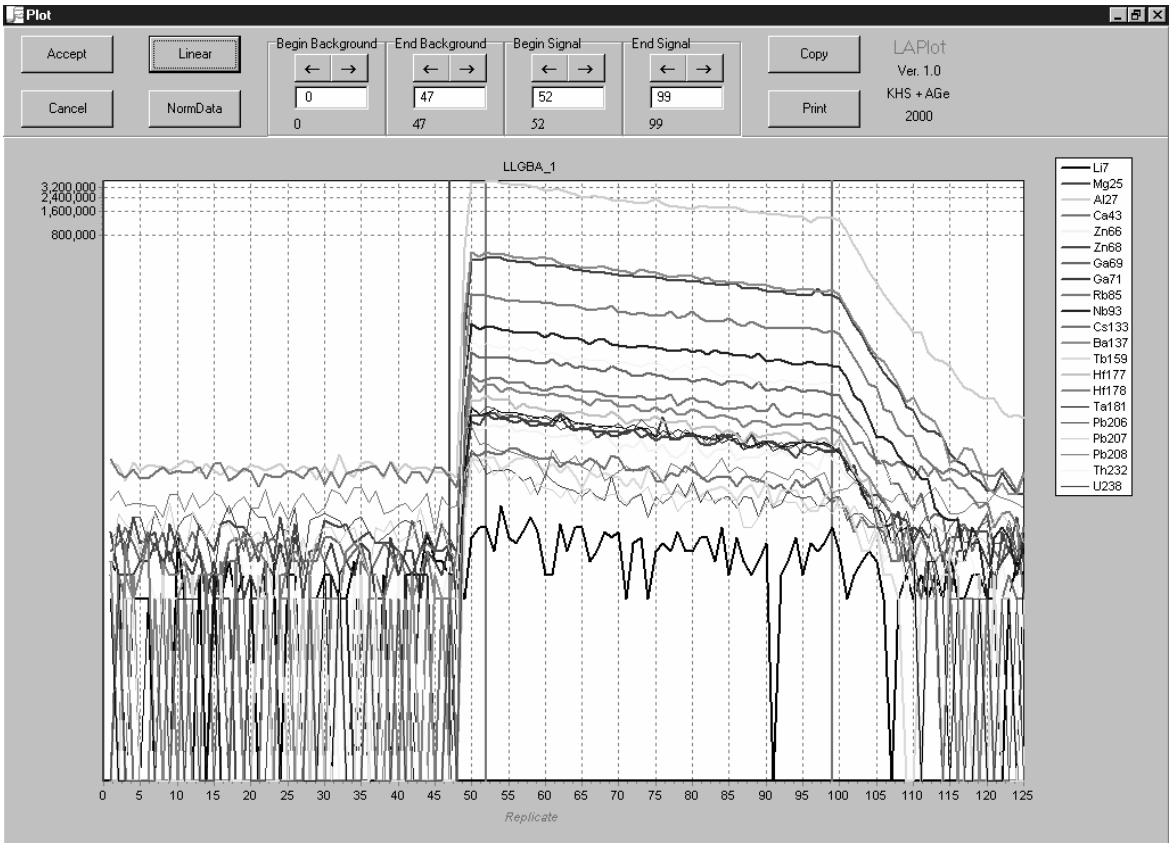


FIG. A8-1: Time resolved signal showing intensities of various analyte elements in an in-house standard glass (LLGBA) in logarithmic scale. Start and end of the background region (replicates 0–47) and of the ablation signal interval (replicates 52–99) are marked on the x-axis by vertical lines.

## SUMMARY

Lars-C is written in Excel-VBA (for Windows 95) and Delphi 3 and runs only under Windows systems. Input files are restricted to the ELAN 6000 *.xl format, but other formats could be easily implemented via another DLL or a short VBA-macro. The software supports data reduction for element concentrations in various materials using time resolved signals, internal standardization and multiple calibration standardization. The resulting Excel-workbook can be changed to the users needs and allows changing data settings easily. Thus, the software is very flexible for users interested in method development, and for users who prefer to work with Excel.

## REFERENCES

ELLENDORF, B. (1999): *Geochemische Untersuchungen an einzelnen Fluid Inclusions in Zechsteinevaporiten mittels Laser-Ramanspektrometrie, Ionenchromatographie und Laser-Ablation-ICP-Massenspektrometrie*. Dissertation, Clausthal-Zellerfeld.

GEBEL, A. (2000): *Einsatz der Laserablation-ICP-MS-Analytik für geochemische Fragestellungen*. Dissertation, Papierflieger, Clausthal-Zellerfeld, http://www.immr.tu-clausthal.de/~mrag/pub/doktor/gebeldr.pdf

LONGERICH, H.P.; JACKSON, S.E.; GÜNTHER, D. (1996): Laser ablation inductively coupled plasma mass spectrometric transient signal data aquisition and analyte concentration calculation. *J. Analyt. Atom. Spectrom.* **11**, 899-904.

# CHAPTER A9: IOLITE: SOFTWARE FOR SPATIALLY RESOLVED LA–(QUAD and MC)–ICP–MS ANALYSIS

John Hellstrom, Chad Paton, Jon Woodhead, Janet Hergt
Isotope and Trace Element Geochemistry Group
School of Earth Sciences, The University of Melbourne
Victoria 3010, Australia
E-mail: jdwood@unimelb.edu.au

## INTRODUCTION

Laser ablation ICP–MS is a uniquely powerful technique for the spatially resolved analysis of geological materials (*e.g.*, Sinclair *et al.* 1998, Treble *et al.* 2005, Desmarchelier *et al.* 2006, Woodhead *et al.* 2007), but has been hindered in this application by the absence of suitably flexible tools for data processing and visualization. Here we describe and release Iolite, our in-house application which has been purpose-developed for spatially resolved LA–ICP–MS. Iolite is implemented as a self-contained package for Igor Pro, a scientific data processing and graphing application by Wavemetrics Inc. of Lake Oswego, Oregon, USA.

LA–ICP–MS is characterized by the ability to acquire very large bodies of data rapidly. The requirement that parameters such as baseline intensities and elemental fractionation factors must be considered for every spot analysis over the course of a day, with reference to standard analyses commonly located within other files, can lead to an overwhelming data-processing burden, often taking far longer than actual data acquisition to complete. The Iolite application grew out of the realization that simultaneous visualization and processing of an entire session's data could not only reduce the data processing burden, but would also greatly improve the consistency and reliability of that data processing. This is particularly true with reference to interpolation of quantities such as baseline intensities and mass or elemental fractionation factors.

The critical distinguishing feature of Iolite is its universal application to both quadrupole (Q)– and multicollector (MC)–ICP–MS data, and the consistent visual display *versus* time of all available raw and processed data over the course of an entire analytical session (regardless of the number of individual time-resolved files involved).

Data processing algorithms are entirely user-defined and can be of any level of complexity, meaning the user has complete control over how the output parameters are calculated. Once time-resolved data processing has been completed, the data can be visualized or exported in a number of ways including as 2- or 3-dimensional spatially resolved data.

Iolite is built around an internal data format in which every imported time-resolved channel (be it a mass or element recorded by a single collector instrument, or a mass collector pair from a multi-collector) is stored as an x,y series *versus* its own absolute date-time. This is a flexible approach as it makes no assumptions about the nature of any stored data except that they are time series, allowing for instance the combination of data sets containing different numbers of measured masses over the course of one or more days, or of simultaneously acquired data where more than one instrument is coupled to a single laser. All available metadata are also collected from the time-resolved source files during data import and are preserved through to data export where they are included with the output data.

The visualization of composite time series covering as long as several days of instrument time allows insight into the best means of interpolating baselines and other quantities, and gives visual verification of the effectiveness of the chosen strategy. Data processing is undertaken after resampling all required data channels (including interpolated baselines and other quantities) onto a single time scale and in all cases considers the entire session's data simultaneously.

Figure A9-1 shows Iolite's main user interface window, containing two and a half hours' data from a Q–ICP–MS and one hour's data from a MC–ICP–MS coupled to the same laser. This amounts to ~35,000 data points on screen and represents a relatively small data set for Iolite, which has been tested with multi-day data sets in excess of 500,000 points in size. Also shown are selected time intervals of baseline, with an uncertainty-weighted baseline spline for the element (arrowed at A) that will be used in subsequent reduction of the data set.

Mineralogical Association of Canada Short Course 40, Vancouver, B.C., p. 343–348.

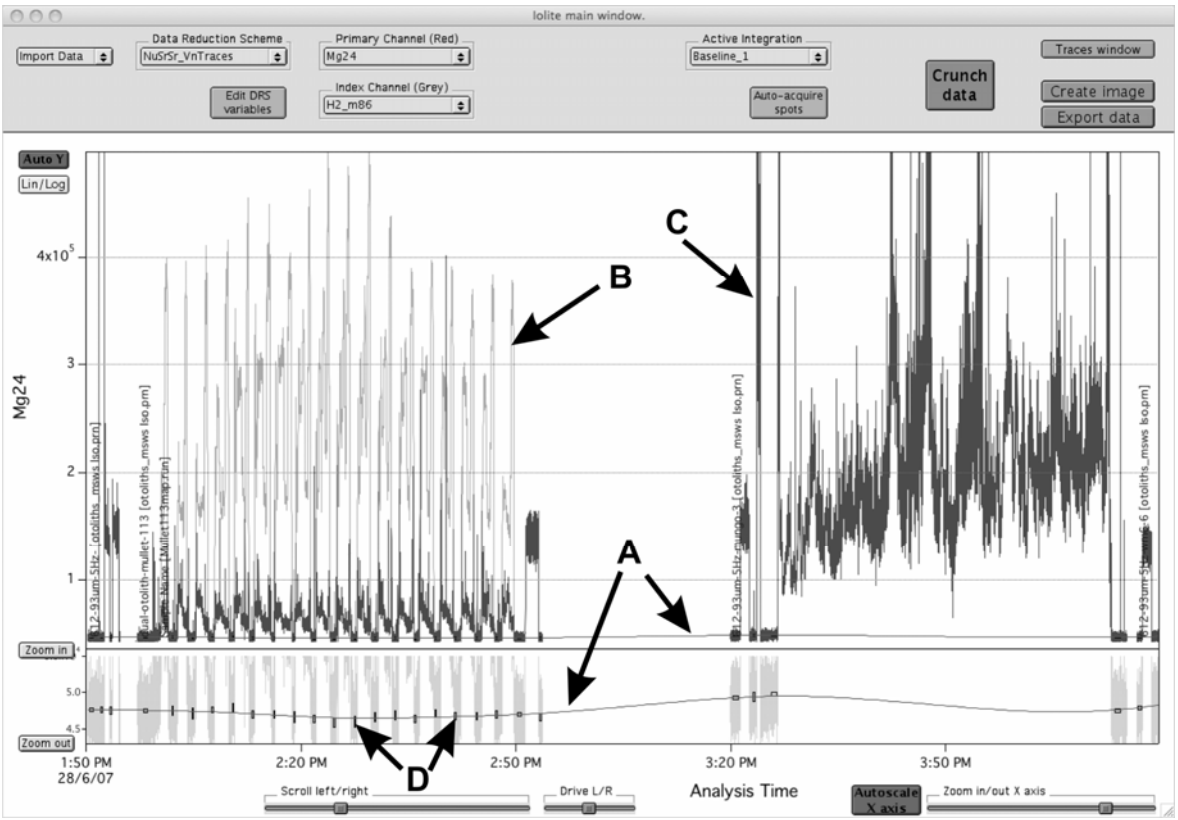


FIG. A9-1. The main Iolite overview window, displaying two raw channels vs time. In this instance one of the channels displayed (Mass 86[V] in collector H2, **B**) is loaded from a multi-collector instrument and the other ($^{24}$Mg[CPS], **C**) from a single-collector instrument connected to the same laser and acquired over the same time period. The lower panel shows a zoom view of the baseline region in which only $^{24}$Mg is evident (the baseline for Mass 86 is not apparent at this scale). User-selected baseline integrations for the selected primary channel ($^{24}$Mg[CPS]) are shown as black boxes (**D**, where height is dependent on the standard error of the enclosed baseline data) and the uncertainty-weighted spline curve through them (**A**) is the interpolated baseline, those for all other channels being calculated in the same way). This particular data reduction scheme has been written to produce simultaneous Sr isotope ratio and trace element concentration data from calcium carbonate samples, in this instance used to compare isotopic and elemental images of the surface of an otolith. After 3:00 PM in the data set only single-collector data have been recorded, in this instance to produce an elemental line profile. Both otolith traverses are bracketed by analyses of the NIST 612 glass, which are visible as short integrations with ~150,000 CPS of $^{24}$Mg. Fractionation factors determined from these may be interpolated in a similar manner to the baselines.

## FLEXIBLE DATA REDUCTION MODULES

Iolite was designed for a mixed research environment featuring both Q– and MC–ICP–MS, such that new techniques and data reduction algorithms could be added as required into the future with as few constraints as possible. All data reduction is handled by plug-in data reduction schemes (DRS) which can be created or edited by end users of the software and are by design essentially unconstrained in their capability. The Igor Pro macro language is relatively easy to follow, and several well annotated DRS templates are provided. This means that new users are soon able to customize any of the various built-in DRSs where required for their own purposes.

The first task of a DRS is to specify which data channels if any are required to be loaded into memory to operate, *i.e.*, MC–ICP–MS techniques such as *in situ* Hf or Sr isotope analysis require specific combinations of mass collector pairs, whereas a generalized elemental procedure may be able to operate on any available mass channels from a single collector instrument. A DRS generally also specifies the requirement of an interpolated baseline for each available channel, which is automatically created after the user has defined one or more time intervals as baseline integrations. Similarly, a DRS also commonly requires user input to define integration windows locating analyses of one or more specific standards over the course of a session.

Once all required data channels are available a DRS proceeds by interpolating the required channels onto a common timescale (although redundant in many cases, this allows for the processing of complex data sets, *e.g.*, Figure A9-1). From this point any desired data processing may be undertaken, usually beginning with the subtraction of interpolated baselines from some or all channels. Output time series as created and defined by a DRS are available for visualization, plotted against as many as twelve other data series at any one time. These may include raw input data, intermediate series used by the DRS during processing, or finalized output values (Figs. A9-2a and 2b). The ability to view intermediate and output channels *versus* time is particularly useful when viewing ratios (*e.g.*, U–Pb, where the effectiveness of down-hole fractionation correction for each spot analysis can be viewed with ease). Data processing can be iterative, in that baseline or standard integrations can be added or redefined and the DRS re-run, or indeed more than one DRS can be run on a given data set to compare the effect of different data reduction algorithms.

Data reduction schemes can call on many of Iolite's built-in functions, which include routines for masking output time series to include only those intervals in which a selected ion beam is over a given intensity threshold, or automatically generating a time series showing seconds since ablation last began (as required by down-hole fractionation correction schemes).

## DATA VISUALIZATION AND EXPORT

Once data reduction is complete, all output parameters are held in memory as time series on a common time scale, covering an entire analytical session at the sampling frequency of the original ICP–MS data (*i.e.*, usually at greater than 1 Hz). Data may then be visualized and exported in three ways, each considered below.

Data are commonly usefully exported as the mean values of individual integration intervals, for instance as required for discrete spot analyses. The

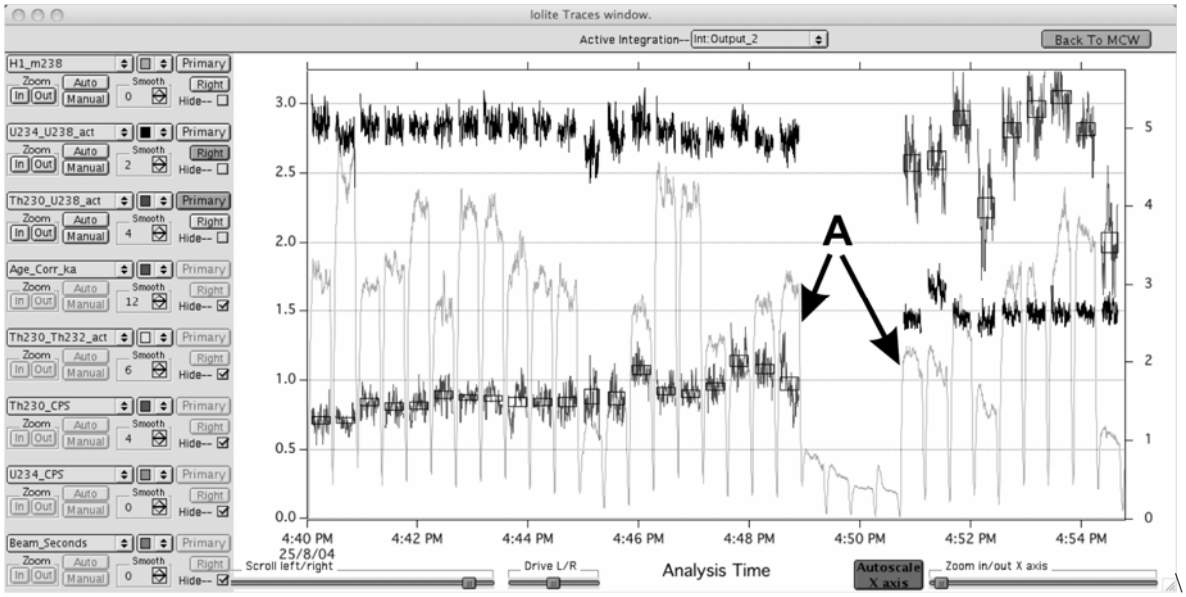


FIG. A9-2a. Iolite's secondary time-resolved window shown here is used to provide a more detailed picture, with as many as twelve different parameters simultaneously displayed *versus* time. All raw input channels and all output parameters are available for display, as well as any intermediate channels created by the currently active data reduction scheme. In this example 15 minutes from a multi-day MC–ICP–MS U–Th data set are shown, being a series of discrete spot analyses traversing a sample of high-uranium calcite. Of the three time series visible, two have been automatically masked to only appear where the primary channel ($^{238}$U in this case, shown in grey, **A**) is above a user-specified voltage threshold. All displayed time series have independent Y axes and can be adjusted individually by the user, although scales are only displayed for two of them (the traces designated "Primary" and "Right"). Any trace can be smoothed as required for display purposes only, leaving the time series itself unaltered (if smoothing of the actual time series is desired, this can be implemented within the DRS). Square boxes indicate time intervals of the currently selected integration type (in this case an output), and their values for the current Primary trace (box size corresponds to a 2s.e. uncertainty). These time intervals can be created, edited or deleted using a simple on-screen interface.

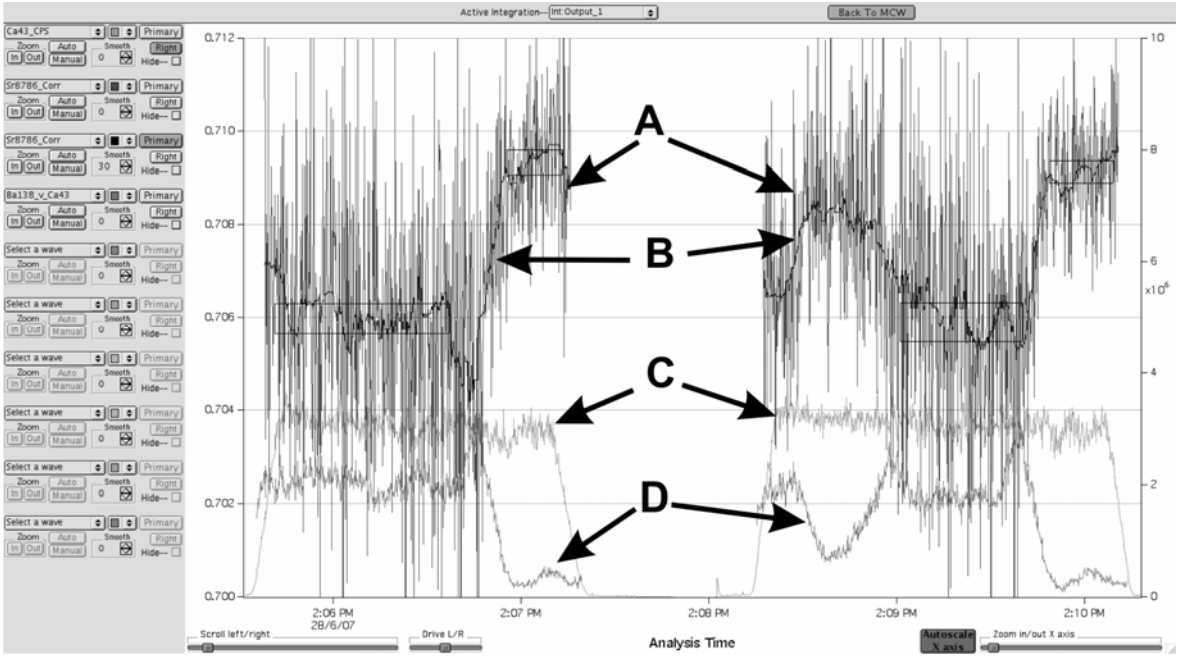


FIG. A9-2b. An additional example in this case showing 2 separate laser traverses conducted across a fish otolith, using simultaneous acquisition of Sr isotope data from the Nu Plasma MC–ICP–MS and trace element abundances from the Varian ICP–MS. The calculated Sr-isotope ratio is shown in dark grey (**A**), together with a user-defined degree of smoothing shown in black (**B**). Additional time series for Ca CPS (grey, **C**) and Ba content, normalized to Ca internal standard (grey, **D**) are also shown for reference. Black boxes indicate regions of interest that have been selected for output (with the height of the box representing the mean and 2σ of the integrated region. These boxes automatically re-calculate as the integration boundaries are edited.

user is able to define each spot interval by dragging the mouse in either of Iolite's two time series windows (Figs. A9-1 and A9-2), or the software can attempt to locate spot analyses automatically by searching the time series data for laser-on and laser-off events. In either case, the user is able to add, modify or delete individual integrations at any stage via the graphical interface. The mean and standard error for each defined integration are then calculated for all output parameters and exported to disc as delimited text, together with the start time, sequence number and original file and/or sample name of each spot analysis.

Iolite's primary design intention is for the processing and display of spatially resolved LA–ICP–MS data, the simplest form of which is linear scanning. Temporally resolved data are transformed to spatially resolved results using the known scan rate, or drill rate, for depth profiling (Woodhead *et al.* 2004). In some cases time series data are resampled to achieve constant distance spacing, as single collector ICP–MS data are not always obtained at a constant sample rate (individual time slices can vary in length according to per-scan changes in detector mode). The output linear scan data may then be filtered and down-sampled for display and export. As well as using the many display, print and graphical export options built into Igor Pro, scan data can be output as delimited text for display and manipulation in other software packages.

Two-dimensional imaging is the most evolved and most automated of Iolite's data visualization modes. Image data are expected to comprise four or more parallel linear scans, each of the same length and duration. An image can be created by selecting any such block of data and triggering an algorithm that automatically determines the number of scan rows, their start time, duration and time offset. All selected data are then resampled to constant time spacing, filtered and down-sampled. Individual scan-lines identified by the algorithm are then reassembled as a two-dimensional array for each output channel of the DRS. All such arrays are then displayed onscreen as thumbnail images, along with an interface for constructing composite three-dimensional displays (Fig. A9-3). A manual mode exists to give more control over image construction, for instance, to change the degree of filtering and down-sampling, to build an image from more than

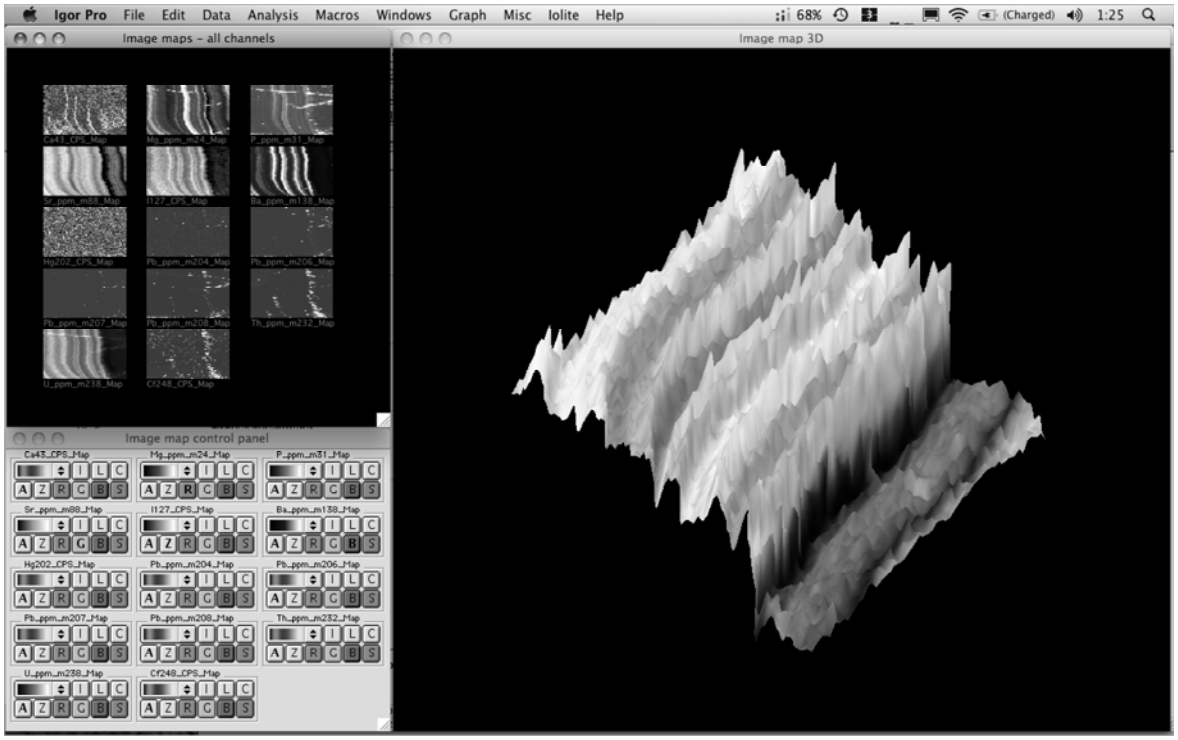


FIG. A9-3. Part of Iolite's two-dimensional imaging interface, showing thumbnail images of each available output channel of the currently selected data reduction scheme for a speleothem calcite sample. The three dimensional image is modified using the control panel at lower left, and can be either a red-green-blue composite of separate output channels, or an indexed colour map using any of Igor Pro's 58 built-in colour scales. The Z axis can be set independently, allowing 3-D visualization of between one and four output channels at one time. In this example, elemental abundances have been calculated using an external standard via normalization to calcium. The 3-D plot is a combination of magnesium, barium, strontium (originally colored red, green and blue, respectively) and iodine (Z axis). See Plate 4 for colored version.

one discrete block of scan lines, or for rare cases where the automatic mode fails to determine the required variables for an image. Once constructed and edited, images can be exported as formatted 2- or 3-dimensional image plots (*e.g.*, Woodhead *et al.* 2007, 2008), or as two-dimensional plain text data arrays for each output channel.

## STANDARDS

An unlimited number of standard materials can be defined within Iolite by any user via a simple delimited text format. Each text file contains the name of a standard and some other basic information including its matrix and source citation, followed by rows containing parameters (*e.g.*, "Ca", "87Sr/86Sr", "[234U/238U]", *etc.*), their values, and optionally their units and/or uncertainties. All standards so defined are available to any data reduction scheme through simple function calls, allowing a DRS to require analyses of either a specific standard or any standard for which a specific parameter is defined.

## COMPATIBILITY AND AVAILABILITY

The Iolite package is freely available from http://www.earthsci.unimelb.edu.au/isotope/iolite. Although the underlying source code is not released, the plug-in data reduction modules are open source by design and form the environment where all user-defined time-resolved data processing takes place.

Data may be imported from any ICP–MS for which a time-resolved import module has been written, provided the instrument's export data format includes enough information to calculate the absolute time of each time slice of data stored within the file. At the time of writing, import modules exist for Varian 810 and Nu Plasma mass spectrometers, with modules for other instruments in development.

Iolite's host environment, Igor Pro, runs natively on recent versions of both Apple Mac OS X and Microsoft Windows. Igor Pro was chosen for its smooth handling of data sets containing tens of independent channels at hundreds of thousands of points each, its high level compiled macro language and its extensive 2- and 3-dimensional data visualization capabilities. Igor Pro is available from www.wavemetrics.com as a fully functional 30-day trial version, after which time it will revert to a limited functionality demonstration version until registered.

Data within the Iolite package can be saved to disk as Igor Pro "Packed Experiment" files which contain all time series and other data in memory plus all open graphs, control panels and spreadsheets and a detailed data processing history. These can be reopened for further processing or data export at any time.

## DEVELOPMENT

Iolite was developed from an original concept by John Hellstrom, under a Hermon Slade Foundation Grant to Janet Hergt and Jon Woodhead. Ongoing development is by John Hellstrom, Chad Paton and Jon Woodhead with the assistance and input of members of the Isotope and Trace Element Geochemistry Group, The University of Melbourne.

## REFERENCES

DESMARCHELIER, J., HELLSTROM, J. & MCCULLOCH, M. (2006): Rapid trace element analysis of speleothems by ELA–ICP–MS. *Chem. Geol.* **231,** 102-117.

SINCLAIR, D. J., KINSLEY L. P. J. & MCCULLOCH M. T. (1998): High resolution analysis of trace elements in corals by laser-ablation ICP–MS. *Geochim. Cosmochim. Acta* **62**, 1889-1901.

TREBLE, P.C., CHAPPELL, J. & SHELLEY, J.M.G. (2005): Complex speleothem growth processes revealed by trace element mapping and scanning electron microscopy of annual layers. *Geochim. Cosmochim. Acta* **69**, 4855-4863.

WOODHEAD, J., HERGT, J., SHELLEY, M., EGGINS, S. & KEMP, R. (2004): Zircon Hf-isotope analysis with an excimer laser, depth profiling, ablation of complex geometries, and concomitant age estimation. *Chem. Geol.* **209***,* 121-135.

WOODHEAD, J., HELLSTROM, J., HERGT, J., GREIG, A. & MAAS, R (2007): Isotopic and elemental imaging of geological materials by laser ablation Inductively Coupled Plasma mass spectrometry. *J. Geostandards & Geoanalyt. Res.* **31**, 331-343.

WOODHEAD, J., HELLSTROM, J., PATON, C., HERGT, J., GREIG, A. & MAAS, R. (2008): A guide to depth profiling and imaging applications of LA–ICP–MS. *In* Laser Ablation ICP–MS in the Earth Sciences: Current Practices and Outstanding Issues (P. Sylvester, *ed*.). *Mineral. Assoc. Can. Short Course Series* **40**, 135-145.